A JOURNEY TOWARDS EFFICIENT MOLECULAR WOCS: FROM MONONUCLEAR TO POLYNUCLEAR COMPLEXES

Md Asmaul Hoque

UNIVERSITAT ROVIRA i VIRGILI

A Journey towards Efficient Molecular WOCs:
From Mononuclear to Polynuclear Complexes

Md Asmaul Hoque

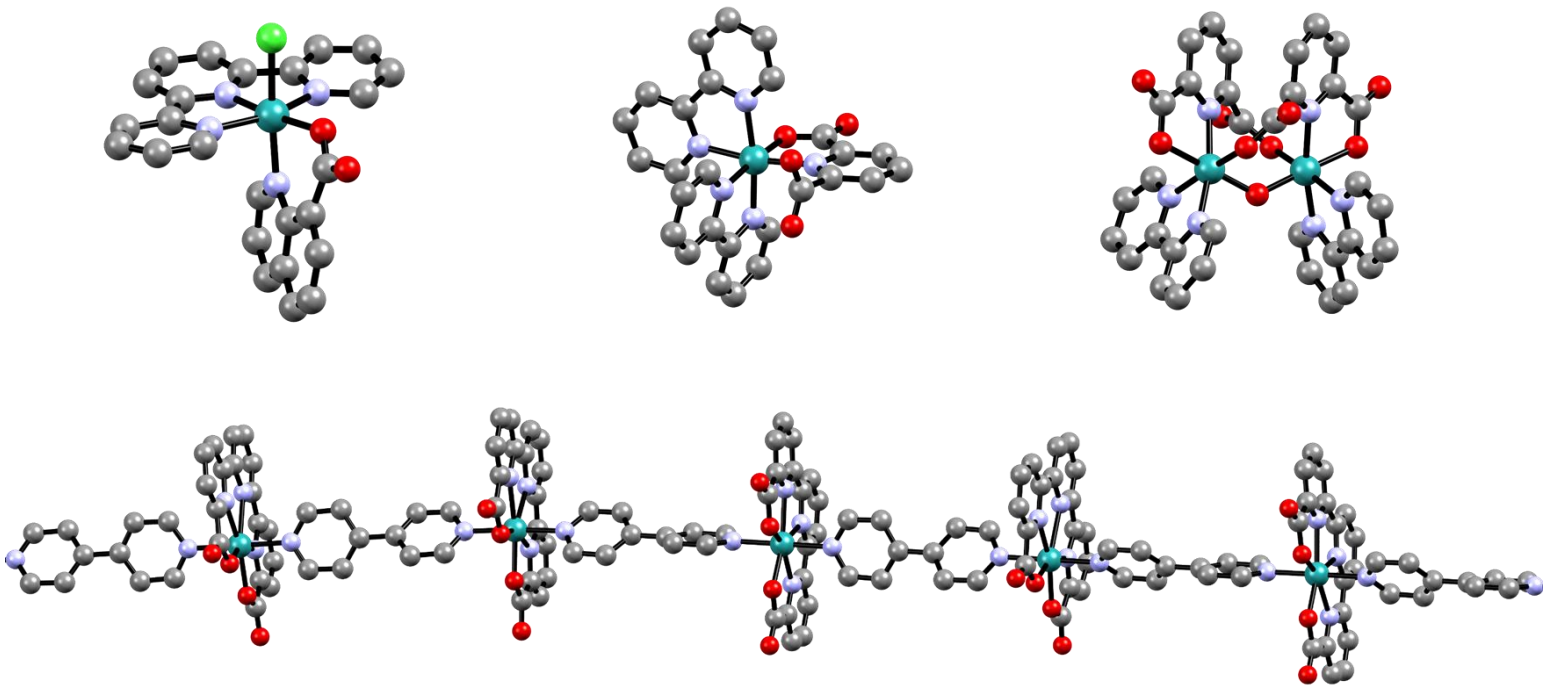

DOCTORAL THESIS
2019

UNIVERSITAT ROVIRA I VIRGILI
A JOURNEY TOWARDS EFFICIENT MOLECULAR WOCS: FROM MONONUCLEAR TO POLYNUCLEAR COMPLEXES
Md Asmaul Hoque

Md Asmaul Hoque

A Journey towards Efficient Molecular WOCs:
From Mononuclear to Polynuclear Complexes

DOCTORAL THESIS

Supervised by

Prof. Antoni Llobet

&

Dr. Carolina Gimbert-Suriñach

Institute of Chemical Research of Catalonia

Tarragona

2019

UNIVERSITAT ROVIRA I VIRGILI
A JOURNEY TOWARDS EFFICIENT MOLECULAR WOCS: FROM MONONUCLEAR TO POLYNUCLEAR COMPLEXES
Md Asmaul Hoque

ICIQ-Institut Català d'Investigació Química

Avgda, Països Catalans, 16,

43007 Tarragona (Spain)

We *STATE* that the present study, entitled "*A Journey towards Efficient Molecular WOCs: From Mononuclear to Polynuclear Complexes*", presented by Md Asmaul Hoque for the award of the degree of Doctor, has been carried out under our supervision at the group of Antoni Llobet in the Institute of Chemical Research of Catalonia and that it fulfills all the requirements to be eligible for the International Doctor Distinction.

Tarragona, 4th June, 2019

Doctoral Thesis Supervisors

Prof. Antoni Llobet

Group leader

Dr. Carolina Gimbert-Suriñach

Scientific Coordinator

Institute of Chemical Research of Catalonia

Acknowledgements

Undertaking this PhD has been one of the most exciting and challenging experiences of my life. It would not have been possible without the support, encouragement and guidance that I have received from the amazing people around me.

First, I would like to express my utmost and sincere gratitude to my supervisors Prof. Antoni Llobet and Dr. Carolina Gimbert-Suriñach for providing me the opportunity to join their outstanding research group. I would like to thank them for their endless positive and enthusiastic attitude, immense support, encouragement, kind advices and valuable suggestions throughout my studies. Without their guidance and constant feedback, this work would not have been possible. I would like to thank Mª Jose for all the administrative support that I have come across during my stay in Tarragona.

I thank all the group members during the journey from the beginning Lorenzo, Sam, Serena, Roc, Pablo, Sergi, CJ, Abi, Prima, Laura, Navid, Andrew, Ludo, Marcos, JanH, JanO, Yuanyuan, Dooshaye, Tingting and Martina. A Special thanks to Nataliia for being a friend inside and outside the lab, helping, and encouraging me during the tough time. I thank Marta for constant positive support and helping me with some administrative works. Outside the lab I would like to thank Jordi Bennet for providing mental support and being so friendly during my stay in Tarragona. I thank Lucas, Alicia, Aurelian and Hélène for being friend and spending some quality time. A very big thanks to all of you for the enormous support you have given me during my difficult situations. The help from the research support area during this study are highy acknowledged specially NMR, crystallography, ChromTae, RMN, Chem Reactions, Fernando, X-ray, compres, logística and manteniment units. Without these instrumental supports, this work would not be possible.

I would like to acknowledge Prof. Surendranath Yogesh from the Massachusetts Institute of Technology (MIT) in USA for giving me the opportunity to work in his esteemed research group. I thank all the group people there for helping me in the lab whenever necessary. Thanks to Mike for the constant support and nice discussions inside and outside the lab and helping me to understand the chemistry occurring in there.

I love to thank my desi friends in Spain and Europe. My thanks will start with Bala, who help me from the beginning and made me feel as my guardian outside my home. I would like to thank Suvada, Venkat, Rohit, Tarun, Murali, Tamalda, Sayantanda, Prathap, Roshita, Noufal,

Suvendu, Sukruth, Sachin, Parijat, Pankaj and Deepika. A special thanks to my flatmates Rajesh, David, Indrajeet and Anvesh for their support in all aspect. I thank to Raju, Santanu and Basudevda for being the compatible friend. A very big thanks to all of you guys for your prompt support when I needed. Thanks a lot, to you people for giving the company and not making me feel the deficiency of motherland love.

My sincere thanks to those people, my parents Asraful Hoque and Tajmira Bibi, my sisters and brothers, without whom I am nothing. Their constant support helps me to grow up the way I am. The last but not the least, I am thankful to my love Sabnam who stands beside me like the roof.

Finally, I would like to thank the funding agencies for the support during the research work.

“AGAUR” foundation for PhD grant (Ref: 2016 FI_B 01011). A.L. thanks MINECO, FEDER and AGAUR for grants CTQ2016-80058-R, CTQ2015-73028-EXP, SEV 2013-0319, ENE2016-82025-REDT, CTQ2016-81923-REDC, and 2017-SGR-1631.

Table of Contents

Acknowledgements ___ *III*

Table of Contents ___ *V*

Abbreviations ___ *IX*

Abstract ___ *XI*

Chapter 1 ___ *1*

General Introduction ___ *1*

1. 1. Photosynthesis: an Inspiration to Sustainable Energy Schemes ___ **3**

1. 2. General Aspects of Water Oxidation Catalysis ___ **8**

1. 3. Molecular Water Oxidation Catalysis ___ **9**

1. 4. Molecular Anodes ___ **22**

1. 5. References ___ **33**

Chapter 2 ___ *37*

Objectives ___ *37*

Chapter 3 ___ *43*

3A. Synthesis, Characterization and Water Oxidation Activity of Isomeric Ru-Complexes ___ *44*

3A. 1. Introduction ___ **46**

3A. 2. Experimental Section ___ **48**

3A. 3. Results and Discussion ___ **52**

3A. 4. Conclusion ___ **64**

3A. 5. References ___ **65**

3A. 6. Supporting Information ___ **67**

3B. Synthesis, Electrochemical Characterization and Water Oxidation Catalysis of Ru Complexes Containing the 2,6-Pyridinedicarboxylato Ligand ___ *91*

3B. 1. Introduction ___ **93**

3B. 2. Experimental Section ___ **94**

3B. 3. Results and Discussion ___ **98**

3B. 4. Conclusion ___ **112**

3B. 5. References ___ **113**

3B. 6. Supporting Information ___ **115**

Chapter 4 ___ *127*

4. Water Oxidation to Dioxygen Catalysis by Mononuclear Ru complexes bearing the 2,6-pyridinedicarboxylato Ligand _____ *128*

4. 1. Introduction _____ **130**

4. 2. Experimental Section _____ **131**

4. 3. Results and Discussion _____ **136**

4. 4. Conclusion _____ **146**

4. 5. References _____ **147**

4. 6. Supporting Information _____ **149**

Chapter 5 _____ *171*

5. New Functional Coordination Oligomers Strongly Attached to MWCNT via Multiple CH-π Interactions as Powerful Molecular Electroanodes for Water Oxidation Catalysis _____ *172*

5. 1. Introduction _____ **175**

5. 2. Results and Discussion _____ **177**

5. 3. Conclusion _____ **187**

5. 4. Reference _____ **188**

5. 5. Supporting Information _____ **190**

Chapter 6 _____ *233*

6. A Powerful Hybrid Molecular Electroanode for Efficient Water Oxidation Based on 2D Ru Coordination Polymer _____ *234*

6. 1. Introduction _____ **236**

6. 2. Results and Discussion _____ **238**

6. 3. Conclusion _____ **244**

6. 4. References _____ **244**

6. 5. Supporting Information _____ **246**

Chapter 7 _____ *261*

7. Anchoring Strategies for Molecular Water Oxidation Catalysts on Solid Surfaces _____ *262*

7. 1. Introduction _____ **264**

7. 2. Experimental Section _____ **266**

7. 3. Results and Discussion _____ **271**

7. 4. Conclusion _____ **302**

7. 5. References _____ **304**

7. 6. Supporting Information _____ **305**

Chapter 8 _____ ***317***

8. Structural and Spectroscopic Characterization of Reaction Intermediates Involved in a Dinuclear Co-Hbpp Water Oxidation Catalyst _____ ***318***

8. 1. Introduction _____ **320**

8. 2. Results and Discussion _____ **322**

8. 3. Conclusion _____ **328**

8. 4. References _____ **329**

8. 5. Supporting Information _____ **330**

Chapter 9 _____ ***367***

General Conclusions _____ ***367***

Abbreviations

1D	Monodimensional
2D	Bidimensional
bpp^-	3,5-bis(2-pyridyl)pyrazolate
bpy	2,2'-bipyridine
CAN	Cerium Ammonium Nitrate
COSY	Correlation Spectroscopy
CPE	Controlled Potential Electrolysis
CV	Cyclic Voltammetry
CH_3CN	Acetonitrile
d	doublet
δ	Chemical shift
DCM	Dichloromethane
DFT	Density Functional Theory
DMSO	Dimethyl sulfoxide
DPV	Differential Pulse Voltammetry
E	Potential
E½	Half wave potential
ESI-MS	Electrospray Ionization Mass Spectrometry
FE	Faradaic Efficiency
FOWA	Foot of the Wave Analysis
FTO	Fluorine doped Tin Oxide
GC	Glassy Carbon
GCC	Graphite Conjugated Catalyst
H2bda	[2,2'-bipyridine]-6,6'-dicarboxylic acid
hv	Light
H2tda	[2,2':6',2''-terpyridine]-6,6'-dicarboxylic acid
HSQC	Heteronuclear Single Quantum Coherence spectroscopy
HMBC	Heteronuclear Multiple Bond Correlation spectroscopy
J	Coupling constant
λ	Wavelenght
M	Molar
I	Ionic strength
ITO	Indium doped Tin Oxide
I2M	Bimolecular Interaction Mechanism
i	Current
j	Current density
m/z	Mass-to-Charge ratio
MLCT	Metal to Ligand Charge Transfer
MS	Mass Spectrometry
MOF	Metal-Organic Framework
MWCNT	Multiwall Carbon Nanotubes
η	Overpotential
NHE	Normal Hydrogen Electrode
NMR	Nuclear Magnetic Resonance
NOESY	Nuclear Overhauser Spectroscopy
OEC	Oxygen Evolving Center

PCET	Proton Coupled Electron Transfer
PEC	Photoelectrochemical cell
PRC	Proton Reduction Catalyst
PR	Proton Reduction
PEM	Proton Exchange Membrane
ppm	Parts per million
PSI	Photosystem I
PSII	Photosystem II
PV	Photovoltaic
py	Pyridine
RT	Room Temperature
S	Surface of the electrode
s	Singlet
SCE	Saturated Calomel Electrode
t	Triplet
TBAH	Tetra(N-butyl)ammonium hexafluorophosphate
TEA	Triethylamine
TOF	Turnover Frequency
TONs	Turnover Numbers
TFE	Trifluoroethanol
TiO_2	Titanium dioxide
trpy	2,2':6',2''-terpyridine
UV-vis	Ultraviolet-visible Spectroscopy
v	Scan rate
UiO	University of Oslo
vs.	versus
WNA	Water Nucleophilic Attack
WO	Water Oxidation
WOC	Water Oxidation Catalyst
WS	Water Splitting

Abstract

Chapter 1. General Introduction

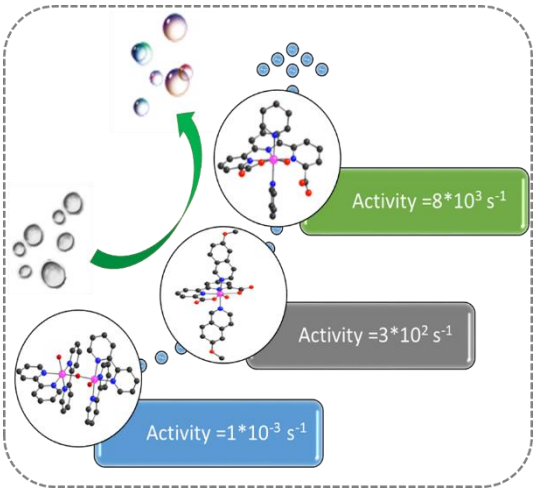

This chapter includes a brief discussion about the natural photosynthesis process as an inspiration towards renewable energy schemes followed by a description of new technologies based on artificial photosynthesis. A brief overview on the development of molecular water oxidation catalysts during the last years have been documented starting with homogeneous catalytic activities all the way to solid surfaces where molecular heterogeneous catalysts have been used with the aim of building efficient water splitting devices.

Chapter 2. Objectives

Chapter 3. Mononuclear Ruthenium Complexes Containing Pyridine Carboxylate ligands: Isomerization, Electronic Properties and Water Oxidation Activities

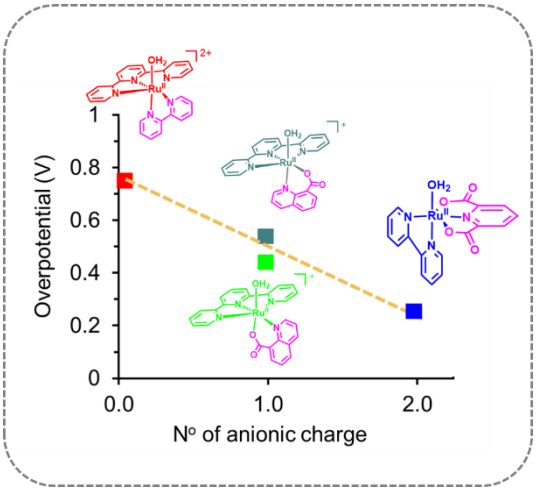

Synthesis, characterization, redox properties, electronic effects and water oxidation activity of a series of ruthenium complexes containing pyridine carboxylate ligands are reported in this chapter. It is shown that the electronic perturbation to the metal center exerted by different orientation and geometry of the ligands together with the electron donating properties produce dramatic effects in both redox properties and water oxidation catalytic performance of the systems.

Chapter 4. Catalytic Oxidation of Water to Dioxygen by Mononuclear Ru Complexes Bearing a 2,6-Pyridinedicarboxylato Ligand

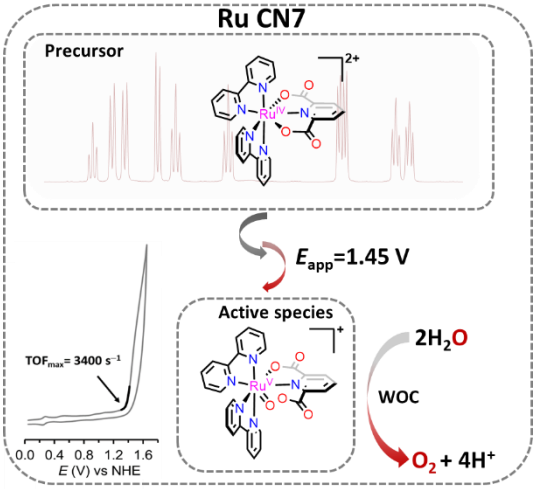

We report the synthesis, characterization and water oxidation activity of Ru complexes containing the pyridine dicarboxylate ligand. Under high anodic potentials, they evolve towards the formation of Ru-aquo complexes that are powerful and rugged water oxidation catalysts. These complexes operate water oxidation catalysis with active species that involve six coordination and seven coordination for the Ru centers. The present work uncovers and highlights the complexity involved in water oxidation catalytic processes when transition metal complexes are exposed to high oxidation potentials needed for the catalysis.

Chapter 5. New Functional Coordination Oligomers Strongly Attached to MWCNT via Multiple CH-π Interactions as Powerful Molecular Electroanodes for Water Oxidation Catalysis

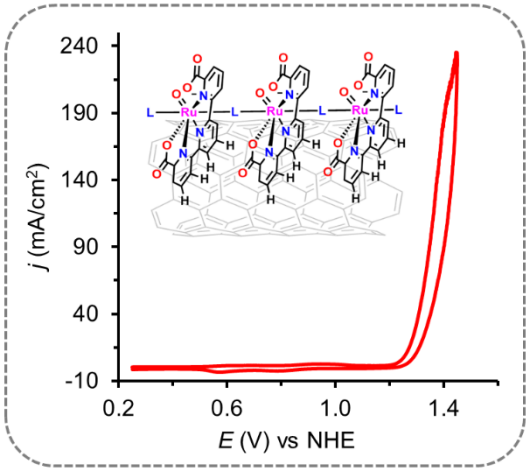

Linear coordination polymers with general formula {[Ru(tda)(4,4-bpy)]$_n$(4,4-bpy)} using 4,4'-bypridine as bridging ligand are synthesized and characterized. These materials show a unique anchoring strategy on multiwall carbon nanotubes via several CH-π interactions. The molecular hybrid materials are very active and rugged electroanodes for water oxidation reaching extremely high current densities up to 240 mA/cm^2 at 1.45 V in pH 7 and are comparable to commercial electrolyzers with much less catalyst loading.

Chapter 6. New Hybrid Powerful Molecular Electroanode for Efficient Water Oxidation based on 2D Ru Coordination Polymer

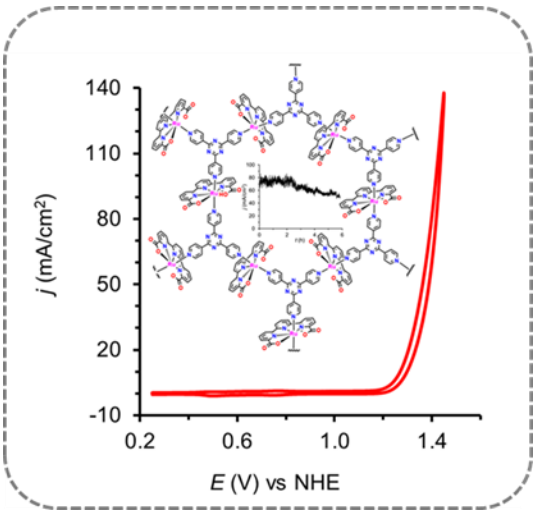

A functional coordination polymer with 2 dimensional framework with a ruthenium catalyst as a core unit and 2,4,6-tris(4-pyridyl)-1,3,5-triazine as a linker is reported. This material shows solid state interactions between different layers and changes its properties from solution to solid state. It strongly and massively anchores on the surface of multiwall carbon nanotubes. This new hybrid material is a precursor of extremely active and robust water oxidation catalyst that shows impressive catalytic current densities in the range of 0.1-0.2 A/cm^2 with over 1 million Turnover number in 6 h.

Chapter 7. Anchoring Strategies for Molecular Water Oxidation Catalysts on Solid Surfaces

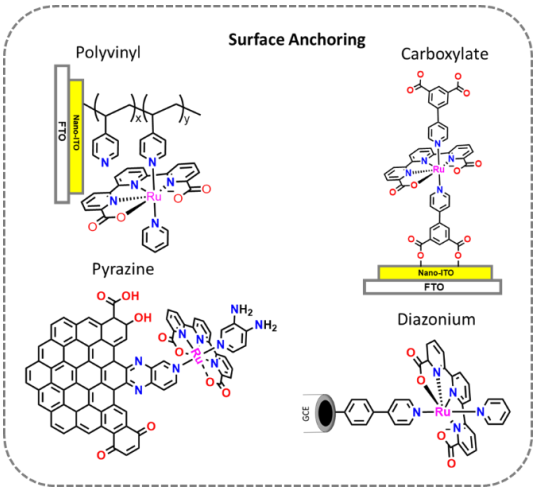

Mononuclear complexes based on the [Ru(tda)(Py')(py")] as a catalyst precursor are described (where tda = 2,2':6',2"-terpyridine-6,6"-dicarboxylate, py' and py" = functionalized pyridine). Here the pyridine py' or py" contain a functional group that allows attaching the complex to conductive substrates via covalent bonding. For instance, carboxylate and vinyl groups are used to attach the complex onto metal oxides, diazonium salts for C-C bonding attachment to graphitic materials or pyrazine linkages to anodized graphitic materials. Finally, non-covalent interactions are explored as a means to heterogenize mononuclear and coordination polymers on graphitic materials or metal oxides.

Chapter 8. Structural and Spectroscopic Characterization of Reaction Intermediates Involved in a Dinuclear Co-Hbpp Water Oxidation Catalyst

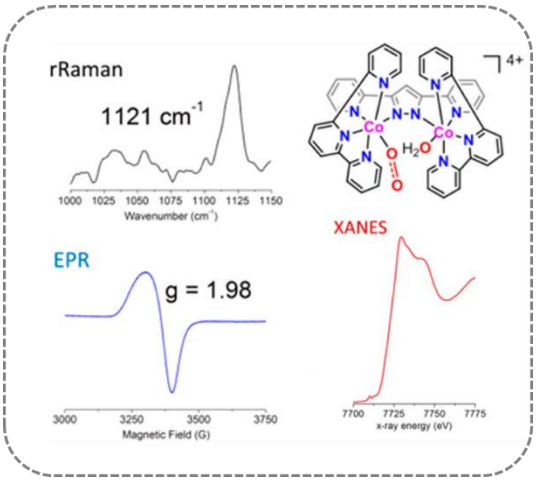

An end-on superoxido intermediate involved in the water oxidation reaction catalysed by a dinuclear Co- complex is characterized by resonance Raman, Electron paramagnetic resonance and X-ray absorption spectroscopy and complemented by Density Functional Theory. Isotopic labeling experiments under turnover conditions prove that this is a key intermediate of the water oxidation reaction.

Chapter 9. General Conclusions

Chapter 1

General Introduction

This chapter includes a brief discussion about the natural photosynthesis process as an inspiration towards renewable energy schemes followed by a description of new technologies based on artificial photosynthesis. A brief overview on the development of molecular water oxidation catalysts during the last years have been documented starting with homogeneous catalytic activities all the way to solid surfaces where molecular heterogeneous catalysts have been used with the aim of building efficient water splitting devices.

Chapter 1

Table of Contents

1. Photosynthesis: an Inspiration to Sustainable Energy Schemes

1. 1. Natural Photosynthesis

1. 2. Artificial Photosynthesis

2. General Aspects of Water Oxidation Catalysis

3. Molecular Water Oxidation Catalysis

3. 1. Proton Coupled Electron Transfer (PCET) process

3. 2. Mechanism of Water Oxidation Reaction

3. 3. Coordination Environments

3. 4. Effect of Secondary Coordination Sphere

3. 5. First Row Transition Metal Complexes

4. Molecular Anodes

4. 1. Design of Molecular Anodes

4. 2. Examples of Molecular Anodes

4. 3. Performance of Molecular Anodes

4. 4. Polymers

5. References

Chapter 1

1. 1. Photosynthesis: an Inspiration to Sustainable Energy Schemes

1. 1. 1. Natural Photosynthesis

Natural photosynthesis is a process carried out by green plants, algae or cyanobacteria that converts light energy from sun to chemical energy, that is, organic molecules that are the building blocks of all living organisms, oil, coal and natural gas. In this process, sunlight absorbed by chlorophyll provides energy to oxidize water in photosystem II and produces oxygen as a side product together with a set of protons and electrons. Later these protons and electrons combine with CO_2 in photosystem I through the Calvin cycle, and produce carbohydrates where solar energy is being stored as a chemical energy (Figure 1).[1,2]

Figure 1. Reduction of carbon dioxide (CO_2) into carbohydrates (e.g. $C_6H_{12}O_6$, glucose) which is accompanied by the oxidation of water (H_2O) to dioxygen (O_2). This photosynthetic process is carried out by the action of light.

Photosystem II is the first link in the chain of the photosynthesis process (Figure 2). This is a multi-subunit membrane protein complex located in the thylakoid membranes of the plants. Initially Chlorophyll P680 in photosystem II absorbs light from sun and one electron is promoted to higher energy and transferred to photosystem I through a complex electron chain.[3,4] Then, the electron deficient chlorophyll abstracts one electron from water mediated by tyrosine. This process takes place in the oxygen evolving complex (OEC)[5] that after five intermediate states produces oxygen from water. A detailed structural and mechanistic study reveals that this OEC is a Mn_4CaO_5 cluster where five oxygen atoms connect all five metals, and four water molecules complete their coordination sphere (Figure 3).[6,7]

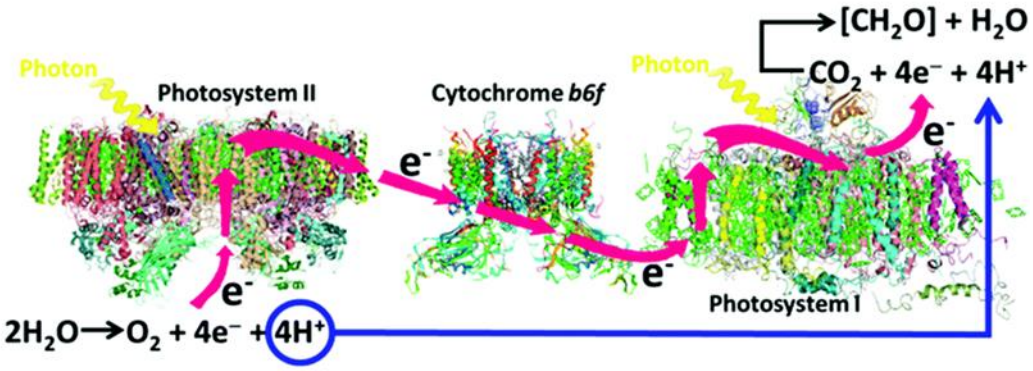

Figure 2. Representation of the natural photosynthesis process and the role of different units involved in it. Figure adapted from the reference paper.[8]

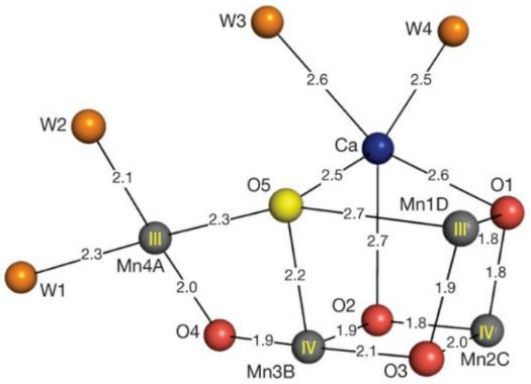

Figure 3. Structure of the oxygen evolving complex (OEC) Mn_4CaO_5 present in Photosystem II at 1.95 Å resolution. All the atoms are properly labelled with the element symbol. W: water molecule. Figure adapted from the reference paper.[7]

The OEC in Figure 3 together with other enzyme cofactors in nature are the inspiration to many scientists. The research community aims to find suitable artificial (man-made) catalysts for valuable reactions such as the water oxidation to dioxygen, for its fundamental role in new sustainable energy schemes.

1. 1. 2. Artificial Photosynthesis

It is well known that sun is the ultimate source of renewable energy for the living lives. The energy provided by sun on the surface of earth in the form of solar irradiation in one hour is more than enough for the global energy demands for one year.[9] The enormous energy power supply of sun drives the scientific communities to focus on the development of technologies that can take the advantage of this energy source (Figure 4). In solar thermal technologies, the heat provided by the sun is captured and used for several applications like heating,

cooking or any mechanical energy that eventually converts to electricity.[10] On the other hand, photovoltaics (PV) solar technologies capture the sunlight and directly converts it into electricity. Since the discovery of these technologies, they have had significant growth and nowadays, they provide nearly 5% of total global energy consumption (Figure 4, right).[11] However, the major drawback of these technologies is that they are unable to store the solar energy for further use, where most of the energy consuming sectors run through combustion of fuel to get the required energy when and where it is needed.

In this regard, plants in nature have probably developed the most efficient power supply in the world with the complex photosynthesis process in Figure 2. This process shows the most successful pathway of energy generation and storage system using the sunlight starting with unlimited source of raw materials like water and carbon dioxide (Figure 4, left). Due to very intense use of fuels generated by natural photosynthesis by human beings, fuel source is getting limited. Thus, scientists are seeking alternative ways to perform this process, that we generally call artificial photosynthesis processes (Figure 4, middle).

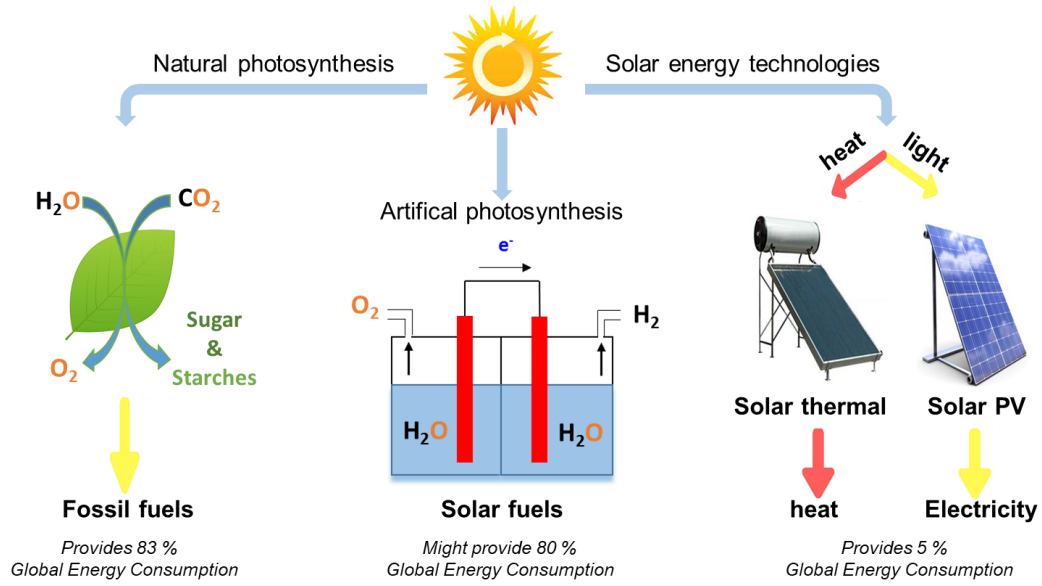

Figure 4. Solar energy conversion schemes.

Artificial photosynthesis is a very promising technology that can mimic the natural photosynthesis process and harvest the solar energy into fuel as chemical bonds. In this case, energy taken from the sunlight can be used to split water to oxygen and hydrogen in the overall water splitting reaction.[12-14] This process involves two half reactions: oxidation of water (H_2O) to oxygen (O_2) (eq. 1) and reduction of protons (H^+) to hydrogen (H_2) (eq. 2). Alternatively, other processes can be designed by using the protons and electrons obtained from the above process to reduce carbon dioxide (CO_2) or nitrogen (N_2) to hydrocarbon

(simplified as $[CH_2O]_n$) (eq. 3)[15] or ammonia (NH_3) (eq. 4).[16] All these products are known as solar fuels where solar energy is stored into them as a chemical energy.

$$2H_2O \rightarrow O_2 + 4H^+ + 4e^- \quad \text{(eq. 1)}$$

$$4H^+ + 4e^- \rightarrow 2H_2 \quad \text{(eq. 2)}$$

$$CO_2 + 4H^+ + 4e^- \rightarrow [CH_2O] + H_2O \quad \text{(eq. 3)}$$

$$N_2 + 6H^+ + 6e^- \rightarrow 2NH_3 \quad \text{(eq. 4)}$$

An ideal photosynthetic device should contain three main components: a) Light absorber that absorbs light from the sun and transfers the energy to the following steps, b) Catalysts that facilitate redox reactions and the breaking/formation of chemical bonds in order to get solar fuels as desired products and c) A membrane that separates the anode and cathode in the cell that allow to obtained the products separately in order to store them for later use. (see for example an example of photoelectrochemical cell (PEC) in Figure 5). Significant efforts have been made towards designing these devices during the past decades and they can broadly be categorized in three different groups: i) PV/electrolyzer, ii) Integrated photoelectrochemical cell (PEC, see example in Figure 5) and mixed colloid devices.[17,18]

PV/electrolyzer set-ups consist of two main parts, the photovoltaic cell and an electrolyzer. The former absorbs light and transfers the electricity generated to the electrolyzer, which consists of an anode and a cathode made by heterogeneous catalysts in an electrolytic solution for water splitting. This set-up is now well advanced but high cost of the PV cell inhibits it for industrial stage practical application.[19,20] On the other hand, mixed colloid devices are comparatively simple and low cost technology where light absorber and catalysts are in one single particle that performs the overall light induced water splitting and produce H_2 and O_2 in the same compartment. However, the development of such devices is in its infancy showing low efficiency and still needs an enormous improvement.[17,21] Integrated PEC is in intermediate state and represents the compromise between the efficiency of PV/electrolyzer and the less complexity of mixed colloid system. An example of PEC cell is given in Figure 5.

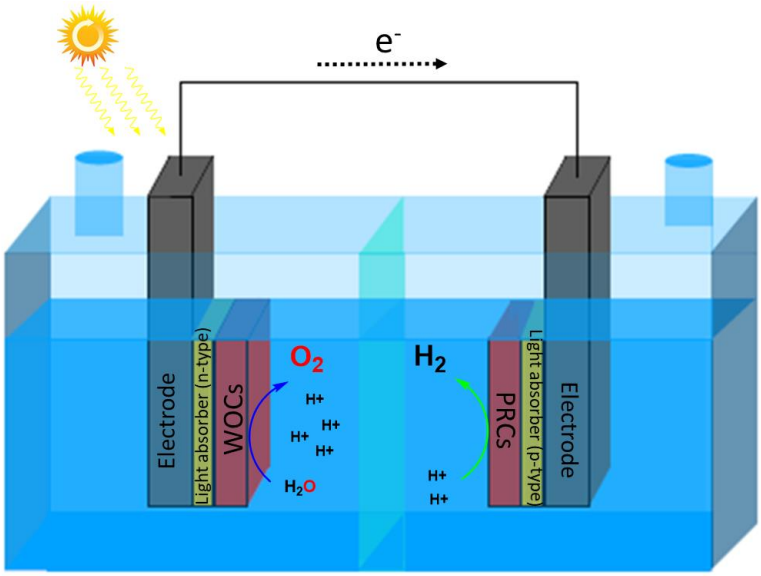

Figure 5. Schematic representation of a photoelectrochemical water splitting device (PEC). WOC: water oxidation catalyst; PRC; proton reduction catalyst.

The PEC cell consists of three main components:

a) Photoanode: an electrode containing a photoactive semiconductor material (n-type) and a heterogeneous water oxidation catalyst (WOC) to produce oxygen.
b) Photocathode: an electrode with photoactive semiconductor material (p-type) and a heterogeneous proton reduction catalyst (PRC) for hydrogen production.
c) Membrane: a junction that separates the cell into two compartments, allow the proton movement between them, and avoid products mixture.

In a photoelectrochemical cell (Figure 5), the process starts with the absorption of sunlight by photoactive n-type semiconductor material that generates an electron-hole pair. Then the hole is filled by an electron from the oxidation of the catalyst that after repeating the process up to 4 times, it finally leads to oxidation of water to oxygen on the surface of the photoanode. On the other hand, similar phenomena also happen in the photocathode with p-type semiconductor yet in this case, the electron is taken by catalyst that once reduced leads to the conversion of protons to generate hydrogen. To avoid the charge accumulation, the electron flow through an external circuit and the proton flow through a membrane should be possible. Importantly the design of the individual components in this artificial photosynthetic device can be improved independently bringing performance at highest level. This photosynthetic device can be extendable for the generation of other types of solar fuel such as NH_3 and hydrocarbons. In all these cases, water oxidation is the main counter reaction,

which occurs in the anode with simultaneous reduction reactions that take place in the cathode. Thus, the development of (photo)anodes where oxidation of water to molecular oxygen takes place is a highly pursued goal.

1. 2. General Aspects of Water Oxidation Catalysis

The oxidation reaction of water to molecular oxygen involves the breaking of 4 O-H bonds from two water molecule to generate a O=O double bond. This process requires the removal of four protons and four electrons, thus becoming thermodynamically uphill (E^0 = 1.23 V *vs.* NHE, Figure 6). The involvement of breaking and forming of multiple bonds make the process highly complex with high kinetic barriers. The additional potential required to overcome this kinetic barrier to make the process feasible is known as overpotential (η) (Figure 6, dotted orange line).[22]

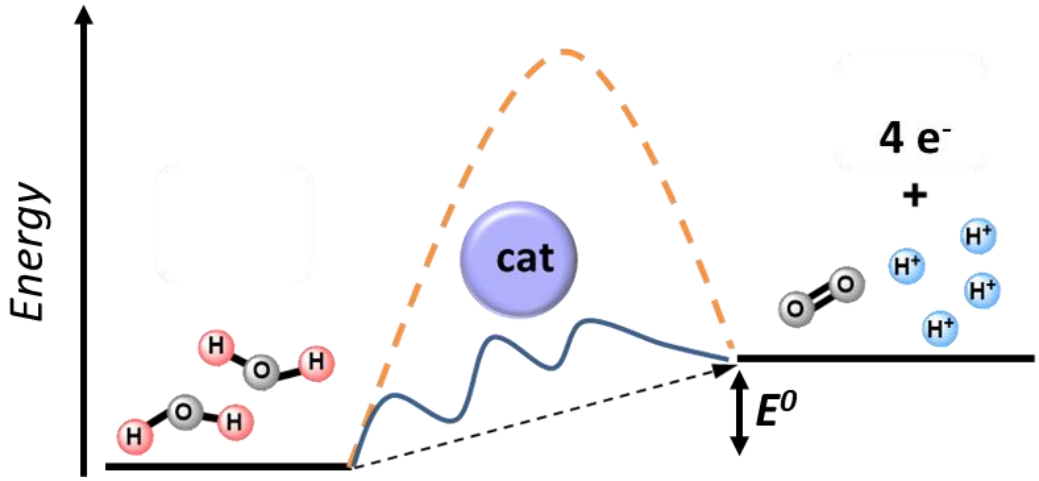

Figure 6. Schematic representation of the thermodynamics of the water oxidation reaction to give molecular oxygen and the high kinetic energy barrier involved (dashed orange line). The kinetic barrier is lowered by the action of a water oxidation catalyst (cat, blue solid line).

In order to lower the high energy barrier, it is possible to use suitable catalysts that go through lower energy intermediates and transitions states (Figure 6, blue solid line). Nature has fulfilled this goal with the oxygen evolving complex present in photosystem II, the Mn_5CaO_5 cubane cluster in Figure 3 discussed above.[7] It has a capacity to oxidize water to molecular oxygen at a mild overpotential of 0.43 V with high turnover frequency in the range of 100-400 s^{-1}. The remarkable feature of this cluster as an efficient water oxidation catalyst is now known, thanks to the well-advanced electrochemical and spectroscopic techniques.[23-26]

Inspired by the performance of this cluster in nature, the scientific community has invested their efforts towards designing highly efficient artificial water oxidation catalysts (WOC). They are broadly classified in two categories, i) metal oxide based catalysts and ii) molecular catalysts. The first artificial water oxidation catalyst was discovered by Glazer and Coehn in 1902 based on nickel oxide.[27] Since then a tremendous progress has been achieved in the field of water oxidation based on different metal oxides in terms of current density and overpotential by varying the morphology and particles size.[28-30]

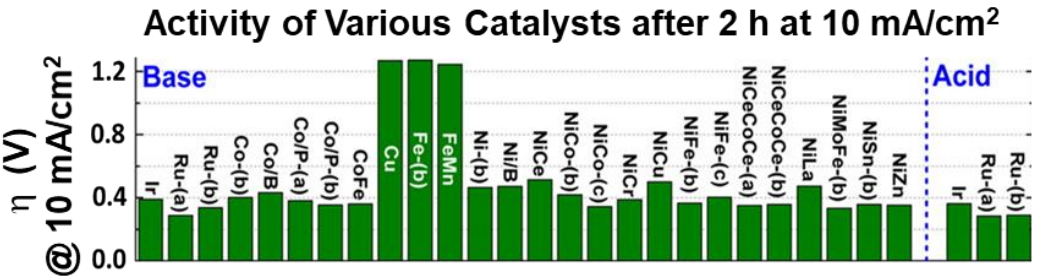

Figure 7. Plot of overpotential required to achieve a current density of 10 mA/cm^2 for water oxidation with different metal oxides in extreme basic (pH 14) and acidic (pH 0) conditions. Figure adapted from the reference paper.[31]

Recently Jaramillo *et al.* have reported a benchmark list of water oxidation catalytic performance of a bunch of metal oxides based on first row transition and noble metal oxides by electrochemical techniques under highly acidic and basic conditions (Figure 7).[31] They show that most of the metal oxide catalysts are highly active for water oxidation at basic pHs with a current density of 10 mA/cm^2 with moderate overpotential in the range of 0.35 to 0.5 V. On the other hand, in acidic pHs just few catalysts with nobel transition metal based oxides (RuO_2 and IrO_2) are capable of performing similar activity. Even though a significant growth on the performance of these catalysts has been achieved, they are limited with respect to their low turnover frequency, in part due to the lack of knowledge of understanding of their real active sites.[32]

1. 3. Molecular Water Oxidation Catalysis

The journey on molecular water oxidation catalysis started by the discovery of the so called blue dimer in 1982 by T. J Meyer. This oxo bridged dinuclear ruthenium complex with the formula *cis,cis*-{[Ru^{II}(bpy)$_2$(H_2O)]$_2$(μ-O)}$^{4+}$, (**1** in Chart 1 (bpy is 2, 2′-bipyridine)) has the capacity to oxidized water to molecular oxygen and is the first well-characterized catalyst that can carry out the reaction chemically and electrochemically.[33] The vast spectroscopic and

electrochemical techniques together with Density Functional Theory (DFT) helped for the detailed mechanistic understanding together with activity performance.

Compound **1** has been the source of inspiration to the scientific community for the further design of artificial molecular catalysts with the purpose of achieving high efficiency and fast reaction kinetics. Since then an enormous progress was achieved with different transition metal complexes such as Mn,[34] Fe,[35,36] Co,[37,38] Ni,[39] Cu,[40-43] Ir[44-46] or Ru[47-49] as metal centers with different ligand scaffolds. In particular, the rich coordination chemistry of ruthenium as well as its wide access of formal oxidation states are some of the reasons why this metal has been the core of most detailed electrochemical, kinetic, spectroscopic and mechanistic studies on water oxidation catalysis over the last 4 decades. From now, onwards the discussion will be mainly focused on the most relevant ruthenium complexes for water oxidation catalysis together with a brief description of complexes with other transition metals when particularly relevant.

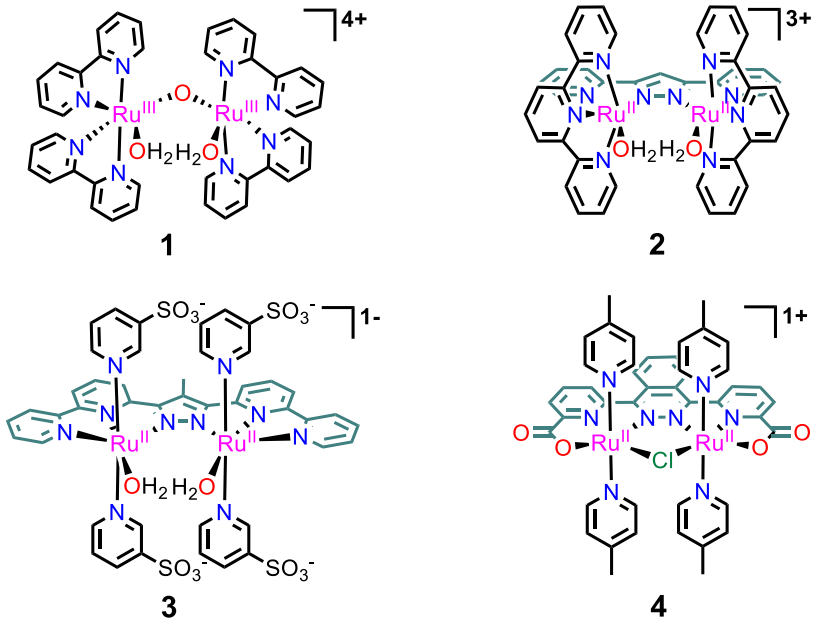

Chart 1. Structural representation of dinuclear Ruthenium complexes **1**, **2**, **3** and **4.**

Since the discovery of the blue dimer, **1**, scientists proposed that only dinuclear diaquo complexes are capable of carrying out water oxidation, because they can remove $2H^+$ and $2e^-$ from each Ru–OH_2 group, facilitating the process. Thus, a number of dinuclear complexes with a Ru-O-Ru bridge were reported in the literature; however, the unavailability of rational synthetic strategies for the preparation of oxo-bridged complexes limited the extension of this family of catalysts.[50,51] After almost 22 years, in 2004, Llobet *et al.* realized that the oxo-bridged is not crucial for the WO activity and reported a dinuclear Ru-complex *cis*,*cis*-

Chapter 1

{[Ru^{II}(trpy)(H_2O)]$_2$(μ-bpp)}$^{3+}$, **2** in Chart 1, by replacing the oxo bridge with a N-donor bpp^- ligand (bpp^- is bis (2-pyridyl)-3,5-pyrazolate).[52] This new bridge shows better electronic communication between the two metal centers and helps to rigidly hold the Ru-OH_2 groups in the proper orientation for further reaction steps in the catalytic cycle. As a result, **2** shows better performance than **1** with 70 % efficiency and 3.5 times higher turnover frequency (0.014 s^{-1} for **2** and 0.004 s^{-1} for **1**). Later, the same group redesigned another dinuclear complex {[Ru^{II}(py-SO_3)$_2$(H_2O)]$_2$(μ-Mebbp)}$^-$, **3** in Chart 1 by changing the bpp^- bridging ligand with $Mebbp^-$ (Mebbp is 4-methyl bis (2, 2′-bipyridyl)-3,5-pyrazolate)[53] and showed remarkable performance with 90% efficiency and TOF = 0.07 s^{-1}. The better efficiency of **3** is due to the replacement of the CH_2-group in the pyrazole ring by a methyl group preventing the oxidative degradation at the high water oxidation potential. Other examples of dinuclear complexes include complex {[Ru^{II}(py-Me)$_2$]$_2$(μ-bcpp)(μ-Cl)}$^-$,**4** in Chart 1[54] by changing the bridging ligand backbone with bcpp where $bcpp^{2-}$ is 1,4-bis (6'-COO-pyrid-2'-yl)phthalazine with high TOF up to 1.2 s^{-1}.

A breakthrough came in 2005 with the realization that mononuclear complexes are also capable of oxidizing water to dioxygen. Thummel *et al.* reported for the first time a new ruthenium polypyridyl complex [Ru(tnp)(Me-py)$_2$(OH_2)]$^{2+}$, **5** in Chart 2 (tnp is 2,2'-(4-(*tert*-butyl)pyridine-2,6-diyl)bis(1,8-naphthyridine))[55] that was a potential candidate for water oxidation catalysis. At that time, it was a puzzle to the scientific community because it was assumed that a minimum of two Ru-OH_2 centers are needed to be able to remove $2H^+$ and $2e^-$ from each Ru–OH_2 group to generate dioxygen from water. The puzzle was solved a few year later, when Meyer *et al.* reported a detailed mechanistic study of [Ru(trpy)(bpm)(OH_2)]$^{2+}$, **7** in Chart 2 and showed that single site Ru center is capable of performing water oxidation by a series of H^+/e^- transfers processes.[56] Since then a revolution happened in the field of water oxidation. The straightforward synthesis and isolation of mononuclear complexes with less complexity compared to dinuclear ones allowed the scientific community to broaden the field. Since then many research groups put their efforts on studying mononuclear ruthenium complexes as WOCs affording the better understanding of the mechanism and the performance by changing the ligand scaffolds in the coordination environments. Meyer and Llobet groups provided several examples of ruthenium complexes with the general formula [Ru(trpy)(BL)(OH_2)]$^{2+}$, by using the different bidentate ligands such as BL = 2,2′-bipyridine, **6**; 2,2′-bipyrimidine, **7**; 3,5-bis(2-pyridyl)pyrazole, **8**[56-58] (Chart 2). However, all these mononuclear complexes are less efficient than that of the analogous dinuclear complexes. Later Sun *et al.* reported another set of ruthenium complexes with the tridentate ligands 2,2′-

bipyridine-6-carboxylate, **9** and 2,6-pyridine dicarboxylate, **10** in Chart 2, although the real catalytic species of these complexes were not elucidated.[59] Incorporation of sigma donating carboxylate ligand improves the water oxidation catalytic activity of complexes **9** and **10** compared to previous mononuclear complexes with neutral N-donor ligands. Table **1** shows the summary of the catalytic data of the mononuclear complexes presented in chart 2 and 3.

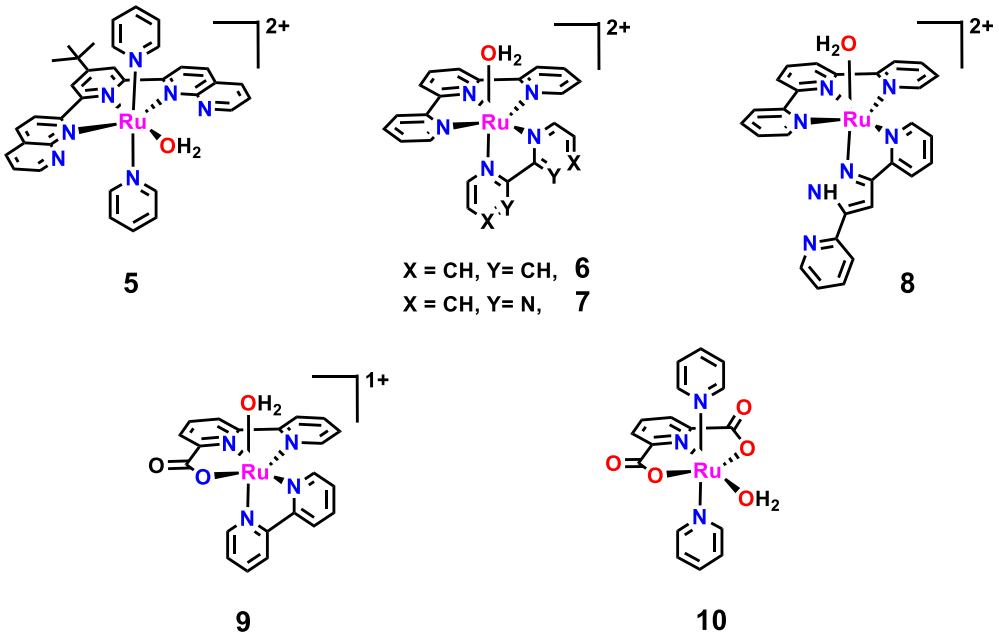

Chart 2. Structural representation of mononuclear Ruthenium complexes **5**, **6**, **7**, **8**, **9** and **10**.

The water oxidation field further speeded up by the discovery of the so called Ru-bda complexes by Sun *et al*. They reported complex [Ru(bda)(Me-py)$_2$(O)], **11** (Chart **3**) (bda^{2-} is [2,2'-bipyridine]-6,6'-dicarboxylate, Me-py is 4-methyl pyridine)[60] where tetradentate bda^{2-} ligand coordinate with Ru in equatorial position and 4-methyl pyridine in axial position with a TOF value of 32 s^{-1} with only 180 mV overpotenital in pH 1 (Table 1). Together with the excellent performance of this catalyst, they also found that it shows some interesting and unique properties: i) in absence of any coordinated solvent, it shows a highly distorted octahedral geometry with the two carboxylate groups coordinated to the Ru, in contrast, in aqueous solvent, water coordinates to Ru leaving one dangling carboxylate; ii) at high oxidation states Ru^{IV} and Ru^{V}, the complex adopts a pentagonal bipyramidal geometry with coordination number 7;[60] iii) the water oxidation catalysis follows a second order kinetics associated with a bimolecular rate-determining step for the formation of O-O bond and iv) the presence of two anionic charges provided by carboxylate group of bda^{2-} ligand help to stabilize the high oxidation state of the metal center. Since then Ru-bda family opened a new era in the field of molecular water oxidation field. After that, dozens of complexes were

reported with the Ru-bda family and they displayed dramatic improvement in the catalytic performance by fine-tuning of the axial ligands. For instance complex **12** in Chart 3 shows TOF of 310 s^{-1} which is one order of magnitude higher with respect to the parent complex **11**, by changing the axial 4-methyl pyridine with π-extended hydrophobic isoquinoline, which favors the binuclear nature of the mechanism for the O-O bond formation by π-interactions between two metal complexes.[61]

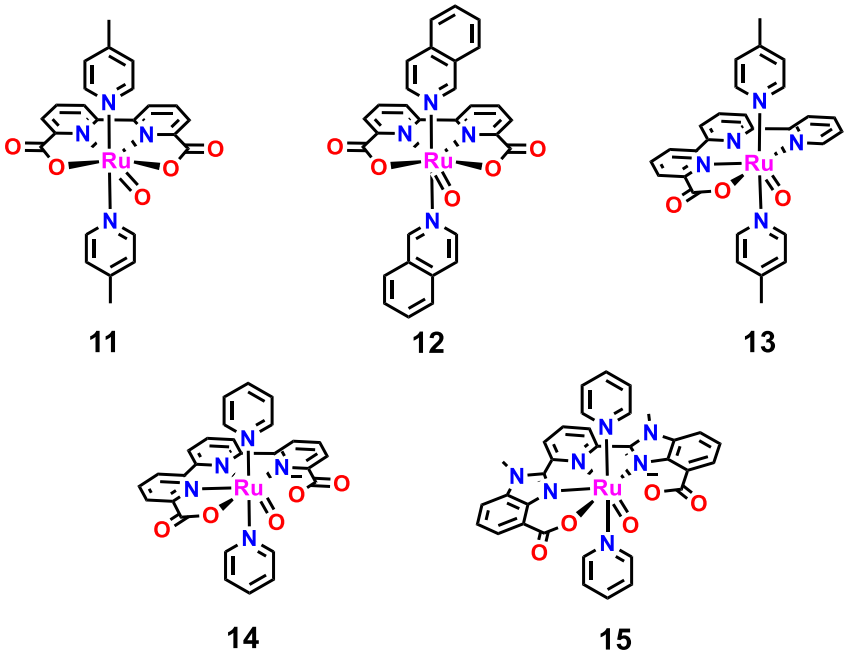

Chart 3. Structural representation of mononuclear seven coordinated Ruthenium complexes **11**, **12**, **13, 14** and **15.**

Another compound of this family of complexes is Ru(tpc)(Me-Py)$_2$(O)], **13**, where equatorial bda ligand was replaced by tpc ([2,2':6',2''-terpyridine]-6-carboxylic acid) with one less carboxylate group.[62] They found that this complex undergoes water oxidation catalysis with a seven coordination environment by aquo connection to the metal center in aqueous solution. However, the activity drastically decreases compared to the Ru-bda family and was proposed to proceed through a high-energy pathway for the O-O bond formation mechanism making this catalyst slower in kinetics. This result is an indication of the crucial role of a second carboxylate group in the equatorial plane. Indeed, this had been previously proven by the discovery of Ru-tda complex in 2015 by Llobet *et al*. They synthesized [Ru(tda)(py)$_2$], (tda^{2-} is [2,2′:6′,2′′-terpyridine]-6,6′′-dicarboxylate, py is pyridine) by incorporation of the tda pentadentate ligand in the equatorial position of the Ru and pyridine in axial position, which was a water oxidation catalyst precursor.[63] They were able to prepare electrochemically *in situ* the active catalyst Ru^{IV}(tda)(py)$_2$(O)], **14** in Chart 3 with seven coordination environment at high oxidation states by incorporation of hydroxo/oxo ligand.

Table 1. Catalytic data of mononuclear complexes with different number of anionic ligands (n^-), geometry of the Ru^{IV}=O species and type of mechanism involved.

Complex	n^{-a}	Geometry Ru^{IV}=O	TOF (s^{-1})	$E^1(Ru^{V/IV}=O)$ (V)[d]	Mechanism
$[Ru(trpy)(bpy)(OH_2)]^{2+}$, **6**[57]	0	CN6	0.01[b]	1.86	WNA
$[Ru(bpc)(bpy)(OH_2)]^{2+}$, **9**[64]	1	CN6	0.16[b]	1.59	WNA
$[Ru(pdc)(Me\text{-}Py)_2(OH_2)]^{2+}$, **10**[59]	2	CN6	0.23[b]	-	WNA
$[Ru(bda)(Me\text{-}Py)_2(O)]$, **11**[60]	2	CN7	32[b]	1.12	I2M
$[Ru(bda)(isoq)_2(O)]$, **12**[61]	2	CN7	310[b]	1.12	I2M
$[Ru(tpc)(Me\text{-}Py)_2(O)]$, **13**[62]	1	CN7	0.17[b]	-	WNA
$[Ru(tda)(py)_2(O)]$, **14**[63]	1	CN7	8000[c]	1.45	WNA
$[Ru(mcbp)(py)_2(O)]$, **15**[65]	1	CN7	1500[c]	1.43	WNA

Abbreviations: (a) n^-: number of anionic ligands coordinated to metal complex; (b) Turn over frequency (TOF) calculated based on the manometric experiment with Ce^{IV} as sacrificial electron acceptor at pH = 1; (c) TOF calculated based on Foot of the Wave Analysis (FOWA) from cyclic voltammetry experiments; (d) redox potential value of the $Ru^{V/IV}$=O redox couple at pH 7.

Catalyst **14** gives an impressive TOF of 8000 s^{-1} in pH 7 based on the "Foot of the Wave Analysis" (FOWA) technique. This result represents the fastest molecular catalyst for water oxidation in terms of TOF reported to date and faster than the oxygen evolving complex in natural photosystem II. The high catalytic activity of this catalyst is mainly due to two ruling factors: i) the pentadentate tda^{2-} ligand with two anionic carboxylate ligand allows the metal center to adopt the seven-coordination environment together with the stabilization of high oxidation states of the metal center and ii) the presence of the dangling carboxylate as a pendant base, which acts as proton acceptor and has a key role during the O-O bond formation step. Having the benefit of the above two ruling parameters, later Åkermark *et al.* reported $[Ru(mcbp)(py)_2(O)]$, **15** in Chart 3 ($mcbp^{2-}$ is 2,6-bis (1-methyl-4-(carboxylate)benzimidazol-2-yl)pyridine) by replacing the equatorial tda^{2-} ligand with $mcbp^{2-}$ showing comparable performance but easier access to the active aquo species.[65]

So far the enormous improvements in the field of artificial molecular water oxidation catalysis have been discussed where the catalytic performance improves up to six orders of magnitude since the discovery of the first molecular catalyst in 1982. The extensive studies on this field over more than 37 years reveal that there are four main fundamental features of the Ruthenium catalysts that allow an exponential increment of their performances; i) Proton coupled electron transfer (PCET) process, ii) Mechanism of O-O bond formation, iii)

coordination environment and iv) effect of secondary coordination sphere. A brief description of all these factors will be discuss hereafter.

1. 3. 1. Proton Coupled Electron Transfer (PCET) process

As mentioned earlier, the oxidation of water to molecular oxygen involves the removal of multiple protons and electrons from two water molecules. Thus, complexes that can access multiple redox states are highly desired to carry out this catalytic process. Proton coupled electron transfer (PCET) is a chemical reaction that transfer both a proton and an electron in a concerted manner. On the other hand, in electron transfer process, only the electron is transferred from one species to the other. When a single electron is removed from the complex, a columbic charge is built up on the metal center and the complex reach a higher energy. Consequently, it hinders the removal of the subsequent electron from the metal center. In the case of PCET, the charge built up by the removal of electron is compensated by the removal of one proton. This helps to stabilize high oxidation states of the metal center with lower potential.[66-69]

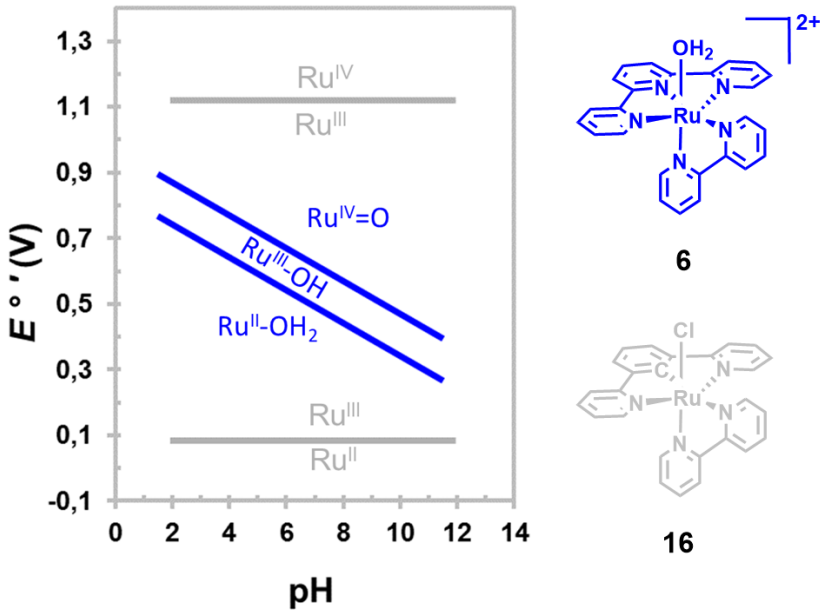

Figure 8. Pourbaix diagram of complexes **6** and **16**.

The effect of PCET can nicely be observed in the Pourbaix diagram of the complexes of **6** and **16** in Figure 8.[57,70] The potential of the $Ru^{III/II}$ and $Ru^{IV/III}$ redox couples of complex **16** are completely pH independent, as it involves only electron transfer process in different oxidation states without any proton transfer. As a result, the difference between these two redox couples are as high as 1000 mV. In comparison, complex **6** undergoes PCET process due to the presence of Ru-OH_2 group in the metal center and the redox couples are pH dependent. The

potential difference between these two couples are now only 100 mV, thus achieving high oxidation state of the metal center becomes easier. Interestingly this diagram provides another interesting feature on the effect of the overall charge of the complex. Complex **16** is neutral in its oxidation state II whereas **6** is double positive charged in the pH range from 2 to 12. Consequently, the potential of the $Ru^{III/II}$ couple of **16** is much lower than that of **6**. However, at oxidation state IV, both complexes are double positively charged but due to the PCET effect, the potential of $Ru^{IV/III}$ couple of **6** is lower than the **16**. The ability to stabilize the high oxidation state of the metal center by PCET process helps to reach the reactive Ru=O moiety at low potential and boost up for the formation of O-O bond in water oxidation catalysis.

1. 3. 2. Mechanism of Water Oxidation Reaction

Thanks to the availability of electrochemical, spectroscopic and analytical techniques as well as complementary information provided by computational studies, it has been possible to obtain a detailed understanding of the mechanism in the water oxidation catalytic cycle, mainly by means of study of Ru based complexes. Various reaction pathways have been proposed for the formation of O-O bond, which can be extended to other transition metal complexes besides Ruthenium. Two classes of mechanistic pathways have been proposed as can be seen in Figure 9: i) water nucleophilic attack (WNA) and ii) interaction of two metal oxo units (I2M).

In the WNA mechanism, a high oxidation state Ru=O species with electrophilic properties is formed via several consecutive oxidation steps. Nucleophilic attack by a water molecule on the Ru=O occurs, resulting in the formation of a Ru-O-O-H hydroperoxo species. Further PCET step generates $Ru\text{-}O\text{-}O^{-}$ superoxo intermediate, which releases O_2 and is converted into the initial complex with the incorporation of H_2O. The mononuclear complexes **5**, **6**, **7**, **8**, **9**, **10**, **13**, **14** and **15** have been proposed to undergo the WNA mechanism for the water oxidation (Figure 9, top).[56-58,62-64] The blue dimer, **1** also undergoes WNA mechanism due to the free rotation of the Ru-O-Ru bonds.[71]

Chapter 1

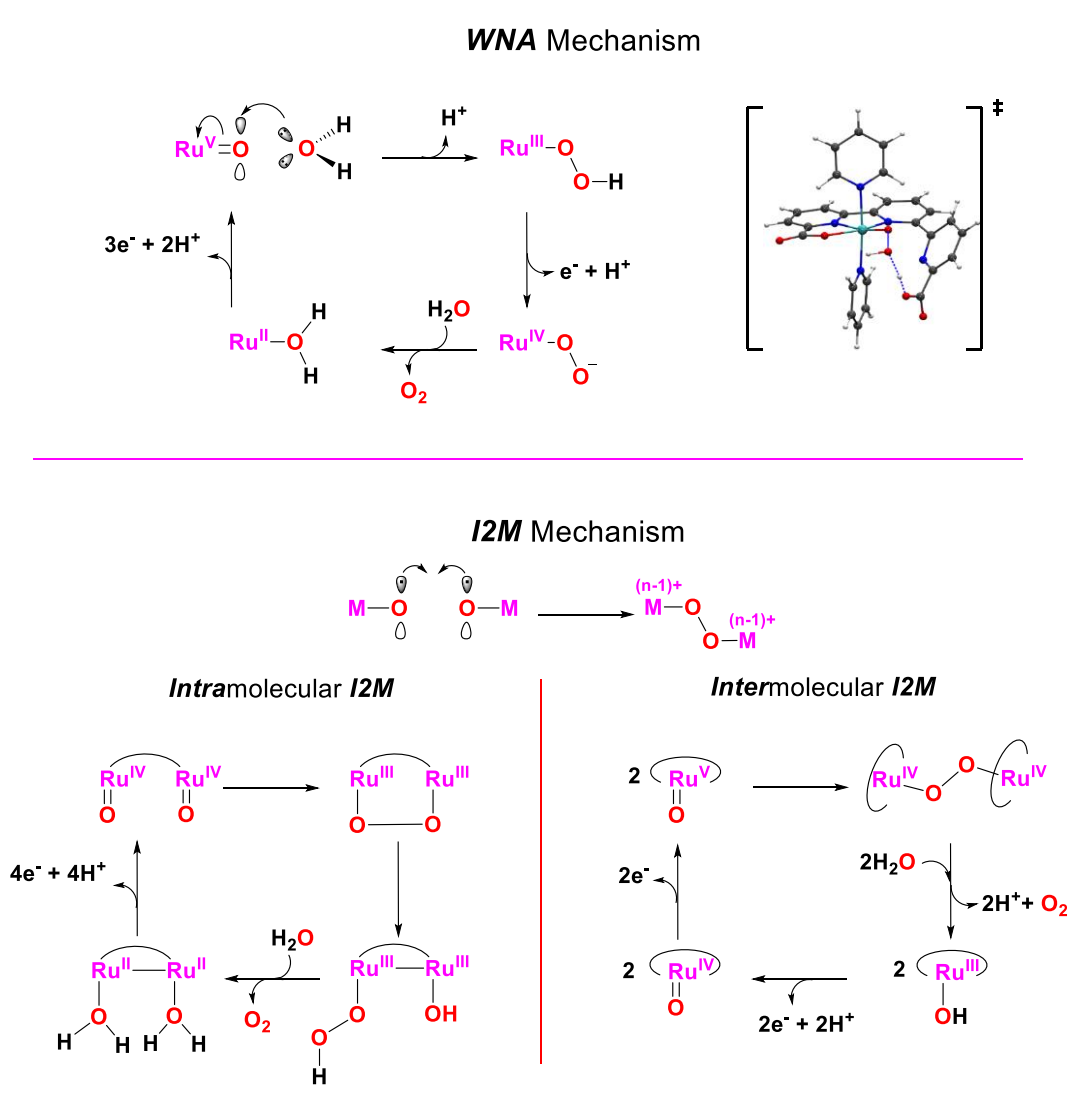

Figure 9. Two mechanistic pathways for the formation of O-O bond. Top: Schematic WNA mechanism (left) and transition state involved in the O-O formation for complex **14** following WNA mechanism (right). Bottom: Schematic I2M mechanism.

In the I2M mechanism,[53] the coupling of two high valent Ru-O oxyl radicals affords a Ru-O-O-Ru peroxo species that releases O_2 and returns to the initial complex with incorporation of H_2O. The dinuclear complex **2**, undergoes intramolecular I2M mechanism, where two Ru-OH_2 centers are at close proximity, allowing coupling between them (Figure 9, bottom left).[72] The mononuclear complexes **11** and **12** are proposed to follow intermolecular I2M mechanism where two discrete molecules are involved (Figure 9, bottom right).[61]

The difference in mechanism has a great influence in the performance of their catalytic activities. For example, bimolecular nature of complex **11** reveals that the catalytic activity can be improved when axial Me-Py ligand is replaced by isoquinoline (**12**) that can favor the bimolecular interaction by additional π-π interaction between the two molecules during the catalysis process. This additional π-π interaction executed by isoquinoline ligand helps to

stabilize the Ru-O-O-Ru peroxo intermediate via dimerization process and boosts up the activity from 32 s^{-1} to 310 s^{-1}. Detailed understanding of the mechanism of the reaction is crucial when the knowledge of homogeneous catalytic activity is transferred to solid surface where catalyst attached to the surface has mobility restrictions.[73]

1. 3. 3. Coordination Environments

Most of the molecular ruthenium water oxidation catalysts have octahedral geometry with coordination number 6 (Chart 1 and 2). The crystal field splitting[74] of octahedral (O_h) type geometry predicts that the d-orbitals of Ru split into two sets of orbitals: i) triply degenerate t_{2g} and doubly degenerate e_g orbitals as can be seen in Figure 10a (top). In some cases, ruthenium complexes with oxidation state IV or more can form seven coordination around the metal center with pentagonal bipyramidal geometry (D_{5h}).[75,76] In this case d-orbitals split into 3 sets of orbitals (e_1", e_2´ and a_1´) in Figure 10a (bottom)**.** Ru complexes at oxidation state IV with O_h geometry are in general paramagnetic but the Ru-complex with D_{5h} geometry are diamagnetic in nature if the crystal filed is strong. The judicious choice of the ligands can favor either octahedral or pentagonal bipyramidal geometry. Complexes **1**-**10** with polypyridine ligands are in octahedral geometry at oxidation state II-IV. In contrast, complexes **11**-**15** are octahedral in oxidation II-III but at oxidation state IV, all of them are heptacoordinated pentagonal bipyramidal geometry.[77] Seventh coordination stabilizes the electron deficient Ru^{IV}/ Ru^{V} center by providing the electron density and that is very crucial for the formation of an O-O bond. Moreover, this extra coordination stabilizes d_{xz}, d_{yz} orbital by lowering the energy of these orbitals as compared to O_h geometry. All the heptacoordinated complexes with anionic carboxylate ligands provide additional electron density to the high valent redox states. This stabilization is reducing the overall potential of the redox couples and thereby facilitates the catalysis.

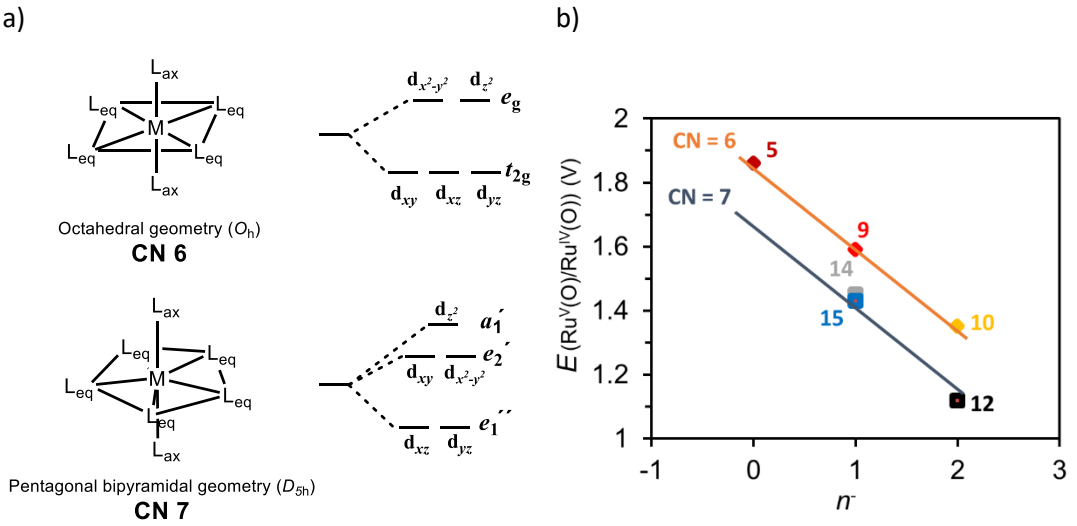

Figure 10. a) Representation of metal ligand bonds in octahedral (CN6) and pentagonal bipyramidal geometry (CN7) (left). Crystal field splitting of d orbitals for CN6 and CN7 complexes (right). b) Correlation of redox potential of $Ru^{V/IV}$=O with the number of anionic ligands.

Taking the advantages of all these parameters discussed above, complex **12** is one of the best catalysts with only 150 mV overpotenital thanks to the two carboxylates coordinated to the metal. In addition, complex **14** also has all these ruling parameters with an additional pyridine ring in the equatorial plane, which enables seven coordination environments at Ru^{IV} where 3 pyridine N and 2 carboxylate O are connected. In neutral or basic condition, there is an equilibrium in oxidation state IV between one of the carboxylate and OH^- ligand present in the electrolyte solution. Coordination of OH^- group to the metal center makes this the fastest catalyst reported to date with impressive TOF of 8000 s^{-1} in pH 7. Figure 10b shows the correlation between the number of anionic ligand (n^-) and $Ru^{IV/V}$=O redox couple of the complexes with coordination number 6 and coordination number 7. Upon addition of one carboxylate ligand in the place of neutral pyridine in the first coordination sphere of the metal, the potential of IV/V redox couple is reduced to by approximately 250 mV.[78] Moreover, seven coordinated complexes reduce the potential around 200 mV as compared to six coordination with the same number of anionic ligands,[48] clearly highlighting the role of additional seventh coordination in the stabilization of high valent metal-oxo with lowering the potential.

1. 3. 4. Effect of Secondary Coordination Sphere

In the previous section the crucial role of the primary coordination sphere play on the properties of the transition metal complexes has been discussed, where ligands are directly connected to the metal. Secondary coordination sphere where ligands are not directly connected to the metal center, sometimes also play a subtle but important role on the reactivity of the complexes. Theses secondary coordination sphere effects include Hydrogen

bonding, supramolecular π-π interaction, accessible pendant base, steric effect etc. All of them can influence on the kinetics and the mechanism of the reaction including substrate activation.[79-81] In complex **14**, the dangling carboxylate present in the equatorial ligand plays the most crucial role on the kinetics of the water oxidation. This dangling carboxylate acts as a pendant base and is involved in intramolecular H-bonding with the aquo group connected to the metal (Figure 9 top, right). This helps to remove the protons from the entering aquo group and drastically reduces the activation barrier during the formation of O-O bond via WNA mechanism in the catalytic cycle (Figure 9 top).[63] This makes the catalyst the fastest reported so far in the literature (see TOF values in Table 1). In comparison, complex **13** shows similar geometric environment as in **14**, but due to the absence of the pendant base, it is a worse catalyst with four orders of magnitude lower catalytic activity (compare entries **13** and **14** of Table 1).

As already discussed in section 1.3.2, the supramolecular π-π interactions also play an important role in the mechanism of complexes **11** and **12** with axial Me-py or π-extended isoquinoline ligands, respectively. These complexes undergo intermolecular I2M mechanism, where two high valent metal oxo dimerize. π-extended axial ligands favor the dimerization step and lower the activation barrier in the O-O bond formation steps.[82]

Recently Würthner *et al.* reported a trinuclear macrocyclic complex **17** with the incorporation of Ru-bda complex connected through a 1,4-bis (pyrid-3-yl) benzene ligand (Figure 11, left).[83,84] This complex creates a cavity in the macrocycle and traps a large number of water molecules through H-bonding. The presence of this H-bonding interaction with Ru-OH groups disfavor the dimerization steps and thus the complex undergoes water nucleophilic attack (WNA) with TOF values of more than 100 s^{-1}. Later Reek *et al.* incorporated the same Ru-bda molecule with 3-pyridylsulfonate as axial ligands inside the cavity of a nanosphere made of endohedral guanidinium site **18** (Figure 11, right). The self-assemble process of 12 units of Pt(II) and 24 units of L-gua^{+} generates a nanosphere with the internal cavity size approximately 4.3-4.9 nm. The sulfonate group present in the Ru-bda complex interacts with guanidinium sites through H-bonding interaction and generates a supramolecular structure where the ruthenium complex is encapsulated inside the nanosphere.[85] The preorganization of molecular catalyst in the cavity of the nansphere enhances the water oxidation activity to 125 s^{-1}.

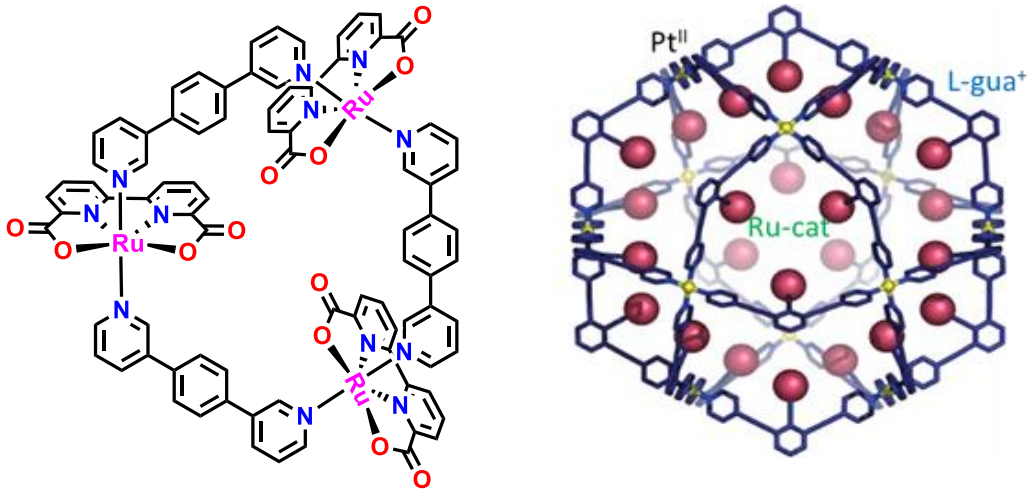

17 18

Figure 11. Left, structure of trinuclear macrocycle complex [Ru(bda)(μ-1,4-bpb)]$_3$, **17.** Right, nanosphere made of self-assembled Pt and L-gua$^+$ ([Pt$_{12}$(L-gua)$_{24}$]). Red balls indicates guanidinium group of the L-gua$^+$ ligand where the [Ru^{II}(bda)(3-SO$_3$-py)$_2$]$^{2-}$ encapsulates by H-bonding interaction. Figures are adapted from the reference papers.[83,86]

1. 3. 5. First Row Transition Metal Complexes

In general, first row transition metals such as Mn, Fe, Co, Ni and Cu are more abundant and cheap and harmless to the environment. From a practical point of view, designing catalyst based on first row transition metals is highly desired. For this reason, the knowledge on the performance and mechanism of water oxidation acquired from the ruthenium complexes have later been translated to the first row transition metal complexes. Some of the representative complexes carrying out water oxidation based on first row transition metal complexes are shown in Chart 4**.** In 1999, Brudvig reported a dinuclear oxo bridged Mn complex (**19**), which is capable of oxidation water to dioxygen with TOF of 0.003 s^{-1}.[87] However, it is important to point out that significant catalysis is only achieved using peroxides as sacrificial oxidant. It is thus very difficult to distinguish between peroxide disproportion and real water oxidation for this complex. In 2015, Thummel *et al.* showed that the dinuclear oxo-bridge Fe complex (**20**) undergoes water oxidation with TOF of 2.2 s^{-1}.[88] However the chemical irreversibility of the electroactive species displayed in the CV reported for this complex clearly point out that **20** is at most a precursor to a catalyst and that most likely the active species are basically not molecular but FeOx. A dinuclear Co complex (**21**) was also reported to show modest catalytic activity reported by Llobet group.[38] The same group reported a Cu based mononuclear complex (**22**) and showed that the introduction of electron donating groups in the ligand backbone can reduced the overpotential all the way to 540 mV, due to the involvement of a ligand oxidation step during the catalytic process.[43]

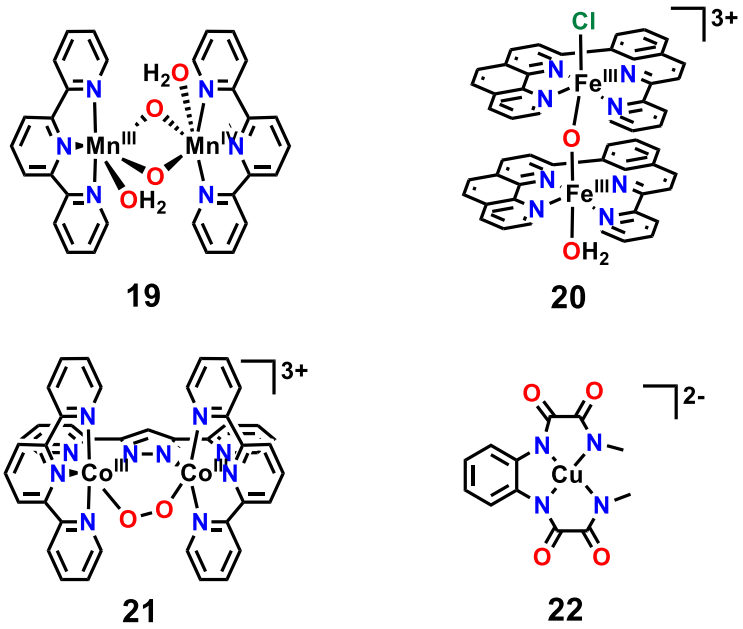

Chart 4. Representative WOCs based on 1st raw transition metal complexes.

In terms of the performance of the water oxidation reaction, first row transition metal complexes are slower in kinetics as compared to the ruthenium complexes. The main disadvantage of this family of complexes is the easy substitution of ligand scaffolds with water that leads to metal-multi aquo complexes that sometimes end up converting into the corresponding metal oxides, which are the real active catalyst as already proven long ago.[89]

1. 4. Molecular Anodes

The study of heterogeneous catalysts based on transition metal based oxides or hydroxides in WOC as an anode is dated back to more than a half century ago.[27] Such anodes exhibit greater stability and can be readily integrated into functional energy conversion devices such as photoelectrochemical cell for water splitting in Figure 5. However, the catalytic activity of such heterogeneous catalysts is difficult to control as its active site is less amenable to systematic modification. In comparison, molecular WOCs can display ligand fine-tuning around the metal center, which represent a powerful strategy to optimize the kinetics and/or thermodynamics of the water oxidation. In addition, the plethora of various analytic/spectroscopic techniques offer direct insights into the catalytic path and reaction intermediates. However, this approach often experiences low reaction rates because catalytic turnover only occurs when the catalyst is in diffusive contact with the electrodes. Moreover, molecular catalysts are still seriously lacking behind heterogeneous in terms of stability and robustness. Thus, construction of a molecularly well-defined and tunable heterogeneous

WOC (i.e. molecular anode) combining advantages of both systems are highly desirable and could open a new field of research successfully transferring the catalytic features of the molecular catalyst onto the solid surface.

1. 4. 1. Design of Molecular Anodes

A molecular anode can be designed in many different ways depending on how the molecular catalyst moiety is deposited/anchored on the conductive support. The most studied molecular anodes are based on the incorporation of a specific functional group in the ligand scaffold of the molecular catalyst so that the interaction with the anchorage support does not change the intrinsic coordination properties of the catalyst. The desired requirements for the anchoring support should be conductive and stable under the working condition. The anchoring group should also be hydrolytically and oxidatively stable at working pHs in order to avoid loss of catalyst. A less explored but the most promising way of designing molecular anode is by using polymerization reactions with either well-defined molecular catalyst or discrete coordination polymer.

Metal Oxide as Conductive Supports

Most of the examples of the molecular anodes reported in the literature are based on the immobilization of the molecular catalyst on a variety of metal oxide surfaces[90] such as fluorine doped tin oxide (FTO), tin doped indium oxide (ITO), nanoparticles of TiO_2 or In_2O_3. The most common and widely used anchoring groups are carboxylate, phosphonate, sulphonate, silicate, hydroxamate, or silatrane groups that can generate covalent bond with the conductive metal oxide (Figure 12 left). Fourier-transform infrared spectroscopy and computational studies help to identify the different binding modes of the anchoring group and have shown monodentate, bidentate, tridentate, chelating or bridging modes/connections through the oxygens depending on the anchoring group and the metal oxide surface.[91-93] The main disadvantages of these anchoring groups are the relatively poor stability in aqueous solution and hydrolysis in different pH ranges. The carboxylate group is moderately stable only in low pH (<4).[94] In comparison, phosphonate groups are more stable than carboxylates in pH <7. Hydroxamic acid and silatranes form strong bonds on the surface and are stable over a wide pH ranges from acidic, neutral to basic condition.

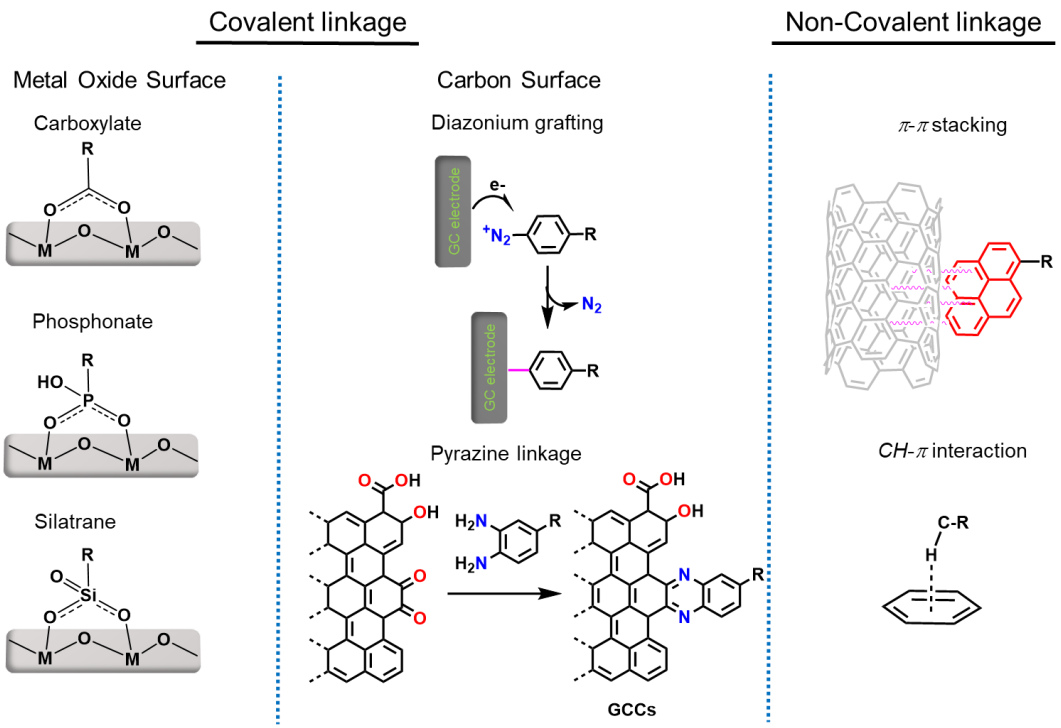

Figure 12. Schematic representation of the strategies for the immobilization of molecular catalysts on metal oxide and carbon surfaces.

Carbon Material as Conductive Support

Anchorage of molecular catalyst on graphitic carbon surface is a very attractive strategy and widely used to generate powerful molecular anodes. This carbon material is comparatively cheap with good electronic conductivity and has been broadly used in electrochemistry as a working electrode. Depending on the arrangement of the carbon atom on the material, it can range from flat glassy carbon electrode to nanostructure carbon material. Among them, the most widely used carbon materials are multiwall carbon nanotubes due to their high surface area, high thermal and chemical stability, excellent electrical conductivity and insolubility in most solvents. The scope of anchoring ways for the molecular catalysts on these materials are very wide ranging from covalent bonding to non-covalent interaction.

Generating a covalent bond between a molecular catalyst and a carbon surface can be achieved in many different ways (Figure 12 middle). One of the potential ways is by doing the dediazonation reaction *i.e,* the loss of dinitrogen from a diazonium salt with the formation of an aryl radical by homolytic cleavage between the aryl group and the nitrogen. Electro-reduction of diazonium salts on carbon surfaces give a covalent linkage between the surface and the appended molecule through C-C bond. This bond is highly stable from a chemical point of view in aqueous solution with a wide potential window.[95] Although this method has

been mainly used on carbon surfaces, there are a few examples that show that it is possible to employ this reaction on metal oxide surfaces where they can form C-O covalent bond.[96]

A new and simple method of anchoring the molecular catalyst on graphite surfaces is through the aromatic pyrazine linkage, which exploits the native surface chemistry of graphite. In this case, the ortho-quinone moieties on graphite edge planes can condense site-selectively with ortho-phenylenediamines under mild conditions, producing well-defined graphite conjugated catalysts (GCCs) (Figure 12, middle-bottom), which are active for both oxygen reduction and CO_2 reduction.[97] This new materials shows very strong electronic coupling between the appended molecule and the surface of the electrode.

Finally, the most extensive studied methods are non-covalent interaction on carbon material mainly based on π-π stacking, where the molecular catalyst connected with pyrene groups binds strongly with the π-system of a nanostructured carbon material. This strong binding does not require any chemical reaction and is as simple as adding the pyrene decorated molecular catalyst to this carbon material (Figure 12**,** right).[98] Similarly, in the CH-π interaction, the C-H proton interacts with the π-system of aromatic ring.[99]

Polymers Containing Molecular Catalyst on Conductive Substrates

The use of polymers made of monomers containing the molecular catalyst functionality has been used to generate molecular anodes for the water oxidation reactions. This can be achieved mainly in two different ways as illustrated in Figure 13: i) photochemically or electrochemically polymerization of well-defined molecular catalyst with specific functional group on the surface of the electrode using conventional organic polymer chemistry, and ii) designing coordination polymers with molecular catalysts and use them as an electrode material on the surface or directly growing them on the surface.

In the first group, we find the polymerization of vinyl pyridine under UV-light that produces polyvinyl pyridine films on the electrode's surface. The dangling pyridines of the resulting polymer can react with molecular catalyst precursors and give hybrid electrodes.[100] On the other hand, the molecular catalyst with N-substituted pyrroles[101] or C-substituted thiophenes under anodic electropolymerization conditions generate polymeric complexes that directly deposit on the electrode surface and behave as a molecular anodes.[102]

Chapter 1

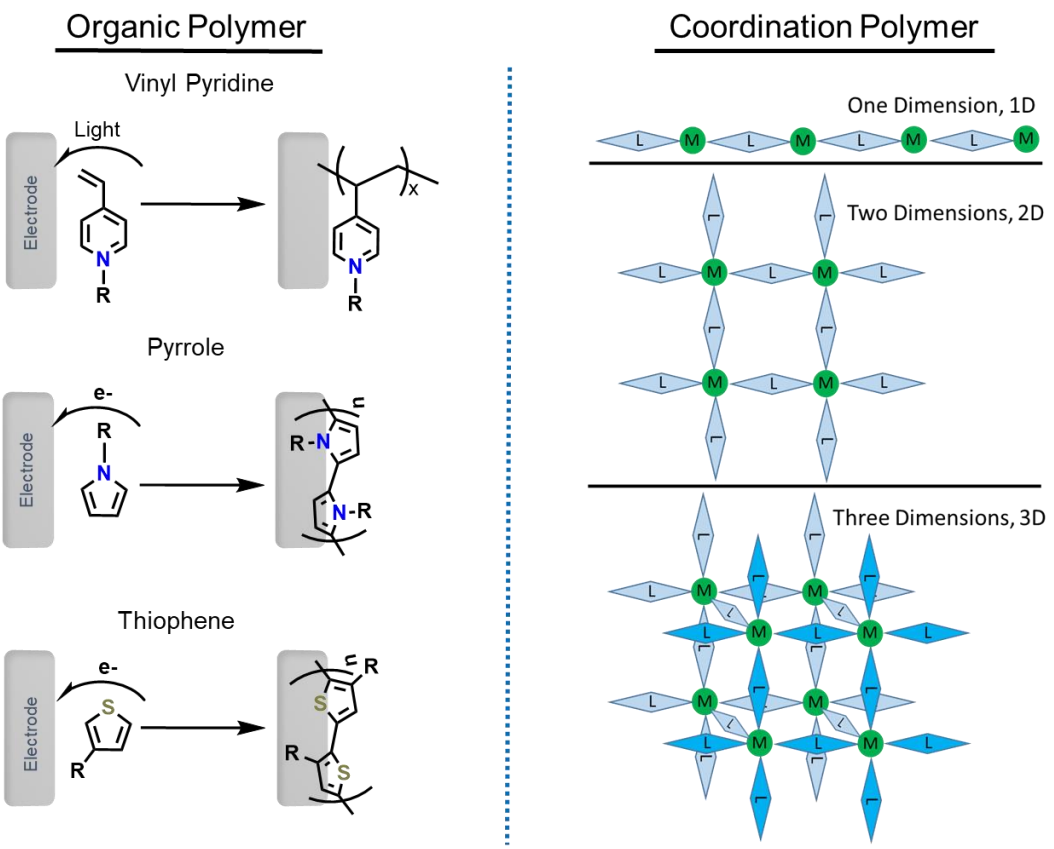

Figure 13. Schematic representation of the strategies for the immobilization of molecular catalysts by ligand polymerization on the surface (left) or generating coordination polymers (right).

In the second group, coordination polymers are inorganic or organometallic polymers that structurally contain metal centers linked with organic ligands. More formally, a coordination polymer is a coordination compound with repeating coordination entities extending in 1, 2 or 3 dimensions (Figure 13, right).[103] Designing a coordination polymer with well-characterized molecular water oxidation catalyst using different bridging ligand is nowadays a very hot topic in the field.[104] In most of the cases, these polymers are insoluble in water and used as a heterogeneous materials. Metal-Organic Frameworks (MOFs) are a class of coordination polymers with high porosity, crystallinity, highly ordered internal pores and large surface area. They can be synthesized separately or can be grown directly on the surface. For their relatively simple synthetic tunability and the possibility to incorporate large number of catalytic sites, MOFs provide appealing working framework for a wide range of electrocatalytic studies,[105,106] also for water oxidation catalysis.[107] With these advantages, they can potentially incorporate a large number of accessible catalytic sites for versatile applications and can be synthetically tuned to achieve the desired properties.

1. 4. 2. Examples of Molecular Anodes

This part will focus on specific examples of molecular anodes for water oxidation reported in the literature that exhibit interesting features and/or best performances. Chart 5 shows the molecular catalysts used to generate molecular anodes that are analogous to the homogeneous catalysts reported previously in the literature. During the last decade, Llobet's and Meyer's groups provided several examples of immobilization of ruthenium molecular catalysts on oxide surfaces. They have modify the active ruthenium molecular catalysts **23** [108]and **24** by introducing the PO_3H_2 group in the trpy or bpy ligand respectively. The resulting phosphonate modified complexes **23** and **24** were then anchored on TiO_2 nanoparticles coated FTO surface or directly on FTO surface generating **23**@TiO_2@FTO and **24**@FTO anodes, respectively. Llobet *et al.* followed the similar strategy to immobilize complex **25** through a carboxylate group. Here they replace the methyl group of the Me-bbp ligand by phenyl-carboxylate.[109] This complex was anchored on meso-ITO nanoparticles coated on an ITO electrode to generate the **25**@mesoITO@ITO anode. The same group used Ru-bda catalyst **26**, a well studied and best performing catalyst, on carbon surface via electroreduction of diazonium salt forming C-C covalent bond, herein referred as **26**@GC anode.[73]

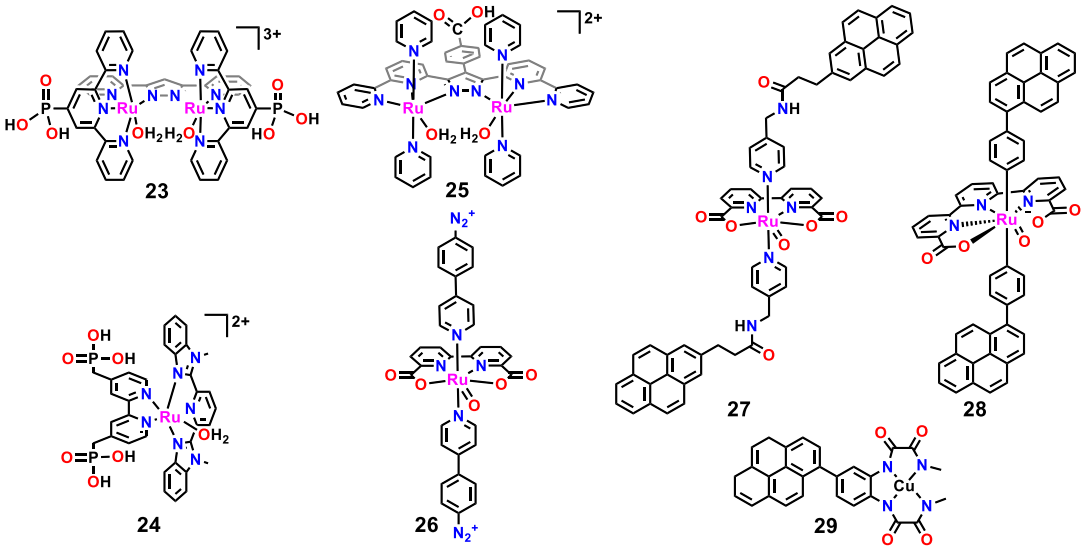

Chart 5. Structure of the molecular catalysts with different anchoring functional groups that have been used for the building of molecular anodes.

Parallely, Sun *et al.* also used carbon materials to anchor the Ru-bda type of catalysts. Initially they have replaced the axial Me-Py ligand of complex [Ru(bda)(Me-py)$_2$(O)], **11** by Pyr-py (Pyr-py is 4-(pyren-1-yl)-*N*-(pyridin-4-ylmethyl)butanamide) ligand to generate a hybrid molecular anode anchored on multiwall carbon nanotubes (MWCNT). The resulting complex

[Ru(bda)(Pyr-py)$_2$(O)], **27** was then attached to MWCNT through π-π stacking and dropcasted on a ITO electrode denoted as **27**@MWCNT@ITO anode for further performing electrochemical water oxidation reaction.[110] Recently, Llobet group employed the same strategy to anchor the best ruthenium molecular catalyst [Ru(tda)(Py)$_2$(O)], **14** by changing the axial pyridine ligand with Pyr-py denoted as **28**@MWCNT@GC anode.[98] Later, they incorporated a pyrene group to the tetradentate 1,2-phenylenebis(oxamidate) ligand and synthesized complex **29** and immobilize on graphene surface via same π-π staking and dropcasted onto carbon electrode, denoted as **29**@graphene@GC anode.[111]

1. 4. 3. Performance of Molecular Anodes

Table 2 summarizes the electrochemical data for **23**@TiO_2, **24**@FTO, **25**@mesoITO@FTO, **26**@GC, **27**@MWCNT@ITO, **28**@MWCNT@GC and **29**@graphene@GC anodes together with the catalytic data for the related homogeneous complexes. The above examples will help the reader to better understand and compare the relevant electrochemical features of the best-performing molecular anodes: the catalyst loading, the turnover frequencies, the current density and the overpotential.

Table 2. Electrochemical data for molecular anodes together with catalytic activity of the analogous homogeneous complexes.

	Γ (nmol/cm^2)	TOF het. (TOF hom.) s^{-1}	j /time (μA/cm^2)/ (min)	η (mV)	Ref. het. (Ref. hom.)
23@TiO_2@FTO	10	0 (0.01)[a]	0[a]/--	--	108 ([52])
24@FTO	0.1	0.36[b] (0.15)[c]	5[b]/480[b]	680	112 ([57])
25@*meso*ITO@ITO	0.5	0.45[d] (0.07)[e]	140[d]/--	520	109 ([53])
26@GC	0.2	1.8[f] (53)	150[f]/2[f]	450	73 ([60])
27@MWCNT@ITO	1.8	0.3[g] (30)[h]	220[g]/420[g]	580	110 ([61])
28@MWCNT@GC	0.3	8000[i] (8000)[i]	700[j]/150[j]	630	98 ([63])
29@graphene@GC	0.05	540[k] (128)[k]	300[l]/30[l]	730	111 ([43])

Experimental details: (a) Ce^{IV} (100 mM) and **2** (1 mM) at pH 1; (b) Chronoamperometry at E = 1.85 V at pH 5; (c) Ce^{IV}(100 mM) and complex **5** (1 mM) at pH 1; (d) Chronoamperometry using a Rotating Disk Electrode at E = 1.69 V at pH 1; (e) Ce^{IV} (100 mM) and **3** (1 mM) at pH 1; (f) Chronoamperometry at E = 1.27 V at pH 7; (g) Chronoamperometry at E = 1.4 V at pH 7; (h) Ce^{IV} (365 μM) at pH 1 and complex **9** (62.5 μM); (i) Foot of the wave analysis from CV at pH 7; (j) Chronoamperometry at E = 1.45 V at pH 7; (k) Foot of the wave analysis from CV at pH 12; (l) Chronoamperometry at E = 1.25 V at pH 12.

Chapter 1

One of the important parameters of the efficient molecular anodes is the catalyst loading on the surface that directly influences the current density and stability of the anode. Using electrodes with high surface area can improve these parameters. In this regard, the use of TiO_2 or meso-ITO nanoparticles on flat FTO can boost the catalyst loading. For example, catalyst loading of **23**@TiO_2@FTO is two orders of magnitude higher than the catalyst **24**@FTO,[108,112] where mesoporous TiO_2 increases the surface area significantly. On the other hand, using highly porous carbon material such as MWCNT or graphene also increases the surface area as compared to flat glassy carbon electrode. This is illustrated in the Table 2 for **27**@MWCNT@ITO, in which catalyst loading is one order of magnitude higher than **26**@GC,[73,110] where catalyst is directly anchored on the flat glassy carbon surface. Another important parameter in this case is the type of anchoring group of the catalyst that can also help to boost the catalyst loading.

The second crucial parameter of the molecular anode is the specific activity of the catalyst. Turnover frequency (TOF) of the catalyst on the solid support gives the information about the specific activity of the molecular anode. The performance of these molecular anodes depend on the mechanism of O-O bond formation step carried out by the catalyst for water oxidation. The catalysts that undergo WNA and intra-I2M mechanisms do not require any translational movement and thus anchoring process does not interfere in the O-O bond formation step. For this reason, **24**@FTO and **25**@*meso*ITO@ITO[109] anodes have shown comparable activity with their analogous homogeneous counterparts and in some cases working even better due to the enhanced contact of the catalyst with the electrode. In sharp contrast, in the case of catalysts of the Ru-bda family when anchored on carbon surface by covalent bond (**26**@GC) or π-π stacking (**27**@MWCNT@ITO), the water oxidation activity goes down drastically with respect to their homogeneous counterparts. The main reason for the fast catalysis in homogeneous solution is the bimolecular nature of the Ru-bda complexes that follows inter-I2M mechanism where two Ru-O group dimerize for the formation of O-O bond.[61] For **26**@GC and **27**@MWCNT@ITO,[73] such mechanism is drastically hindered as they are restricted with their translation mobility which results in limited accessibility to the second molecule thus increasing difficulties for dimerization during O-O bond formation. As a result, they lose their activity or force the catalyst to follow WNA mechanism that follows higher energy pathway slowering the kinetics and eventually leading to catalyst degradation to RuO_2. With **23**@TiO_2 anode, the catalytic activity is completely lost when complex **23** is anchored on metal oxide surface. In this case, the position of active Ru-OH_2 site is inward towards oxide surface and

coordinates on the surface, blocking the catalytic activity. That reveals the importance of the anchoring architecture in order to retain the catalytic activity.

Finally, **28**@MWCNT@GC[98] anode containing the best molecular water oxidation catalyst with Ru-tda family functionalized with pyrene moiety in axial pyridine ligand is the best molecular electroanode reported to date. In this case, the catalytic activity in homogeneous phase has been completely translated to solid surface with the same reaction kinetics due to the unimolecular WNA mechanism. The **29**@graphene@GC anode[111] is the only reported example that shows a drastic increase in activity with respect to its homogeneous counterpart. In this case, the anchoring group and the graphene surface are integral part of the catalyst and lower the activation energy for O-O bond formation that facilitates oxidation of water to molecular oxygen both from thermodynamic and kinetic perspective.

From the practical point of view, current density (*j*, mA/cm^2) is the most important parameter for an oxygen evolving molecular anode. An ideal anode in a photoelectrochemical cell or any commercial cell must maintain current density over 10 mA/cm^2 for unlimited time with lowest over potential. In any molecular anodes, this current density is directly proportional to the product of loading of the catalyst (Γ) and the turnover frequency (TOF) of the catalyst. As can be seen in Table 2, Ru-bda family of complexes on solid surfaces experienced an improvement on the current density starting with **26**@GC (150 μA/cm^2) to **27**@MWCNT/ITO (220 μA/cm^2).[110] However, here the current density relies on the higher loading of complexes on the carbon electrodes (flat glassy carbon *vs.* MWCNT on ITO) rather than on the higher activity of the molecular catalyst. Moreover, stability of the electrode is a big issue in this case. Interestingly, **28**@MWCNT@GC shows a current density (700 μA/cm^2) over more than 12 h with very low loading of the catalyst and clearly indicates that this current density mainly relies on the high activity of the catalyst. The current density of the **28**@MWCNT@GC electrode could reach the commercially relevant values of 10 mA/cm^2 if the catalyst loading (Γ) can be increased.[98]

Another important parameter required for efficient photoelectrochemical water splitting devices is the working potential associated with the overpotential of the catalyst on the surface of the electrode. Among the reported molecular anodes, **26**@GC shows the lowest overpotential as compared to others but with limited current density. For practical use, a molecular anode with high current density and low overpotential is highly desired. Encouraged by this challenge, the development of a molecular anode with fast molecular catalyst, high catalyst loading and low overpotential would fill up the important gap; if

successful, these systems would represent a significant step forward for more prolific use of molecular catalyst in energy conversion device.

1. 4. 4. Polymers

Using the concept of polymerization of active sites on the surface (both organic polymers and coordination polymers) in order to achieve high catalyst loading on molecular anodes have experienced a limited progress in the field of water oxidation. Chart 6 shows some representative examples of molecular catalysts that have been used in the polymerization reaction strategy. In 2008, Llobet *et al.* showed that the anodic electropolymerization of N-substituted pyrroles is a potential way of anchoring molecular catalysts on the conductive solid surface. They used N-substituted pyrroles functionalized in the trpy ligand of complex **30** for anchoring on FTO surface denoted as **30**@FTO. The loading of complex in this molecular anode was 1 nmol/cm^2 and was working much better than its homogeneous analogue using Ce^{IV} as an oxidant.[101] Later Sun *et al*. have extended their study by using thiophene in complex **31** for anchoring on carbon surface by the electroanodization technique denoted as **31**@GC.[102] This anode showed loadings of 0.9 nmol/cm^2 with a current density of 1.5 mA/ cm^2 at 1.3 V in pH 7 for more than 7 h. Recently, Meyer *et al.* immobilized complex **32** by electropolymerization of a vinyl group on metal oxide surfaces and have shown that the loading of the catalyst on the surface depends on the number of CV cycles within a selected potential windows. They can achieve loadings as high as 50 nmol/cm^2 after 250 CV cycles. This **32**@mesoITO@FTO anode performs as an efficient water oxidation catalyst with 0.5 mA/cm^2 current density over 3 h in pH 7.[113] This method of anchoring is very promising in terms of catalyst loading that can be enormously improved than other covalent anchoring strategies.

On the other hand, Najafpur reported for the first time the coordination polymer **33** based on Ru-polypyridine complexes for water oxidation.[114] The hydrophobic linear polymer was dropcasted on the carbon surface to generate the molecular anode **33**@GC. This molecular anode was active for water oxidation but its efficiency was very low. Later Li *et al.* reported a cross-linked coordination polymer based on Ru-bda catalyst, dropcasted on ITO surface with nafion binder and used as molecular anode (**34**@ITO).[104] This anode was active for water oxidation with 0.4 mA/cm^2 current density at 750 mV overpotential and retained their molecular nature during catalytic turnovers.

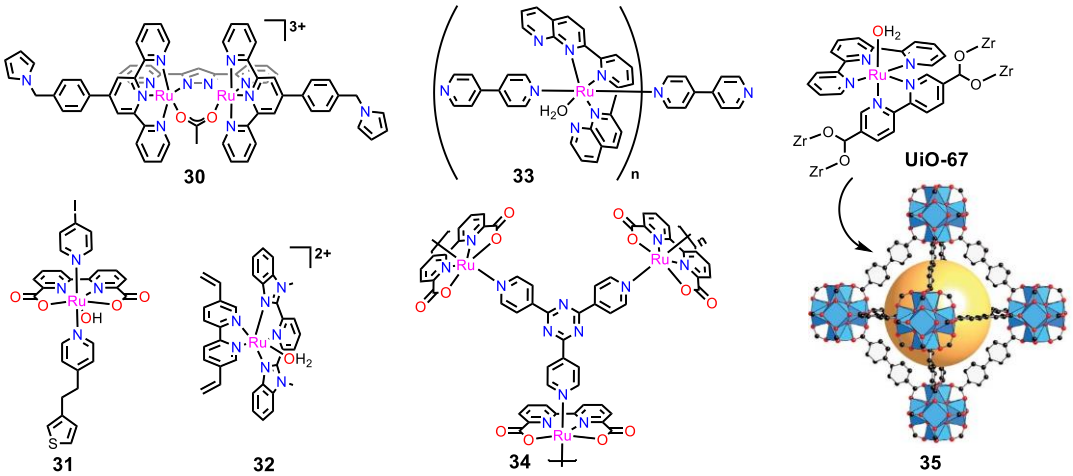

Chart 6. Structure of the molecular catalysts with different function group for polymerization, coordination polymers and MOFs.

MOFs are another class of coordination polymers with high porosity and large surface area. This material is a potential candidate for generating molecular anodes by incorporating well-defined molecular water oxidation catalyst. Morris and Ott groups incorporated the famous Ru-based mononuclear WOC, $[Ru(tpy)(bpy)OH_2]^{2+}$, **6** into the UiO-67 MOF backbone by changing the bpy ligand with dcbpy (5,5- dicarboxy-2,2'-bipyridine) as a linker, designated as Ru-bpy-MOF, **35**.[115] This framework shows comparable electrochemical behavior to that of the homogeneous solution. Ru-bpy-MOF (**35**@FTO) exhibits a stable current density for electrochemical water oxidation over 1 h with TOF (0.2±0.1) s^{-1} at 1.71 V in neutral pH.[116] Their results demonstrate that this is a promising way to immobilize molecular catalyst with high loading into a highly robust and porous MOF scaffold.

1. 5. References

(1) McEvoy, J. P.; Brudvig, G. W. *Chem. Rev.* **2006**, *106*, 4455.
(2) Nelson, N.; Ben-Shem, A. *Nat. Rev. Mol. Cell Biol.* **2004**, *5*, 971.
(3) Amunts, A.; Drory, O.; Nelson, N. *Nature* **2007**, *447*, 58.
(4) Crowe, S. A.; Døssing, L. N.; Beukes, N. J.; Bau, M.; Kruger, S. J.; Frei, R.; Canfield, D. E. *Nature* **2013**, *501*, 535.
(5) Ferreira, K. N.; Iverson, T. M.; Maghlaoui, K.; Barber, J.; Iwata, S. *Science* **2004**, *303*, 1831.
(6) Umena, Y.; Kawakami, K.; Shen, J.-R.; Kamiya, N. *Nature* **2011**, *473*, 55.
(7) Suga, M.; Akita, F.; Hirata, K.; Ueno, G.; Murakami, H.; Nakajima, Y.; Shimizu, T.; Yamashita, K.; Yamamoto, M.; Ago, H. *Nature* **2015**, *517*, 99.
(8) Zhang, B.; Sun, L. *Chem. Soc. Rev.* **2019**, *48*, 2216.
(9) *Energy...beyond oil; Armstron, F. B., Katherine, Ed.; Oxford University Press: UK, 2007*.
(10) Arshad, M. In *Clean Energy for Sustainable Development*; Rasul, M. G., Azad, A. k., Sharma, S. C., Eds.; Academic Press: 2017, p 73.
(11) *Key world energy statistics 2017, International Energy Agency, 2017.*
(12) Navarro Yerga, R. M.; Alvarez Galvan, M. C.; Del Valle, F.; Villoria de la Mano, J. A.; Fierro, J. L. *ChemSusChem: Chemistry & Sustainability Energy & Materials* **2009**, *2*, 471.
(13) Graetzel, M. *Acc. Chem. Res.* **1981**, *14*, 376.
(14) Berardi, S.; Drouet, S.; Francas, L.; Gimbert-Suriñach, C.; Guttentag, M.; Richmond, C.; Stoll, T.; Llobet, A. *Chem. Soc. Rev.* **2014**, *43*, 7501.
(15) Appel, A. M.; Bercaw, J. E.; Bocarsly, A. B.; Dobbek, H.; DuBois, D. L.; Dupuis, M.; Ferry, J. G.; Fujita, E.; Hille, R.; Kenis, P. J. *Chem. Rev.* **2013**, *113*, 6621.
(16) Schrock, R. R. *Proc. Natl. Acad. Sci.* **2006**, *103*, 17087.
(17) McKone, J. R.; Lewis, N. S.; Gray, H. B. *Chem. Mater.* **2013**, *26*, 407.
(18) Montoya, J. H.; Seitz, L. C.; Chakthranont, P.; Vojvodic, A.; Jaramillo, T. F.; Nørskov, J. K. *Nat. Mater.* **2017**, *16*, 70.
(19) Khaselev, O.; Turner, J. A. *Science* **1998**, *280*, 425.
(20) Bonke, S. A.; Wiechen, M.; MacFarlane, D. R.; Spiccia, L. *Energy Environ. Sci.* **2015**, *8*, 2791.
(21) Fabian, D. M.; Hu, S.; Singh, N.; Houle, F. A.; Hisatomi, T.; Domen, K.; Osterloh, F. E.; Ardo, S. *Energy Environ. Sci.* **2015**, *8*, 2825.
(22) Liu, F.; Concepcion, J. J.; Jurss, J. W.; Cardolaccia, T.; Templeton, J. L.; Meyer, T. J. *Inorg. Chem.* **2008**, *47*, 1727.
(23) Blomberg, M. R.; Borowski, T.; Himo, F.; Liao, R.-Z.; Siegbahn, P. E. *Chem. Rev.* **2014**, *114*, 3601.
(24) Cox, N.; Pantazis, D. A.; Neese, F.; Lubitz, W. *Acc. Chem. Res.* **2013**, *46*, 1588.
(25) Nocera, D. G. *Acc. Chem. Res.* **2012**, *45*, 767.
(26) Dismukes, G. C.; Brimblecombe, R.; Felton, G. A.; Pryadun, R. S.; Sheats, J. E.; Spiccia, L.; Swiegers, G. F. *Acc. Chem. Res.* **2009**, *42*, 1935.
(27) Coehn, A.; Gläser, M. *Z. anorg. allg.* **1902**, *33*, 9.
(28) Matsumoto, Y.; Sato, E. *Mater. Chem. Phys.* **1986**, *14*, 397.
(29) McCrory, C. C.; Jung, S.; Peters, J. C.; Jaramillo, T. F. *J. Am. Chem. Soc.* **2013**, *135*, 16977.
(30) Song, F.; Bai, L.; Moysiadou, A.; Lee, S.; Hu, C.; Liardet, L.; Hu, X. *J. Am. Chem. Soc.* **2018**, *140*, 7748.
(31) McCrory, C. C.; Jung, S.; Ferrer, I. M.; Chatman, S. M.; Peters, J. C.; Jaramillo, T. F. *J. Am. Chem. Soc.* **2015**, *137*, 4347.
(32) Feng, X.; Jiang, K.; Fan, S.; Kanan, M. W. *J. Am. Chem. Soc.* **2015**, *137*, 4606.
(33) Gersten, S. W.; Samuels, G. J.; Meyer, T. J. *J. Am. Chem. Soc.* **1982**, *104*, 4029.
(34) Cady, C. W.; Crabtree, R. H.; Brudvig, G. W. *Coord. Chem. Rev.* **2008**, *252*, 444.

(35) Ellis, W. C.; McDaniel, N. D.; Bernhard, S.; Collins, T. J. *J. Am. Chem. Soc.* **2010**, *132*, 10990.
(36) Okamura, M.; Kondo, M.; Kuga, R.; Kurashige, Y.; Yanai, T.; Hayami, S.; Praneeth, V. K. K.; Yoshida, M.; Yoneda, K.; Kawata, S.; Masaoka, S. *Nature* **2016**, *530*, 465.
(37) Leung, C.-F.; Ng, S.-M.; Ko, C.-C.; Man, W.-L.; Wu, J.; Chen, L.; Lau, T.-C. *Energy Environ. Sci.* **2012**, *5*, 7903.
(38) Rigsby, M. L.; Mandal, S.; Nam, W.; Spencer, L. C.; Llobet, A.; Stahl, S. S. *Chem. Sci.* **2012**, *3*, 3058.
(39) Han, Y.; Wu, Y.; Lai, W.; Cao, R. *Inorg. Chem.* **2015**, *54*, 5604.
(40) Barnett, S. M.; Goldberg, K. I.; Mayer, J. M. *Nat. Chem.* **2012**, *4*, 498.
(41) Zhang, M.-T.; Chen, Z.; Kang, P.; Meyer, T. J. *J. Am. Chem. Soc.* **2013**, *135*, 2048.
(42) Zhang, T.; Wang, C.; Liu, S.; Wang, J.-L.; Lin, W. *J. Am. Chem. Soc.* **2013**, *136*, 273.
(43) Garrido-Barros, P.; Funes-Ardoiz, I.; Drouet, S.; Benet-Buchholz, J.; Maseras, F.; Llobet, A. *J. Am. Chem. Soc.* **2015**, *137*, 6758.
(44) Hull, J. F.; Balcells, D.; Blakemore, J. D.; Incarvito, C. D.; Eisenstein, O.; Brudvig, G. W.; Crabtree, R. H. *J. Am. Chem. Soc.* **2009**, *131*, 8730.
(45) Woods, J. A.; Lalrempuia, R.; Petronilho, A.; McDaniel, N. D.; Müller-Bunz, H.; Albrecht, M.; Bernhard, S. *Energy Environ. Sci.* **2014**, *7*, 2316.
(46) Nieto, J.; Jiménez, M. V.; Alvarez, P.; Pérez-Mas, A. M.; González, Z.; Pereira, R.; Sánchez-Page, B.; Pérez-Torrente, J. J.; Blasco, J.; Subías, G. *ACS Appl. Energy Mater.* **2019**.
(47) Matheu, R.; Garrido-Barros, P.; Gil-Sepulcre, M.; Ertem, M. Z.; Sala, X.; Gimbert-Suriñach, C.; Llobet, A. *Nat. Rev. Chem.* **2019**, *3*, 331.
(48) Matheu, R.; Ertem, M. Z.; Gimbert-Suriñach, C.; Sala, X.; Llobet, A. *Chem. Rev.* **2019**, *119*, 3453.
(49) Xie, Y.; Shaffer, D. W.; Lewandowska-Andralojc, A.; Szalda, D. J.; Concepcion, J. J. *Angew. Chem. Int. Ed.* **2016**, *55*, 8067.
(50) Rotzinger, F. P.; Munavalli, S.; Comte, P.; Hurst, J. K.; Graetzel, M.; Pern, F. J.; Frank, A. J. *J. Am. Chem. Soc.* **1987**, *109*, 6619.
(51) Nazeeruddin, M. K.; Rotzinger, F. P.; Comte, P.; Grätzel, M. *J. Chem. Soc., Chem. Commun.* **1988**, 872.
(52) Sens, C.; Romero, I.; Rodríguez, M.; Llobet, A.; Parella, T.; Benet-Buchholz, J. *J. Am. Chem. Soc.* **2004**, *126*, 7798.
(53) Neudeck, S.; Maji, S.; López, I.; Meyer, S.; Meyer, F.; Llobet, A. *J. Am. Chem. Soc.* **2013**, *136*, 24.
(54) Xu, Y.; Fischer, A.; Duan, L.; Tong, L.; Gabrielsson, E.; Åkermark, B.; Sun, L. *Angew. Chem. Int. Ed.* **2010**, *49*, 8934.
(55) Zong, R.; Thummel, R. P. *J. Am. Chem. Soc.* **2005**, *127*, 12802.
(56) Concepcion, J. J.; Jurss, J. W.; Templeton, J. L.; Meyer, T. J. *J. Am. Chem. Soc.* **2008**, *130*, 16462.
(57) Wasylenko, D. J.; Ganesamoorthy, C.; Henderson, M. A.; Koivisto, B. D.; Osthoff, H. D.; Berlinguette, C. P. *J. Am. Chem. Soc.* **2010**, *132*, 16094.
(58) Roeser, S.; Farràs, P.; Bozoglian, F.; Martínez-Belmonte, M.; Benet-Buchholz, J.; Llobet, A. *ChemSusChem.* **2011**, *4*, 197.
(59) Tong, L.; Wang, Y.; Duan, L.; Xu, Y.; Cheng, X.; Fischer, A.; Ahlquist, M. r. S.; Sun, L. *Inorg. Chem.* **2012**, *51*, 3388.
(60) Duan, L.; Fischer, A.; Xu, Y.; Sun, L. *J. Am. Chem. Soc.* **2009**, *131*, 10397.
(61) Duan, L.; Bozoglian, F.; Mandal, S.; Stewart, B.; Privalov, T.; Llobet, A.; Sun, L. *Nat. Chem.* **2012**, *4*, 418.
(62) Fan, T.; Duan, L.; Huang, P.; Chen, H.; Daniel, Q.; Ahlquist, M. r. S.; Sun, L. *ACS Catal.* **2017**, *7*, 2956.

(63) Matheu, R.; Ertem, M. Z.; Benet-Buchholz, J.; Coronado, E.; Batista, V. S.; Sala, X.; Llobet, A. *J. Am. Chem. Soc.* **2015**, *137*, 10786.
(64) Tong, L.; Inge, A. K.; Duan, L.; Wang, L.; Zou, X.; Sun, L. *Inorg. Chem.* **2013**, *52*, 2505.
(65) Shatskiy, A.; Bardin, A. A.; Oschmann, M.; Matheu, R.; Benet-Buchholz, J.; Eriksson, L.; Kärkäs, M. D.; Johnston, E. V.; Gimbert-Suriñach, C.; Llobet, A.; Åkermark, B. *ChemSusChem.* **2019**, *12*, 2251.
(66) Binstead, R. A.; Moyer, B. A.; Samuels, G. J.; Meyer, T. J. *J. Am. Chem. Soc.* **1981**, *103*, 2897.
(67) Weinberg, D. R.; Gagliardi, C. J.; Hull, J. F.; Murphy, C. F.; Kent, C. A.; Westlake, B. C.; Paul, A.; Ess, D. H.; McCafferty, D. G.; Meyer, T. J. *Chem. Rev.* **2012**, *112*, 4016.
(68) Gagliardi, C. J.; Vannucci, A. K.; Concepcion, J. J.; Chen, Z.; Meyer, T. J. *Energy Environ. Sci.* **2012**, *5*, 7704.
(69) Savéant, J.-M. *Energy Environ. Sci.* **2012**, *5*, 7718.
(70) Ono, T.; Qu, S.; Gimbert-Suriñach, C.; Johnson, M. A.; Marell, D. J.; Benet-Buchholz, J.; Cramer, C. J.; Llobet, A. *ACS Catal.* **2017**, *7*, 5932.
(71) Moonshiram, D.; Alperovich, I.; Concepcion, J. J.; Meyer, T. J.; Pushkar, Y. *Proc. Natl. Acad. Sci.* **2013**, *110*, 3765.
(72) Romain, S.; Bozoglian, F.; Sala, X.; Llobet, A. *J. Am. Chem. Soc.* **2009**, *131*, 2768.
(73) Matheu, R.; Francàs, L.; Chernev, P.; Ertem, M. Z.; Batista, V.; Haumann, M.; Sala, X.; Llobet, A. *ACS Catal.* **2015**, *5*, 3422.
(74) *Miessler, G. L.; Tarr, D. A. Inorg. Chem.; Pearson Prentice Hall, 2003.*
(75) Kojima, T.; Hirai, Y.; Ishizuka, T.; Shiota, Y.; Yoshizawa, K.; Ikemura, K.; Ogura, T.; Fukuzumi, S. *Angew. Chem. Int. Ed.* **2010**, *49*, 8449.
(76) Muckerman, J. T.; Kowalczyk, M.; Badiei, Y. M.; Polyansky, D. E.; Concepcion, J. J.; Zong, R.; Thummel, R. P.; Fujita, E. *Inorg. Chem.* **2014**, *53*, 6904.
(77) Zhang, B.; Sun, L. *J. Am. Chem. Soc.* **2019**, *141*, 5565.
(78) Matheu, R.; Ertem, M. Z.; Gimbert-Surinach, C.; Benet-Buchholz, J.; Sala, X.; Llobet, A. *ACS Catal.* **2017**, *7*, 6525.
(79) De Grotthuss, C. *Biochim. Biophys. Acta Bioenerg.* **2006**, *1757*, 871.
(80) Kabbe, G.; Dreßler, C.; Sebastiani, D. *Phys. Chem. Chem. Phys.* **2017**, *19*, 28604.
(81) Vigara, L.; Ertem, M. Z.; Planas, N.; Bozoglian, F.; Leidel, N.; Dau, H.; Haumann, M.; Gagliardi, L.; Cramer, C. J.; Llobet, A. *Chem. Sci.* **2012**, *3*, 2576.
(82) Richmond, C. J.; Matheu, R.; Poater, A.; Falivene, L.; Benet-Buchholz, J.; Sala, X.; Cavallo, L.; Llobet, A. *Chem. Eur. J.* **2014**, *20*, 17282.
(83) Schulze, M.; Kunz, V.; Frischmann, P. D.; Würthner, F. *Nat. Chem.* **2016**, *8*, 576.
(84) Kunz, V.; Lindner, J. O.; Schulze, M.; Röhr, M. I.; Schmidt, D.; Mitrić, R.; Würthner, F. *Energy Environ. Sci.* **2017**, *10*, 2137.
(85) Yu, F.; Poole III, D.; Mathew, S.; Yan, N.; Hessels, J.; Orth, N.; Ivanović-Burmazović, I.; Reek, J. N. *Angew. Chem.* **2018**, *130*, 11417.
(86) Sato, S.; Iida, J.; Suzuki, K.; Kawano, M.; Ozeki, T.; Fujita, M. *Science* **2006**, *313*, 1273.
(87) Limburg, J.; Vrettos, J. S.; Liable-Sands, L. M.; Rheingold, A. L.; Crabtree, R. H.; Brudvig, G. W. *Science* **1999**, *283*, 1524.
(88) Wickramasinghe, L. D.; Zhou, R.; Zong, R.; Vo, P.; Gagnon, K. J.; Thummel, R. P. *J. Am. Chem. Soc.* **2015**, *137*, 13260.
(89) Hong, D.; Mandal, S.; Yamada, Y.; Lee, Y.-M.; Nam, W.; Llobet, A.; Fukuzumi, S. *Inorg. Chem.* **2013**, *52*, 9522.
(90) Bullock, R. M.; Das, A. K.; Appel, A. M. *Chem. Eur. J.* **2017**, *23*, 7626.
(91) Ernstorfer, R.; Gundlach, L.; Felber, S.; Storck, W.; Eichberger, R.; Willig, F. *J. Phys. Chem. B* **2006**, *110*, 25383.
(92) Brennan, B. J.; Portolés, M. J. L.; Liddell, P. A.; Moore, T. A.; Moore, A. L.; Gust, D. *Phys. Chem. Chem. Phys.* **2013**, *15*, 16605.

(93) Bae, E.; Choi, W.; Park, J.; Shin, H. S.; Kim, S. B.; Lee, J. S. *J. Phys. Chem. B* **2004**, *108*, 14093.
(94) Materna, K. L.; Crabtree, R. H.; Brudvig, G. W. *Chem. Soc. Rev.* **2017**, *46*, 6099.
(95) Garrido-Barros, P.; Matheu, R.; Gimbert-Suriñach, C.; Llobet, A. *Curr. Opin. Electrochem.* **2019**, DOI: 10.1016/j.coelec.2019.04.027.
(96) Bangle, R.; Sampaio, R. N.; Troian-Gautier, L.; Meyer, G. J. *ACS Appl. Mater. Interfaces.* **2018**, *10*, 3121.
(97) Oh, S.; Gallagher, J. R.; Miller, J. T.; Surendranath, Y. *J. Am. Chem. Soc.* **2016**, *138*, 1820.
(98) Creus, J.; Matheu, R.; Peñafiel, I.; Moonshiram, D.; Blondeau, P.; Benet-Buchholz, J.; García-Antón, J.; Sala, X.; Godard, C.; Llobet, A. *Angew. Chem. Int. Ed.* **2016**, *55*, 15382.
(99) Neel, A. J.; Hilton, M. J.; Sigman, M. S.; Toste, F. D. *Nature* **2017**, *543*, 637.
(100) Wadsworth, B. L.; Beiler, A. M.; Khusnutdinova, D.; Jacob, S. I.; Moore, G. F. *ACS Catal.* **2016**, *6*, 8048.
(101) Mola, J.; Mas-Marza, E.; Sala, X.; Romero, I.; Rodríguez, M.; Viñas, C.; Parella, T.; Llobet, A. *Angew. Chem. Int. Ed.* **2008**, *47*, 5830.
(102) Wang, L.; Fan, K.; Chen, H.; Daniel, Q.; Philippe, B.; Rensmo, H.; Sun, L. *Catal. Today* **2017**, *290*, 73.
(103) Batten, S. R.; Champness, N. R.; Chen, X.-M.; Garcia-Martinez, J.; Kitagawa, S.; Öhrström, L.; O'Keeffe, M.; Suh, M. P.; Reedijk, J. *Pure Appl. Chem.* **2013**, *85*, 1715.
(104) Zheng, T.; Li, L. *New J. Chem.* **2018**, *42*, 2526.
(105) Kornienko, N.; Zhao, Y.; Kley, C. S.; Zhu, C.; Kim, D.; Lin, S.; Chang, C. J.; Yaghi, O. M.; Yang, P. *J. Am. Chem. Soc.* **2015**, *137*, 14129.
(106) Zhang, T.; Lin, W. *Chem. Soc. Rev.* **2014**, *43*, 5982.
(107) Liu, Q.; Xie, L.; Shi, X.; Du, G.; Asiri, A. M.; Luo, Y.; Sun, X. *Inorg. Chem. Front.* **2018**, *5*, 1570.
(108) Francàs, L.; Richmond, C.; Garrido-Barros, P.; Planas, N.; Roeser, S.; Benet-Buchholz, J.; Escriche, L.; Sala, X.; Llobet, A. *Chem. Eur. J.* **2016**, *22*, 5261.
(109) Odrobina, J.; Scholz, J.; Pannwitz, A.; Francàs, L.; Dechert, S.; Llobet, A.; Jooss, C.; Meyer, F. *ACS Catal.* **2017**, *7*, 2116.
(110) Li, F.; Zhang, B.; Li, X.; Jiang, Y.; Chen, L.; Li, Y.; Sun, L. *Angew. Chem. Int. Ed.* **2011**, *50*, 12276.
(111) Garrido-Barros, P.; Gimbert-Suriñach, C.; Moonshiram, D.; Picón, A.; Monge, P.; Batista, V. S.; Llobet, A. *J. Am. Chem. Soc.* **2017**, *139*, 12907.
(112) Chen, Z.; Concepcion, J. J.; Jurss, J. W.; Meyer, T. J. *J. Am. Chem. Soc.* **2009**, *131*, 15580.
(113) Wu, L.; Nayak, A.; Shao, J.; Meyer, T. J. *Proc. Natl. Acad. Sci.* **2019**, DOI: 10.1073/pnas.1902455116.
(114) Najafpour, M. M. *Mol. Cryst. Liq. Cryst.* **2010**, *517*, 167.
(115) Johnson, B. A.; Bhunia, A.; Ott, S. *Dalton. Trans.* **2017**, *46*, 1382.
(116) Lin, S.; Pineda-Galvan, Y.; Maza, W. A.; Epley, C. C.; Zhu, J.; Kessinger, M. C.; Pushkar, Y.; Morris, A. J. *ChemSusChem.* **2017**, *10*, 514.

Chapter 2

Objectives

Chapter 2

II

Over the last 4 decades, the field of molecular water oxidation catalysis has witnessed a tremendous progress by improving the performance up to six orders of magnitude higher than the first reported molecular catalyst. The journey through the most relevant achievements in the field has been summarized in the previous chapter. Despite the success, there are still several challenges that need to be addressed from a practical application standpoint. This thesis will focus on some of these challenges highlighted in the following objectives.

First of all, the catalyst should work very fast with minimum overpotential. In objectives, 1 and 2 below, the synthesis of new ruthenium water oxidation catalysts with different number of coordinated carboxylate groups will be discussed. The anionic ligand is expected to be responsible of lowering the working potential, while geometrical and secondary effects of the ligands will be explored as a way to enhance catalytic performance.

Secondly, in order to transfer the high catalytic activity of homogeneous catalysts into solid supports with the ultimate goal of building powerful water splitting devices, the design of molecular catalysts that are efficient, robust and easily transferable to heterogeneous phase is highly desirable. Thus, the third objective of this thesis is focused on the development of molecular water oxidation catalysts that can be supported on conductive substrates, starting from mononuclear complexes all the way to coordination polymers. In objective 4, the new family of materials will be used to understand the ruling factors and mechanistic details of the catalysis on surfaces.

Finally, the last challenge addressed in this thesis is to explore water oxidation catalysts made of cheap and abundant first row transition metals. Advances in this line are summarized in objective 5 and are based on getting mechanistic insights of the water oxidation catalysis by a dinuclear cobalt complex that is active for the water oxidation reaction.

Chapter 2

Objective 1

With the aim of lowering the overpotential of the water oxidation catalysis, ruthenium complexes with pyridine type of ligands including one anionic ligand, e.g. 8-quinolinecarboxylate (qc) and 2-picolinate (pic), will be used. Their influence on geometrical and electronic effects on the overpotential and kinetics of the process will also be explored.

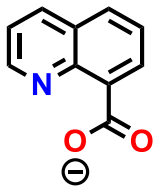

qc

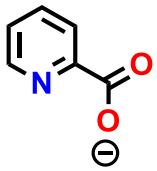

pic

Objective 2

Following the same goal as in objective 1 above, pyridyl-2,6-dicarboxylate (pdc) will be use as ligand in ruthenium complexes with the objective of not only reducing the overpotential by introduction of a second carboxylate group, but also to achieve seven coordinated ruthenium intermediates ensuring fast kinetics of the water oxidation catalysis.

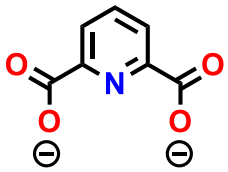

pdc

Objective 3

The development of molecular catalysts that can be incorporated into anodes for the water oxidation reaction. This objective will be achieved with two main families of complexes: i) mononuclear ruthenium complexes with functional groups that allow them to be incorporated into conductive substrates and ii) coordination polymers based on the fastest ruthenium catalyst reported in the literature ($[Ru(tda)(py')_2]$, where tda = 2,2':6',2''-terpyridine-6,6''-dicarboxylate and py' = functionalized pyridine) as a core unit. Two organic linkers will be used as bridging building blocks with different arrays, *i.e.*, 4,4´-bipyridine (4,4'-bpy) and 2,4,6-tri(pyridin-4-yl)-1,3,5-triazine (tpt) to form 1-dimensional or 2-dimentional polymers, respectively.

Core unit **Linker**

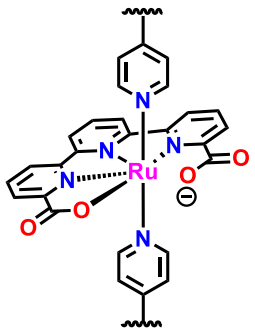

[Ru(tda)(py')$_2$]

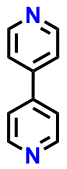

4,4´-bipyridine (4,4'-bpy)

1D

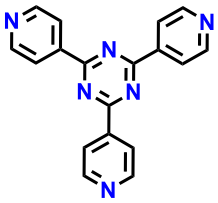

2,4,6-tri(pyridin-4-yl)-1,3,5-triazine (tpt)

2D

Objective 4

The objective here is to develop hybrid molecular anodes with the ruthenium complex and the coordination polymer prepared in objective 3 above in order to generate powerful molecular electroanodes for water splitting devices.

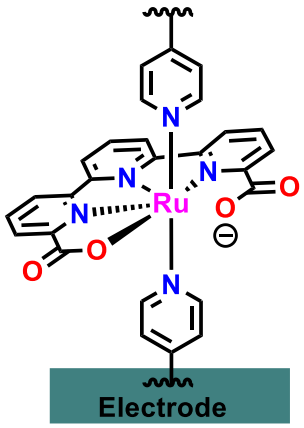

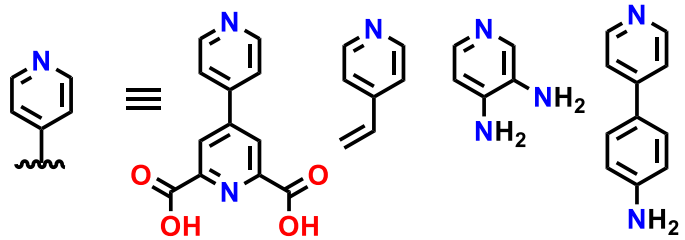

Chapter 2

Objective 5

The last objective of this thesis is the detailed mechanistic understanding of the water oxidation reaction by a dinuclear cobalt complex $\{[Co^{III}(trpy)]_2(\mu\text{-bpp})(\mu\text{-OO})\}^{3+}$, based on the trapping and characterization of intermediates involved in the catalytic cycle and isotopic labelling experiments.

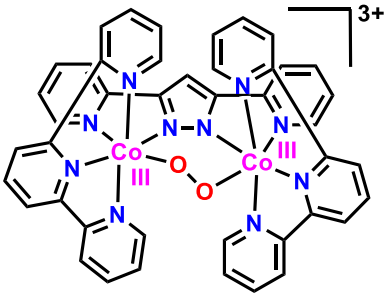

$\{[Co^{III}(trpy)]_2(\mu\text{-bpp})(\mu\text{-OO})\}^{3+}$

Chapter 3

Synthesis, characterization, redox properties, electronic effects and water oxidation activity of a series of ruthenium complexes containing pyridine carboxylate ligands are reported in this chapter. It is shown that the electronic perturbation to the metal center exerted by different orientation and geometry of the ligands together with the electron donating properties produce dramatic effects in both redox properties and water oxidation catalytic performance of the systems.

Chapter 3A

3A. Synthesis, Characterization and Water Oxidation Activity of Isomeric Ru-Complexes

Md Asmaul Hoque,[1,2] Somnath Maji,[1] Jordi Benet-Buchholz,[1] Carolina Gimbert-Suriñach,[1] Goutam Kumar Lahiri,[4] Antoni Llobet[1,3]

[1] Institute of Chemical Research of Catalonia (ICIQ), Barcelona Institute of Science and Technology, Av. Països Catalans 16, 43007 Tarragona, Spain

[2]Departament de Química Física i Inorganica, Universitat Rovira i Virgili, Campus Sescelades, C/Marcel·lí Domingo, s/n, 43007 Tarragona, Spain

[3]Universitat Autònoma de Barcelona, Departament de Química, Cerdanyola del Vallès, 08193 Barcelona, Spain

[4]Department of Chemistry, Indian Institute of Technology Bombay, Powai, Mumbai 400076, India

III

Contributions

Md Asmaul Hoque synthesized and characterized all the new compounds and performed the electrochemical, spectroscopic analysis together with the catalytic tests and prepared the manuscript.

Chapter 3A

Abstract

We report the synthesis and characterization of the isomeric ruthenium complexes with the general formula *cis*- and *trans*-[Ru(trpy)(qc)X]$^{n+}$ (trpy is 2,2':6',2"-terpyridine, qc is 8-quinolinecarboxylate, *cis*-**1** and *trans*-**1**, X = Cl, n = 0; *cis*-**2** and *trans*-**2**, X = OH_2, n = 1) with respect to the relative disposition of the carboxylate and X ligands. For comparison purposes, another set of Ruthenium complexes with general formula *cis*- and *trans*-[Ru(trpy)(pic)(OH_2)]$^{+}$ (pic is 2-picolinate (*trans*-**3**, *cis*-**3**) have been prepared. The complexes with qc ligand show a more distorted geometry as compared to the complexes with pic ligand. In all the cases, *trans*-isomers show lower redox potential values for all the redox couples relative to the *cis*-isomers. Complexes *cis*-**2** and *trans*-**2** with six-member chelate ring show higher catalytic activity than *cis*-**3** and *trans*-**3**. Overall, it was shown that the electronic perturbation to the metal center exerted by different orientation and geometry of ligands produced dramatic effects both in redox properties and in catalytic performance of the systems.

Graphical Abstract

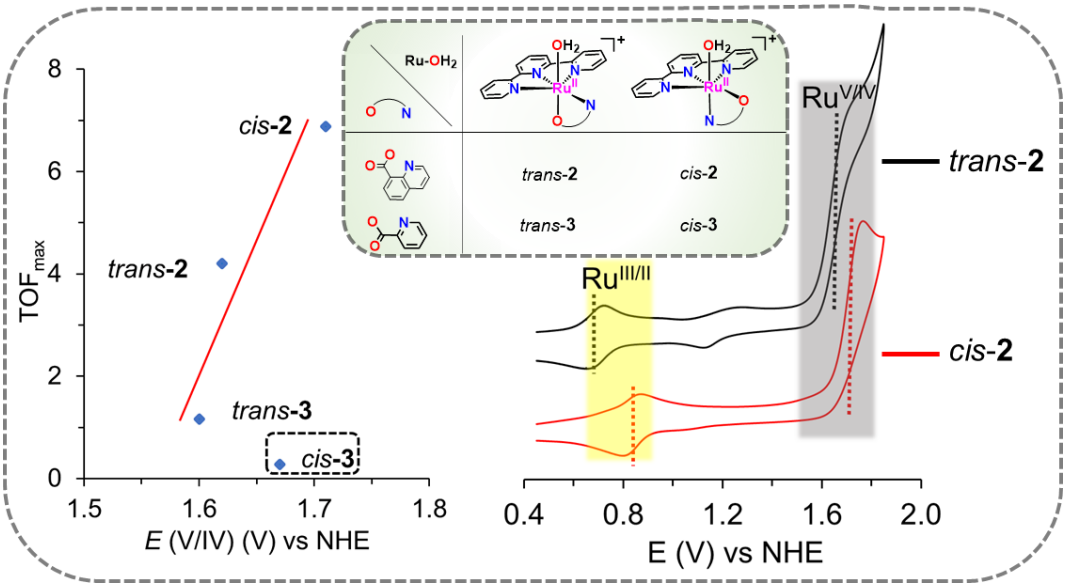

Keywords: Ruthenium, Isomers, Geometry, Redox properties, Water oxidation catalysis

Chapter 3A

3A. 1. Introduction

The conversion of solar energy to chemical energy is considered a promising option for the generation of renewable and clean fuel for transportation.[1] One way of achieving this goal is by performing light induced water splitting into hydrogen and oxygen as indicated in equation 1, catalyzed by suitable molecular catalysts,

$2H_2O + h\nu \rightarrow 2H_2 + O_2$, $\Delta E^o = 1.23$ V vs. NHE.[2] (1)

In this process, the water oxidation half reaction is particularly challenging due to the large endothermicity and mechanistic complexity of the process that requires the transfer of four electrons and the generation of an O-O bond.[3] For this reason, the study of new molecular water oxidation catalysts (WOC) has become one of the main research areas in the field, achieving tremendous progress in the last ten years. Among the most studied catalysts are those based on ruthenium, starting from the first well characterized synthetic molecular WOC by T. J. Meyer, (*cis*,*cis*-$[(bpy)_2(H_2O)Ru^{III}ORu^{III}(OH_2)(bpy)_2]^{4+}$, where bpy is 2,2'-bipyridine)[4] to the recently reported fastest molecular WOC based on mononuclear complexes as catalyst precursors with auxiliary ligands containing carboxylate groups $[Ru(bda)(isoq)_2]$,[5] $[Ru(tda)(py)_2]$[6], $[Ru(pdc)(bpy)_2]$[7] and $[Ru(mcbp)(py)_2]$[8] (bda^{2-} is (2,2'-bipyridine)-6,6'-dicarboxylate, tda^{2-} is 2,2':6',2"-terpyridine-6,6"-dicarboxylate, pdc^{2-} is pyridine-2,6-dicarboxylate, $mcbp^{2-}$is 2,6-bis(1-methyl-4-(carboxylate)benzimidazol-2-yl)pyridine, isoq is Isoquinoline and py is pyridine). Further, these catalyst precursors have also been successfully used in water oxidation reactions triggered by light.[9-13]

The ability of Ru-OH_2 derivatives to undergo facile pH-dependent proton-coupled electron-transfer (PCET) processes leading to the formation of highly oxidized Ru^V=O species is a key because it can do O-O bond formation via water nucleophilic attack (WNA)[14-16] due to the electrophilicity of the Ru=O intermediate or dimerization through oxyl radical formation (I2M).[5,17] This significant information based on spectroscopic, electrochemical and analytical techniques together with the valuable complementary information provided by computational studies, allow the scientific community to rationally design powerful and oxidatively rugged molecular water oxidation catalyst.[18-23]

The present report describes the synthesis, structural and spectroscopic characterization as well as the water oxidation catalytic activity of single site Ru-aquo isomeric complexes and their precursors with general formula *cis*- and *trans*-[Ru(trpy)(qc)Cl] (*trans*-**1**, *cis*-**1**) and *cis*- and *trans*-$[Ru(trpy)(qc)(OH_2)]^+$ (*trans*-**2**, *cis*-**2**), where trpy is 2,2':6',2"-terpyridine and qc is 8-

quinolinecarboxylate. In addition, two other similar complexes *cis*- and *trans*-[Ru(trpy)(pic)(OH_2)]$^+$ where pic is 2-picolinate (*trans*-**3**, *cis*-**3**) have also been studied (Chart 1 and Scheme 1). The choice of qc and pic ligands are of special interest as they are not only introducing a σ-donating carboxylate moiety in the catalyst that can help to reduce the overpotential for the water oxidation reaction but also they can create different isomeric compounds (*cis* and *trans* in respect to the Ru-OH_2 group) along with different geometric configuration with different ring size around the metal center (six-membered ring for qc and five-membered ring for pic). It has been shown that electronic perturbation to the metal center exerted by relative disposition and geometry of the qc or pic ligands with regard to the aquo ligand around the metal center produce dramatic effect both in redox properties and catalytic performance.

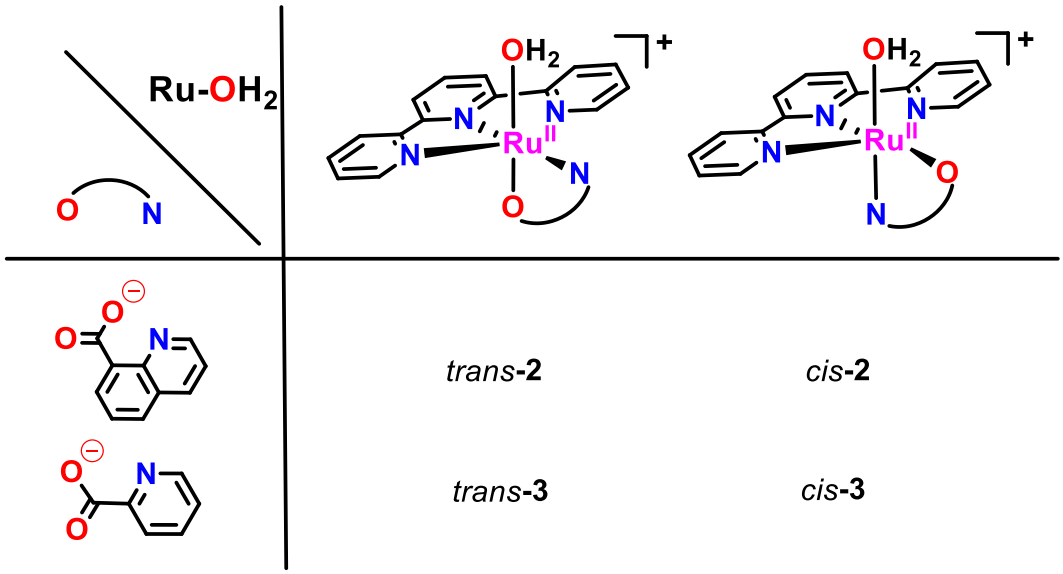

Chart 1. Ruthenium-aquo complexes studied in this work.

3A. 2. Experimental Section

Materials

The precursor complex $[RuCl_3(trpy)]$ (trpy = 2,2':6',2"-terpyridine), *trans*-$[Ru^{II}(trpy)(pic)Cl]$, *cis*-$[Ru^{II}(trpy)(pic)Cl]$, *trans*-$[Ru^{II}(trpy)(pic)(OH_2)]ClO_4$ and *cis*-$[Ru^{II}(trpy)(pic)(OH_2)]ClO_4$ were prepared according to the literature procedures.[24,25] The ligand 8-quinolinecarboxylic acid and other reagents and chemicals were obtained from Aldrich and used as received. When required, solvents were dried by following the standard procedures, distilled under nitrogen and used immediately. High purity de-ionized water used for the electrochemistry experiments were obtained by passing distilled water through a nanopure Milli-Q water purification system. For other spectroscopic and electrochemical studies, HPLC-grade solvents were used.

Instrumentation and Methods

NMR spectra were recorded on a 500 MHz Bruker Avance Ultrashield NMR spectrometer. UV/Vis spectroscopy was performed on a Cary 50 (Varian) UV/Vis spectrophotometer in 1 cm quartz cuvettes. ESI-Mass spectra were recorded using micromass Q-TOF mass spectrometer. Elemental analyses were carried out on Perkin-Elmer 240C elemental analyzer. Cyclic voltammetry (CV), differential pulse voltammetry (DPV) experiments were performed on an IJ-Cambria CHI-660 potentiostat using a three-electrode cell. Typical CV experiments were carried out at a scan rate of 100 mVs^{-1}. The DPV parameters were ΔE = 4 mV, Amplitude = 50 mV, Pulse width = 0.05 s, Sampling width = 0.0167 s, Pulse period = 0.5 s. A glassy carbon disk (ϕ = 0.3 cm, S = 0.07 cm^2) was used as working electrode(WE), Pt disk as counter electrode (CE), and a Hg/Hg_2SO_4 (K_2SO_4 saturated) as a reference electrode (RE). All potentials were converted to NHE by adding 0.65 V. Glassy carbon electrodes were polished with 0.05 µm alumina (Al_2O_3) and rinsed with water and acetone followed by blow-drying before each measurement. CVs and DPVs were iR compensated by the potentiostat in all the measurements. In organic solvent, all the complexes were dissolved in CH_3CN containing the necessary amount of $[(n\text{-}Bu)_4N][PF_6]$ (TBAH) as supporting electrolyte to yield a 0.1 M ionic strength solution. In aqueous solution, the electrochemical experiments were carried out in 0.1 M CF_3SO_3H (pH 1.0). $E_{1/2}$ values reported in this work were estimated from CV experiments as the average of the oxidative and reductive peak potentials ($E_{p,a} + E_{p,c}$)/2 or taken as E (I_{max}) from DPV measurements. The Pourbaix diagrams were built using the following buffers: sodium dihydrogen phosphate/phosphoric acid up to pH = 4 (pK_a = 2.12), sodium hydrogen phosphate/sodium dihydrogen phosphate up to pH = 9 (pK_a = 7.67), sodium hydrogen

phosphate/sodium phosphate up to pH = 13 (pK_a = 12.12) and also 0.1 M CF_3SO_3H for pH = 1.0. The concentration of the species was approximately 1 mM. The pH of the solutions was determined by a pHmeter (CRISON, Basic 20^+) calibrated before measurements through standard solutions at pH 4.01, 7.00 and 9.21.

Online manometric measurements were performed on a Testo 521 differential pressure manometer with an operating range of 0.1-10 kPa and accuracy within 0.5% of the measurements. The manometer was coupled to thermostatic reaction vessels for dynamic monitoring of the headspace pressure above each reaction solution. The manometer's secondary ports were connected to thermostatic reaction vessels containing the same solvents and headspace volumes as the sample vials. Each measurement for a reaction solution (2.0 mL) was performed at 298 K.

Single Crystal X-Ray Structure Determinations

Crystal Preparation: Single crystals of *cis*-**1**, *trans*-**1**, *trans*-**2** and *cis*-[Ru^{II}(trpy)(pic)Cl] were grown by slow evaporations of 1:1 methanol:dichloromethane, 1:1 dichloromethane:diethylether, 1:1 dichloromethane: toluene and 1:1 methanol:dichloromethane, respectively. The crystals used for structure determination were selected using a Zeiss stereomicroscope using polarized light and prepared under inert conditions immersed in perfluoropolyether as protecting oil for manipulation.

Data Collection: Crystal structure determination for sample *cis*-**1**, *trans*-**1** and *cis*-[Ru^{II}(trpy)(pic)Cl] were carried out using a Apex DUO Kappa 4-axis goniometer equipped with an APPEX 2 4K CCD area detector, a Microfocus Source E025 IuS using MoK_α radiation, Quazar MX multilayer Optics as monochromator and an Oxford Cryosystems low temperature device Cryostream 700 plus (T = -173 ˚C). Crystal structure determination for samples Full-sphere data collection was used with ω and φ scans. *Programs used:* Data collection APEX-2,[26] data reduction Bruker Saint[27] V/.60A and absorption correction SADABS.[28]

Crystal structure determination for sample *trans*-**2** was carried out at -123 ˚C using a Xcalibur Sapphire3 goniometer using MoK_α radiation. *Programs used:* Data collection and reduction with CrysAlisPro[29] V/.60A and absorption correction with Scale3 Abspack scaling algorithm.[30]

Structure Solution and Refinement: Crystal structure solution was achieved using the computer program SHELXT.[31] Visualization was performed with the program SHELXle.[32] Missing atoms were subsequently located from difference Fourier synthesis and added to the

atom list. Least-squares refinement on F^2 using all measured intensities was carried out using the program SHELXL 2015.[33] All non-hydrogen atoms were refined including anisotropic displacement parameters. *cis*-**1**: The asymmetric unit contains two different compounds of the metal complex sharing its position (ratio 90:10) and one and half water molecules disordered in four positions (ratio: 0.50:0.50:0.25:0.25). The metal complex is coordinated with 90 % ratio to a chloro anion and with 10 % to a methanolate. *trans*-**2**: The asymmetric unit contains one molecule of the metalorganic complex coordinated to a water molecule, one additional water molecule and one PF_6^- anion. The PF_6^- anion is disordered in two orientations (ratio 91:9). *cis*-[Ru^{II}(trpy)(pic)Cl]: The asymmetric unit contains one molecule of the metal complex and 0.75 molecules of dichloromethane. The dichloromethane molecules are highly disordered in four orientations/positions.

Synthesis of Isomeric [Ru^{II}(trpy)(qc)Cl] (*trans*-1 and *cis*-1). In a 100 mL two neck round bottom flask, [$RuCl_3$(trpy)] (100 mg, 0.23 mmol), 8-quinolinecarboxylic acid (Hqc) (55 mg, 0.32 mmol) and NEt_3 (0.2 mL, 1.5 mmol) were dissolved in 20 mL of degassed ethanol. The mixture was heated to reflux for 6 h under nitrogen atmosphere. The mixture was then evaporated to dryness and the resulting dark solid was dissolved in the minimum volume of CH_2Cl_2 and purified by chromatography using a neutral alumina column. The blue-violet solution corresponding to the major isomer *trans*-**1** was eluted first with CH_2Cl_2:CH_3OH (20:1) followed by the red-violet solution of the minor isomer *cis*-**1** with CH_2Cl_2:CH_3OH (10:1) mixture. On removal of the solvent under reduced pressure the pure isomeric complexes *trans*-**1** and *cis*-**1** were obtained in the solid state.

***trans*-1:** Yield, 85 mg (0.16 mmol, 70%). Anal. Calcd. for ($C_{25}H_{17}N_4ClO_2Ru$): C, 55.35%; H, 3.16%; N, 10.33%. Found: C, 55.57%; H, 2.96%; N, 10.51%. λ [nm](ε[$M^{-1}cm^{-1}$]) in dicholoromethane: 578(11760), 420(10590), 328(38760), 315(34350), 281(38920), 233(74070). ESI^+-MS (*m/z*): 543.30 ([*trans*-**1**+H]$^+$, Calcd. 543.01), 507.30 ([*trans*-**1**-Cl]$^+$, Calcd. 507.03). ^{1}H NMR (500 MHz [d_6]- DMSO) δ: 10.43 (H^7, d, *J*= 4.86 Hz, 1H), 8.81 (H^9, d, *J*= 8.01 Hz, 1H), 8.63 ($H^{4\&5}$, dd, *J*= 7.7 Hz and *J*=2.83 Hz, 4H), 8.51 (H^{12}, d, *J*= 7.45Hz, 1H), 8.40 (H^{10}, d, *J*= 7.82, 1H), 8.0 (H^1, d, *J*= 5.47 Hz, 2H), 7.92 ($H^{3,6\&8}$, m, 4H), 7.77 (H^{11}, t, *J*= 7.7 Hz, 1H), 7.41 (H^2, t, *J*= 6.5 Hz, 2H). ^{13}C-NMR (125 MHz, [d_6]- DMSO) δ: 169.1, 160.6, 160.4, 158.5, 152.2, 147.8, 138.2, 136.7, 136.2, 133.7, 131.3, 130.6, 130.5, 127.2, 127.0, 123.2, 121.9 and 121.5.

***cis*-1:** Yield, 6 mg (0.01 mmol, 4%). Anal. Calcd. for ($C_{25}H_{17}N_4ClO_2Ru$): C, 55.35%; H, 3.16%; N, 10.33%. Found: C, 55.27%; H, 3.10%; N, 10.58%. λ [nm](ε[$M^{-1}cm^{-1}$]) in acetonitrile: 545(11360), 483(sh), 372(11300), 317(46680), 279(42080), 235(79690). ESI^+-MS (*m/z*): 543.19

([*cis*-**1**+H]$^+$, Calcd. 543.01), 507.10 ([*cis*-**1**-Cl]$^+$, Calcd. 507.03). ^{1}H NMR (500MHz [d_6]-DMSO) δ: 9.0 (H^7, dd, *J*= 4.86 Hz, and *J*= 1.7 Hz, 1H), 8.62 ($H^{1,4\&5}$, m, 6H), 8.06 (H^{10} dd, *J*= 8.31 Hz and *J*= 1.31 Hz, 1H), 7.95 ($H^{2\&9}$, m, 3H), 7.82 (H^6, t, *J*=7.98, 1H), 7.73 (H^8, t, *J*= 7.74 Hz, 1H), 7.56 (H^3, dt, *J*= 5.65 Hz and *J*= 1.14 Hz, 2H), 7.05 (H^{12}, dd, *J*= 5.41 and Hz *J*= 1.43 Hz, 1H), 6.82 (H^{11}, dd, *J*= 8.16 Hz and *J*= 5.45 Hz, 1H). ^{13}C-NMR (125MHz, [d_6]-DMSO) δ: 169.1, 161.4, 159.7, 153.7, 151.5, 148.2, 137.4, 136.7, 136.4, 133.3, 131.6, 129.3, 129.1, 127.6, 127.1, 123.4, 122.5 and 121.3.

III

Synthesis of *trans*-[Ru^{II}(trpy)(qc)(H_2O)](PF_6) (*trans*-2). In a 50 mL two neck round bottom flask, *trans*-**1** (100 mg, 0.18 mmol) was dissolved in 20 mL of acetone: water mixture (3:1, *v/v*) and $TlNO_3$ (60 mg, 0.23 mmol) was added to the solution and stirred for 1 h at reflux. The initial blue-violet color of the solution was changed to red-violet with the precipitation of TlCl. The cooled solution was filtered over Celite® to remove TlCl. The filtrate was then concentrated to approx. 2 mL in vacuum and 3 mL saturated solution of NH_4PF_6 was added. The resulting solution was allowed to stand at 0˚C for complete precipitation. It was then filtered and the residue washed with ice-cold water for several times and dried in vacuum over P_4O_{10}. Yield: 110 mg (0.16 mmol, 88%). Anal. Calcd. for ($C_{25}H_{19}N_4O_3RuPF_6$): C, 44.78%; H, 2.86%; N, 8.36%. Found: C, 44.98%; H, 2.95%; N, 8.62%. ESI$^+$-MS (*m/z*): 507.10 ({*trans*-**2**-PF_6-OH_2}$^+$, Calcd. 507.03). ^{1}H NMR (500MHz, [d_2]-D_2O) δ: 9.59 (H^7, d, *J*= 5.52 Hz, 1H), 8.73 (H^9, d, *J*= 8.41 Hz, 1H), 8.39 ($H^{4,5,10\&12}$, m, 6H), 8.08 (H^1, d, *J*= 5.60Hz, 2H), 7.89 ($H^{3,8\&11}$, m, 4H), 7.77 (H^6, t, *J*= 7.65 Hz, 1H), 7.31 (H^2, t, *J*= 6.93 Hz, 2H). ^{13}C- NMR (125MHz, [d_2]-D_2O) δ: 175.2, 160.7, 160.3, 155.3, 153.2, 147.6, 138.8, 137.5, 137.2, 135.4, 134.0, 130.7, 127.1, 127.0, 123.4, 123.2, 122.1 and 121.8.

Synthesis of *cis*-[Ru^{II}(trpy)(qc)(H_2O)]$^+$ (*cis*-2). In a 25 mL two neck round bottom flask, *cis*-**1** (5 mg, 0.01 mmol) was dissolved and $TlNO_3$ (5 mg, 0.02 mmol) was suspended in 4 mL of acetone:water mixture (3:1, *v/v*) and stirred for 1 h at reflux. The initial red-violet color of the solution was changed to red with the precipitation of TlCl. The cooled solution was filtered to remove TlCl. The filtrate was dried in vacuum over P_4O_{10} and dissolved in D_2O for NMR and pH 1 for electrochemistry. ^{1}H NMR (500MHz, [d_2]-D_2O) δ: 8.97 (H^7, d, *J*= 7.63 Hz, 1H), 8.56 (H^1, d, *J*= 5.48 Hz, 2H), 8.37 (H^5, d, *J*= 8.25 Hz, 2H), 8.31 (H^4, d, *J*= 8.11 Hz, 2H), 7.98 (H^9, d, *J*= 8.09 Hz, 1H), 7.88 ($H^{3,6\&10}$, m, 4H), 7.72 (H^8, t, *J*= 7.96 Hz, 1H), 7.40 (H^2, t, *J*= 6.65 Hz, 2H), 7.30 (H^{12}, d, *J*= 5.37 Hz, 1H), 6.62 (H^{11}, dd, *J*= 7.95 Hz and *J*= 5.93 Hz, 1H).

3A. 3. Results and Discussion

3A. 3. 1. Synthesis, Spectroscopic and Structural Characterization

The synthetic strategy used for the preparation of the complexes described in this work is outlined in Scheme 1. The reaction of 8-quinolinecarboxylic acid with the ruthenium precursor complex [$RuCl_3$(trpy)] in the presence of NEt_3 in EtOH results in a 15:1 mixture of isomeric complexes of *trans*- and *cis*-[Ru^{II}(trpy)(qc)Cl] (*trans*-**1** and *cis*-**1**) respectively**.** The *cis* and *trans* assignment refers to the relative disposition of the chlorido and carboxylato ligands. Both isomers can be separated by column chromatography and are stable in the solid state and in solution. The corresponding *trans* and *cis* isomeric aquo complexes [Ru(trpy)(qc)(OH_2)]$^+$ (*trans*-**2** and *cis*-**2**) have been synthesized *via* substitution of the chlorido ligand by an H_2O using $TlNO_3$ in acetone:H_2O (3:1) as the solvent mixture and formation of insoluble TlCl. Complexes *trans*-**1,** *cis*-**1**, *trans*-**2** and *cis*-**2** have been thoroughly characterized by means of analytical, spectroscopic and electrochemical techniques.

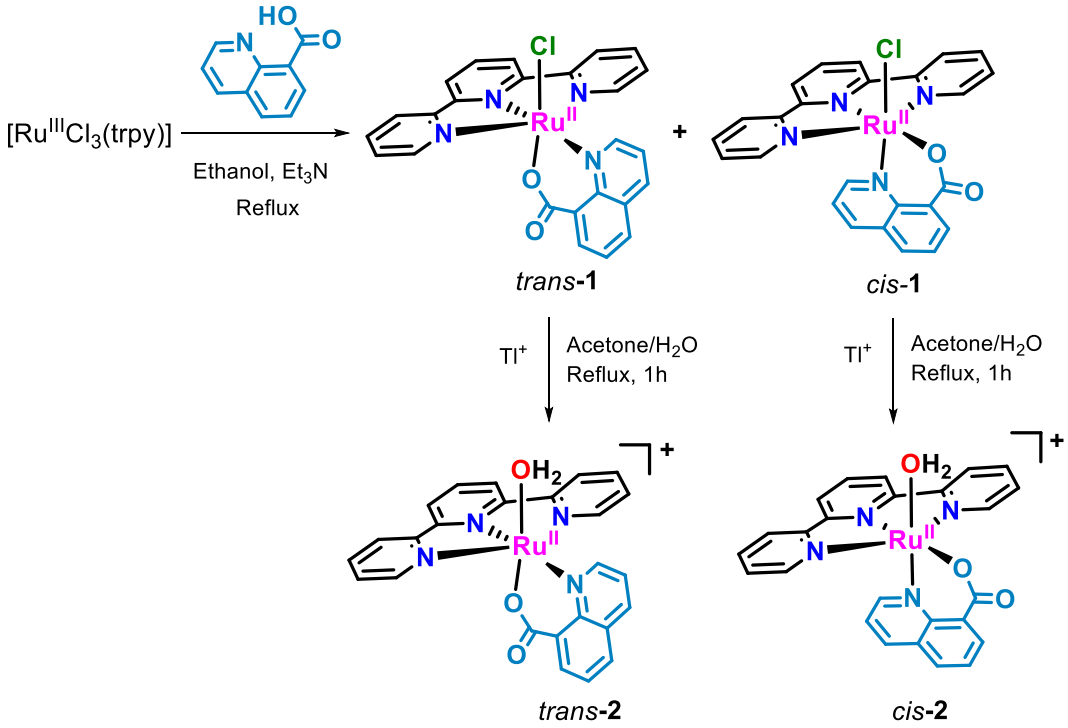

Scheme 1. Synthetic strategy and labelling scheme used for the ligands and complexes described in this work.

Chapter 3A

Single crystals of the complexes *trans*-**1**, *cis*-**1** and *trans*-**2** together with the related picolinate derivative *cis*-[Ru(trpy)(pic)Cl] were obtained and their ORTEP structures are shown in Figure 1. All the complexes display the typical slightly distorted octahedral geometry around the ruthenium, as expected for low-spin d^6 Ru^{II}.[34,35] The bidentate ligand 8-quinolinecarboxylate occupies both axial and equatorial positions and is bonded to the ruthenium metal *via* the anionic oxygen atom O1 (carboxylate) and neutral nitrogen atom N1 (quinoline) (See Figure 1 for labeling key) donors forming a six-membered chelate ring. The meridional configuration of trpy introduces expected geometrical constraint as has been reflected in smaller *trans* angle involving the trpy ligand, N2-Ru-N4 of 159.6(5)° and 159.26(13) in *trans*-**1** and *trans*-**2**, respectively. The central Ru-N3(trpy) bond length of 1.924(11) Å or 1.942(4) Å in *trans*-**1** and *trans*-**2**, respectively, is significantly shorter than the corresponding distances involving the terminal pyridine rings of trpy, Ru-N2(trpy), 2.082(11)/2.064(4) Å and Ru-N4(trpy), 2.060(10)/2.058(3) Å in *trans*-**1**/*trans*-**2**, respectively, while the Ru-N1(qc) in *trans* to the Ru-N3(trpy) bonds are slightly longer, 2.083(10) Å/2.085(3) Å.[36] The Ru-O1(qc) bond length of 1.966(7) Å in the aquo derivative *trans*-**2** is appreciably shorter than that in *trans*-**1** (2.050(3) Å). The Ru-O3(H_2O) bond distance of 2.094(3) Å in *trans*-**2** agrees well with the reported analogous ruthenium-aquo species.[37]

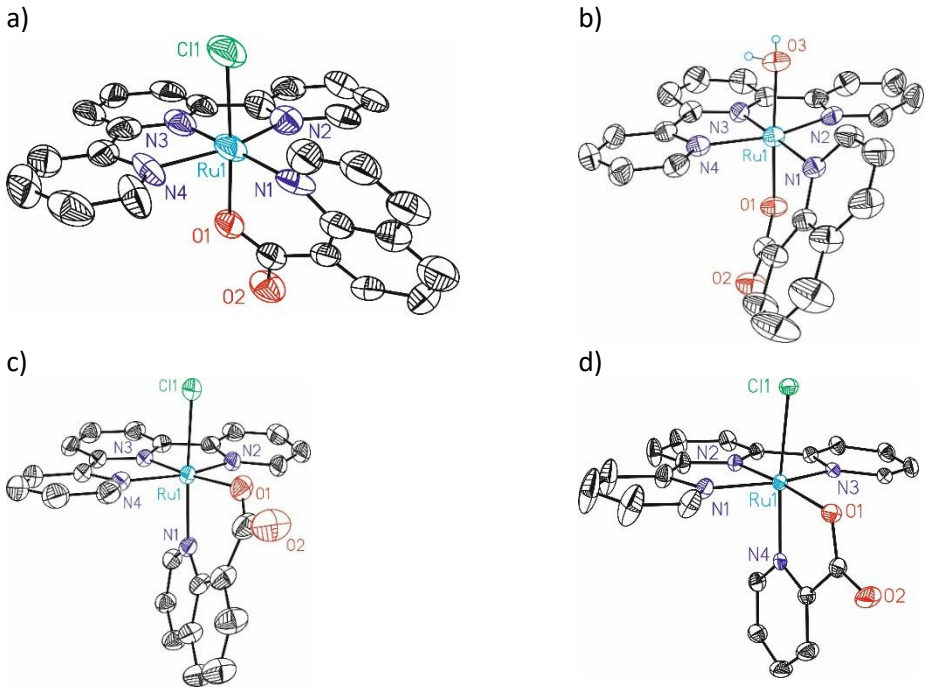

Figure 1. ORTEP diagrams of (a) *trans*-[Ru(trpy)(qc)Cl] (*trans*-**1**), (b) *trans*-[Ru(trpy)(qc)(OH_2)]$^+$ (*trans*-**2**), (c) *cis*-[Ru(trpy)(qc)Cl] (*cis*-**1**) and (d) *cis*-[Ru(trpy)(pic)Cl]. Thermal ellipsoids are drawn at 50% probability. The solvents of crystallization and hydrogen atoms are omitted for clarity, except for the OH_2 ligand.

The Ru-Cl bond distances in *trans*-**1** (2.311(3) Å) is 0.08 Å shorter than that in *cis*-**1** (2.393(12) Å).[38] We attribute this difference to the electronegativity of the Cl ligand and due to the presence of strong σ–donating negatively charge O^- of qc trans to Cl^- in *trans*-**1** as compared to *cis*-**1**, where the neutral N of the qc is trans to Cl^-. This in turn makes the Ru-O bond shorter in *trans*-**1** (1.966(7) Å) relative to *cis*-**1** (2.085(3) Å). On the other hand, the Ru-N(qc) distance in *cis*-**1** (2.061(3) Å) is shorter than that in *trans*-**1** (2.083(10) Å), mainly due to the enhanced $Ru^{II}\rightarrow$quinoline back-bonding via involvement of σ- and π-donating chlorido ligand trans to N1(qc) in *cis*-**1**. They also show appreciable differences in the trans angle involving qc-Ru-Cl: O1-Ru-Cl at 176.12(5)˚ in *trans*-**1** vs N1-Ru-Cl at 172.93(10)˚ in *cis*-**1**; the bulkier quinoline ring trans to Ru-Cl in *cis*-**1** makes it relatively bent (Figure S12 and Tables S2-S3). Interestingly, the dihedral angles between the planes of qc and trpy in *cis*-**1**, qc-Ru-trpy, is 76.2˚ and for the analog complex having the picolinate ligand *cis*-[Ru(trpy)(pic)Cl], the angle pic-Ru-trpy is 87.6˚ (Figure S13). This difference clearly indicates the presence of more distortion in the complex containing the qc ligand as compared to that of the complex containing the pic ligand.

Chapter 3A

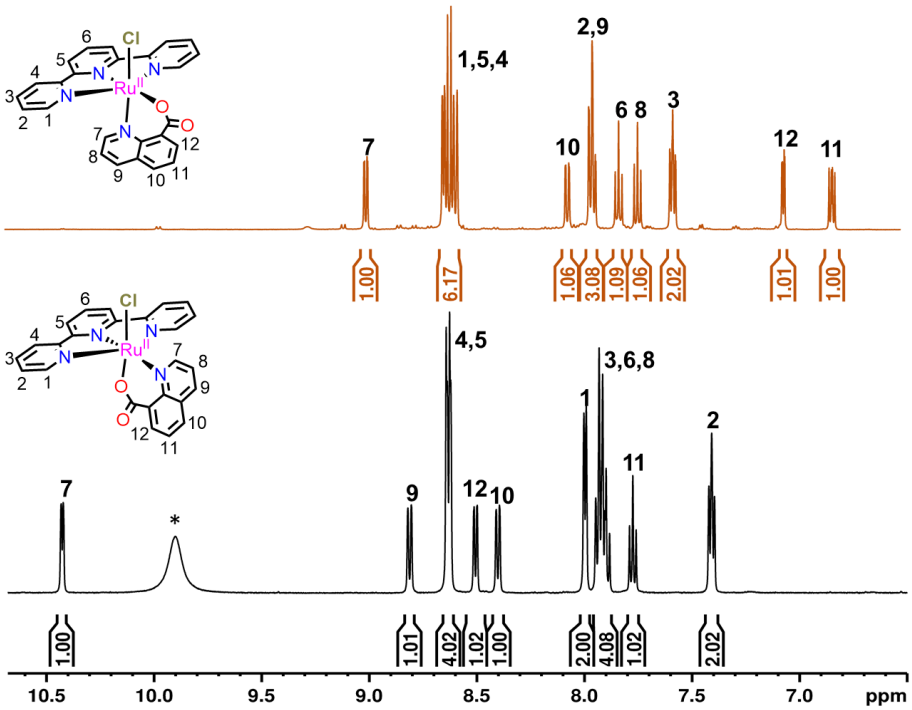

Figure 2. ^{1}H NMR spectra in ([d_6]-DMSO (500 MHz, 298 K) and assignment for complexes (top) *cis*-**1** and (bottom) *trans*-**1**. Asterisk is unidentified species.

The ^{1}H NMR spectra of *trans*-**1** and *cis*-**1** are quite distinct, as expected (Figure 2). In both cases, the symmetric nature of the complexes observed in the solid state is maintained in solution as indicated by a single set of signals for the trpy ligand. A characteristic feature of *trans*-**1** is the typical signal at low field δ = 10.4 ppm[39] for a proton in *ortho* to the quinoline nitrogen of the bidentate ligand (proton H^7) de-shielded due to the diamagnetic anisotropy generated by the chlorido ligand,[40,41] allowing us to fully assign all the signals. A further clue in this direction is given by the NOE signal between H^7 and H^1 (with a distance of 2.72 Å in the solid state structure, see Figure S1-S3). None of these features are present in the spectrum of *cis*-**1**, so its assignment is based on intensities of the integrals with the help of 2-dimensional experiments also shows that the structures remain similar in solution to those described in the solid state (Figure S4-S6). The NMR analysis of complexes *trans*-**2** and *cis*-**2** were performed in deuterated water to avoid ligand exchange with coordinating ligands such as DMSO. Compound *trans*-**2** also shows the typical downfield signal of H7 due to anisotropic effects with the aquo ligand (δ = 9.6 ppm, Figure S7 and S11).

3A. 3. 2-Electrochemical Characterization

The redox properties of all the complexes were analyzed by cyclic voltammetry (CV) and differential pulse voltammetry (DPV) in acetonitrile (CH_3CN) containing 0.1 M of [(*n*-Bu)$_4$N][PF_6] (TBAH) for complexes *trans*-**1** and *cis*-**1** and 0.1 M ionic strength buffered aqueous solutions at different pHs for complexes *trans*-**2** and *cis*-**2**. All redox potentials reported in this work were meausured with Hg/Hg_2SO_4 reference electrode and referred to the NHE electrode.

In acetonitrile solution, both *trans*-**1** and *cis*-**1** isomers show a chemically reversible and electrochemically quasi-reversible one-electron oxidation wave at $E_{1/2}$ = 0.58 V (ΔE = 60 mV) and $E_{1/2}$ = 0.67 V (ΔE = 63 mV) respectively, assigned to the $Ru^{III/II}$ redox couple (Figure S14). The slight cathodic shift of the $Ru^{III/II}$ couple observed for *trans*-**1** as compared to *cis*-**1** is attributed to the higher electron-density on the ruthenium provided by the chlorido and carboxylato moieties when they are in trans relative position. This trend is in agreement with the shorter Ru-O and Ru-Cl distances observed in the solid state structure of *trans*-**1** as compared to *cis*-**1** and highlights the strong influence of the relative position (*trans vs. cis*) of the ligands.

The redox chemistry of the aquo complexes *trans*-**2** and *cis*-**2** were studied in pH 1 (0.1 M triflic acid) solution and the appropriate phosphate buffer for measurement at pH > 1 (Figure S16). Both isomers exhibit two successive pH dependent redox couples associated with proton coupled electron-transfer (PCET) processes with the formation of the Ru^{III} and Ru^{IV} species with different level of protonation of the aquo group, hydroxo or aquo depending on the pH (Equations 2 and 3). Further scanning to more positive potentials shows a third pH independent oxidation leading to the [Ru^{V}=O] (Equation 4) which is followed by a large anodic current attributed to the electrocatalytic oxidation of water to produce oxygen gas (Figure 3a).

$$[Ru^{II}(trpy)(qc)(H_2O)]^+ \rightarrow [Ru^{III}(trpy)(qc)(HO)]^+ + H^+ + e^- \quad (2)$$

$$[Ru^{III}(trpy)(qc)(HO)]^+ \rightarrow [Ru^{IV}(trpy)(qc)(O)]^+ + H^+ + e^- \quad (3)$$

$$[Ru^{IV}(trpy)(qc)(O)]^+ \rightarrow [Ru^{V}(trpy)(qc)(O)]^{2+} + e^- \quad (4)$$

Interestingly, the $[Ru^{III}\text{-}OH_2]^{2+}/[Ru^{II}\text{-}OH_2]^+$ redox couple for *trans*-**2** in pH 1 (0.67 V), is 150 mV lower as compare to *cis*-**2** (0.82 V), and this is due to the *trans* influence of the carboxylate

group to the aquo ligand making the metal center electronically richer, hence easy to oxidize. On the other hand $[Ru^{V}\text{-}O]^{2+}/[Ru^{IV}\text{-}O]^{+}$ redox couple is only 90 mV lower (Table 1).

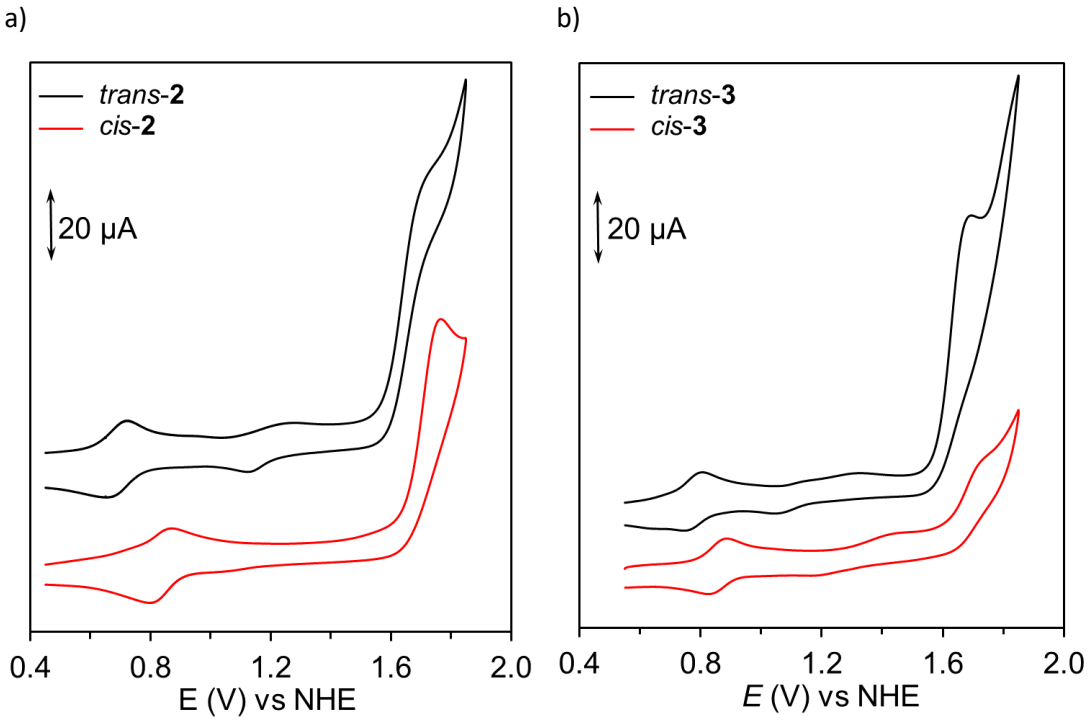

Figure 3. a) CVs of *trans*-**2** (black) and *cis*-**2** (red), b) CVs of *trans*-**3** (black) and *cis*-**3** (red) in 0.1 M triflic acid (pH 1). Working electrode: glassy carbon disk; counter electrode: platinum disk; reference electrode: Hg/Hg_2SO_4.

The Pourbaix diagrams for *trans*-**2** and *cis*-**2** (Figure 4) reveal that the $[Ru^{III}\text{-}OH]^{+}/[Ru^{II}\text{-}OH_2]^{+}$ and $[Ru^{IV}\text{-}O]^{+}/[Ru^{III}\text{-}OH]^{+}$ redox processes each change by approximately 59 mV per pH decade over a large pH range (10 > pH > 2) for *trans*-**2** and (10 > pH > 3) for *cis*-**2** (Figure 4) respectively. The $Ru^{III/II}$ redox processes of *trans*-**2** (at pH < 2) and *cis*-**2** (at pH < 3) are not associated with the loss of a proton based on the pH-independent behavior of the $[Ru^{III}\text{-}OH_2]^{2+}/[Ru^{II}\text{-}OH_2]^{+}$ redox couple. Consequently, the higher oxidation step is accompanied with the loss of two protons (i.e. $[Ru^{IV}\text{-}O]^{+}/[Ru^{III}\text{-}OH_2]^{2+}$) in strongly acidic medium. This assignment is corroborated by the slope of -120 mV/pH below pH 2.0 for *trans*-**2** and -121 mV/pH below pH 3.0 for *cis*-**2**. At pH >10, the potentials for the $Ru^{IV/III}$ couple continue to vary linearly with pH, with a slope near to -59 mV/pH unit, while the potentials for the $Ru^{III/II}$ couple become pH independent as a consequence of no loss of proton from $[Ru^{II}\text{-}OH]$ with $pK_a \approx 10.6$. The $[Ru^{V}\text{-}O]^{2+}/[Ru^{IV}\text{-}O]^{+}$ redox couple remains relatively constant at ~1.62 V and ~1.71 V vs NHE for *trans*-**2** and *cis*-**2** respectively, over the whole pH 1-13 range.

It is worth mentioning that *cis*-**2** over time in aqueous solution slowly converts to *trans*-**2** as can be seen in Figure S16b and Figure S18. This is in good agreement with lower isolated yield

of the *cis*-**1** compared to the *trans*-**1** indicating that the latter is thermodynamically more stable.

a)

b)

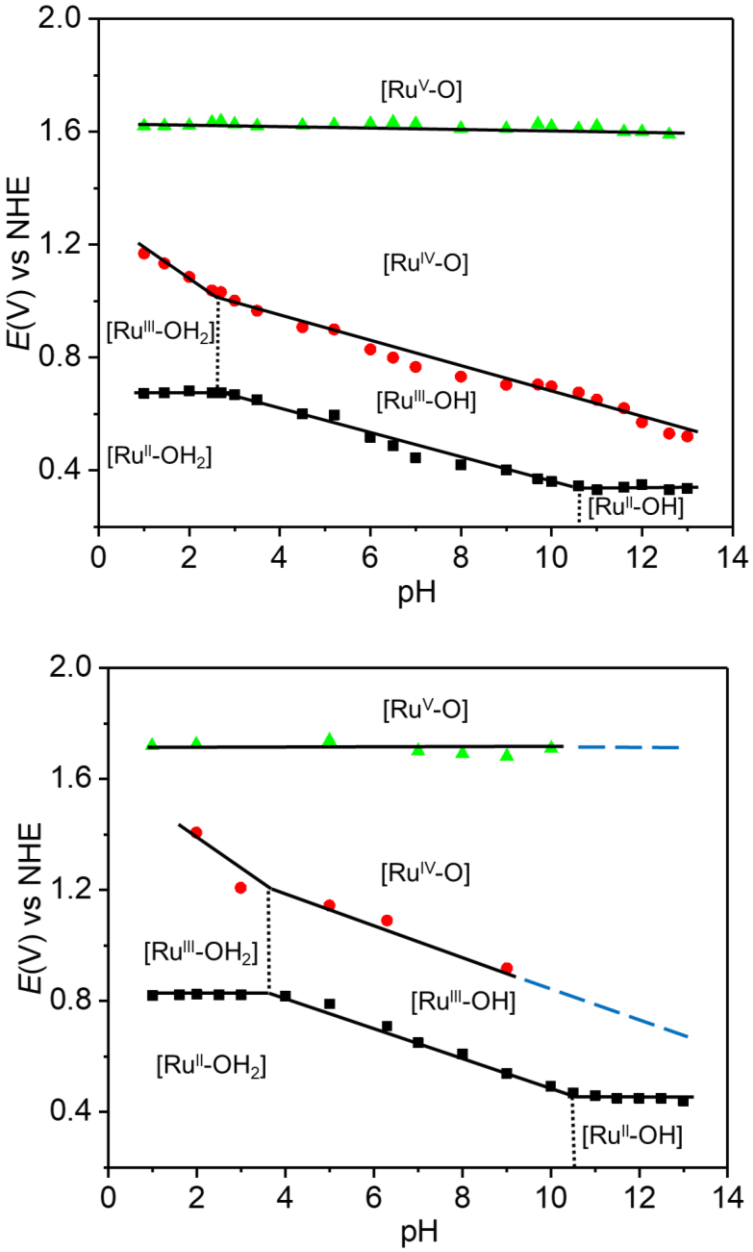

Figure 4. Pourbaix diagram of a) *trans*-[(trpy)(qc)$Ru^{II}(OH_2)]^+$, *trans*-**2** and b) *cis*-[(trpy)(qc)$Ru^{II}(OH_2)]^+$, *cis*-**2**. The black solid lines indicate the redox potentials for the different redox couples, whereas the dashed vertical lines indicate the p*K*a. The zone of stability of the different species are indicated only with the Ru symbol, its oxidation state, and the degree of protonation of the aquo ligand. For instance, "Ru^V-O" is used to indicate the zone of stability of *trans*-[(trpy)(qc)$Ru^V(O)]^{2+}$ for the *trans*-**1** (left) and *cis*-[(trpy)(qc)$Ru^V(O)]^{2+}$ for the *cis*-**2** (right). Blue dotted line correspond to the imaginary line and extended of the corresponding redox potential.

Chapter 3A

In order to get more insights into the *trans vs. cis* influence on the redox potentials and catalytic activity, we have extended our study to two similar mononuclear Ru-trpy-OH_2 complexes containing the 2-picolinate (pic) bidentate ligand, namely, *trans*-**3** and *cis*-**3** in Chart 1. These two complexes are of interest because they form a five-membered chelate ring around the metal center as opposed to the 8-quinolinecarboxylate (qc) that makes six-membered chelate rings, allowing to further study geometric effects. Complexes *trans*-**3** and *cis*-**3** have been synthesized and characterized according to the literature procedure.[25] Here we have extensively studied their electrochemical and water oxidation properties.

As shown in the CVs in Figure 3b and the Pourbaix diagrams in Figure S17, complexes *trans*-**3** and *cis*-**3** also show two successive pH dependent redox couples associated with PCET processes and a third pH independent oxidation couple related to electrochemical oxidation of water to dioxygen. The redox potentials for the four Ru-aquo complexes in Chart 1 are summarized in Table 1 together with other relevant Ru-aquo complexes previously described in the literature.

An interesting feature arising from the comparison of the potentials is that at pH 1.0 the $Ru^{III/II}$ redox couple for *trans*-**2** is around 90 mV lower compared to the related *trans*-Ru(trpy)(pic) complex, *trans*-**3**. Considering that both complexes have a similar trans influence of the carboxylate group, we attribute this phenomenon to the higher distortion of the dihedral plane between the quinolinate and trpy ligands in *trans*-**2** as compared to that of the picolinate and trpy ligands in *trans*-**3** (*e.g.* Figure S13). As a consequence, we expect that the hydrogen bonding between the aquo/hydroxido group and the C-H group in the ortho position of the pyridine of the qc ligand is less pronounced in *trans*-**2** than in *trans*-**3** (Figure S20 and Scheme 2). Such hydrogen bond lowers the electron density of the metal center, thus increasing the oxidation potential for the $Ru^{III/II}$ couple. On the other hand, for *cis*-**2** the $Ru^{III/II}$ redox couple is only 40 mV lower than *cis*-**3**, because of the absence of H-bonding and therefore this small difference is associated solely to slight changes in the geometry between the two complexes. Indeed, as shown in Figures S13, dihedral angles between the qc-trpy and pic-trpy planes in *cis*-**1** and *cis*-[Ru^{II}(trpy)(pic)Cl] are significantly different (76.2° and 87.6°, respectively).

In contrast, the third oxidation $[Ru^{V}=O]^{2+}/[Ru^{IV}=O]^{+}$ for *trans*-**2** is around 20 mV higher compared to the related *trans*-**3** and the same trend is observed for *cis*-**2**, which shows an anodic shift of 40 mV higher compared to *cis*-**3**, indicative of no influence of the hydrogen bond at higher oxidation states.

The *cis*-isomers always show pK_a values higher than the corresponding *trans*-isomers (compare entry 2 with 3 and entry 4 with 5 in Table 1 and Figure 4). We attribute this trend once more to the H-bonding present in the *trans*-isomers, which picks up part of the electron density of the metal center and thus makes it more acidic than the *cis*-isomers. On the other hand, the pK_a^{III} value for the [Ru^{III}-OH] with singly negatively charged carboxylate ligand of all these complexes are higher as compared to other Ru-aquo complexes with neutral ligand such as $[Ru(trpy)(bpy)(OH_2)]^{2+}$ as expected (Table 1).

Density Functional Theory (DFT) was used in collaboration with Dr. M. Z. Ertem to calculate potentials for the $Ru^{III/II}$, $Ru^{IV/III}$ and $Ru^{V/IV}$ couples and they agree reasonably well with experimental values at M06 level of theory (see Table S1). Although the difference between the two isomers is rather low, it follows the same trend observed in the experiments in Figure 5.

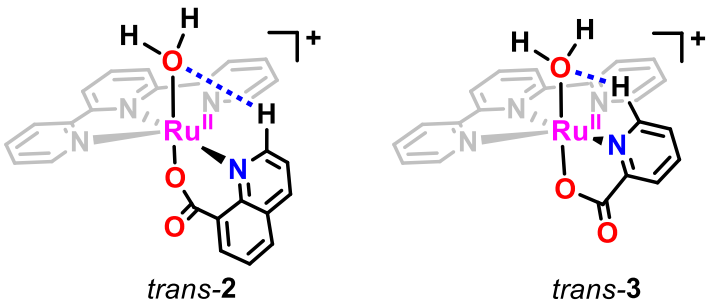

Scheme 2. H-bonding interaction present in *trans*-**2** and *trans*-**3**, that is expected to be more pronounced for the latter due to less distortion of the molecule.

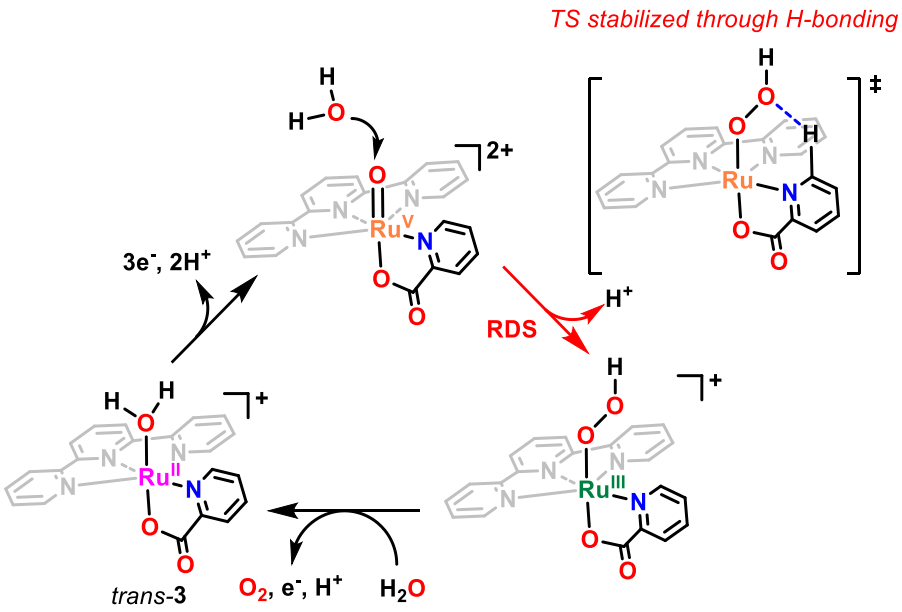

Scheme 3. Proposed reaction intermediates involved in the water oxidation catalytic cycle with *trans*-**3**.

3A. 3. 3 Water Oxidation Catalysis: Performance and Mechanism

The kinetics of the water oxidation catalysis by the Ru-aquo complexes in Chart 1 where assessed electrochemically, by using the "foot of the wave analysis" (FOWA), which allows us to calculate the apparent kinetic constant (k_{obs}) from cyclic voltammetry experiments.[42-44] This method uses the relationship in equation 5 for a first order kinetics,

$$\frac{i}{i_p} = \frac{4*2.24*\sqrt{\frac{RTk_{obs}}{Fv}}}{1+\exp(\frac{F(E^0_{P/Q}-E)}{RT})} \qquad (5)$$

where i is the current intensity in the presence of substrate, i_p is the current intensity in the absence of substrate (we approximate this current to the current associated with the $Ru^{III/II}$ couple), $E^0_{P/Q}$ is the standard potential for the redox couple that starts the catalysis (1.62 V for *trans*-**2**, 1.71 V for *cis*-**2**, 1.60 V *trans*-**3** and 1.67 for *cis*-**3** extracted from the DPVs in Figure S15), F is the faraday constant, v is the scan rate, and R is 8.314 J mol^{-1} K^{-1}. K_{obs} or TOF_{max} can be extracted from the plot of i/i_p versus $1/\{1 + \exp[(F/RT)(E_{P/Q} - E)]\}$ as shown in Figure S19.

From these calculations we get TOF_{max} of 4.2 s^{-1} for *trans*-**2**, 6.88 s^{-1} for *cis*-**2**, 1.16 s^{-1} for *trans*-**3** and 0.28 s^{-1} for *cis*-**3**. When this TOF values are plotted against the $E_{1/2}(Ru^{V/IV})$ potentials (Figure 5b) we see the expected trend according to Marcus theory that predicts higher rates for higher driving force in outer sphere electron transfer processes.

The water oxidation to dioxygen catalytic properties of complexes *trans*-**2**, *trans*-**3** and *cis*-**3** were also tested using a sacrificial oxidant, *i.e.,* $(NH_4)_2[Ce(NO_3)_6]$ and the observed catalytic rates follow exactly the same trend as observed in the electrocatalysis, that is, TOF_i (*trans*-**2**) > TOF_i (*trans*-**3**) > TOF_i (*cis*-**3**) (Figure 5a and Table 1). Although *trans*-**2** is still the fastest with TOF_i of 0.68 s^{-1} it is less robust than compound *trans*-**3** with a TOF_i of 0.24 s^{-1} (TON = 14.90, 60% efficiency and TON = 19.87, 80% efficiency, respectively). Complex *cis*-**3** produces 8.4 TON (42% efficiency) with a TOF_i of 0.11 s^{-1} under the same conditions.

The fact that the rates of oxygen generation, both chemical and electrochemical, increase with the redox potential clearly indicate that the rds is the O-O bond formation step proposed in Scheme 3. The origin of the slow catalytic activity of *cis*-**3** with a relatively high $Ru^{V/IV}$ redox potential is not clearly understood but it might be related to the lack of H-bonding reducing the TS energy as indicated in Scheme 3 for *trans*-**3**. DFT calculations are currently underway to further shed some light at this effect. Preliminary results of a water nucleophilic attack

(WNA) mechanism for the quinoline complexes are given in Scheme S1 and Table S1 in the supporting information.

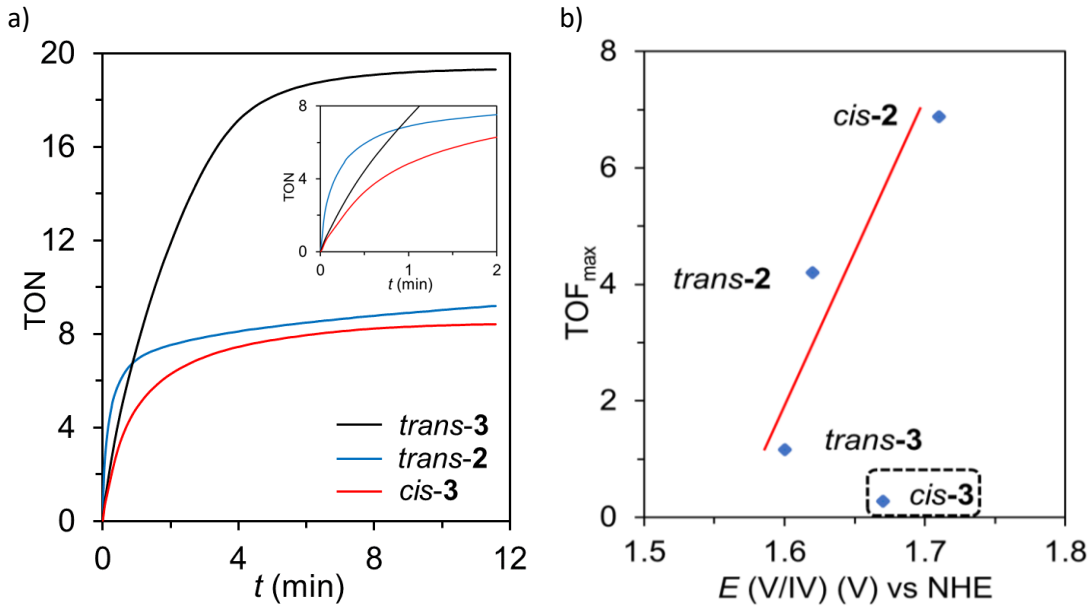

Figure 5. a) Oxygen evolution profile obtained for *trans*-**2** (blue), *trans*-**3** (black) and *cis*-**3** (red). Experimental conditions: 1 mM of complex and 100 mM of Ce^{IV} in 0.1 M triflic acid (2 mL total volume) at 25 ˚C. TON_{max} = 25. Inset: same profile for first 2 min. b) Plot of TOF_{max} *vs*. E^o ($Ru^{V/IV}$) for all four complexes obtained from FOWA.

Chapter 3A

Table 1. Thermodynamic and catalytic data for Ru-aqua caborxylate and related complexes described in the literature at pH 1.

		$E_{1/2}$ (V) *vs.* NHE				pK_a				
Entry	Complexes[a]	V/IV	IV/III	III/II	[b]ΔE (mV)	Ru^{II}-OH_2	Ru^{III}-OH_2	TON[c]	TOF[d]	TOF_{max}[e]
1[45]	$[Ru(trpy)(bpy)(H_2O)]^{2+}$	1.92	1.22	1.06	110	9.7	1.7	18.3	0.01	-
2[f]	*cis*-**2**	1.71(1.41)	1.36(1.14)	0.82(0.59)	540(550)	10.6	3.8	-		6.8
3[f]	*trans*-**2**	1.62(1.50)	1.20(1.00)	0.67(0.44)	530(560)	10.6	2.7	14.9	0.68	4.2
4[25,f]	*cis*-**3**	1.67	1.31	0.86	450	10.1	3.7	8.6	0.11	0.3
5[25,f]	*trans*-**3**	1.60	1.09	0.76	330	10.1	2.0	19.7	0.24	1.2
6	$[Ru(pdc)(bpy)(H_2O)]^{+}$	1.41	0.73	0.25	480	11	4	-		
7[46]	$[Ru(bpc)(bpy)(H_2O)]^{+}$	1.57	1.29	0.81	480	10.6	2.6	-	0.16	-

[a]Ligand abbreviations: trpy = 2,2':6',2"-terpyridine, bpy = 2,2'-bipyridine, pic = 2-picolinate, qc = 8-quinolinecarboxylate, bpc = 2,2'-bipyridine-6-carboxylate, pdc = 2,6-pyridinedicarboxylate. [b]ΔE= $E_{1/2}$(IV/III)-$E_{1/2}$(III/II); [c]TON stands for Turn Over Numbers; [d]TOF stands for initial Turn Over Frequency in s^{-1}; These values are extracted for the catalytic reactions involving 1.0 mM Cat/100 mM Ce^{IV} in a 0.1 M triflic acid solution with a total volume of 2 mL; [e]TOF_{max} stands for Maximum Turn Over Frequency reported in s^{-1}; values extracted from Foot of the Wave Analysis of CV and DPV experiment in pH 1 (entry 2-5); [f] this work; Redox potential values in parenthesis are calculated from DFT (M06).

3A. 4. Conclusion

In summary, we have synthesized and characterized a series of ruthenium complexes with bidentate ligands containing carboxylate groups with different isomeric forms. In all the complexes, *trans*-isomers show lower potential of their redox couple as compared to *cis*-isomers due to the different extend of trans influence of the carboxylate group in the quinolinato or picolinato ligands. Complexes *cis*-**2** and *trans*-**2** with 6-member chelate ring around the Ruthenium are faster water oxidation catalysts as compare to *cis*-**3** and *trans*-**3** (5-member chelate ring around the Ruthenium). We conclude that the higher the driving force in outer sphere electron transfer processes, better is the rate. The pK_a value for Ru^{III}-OH of *cis*-isomers are always higher than those of the corresponding *trans*-isomers due to the presence of an H-bonding interaction in the *trans*-isomer, making this more acidic in nature.

3A. 5. References

(1) Lewis, N. S. *Science* **2016**, *351*, 1920.
(2) Berardi, S.; Drouet, S.; Francas, L.; Gimbert-Surinach, C.; Guttentag, M.; Richmond, C.; Stoll, T.; Llobet, A. *Chem. Soc. Rev.* **2014**, *43*, 7501.
(3) Sala, X.; Maji, S.; Bofill, R.; Garcia-Anton, J.; Escriche, L. s.; Llobet, A. *Acc. Chem. Res.* **2013**, *47*, 504.
(4) Gersten, S. W.; Samuels, G. J.; Meyer, T. J. *J. Am. Chem. Soc.* **1982**, *104*, 4029.
(5) Duan, L.; Bozoglian, F.; Mandal, S.; Stewart, B.; Privalov, T.; Llobet, A.; Sun, L. *Nat. Chem.* **2012**, *4*, 418.
(6) Matheu, R.; Ertem, M. Z.; Benet-Buchholz, J.; Coronado, E.; Batista, V. S.; Sala, X.; Llobet, A. *J. Am. Chem. Soc.* **2015**, *137*, 10786.
(7) Hoque, M. A.; Benet-Buchholz, J.; Llobet, A.; Gimbert-Suriñach, C. *ChemSusChem.* **2019**, *12*, 1949.
(8) Shatskiy, A.; Bardin, A. A.; Oschmann, M.; Matheu, R.; Benet-Buchholz, J.; Eriksson, L.; Kärkäs, M. D.; Johnston, E. V.; Gimbert-Suriñach, C.; Llobet, A.; Åkermark, B. *ChemSusChem.* **2019**, *12*, 2251.
(9) Wang, L.; Duan, L.; Tong, L.; Sun, L. *J. Catal.* **2013**, *306*, 129.
(10) Roeser, S.; Farràs, P.; Bozoglian, F.; Martínez-Belmonte, M.; Benet-Buchholz, J.; Llobet, A. *ChemSusChem.* **2011**, *4*, 197.
(11) Berardi, S.; Francàs, L.; Neudeck, S.; Maji, S.; Benet-Buchholz, J.; Meyer, F.; Llobet, A. *ChemSusChem.* **2015**, *8*, 3688.
(12) Li, H.; Li, F.; Zhang, B.; Zhou, X.; Yu, F.; Sun, L. *J. Am. Chem. Soc.* **2015**, *137*, 4332.
(13) Francàs, L.; Matheu, R.; Pastor, E.; Reynal, A.; Berardi, S.; Sala, X.; Llobet, A.; Durrant, J. R. *ACS Catal.* **2017**, *7*, 5142.
(14) Concepcion, J. J.; Tsai, M.-K.; Muckerman, J. T.; Meyer, T. J. *J. Am. Chem. Soc.* **2010**, *132*, 1545.
(15) Vigara, L.; Ertem, M. Z.; Planas, N.; Bozoglian, F.; Leidel, N.; Dau, H.; Haumann, M.; Gagliardi, L.; Cramer, C. J.; Llobet, A. *Chem. Sci.* **2012**, *3*, 2576.
(16) Pushkar, Y.; Moonshiram, D.; Purohit, V.; Yan, L.; Alperovich, I. *J. Am. Chem. Soc.* **2014**, *136*, 11938.
(17) Pushkar, Y.; Pineda-Galvan, Y.; Ravari, A. K.; Otroshchenko, T.; Hartzler, D. A. *J. Am. Chem. Soc.* **2018**, *140*, 13538.
(18) Barnett, S. M.; Goldberg, K. I.; Mayer, J. M. *Nat. Chem.* **2012**, *4*, 498.
(19) Okamura, M.; Kondo, M.; Kuga, R.; Kurashige, Y.; Yanai, T.; Hayami, S.; Praneeth, V. K.; Yoshida, M.; Yoneda, K.; Kawata, S. *Nature* **2016**, *530*, 465.
(20) Sens, C.; Romero, I.; Rodríguez, M.; Llobet, A.; Parella, T.; Benet-Buchholz, J. *J. Am. Chem. Soc.* **2004**, *126*, 7798.
(21) Neudeck, S.; Maji, S.; López, I.; Meyer, S.; Meyer, F.; Llobet, A. *J. Am. Chem. Soc.* **2013**, *136*, 24.
(22) Schulze, M.; Kunz, V.; Frischmann, P. D.; Würthner, F. *Nat. Chem.* **2016**, *8*, 576.
(23) Gimbert-Suriñach, C.; Moonshiram, D.; Francàs, L.; Planas, N.; Bernales, V.; Bozoglian, F.; Guda, A.; Mognon, L.; López, I.; Hoque, M. A. *J. Am. Chem. Soc.* **2016**, *138*, 15291.
(24) Sullivan, B. P.; Calvert, J. M.; Meyer, T. J. *Inorg. Chem.* **1980**, *19*, 1404.
(25) Llobet, A.; Doppelt, P.; Meyer, T. J. *Inorg. Chem.* **1988**, *27*, 514.
(26) *Data collection with APEX II version v2013.4-1. Bruker (2007). Bruker AXS Inc., Madison, Wisconsin, USA.*
(27) *Data reduction with Bruker SAINT version V8.30c. Bruker (2007). Bruker AXS Inc., Madison, Wisconsin, USA.*
(28) Blessing, R. H. *Acta Cryst. A* **1995**, *51*, 33.
(29) *Data collection and reduction with CrysAlisPro 1.171.39.12b (Rigaku OD, 2015).*

(30) *Empirical absorption corrrection using spherical harmonics implemented in Scale3 Abspack scaling algorithm, CrysAlisPro 1.171.39.12b (Rigaku OD, 2015).*
(31) SHELXT; Sheldrick, G. M. *Acta Cryst.* **2015**, *A71*, 3.
(32) SHELXle; C.B. Huebschle, G. M. S. B. D. *J.Appl.Cryst.* **2011**, *44*, 1281.
(33) Sheldrick, G. M. *Acta Cryst. C* **2015**, *71*, 3.
(34) Mandal, A.; Hoque, M. A.; Grupp, A.; Paretzki, A.; Kaim, W.; Lahiri, G. K. *Inorg. Chem.* **2016**, *55*, 2146.
(35) Maji, S.; López, I.; Bozoglian, F.; Benet-Buchholz, J.; Llobet, A. *Inorg. Chem.* **2013**, *52*, 3591.
(36) Chanda, N.; Mobin, S. M.; Puranik, V. G.; Datta, A.; Niemeyer, M.; Lahiri, G. K. *Inorg. Chem.* **2004**, *43*, 1056.
(37) Mondal, B.; Paul, H.; Puranik, V. G.; Lahiri, G. K. *J. Chem. Soc., Dalton Trans.* **2001**, 481.
(38) Patra, S.; Sarkar, B.; Ghumaan, S.; Patil, M. P.; Mobin, S. M.; Sunoj, R. B.; Kaim, W.; Lahiri, G. K. *Dalton. Trans.* **2005**, 1188.
(39) Chowdhury, A. D.; Das, A.; Mobin, S. M.; Lahiri, G. K. *Inorg. Chem.* **2011**, *50*, 1775.
(40) Mognon, L.; Benet-Buchholz, J.; Rahaman, S. W.; Bo, C.; Llobet, A. *Inorg. Chem.* **2014**, *53*, 12407.
(41) Mognon, L.; Benet-Buchholz, J.; Llobet, A. *Inorg. Chem.* **2015**, *54*, 11948.
(42) Costentin, C.; Drouet, S.; Robert, M.; Savéant, J.-M. *Science* **2012**, *338*, 90.
(43) Costentin, C.; Drouet, S.; Robert, M.; Savéant, J.-M. *J. Am. Chem. Soc.* **2012**, *134*, 11235.
(44) Matheu, R.; Neudeck, S.; Meyer, F.; Sala, X.; Llobet, A. *ChemSusChem.* **2016**, *9*, 3361.
(45) Takeuchi, K. J.; Thompson, M. S.; Pipes, D. W.; Meyer, T. J. *Inorg. Chem.* **1984**, *23*, 1845.
(46) Tong, L.; Inge, A. K.; Duan, L.; Wang, L.; Zou, X.; Sun, L. *Inorg. Chem.* **2013**, *52*, 2505.

3A. 6. Supporting Information

Table of Contents

NMR

Figure S1-S3. NMR spectra of *trans*-[Ru^{II}(trpy)(qc)Cl], *trans*-**1**

Figure S4- S6. NMR spectra of *cis*-[Ru^{II}(trpy)(qc)Cl], *cis*-**1**

Figure S7-S9. NMR spectra of *trans*-[Ru^{II}(trpy)(qc)(OH_2)]$^+$, *trans*-**2**

Figure S10-S11. NMR spectra of *cis*-[Ru^{II}(trpy)(qc)(OH_2)]$^+$, *cis*-**2**

Electrochemistry and Manometry

Figure S12. View of the trans angles in crystal structure

Figure S13. View of the distortion of the angle in crystal structure

Figure S14. CV of *trans*-[Ru^{II}(trpy)(qc)Cl], *trans*-**1** and *cis*-[Ru^{II}(trpy)(qc)Cl], *cis*-**1** in acetonitrile

Figure S15. DPVs of *trans*-[Ru^{II}(trpy)(qc)(OH_2)]$^+$, *trans*-**2,** *cis*-[Ru^{II}(trpy)(qc)(OH_2)]$^+$, *cis*-**2**, *trans*-[Ru^{II}(trpy)(pic)(OH_2)]$^+$, *trans*-**3** and *cis*-[Ru^{II}(trpy)(pic)(OH_2)]$^+$, *cis*-**3** in pH 1 triflic acid

Figure S16. DPVs of a) *trans*-**2** and b) *cis*-**2** at different pHs

Figure S17. Pourbaix diagram of A) *trans*-**3** and B) *cis*-**3**

Figure S18. DPVs of *trans*-**2** and *cis*-**2** at pH 10.5 phosphate buffer

Figure S19. FOWA of *trans*-**2,** *cis*-**2,** *trans*-**3** and *cis*-**3** at pH 1 triflic acid

Figure S20. ORTEP views of *trans*-**2**

Figure S21. Plot of TOFi *vs*. time obtained from manometry experiment for *trans*-**2**, *trans*-**3** and *cis*-**3.**

Figure S22. On line mass spectrometry experiments

Scheme S1. Mechanism pathway studied with Density Functional Theory

Table S1. Computational data

Table S2-S3. Selected Crystallographic Parameters

a)

b)

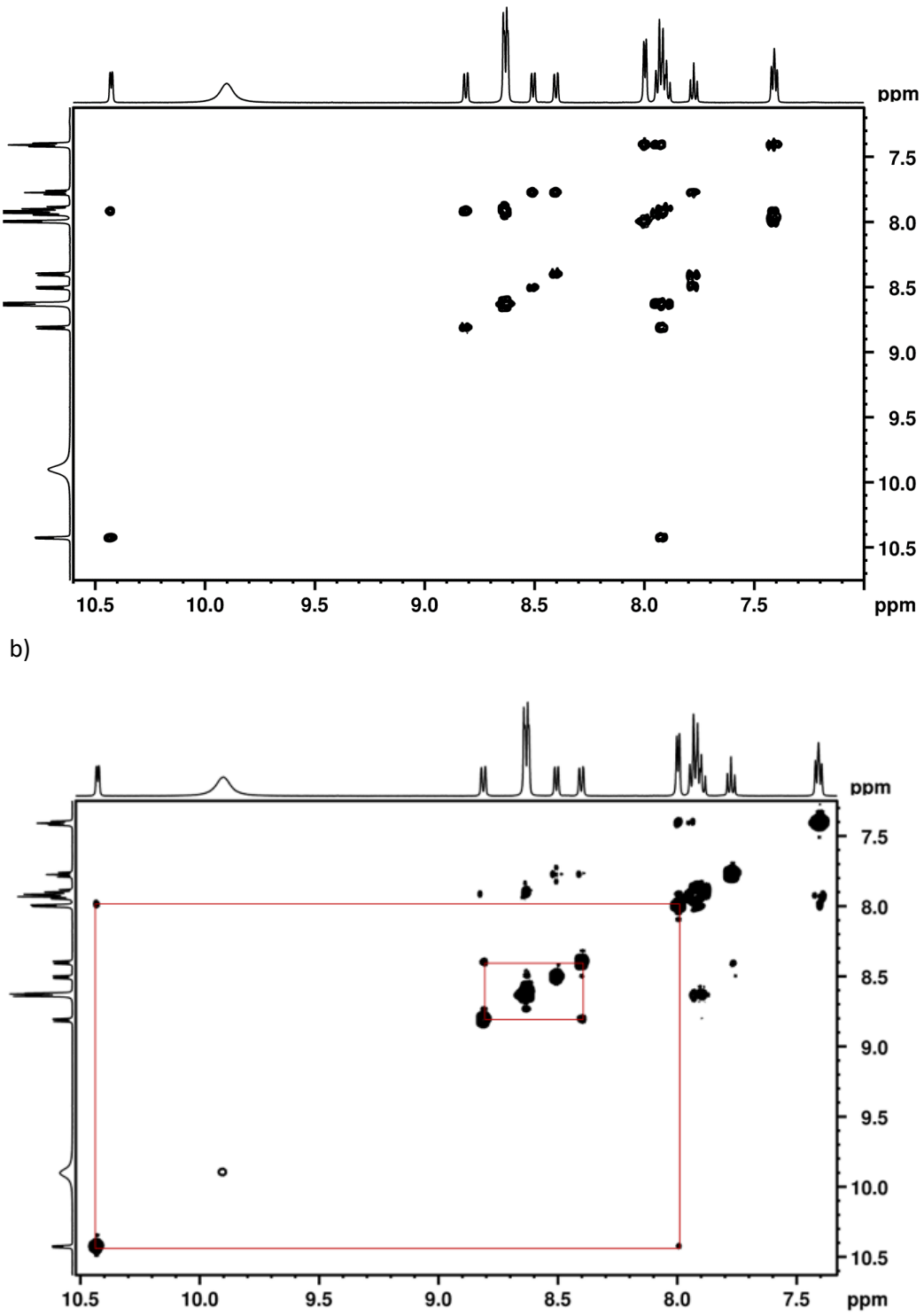

Figure S1. NMR spectra (500 MHz, 298 K, [d_6]-DMSO) for complex *trans*-**1**. a) COSY and b) NOESY.

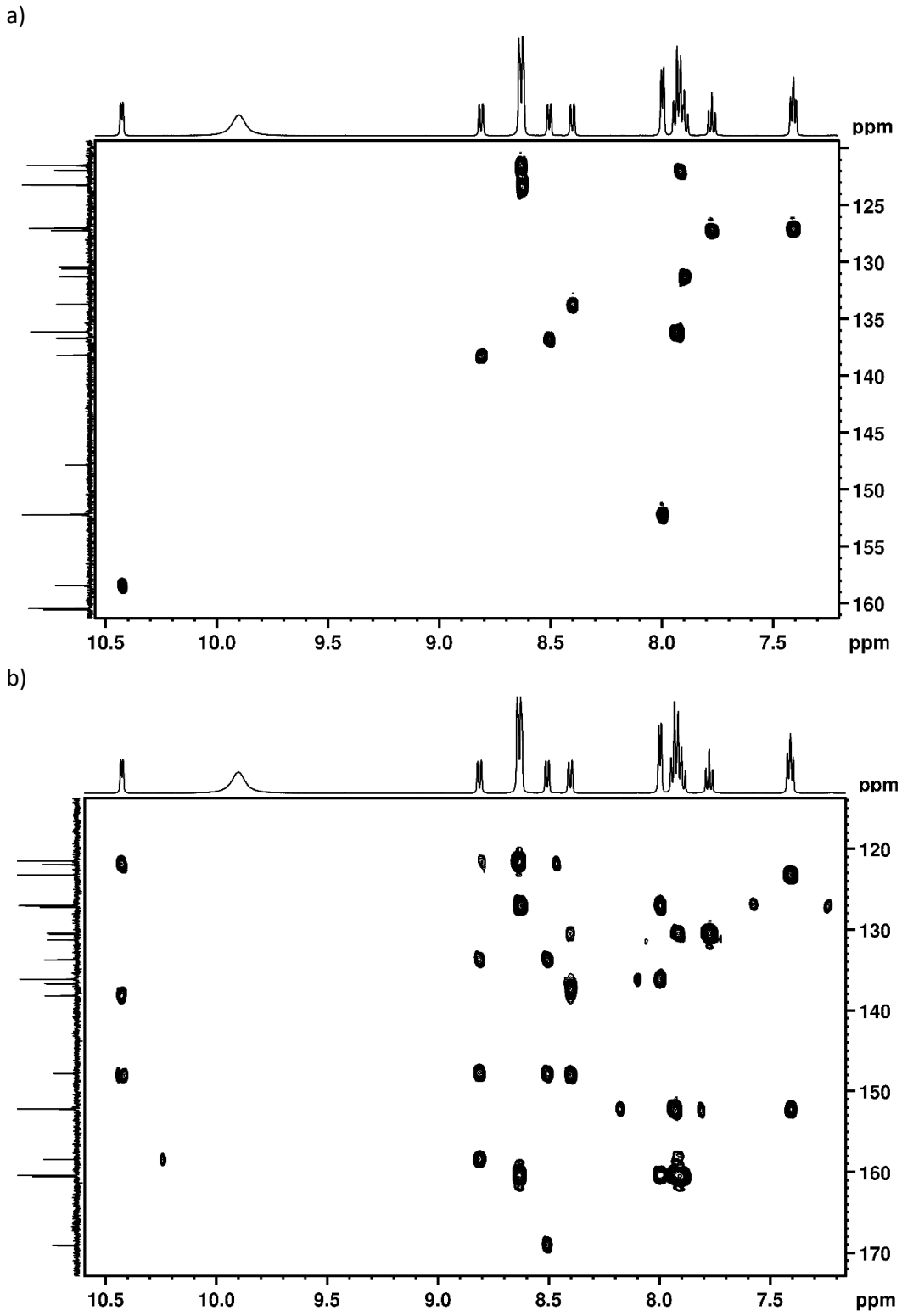

Figure S2. NMR spectra (500 MHz, 298 K, [d_6]-DMSO) for complex *trans*-**1**. a) HSQC and b) HMBC.

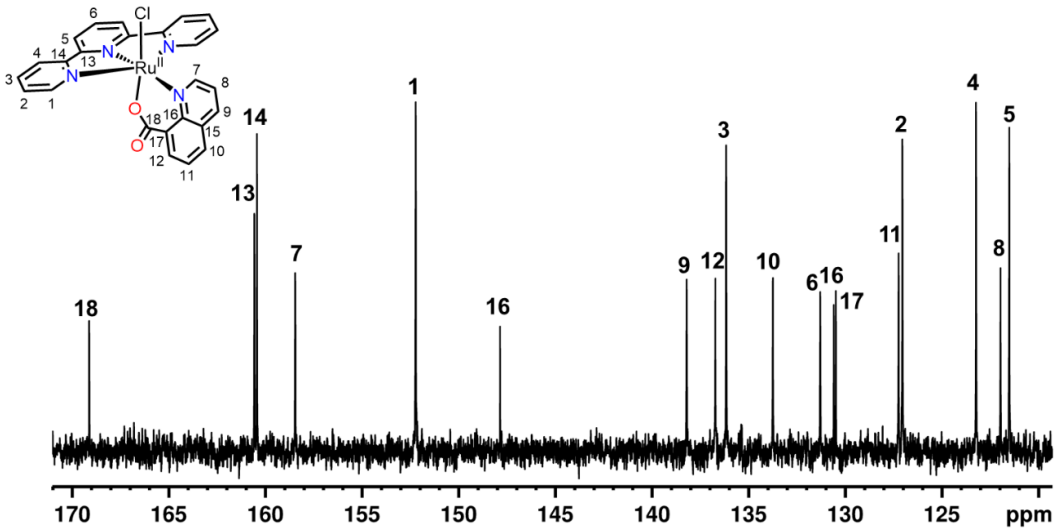

Figure S3. ^{13}C NMR spectra (125 MHz, 298 K, [d_6]-DMSO) for complex *trans*-**1**.

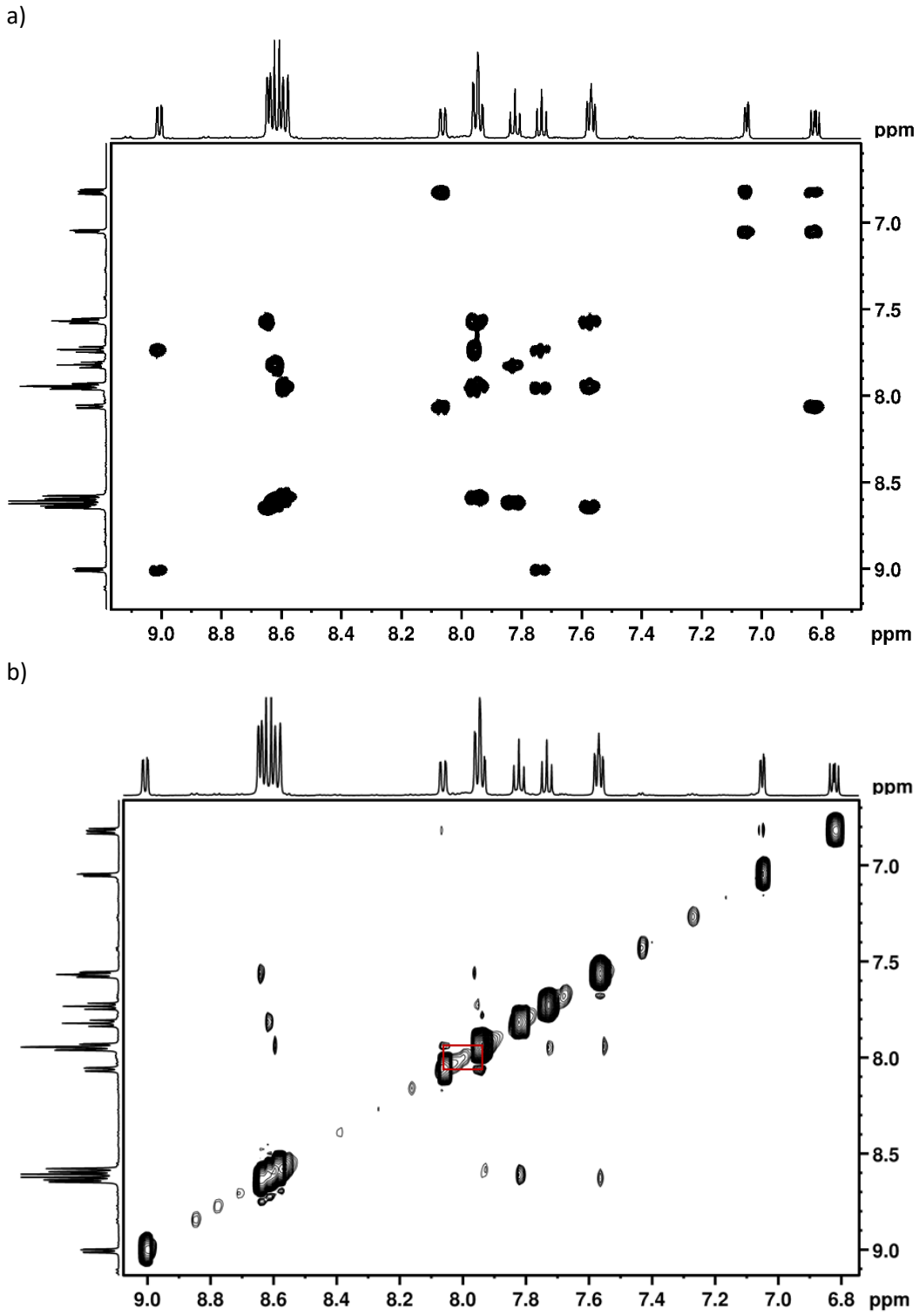

Figure S4. NMR spectra (500 MHz, 298 K, [d_6]-DMSO) for complex *cis*-**1**. a) COSY and b) NOESY.

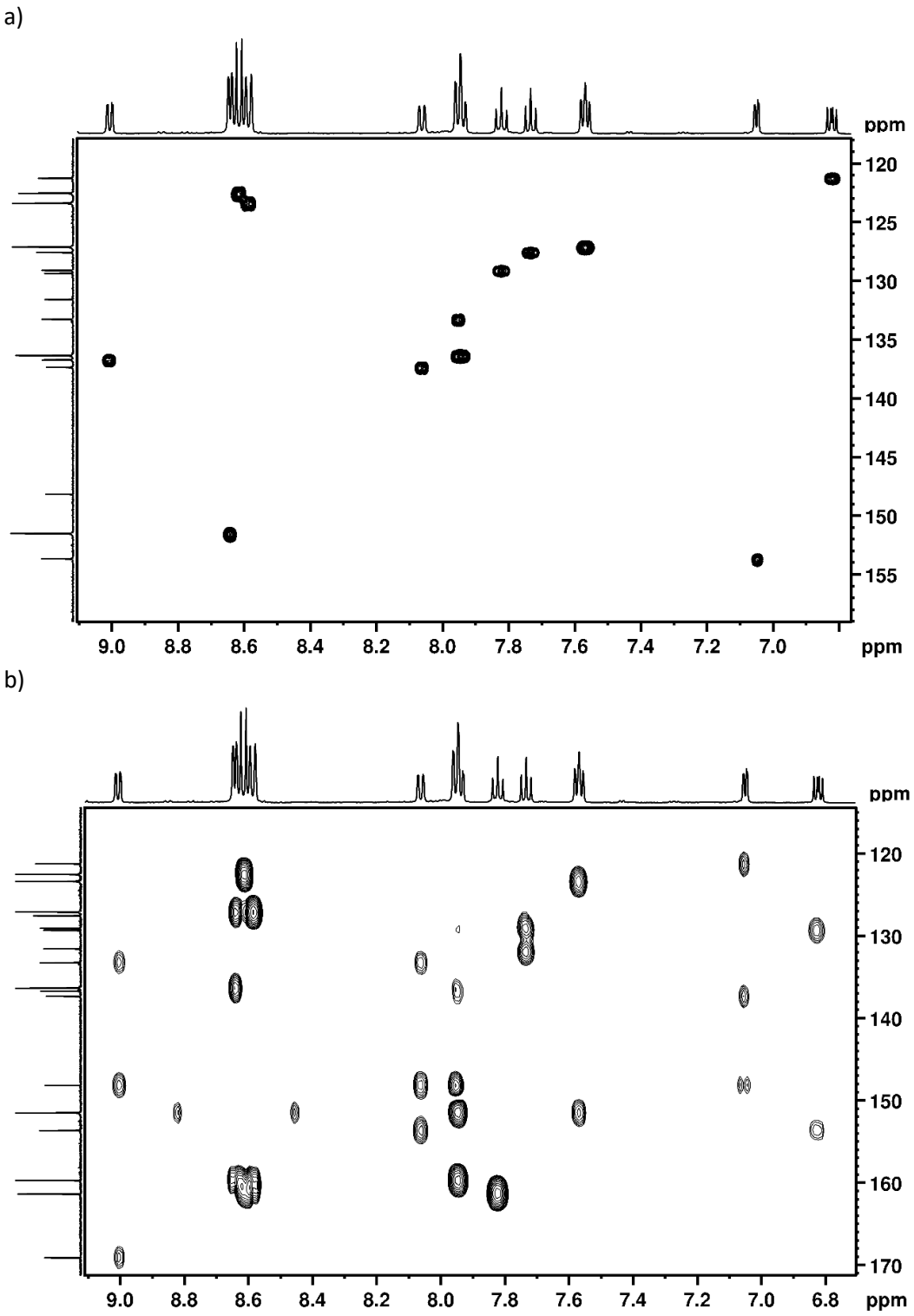

Figure S5. NMR spectra (500 MHz, 298 K, [d_6]-DMSO) for complex *cis*-**1**. a) HSQC and b) HMBC.

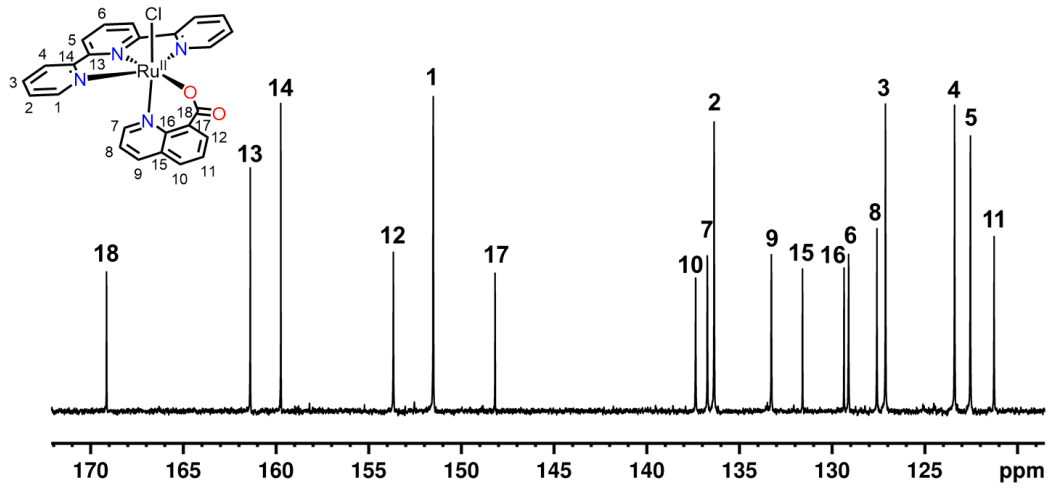

Figure S6. ^{13}C NMR spectra (125 MHz, 298 K, [d_6]-DMSO) for complex *cis*-**1**.

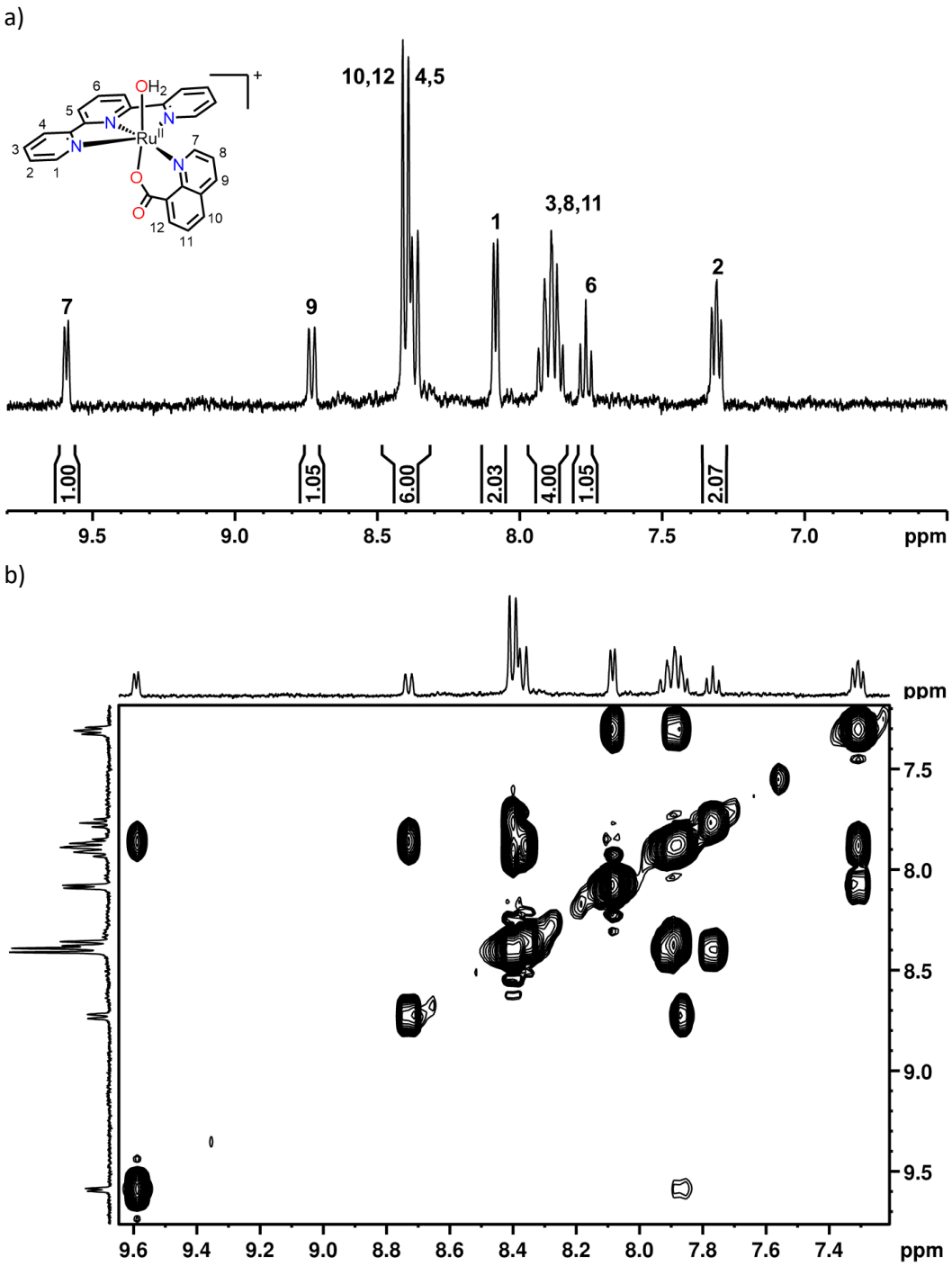

Figure S7. NMR spectra (500 MHz, 298 K, [d_2]-D_2O) for complex *trans*-**2**. a) ^{1}H NMR and b) COSY.

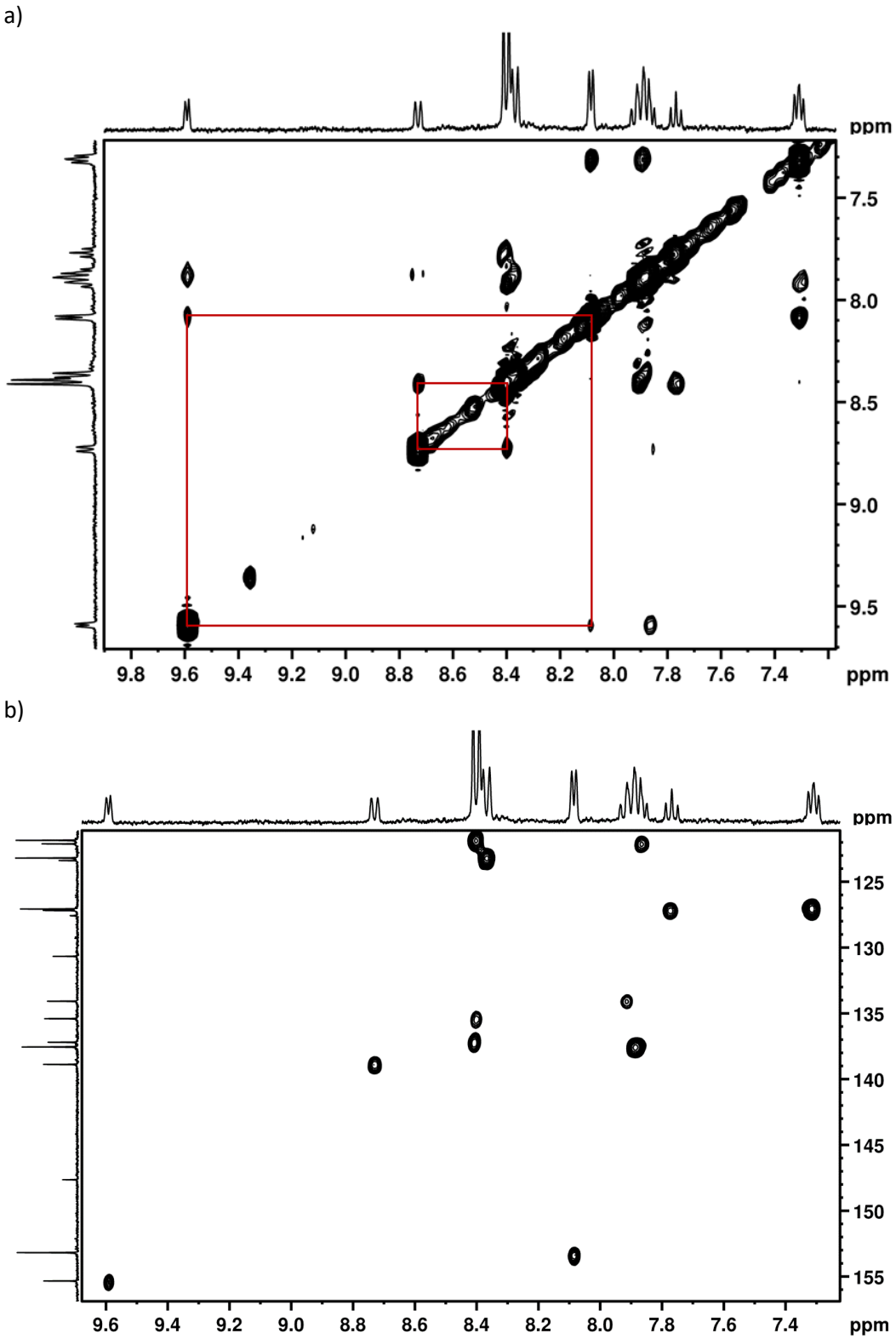

Figure S8. NMR spectra (500 MHz, 298 K, [d_2]-D_2O) for complex *trans*-**2** a) NOESY and b) HSQC.

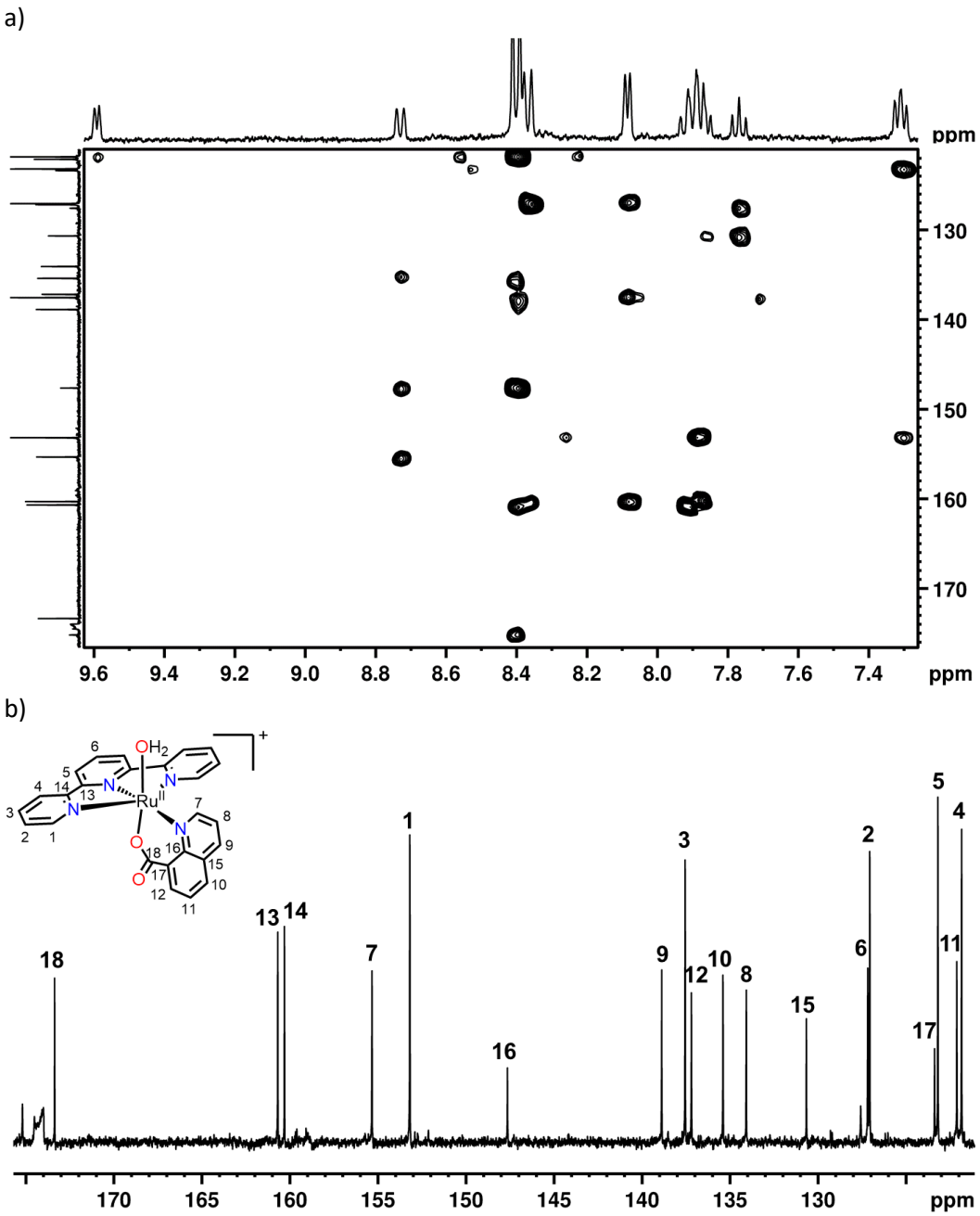

Figure S9. NMR spectra (500 MHz, 298 K, [d_2]-D_2O) for complex *trans*-**2**. a) HMBC and b) ^{13}C NMR (125 MHz, 298 K, [d_2]-D_2O).

Chapter 3A

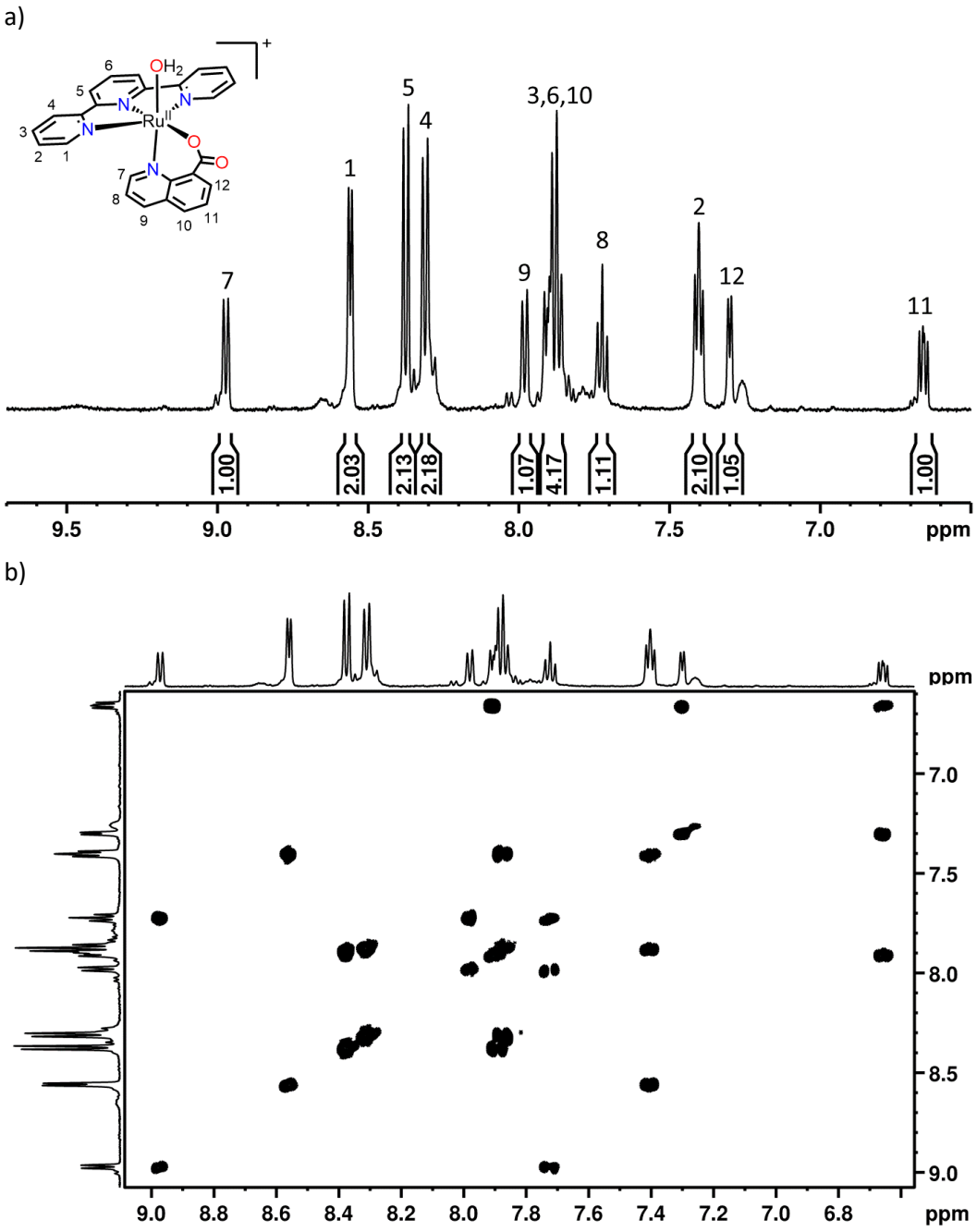

Figure S10. NMR spectra (500 MHz, 298 K, [d_2]-D_2O) for complex *cis*-**2** a) ^{1}H NMR, and b) COSY.

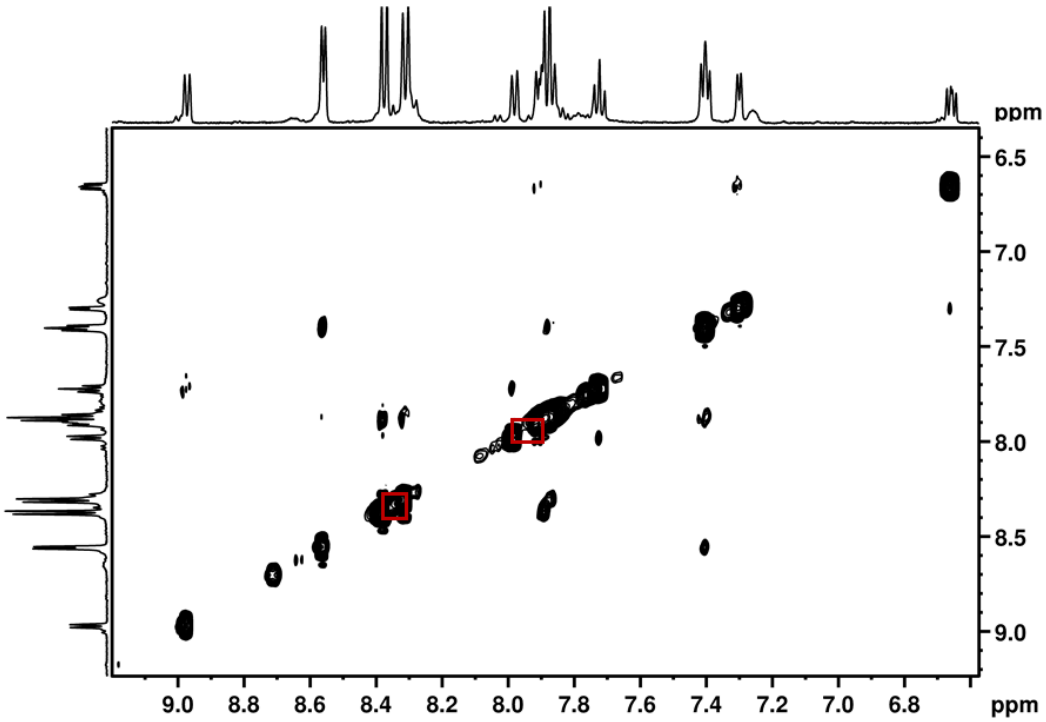

Figure S11. NMR spectra (500 MHz, 298 K, [d_2]-D_2O) for complex *cis*-**2**. NOESY.

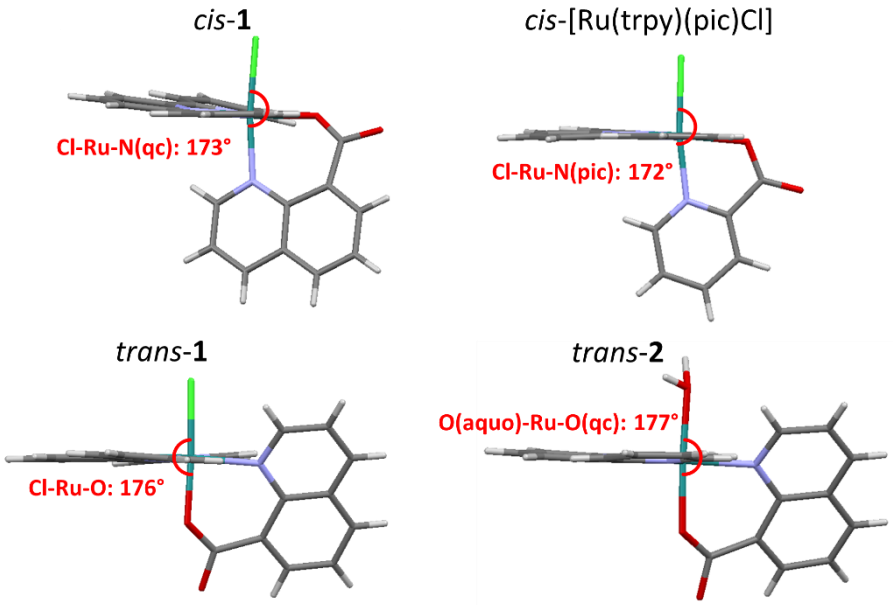

Figure S12. View of the trans angles for complexes, *cis*-**1**, *cis*-[Ru(trpy)(pic)Cl], *trans*-**1** and *trans*-**2**.

trans-**2**

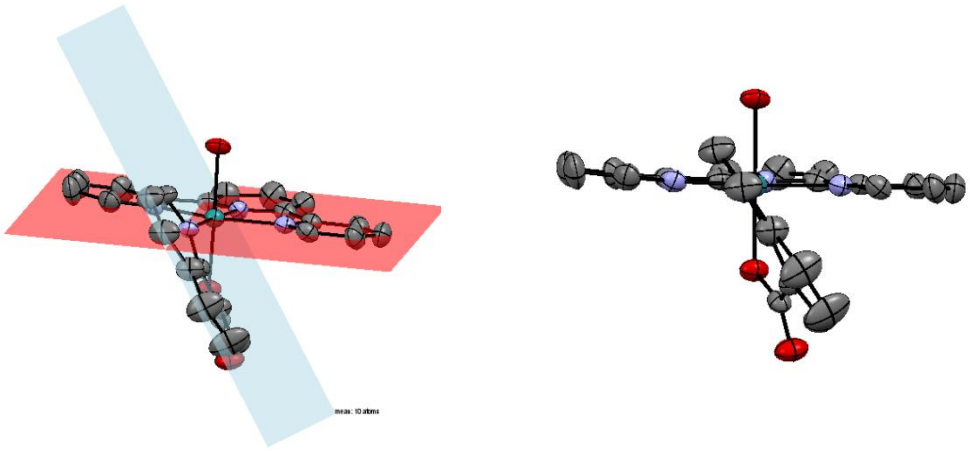

cis-**1**

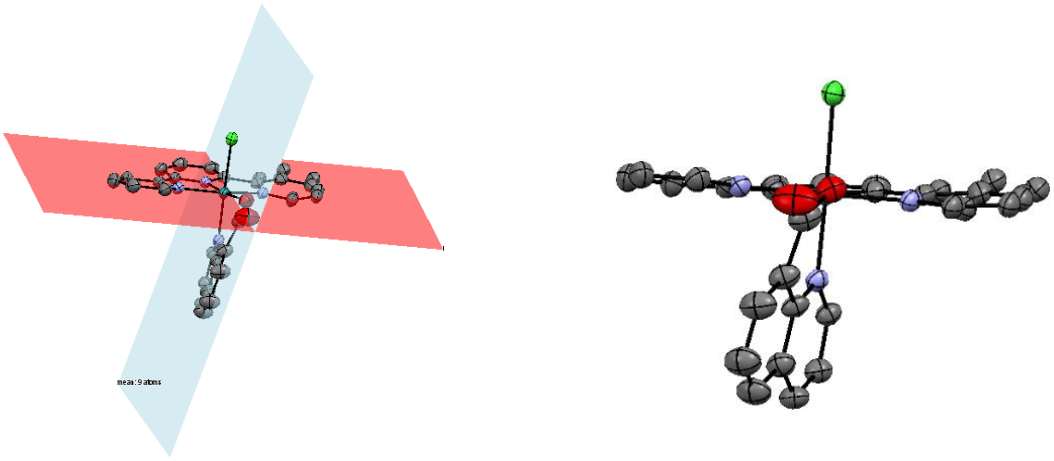

cis-[Ru(trpy)(pic)Cl]

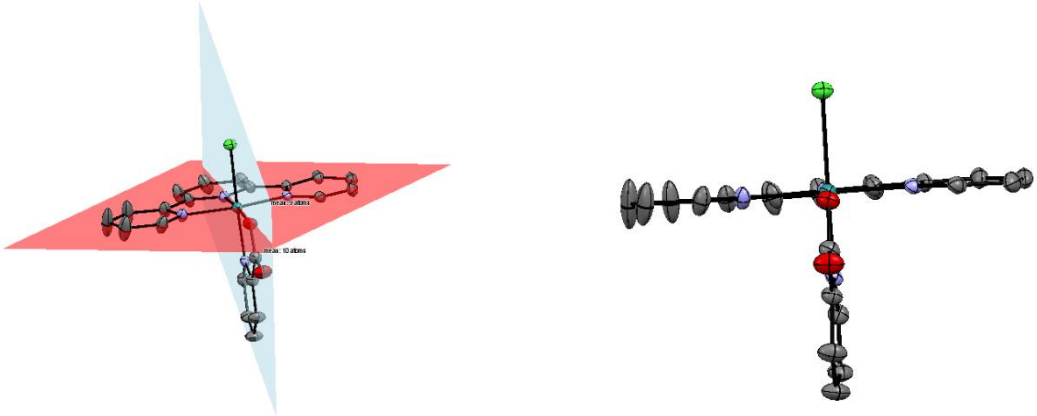

Figure S13. View of the distortion of the angle between trpy and qc planes in t*rans*-**2** (top) and *cis*-**1** (middle) (57.1˚ and 76.2˚, respectively) and for the trpy and pic planes in *cis*-[Ru(trpy)(pic)Cl] (87.6˚, bottom). It is clear that the picolinate ligand shows less distortion from the ideal 90˚ as compared to the quinolinate ligand.

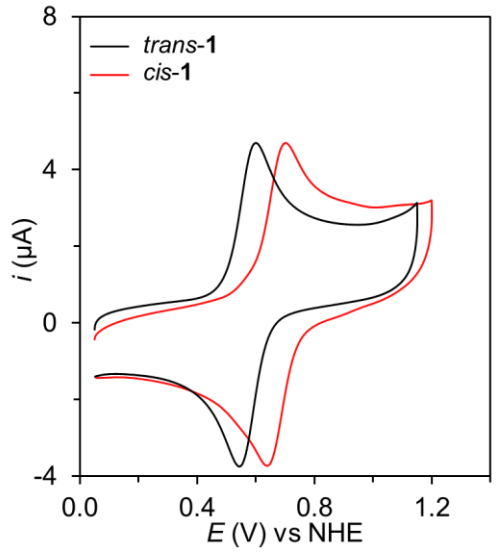

Figure S14. Cyclic Voltammograms of 1 mM of *trans*-**1** and *cis*-**1** in CH_3CN (0.1 M TBAH).

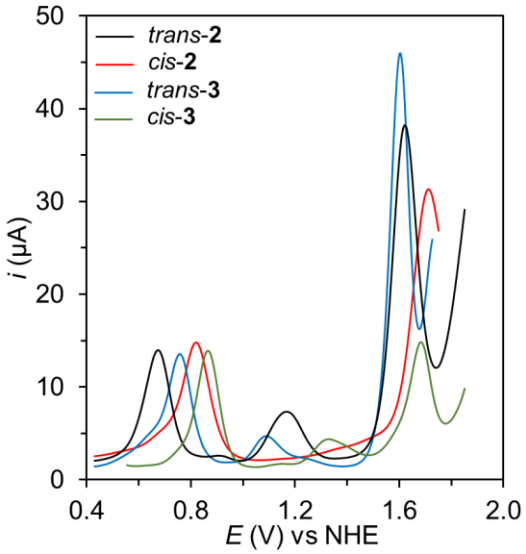

Figure S15. DPVs of *trans*-**2** (black), *cis*-**2** (red), *trans*-**3** (blue) and *cis*-**3** (green) at pH 1.0.

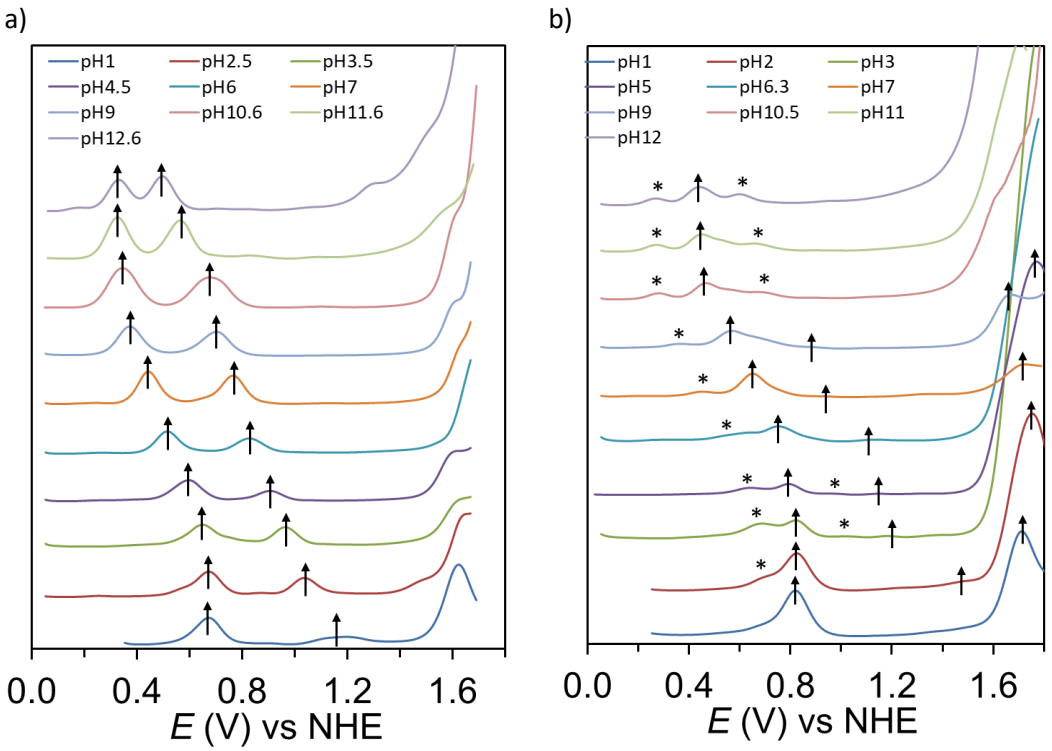

Figure S16. DPVs of a) *trans*-**2** and b) *cis*-**2** at different pHs.Asterisk in the Figure b indicates the redox waves of *trans*-**2**. This indicates that *cis*-**2** slowly converts to *trans*-**2**.

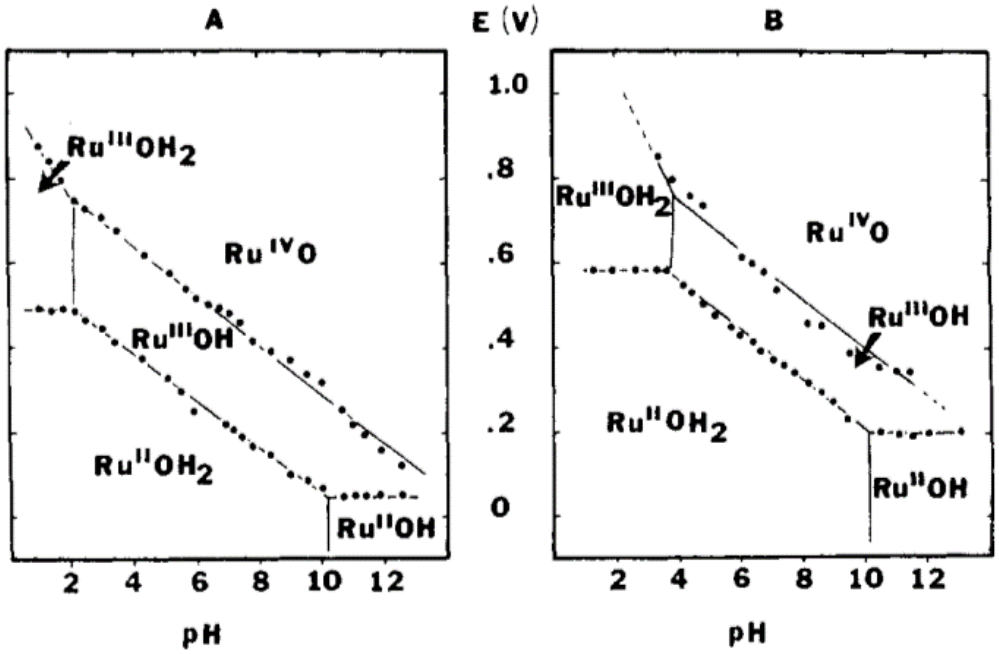

Figure S17. Pourbaix diagram derived from electrochemical measurements on complexes. (A) *trans*-[Ru^{II}(trpy)(pic)(OH_2)]$^+$ and (B) *cis*-[Ru^{II}(trpy)(pic)(OH_2)]$^+$. The pH-potential regions of stability for the various oxidation states and their dominant proton composition are indicated by using abbreviations such as $Ru^{II}OH_2$, for example, for *trans*-[Ru(trpy)(pic)(OH_2)]$^+$. The p*K*a values are shown by the vertical line in the various *E*-pH regions. Redox potential value reported in this plot is vs SSCE (A. Llobet, P. Doppelt, T. J. Meyer, *Inorg. Chem.* **1988**, *27*, 514.)

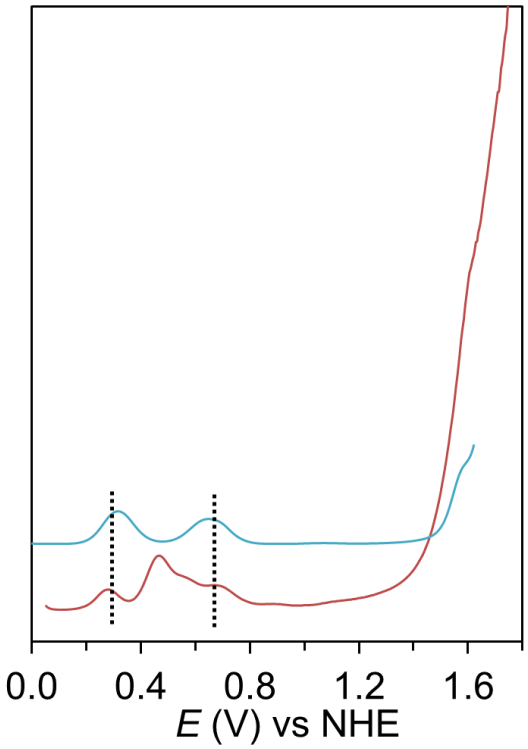

Figure S18. DPVs of *trans*-**2** (light blue), *cis*-**2** (red) at pH10.5 phosphate buffer. The conversion of *cis*-**2** to *trans*-**2** over 1 h in aqueous solution.

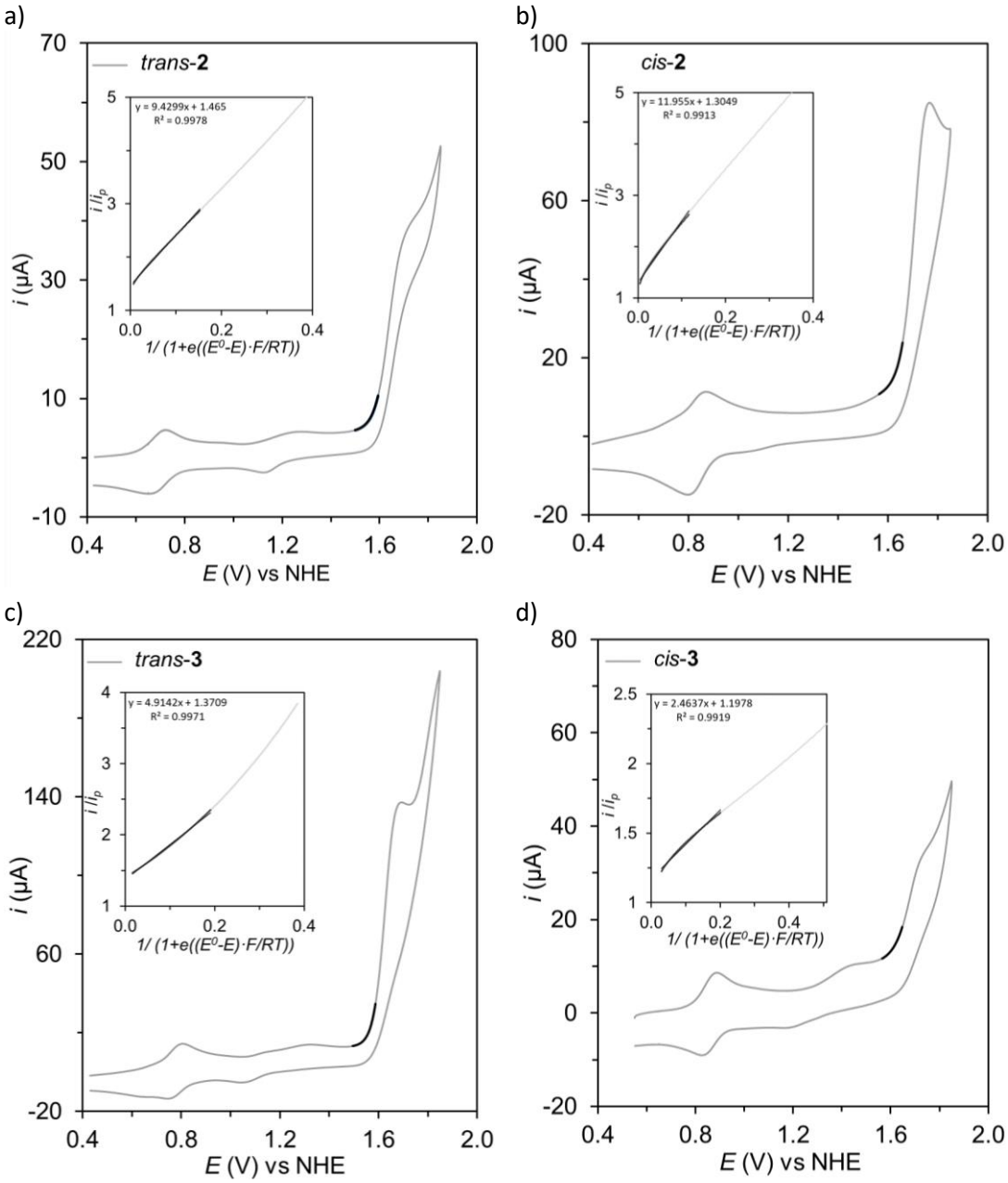

Figure S19. Grey solid line shows a CV of a) *trans*-**2** (top, left), b) *cis*-**2** (top, right), c) *trans*-**3** (bottom, left) and d) *cis*-**3** (bottom, right) at pH 1.0. The black solid line indicates the data points used for the FOWA. (Inset) i/i_p vs. $1/\{1+e\ [(E^0-E)(F/RT)]\}$ plot assuming a WNA mechanism and the used equation. The fitting points for the extraction of rate constants at the foot of the waves are represented as a black solid line in all graphs.

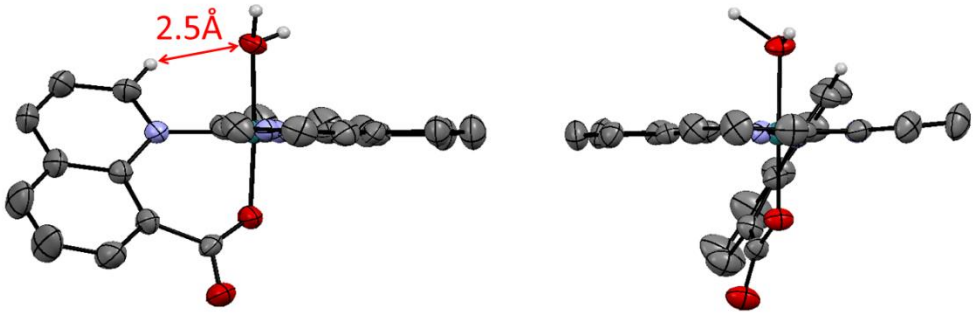

Figure S20. ORTEP views of *trans*-**2** to highlight the H-bond between the C-H group in *ortho* position of the pyridine ring of qc ligand and the aquo ligand coordinated to the Ru^{II} center.

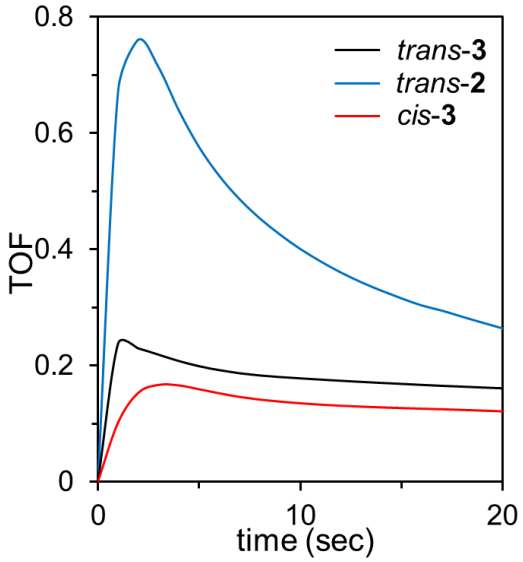

Figure S21. Plot of TOF_i *vs.* time obtained from Manometry experiment *trans*-**2** (blue), *trans*-**3** (black) and *cis*-**3** (red)**.** The experimental condition: 1 mM of complexes and 100 mM of Ce(IV) in 0.1 M triflic acid (2 mL total volume) at 25˚C.

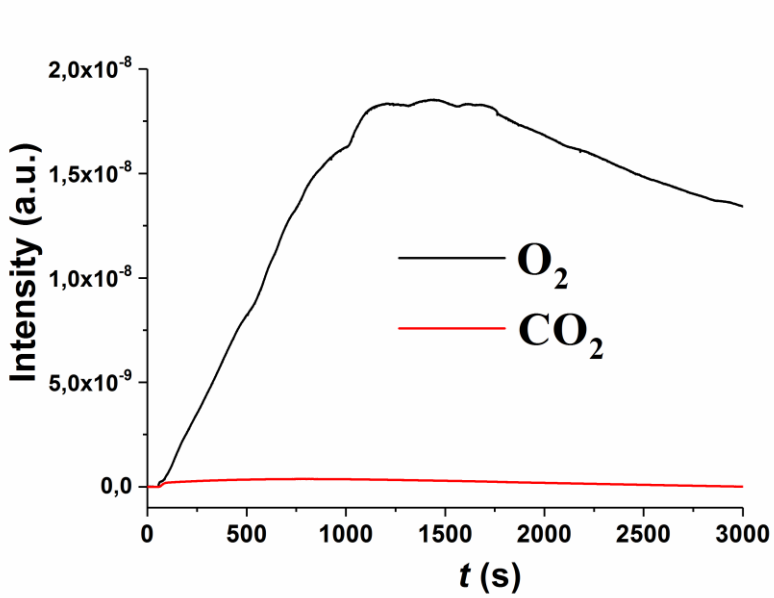

Figure S22. On-line mass spectrometry experiments of a catalysis experiment by *trans*-**2**. Experimental conditions: 1 mM of complex and 100 mM of Ce^{IV} in 0.1 M triflic acid (2 mL total volume) at 25˚C.

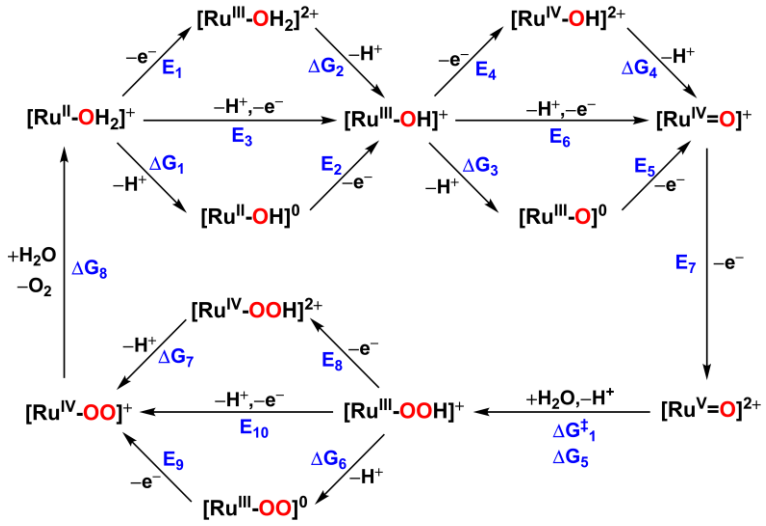

Scheme S1. Mechanism pathway studied with Density Functional Theory of complexes *trans*-**2** and cis-**2**. See Table S1.

Table S1. Summary of redox potentials and free energy calculated for the mechanistic scheme in Scheme S1.

ΔG in kcal/mol, E in V vs NHE at pH 0		**M06-L**		**M06**	
		cis-**2**	*Trans*-**2**	*cis*-**2**	*Trans*-**2**
1st PCET	E_1	0.31	0.37	0.40	0.40
	ΔG_2	5.6	1.8	4.3	1.1
	ΔG_1	16.1	14.5	15.5	14.5
	E_2	–0.14	–0.19	–0.08	–0.19
	E_3	0.56	0.44	0.59	0.44
2nd PCET	E_4	1.17	1.26	1.48	1.57
	ΔG_4	–5.8	–11.0	–7.7	–13.0
	ΔG_3	29.3	28.9	33.2	33.5
	E_5	–0.35	–0.47	–0.30	–0.45
	E_6	0.92	0.78	1.14	1.00
Ru^{IV}=O to Ru^{V}=O	E_7	1.04	1.17	1.41	1.50
O - O Bond Formation	$\Delta G^{\ddagger}_1$	underway	underway	underway	underway
	ΔG_5	25.4	22.8	15.8	14.9
3rd PCET	E_8	1.09	1.02	1.45	1.36
	ΔG_7	–8.0	–0.8	–11.7	–2.5
	ΔG_6	13.2	16.6	14.5	18.2
	E_9	0.17	0.27	0.31	0.46
	E_{10}	0.75	0.99	0.94	1.25
O_2 evolution	ΔG_8	–1.2	–1.3	–1.4	–3.1

Chapter 3A

Table S2. Selected crystallographic prameters for *trans*-**1**, *cis*-**1**, *trans*-**2** and *cis*-[Ru^{II}(trpy)(pic)Cl].

	trans-**1**	*cis*-**1**	*trans*-**2**	*cis*-[Ru^{II}(trpy)(pic)Cl]
emperical formula	C29 H17 Cl N4 O4.50 Ru	C25.10 H20.40 Cl0.90 N4 O3.60 Ru	C25 H21 F6 N4 O4 P Ru	C21.75 H16.50 Cl2.50 N4 O2 Ru
formula weight	629.99	568.63	687.50	555.58
crystal system	Monoclinic	Monoclinic	Monoclinic	Monoclinic
space group	P 21/c	C2/c	P 21/c	P2(1)/c
a (Å)	7.5129(14)	17.9064(5)	13.1911(6)	16.0801(16)
b (Å)	14.076(6)	25.1767(7)	14.2906(5)	18.0650(18)
c (Å)	23.225(6)	13.8906(4)	14.5378(6)	7.8128(8)
α (deg)	90	90°	90	90
β (deg)	93.58(2)	127.8524(6)	108.703(5)	100.736(2)
γ (deg)	90	90	90	90
V ($Å^3$)	2451.4(13)	4944.6(2)	2595.79(18)	2229.8(4)
Z	4	8	4	4
μ (mm^{-1})	0.797	0.768	0.750	1.029

T(K)	120(2)	100(2)	293(2)	100(2)
*D*calcd(g cm^{-3})	1.707	1.528	1.759	1.655
F(000)	1264	2297	1376	1110
θ range(deg)	3.25 to 25.00	1.701 to 30.562	3.28 to 25.00	1.712 to 30.584°.
data/restraints/parameters	4293 / 0 / 359	7414/ 1829/ 639	4558 / 0 / 386	6669/ 225/ 363
R1, wR2 [I>2σ(I)]	0.0770, 0.1540	0.0539, 0.1517	0.0407, 0.0742	= 0.0444, 0.1188
R1, wR2(all data)	0.2122, 0.1960	R1 = 0.0769, wR2 = 0.1696	0.0857, 0.0805	0.0517, 0.1239
GOF	0.822	1.035	0.816	1.074
largest diff. peak/hole, (e $Å^{-3}$)	1.048 and -0.782	1.652 and -0.847	0.614 and -0.428	1.508 and -1.254

Table S3. Selected structural parameters for *trans*-**1**, *cis*-**1**, and *trans*-**2**.

bond length (Å)/ bond angle (deg)	*trans*-**1** X-ray	*cis*-**1** X-ray	*trans*-**2** X-ray
Ru-N1	2.083(10)	2.061(3)	2.085(3)
Ru-N2	2.082(11)	2.053(4)	2.064(4)
Ru-N3	1.924(11)	1.926(3)	1.942(4)
Ru-N4	2.060(10)	2.079(3)	2.058(3)
Ru-O1	1.966(7)	2.085(3)	2.050(3)
Ru-Cl	2.311(3)	2.3934(12)	-
Ru-O3	-	-	2.094(3)
O1-C1	1.287(13)	1.233(6)	1.278(5)
C1-O2	1.237(13)	1.270(6)	1.233(5)
O1-Ru-N3	88.0(3)	174.91 (5)	91.37(14)
N1-Ru-Cl	176.12(5)	172.93(10)	178.58(15)
N2-Ru-N4	159.6(5)	159.42(15)	159.26(13)

Chapter 3B

3B. Synthesis, Electrochemical Characterization and Water Oxidation Catalysis of Ru Complexes Containing the 2,6-Pyridinedicarboxylato Ligand

Md Asmaul Hoque,[1,2] Jordi Benet-Buchholz,[1] Carolina Gimbert-Suriñach,[1] Antoni Llobet[1,3]

[1]Institute of Chemical Research of Catalonia (ICIQ), Barcelona Institute of Science and Technology (BIST), Av. Països Catalans 16, 43007 Tarragona, Spain

[2]Departament de Química Física i Inorganica, Universitat Rovira i Virgili, Campus Sescelades, C/Marcel·lí Domingo, s/n, 43007 Tarragona, Spain

[3]Universitat Autònoma de Barcelona, Departament de Química, Cerdanyola del Vallès, 08193 Barcelona, Spain

III

Contributions

Md Asmaul Hoque has done all the experiments and prepared the manuscript.

Chapter 3B

Abstract

The tridentate meridional ligand pyridyl-2,6-dicarboxylato (pdc) has been used to prepare complexes $Ru^{II}(pdc\text{-}\kappa^3\text{-}N^1O^2)(DMSO)_2Cl]$, **1**^{II} $Ru^{II}(pdc\text{-}\kappa^3\text{-}N^1O^2)(bpy)(DMSO)]$, **2**^{II} and $\{[Ru^{III}(pdc\text{-}\kappa^3\text{-}N^1O^2)(bpy)]_2(\mu\text{-}O)\}$, **5**^{III,III} where bpy: 2,2'-bipyridine. All complexes have been fully characterized through spectroscopic, electrochemical and single crystal X-ray diffraction techniques. Compounds **1**^{II} and **2**^{II} show S→O linkage isomerization of the DMSO ligand upon oxidation from Ru^{II} to Ru^{III} and thermodynamic and kinetic data have been obtained from cyclic voltammetry experiments. Dimeric complex **5**^{III,III} is a precursor of the monomeric complex $[Ru^{II}(pdc\text{-}\kappa^3\text{-}N^1O^2)(bpy)(H_2O)]$, **4**^{II} which is a water oxidation catalyst. The electrochemistry and catalytic activity of **4**^{II} has been ascertained for the first time and compared with related Ru-aquo complexes that are also active for the water oxidation reaction. It shows a TOF_{max} = 0.23 s^{-1} and overpotential of 240 mV in pH 1. The overpotential shown by **4**^{II} is one of the lowest reported in the literature and is associated to the role of the two carboxylato groups of the pdc ligand, providing high electron density to the ruthenium complex.

Graphical Abstract

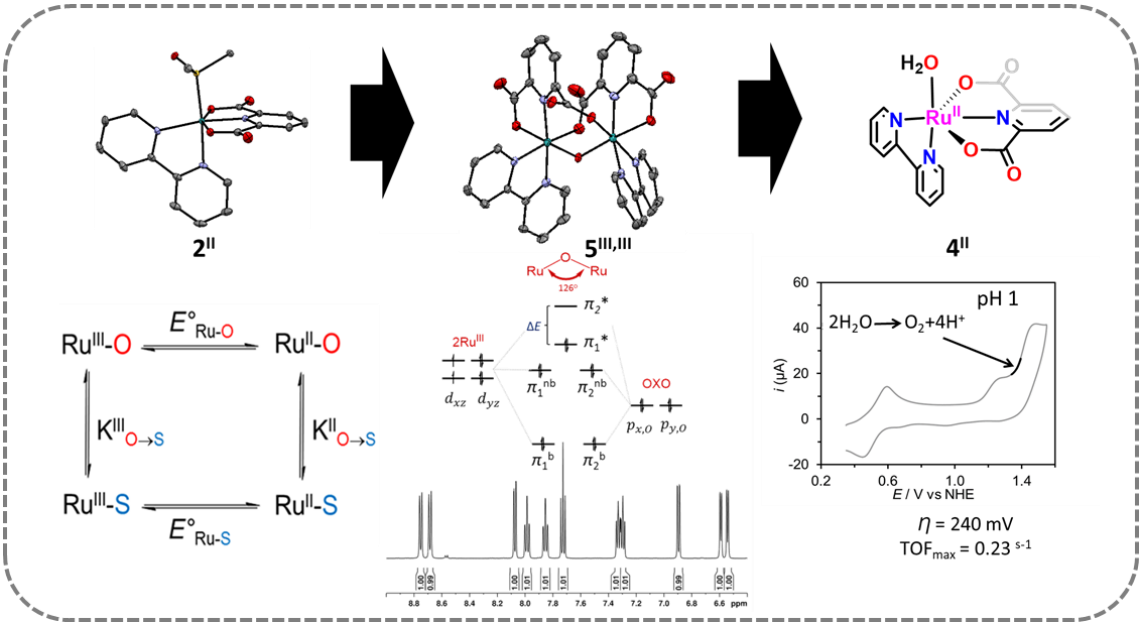

Keywords: Ruthenium, DMSO linkage isomerization, Oxo-bridge, Redox chemistry, Water oxidation

Chapter 3B

3B. 1. Introduction

Homogeneous molecular water oxidation catalysts based on transition metal complexes (Mn, Ru, Ir, Co, Cu, Fe etc)[1-6] have demonstrated that properties of ancillary ligands including electronic parameters, flexibility and orientation can influence the catalytic activity and robustness of catalysts. With the help of spectroscopic, electrochemical and analytical techniques together with the valuable complementary information provided by computational studies it is possible to have a detailed understanding of their mode of action and mechanism.[7-12] For all these reasons significant developments have been carried out based on these type of complexes in terms of their catalytic performance and stability. However, many challenges still remain, including high speed catalysis, robustness and reduced overpotential in order to see molecular catalysts in water splitting devices to generate solar fuels such as hydrogen.

The most extensively studied homogeneous water oxidation catalysts are based on mononuclear ruthenium complexes containing flexible, adaptative, multidentate and equatorial (FAME) ligands containing carboxylate groups that are the fastest water oxidation catalyst reported in the literature[13-18] with a TOF_{max} in the range of 10^2 to 10^4 s^{-1} which exceed by 1-2 orders of magnitude that of the oxygen evolving complex in the natural Photosystem II.[19] Ruthenium complexes are of special interest due to their crucial understanding of the mechanistic pathways responsible for O=O bond formation[7,20] and the electronic perturbation created by ligand environment can influence this pathways.

In the present work we report the synthesis, structural, spectroscopic and electrochemical characterization of ruthenium complexes containing the 2,6 pyridinedicarboxylato ligand (pdc^{2-}); $[Ru^{II}(pdc\text{-}\kappa^3\text{-}N^1O^2)(bpy)(DMSO)]$, $\mathbf{2}^{II}$ and $\{[Ru^{III}(pdc\text{-}\kappa^3\text{-}N^1O^2)(bpy)]_2(\mu\text{-}O)\}$, $\mathbf{5}^{III,III}$, where bpy= 2,2'-bipyridine (Scheme 1), which are derivatives of the water oxidation catalyst $[Ru^{III}(pdc\text{-}\kappa^3\text{-}N^1O^2)(bpy)(H_2O)]^+$, $\mathbf{4}^{III}$. The catalytic activity of $\mathbf{4}^{III}$ is studied and put in context of the best WOCs reported to date.

3B. 2. Experimental Section

Materials

$RuCl_3 \cdot \times H_2O$ was purchased from Alfa-Aesar. The precursor complex $[Ru^{II}(DMSO)_4Cl_2]$ was prepared according to the literature procedure.[21] The ligand precursor 2,6-pyridinedicarboxylic acid (H_2pdc) and other reagents and chemicals were obtained from Aldrich and used as received. When required, solvents were dried by following the standard procedures, distilled under nitrogen and used immediately. High purity de-ionized water used for the electrochemistry experiments was obtained by passing distilled water through a nanopure Milli-Q water purification system. For other spectroscopic and electrochemical studies, HPLC-grade solvents were used.

Instrumentation and Methods

A Bruker Avance 500 MHz was used to carry out NMR spectroscopy. ESI-Mass spectra were recorded using micromass Q-TOF mass spectrometer. Elemental analyses were carried out on Perkin-Elmer 240C elemental analyzer. The pH of the solutions was determined by a pHmeter (CRISON, Basic 20+) calibrated before measurements through a standard solutions at pH 4.01, 7.00 and 9.21. All electrochemical experiments were performed with an IJ-Cambria CHI-660 potentiostat using a three-electrode cell for cyclic voltammetry (CV) and differential pulse voltammetry (DPV) or two compartment cell for bulk electrolysis. $E_{1/2}$ values reported in this work were estimated from CV experiments as the average of the oxidative and reductive peak potentials ($E_{p,a}$ + $E_{p,c}$)/2 or from DPV. The Reference Electrode (RE) was Hg/Hg_2SO_4 (K_2SO_4 saturated) unless indicated and potentials were converted to NHE by adding 0.65 V.

Glassy carbon disk (ϕ = 0.3 cm, S = 0.07 cm^2), Pt disk and Hg/Hg_2SO_4 (K_2SO_4 saturated) were used as Working Electrode (WE), Counter Electrode (CE) and Reference Electrode (RE) respectively, unless explicitly mentioned. Glassy carbon electrodes were polished with 0.05 µm alumina (Al_2O_3) and rinsed with water. CVs and DPVs were iR compensated by the potentiostat in all the measurements unless indicated. Cyclic Voltammograms (CV) were recorded at 100 $mV \cdot s^{-1}$ scan rate, unless explicitly expressed. The DPV parameters were ΔE= 4 mV, Amplitude = 50 mV, Pulse width = 0.05 s, Sampling width = 0.0167 s, Pulse period = 0.5 s. The complexes were dissolved in dichloromethane (DCM) containing the necessary amount of $[(n\text{-}Bu)_4N][PF_6]$ (TBAH) as supporting electrolyte to yield a 0.1 M ionic strength (*I*) solution. In aqueous solution the electrochemical experiments were carried out in 0.1 M triflic acid solution for pH 1 and *I* = 0.1 M phosphate buffer solutions with desired the pH. For

construction of the Pourbaix diagrams, the following buffers were used: dihydrogen phosphate/phosphoric acid up to pH = 4 (pK_a = 2.12), hydrogen phosphate/dihydrogen phosphate up to pH = 9 (pK_a = 7.67), hydrogen phosphate/sodium phosphate up to pH = 13 (pK_a = 12.12) and also 0.1 M CF_3SO_3H for pH = 1.0. For routine bulk electrolysis experiments, a Pt grid was used as a WE, another Pt grid as a CE and a Hg/Hg_2SO_4 (K_2SO_4 saturated) as a RE. Online manometric measurements were performed on a Testo 521 differential pressure manometer with an operating range of 0.1-10 kPa and accuracy within 0.5% of the measurements. The manometer was coupled to thermostatic reaction vessels for dynamic monitoring of the headspace pressure above each reaction solution. The manometer's secondary ports were connected to thermostatic reaction vessels containing the same solvents and headspace volumes as the sample vials. Each measurement for a reaction solution (2.0 mL) was performed at 298 K. For manometric experiment, Control potential electrolysis was carried out for 10 min with 1 mM complex of $\mathbf{5}^{\mathbf{III,III}}$ in pH 1. It was assumed that upon breaking of dimeric complex $\mathbf{5}^{\mathbf{III,III}}$, it produced 2 equivalent of monomeric complex $\mathbf{4}^{\mathbf{II}}$, that means concentration of $\mathbf{4}^{\mathbf{II}}$ becomes 2 mM. This complex was diluted to half with additional pH 1 solution to get 1 mM of $\mathbf{4}^{\mathbf{II}}$.

Single Crystal X-Ray Structure Determinations

Crystal Preparation: Crystals of $[Et_3NH][Ru^{II}(pdc\text{-}\kappa^3\text{-}N^1O^2)(DMSO)_2Cl]$, $\mathbf{1}^{\mathbf{II}}$ $[Ru^{II}(pdc\text{-}\kappa^3\text{-}N^1O^2)(bpy)(DMSO)]$, $\mathbf{2}^{\mathbf{II}}$ and $\{[Ru^{III}(pdc\text{-}\kappa^3\text{-}N^2O^1)(bpy)]_2(\mu\text{-}O)\}$, $\mathbf{5}^{\mathbf{III,III}}$ were grown by slow evaporation of 1:1 methanol : benzene, 1:1 methanol : diethylether and 1:1 dichloromethane: hexane respectively. The crystals used for structure determination were selected using a Zeiss stereomicroscope using polarized light and prepared under inert conditions immersed in perfluoropolyether as protecting oil for manipulation.

Data Collection: Crystal structure determination for compounds $\mathbf{1}^{\mathbf{II}}$, $\mathbf{2}^{\mathbf{II}}$ and $\mathbf{5}^{\mathbf{III,III}}$ were carried out using a Apex DUO Kappa 4-axis goniometer equipped with an APPEX 2 4K CCD area detector, a Microfocus Source E025 IuS using MoK_α radiation, Quazar MX multilayer Optics as monochromator and an Oxford Cryosystems low temperature device Cryostream 700 plus (T = -173 ˚C). Crystal structure determination for samples Full-sphere data collection was used with ω and φ scans. *Programs used:* Data collection APEX-2[22], data reduction Bruker Saint[23] V/.60A and absorption correction SADABS.[24]

Structure Solution and Refinement: Crystal structure solution was achieved using the computer program SHELXT.[25] Visualization was performed with the program SHELXle.[26] Missing atoms were subsequently located from difference Fourier synthesis and added to the

atom list. Least-squares refinement on F^2 using all measured intensities was carried out using the program SHELXL 2015.[27] All non-hydrogen atoms were refined including anisotropic displacement parameters.

Comments to the Structures: $[Et_3NH][Ru^{II}(pdc\text{-}\kappa^3\text{-}N^1O^2)(DMSO)_2Cl]$, **$1^{II}$**: The asymmetric unit contains two molecules of the metal complex (each coordinated to two DMSO molecules), two triethylamonium cations, two water molecules and two benzene molecules. The benzene molecules are disordered in two orientations. $[Ru^{II}(pdc\text{-}\kappa^3\text{-}N^2O^1)(bpy)(DMSO)]$, **$2^{II}$**: The asymmetric unit contains one molecule of the metal complex (coordinated to a DMSO molecule) and two molecules of water. $\{[Ru^{III}(pdc\text{-}\kappa^3\text{-}N^2O^1)(bpy)]_2(\mu\text{-}O)\}$, **$5^{III,III}$**: The asymmetric unit contains two independent molecules of the metal complex and 5.1 molecules of dichloromethane. The dichloromethane molecules are disordered in 11 positions with a ratio: 1.00:0.75:0.60:0.40:0.55:0.45:0.70:0.20:0.25:0.10:0.10.

Synthesis of $[Et_3NH][Ru^{II}(pdc\text{-}\kappa^3\text{-}N^1O^2)(DMSO)_2Cl]\cdot H_2O$, 1^{II}. In a 100 mL two neck round bottom flask, $[Ru^{II}(DMSO)_4Cl_2]$ (450 mg, 0.93 mmol), 2,6-pyridine dicarboxylic acid (155 mg, 0.93 mmol) and triethylamine (0.2 mL) were dissolved in 30 mL of degassed methanol and were reflux for 5 h under N_2 atmosphare. The resulting solution was filtered and the volume was reduced to 5 mL. Then 30 mL of diethyl ether was added to obtain an orange precipitate. The solid was filtered and washed with diethyl ether (3x20 mL) and dried under vacuum. Yield: 460 mg (0.82 mmol, 88%). The characterization data matches with reported complex.[28]

Synthesis of $[Ru^{II}(pdc\text{-}\kappa^3\text{-}N^1O^2)(bpy)(DMSO)]\cdot 1.5H_2O$, 2^{II}. In a 100 mL two neck round bottom flask, $[Et_3NH][Ru^{II}(pdc\text{-}\kappa^3\text{-}N^1O^2)(DMSO)_2Cl]$, **$1^{II}$** (560 mg, 1 mmol) and 2,2´-bipyridine (156 mg, 1 mmol) were dissolved in 40 mL degassed methanol solvent and refluxed for 4 hours under N_2 atmosphere. The mixture was then evaporated to dryness and the resulting solid dissolved in CH_2Cl_2 and purified over neutral alumina using a mixture of CH_2Cl_2/MeOH (100:2) as eluent. The first orange-red fraction was collected an identified with complex **2^{II}**. Yield: 60 mg (0.12 mmol, 12%). Anal. Calc. for ($C_{19}H_{17}N_3O_5RuS\cdot 1.5H_2O$): C, 43.26%; H, 3.82%; N, 7.94%; S, 6.08%. Found: C, 43.35%; H, 3.15%; N, 7.85%; S, 6.18%. ^{1}H-NMR (500 MHz, [d_2]-DCM) δ: 10.61 (d, J=5.7 Hz, 1H), 8.29 (d, J= 8.4 Hz, 2H), 8.24 (d, J=7.7 Hz, 2H), 8.14 (t, J=7.8 Hz, 1H), 7.89 (tt, J=3.5 and 7.8Hz, 2H), 7.61 (t, J=7.3 Hz, 1H), 7.29 (t, J=6.6 Hz, 1H), 6.96 (d, J=5.6 Hz, 1H), 2.65 (s, 6H). ^{13}C-NMR (125 MHz, [d_2]-DCM) δ: 172.6, 158.3, 158.1, 157.4, 154.3, 148.7, 138.4, 137.2, 136.6, 128.9, 127.1, 123.5, 123.1, 51.2 and 42.6. (ESI$^+$-HRMS; MeOH) m/z: calc. for $[M+Na]^+$: 523.9857, found m/z: 523.9830.

Chapter 3B

Synthesis of {[Ru^{III}(pdc-κ^3-N^1O^2)(bpy)]$_2$(μ-O)}·2H_2O, $5^{III,III}$. In a 100 mL two neck round-bottom flask, [Ru^{III}(pdc-κ^3-N^1O^2)(bpy)Cl][15] (100 mg, 0.22 mmol) was dissolved in 40 mL of acetone/water (3:1) followed by addition of triethylamine (0.20 mL) and stirred for 5 minutes under N_2. Then silver perchlorate (120 mg, 0.58 mmol) was added to the reaction mixture and stirred for 30 minutes at 50°C. The precipitated AgCl was filtered through Celite®. The mixture was then evaporated to dryness and the resulting solid was dissolved in CH_2Cl_2 and purified by chromatography with neutral alumina using a mixture of CH_2Cl_2/MeOH (100:4) as eluent. The blue colour fraction was collected and evaporated to drynes to give complex $\mathbf{5^{III,III}}$. Yield 37 mg (0.043 mmol, 20%). Anal. Calc. for ($C_{34}H_{22}N_6O_9Ru_2$·2H_2O): C, 45.54%; H, 2.92%; N, 9.37%. Found: C, 45.31%; H, 2.50%; N, 9.26%. ^{1}H-NMR (500 MHz, [d_6]-DMSO) δ: 8.75 (d, J= 8.1 Hz, 1H), 8.68 (d, J= 8.2 Hz, 1H), 8.07 (dd, J=7.6 Hz and 1.4 Hz, 1H), 7.98 (t, J=7.6 Hz, 1H), 7.87 (td, J= 8.95 Hz and 1.3 Hz, 1H), 7.72 (t, J= 7.75 Hz, 1H), 7.33 (t, J= 7.0 Hz, 1H), 7.29 (t, J-= 7.15 Hz, 1H), 6.89 (dd, J= 7.75 Hz and 1.4 Hz, 1H), 6.59 (d, J= 4.9 Hz, 1H), 6.54 (d, J= 5.3 Hz, 1H). ^{13}C-NMR (125 MHz, [d_6]-DMSO) δ: 173.2, 169.6, 164.6, 159.5, 158.6, 153.9, 152.3, 150.4, 140.9, 140.1, 139.9, 127.4, 125.4, 125.3, 124.8, 123.5 and 123.3. (ESI$^+$-HRMS; MeOH) m/z: calc. for [M+Na]$^+$: 884.9492, found m/z: 884.9441.

3B. 3. Results and Discussion

3B. 3. 1. Synthesis and Characterization of Complexes 1-5

The reaction of 2,6-pyridinedicarboxylic acid (H_2pdc) with the ruthenium precursor complex $[Ru(DMSO)_4Cl_2]$ in the presence of Et_3N as a base in MeOH under reflux gives complex **1^{II}**, which upon treatment with 1 equivalent of bpy gives complex **2^{II}** in 12% isolated yield (Scheme 1, top).

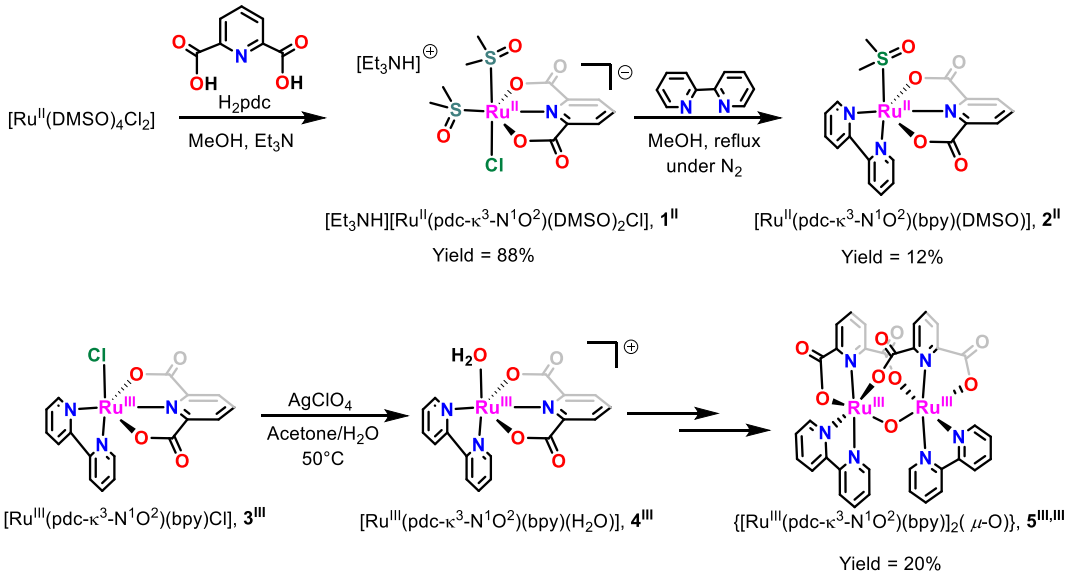

Scheme 1. Synthetic strategy and labelling scheme used for the ligands and complexes described in this work.

On the other hand, when $RuCl_3$ is used as ruthenium source, the analogous complex [Ru^{III}(pdc-κ^3-N^{1}O^2)(bpy)Cl], **3^{III}** with a chlorido ligand instead of DMSO ligand is obtained as we recently reported.[15] The addition of $AgClO_4$ to a solution of **3^{III}** generates an ustable species identified as complex [Ru^{III}(pdc-κ^3-N^{1}O^2)(bpy)(OH$_2$)], **4^{III}** that slowly converts to an oxo bridged dimer **5^{III,III}** (Scheme 1, bottom). This complex was purified by column chromatography and isolated as a blue solid in 20% yield.

Complexes **2^{II}** and **5^{III,III}** were structurally characterized in the solid state by single crystal X-ray diffraction analysis and in solution by NMR spectroscopy. The ORTEP plots of complex **2^{II}** in Figure 1b displays highly distorted octahedral geometry around the ruthenium metal due to the strain imposed by the pdc^{2-} meridional ligand with O-Ru-O angle of 158.1(5)˚ as opposed to the 180˚ expected for an ideal octahedron. Bond distances and angles are very similar to those of **3^{III}** and other related complexes reported in the literature.[15,28,29] The bpy ligand occupies both axial and equatorial positions assuming the κ-N^{1}O^2-pdc^{2-} ligand binds in the equatorial plane.

Chapter 3B

The crystal structure of dimeric complex $\mathbf{5^{III,III}}$ shows that both metal centers exhibit a distorted octahedral geometry (Figure 1c). The Ru-O_{oxo} bond distances are 1.869 (4) Å and 1.885 (4) Å, which are in the range of reported Ru^{III}-O-Ru^{III} type of complexes.[30-33]

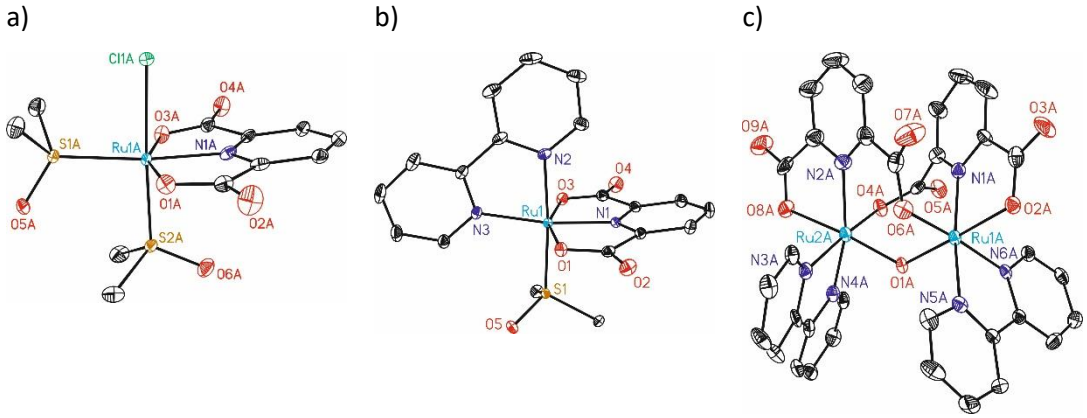

Figure 1. ORTEP plots at 50% probability for a) $[Ru^{II}(pdc\text{-}\kappa^3\text{-}N^1O^2)(DMSO)_2Cl]^-$, $\mathbf{1^{II}}$; b) $[Ru^{II}(pdc\text{-}\kappa^3\text{-}N^1O^2)(bpy)(DMSO)]$, $\mathbf{2^{II}}$ and c) $\{[Ru^{III}(pdc\text{-}\kappa^3\text{-}N^1O^2)(bpy)]_2(\mu\text{-}O)\}$, $\mathbf{5^{III,III}}$.

The angle defined by Ru-O-Ru in complex $\mathbf{5^{III,III}}$ is significantly bent with a value of 125.9(2)˚. As reported before, this angle has a strong influence in the electronic configuration of the molecule, which will be affected by the overlapping of the orbitals of the oxo ligand with those of the Ruthenium centers (see molecular orbital scheme in Figure 2, where the Ru-O bond is taken as z axis). For bent structures such as in $\mathbf{5^{III,III}}$ a high-energy gap between π_1* and π_2* orbitals is expected resulting in the following diamagnetic electronic configuration; $(\pi_1^b)^2$ $(\pi_2^b)^2$ $(\pi_1^{nb})^2$ $(\pi_2^{nb})^2$ $(\pi_1^*)^2$ $(\pi_2^*)^0$.[34,35] In contrast, dinuclear oxo-bridged Ru^{III} complexes with Ru-O-Ru angles close to 180° display a paramagnetic behavior because their π_1* and π_2* orbitals are either degenerate or very close in energy.[30] The diamagnetic and symmetric nature of $\mathbf{5^{III,III}}$ is clear from its ^{1}H NMR spectrum in [d_6]-DMSO solution, which shows two single set of resonances for the pdc^{2-} and the bpy ligands, respectively (Figure 2).

Although bidimensional NMR experiments allowed as to unequivocally assign all the resonances to the respective ligands, it was not possible to distinguish between the two pyridine rings of the bpy ligand, which have been arbitrary labeled as a diamond (♦) and square (■) symbols in the ^{1}H NMR spectrum in Figure 2 (see also Figure S4-S6).

The ^{1}H NMR spectrum of complex $\mathbf{2^{II}}$ in [d_2]-DCM shows a characteristic signal at low field (δ = 10.61 ppm) for a proton deshielded by the through space interaction with the closest DMSO ligand (Figure S1-S3).[36] Protons of the two methyl groups of the DMSO ligand are clearly visible at high field (δ = 2.65 ppm) as expected.

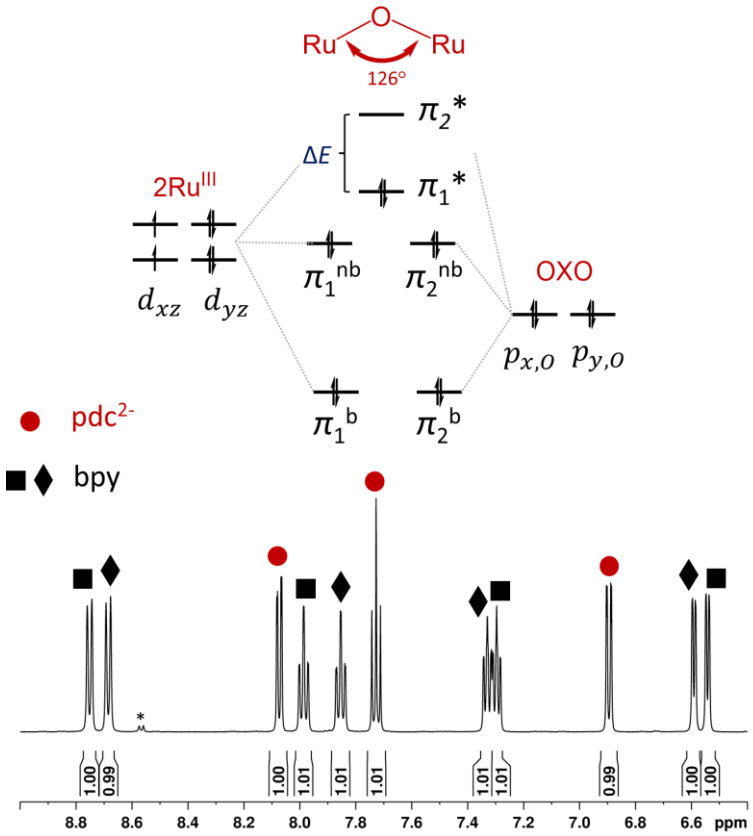

Figure 2. ^{1}H NMR spectrum of complex {[Ru^{III}(pdc-κ^{3}-N^{1}O^{2})(bpy)]$_2$(μ-O)}, **5^{III,III}** in [d$_6$]-DMSO (500 MHz, 298 K). Squares and symbols indicate the signals of the two independent pyridine rings in the bipyridine ligand. Asterisks indicate unidentified signal.

The optical properties of complexes **2^{II}** and **5^{III,III}** were investigated by UV–vis spectroscopy in DCM (Figure 3). Both compounds show π–π* transitions due to the aromatic ligands below 350 nm and weaker metal to ligand charge transfer (MLCT) d–π* bands showing between 350 and 500 nm. In addition, complex **5^{III,III}** has a prominent band at 617 nm that is typical of Ru^{III}-O-Ru^{III} type of complexes.[30,37]

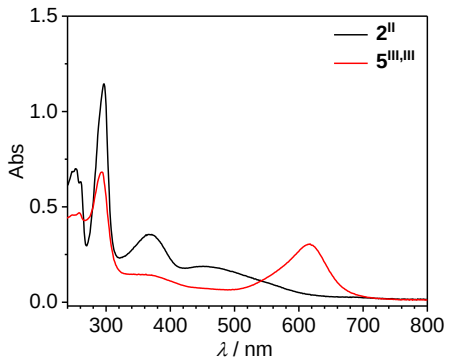

Figure 3. UV–vis spectra of 0.2 mM of complexes **2^{II}** (black) and **5^{III,III}** (red) in DCM.

3B. 3. 2. Electrochemistry in Organic Solvent

The redox properties of complexes **1**, **2** and **5** were analysed by means of cyclic voltammetry (CV) in DCM containing 0.1 M [(*n*-Bu_4N)]PF_6 (TBAH) as supporting electrolyte. All redox potentials reported in this work are referred to the NHE electrode, and all CV were run at a scan rate of 100 mV/s unless explicitly mention. Glassy carbon disk was used as working electrode, platinum disk as auxiliary electrode and Hg/Hg_2SO_4 as reference electrode.

3B. 3. 2. 1. DMSO Linkage Isomerization of Complexes 1^{II} and 2^{II}

Complexes $\mathbf{1}^{II}$ and $\mathbf{2}^{II}$ are two new examples that show S→O DMSO linkage isomerization by changing oxidation state of the Ru metal center from II to III (Scheme 2). As shown in Figure 4 and Figure S8 complex $\mathbf{1}^{II}$ shows an irreversible wave with $E^1_{p,a}$ = 1.05 V and $E^1_{p,c}$ = 0.87 V associated with the $Ru^{III/II}$-S redox couple. After the anodic scan a new wave appears at $E^2_{p,c}$ = 0.19 V and $E^2_{p,a}$ = 0.32 V assigned to the $Ru^{III/II}$-O couple. This significant anodic shift in potential due to the distinct coordination mode of the DMSO ligand has been observed before and is attributed to the lower π-accepting properties of the S-bonded ligand as compared to the O-bonded DMSO ligand.[36] The peak intensity ratios $[i_{p,c}]/[i_{p,a}]$ depend strongly on the scan rate for both redox couples as a result of the different kinetics of the isomerization processes described in Scheme 2. In addition, the relative intensity of the two redox couples change significantly if a quick controlled potential electrolysis (CPE) is carried out at -0.2 V or at 1.4 V (Figure 4 and Figure S8).

The equilibrium constant $K^{III}_{O\rightarrow S}$ for the Ru^{III}–O/Ru^{III}–S reaction of the square mechanism shown in Scheme 2 can be obtained from the CVs in Figure 4 (bottom), plotting the ratio $[i_{p,c1}]/[i_{p,c2}]$ versus the inverse of the scan rate (v^{-1}) and extrapolating for $v \rightarrow \infty$, where the intensities of the waves correspond to the concentrations at the equilibrium.[38] This mathematical treatment results in $K^{III}_{O\rightarrow S}$ = 0.60 (Figure S8).

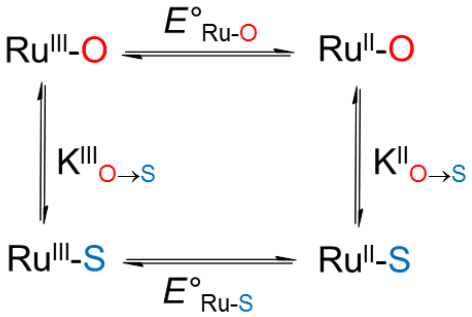

Scheme 2. Square mechanism associated with the S→O DMSO linkage isomerization by changing oxidation state of the Ru metal center.

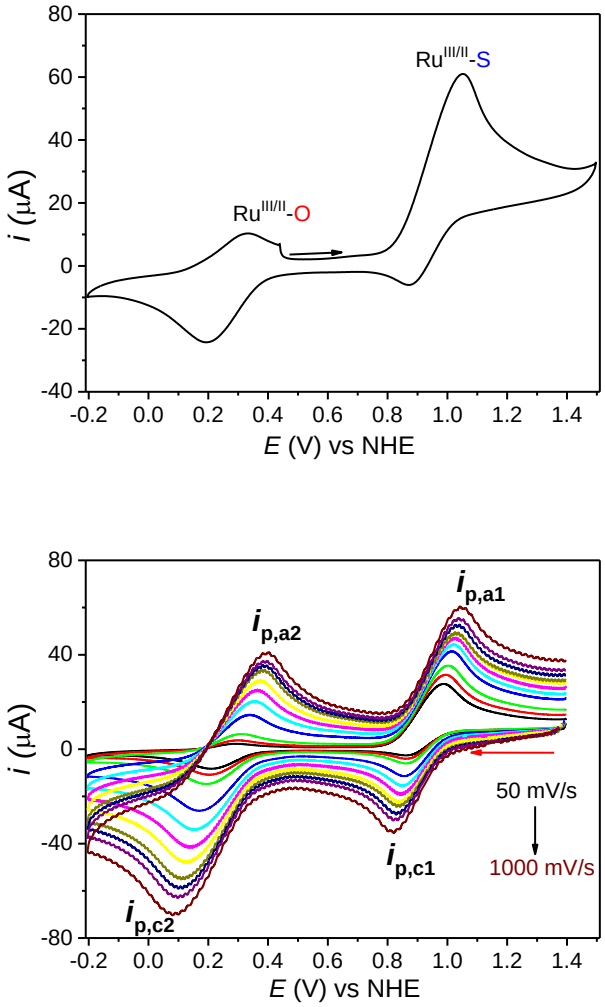

Figure **4**. CVs of 1 mM of **1**^{II} in DCM containing 0.1 M TBAH starting at the open circuit potential (top) and after leaving the potential at 1.4 V for 2 minutes before the scan. Arrows indicate initial scan direction, color code denote scan rate (mV/s): Black: 50 mV/s, red: 70 mV/s, green: 100 mV/ s, blue: 200 mV/s, turquoise: 300 mV/s, pink: 400 mV/s, yellow: 500 mV/s, dark green: 600 mV/s, dark blue: 700 mV/s, purple: 800 mV/s and marron: 1000 mV/s.

In addition, the kinetic constants for the isomerization in the Ru^{III} oxidation state can be calculated using the working curves for a chemical reaction preceding an electron transfer proposed by Shain and co-workers[39] that uses the ratio i_k/i_d where i_k is the measured peak current $i_{p,c1}$, of the CV starting at 1.4 V after a CPE of 2 min (Figure 4), and i_d is the corresponding diffusion current in the absence of a chemical reaction. As an estimated value of i_d, we used $i_{p,a1}$ of the CV starting at -0.2 V after a CPE of 2 min (Figure S8). The values thus obtained are $k^{III}_{O\rightarrow S} = 5.52\times10^{-6}\ s^{-1}$ and $k^{III}_{S\rightarrow O} = 9.21\times10^{-6}\ s^{-1}$.

Assuming $E^0 = E_{1/2}$ and knowing the value of $K^{III}_{O\rightarrow S}$, the thermodynamic cycle in Scheme 2 can be derived and used to calculate $K^{II}_{S\rightarrow O} = 5.89 \times 10^{+11}$.

Chapter 3B

The kinetic isomerization constant $k^{II}_{O\rightarrow S}$ in the Ru^{II} state was calculated from the dependency of $\ln(i_{a2}/v^{1/2})$ versus time[38] and gives a value of 9.39×10^{-2} s^{-1} (Figure S8). The whole cycle is completed by calculating the remaining constant $k^{II}_{S\rightarrow O}$ with a value of 1.59×10^{-13} s^{-1} (equation 1).

$$K^{II}_{O\rightarrow S} = \frac{k^{II}_{O\rightarrow S}}{k^{II}_{S\rightarrow O}} \qquad (1)$$

Analogously to complex **1**^{II}, complex **2**^{II} also shows two electrochemically quasi-reversible redox waves at $E^{1}_{1/2}{}^{III/II}$ = 1.06 V (ΔE = 96 mV) and $E^{2}_{1/2}{}^{III/II}$ = 0.54 V (ΔE = 60 mV) corresponding to $Ru^{III/II}$-S and $Ru^{III/II}$-O redox couples respectively (Figure S9 and S10). Following the same mathematical methodology, we calculated all the equilibrium and rate constants associated with the square mechanism of Scheme 2 for **2**^{II}. All these data are summarized in Table 1 together with the results of **1**^{II} and other relevant compound reported in the literature.

Complexes **1**^{II} and **2**^{II} have the lowest $Ru^{III/II}$ oxidation potentials in Table 1 as a result of the high sigma-donation of the carboxylate groups in the pdc ligand (compare entries 1 and 2 with entries 3-7). Interestingly the complexes having only one DMSO, such as **2**^{II}, show slower $K^{II}_{O\rightarrow S}$ rate as compared to the complexes having two DMSO ligands such as **1**^{II} with the exception of complex *cis, trans*-$[Ru(HPhpp)(DMSO)_2Cl_2]$ in entry 5 (where HPpp is 2-(5-phenyl-1*H*-pyrazol-3-yl)pyridine). Although it is not trivial to compare thermodynamic and kinetic values of complexes with distinct coordination sphere and different relative disposition of chlorido and DMSO ligands, a general trend is observed for all the complexes in Table 1; the values of the linkage isomerization constants $K^{II}_{O\rightarrow S}$ are very high, in the order of 10^8-10^{12}, indicating that Ru^{II}-O species are much less stable and convert to the Ru^{II}-S at low oxidation state. On the other hand, the tendency to isomerize for Ru^{III}-S to the corresponding Ru^{III}-O is less favored for all complexes with equilibrium constants in the range of 0.13-1.7.

Chapter 3B

Table 1. Thermodynamics and kinetics data for the S→O linkage isomerization process of complexes **1**^{II} and **2**^{II} and related compounds reported in the literature.

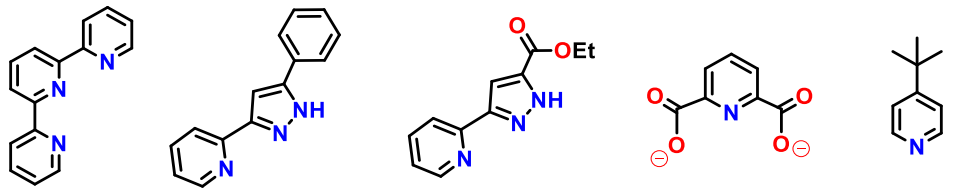

Ligand labels for the Ru-DMSO complexes in the Table

Entry	Complex	$E_{1/2}$(Ru-S)[a]	$E_{1/2}$(Ru-O)[a]	$K^{III}_{(O\rightarrow S)}$	$k^{III}_{O\rightarrow S}[s^{-1}]$	$k^{III}_{S\rightarrow O}[s^{-1}]$	$K^{II}_{(O\rightarrow S)}$	$k^{II}_{O\rightarrow S}[s^{-1}]$	$k^{II}_{S\rightarrow O}[s^{-1}]$
1[b]	[Ru(pdc)(DMSO)$_2$Cl]$^-$, **1**^{II}	0.96	0.26	0.59	4.7×10^{-1}	7.9×10^{-1}	$5.9 \times 10^{+11}$	9.4×10^{-2}	1.6×10^{-13}
2[b]	[Ru(pdc)(bpy)(DMSO)], **2**^{II}	1.06	0.54	0.91	8.9×10^{-1}	9.8×10^{-1}	$8.0\times 10^{+8}$	6.9×10^{-2}	1.2×10^{-10}
3[40]	*out*-[Ru(HPpp)(trpy)(DMSO)]$^{+,c}$	1.22	0.65	0.13	7.7×10^{-2}	6.0×10^{-1}	$5.5 \times 10^{+8}$	2.5×10^{-1}	4.6×10^{-10}
4[41]	*cis(in), cis(out)*-[Ru(HPpp)(DMSO)$_2$Cl$_2$][c]	1.27	0.70	1.7	2.8×10^{-1}	1.7×10^{-1}	$5.2 \times 10^{+11}$	4.9×10^{-1}	9.3×10^{-14}
5[41]	*cis, trans*-[Ru(HPpp)(DMSO)$_2$Cl$_2$][c]	1.22	0.63	0.20	5.7×10^{-2}	2.2×10^{-1}	$5.3 \times 10^{+8}$	8.7×10^{-2}	1.6×10^{-10}
6[36]	*cis(in),cis(out)*-[Ru(Hppc)(DMSO)$_2$Cl$_2$][d]	1.37	0.69	0.41	2.0×10^{-1}	4.9×10^{-1}	$2.1 \times 10^{+11}$	9.3×10^{-2}	4.5×10^{-13}
7[38]	*cis, cis, cis*-[Ru(tbpy)$_2$(DMSO)$_2$Cl$_2$][e]	1.51	0.79	0.63	1.2	1.9	$2.1 \times 10^{+12}$	1.0×10^{-2}	5.0×10^{-14}

[a]Potentials are given in volts versus the NHE electrode. CV experiments were performed in CH_2Cl_2 /TBAH (0.1 M) solvent for all complexes except for [Ru(tbpy)$_2$(DMSO)$_2$Cl$_2$] in entry 7 that was analyzed in CH_3CN/TEAP (0.1 M) where TEAP is tetraethylammonium perchlorate. [b]This work. [c]HPpp: 2-(5-phenyl-1*H*-pyrazol-3-yl)pyridine. [d]Hppc: ethyl 3-(pyridin-2-yl)-1*H*-pyrazole-5-carboxylate. [e]tbpy: 4-(*tert*-butyl)pyridine.

3B. 3. 2. 2. Redox Behavior of Dimeric Compound $5^{III,III}$

The oxo bridged dinuclear complex $\mathbf{5}^{III,III}$ shows two one-electron reversible waves at $E^{III,III/IV,III}_{1/2}$ = 0.86 V (ΔE = 84 mV) and $E^{IV,III/IV,IV}_{1/2}$ = 1.75 V (ΔE = 105 mV) in trifluoroethanol solvent containing 0.1 M TBAH (Figure 5). The high reversibility of both redox processes highlight the stability of the dimeric structure of **5**, that doesn't rearrange or react upon oxidation in organic solvents.

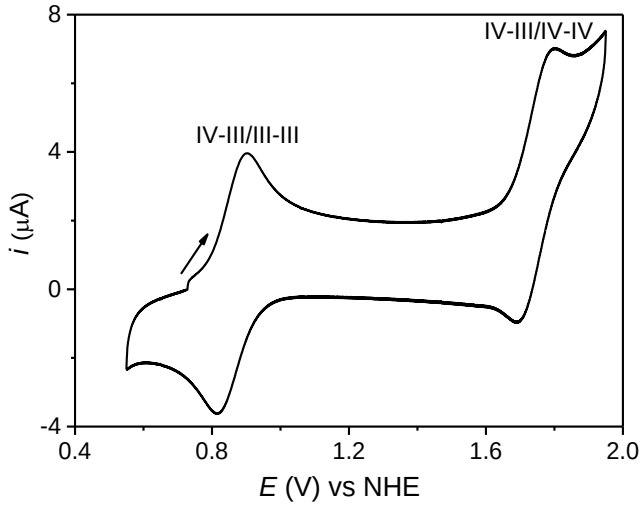

Figure 5. CV of 0.5 mM of $\mathbf{5}^{III,III}$ in trifluoroethanol containing 0.1 M TBAH.

Chapter 3B

3B. 3. 3. Electrochemistry of $\mathbf{5^{III,III}}$ in Aqueous Solution

3B. 3. 3. 1. Conversion of $\mathbf{5^{III,III}}$ into $\mathbf{4^{II}}$

The redox properties of the oxo-bridged dimer $\mathbf{5^{III,III}}$ in aqueous solution were analysed in pH 1 triflic acid solution (Figure 6). It shows a one-electron oxidation wave at $E_{1/2}$ = 0.85 V (ΔE = 67 mV) associated with the Ru^{IV}-O-Ru^{III}/Ru^{III}-O-Ru^{III} redox couple, that is consistent with that observed in organic solvents in Figure 5. A subsequent cathodic scan all the way down to 0.05 V shows a chemically irreversible wave at $E_{p,c}$ = 0.30 V, that we attribute to a $2e^-/1H^+$ transfer as reported for similar complexes that also contain a dinuclear oxo-bridged motive, which is prone to protonation upon reduction.[30] This proton couple electron transfer (PCET) process is followed by the breaking of the resulting Ru-OH-Ru bridge and the formation of the corresponding mononuclear complex [Ru^{II}(pdc-κ^3-N^1O^2)(bpy)(H_2O)], $\mathbf{4^{II}}$ as shown in Scheme 1 and indicated in equations 2-4. Upon repetitive CV cycles in the potential range from 0.05 V to 0.95 V, a new redox wave appears at $E^{III/II}{}_{1/2}$ = 0.52 V with concomitant disappearance of the redox couples associated with $\mathbf{5^{III,III}}$ (Figure 6, top). This can be further prove by a quick control potential electrolysis. It was carried out at E_{app} = 0.05 V for 10 min. As can be seen from Figure 6 (bottom) all the starting complex $\mathbf{5^{III,III}}$ completely converts to the new complex $\mathbf{4^{II}}$.

$$\mathrm{Ru^{III}-O-Ru^{III}} \; - \; 1\mathrm{e^-} \rightarrow \mathrm{Ru^{III}-O-Ru^{IV}} \quad E_{\frac{1}{2}} = 0.85\mathrm{V} \qquad (2)$$

$$\mathrm{Ru^{III}-O-Ru^{III}}(\mathbf{5^{III,III}}) \; + \; 1\mathrm{e^-} + 1\mathrm{H^+} \rightarrow \mathrm{Ru^{II}-(OH)-Ru^{II}} \quad E_{\frac{1}{2}} = 0.3\mathrm{V} \qquad (3)$$

$$\mathrm{Ru^{II}-(OH)-Ru^{II}} \; + \; \mathrm{H_2O} + 1\mathrm{H^+} \rightarrow 2\mathrm{Ru^{II}-OH_2}(\mathbf{4^{II}}) \qquad (4)$$

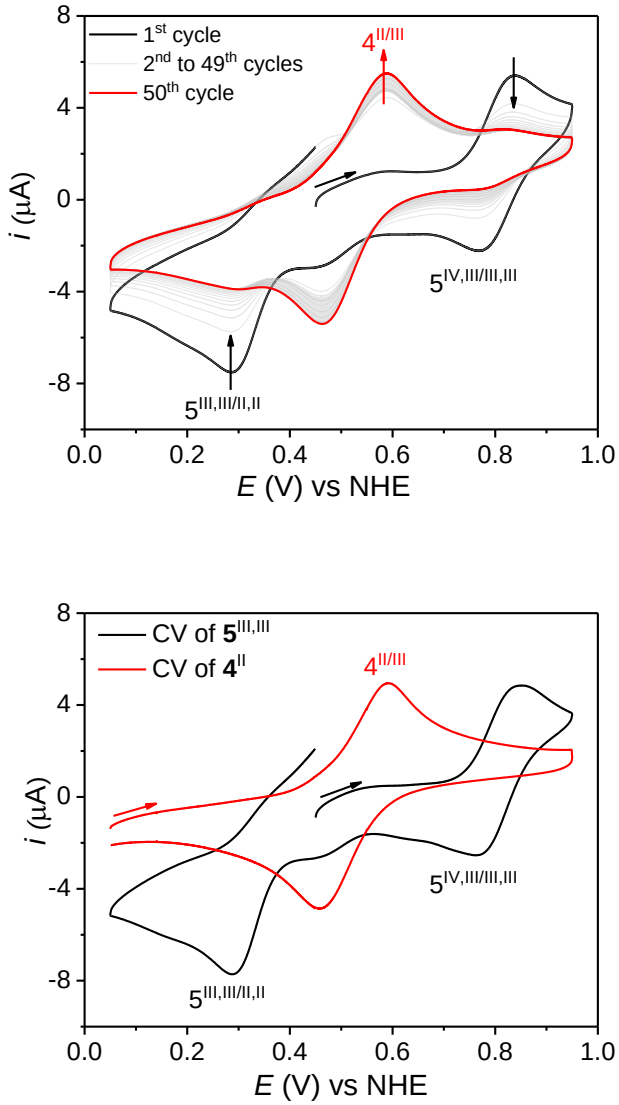

Figure 6. Top) Repetitive CV experiments of 1 mM of $\mathbf{5}^{\mathbf{III,III}}$ in pH 1.0 triflic acid solution showing the generation of the new complex $\mathbf{4}^{\mathbf{II}}$ after breaking the oxo-bridge (see equations 2-4 in main text); 1st cycle (black), 2nd to 49th cycles (grey) and 50th cycle (red), vertical black arrows indicate disappearance of the waves associated with $\mathbf{5}^{\mathbf{III,III}}$ and red vertical arrow indicates appearance of the redox waves with $\mathbf{4}^{\mathbf{II}}$. Bottom) CV of complex $\mathbf{5}^{\mathbf{III,III}}$ before (black) and after (red) a CPE at E_{app} = 0.05 V, showing clean conversion to complex $\mathbf{4}^{\mathbf{II}}$.

3B. 3. 3.2. Electrochemistry of 4^{II} and Water Oxidation Catalysis

Complex $\mathbf{4}^{\mathbf{II}}$ is a mononuclear Ru-OH_2 type of complex that has been previously proposed to act as a water oxidation catalyst but it has never been prepared in pure form due to the low stability upon work up procedures from the reaction starting with the chlorido precursor $\mathbf{3}^{\mathbf{III}}$ (Scheme 1).[15] Thus, the *in situ* generation of $\mathbf{4}^{\mathbf{II}}$ from the dimeric complex $\mathbf{5}^{\mathbf{III,III}}$ is a useful, alternative methodology to isolate this complex in solution and to fully analyze its

electrochemical behavior as well as the kinetic data associated with their capacity to oxidize water.

As shown in Figure 7, compound **4**^{II} shows two one-electron waves at $E_{1/2}$ = 0.52 V (ΔE = 130 mV) and $E_{p,a}$ = 1.19 V corresponding to the III/II and IV/III redox couples respectively. Both waves are pH dependent as expected for a Ru-aquo type of complex that is involved in PCET (Figure S11). The $Ru^{IV/III}$ wave is not reversible because it is partially overlapping with a third irreversible wave that is pH independent and that we attribute to the $Ru^{V/IV}$ couple followed by electrocatalytic oxidation of water. A manometry experiment using a 1 mM solution of **4**^{II} and 100 mM of $(NH_4)_2[Ce(NO_3)_6]$ as sacrificial electron acceptor in pH 1 shows the evolution of gas with a calculated turnover number of TON = 1.2 (Figure S12). The poor catalytic activity observed under this chemical oxidation is consistent with the limited catalytic current observed in the CV of Figure 7, which hardly exceeds the current intensity equivalent to one-electron transfer.

The Pourbaix diagram of complex **4**^{II} in Figure 7 is fully consistent with reported data[15] and reveals that the $[Ru^{III}\text{-}OH]/[Ru^{II}\text{-}OH_2]$ and $[Ru^{IV}\text{-}O]/[Ru^{III}\text{-}OH]$ redox processes each changes by approximately 59 mV per pH decade over a large pH range (11 > pH > 4). The oxidation of **4**^{II} at pH < 4 is not associated with the loss of a proton based on the pH-independent behavior of the $[Ru^{III}\text{-}OH_2]/[Ru^{II}\text{-}OH_2]$ redox couple. Consequently, the higher oxidation step is accompanied with the loss of two protons (i.e. $[Ru^{IV}\text{-}O]/[Ru^{III}\text{-}OH_2]$) in strongly acidic medium. This assignment is corroborated by the slope of -118 mV/pH below pH 4.0 for **4**^{II}. At pH > 11, the potentials for the $Ru^{III/II}$ become pH independent as a consequence of a loss of a proton from $[Ru^{II}\text{-}OH_2]$ with $pK_a \approx 11$. The $[Ru^{V}\text{-}O]^+/[Ru^{IV}\text{-}O]$ redox couple remains relatively constant at ~1.41 V over the whole pH 0-13 range. The pK_a^{III} value for the $[Ru^{III}\text{-}OH]$ derived from **4**^{II} is higher as compared to other Ru-aquo complexes with neutral ligand such as $[Ru(trpy)(bpy)(OH_2)]^{2+}$ (pK_a^{III} = 4 and 1.7 respectively),[42] mainly due to the presence of two negatively charged carboxylate groups around the ruthenium center, that makes the complex more basic in nature as expected.

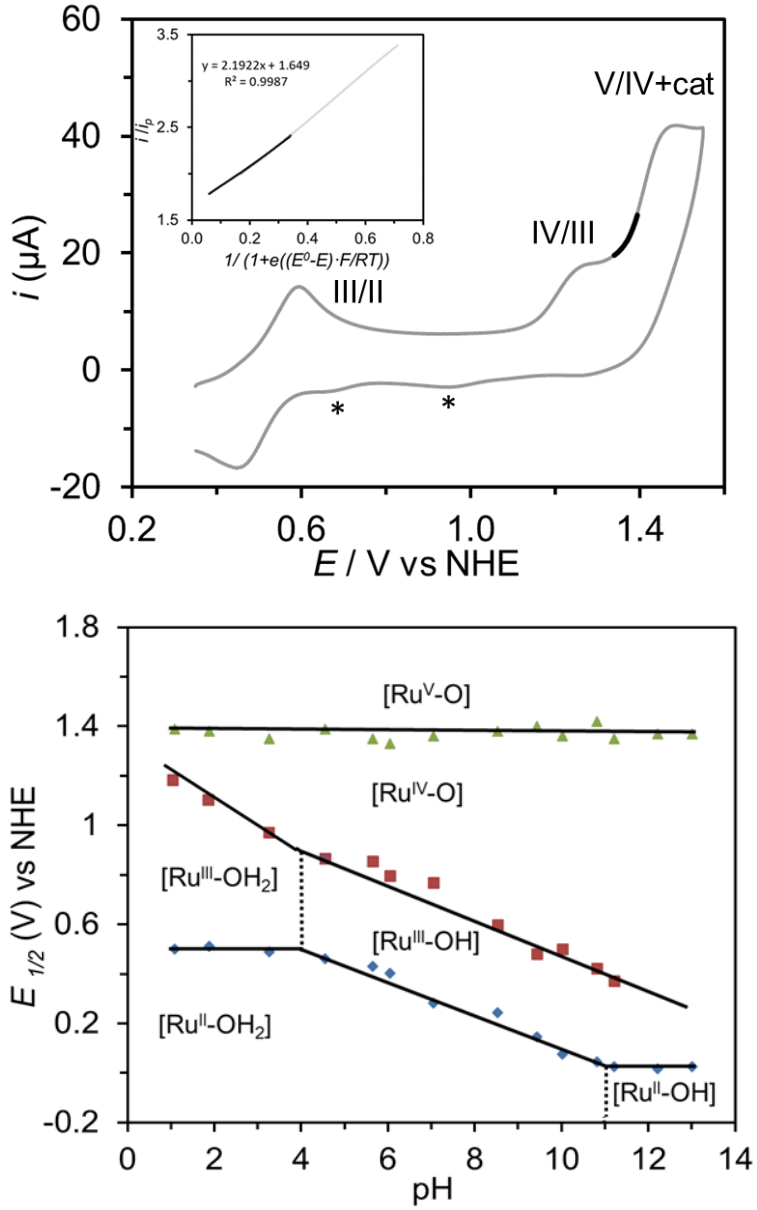

Figure 7. Electrochemical characterization of **4**^{II} in pH 1 generated *in situ* from **5**^{III,III} after a CPE at E_{app} = 0.05 V for 10 min. Top) CV and foot of the wave analysis (FOWA) of **4**^{II}. Asterisks indicate unidentified species. Bottom) Pourbaix diagram of **4**^{II}; black solid lines indicate the redox potentials for the different redox couples at varying pH, whereas the dashed vertical lines indicate pK_a values. The zone of stability of the different species are indicated only with the Ru symbol, its oxidation state, and the degree of protonation of the aquo ligand. For instance, [Ru^{IV}-O] is used to indicate the zone of stability of complex **4**^{IV} [Ru^{IV}(O)(pdc-κ^3-N^{1}O^2)(bpy)].

A "foot of the wave analysis" (FOWA) of the CV in Figure 7 allowed us to calculate the apparent rate constant for the water oxidation catalytic process. Assuming a unimolecular mechanism, this method developed by Sáveant and coworker[43,44] consists of using the relationship in equation 5,

$$\frac{i}{i_p} = \frac{4*2.24*\sqrt{\frac{RTk_{obs}}{Fv}}}{1+\exp(\frac{F\left(E^0_{P/Q} - E\right)}{RT})} \qquad (5)$$

Where k_{obs} is the unimolecular apparent rate constant or maximum turnover frequency (TOF_{max}), i is the current intensity in the presence of substrate, i_p is the current intensity in the absence of substrate (we approximate this current to the current associated with the $Ru^{III/II}$ couple), $E^0_{P/Q}$ is the standard potential for the redox couple where the catalysis starts (1.41 V for **4**^{II} extracted from the DPVs in Figure S11), F is the faraday constant, v is the scan rate, and R is 8.314 J mol^{-1} K^{-1}.

From the plot of i/i_p versus 1/{1 + exp[(F/RT)($E_{P/Q}$ − E)]} shown in Figure 7 a TOF_{max} = 0.23 s^{-1} is obtained. This value is comparable to the catalytic rates of relevant ruthenium-aquo complexes reported in the literature, that are believed to follow a mechanistic pathway where the O-O bond formation through a nucleophilic attack of a water molecule to the Ru^{V}=O species is the rate determining step of the reaction (Table 2, entries 1-6). Importantly, the overpotential of the catalytic reaction at pH 1, dictated by the $E_{1/2}$ ($Ru^{V/IV}$), is only 240 mV, being one of the lowest ever reported in the literature. This is a consequence of the two carboxylate groups in the pdc ligand that provide high electron density to the ruthenium center, allowing to reach higher oxidation states within a narrow potential range. This record value of overpotential is only overcome by complex [Ru^{IV}(bda)(4-Pic)$_2$(O)] in Table 1 and its derivatives (compare entries 8 and 9, where bda is [2,2'-bipyridine]-6,6'-dicarboxylato and 4-Pic is 4-picoline), that also contain two carboxylate groups in the bda ligand framework, but also the possibility to reach seven coordination intermediate species that give extra-stabilization of the high valent ruthenium intermediates involved in the catalysis.[17] In contrast, catalyst **4**^{II} undergoes a catalytic pathway where only six coordinated species are involved, as suggested in a previous reported work.[15]

Chapter 3B

Table 2. Electrochemical and water oxidation catalytic data of **4^{II}** and selected complexes reported in the literature at pH 1.

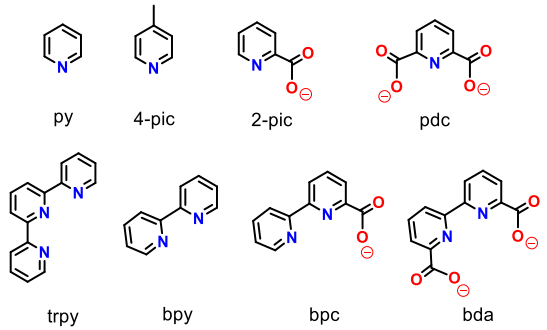

Ligand labels for the Ru-complexes in the Table

Entry	Complex	N[a]	$E_{1/2}$ ($Ru^{III/II}$) (V)	$E_{1/2}$ ($Ru^{IV/III}$) (V)	$E_{1/2}$ ($Ru^{V/IV}$) (V)	TOF[b] (s^{-1})	TOF_{max}[c] (s^{-1})
1[42]	$[Ru^{II}(trpy)(bpy)(H_2O)]^{2+}$	0	1.06	1.22	1.92	0.01	[d]
2[45]	$[Ru^{II}(bpc)(bpy)(H_2O)]^{+}$	1	0.81	1.29	1.57	0.16	[d]
3[46]	*cis*-$[Ru^{II}(trpy)(qc)(H_2O)]^{+}$	1	0.82	1.36	1.71	[d]	6.8
4[46]	*trans*-$[Ru^{II}(trpy)(qc)(H_2O)]^{+}$	1	0.67	1.20	1.62	0.68	4.2
5[46]	*cis*-$[Ru^{II}(trpy)(2\text{-}pic)(H_2O)]^{+}$	1	0.86	1.31	1.67	0.11	0.3
6[46]	*trans*-$[Ru^{II}(trpy)(2\text{-}pic)(H_2O)]^{+}$	1	0.76	1.09	1.60	0.24	1.2
7[10]	$[Ru^{IV}(bda)(4\text{-}Pic)_2(O)]$	2	0.61	1.1	1.35	33[e]	11[e]
8[f]	$[Ru^{II}(pdc)(bpy)(H_2O)]^{+}$, **4^{II}**	2	0.52	1.19	1.41	0.01	0.23

N[a]: number of carboxylate groups in the ligand framework, that are coordinated to the ruthenium center. [b]TOF: stands for initial Turn Over Frequency in s^{-1}. These values are extracted for the catalytic reactions involving 1 mM Cat/100 mM Ce^{IV} in a 0.1 M triflic acid solution with a total volume of 2 mL. [c]TOF_{max}: stands for Maximum Turn Over Frequency reported in s^{-1}; values extracted from Foot of the Wave Analysis of CV and DPV experiment in pH 1, [d]Not available. [e]A bimolecular mechanism involving two seven coordinated Ru=O species is ruling the water oxidation catalysis by $[Ru^{IV}(bda)(4\text{-}Pic)_2(O)]$. [f]This work.

3B. 4. Conclusion

In this work, the synthesis of two ruthenium complexes containing the meridional 2,6-pyridinedicarboxylato (pdc) ligand [Ru^{II}(pdc-κ^3-N^1O^2)(bpy)(DMSO)], **2^{II}** and {[Ru^{III}(pdc-κ^3-N^1O^2)(bpy)]$_2$(μ-O)}, **$5^{III,III}$** has been described. Both complexes have been fully characterized by spectroscopic, single crystal x-ray diffraction and electrochemical techniques.

Complex **2^{II}** and its precursor [Ru^{II}(pdc-κ^3-N^1O^2)$(DMSO)_2Cl]^-$, **1^{II}** show Ru-DMSO linkage isomerization process (Ru-S/Ru-O) upon oxidation. Cyclic voltammetry experiments allowed us to quantitatively describe all the thermodynamic and kinetic constants involved in this process for both compound and the values have been compared with related Ru-DMSO complexes reported in the literature. A general trend observed from this comparison is that the linkage isomerization constants at oxidation state Ru^{II} ($K^{II}_{O\rightarrow S}$) are all very high, in the order of 10^8-10^{12}, indicating that Ru^{II}-O species was unstable and immediately isomerizes to the Ru^{II}-S.

The dimeric complex **$5^{III,III}$** is characterized by a bridging oxo group, whose Ru-O-Ru angle of 126° determines a diamagnetic electronic configuration $(\pi_1^b)^2(\pi_2^b)^2(\pi_1^{nb})^2(\pi_2^{nb})^2(\pi_1^*)(\pi_2^*)^0$, allowing to analyze this complex with NMR techniques. Upon reduction in pH 1 aqueous solution, compound **$5^{III,III}$** converts to the monomeric derivative **4^{II}** [Ru^{II}(pdc-κ^3-N^1O^2)(bpy)(OH_2)], a Ru-aquo complex that is active for the water oxidation catalysis with an overpotential of only 240 mV in acidic pH due to the presence of two carboxylates groups connected to the ruthenium with TOF_{max} = 0.23 s^{-1}.

3B. 5. References

(1) Yagi, M.; Narita, K. *J. Am. Chem. Soc.* **2004**, *126*, 8084.
(2) Berardi, S.; Drouet, S.; Francas, L.; Gimbert-Suriñach, C.; Guttentag, M.; Richmond, C.; Stoll, T.; Llobet, A. *Chem. Soc. Rev.* **2014**, *43*, 7501.
(3) Savini, A.; Bellachioma, G.; Bolaño, S.; Rocchigiani, L.; Zuccaccia, C.; Zuccaccia, D.; Macchioni, A. *ChemSusChem.* **2012**, *5*, 1415.
(4) Rigsby, M. L.; Mandal, S.; Nam, W.; Spencer, L. C.; Llobet, A.; Stahl, S. S. *Chem. Sci.* **2012**, *3*, 3058.
(5) Garrido-Barros, P.; Funes-Ardoiz, I.; Drouet, S.; Benet-Buchholz, J.; Maseras, F.; Llobet, A. *J. Am. Chem. Soc.* **2015**, *137*, 6758.
(6) Kottrup, K. G.; D'Agostini, S.; van Langevelde, P. H.; Siegler, M. A.; Hetterscheid, D. G. *ACS Catal.* **2018**, *8*, 1052.
(7) Concepcion, J. J.; Tsai, M.-K.; Muckerman, J. T.; Meyer, T. J. *J. Am. Chem. Soc.* **2010**, *132*, 1545.
(8) Wasylenko, D. J.; Ganesamoorthy, C.; Henderson, M. A.; Koivisto, B. D.; Osthoff, H. D.; Berlinguette, C. P. *J. Am. Chem. Soc.* **2010**, *132*, 16094.
(9) Polyansky, D. E.; Muckerman, J. T.; Rochford, J.; Zong, R.; Thummel, R. P.; Fujita, E. *J. Am. Chem. Soc.* **2011**, *133*, 14649.
(10) Duan, L.; Bozoglian, F.; Mandal, S.; Stewart, B.; Privalov, T.; Llobet, A.; Sun, L. *Nat. Chem.* **2012**, *4*, 418.
(11) Gimbert-Suriñach, C.; Moonshiram, D.; Francàs, L.; Planas, N.; Bernales, V.; Bozoglian, F.; Guda, A.; Mognon, L.; López, I.; Hoque, M. A. *J. Am. Chem. Soc.* **2016**, *138*, 15291.
(12) Funes-Ardoiz, I.; Garrido-Barros, P.; Llobet, A.; Maseras, F. *ACS Catal.* **2017**, *7*, 1712.
(13) Zhang, B.; Sun, L. *J. Am. Chem. Soc.* **2019**, *141*, 5565.
(14) Matheu, R.; Ertem, M. Z.; Benet-Buchholz, J.; Coronado, E.; Batista, V. S.; Sala, X.; Llobet, A. *J. Am. Chem. Soc.* **2015**, *137*, 10786.
(15) Hoque, M. A.; Benet-Buchholz, J.; Llobet, A.; Gimbert-Suriñach, C. *ChemSusChem.* **2019**, *12*, 1949.
(16) Shatskiy, A.; Bardin, A. A.; Oschmann, M.; Matheu, R.; Benet-Buchholz, J.; Eriksson, L.; Kärkäs, M. D.; Johnston, E. V.; Gimbert-Suriñach, C.; Llobet, A.; Åkermark, B. *ChemSusChem.* **2019**, *12*, 2251.
(17) Matheu, R.; Ertem, M. Z.; Gimbert-Suriñach, C.; Sala, X.; Llobet, A. *Chem. Rev.* **2019**, *119*, 3453.
(18) Matheu, R.; Garrido-Barros, P.; Gil-Sepulcre, M.; Ertem, M. Z.; Sala, X.; Gimbert-Suriñach, C.; Llobet, A. *Nat. Rev. Chem.* **2019**, *3*, 331.
(19) Dismukes, G. C.; Brimblecombe, R.; Felton, G. A.; Pryadun, R. S.; Sheats, J. E.; Spiccia, L.; Swiegers, G. F. *Acc. Chem. Res.* **2009**, *42*, 1935.
(20) Vigara, L.; Ertem, M. Z.; Planas, N.; Bozoglian, F.; Leidel, N.; Dau, H.; Haumann, M.; Gagliardi, L.; Cramer, C. J.; Llobet, A. *Chem. Sci.* **2012**, *3*, 2576.
(21) Evans, I.; Spencer, A.; Wilkinson, G. *J. Chem. Soc., Dalton Trans.* **1973**, 204.
(22) *Data collection with APEX II version v2013.4-1. Bruker (2007). Bruker AXS Inc., Madison, Wisconsin, USA.*
(23) *Data reduction with Bruker SAINT version V8.30c. Bruker (2007). Bruker AXS Inc., Madison, Wisconsin, USA.*
(24) Blessing, R. H. *Acta Cryst. A* **1995**, *51*, 33.
(25) Sheldrick, G. M. *Acta Cryst. A* **2015**, *71*, 3.
(26) Hübschle, C. B.; Sheldrick, G. M.; Dittrich, B. *J. Appl. Crystallogr.* **2011**, *44*, 1281.
(27) Sheldrick, G. M. *Acta Cryst. C* **2015**, *71*, 3.
(28) Xie, Y.-F.; Zhu, H.; Shi, H.-T.; Jia, A.-Q.; Zhang, Q.-F. *Inorg. Chim. Acta* **2015**, *428*, 147.
(29) An, J.; Duan, L.; Sun, L. *Faraday Discuss.* **2012**, *155*, 267.
(30) López, I.; Maji, S.; Benet-Buchholz, J.; Llobet, A. *Inorg. Chem.* **2014**, *54*, 658.

(31) Ishitani, O.; White, P. S.; Meyer, T. J. *Inorg. Chem.* **1996**, *35*, 2167.
(32) Lebeau, E. L.; Adeyemi, S. A.; Meyer, T. J. *Inorg. Chem.* **1998**, *37*, 6476.
(33) López, I.; Ertem, M. Z.; Maji, S.; Benet-Buchholz, J.; Keidel, A.; Kuhlmann, U.; Hildebrandt, P.; Cramer, C. J.; Batista, V. S.; Llobet, A. *Angew. Chem. Int. Ed.* **2014**, *53*, 205.
(34) Llobet, A.; Curry, M. E.; Howard, T.; Mayer, T. J. *Inorg. Chem* **1989**, *28*, 3131.
(35) Neubold, P.; Wieghardt, K.; Nuber, B.; Weiss, J. *Inorg. Chem.* **1989**, *28*, 459.
(36) Mognon, L.; Benet-Buchholz, J.; Llobet, A. *Inorg. Chem.* **2015**, *54*, 11948.
(37) Llobet, A.; Doppelt, P.; Meyer, T. J. *Inorg. Chem.* **1988**, *27*, 514.
(38) Silva, D. O.; Toma, H. E. *Can. J. Chem.* **1994**, *72*, 1705.
(39) Nicholson, R. S.; Shain, I. *Anal. Chem.* **1964**, *36*, 706.
(40) Benet-Buchholz, J.; Comba, P.; Llobet, A.; Roeser, S.; Vadivelu, P.; Wiesner, S. *Dalton. Trans.* **2010**, *39*, 3315.
(41) Roeser, S.; Maji, S.; Benet-Buchholz, J.; Pons, J.; Llobet, A. *Eur. J. Inorg. Chem.* **2013**, *2013*, 232.
(42) Takeuchi, K. J.; Thompson, M. S.; Pipes, D. W.; Meyer, T. J. *Inorg. Chem.* **1984**, *23*, 1845.
(43) Costentin, C.; Drouet, S.; Robert, M.; Savéant, J.-M. *J. Am. Chem. Soc.* **2012**, *134*, 11235.
(44) Matheu, R.; Neudeck, S.; Meyer, F.; Sala, X.; Llobet, A. *ChemSusChem.* **2016**, *9*, 3361.
(45) Tong, L.; Inge, A. K.; Duan, L.; Wang, L.; Zou, X.; Sun, L. *Inorg. Chem.* **2013**, *52*, 2505.
(46) *Chapter 3A, Unpublished.*

3B. 6. Supporting Information

Table of Contents

NMR Spectroscopy and Mass Spectrometry

Figure S1-S3. NMR spectra of $\mathbf{2}^{II}$

Figure S4-S6. NMR spectra of $\mathbf{5}^{III,III}$

Figure S7. ESI-MS of complexes $\mathbf{2}^{II}$ and $\mathbf{5}^{III,III}$

Electrochemistry

Figure S8. Electrochemical data of $\mathbf{1}^{II}$ for linkage isomerization

Figure S9-S10. Electrochemical data of $\mathbf{2}^{II}$ for linkage isomerisation

Figure S11. DPV of $[Ru^{III}(pdc\text{-}\kappa^3\text{-}N^1O^2)(bpy)OH_2]$, $\mathbf{4}^{II}$ in different pHs

Figure S12. Manometry data for complex $\mathbf{4}^{II}$

a)

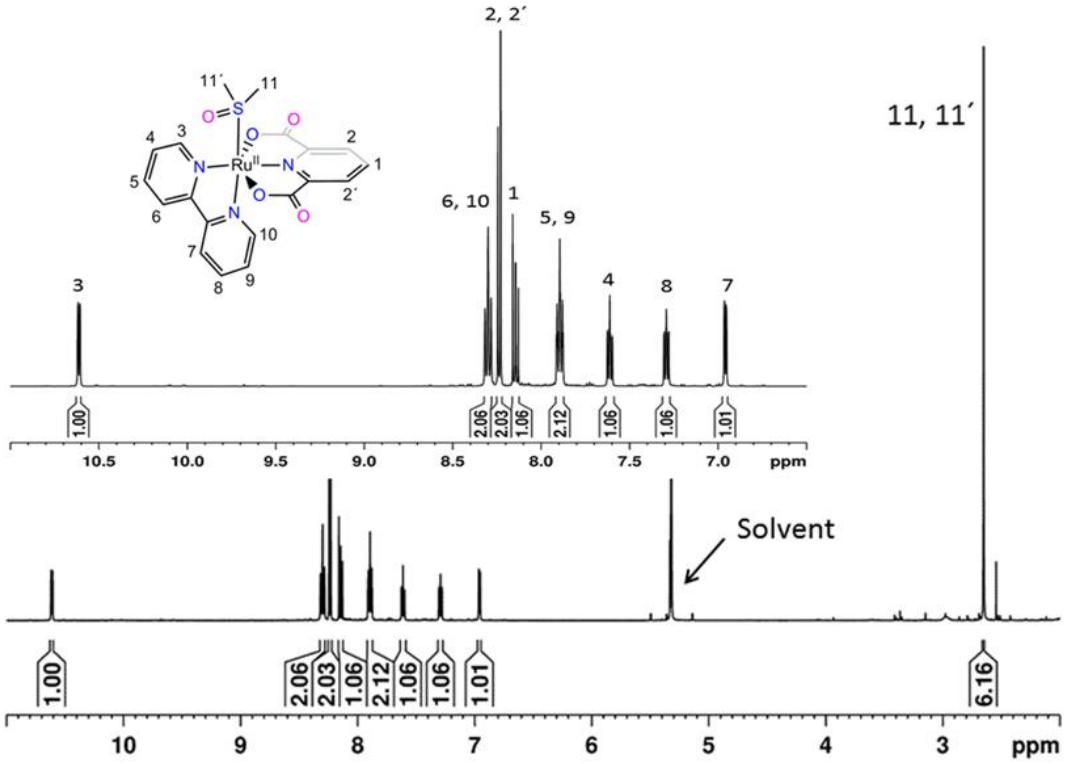

b)

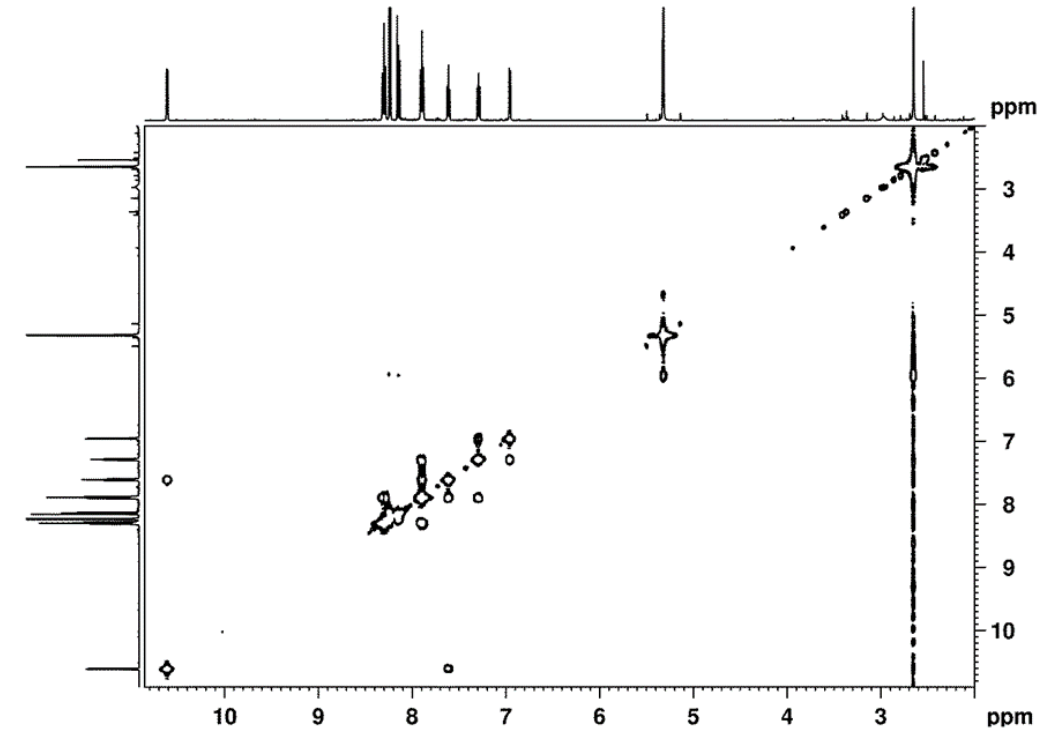

Figure S1. NMR spectra (500 MHz, 298 K, [d_2]-DCM) for complex **2^{II}**. a) ^{1}H NMR and b) COSY.

a)

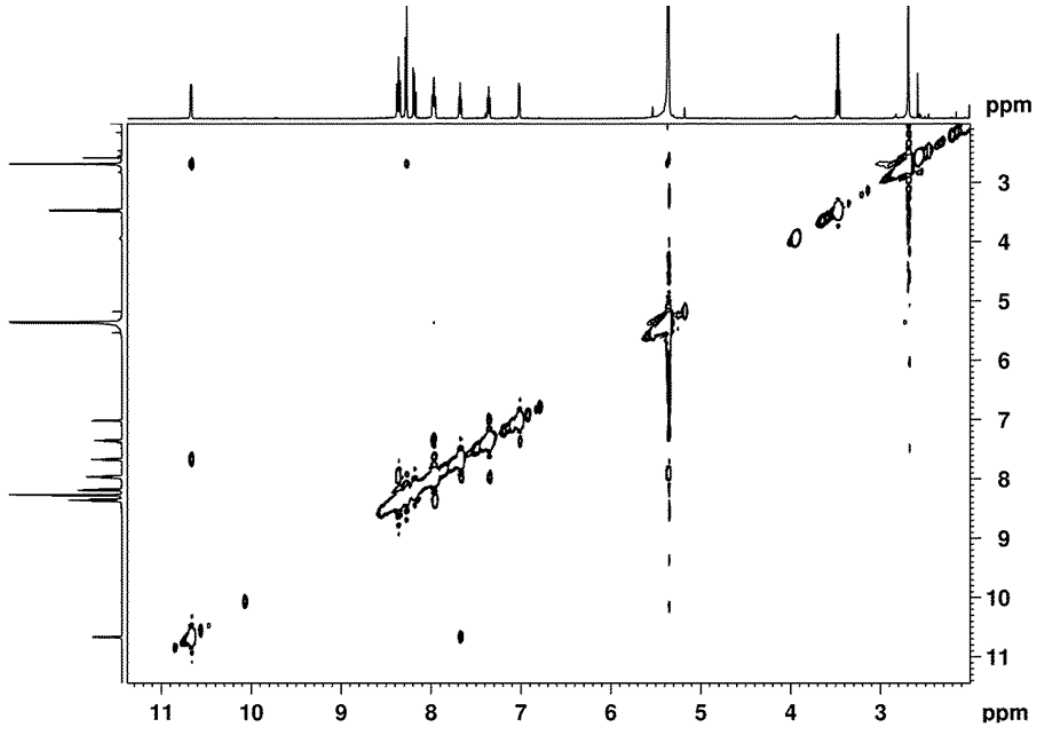

b)

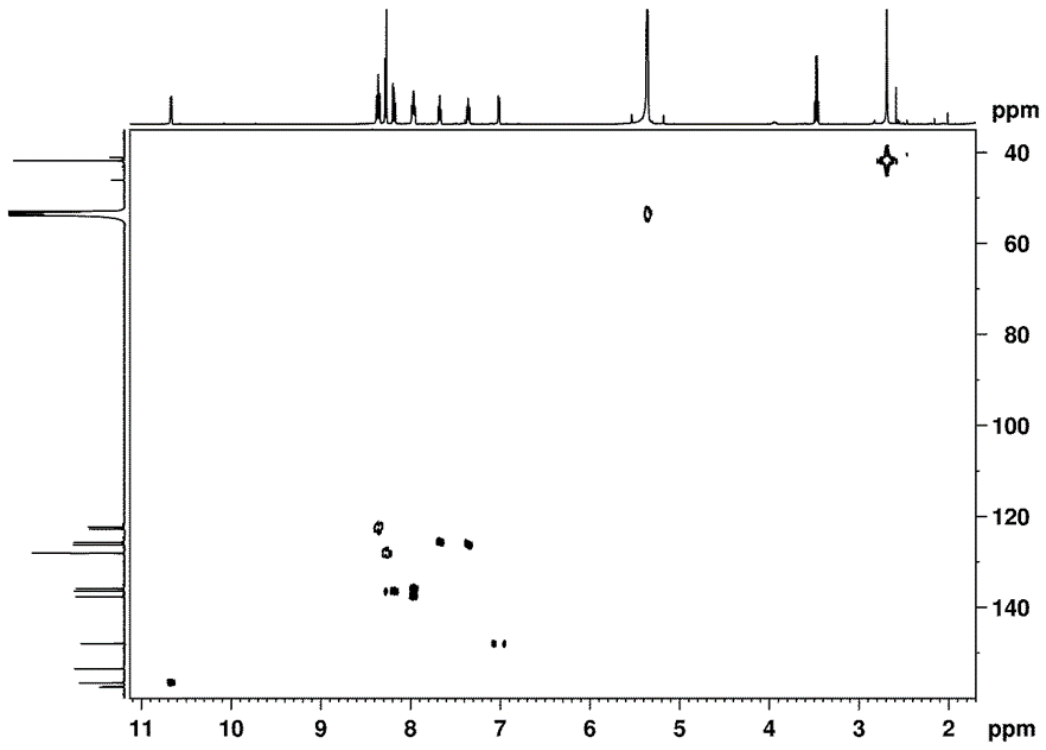

Figure S2. NMR spectra (500 MHz, 298 K, [d_2]-DCM) for complex **2**^{II}; a) NOESY and b) HSQC.

a)

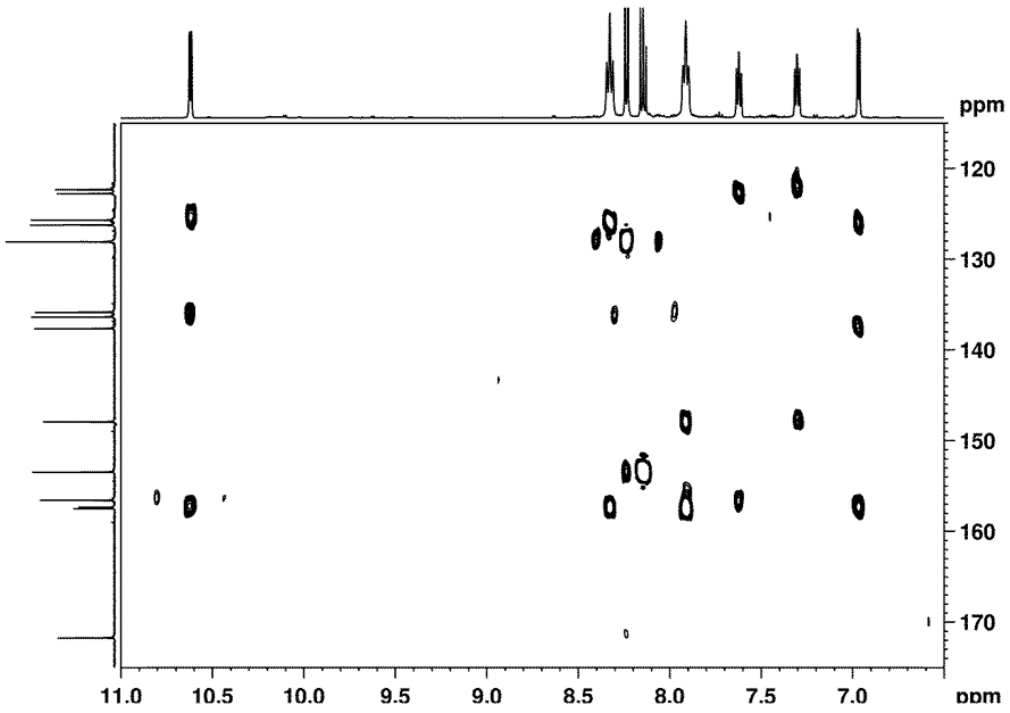

b)

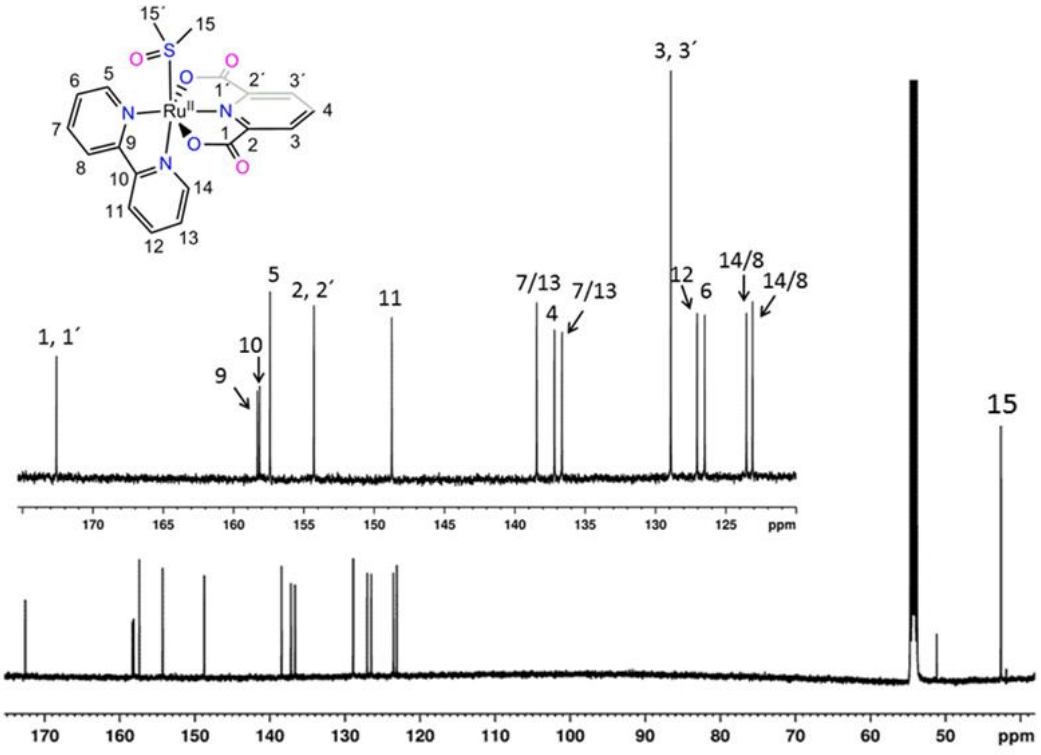

Figure S3. NMR spectra (500 MHz, 298 K, [d_2]-DCM) for complex **2**^{II}; a) HMBC and b) ^{13}C NMR (125 MHz, 298 K, [d_2]-DCM).

a)

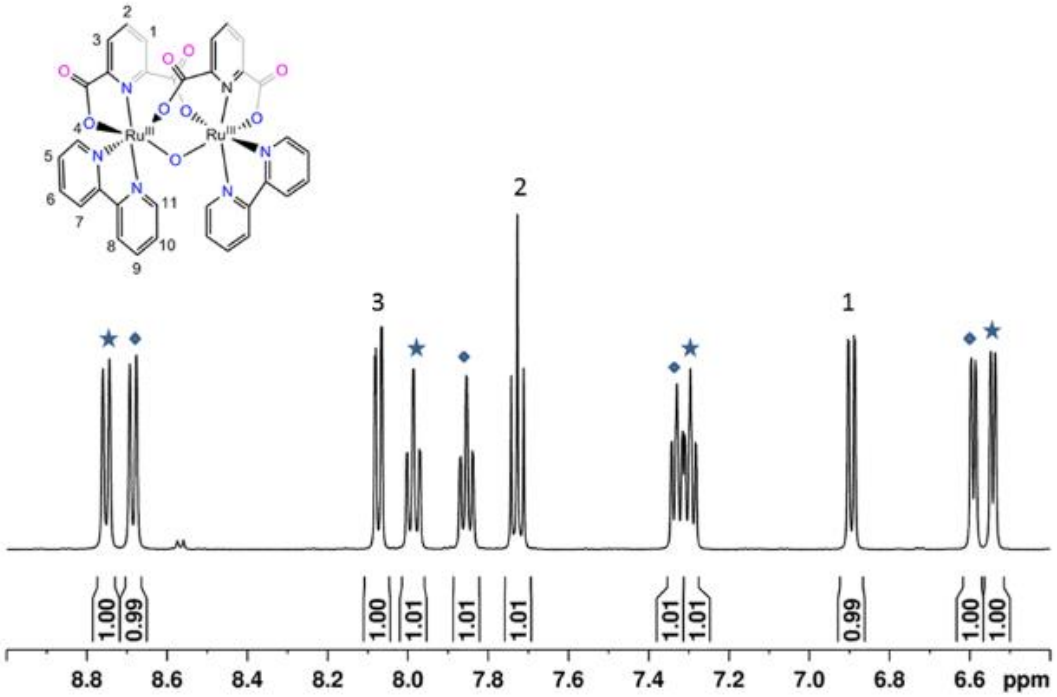

b)

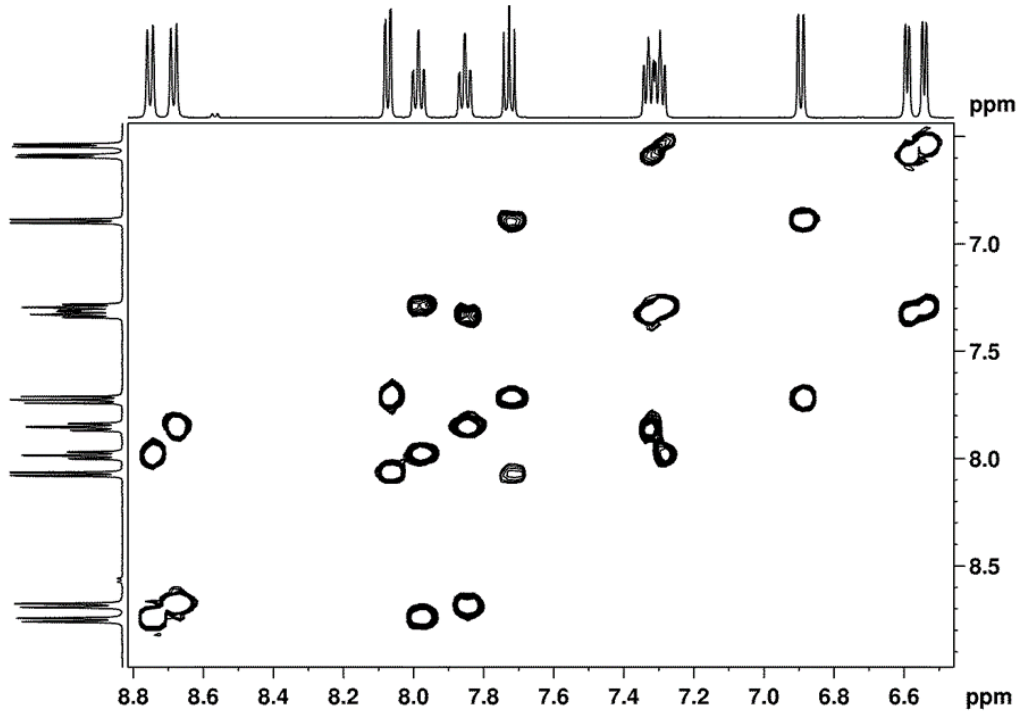

Figure S4. NMR spectra (500 MHz, 298 K, [d_6]-DMSO) for complex $\mathbf{5}^{III,III}$; a) ^{1}H NMR and b) COSY.

a)

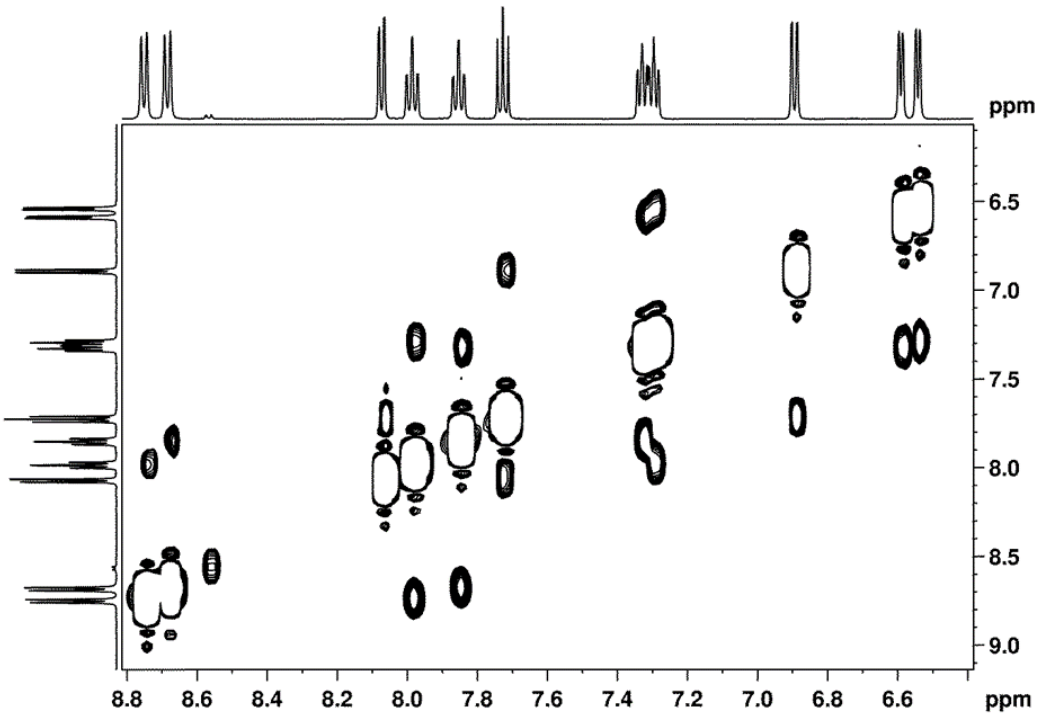

b)

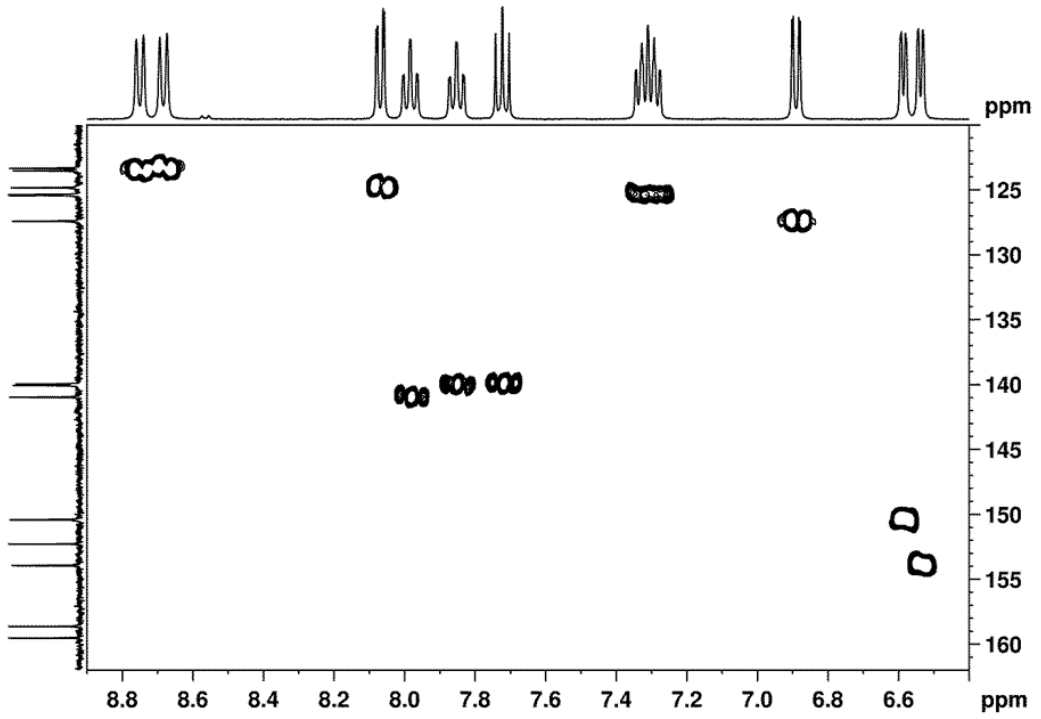

Figure S5. NMR spectra (500 MHz, 298 K, [d_6]-DMSO) for complex $\mathbf{5}^{III,III}$; a) NOESY and b) HSQC.

a)

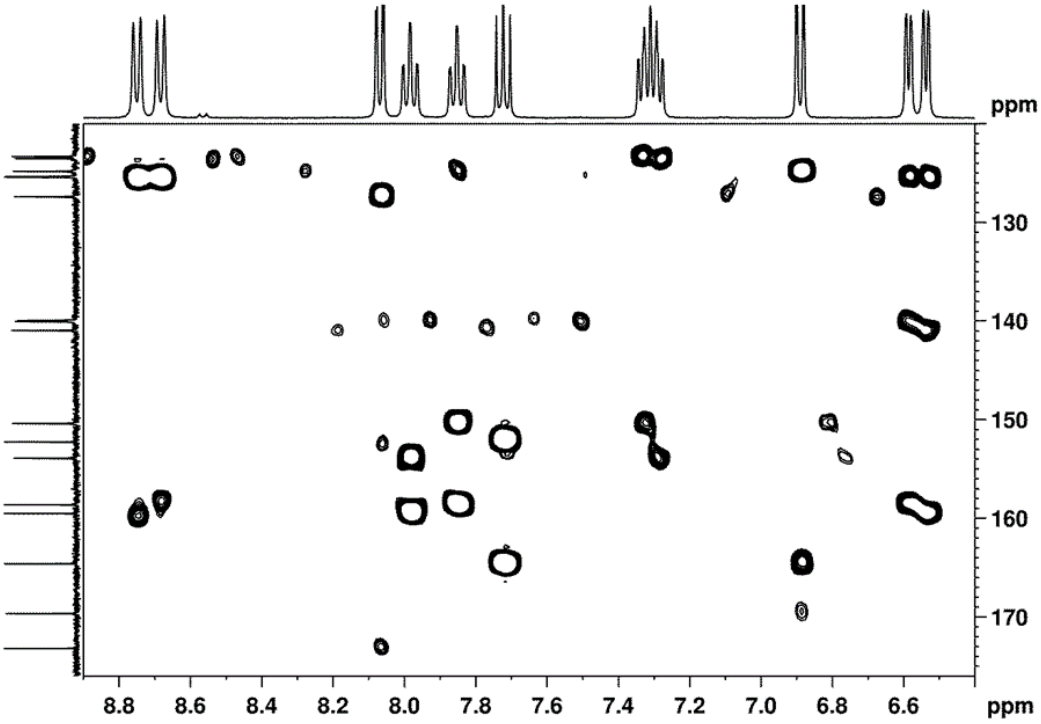

b)

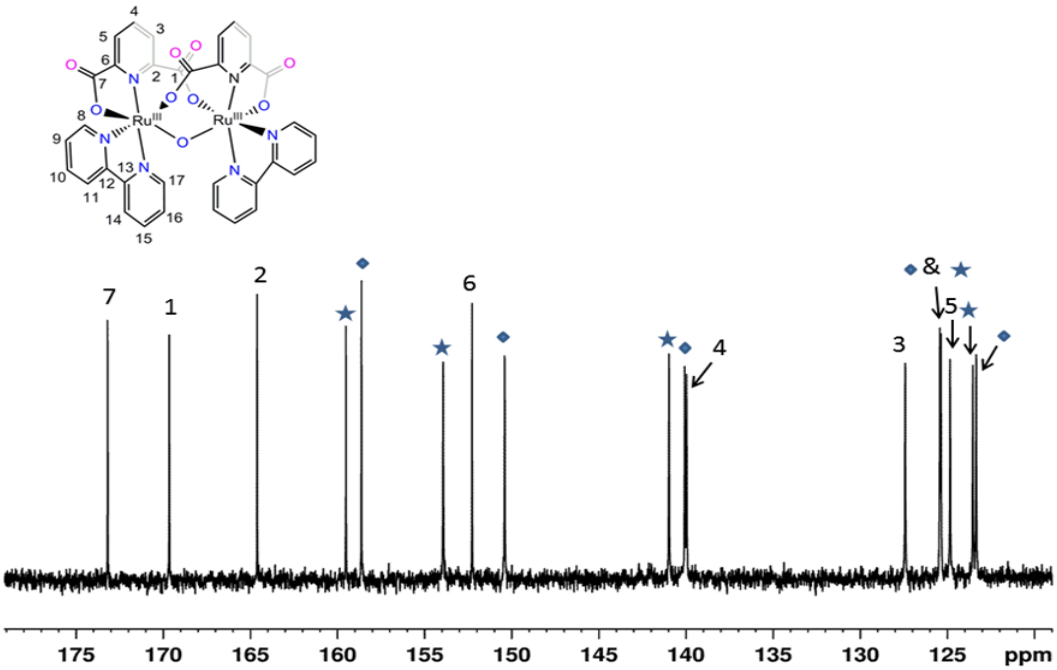

Figure S6. NMR spectra (500 MHz, 298 K, [d_6]-DMSO) for complex $\mathbf{5}^{III,III}$; a) HMBC and b) ^{13}C NMR (125 MHz, 298 K, [d_6]-DMSO).

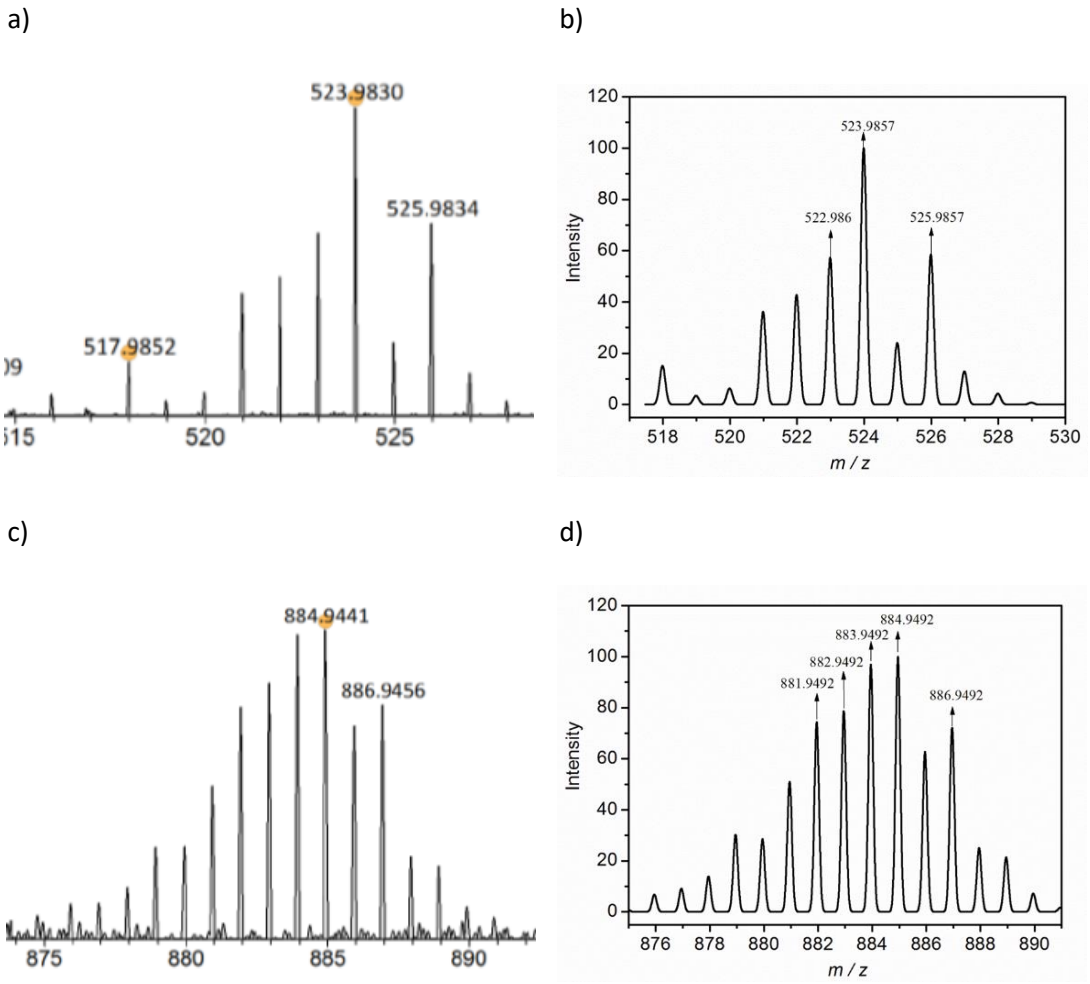

Figure S7. (Left) Experimental ESI-MS of complexes a) $\mathbf{2}^{II}$ and c) $\mathbf{5}^{III,III}$ **(**Right) Simulated ESI-MS of complexes b) $\mathbf{2}^{II}$ and d) $\mathbf{5}^{III,III}$.

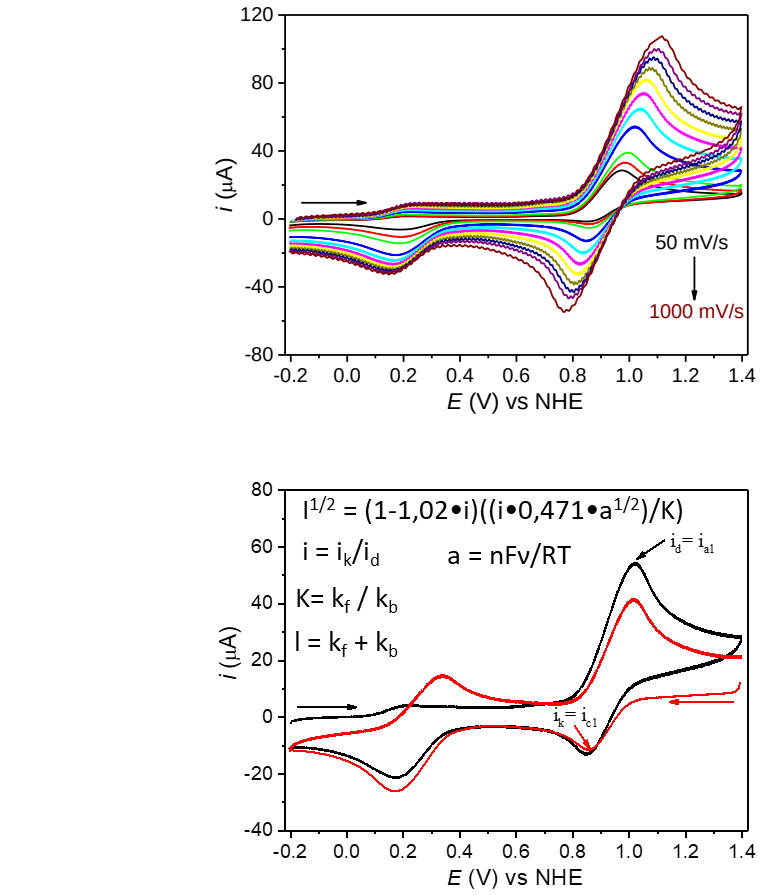

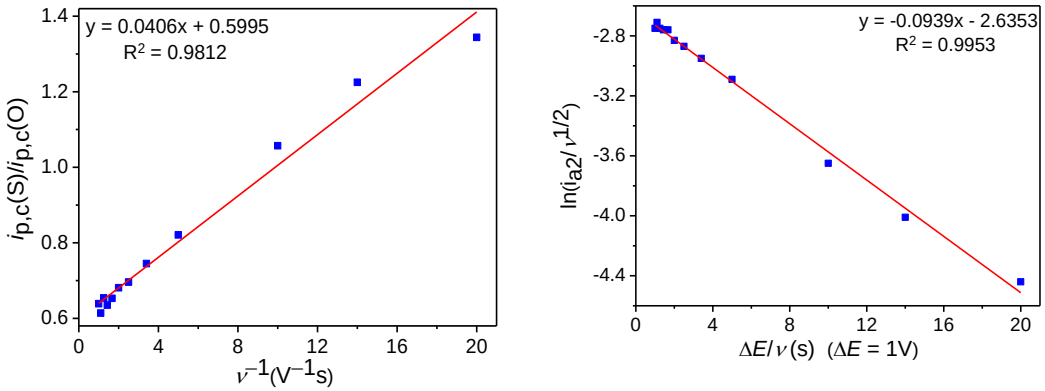

Figure S8. CV experiments of 1 mM of $\mathbf{1}^{II}$ in DCM containing 0.1 M TBAH [*n*-Bu_4NPF_6] and plots for the calculation of $k^{III}{}_{O\rightarrow S}$ and $k^{III}{}_{S\rightarrow O}$. **Top)** Scan rate dependence of the CV after leaving the potential at -0.2 V for 2 minutes before the scan. Black: 50 mV/s, red: 70 mV/s, green: 100 mV/ s, blue: 200 mV/s, turquoise: 300 mV/s, pink: 400 mV/s, yellow: 500 mV/s, dark green: 600 mV/s, dark blue: 700 mV/s, purple: 800 mV/s and marron: 1000 mV/s. **Middle)** Anodic and cathodic CV scans after leaving the potential at 1.4 V (red) and -0.2 V (black) for 2 minutes at a scan rate of 200 mV/s used to calculate $k^{III}{}_{O\rightarrow S}$ and $k^{III}{}_{S\rightarrow O}$. Arrows indicate the initial scan direction. **Bottom)** Plot of $i_{p,c1}/i_{p,c2}$ *vs.* ν^{-1}, plus its linear fitting extrapolating $\nu\rightarrow\infty$ to obtain $K^{III}{}_{(O\rightarrow S)}$ for complex $\mathbf{1}^{II}$ (left) and Plot of $\ln(i_{a2}/\nu^{1/2})$ *vs.* $\Delta E/\nu$ (with ΔE = 1 V) to obtain k_f of $K^{II}{}_{(O\rightarrow S)}$ for complex $\mathbf{1}^{II}$ (right).

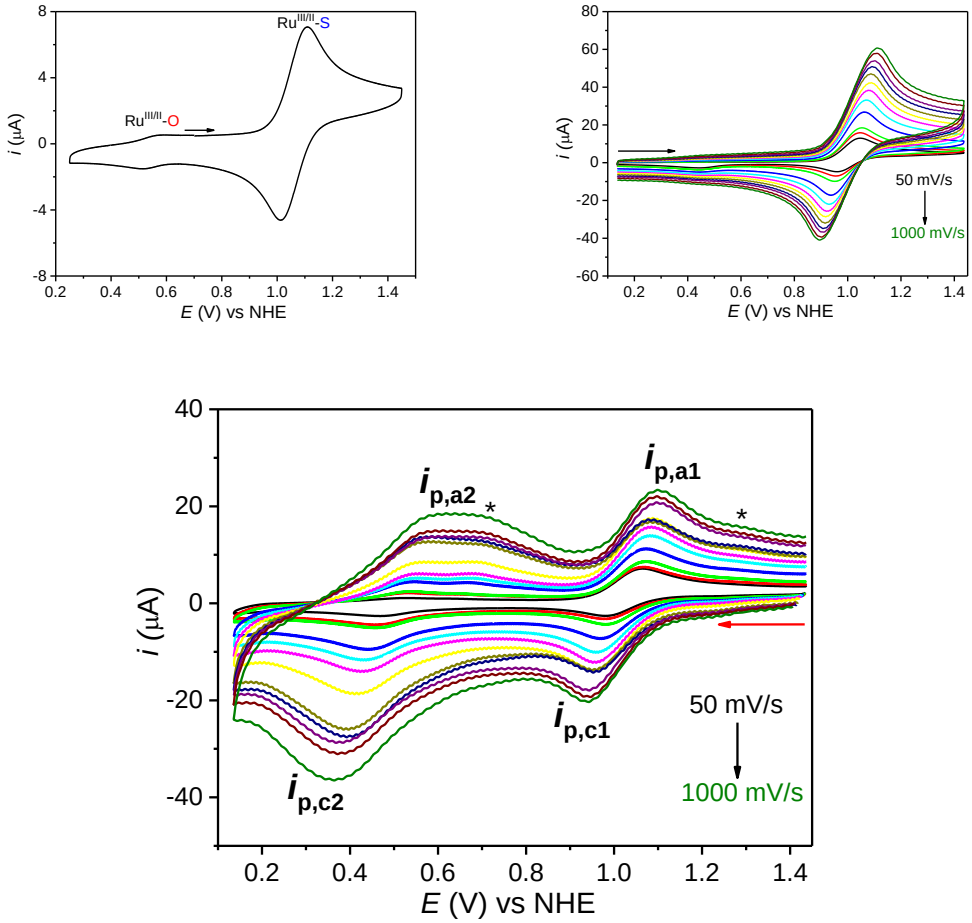

Figure S9. CV experiments of 1 mM of **2^{II}** in DCM containing 0.1 M TBAH [*n*-Bu$_4$NPF$_6$]. **Top)** left, CV at 100 mV scan rate. Right**,** CVs at different scan rates after leaving the potential at 0.14 V for 2 minutes before the scan. Arrows indicate initial scan direction. Colour code denote scan rate (mV/s). Black: 50 mV/s, red: 70 mV/s, green: 100 mV/ s, blue: 200 mV/s, turquoise: 300 mV/s, pink: 400 mV/s, yellow: 500 mV/s, dark green: 600 mV/s, dark blue: 700 mV/s, purple: 800 mV/s, marron: 900 mV/s: and grassy green: 1000 mV/s. **Bottom)** CVs at different scan rates after leaving the potential at 1.44 V for 2 minutes before each scan. Black: 50 mV/s, red: 70 mV/s, green: 100 mV/ s, blue: 200 mV/s, turquoise: 300 mV/s, pink: 400 mV/s, yellow: 500 mV/s, dark green: 600 mV/s, dark blue: 700 mV/s, purple: 800 mV/s, marron: 900 mV/s: and grassy green: 1000 mV/s. Asterisks indicate side products formed after applying anodic potential (1.44 V), that do not appear when applying reductive potential (0.14 V).

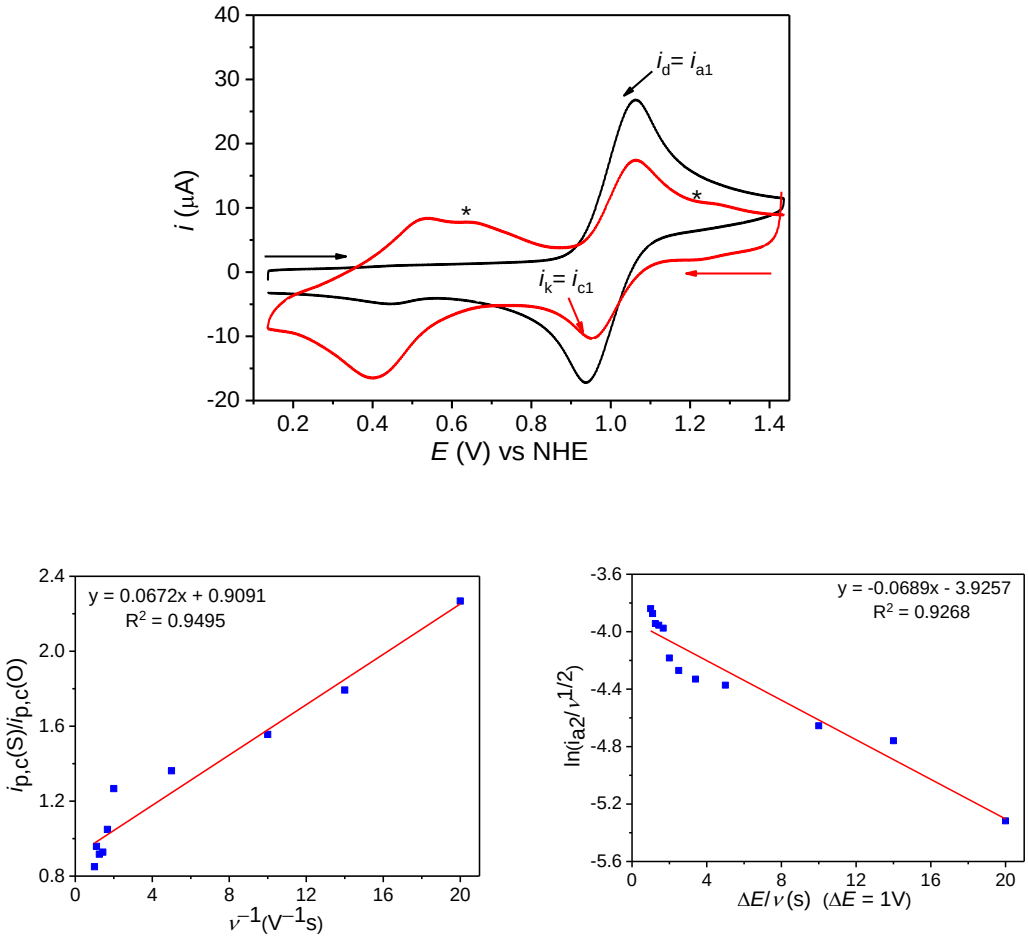

Figure S10. CV experiments of 1 mM of **2^{II}** in DCM containing 0.1 M TBAH [*n*-Bu_4NPF_6] and plots for the calculation of $k^{III}{}_{O\rightarrow S}$ and $k^{III}{}_{S\rightarrow O}$. **Top)** Anodic and cathodic CV scans after leaving the potential at 1.44 V (red) and 0.14 V (black) for 2 minutes at a scan rate of 200 mV/s used to calculate $k^{III}{}_{O\rightarrow S}$ and $k^{III}{}_{S\rightarrow O}$. Arrows indicate the initial scan direction. **Bottom)** Plot of $i_{p,c1}/i_{p,c2}$ *vs.* ν^{-1}, plus its linear fitting extrapolating $\nu\rightarrow\infty$ to obtain $K^{III}{}_{(O\rightarrow S)}$ for complex **2^{II}** (left) and plot of $\ln(i_{a2}/\nu^{1/2})$ *vs.* $\Delta E/\nu$ (with ΔE = 1 V) to obtain k_f of $K^{II}{}_{(O\rightarrow S)}$ for complex **2^{II}** (right).

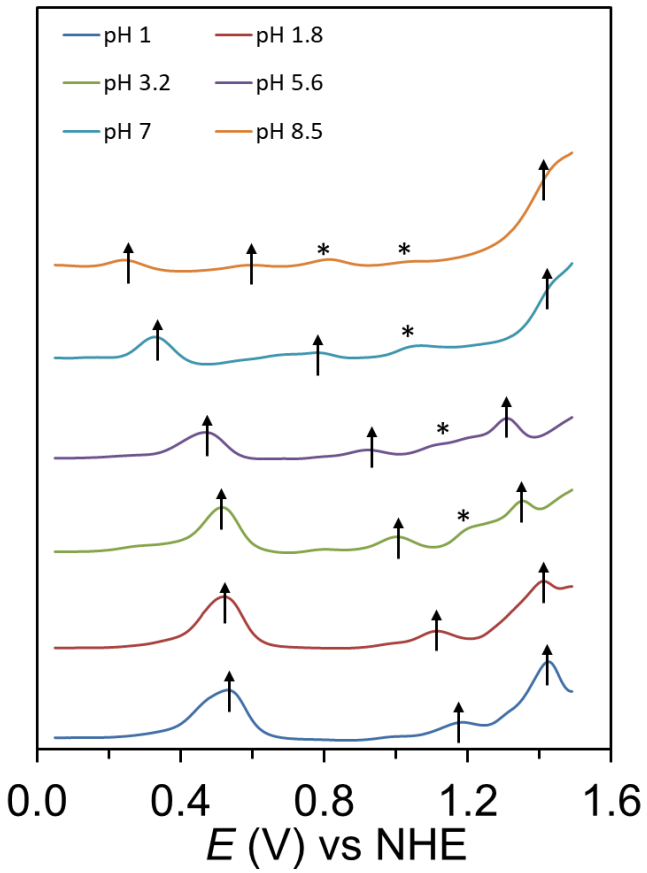

Figure S11. DPV of [Ru^{III}(pdc-κ^3-N^{1}O^2)(bpy)OH_2], **4^{II}** with initial concentration 2 mM in pH 1. Asterisks indicate unidentified species.

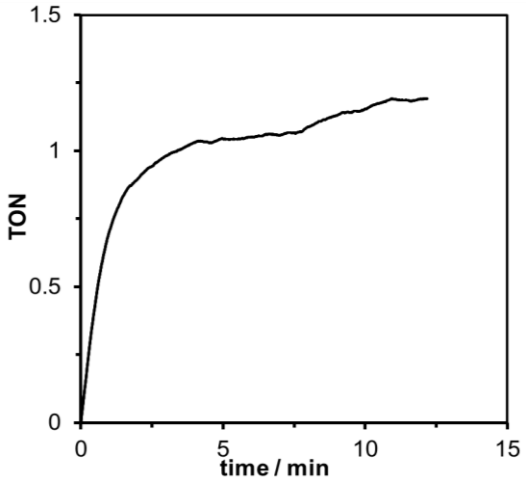

Figure S12. Gas evolution profile obtained for a water oxidation catalytic mixture containing **4^{II}** and Ce^{IV} as sacrificial electron acceptor. Experimental conditions: 1 mM of **4^{II}** and 100 mM of Ce^{IV} ammonium nitrate in 0.1 M triflic acid (2 mL total volume) at 25˚C.

Chapter 4

We report the synthesis, characterization and water oxidation activity of Ru complexes containing the pyridine dicarboxylate ligand. Under high anodic potentials, they evolve towards the formation of Ru-aquo complexes that are powerful and rugged water oxidation catalysts. These complexes operate water oxidation catalysis with active species that involve six coordination and seven coordination for the Ru centers. The present work uncovers and highlights the complexity involved in water oxidation catalytic processes when transition metal complexes are exposed to high oxidation potentials needed for the catalysis.

Chapter 4

4. Water Oxidation to Dioxygen Catalysis by Mononuclear Ru complexes bearing the 2,6-pyridinedicarboxylato Ligand

Md Asmaul Hoque,[1,2] Jordi Benet-Buchholz,[1] Antoni Llobet,[1,3] Carolina Gimbert-Suriñach[1,*]

[1]Institute of Chemical Research of Catalonia (ICIQ), Barcelona Institute of Science and Technology (BIST), Av. Països Catalans 16, 43007 Tarragona, Spain

[2]Departament de Química Física i Inorganica, Universitat Rovira i Virgili, Campus Sescelades, C/Marcel·lí Domingo, s/n, 43007 Tarragona, Spain

[3]Universitat Autònoma de Barcelona, Departament de Química, Cerdanyola del Vallès, 08193 Barcelona, Spain

IV

Published Article: **Hoque, M. A.**; Benet-Buchholz, J.; Llobet, A.; Gimbert-Suriñach, C. *ChemSusChem.* **2019**, *12*, 1949.

Contributions

Md Asmaul Hoque has done all the experiments and prepared the manuscript.

Chapter 4

Abstract

The synthesis, purification and isolation of mononuclear Ru complexes containing the tridentate dianionic meridional ligand pyridyl-2,6-dicarboxylato (pdc^{2-}) of general formula $[Ru^{III}(pdc\text{-}\kappa^3\text{-}N^1O^2)(bpy)Cl]$, **1**^{III} and $[Ru^{II}(pdc\text{-}\kappa^2\text{-}N^1O^1)(bpy)_2]$, **2**^{II} (bpy is 2,2'-bipyridne) are reported. These two complexes and their derivatives have been thoroughly characterized based on spectroscopic (UV-vis, NMR), electrochemical (CV, DPV and Coulometry) and three of them by single crystal X-ray diffraction techniques. Under a high anodic applied potential both complexes evolve towards the formation of Ru-aquo derivative species namely, $[Ru^{III}(pdc\text{-}\kappa^3\text{-}N^1O^2)(bpy)(OH_2)]^+$, **1-O** and $[Ru^{IV}(O)(pdc\text{-}\kappa^2\text{-}N^1O^1)(bpy)_2]$, **2-O**. These two complexes are active catalysts for the oxidation of water to dioxygen reaction and their catalytic activity is analyzed based on electrochemical techniques. A TOF_{max} = 2.4-3.4 x10^3 s^{-1}, has been calculated for **2-O**.

IV

Graphical Abstract

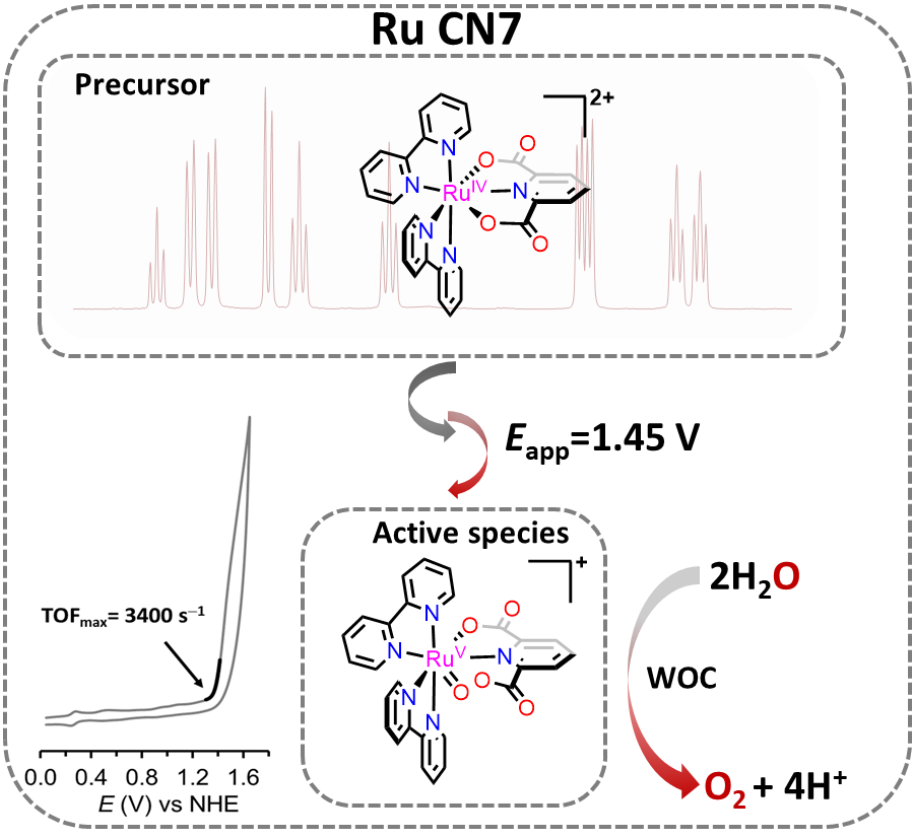

Keywords: Water oxidation, Redox properties, Transition metal complexes, Ru complexes, Redox catalysis

Chapter 4

4. 1. Introduction

Water oxidation (WO) catalysis is one of the key process involved in the light induced water splitting (WS) reaction. This process generates hydrogen as a clean fuel from an inexhaustible source of energy, sunlight.[1] The overall reaction is depicted in Eq. 1, that can be split in the respective two half reactions in Eq. 2 (WO) and Eq. 3 for proton reduction (PR).[2] Given the beneficial impact of such a sustainable process on our society, the development of efficient catalysts to perform the WO reaction has experienced increasing interest.[3-5] Among the most efficient catalysts described to date, ruthenium coordination complexes containing flexible, adaptative, multidentate and equatorial (FAME) ligands have shown to perform remarkably well.[3,6] Another key feature of the best performing WO catalysts is the presence of carboxylate groups in the coordination sphere of the metal center, providing stability to the metal high oxidation states and lowering the overpotential of the reaction.[7-14] In addition, the presence of dangling carboxylate group, strategically situated so that it can intramolecularly accept a proton at the water nucleophilic attack stage, significantly reduces the energy of activation at this step and thus greatly increases reaction rate.[3,7,15]

$$2H_2O + 4h\upsilon \rightarrow 2H_2 + O_2 \quad (1)$$
$$2H_2O + \rightarrow O_2 + 4H^+ + 4e^- \quad (2)$$
$$4H^+ + 4e^- \rightarrow 2H_2 \quad (3)$$

Ruthenium complexes have also been crucial to understand the mechanistic pathways responsible for the O-O[16-18] bond formation and how the coordination sphere around the metal center influence these pathways. Other factors such as the pK_a of ruthenium aquo (Ru-OH_2) intermediate species have also been shown to strongly impact the performance of the water oxidation catalysts.[19,20] All these insights are of paramount importance because they have allowed the rational design of catalysts that nowadays can perform as fast as 7,900 s^{-1} at neutral pH.[15]

In this work, we explore the water oxidation catalytic activity of Ru complexes containing the meridional tridentate dianionic ligand 2,6-pyridinedicarboxylato (pdc^{2-}), which can show different coordination modes.[21] For instance, it can coordinate in a tridentate κ-N^1O^2 meridional fashion and provide a strong sigma donation to the metal center[21-23] but also it can bind in a bidentate κ-N^1O^1 mode leaving a pendant carboxylate.[21] We report the preparation, purification and isolation of two new Ru complexes [Ru^{III}(pdc-κ^3-N^1O^2)(bpy)Cl], **1**^{III} and [Ru^{II}(pdc-κ^2-N^1O^1)$(bpy)_2$], **2**^{II} shown in Scheme 1, that in addition to the pdc^{2-} ligand also contain one or two neutral bidentate 2,2'-bipyridne (bpy) ligands respectively. We have studied the spectroscopic, redox and structural properties of these two complexes and we

have also shown that they are precursors to Ru complexes capable of catalytically oxidize water to dioxygen. The activity of the catalysts are evaluated based on electrochemical techniques.

4. 2. Experimental Section

Materials

$RuCl_3 \cdot \times H_2O$ was purchased from Alfa-Aesar. The precursor complex $[Ru(DMSO)_4Cl_2]$ was prepared according to a reported procedure.[24] 2,6-pyridindicarboxylic acid (H_2pdc) and other chemicals were obtained from Aldrich and used as received. Solvents were dried with a SPS® system and degassed by bubbling nitrogen before starting the reactions. High purity de-ionized water used for the electrochemistry experiments was obtained by passing distilled water through a nanopure Mili-Q water purification system. For other spectroscopic and electrochemical studies, HPLC-grade solvents were used.

Instrumentation and Methods

A Bruker Avance 500 MHz were used to carry out NMR spectroscopy. ESI-Mass spectra were recorded using micromass Q-TOF mass spectrometer. Elemental analyses were carried out on Perkin-Elmer 240C elemental analyzer. The EPR experiments were carried out at 4 K on frozen solutions by using a X-band spectrometer (Bruker ELEXYS E580). The pH of the solutions was determined by a pHmeter (CRISON, Basic 20^+) calibrated before measurements through standard solutions at pH 4.01, 7.00 and 9.21. Oxygen evolution was analyzed with a gas phase Clark type oxygen electrode (Unisense Ox-N needle microsensor) and calibrated by the addition of small quantities of oxygen (99%) at the end of the experiment. All electrochemical experiments were performed in an IJ-Cambria CHI-660 potentiostat using a three-electrode one compartment cell for cyclic voltammetry (CV) and differential pulse voltammetry (DPV) or two compartment cell for bulk electrolysis. $E_{1/2}$ values reported in this work were estimated from CV experiments as the average of the oxidative and reductive peak potentials ($E_{p,a}$ + $E_{p,c}$)/2 or from DPV. The Reference Electrode (RE) was Hg/Hg_2SO_4 (K_2SO_4 saturated) and potentials were converted to NHE by adding 0.65 V. Glassy carbon disk (ϕ = 0.3 cm, S = 0.07 cm^2), Pt disk and Hg/Hg_2SO_4 (K_2SO_4 saturated) were used as Working Electrode (WE), Counter Electrode (CE) and Reference Electrode (RE) respectively, unless explicitly mentioned. Glassy carbon electrodes were polished with 0.05 µm alumina (Al_2O_3) and rinsed with water. CVs and DPVs were iR compensated by the potentiostat in all the measurements. CVs were recorded at 100 $mV \cdot s^{-1}$ scan rate. DPV parameters were ΔE = 4 mV, Amplitude = 50 mV, Pulse width =

0.05 s, Sampling width = 0.0167 s, Pulse period = 0.5 s. The complexes were dissolved in dichloromethane or acetone containing [(*n*-Bu)$_4$N][PF$_6$] (0.1 M) as supporting electrolyte. In aqueous solution the electrochemical experiments were carried out in *I* = 0.1 M phosphate buffer solutions with desired pH. The Pourbaix diagrams were built using the following buffers: sodium dihydrogen phosphate/phosphoric acid up to pH = 4 (pK_a = 2.12), sodium hydrogen phosphate/ sodium dihydrogen phosphate up to pH = 9 (pK_a = 7.67), sodium hydrogen phosphate/sodium phosphate up to pH = 13 (pK_a = 12.12) and also 0.1 M CF_3SO_3H for pH=1.0. For routine bulk electrolysis experiments in figure 4C, a Pt grid was used as a WE, another Pt grid as a CE and a Hg/Hg_2SO_4 (K_2SO_4 saturated) as a RE. For the bulk electrolysis experiment for oxygen detection, a glassy carbon rod (*S* = 8.2 cm^2) was used as a working electrode and Ag/AgCl (sat. KCl) as a RE.

For Figure S11, to generate [Ru^{III}(pdc-κ^3-N^{1}O^2)(bpy)(OH$_2$)]$^+$, **1-O** complex from 1 mM of [Ru^{III}(pdc-κ^3-N^{1}O^2)(bpy)Cl], **1**^{III} bulk electrolysis experiment was carried out in three-electrode one compartment cell for 5 min at E_{app} = 1.6 V without stirring. A glassy carbon disk was used as a WE, Pt disk as a CE and a Hg/Hg_2SO_4 (K_2SO_4 saturated) as a RE. For Figure S15, to see the coordination of DMSO, [Ru^{II}(pdc-κ^2-N^{1}O^1)(bpy)(dmso)Cl], to the complex [Ru^{III}(pdc-κ^3-N^{1}O^2)(bpy)Cl], **1**^{III} bulk electrolysis experiment was carried out in three-electrode one compartment cell for 2 min at E_{app} = 0 V without stirring. A glassy carbon disk was used as a WE, Pt disk as a CE and a Hg/Hg_2SO_4 (K_2SO_4 saturated) as a RE. iR compensation by the potentiostat was not applied in this technique.

Single Crystal X-Ray Structure Determinations

Crystal Preparation: Crystals of [Ru^{III}(pdc-κ^3-N^{1}O^2)(bpy)Cl], **1**^{III}, was obtained from reaction in methanol solvent. [Ru^{II}(pdc-κ^2-N^{1}O^1)(bpy)$_2$], **2**^{II} and [Ru^{III}(Hpdc-κ^2-N^{1}O^1)(bpy)$_2$]$^{2+}$, **2**^{III} were grown by slow evaporation of methanol:hexane and water:acetonitrile respectively. The measured crystals were prepared under inert conditions immersed in perfluoropolyether as protecting oil for manipulation.

Data Collection: Crystal structure determination for compounds **1**^{III}, **2**^{II} and **2**^{III} were carried out using a Rigaku diffractometer equipped with a Pilatus 200K area detector, a Rigaku MicroMax-007HF microfocus rotating anode with MoK$_\alpha$ radiation, Confocal Max Flux optics and an Oxford Cryosystems low temperature device Cryostream 700 plus (*T* = -173 ˚C). Full-sphere data collection was used with ω and φ scans. *Programs used:* Data collection and

reduction with CrysAlisPro[25] V/.60A and absorption correction with Scale3 Abspack scaling algorithm.[26]

Structure Solution and Refinement: Crystal structure solution was achieved using the computer program SHELXT.[27] Visualization was performed with the program SHELXle.[28] Missing atoms were subsequently located from difference Fourier synthesis and added to the atom list. Least-squares refinement on F^2 using all measured intensities was carried out using the program SHELXL 2015.[29] All non-hydrogen atoms were refined including anisotropic displacement parameters.

Comments to the Structures: [Ru^{III}(pdc-κ^3-N^1O^2)(bpy)Cl], **1^{III}**: The asymmetric unit contains one molecule of the metal complex and one methanol molecule. [Ru^{II}(pdc-κ^2-N^1O^1)(bpy)$_2$], **2^{II}** : The asymmetric unit contains one molecule of the metal complex and two molecules of water. [Ru^{III}(Hpdc-κ^2-N^1O^1)(bpy)$_2$]$^{2+}$, **2^{III}**: The asymmetric unit contains one molecule of the metal complex, 1 ½ PF_6-anions, 1.75 molecules of acetonitrile and 0.25 molecules of dichloromethane. In this metal complex one of the carboxylates is protonated with 0.5 occupancy (although hydrogen atoms can only be localized with difficulties, the distances indicate unambiguously that one of the oxygen atoms is protonated). In one of the solvent position, an acetonitrile and a dichloromethane molecule are sharing its position by disorder with a ratio of respectively 75:25.

Synthesis of [Ru^{III}(pdc-κ^3-N^1O^2)(bpy)Cl], 1^{III}. In a 100 mL two neck round-bottom flask, $RuCl_3.xH_2O$ (262 mg, *ca.* 1 mmol) and LiCl (42 mg, 1mmol) were dissolved in 20 mL of degassed methanol. Then, a 10 mL degassed aqueous solution of 2,6-pyridine dicarboxylic acid (167 mg, 1 mmol) and sodium carbonate (106 mg, 1mmol) were added slowly to the reaction mixture. After 20 minutes of stirring at room temperature, 10 mL of a degassed methanol solution of 2,2´-bipyridine (156 mg, 1 mmol) was added slowly and refluxed for 4 h under N_2 atmosphere. The resulting orange-red crystalline solid was filtered and washed with methanol and diethyl ether (320 mg, 0.70 mmol, Yield: 70 %). Single crystals were selected from this batch to perform single crystal X-ray diffraction analysis. Anal. Calc. for ($C_{17}H_{11}ClN_3O_4Ru{\cdot}CH_3OH$): C, 44.13%; H, 3.09%; N, 8.58%; S. Found: C, 43.95%; H, 2.76%; N, 8.58%. ESI^+-HRMS (MeOH) m/z calc. for $[M+Na]^+$: 480.9406, found m/z: 480.9376.

Synthesis of [Ru^{II}(pdc-κ^2-N^1O^1)(bpy)(DMSO)Cl] *in situ*. In a NMR tube or in a UV-Vis spectroscopy cell, 20 μL of triethylamine were added to a solution of 0.5 mL [Ru^{III}(κ^3-pdc)(bpy)Cl] in [d_6]-DMSO for the NMR and DMSO for the UV-vis. ^{1}H-NMR (500 MHz, [d_6]-DMSO + triethylamine) δ: 9.31 (d, J = 4.9 Hz, 1H), 8.48 (d, J = 5.05 Hz, 1H), 8.29 (t, J = 8.35 Hz,

2H), 7.88 (t, *J* = 7.55 Hz, 1H), 7.81 (m, 3H), 7.38 (dd, *J* = 12.2 Hz and 5.05 Hz, 2H), 7.05 (dd, *J* = 7.1 Hz and 2.1 Hz, 1H). ^{13}C-NMR (125 MHz, [d_6]-DMSO + triethylamine) *δ*: 172.3, 167.8, 164.3, 161.4, 161.2, 155.4, 152.9, 150.3, 137.2, 134.9, 134.7, 124.5, 123.8, 123.7, 122.9, 121.9 and 121.4.

Synthesis of [Ru^{III}(pdc-κ^3-N^{1}O^2)(bpy)(OH$_2$)] *in situ*, 1-O. In a 100 mL two neck round-bottom flask, [Ru^{III}(pdc-κ^3-N^{1}O^2)(bpy)Cl] (100 mg, 0.21 mmol) and $AgClO_4$ (50 mg, 0.24 mmol) in 40 mL of a mixture of acetone: water (75:25) were heated at reflux under N_2 atmosphere for 3 h. The color of the solution changed from orange red to green. A CV analysis of the reaction crude mixture shows almost complete conversion of the starting material to a new species with a Ru$^{III/II}$ couple consistent with the corresponding Ru-OH$_2$ complex (Figure S14 in the supporting information). After several attempts to purify this compound, it was not possible to isolate it in a pure form due to the formation of higher nuclearity oxo-bridged species as suggested by UV-Vis spectroscopy, which showed typical absorptions in the range of 650-800 nm.

Synthesis of [Ru^{II}((pdc-κ^2-N^{1}O^1)(bpy)$_2$]·3H$_2$O, 2^{II}. In a 100 mL two neck round bottom flask [Ru^{II}(pdc-κ^3-N^{1}O^2)(Cl)(DMSO)$_2$][21] (560 mg, 1 mmol) and 2,2´-bipyridine (312 mg, 2 mmol) were dissolved in degassed methanol (40 mL) and refluxed for 4 h. The mixture was then evaporated to dryness and the resulting solid dissolved in CH_2Cl_2 and purified by column chromatography with neutral alumina using a mixture of CH_2Cl_2/MeOH (100:5, v/v) as eluent. A red color fraction was collected giving a solid identified as the product (350 mg, 0.60 mmol, Yield: 60 %). Single crystals were grown by slow evaporation of the complex in a 1:1 mixture of methanol:hexane. Anal. Calc. for ($C_{27}H_{19}N_5O_4Ru$ ·3H_2O): C, 51.31%; H, 3.63%; N, 11.02%. Found: C, 51.26%; H, 3.98%; N, 11.07%. ^{1}H-NMR (500 MHz, [d_4]-MeOD) *δ*: 8.67 (d, *J* = 5.7 Hz, 1H), 8.60 (d, *J* = 5.6 Hz, 1H), 8.58 (d, *J* = 8.1 Hz, 1H), 8.56 (d, *J* = 8.2 Hz, 1H), 8.48 (d, *J* = 8.1 Hz, 1H), 8.33 (d, *J* = 8 Hz, 1H), 8.09-8.06 (m, 3H), 7.97 (t, *J* = 7.7 Hz, 1H). 7.85 (td, *J* = 1.4 and 7.9 Hz, 1H), 7.75-7.70 (m, 2H), 7.62 (t, *J* = 6.5 Hz, 1H), 7.56 (t, *J* = 6.4 Hz, 1H), 7.39 (d, *J* = 5.1 Hz, 1H), 7.34 (dd, *J* = 1.5 and 7.7 Hz, 1H), 7.21 (t, *J* = 6.6 Hz, 1H), 7.06 (t, *J* = 6.7 Hz, 1H). ^{13}C-NMR (125 MHz, [d_4]-MeOD) *δ*: 175.6, 170.7, 165.8, 160.9, 160.4, 160.0, 159.4, 155.5, 154.8, 152.9, 152.5, 150.6, 139.2, 137.8, 137.7, 137.5, 136.3, 127.9, 127.4, 127.4, 126.6, 126.4, 126.4, 124.5, 124.3, 124.3 and 123.8. (ESI$^+$-HRMS; MeOH) m/z calc. for [M]$^+$: 580.0585, found m/z: 580.0563.

Synthesis of [Ru^{III}(Hpdc-κ^2-N^{1}O^1)(bpy)$_2$](PF$_6$)$_2$, 2^{III}. In a 25 mL round bottom flask, a solution of cerium(IV) ammonium nitrate (21 mM, 1.05 eq, 1 mL in pH 1) was added dropwise to a

solution of [Ru^{II}(pdc-κ^2-N^1O^1)$(bpy)_2$] in water (2.0 mM, 10 mL) and the mixture was stirred at room temperature for 15 minutes. A green color precipitate was obtained when a saturated aqueous solution of KPF_6 was added. The solid was filtered and washed with water, methanol and diethyl ether (10 mg, 0.0135 mmol, Yield: 65%). Single crystals were obtained from slow evaporation of a solution in a mixture of water and acetonitrile.

Synthesis of [Ru^{IV}(pdc-κ^3-N^1O^2)$(bpy)_2$]$^{2+}$, 2^{IV}. Inside a NMR tube, a solution of cerium(IV) ammonium nitrate (42 mM, 2.1 eq, 0.1 mL in pD 1) was added dropwise to a solution of [Ru^{II}(pdc-κ^2-N^1O^1)$(bpy)_2$] in deuterated water (2 mM, 1.0 mL) and the mixture was stirred for 5 minutes. ^{1}H-NMR (500 MHz, [d_2]-D_2O) δ: 8.85 (t, J = 7.7 Hz, 1H), 8.77 (d, J = 8.1 Hz, 2H), 8.72 (d, J = 8.2 Hz, 2H), 8.59 (d, J = 7.7 Hz, 2H), 8.52 (t, J = 7.9 Hz, 2H), 8.31 (t, J = 7.9 Hz, 2H), 7.87-7.83 (m, 4H), 7.64 (t, J = 6.8 Hz, 2H). 7.58 (t, J = 6.7 Hz, 2H). ^{13}C-NMR (125 MHz, [d_2]-D_2O) δ: 168.1, 155.1, 151.5, 149.9, 148.9, 147.7, 147.1, 144.8, 142.9, 133.9, 129.9, 128.5, 127.2 and 126.6.

4. 3. Results and Discussion

4. 3. 1. Synthesis, Spectroscopic and Structural Characterization

The complex **1**^{III} was synthesized by slow addition of an aqueous solution of sodium 2,6-pyridindicarboxylate to a MeOH solution of the ruthenium precursor $RuCl_3 \cdot \times H_2O$ followed by addition of 1 equivalent of bpy also in MeOH as indicated in Scheme 1. The final solution was refluxed for 4 h and on cooling an orange-red crystalline solid of the desired complex precipitates with 70% yield. Crystals suitable for single crystal x-ray diffraction studies were obtained and its molecular structure is shown in Figure 1 A.

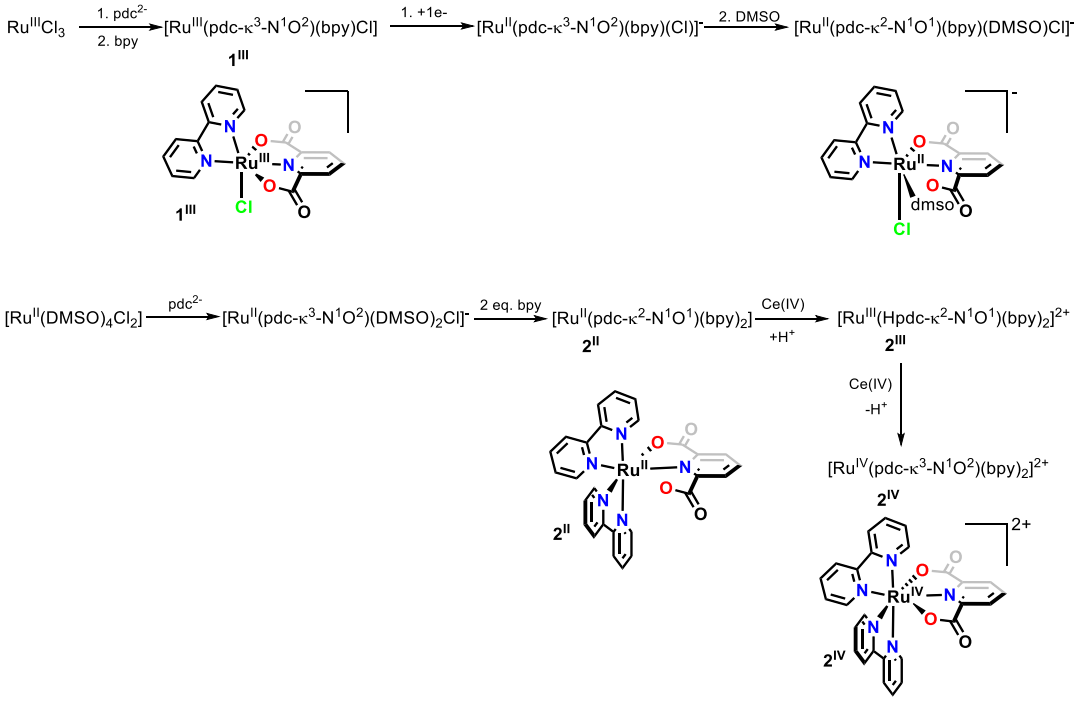

Scheme 1. Synthetic scheme and labelling.

It has a highly distorted octahedral geometry due to the strain imposed by the pdc^{2-} meridional ligand with O-Ru-O angle of 157° as opposed to the 180° expected for an ideal octahedron. It shows similar bond distances and angles to those reported for related complexes.[21-23]

Reduction of **1**^{III} in DMSO with NEt_3, generates a new complex, [Ru^{II}(pdc-κ^2-N^{1}O^1)(bpy)(DMSO)Cl]$^-$, where the pdc^{2-} changes its coordination mode from tridentate κ-N^{1}O^2 to bidentate κ-N^{1}O^1 as evidenced by NMR spectroscopy and Cyclic Voltammetry (CV) experiments (Figures S1 and S15 in the SI). As a consequence of the DMSO coordination the complex loses its Cs symmetry and thus all pdc^{2-} proton resonances are different.

On the other hand, complex **2**^{II} was prepared in 60% yield by reacting the ruthenium precursor [Ru^{II}(κ^3-N^{1}O^2)(Cl)(DMSO)$_2$]$^{-21}$ dissolved in MeOH with 2 equivalents of bpy ligand under reflux. The ^{1}H NMR spectrum of the product shows the non-symmetric nature of the complex with two sets of resonances for the bpy ligands as well as the corresponding non symmetric resonances for the pdc^{2-} protons, in agreement with the bidentate κ-N^{1}O^1 coordination mode of the latter (Figure 2 and Figures S3-S4 in the SI). Upon oxidation with 1 equivalent of cerium(IV) ammonium nitrate (Ce^{IV}), the corresponding Ru^{III} derivative, [Ru^{III}(Hpdc-κ^2-N^{1}O^1)(bpy)$_2$]$^{2+}$, **2**^{III} was isolated.

Single crystals of both the Ru^{II} and Ru^{III} species were obtained and their ORTEP structures are shown in Figures 1B and 1C, respectively. Complex **2**^{II} displays the typical slightly distorted octahedral geometry around the ruthenium, as expected for low-spin d^6 Ru^{II} ion.[30-32] The bpy ligands occupy both axial and equatorial positions assuming the κ-N^{1}O^1-pdc^{2-} ligands binds in the equatorial plane, with a dangling carboxylate not bonded to Ru.

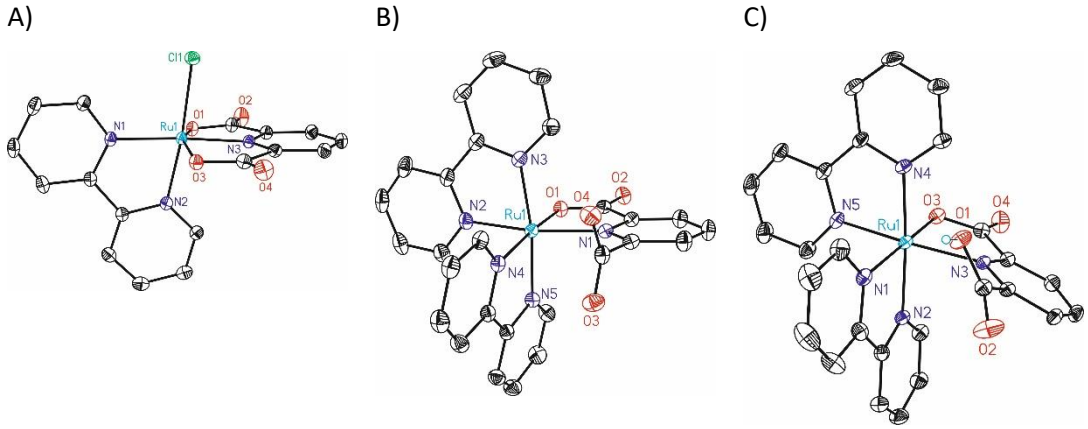

Figure 1. ORTEP plots at 50% probability for [Ru^{III}(pdc-κ^3-N^{1}O^2)(bpy)Cl], **1**^{III} (A), [Ru^{II}(pdc-κ^2-N^{1}O^1)(bpy)$_2$], **2**^{II} (B) and [Ru^{II}(Hpdc-κ^2-N^{1}O^1)(bpy)$_2$]$^{2+}$, **2**^{III} (C).

The one electron oxidized Ru^{III}, **2**^{III} shows a very similar structure with the Hpdc$^-$ ligand also coordinating in a bidentate κ -N^{1}O^1 mode but with the nonbonding carboxylate protonated. The Ru-O bond distance of the Ru^{III} compound is slightly shorter than that of its parent Ru^{II} complex, average 2.00 (1) Å *vs*. 2.08 (1) Å, respectively, as expected.

The addition of two equivalents of Ce^{IV} to a solution of **2**^{II} generates the Ru^{IV} derivative, [Ru^{IV}(pdc-κ^3-N^{1}O^2)(bpy)$_2$]$^{2+}$, **2**^{IV} which slowly converts to the Ru^{III} compound over time as monitored by NMR spectroscopy (see Figures S7 in the SI), hindering the formation of high quality crystals suitable for single crystal X-ray diffraction. However, it was possible to fully characterize the Ru^{IV} species by NMR and UV-Vis spectroscopy (Figure 2, Figures S6 and S9 in the SI). All the analysis are consistent with a diamagnetic compound, corresponding to a low-

spin d^4 Ru^{IV} center with a $(d_{xz}, d_{yz})^4$ electronic configuration and pentagonal bipyramidal geometry.[15,22] $[Ru^{IV}(pdc\text{-}\kappa^3\text{-}N^1O^2)(bpy)_2]^{2+}$ shows less number of resonances in the ^1H NMR spectrum compared to its Ru^{II} derivative $[Ru^{II}(pdc\text{-}\kappa^2\text{-}N^1O^1)(bpy)_2]$ in agreement to the symmetry increase (Figure 2). In addition, they are shifted to lower field in accordance with the higher oxidation state of the Ru center.

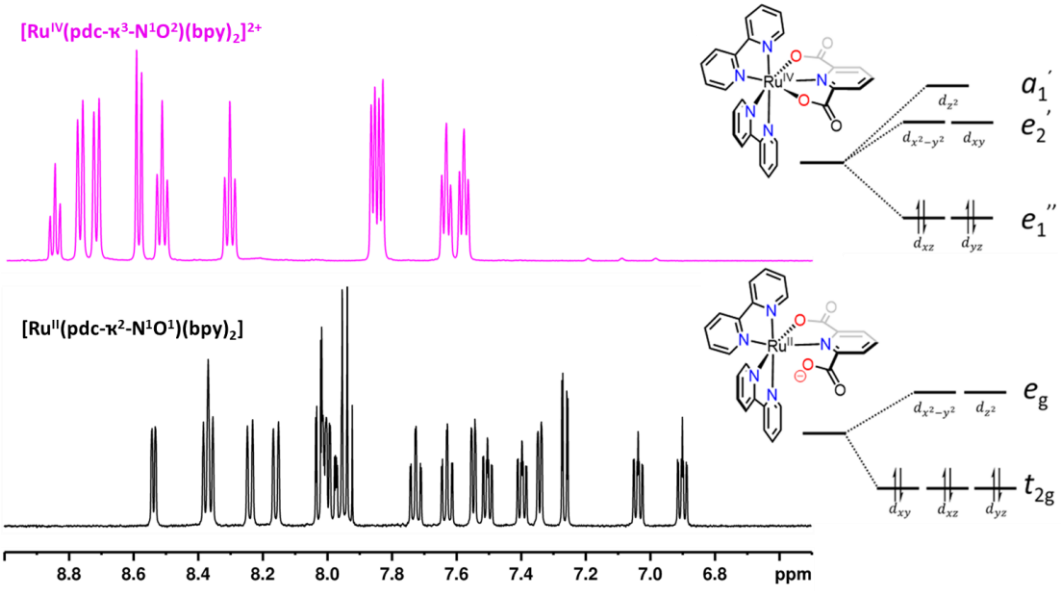

Figure 2. ^1H NMR (500 MHz, 298 K, $[d_2]$-D_2O) of $[Ru^{II}(pdc\text{-}\kappa^2\text{-}N^1O^1)(bpy)_2]$, $\mathbf{2}^{II}$ (black, bottom) and $[Ru^{IV}(pdc\text{-}\kappa^3\text{-}N^1O^2)(bpy)_2]^{2+}$, $\mathbf{2}^{IV}$ (magenta, top). The Crystal Field Splitting of d-orbitals and electronic configuration under 6-coordination-octahedral (O_h) or 7-coordinated pentagonal bipyramidal (D_{5h}) geometries are indicated next to each spectrum.

Complex $\mathbf{2}^{III}$ is low spin d^5 with an unpaired electron. As a consequence, all resonances in the ^1H NMR spectrum are broadened and highly shifted with regard to the Ru^{II} analogue (Figure S5a in the SI). On the other hand, it exhibits typical EPR features of unsymmetrical Ru^{III} complexes with $g_x = 2.69$, $g_y = 2.42$, $g_z = 2.04$ (Figure S5c in the SI). The large g anisotropy and the deviation of the average g factor from the free electron value of 2.0023 point to significant contributions from the heavy metal with its high spin−orbit coupling constant to the spin distribution.[33,34] The Ru^{III} chlorido complex $\mathbf{1}^{III}$ also shows a characteristic signal of the corresponding unpaired electron, but with a broader signature (Figure S5e in the SI).[31] Both Ru^{II} and Ru^{IV} derivatives, $\mathbf{2}^{II}$ and $\mathbf{2}^{IV}$, are EPR-silent as expected for complexes with no unpaired electrons.

The UV−vis spectra of complexes $\mathbf{2}^{II}$, $\mathbf{2}^{III}$ and $\mathbf{2}^{IV}$ were recorded in 0.1 M triflic acid aqueous solutions (pH 1.0) (Figure S9 in the supporting information). Typical Ru−bpy metal to ligand charge transfer (MLCT) bands are observed in the 380−550 nm range for the Ru^{II} compound,

where as a single transition at 360 nm is observed in that range of the spectrum for Ru^{III}, which is essentially featureless for Ru^{IV}. Analogous spectra could be obtained by spectrophotometric redox titration of $\mathbf{2}^{II}$ with Ce^{IV}, exhibiting isosbestic points as displayed in the Figure S10 in the SI.

4. 3. 2. Electrochemical Characterization and Catalysis

The electrochemical behavior of complexes $\mathbf{1}^{III}$ and $\mathbf{2}^{II}$ were analyzed by cyclic voltammetry (CV), differential pulse voltammetry (DPV) and bulk electrolysis experiments in dichloromethane (DCM) containing 0.1 M of $[(n\text{-Bu})_4N][PF_6]$ (TBAH) and 0.1 M ionic strength buffered aqueous solutions at different pHs. All redox potentials reported in this work are referred to the NHE electrode.

In DCM complex $\mathbf{1}^{III}$ shows a reversible redox wave at $E_{1/2}$ = 0.31 V (ΔE = 75 mV) attributed to the $Ru^{III/II}$ couple (Figure 3, left). On the other hand, complex $\mathbf{2}^{II}$ shows two chemically reversible and electrochemically quasi-reversible waves at $E_{1/2}$ = 1.05 V (ΔE = 62 mV) and $E_{1/2}$ = 1.32 V (ΔE = 120 mV) attributed to the $Ru^{III/II}$ and $Ru^{IV/III}$ couples respectively (Figure 3, right).[35] The relatively easy access to the IV/III redox potential at only 270 mV above the III/II is a clear indication of the 7 coordinated nature of the oxidized compound, as already been proven by NMR spectroscopy (Figure 2).

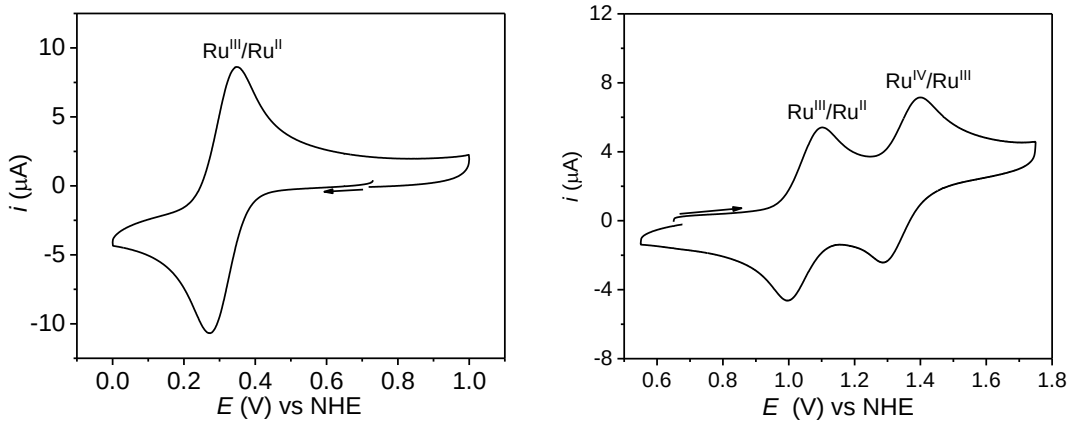

Figure 3. Cyclic voltammetry experiments in dichloromethane-0.1 M $[(n\text{-Bu})_4N][PF_6]$ of a 1 mM solution for $[Ru^{III}(pdc\text{-}\kappa^3\text{-}N^1O^2)(bpy)Cl]$, $\mathbf{1}^{III}$ (left) and $[Ru^{II}(pdc\text{-}\kappa^2\text{-}N^1O^1)(bpy)_2]$, $\mathbf{2}^{II}$ (right). WE: glassy carbon disk; CE: platinum disk; RE: Hg/Hg_2SO_4. Scan rate = 100 mV/s.

The chlorido complex **1**^{III} in aqueous solution at a pH 7 phosphate buffer (phbf), shows a $Ru^{III/II}$ redox wave at $E_{1/2}$ = 0.44 V (ΔE = 65 mV) (Figure S11 in the SI) and a second wave at 1.45 V which is chemically irreversible. It thus indicates that Ru^{IV}-Cl complex is not stable and undergoes oxidative Ru-Cl degradation to form most likely Cl_2 (g) as has been proposed for related complexes. This produces the *in situ* generation of the Ru-OH_2 complex, [Ru^{II}(pdc-κ^3-N^1O^2)(bpy)(H_2O)] that can act as a water oxidation catalyst. Indeed, a bulk electrolysis experiments of **1**^{III} at 1.6 V for 5 minutes at pH 7 involved a charge of 7.2 mC, which implies 0.05 mols of electrons per mol of **1**^{III}. The shape of the current *vs.* time is in agreement with the *in situ* generation of a water oxidation catalyst (Figure S11a in the SI). A CV and DPV analysis of the solution after the bulk electrolysis experiment reveals the generation of three new waves at E = 0.27 V, E = 0.80 V and E = 1.41 V that can be tentatively assigned to the III/II, IV/III and V/IV couples of [Ru^{II}(pdc-κ^3-N^1O^2)(bpy)(H_2O)] respectively (Figures S11b and 11c in the SI). The latter one being responsible for the catalytic phenomenon.

On the other hand, the CV of complex **2**^{II} at pH 7 shows two pH independent redox waves at $E_{1/2}$ = 0.89 V (ΔE = 90 mV) and 1.23 V (ΔE = 70 mV) associated with the III/II and IV/III couples as can be observed in Figure 4A. Figure 4B shows the effect of carrying out 100 repetitive CV within the potential range 0-1.6 V at the same pH. As can be observed in the inset as the number of cycles increases new small waves appear that are indicated with blue arrows together with the presence of a large electrocatalytic wave at 1.4-1.6 V.

In order to get more insights into the new species formed upon cycling, bulk electrolysis experiments at E_{app} = 1.45 V for 2 h were conducted (Figure 4C) which involved a charge of 7.93 C and 4.8 mols of electrons per mol of initial Ru^{II} clearly indicating the presence of an electrocalytic process. The solution generated under these conditions was analyzed by DPV experiments that are shown in Figure 4D. The DPV shows that the waves associated with the initial complex have drastically decreased and a set of new waves appear at E = 0.25 V, E = 0.46 V, E = 0.73 V and E = 1.03 V. Further as shown by DPV at different pH all these waves are pH dependent and therefore involving proton coupled electron transfer (PCET) processes that in turn indicate the presence of Ru-OH_2 groups in the new species generated (Figure S13 in the SI). Finally, a very large and intense wave can be observed at approximately 1.35 V attributed to the catalytic oxidation of water to dioxygen.

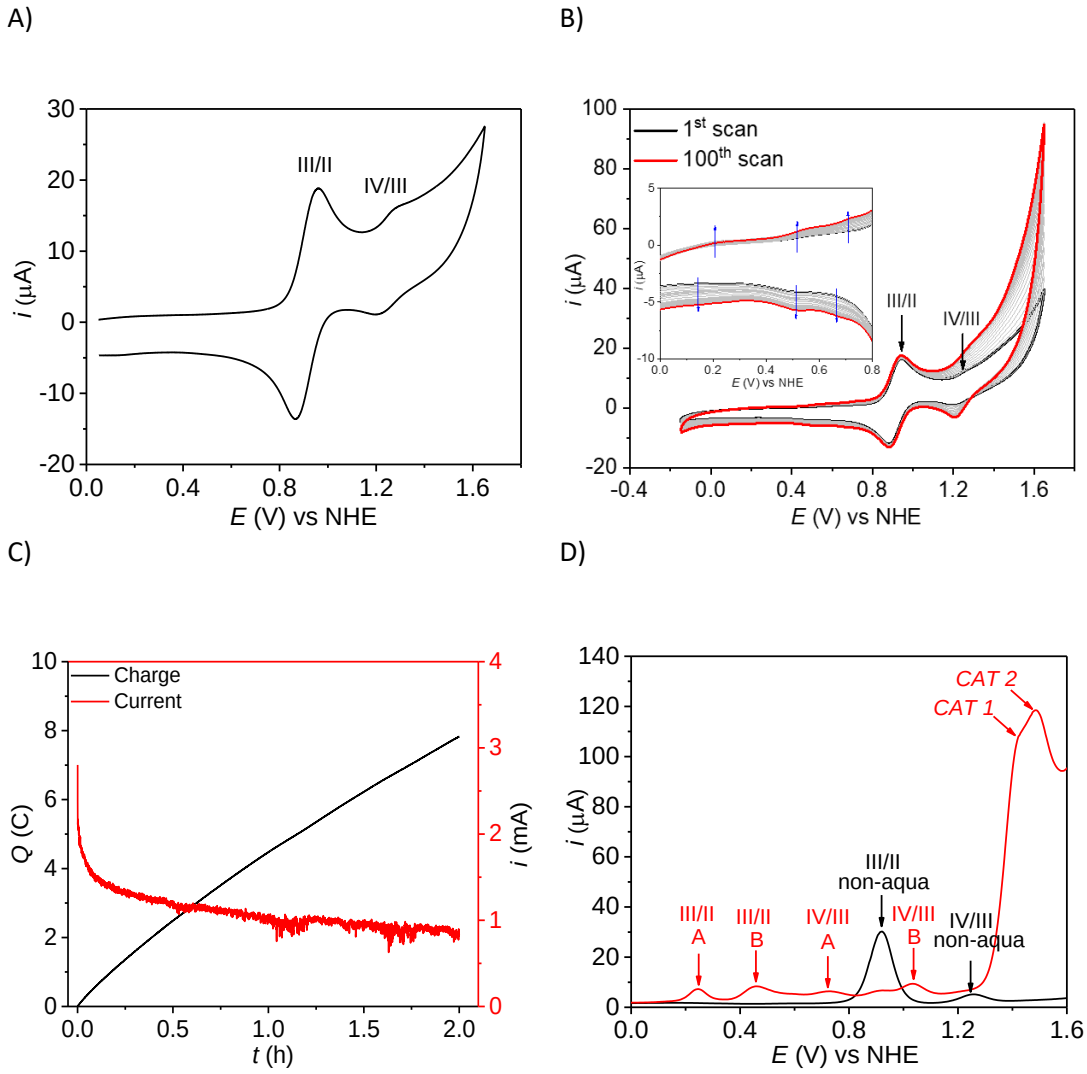

Figure 4. A, CV of a pH 7 phbf solution of 1 mM of $\mathbf{2}^{II}$. B, 100 consecutive CV cycles. Inset, enlargement of the 0-0.8 V range. The blue arrows indicate small new waves growing. C, bulk electrolysis of a pH 8 phbf solution of 2 mM of $\mathbf{2}^{II}$ at E_{app} = 1.45 V for 2 h. D, DPV of a pH 7 phbf solution of 2 mM of $\mathbf{2}^{II}$ (black) and of the solution obtained after the bulk electrolysis in C adjusted to pH 7 (red).

It is important to note that waves at 0.25 and 0.73 V assigned to $[Ru^{II}(pdc\text{-}\kappa^3\text{-}N^1O^2)(bpy)(H_2O)]$, **1-O**, species generated from the coulometry of $\mathbf{1}^{III}$ coincide with those generated by the coulometry of $\mathbf{2}^{II}$, meaning that one of the transformation processes involves bpy ligand loss as indicated in path A of Scheme 2. Further by checking the potential as a function of pH we were able to generate a Pourbaix diagram that is presented in the Figure 5A. The pK_a calculated from the slope changes are 4 for Ru^{II} and 11 for Ru^{III} and are gathered in Table 1 together with similar data for related complexes previously described in the literature.

The strong sigma donating effect of the pyridyldicarboxylato ligand can be clearly observed on the increase of pK_a's (10 → 11 (II); 2 → 4 (III)) and reduction of the V/IV redox couples when comparing for instance with $[Ru(trpy)(bpy)(H_2O)]^{2+}$ (entry 1).[36]

A)

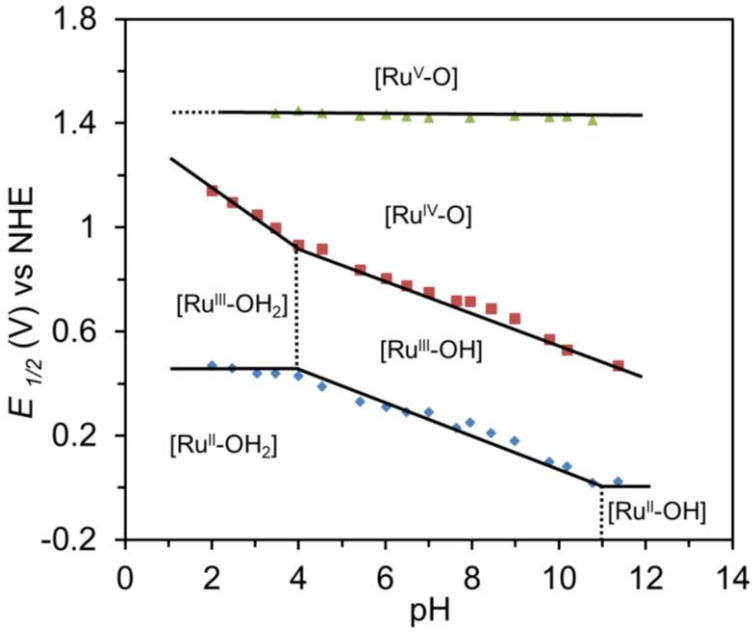

B)

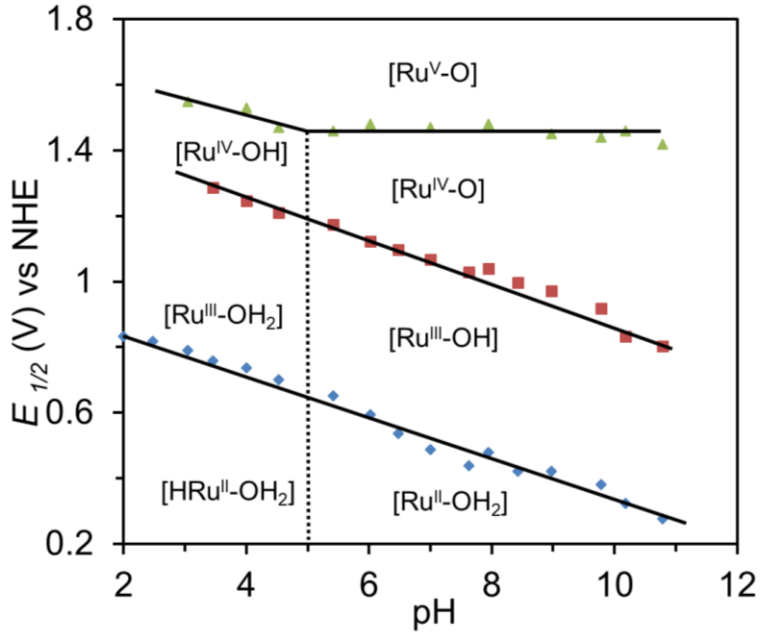

Figure 5. Pourbaix diagrams of [Ru-OH$_2$] species derived from bulk electrolysis of **2**^{II}. A) **1-O** and B) **2-O**. The black solid lines indicate the redox potentials for the different redox couples, whereas the dashed vertical lines indicate the pK_a. The zone of stability of the different species is indicated only with the Ru symbol, its oxidation state, and its degree of protonation of the aquo ligand. For instance, "Ru^{V}-O" is used to indicate the zone of stability of [Ru^{V}(O)(pdc-κ^3-N^{1}O^2)(bpy)]$^+$ for the **1-O** derived species (A) and [Ru^{V}(O)(pdc-κ^2-N^{1}O^1)(bpy)$_2$]$^+$ for the **2-O** derived species (B).

On the other hand, the waves at 0.46 and 1.03 V are assigned to a new species where one of the carboxylate arms of pdc^{2-} is substituted by an oxo group generating the seven coordinated species $[Ru^{IV}(O)(pdc\text{-}\kappa^2\text{-}N^1O^1)(bpy)_2]$, **2-O** (Scheme 2, path B).

The Pourbaix diagram obtained for this complex is presented in Figure 5B. Here the III/II redox potential is significantly higher than for $[Ru^{II}(pdc\text{-}\kappa^3\text{-}N^1O^2)(bpy)(H_2O)]$, **1-O**, since in the present complex the pdc^{2-} ligand acts in a $\kappa\text{-}N^1O^1$ mode and thus only one of the two anionic charges is directly felt by the Ru center. In sharp contrast the V/IV redox potentials are similar which is due to the cancelling effect of CN7 *vs.* CN6 1 vs. 2 anionic charges, a phenomenon that has been previously described for related Ru-aquo complexes.[19,37,38]

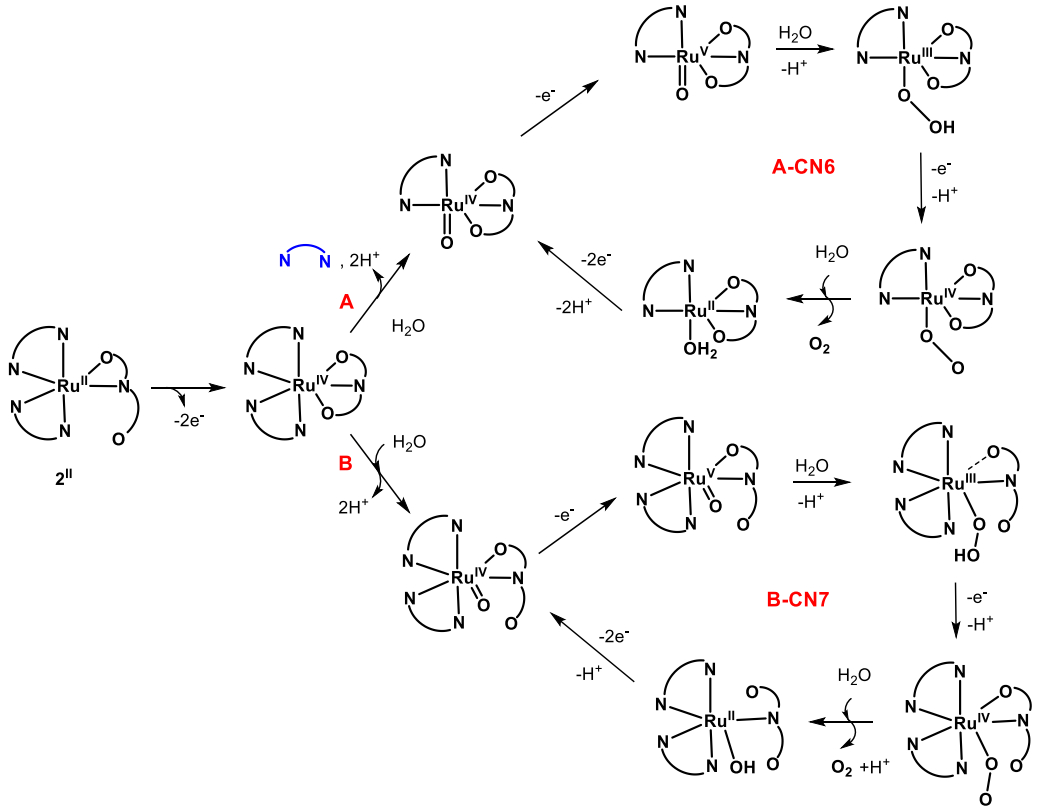

Scheme 2. Generation of water oxidation catalytically active species from $\mathbf{2}^{II}$.

The water oxidation catalytic cycles proposed for **1-O** and **2-O** are presented in Scheme 2. The main differentiating feature for the two cycles is that for **2-O** the high oxidation state species are CN7 and a dangling carboxylate is ready for an intramolecular proton transfer at the O-O bond formation step that is generally the rds, and thus radically decreases the energy of activation at this step as has been previously shown for related complexes.

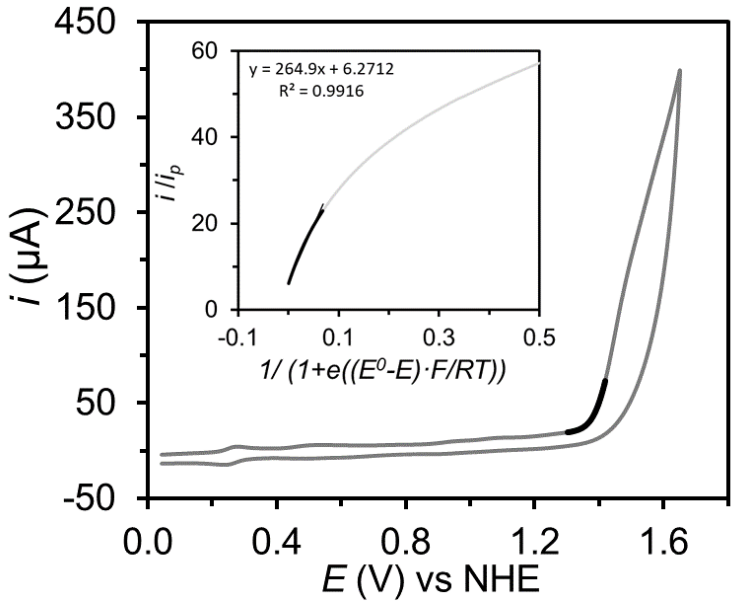

Figure 6. CV of a mixture of 0.92 mM of [Ru^{II}(pdc-κ^3-N^1O^2)(bpy)(H_2O)], **1-O** and 1.08 mM of [Ru^{IV}(O)(pdc-κ^2-N^1O^1)$(bpy)_2$], **2-O** at pH 7.0 phbf. Inset: FOWA plot of the catalytic current. The gray line represents the experimental data used for the FOWA analysis, and the black solid line shows the experimental data used for the extraction of TOF_{max}.

Indeed, a FOWA analysis [39-41] of the catalytic current (see Figure 6) for the mixture of **1-O** and **2-O** gives a TOF_{max} value for the catalytic process of 2.4-3.4 x 10^3 s^{-1}, for **2-O** assuming that the initial current at the foot is solely due to the fastest WOC.

Finally, an analysis of the gas phase of a bulk electrolysis experiments of 1 mM of $\mathbf{2}^{II}$ at an applied potential of 1.45 V for 1.2 h (4.25 C; 15 mols of electrons/mols of $\mathbf{2}^{II}$; 3.5 turnover numbers) confirms the evolution of O_2 gas with a Faradaic efficiency of 90%. (see Figure S16 in the SI).

Chapter 4

Table1. Thermodynamic and catalytic data for Ru-pdc and for related Ru complexes described in the literature at pH = 7.0.

		$E_{1/2}$ (V) vs NHE				pK_a			
Entry	Complexes[a]	V/IV	IV/III	III/II	[b]ΔE	Ru^{II}-OH_2	Ru^{III}-OH_2	Ru^{IV}-OH	TOF[c,d]
1[36]	$[Ru(trpy)(bpy)(H_2O)]^{2+}$	1.86	0.83	0.72	110	9.8	1.7	-	1.5×10^1
2[42]	*cis*-$[Ru(trpy)(pic)(H_2O)]^{1+}$	-	0.80	0.62	180	10.0	3.7	-	-
3[42]	*trans*-$[Ru(trpy)(pic)(H_2O)]^{1+}$	-	0.69	0.45	240	10	2.0	-	-
4[43]	*out*-$[Ru(Hbpp)(trpy)(H_2O)]^{2+}$	-	0.85	0.52	370	11.1	2.8	-	-
5[44]	$[Ru(bpc)(bpy)(H_2O)]^{1+}$	-	-	0.56	-	10.6	2.6	-	1.6×10^2
6[e]	$[Ru(pdc)(bpy)(H_2O)]^{1+}$	1.41	0.73	0.25	480	11	4	-	
7[45]	$Ru(bda)(isq)_2(H_2O)]$	1.11	0.88	0.55	330	5.5	12.9	-	3.0×10^2
8[15]	$[Ru(tda)(py)_2OH]$	1.43	0.87	0.70	170	-	-	Ru^{IV} (5.5)	8.0×10^3
9[e]	$[Ru(pdc)(bpy)_2OH]$	1.47	1.03	0.46	570	-	-	Ru^{IV} (5.0)	3.4×10^3

[a]Ligand abbreviations: trpy = 2,2':6',2"-terpyridine, bpy = 2,2'-bipyridine, pic = 2-picolinate, Hbpp = 3,5-bis(2-pyridyl)pyrazole, bpc = 2,2'-bipyridine-6-carboxylate, pdc = 2,6-pyridinedicarboxylate, bda = 2,2'-bipyridine-6,6'-dicarboxylate, tda = 2,2':6',2"-terpyridine-6,6"-dicarboxylate, py = pyridine. [b]ΔE= E(IV/III)-E(III/II). [c]TOF stands for initial Turn Over Frequencies in cycles per second. These values are extracted for the catalytic reactions involving 1.0 mM Cat/100 mM Ce^{IV} in a 0.1 M triflic acid solution with a total volume of 2 mL (entry 1, 5 and 7). [d]TOF stands for Maximum Turn Over Frequencies per second. This value has been extracted from Foot of the Wave Analysis of CV and DPV experiment in pH7 (entry 8 and 9). [e] this work.

4. 4. Conclusion

In conclusion, two new Ru complexes [Ru^{III}(pdc-κ^3-N^1O^2)(bpy)Cl], **1**^{III}, [Ru^{II}(pdc-κ^2-N^1O^1)$(bpy)_2$], **2**^{II} and their reduced and oxidized species are reported. Under high anodic potentials they evolve towards the formation of Ru-aquo complexes [Ru^{III}(pdc-κ^3-N^1O^2)(bpy)$(OH_2)]^+$, **1-O** and [Ru^{IV}(O)(pdc-κ^2-N^1O^1)$(bpy)_2$], **2-O** that are powerful and rugged water oxidation catalysts. These two complexes operate water oxidation catalysis with active species that involve six coordination for the Ru center in **1-O** and seven coordination in **2-O**. The present work uncovers and highlights the complexity involved in water oxidation catalytic processes when transition metal complexes are exposed to high oxidation potentials needed for water oxidation catalysis.

4. 5. References

(1) Lewis, N. S.; Nocera, D. G. *Proc. Natl. Acad. Sci.* **2006**, *103*, 15729.
(2) Berardi, S.; Drouet, S.; Francas, L.; Gimbert-Surinach, C.; Guttentag, M.; Richmond, C.; Stoll, T.; Llobet, A. *Chem. Soc. Rev.* **2014**, *43*, 7501.
(3) Matheu, R.; Garrido-Barros, P.; Gil-Sepulcre, M.; Ertem, M. Z.; Sala, X.; Gimbert-Suriñach, C.; Llobet, A. *Nat. Rev. Chem.* **2019**, *3*, 331.
(4) Blakemore, J. D.; Crabtree, R. H.; Brudvig, G. W. *Chem. Rev.* **2015**, *115*, 12974.
(5) Cao, R.; Lai, W.; Du, P. *Energy Environ. Sci.* **2012**, *5*, 8134.
(6) Llobet, A.; John Wiley & Sons, Molecular water oxidation catalysis: a key topic for new sustainable energy conversion schemes, 2014.
(7) Garrido-Barros, P.; Gimbert-Suriñach, C.; Matheu, R.; Sala, X.; Llobet, A. *Chem. Soc. Rev.* **2017**, *46*, 6088.
(8) Tong, L.; Thummel, R. P. *Chem. Sci.* **2016**, *7*, 6591.
(9) Xie, Y.; Shaffer, D. W.; Concepcion, J. J. *Inorg. Chem.* **2018**.
(10) Savini, A.; Bellachioma, G.; Bolaño, S.; Rocchigiani, L.; Zuccaccia, C.; Zuccaccia, D.; Macchioni, A. *ChemSusChem.* **2012**, *5*, 1415.
(11) Bucci, A.; Savini, A.; Rocchigiani, L.; Zuccaccia, C.; Rizzato, S.; Albinati, A.; Llobet, A.; Macchioni, A. *Organometallics* **2012**, *31*, 8071.
(12) Savini, A.; Bucci, A.; Nocchetti, M.; Vivani, R.; Idriss, H.; Macchioni, A. *ACS Catal.* **2015**, *5*, 264.
(13) Menendez Rodriguez, G.; Bucci, A.; Hutchinson, R.; Bellachioma, G.; Zuccaccia, C.; Giovagnoli, S.; Idriss, H.; Macchioni, A. *ACS Energy Lett.* **2017**, *2*, 105.
(14) Macchioni, A. *Eur. J. Inorg. Chem.* **2019**, *2019*, 7.
(15) Matheu, R.; Ertem, M. Z.; Benet-Buchholz, J.; Coronado, E.; Batista, V. S.; Sala, X.; Llobet, A. *J. Am. Chem. Soc.* **2015**, *137*, 10786.
(16) Shaffer, D. W.; Xie, Y.; Szalda, D. J.; Concepcion, J. J. *Inorg. Chem.* **2016**, *55*, 12024.
(17) Keidel, A.; López, I.; Staffa, J.; Kuhlmann, U.; Bozoglian, F.; Gimbert-Suriñach, C.; Benet-Buchholz, J.; Hildebrandt, P.; Llobet, A. *ChemSusChem.* **2017**, *10*, 551.
(18) Wasylenko, D. J.; Ganesamoorthy, C.; Henderson, M. A.; Koivisto, B. D.; Osthoff, H. D.; Berlinguette, C. P. *J. Am. Chem. Soc.* **2010**, *132*, 16094.
(19) Matheu, R.; Ertem, M. Z.; Gimbert-Suriñach, C.; Benet-Buchholz, J.; Sala, X.; Llobet, A. *ACS Catal.* **2017**, *7*, 6525.
(20) Matheu, R.; Ertem, M. Z.; Gimbert-Suriñach, C.; Sala, X.; Llobet, A. *Chem. Rev.* **2019**, *119*, 3453.
(21) Xie, Y.-F.; Zhu, H.; Shi, H.-T.; Jia, A.-Q.; Zhang, Q.-F. *Inorg. Chim. Acta* **2015**, *428*, 147.
(22) Duan, L.; Xu, Y.; Gorlov, M.; Tong, L.; Andersson, S.; Sun, L. *Chem.: Eur. J* **2010**, *16*, 4659.
(23) Daniel, Q.; Duan, L.; Timmer, B. J. J.; Chen, H.; Luo, X.; Ambre, R.; Wang, Y.; Zhang, B.; Zhang, P.; Wang, L.; Li, F.; Sun, J.; Ahlquist, M.; Sun, L. *ACS Catal.* **2018**, *8*, 4375.
(24) Evans, I. P.; Spencer, A.; Wilkinson, G. *J. Chem. Soc., Dalton Trans.* **1973**, 204.
(25) *Data collection and reduction with CrysAlisPro 1.171.39.12b (Rigaku OD, 2015).*
(26) *Empirical absorption corrrection using spherical harmonics implemented in Scale3 Abspack scaling algorithm, CrysAlisPro 1.171.39.12b (Rigaku OD, 2015).*
(27) Sheldrick, G. M. *Acta Cryst. A* **2015**, *71*, 3.
(28) Hübschle, C. B.; Sheldrick, G. M.; Dittrich, B. *J. Appl. Crystallogr.* **2011**, *44*, 1281.
(29) Sheldrick, G. M. *Acta Cryst. C* **2015**, *71*, 3.
(30) Matheu, R.; Ghaderian, A.; Francàs, L.; Chernev, P.; Ertem, M. Z.; Benet-Buchholz, J.; Batista, V. S.; Haumann, M.; Gimbert-Suriñach, C.; Sala, X.; Llobet, A. *Chem.: Eur. J* **2018**, *24*, 12838.
(31) Singha Hazari, A.; Ray, R.; Hoque, M. A.; Lahiri, G. K. *Inorg. Chem.* **2016**, *55*, 8160.

(32) Neudeck, S.; Maji, S.; López, I.; Dechert, S.; Benet-Buchholz, J.; Llobet, A.; Meyer, F. *Inorg. Chem.* **2016**, *55*, 2508.
(33) Kaim, W.; Lahiri, G. K. *Angew. Chem. Int. Ed.* **2007**, *46*, 1778.
(34) Mandal, A.; Hoque, M. A.; Grupp, A.; Paretzki, A.; Kaim, W.; Lahiri, G. K. *Inorg. Chem.* **2016**, *55*, 2146.
(35) Kaveevivitchai, N.; Kohler, L.; Zong, R.; El Ojaimi, M.; Mehta, N.; Thummel, R. P. *Inorg. Chem.* **2013**, *52*, 10615.
(36) Takeuchi, K. J.; Thompson, M. S.; Pipes, D. W.; Meyer, T. J. *Inorg. Chem.* **1984**, *23*, 1845.
(37) Mognon, L.; Benet-Buchholz, J.; Llobet, A. *Inorg. Chem.* **2015**, *54*, 11948.
(38) Maji, S.; López, I.; Bozoglian, F.; Benet-Buchholz, J.; Llobet, A. *Inorg. Chem.* **2013**, *52*, 3591.
(39) Costentin, C.; Drouet, S.; Robert, M.; Savéant, J.-M. *J. Am. Chem. Soc.* **2012**, *134*, 11235.
(40) Costentin, C.; Drouet, S.; Robert, M.; Savéant, J. M. *Science* **2012**, *338*, 90.
(41) Matheu, R.; Neudeck, S.; Meyer, F.; Sala, X.; Llobet, A. *ChemSusChem.* **2016**, *9*, 3361.
(42) Llobet, A.; Doppelt, P.; Meyer, T. J. *Inorg. Chem.* **1988**, *27*, 514.
(43) Sens, C.; Rodríguez, M.; Romero, I.; Llobet, A.; Parella, T.; Benet-Buchholz, J. *Inorg. Chem.* **2003**, *42*, 8385.
(44) Tong, L.; Inge, A. K.; Duan, L.; Wang, L.; Zou, X.; Sun, L. *Inorg. Chem.* **2013**, *52*, 2505.
(45) Duan, L.; Bozoglian, F.; Mandal, S.; Stewart, B.; Privalov, T.; Llobet, A.; Sun, L. *Nat. Chem.* **2012**, *4*, 418.

4. 6. Supporting Information

Table of Contents

NMR, UV-Vis and EPR spectroscopy

Figure S1-S2. NMR spectra of $[Ru^{II}(pdc\text{-}\kappa^2\text{-}N^1O^1)(bpy)(DMSO)Cl]^-$

Figure S3-S4. NMR spectra $[Ru^{II}(pdc\text{-}\kappa^2\text{-}N^1O^1)(bpy)_2]$, $\mathbf{2}^{II}$

Figure S5. ^1H NMR and EPR spectra of $[Ru^{III}(Hpdc\text{-}\kappa^2\text{-}N^1O^1)(bpy)_2]^{2+}$, $\mathbf{2}^{III}$

Figure S6. NMR spectra of $[Ru^{IV}(pdc\text{-}\kappa^3\text{-}N^1O^2)(bpy)_2]^{2+}$, $\mathbf{2}^{IV}$

Figure S7. NMR spectra of $[Ru^{IV}(pdc\text{-}\kappa^3\text{-}N^1O^2)(bpy)_2]^{2+}$, $\mathbf{2}^{IV}$ at different time

Figure S8. UV-Vis spectra of $[Ru^{III}(pdc\text{-}\kappa^3\text{-}N^1O^2)(bpy)Cl]$, $\mathbf{1}^{III}$ and $[Ru^{II}(pdc\text{-}\kappa^2\text{-}N^1O^1)(bpy)(DMSO)Cl]^-$

Figure S9. UV-Vis spectra of $[Ru^{II}(pdc\text{-}\kappa^2\text{-}N^1O^1)(bpy)_2]$, $\mathbf{2}^{II}$; $[Ru^{III}(Hpdc\text{-}\kappa^2\text{-}N^1O^1)(bpy)_2]^+$, $\mathbf{2}^{III}$; and $[Ru^{IV}(pdc\text{-}\kappa^3\text{-}N^1O^2)(bpy)_2]^{2+}$,$\mathbf{2}^{IV}$

Figure S10. Redox titration of $[Ru^{II}(pdc\text{-}\kappa^2\text{-}N^1O^1)(bpy)_2]$, $\mathbf{2}^{II}$

Electrochemistry and electrocatalysis

Figure S11. Bulk electrolysis**,** CV and DPV of $[Ru^{III}(pdc\text{-}\kappa^3\text{-}N^1O^2)(bpy)Cl]$, $\mathbf{1}^{III}$ in pH 7 phosphate buffer

Figure S12. DPV of $[Ru^{III}(pdc\text{-}\kappa^3\text{-}N^1O^2)(bpy)Cl]$, $\mathbf{1}^{III}$ and active species generated from $[Ru^{II}(pdc\text{-}\kappa^2\text{-}N^1O^1)(bpy)_2]$, $\mathbf{2}^{II}$ in pH 7 phosphate buffer

Figure S13. DPVs of the active species generated from $[Ru^{II}(pdc\text{-}\kappa^2\text{-}N^1O^1)(bpy)_2]$, $\mathbf{2}^{II}$ in different pH

Figure S14. CV of $[Ru^{III}(pdc\text{-}\kappa^3\text{-}N^1O^2)(bpy)Cl]$, $\mathbf{1}^{III}$ and $[Ru^{III}(pdc\text{-}\kappa^3\text{-}N^1O^2)(bpy)(OH_2)]^+$ in acetone

Figure S15. CV of $[Ru^{III}(pdc\text{-}\kappa^3\text{-}N^1O^2)(bpy)Cl]$, $\mathbf{1}^{III}$ in dichloromethane and dimethyl sulfoxide solvent mixture

Figure S16. Oxygen evolution profile

a)

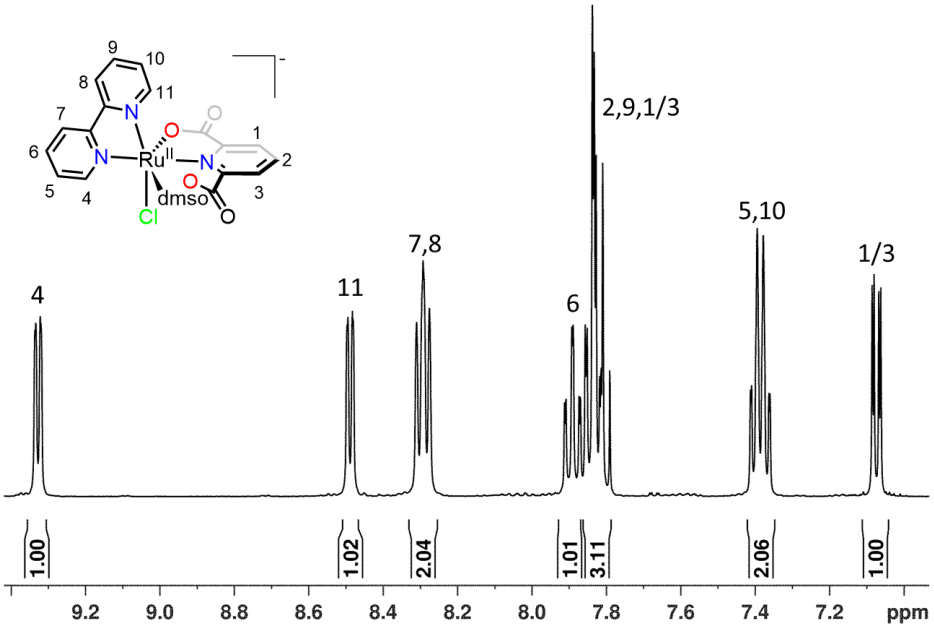
4
11
7,8
6
2,9,1/3
5,10
1/3
1.00
1.02
2.04
1.01
3.11
2.06
1.00
9.2
9.0
8.8
8.6
8.4
8.2
8.0
7.8
7.6
7.4
7.2
ppm
dmso
Cl

b)

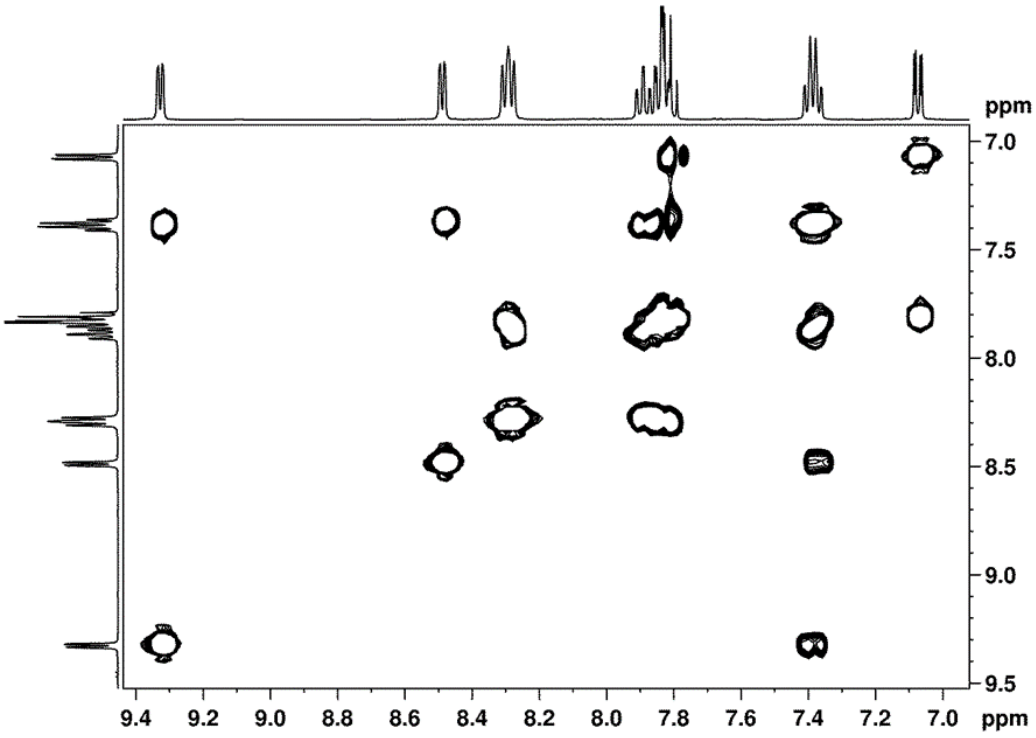
ppm
7.0
7.5
8.0
8.5
9.0
9.5
9.4
9.2
9.0
8.8
8.6
8.4
8.2
8.0
7.8
7.6
7.4
7.2
7.0
ppm

c)

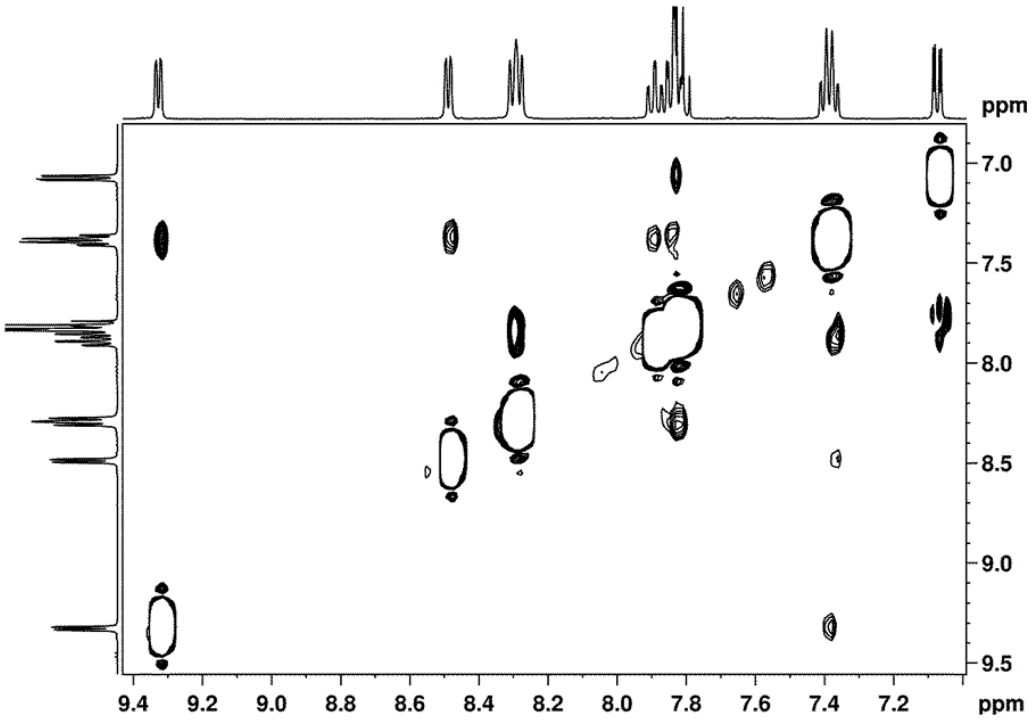

Figure S1. a) ^{1}H NMR spectra (500 MHz, 298 K, [d_6]-DMSO) of [Ru^{II}(pdc-κ^2-N^1O^1)(bpy)(DMSO)Cl]$^-$, **1**^{III} by in situ reduction with excess of triethylamine; b) COSY and c) NOESY.

Chapter 4

a)

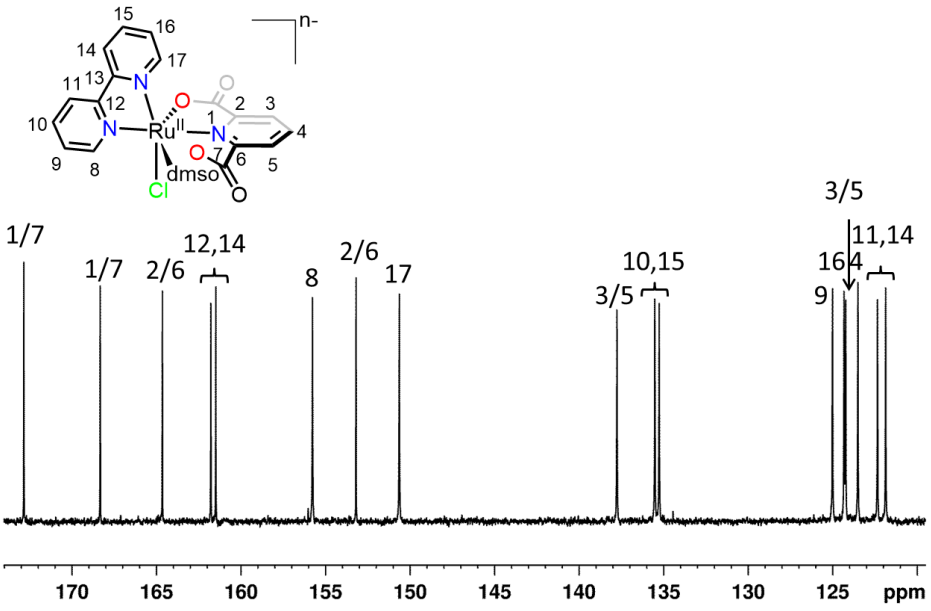
n-
Ru
dmso
Cl
1/7
1/7
2/6
12,14
8
2/6
17
3/5
10,15
3/5
9
16
4
11,14
170
165
160
155
150
145
140
135
130
125
ppm

b)

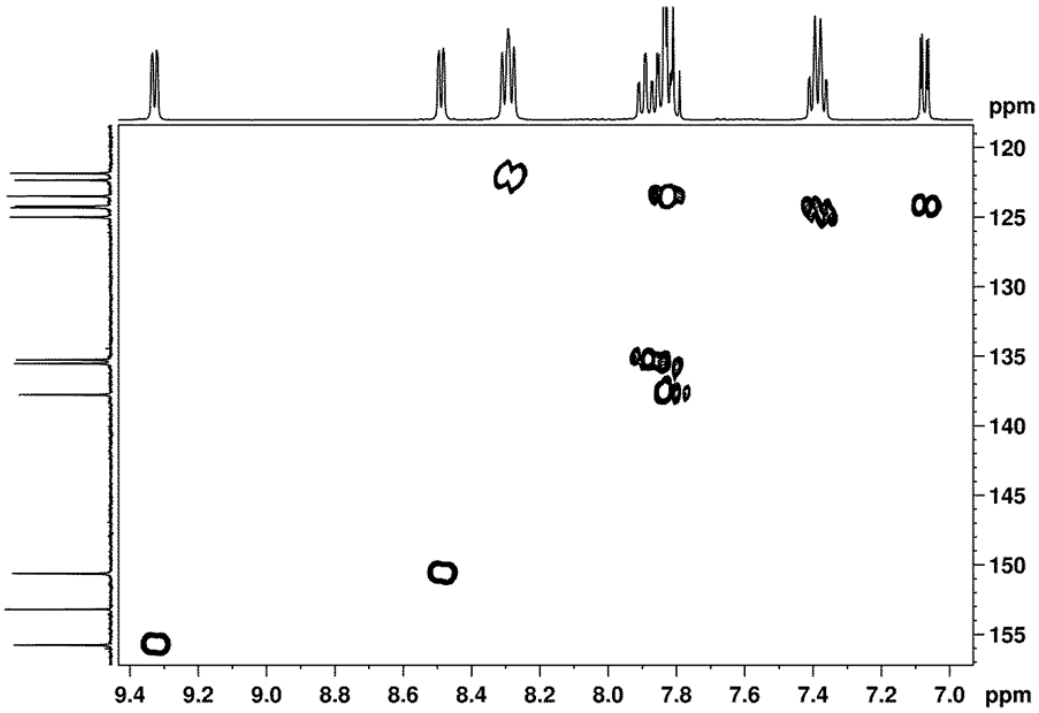
ppm
120
125
130
135
140
145
150
155
9.4
9.2
9.0
8.8
8.6
8.4
8.2
8.0
7.8
7.6
7.4
7.2
7.0
ppm

c)

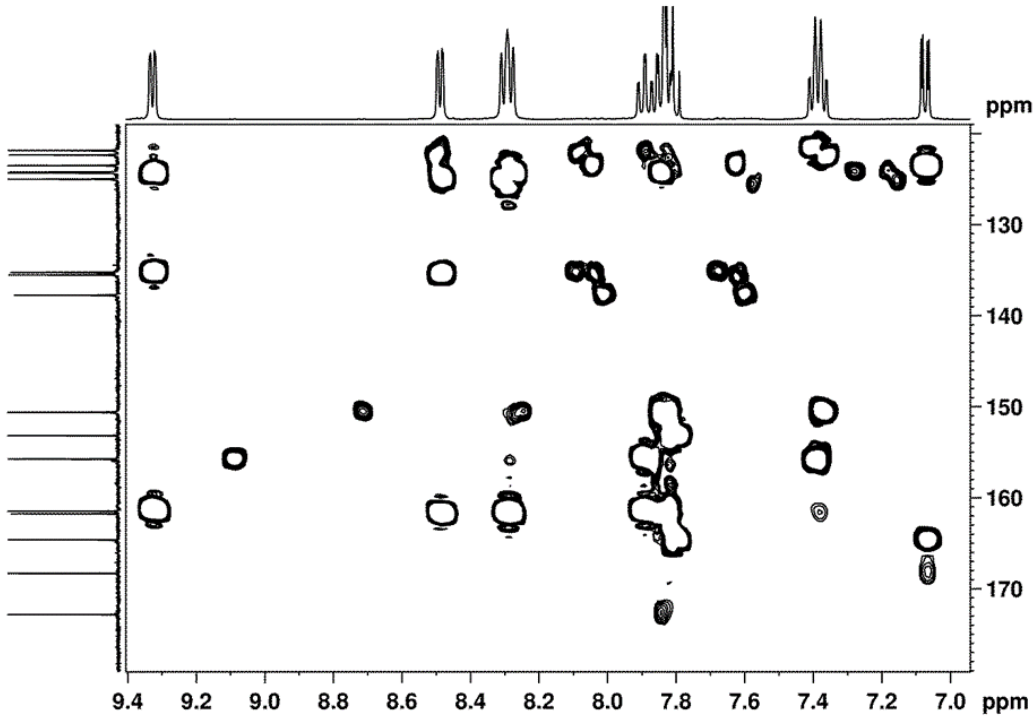

Figure S2. a) ^{13}C NMR spectra (125 MHz, 298 K, [d_6]-DMSO) of [Ru^{II}(pdc-κ^2-N^1O^1)(bpy)(DMSO)Cl]$^-$, **1**^{III} by in situ reduction with excess of triethylamine; b) HSQC and c) HMBC (500 MHz, 298 K, [d_6]-DMSO).

a)

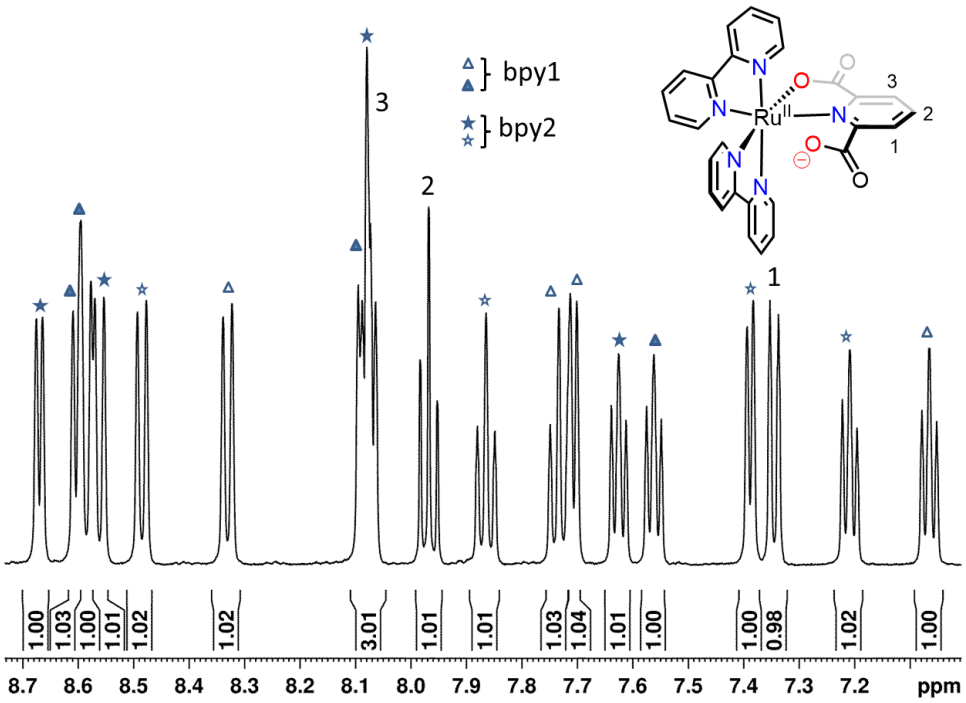
bpy1
bpy2
3
2
1
1.00
1.03
1.00
1.01
1.02
1.02
3.01
1.01
1.01
1.03
1.04
1.01
1.00
1.00
0.98
1.02
1.00
8.7 8.6 8.5 8.4 8.3 8.2 8.1 8.0 7.9 7.8 7.7 7.6 7.5 7.4 7.3 7.2 ppm

b)

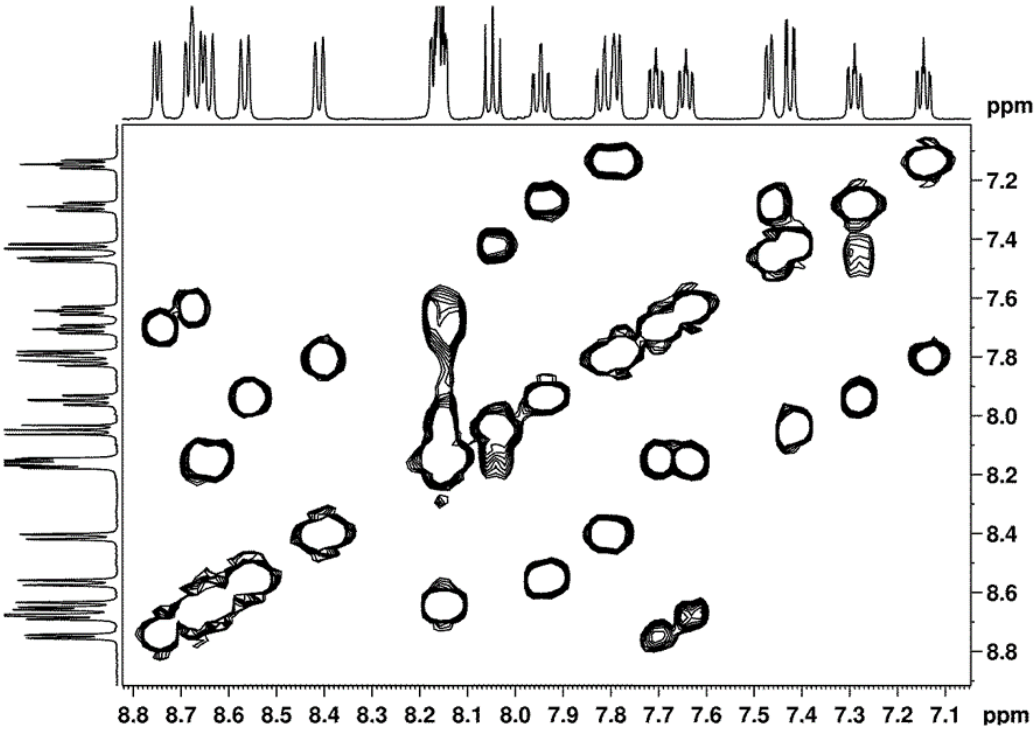
ppm
7.2
7.4
7.6
7.8
8.0
8.2
8.4
8.6
8.8
8.8 8.7 8.6 8.5 8.4 8.3 8.2 8.1 8.0 7.9 7.8 7.7 7.6 7.5 7.4 7.3 7.2 7.1 ppm

c)

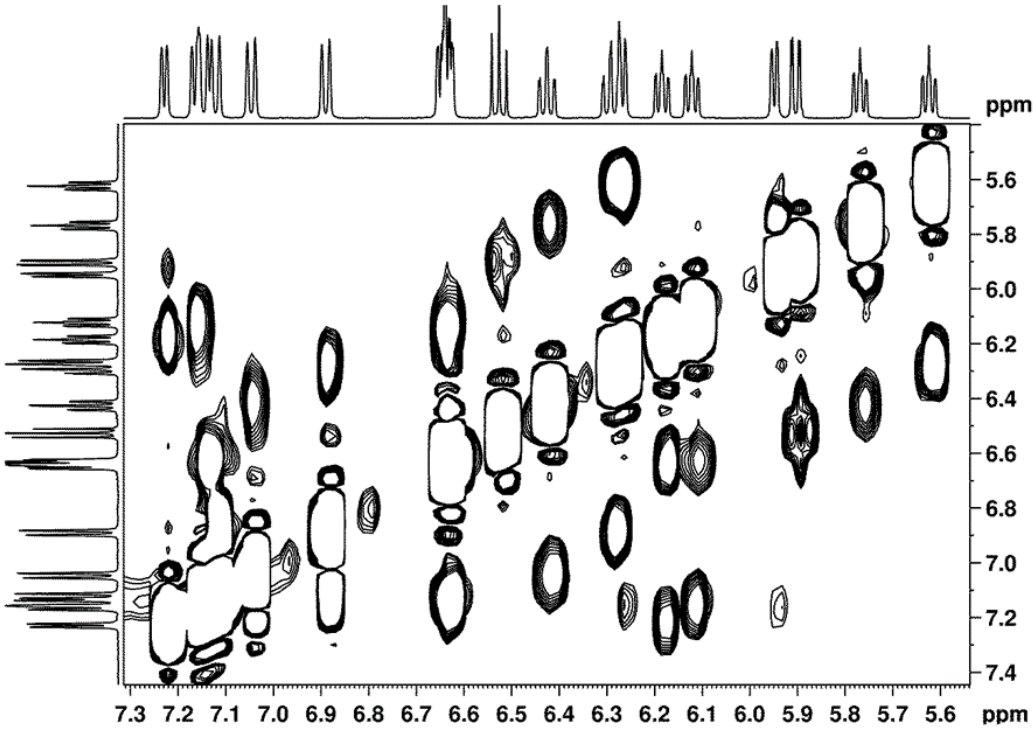

Figure S3. a) ^{1}H NMR spectrum (500 MHz, 298 K, [d_4]-MeOD) of [Ru^{II}(pdc-κ^2-N^1O^1)(bpy)$_2$], **2**^{II}; b) COSY and c) NOESY. Triangles and stars indicate set of bpy ligands.

a)

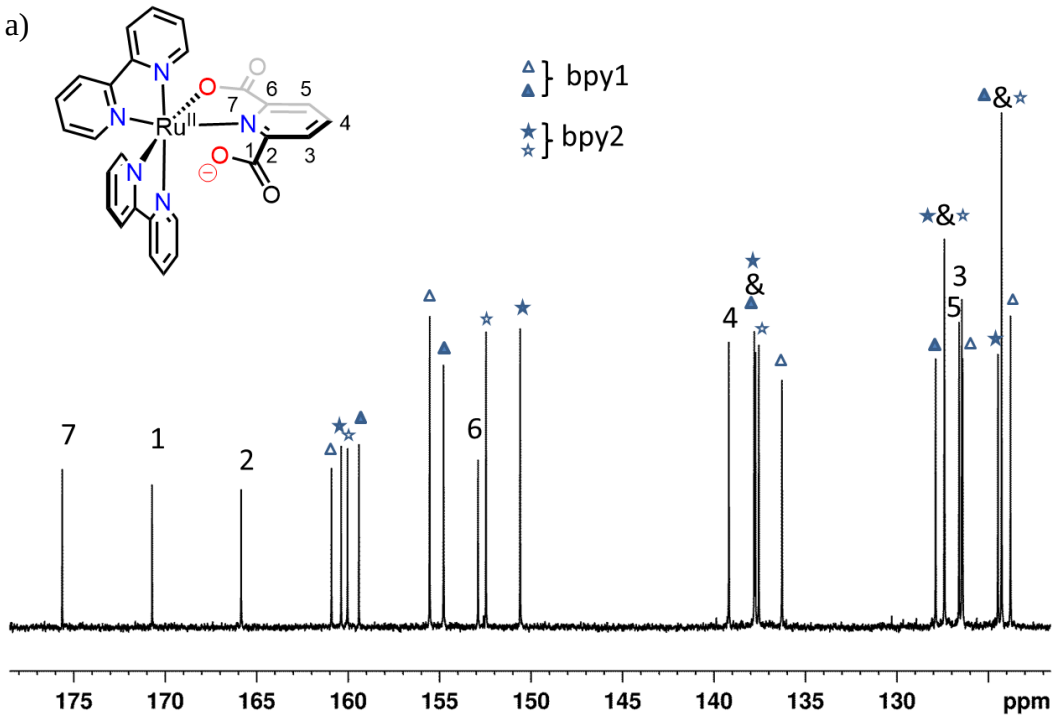
bpy1
bpy2
7
1
2
6
4
3
5
175
170
165
160
155
150
145
140
135
130
ppm

b)

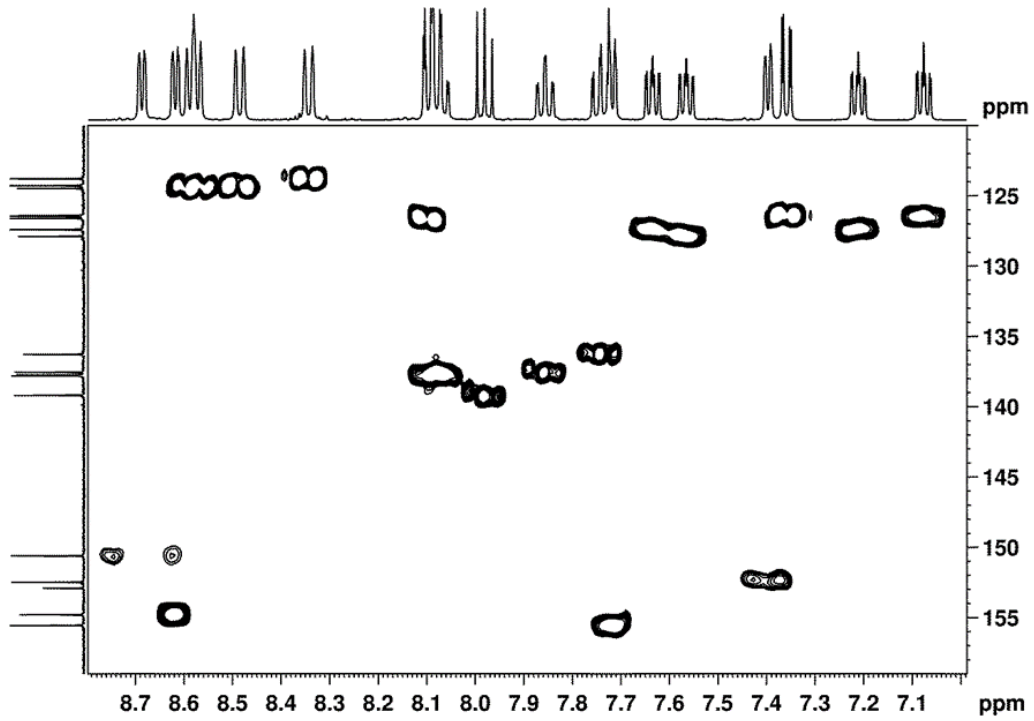
ppm
125
130
135
140
145
150
155
8.7
8.6
8.5
8.4
8.3
8.2
8.1
8.0
7.9
7.8
7.7
7.6
7.5
7.4
7.3
7.2
7.1
ppm

c)

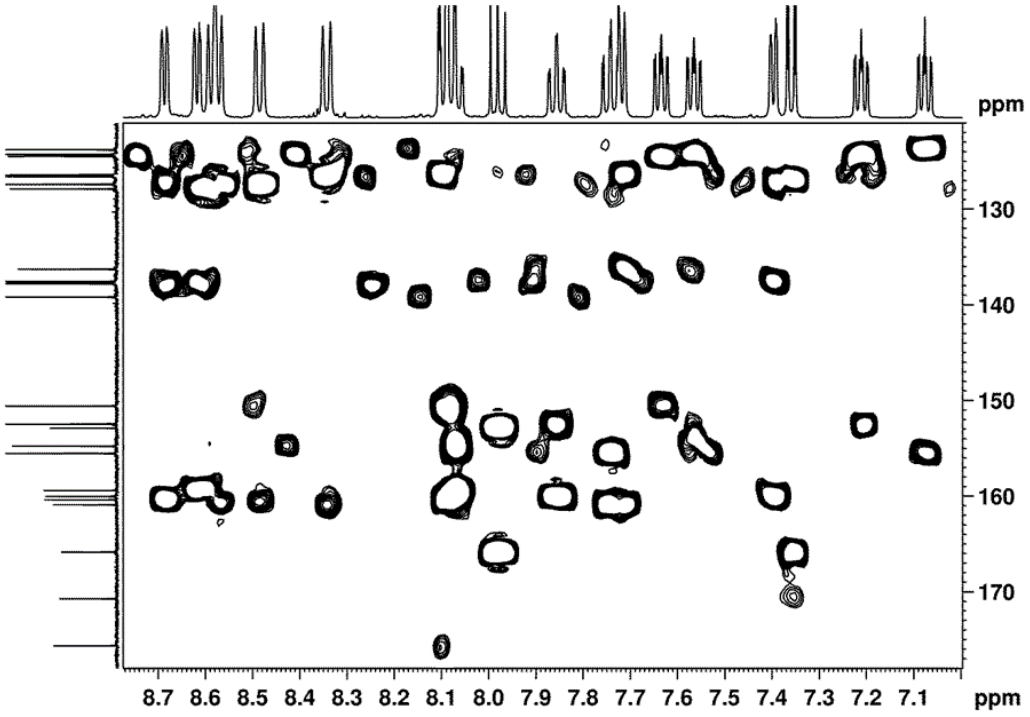

Figure S4. a) ^{13}C NMR spectra (125 MHz, 298 K, [d$_4$]-MeOD) of [Ru^{II}(pdc-κ^2-N^{1}O^1)(bpy)$_2$], **2**^{II}; b) HSQC and c) HMBC (500 MHz, 298 K, [d$_4$]-MeOD).

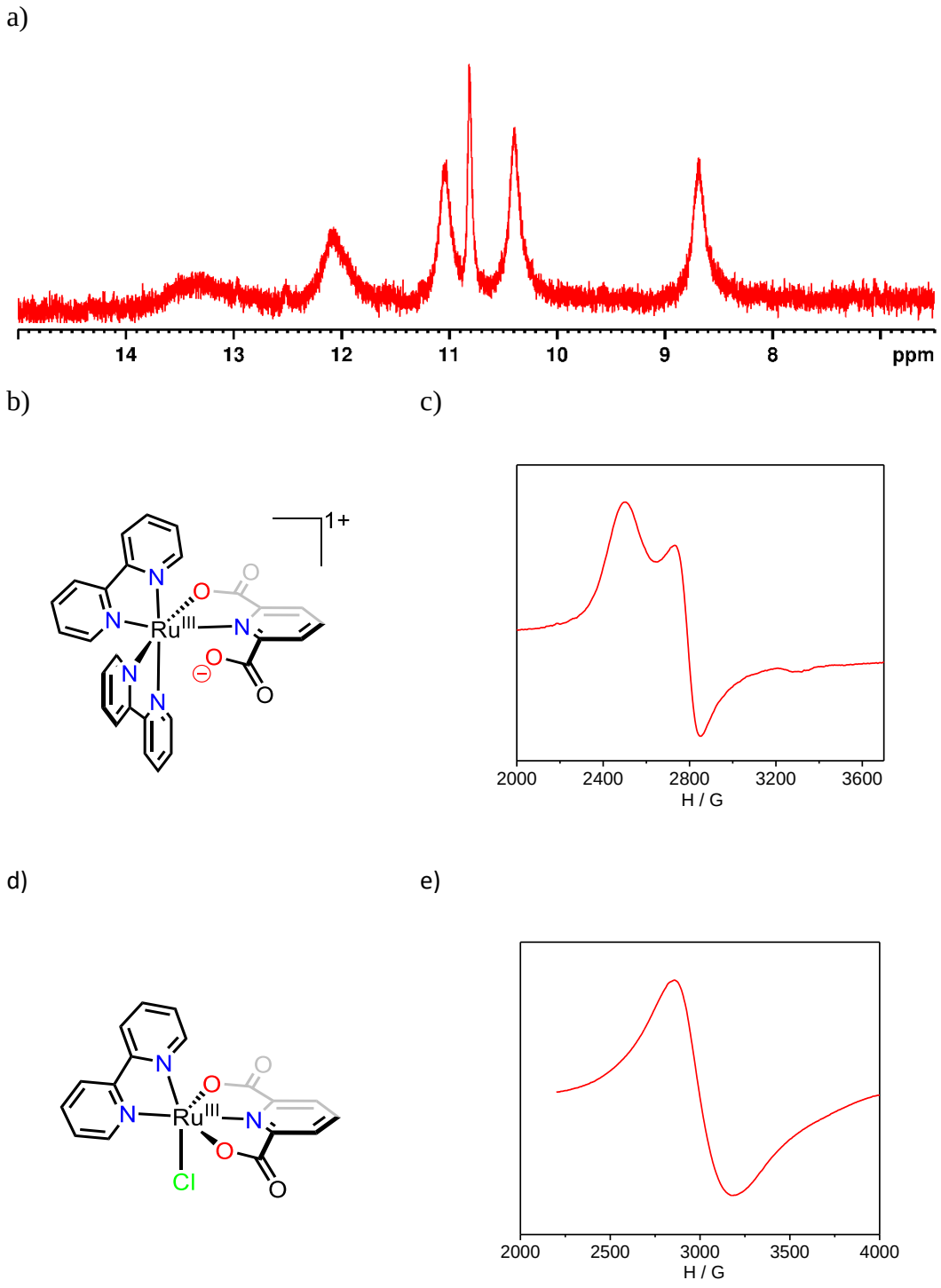

Figure S5. a) ^{1}H NMR spectrum (500 MHz, 298 K, [d$_2$]-D$_2$O) of [Ru^{III}(Hpdc-κ^2-N^{1}O^1)(bpy)$_2$]$^+$, **2^{III}**; b and c) ChemDraw structure and EPR spectrum of [Ru^{III}(Hpdc-κ^2-N^{1}O^1)(bpy)$_2$]$^+$, **2^{III}** measured at 4 K. The compound was prepared *in situ* by adding one equivalent of Ce^{IV} to a solution of [Ru^{II}(pdc-κ^2-N^{1}O^1)(bpy)$_2$], **2^{II}** in water. d) and e) ChemDraw structure and EPR spectrum of [Ru^{III}(pdc-κ^3-N^{1}O^2)(bpy)Cl], **1^{III}** in DMSO solvent measured at 4 K.

a)

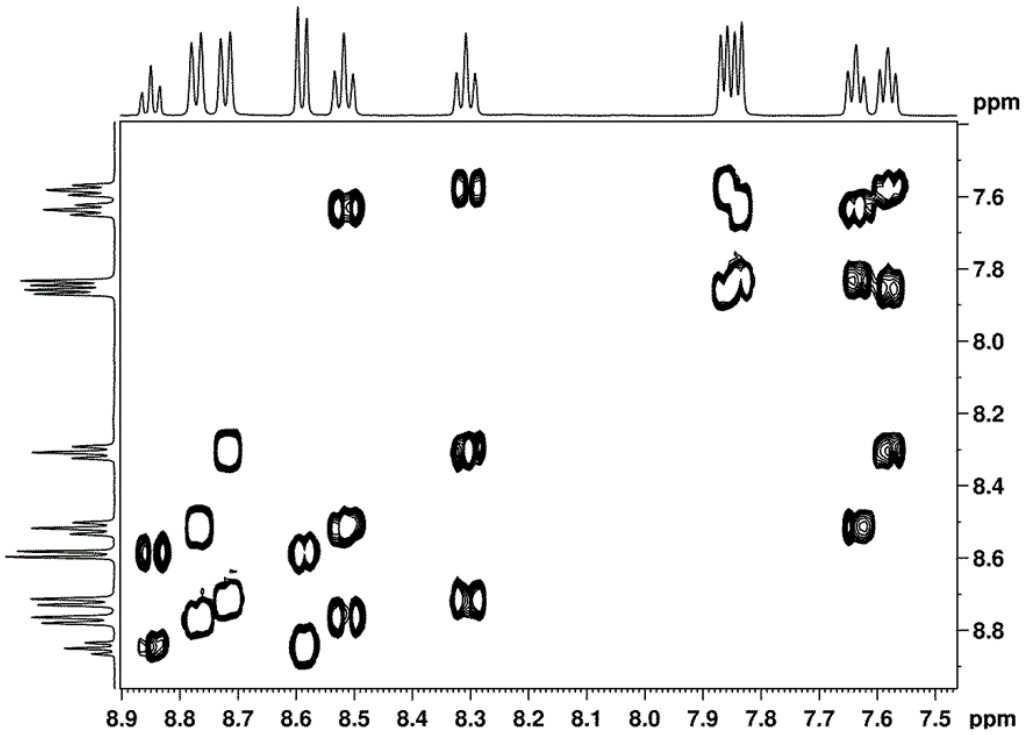
ppm
7.6
7.8
8.0
8.2
8.4
8.6
8.8
8.9 8.8 8.7 8.6 8.5 8.4 8.3 8.2 8.1 8.0 7.9 7.8 7.7 7.6 7.5 ppm

b)

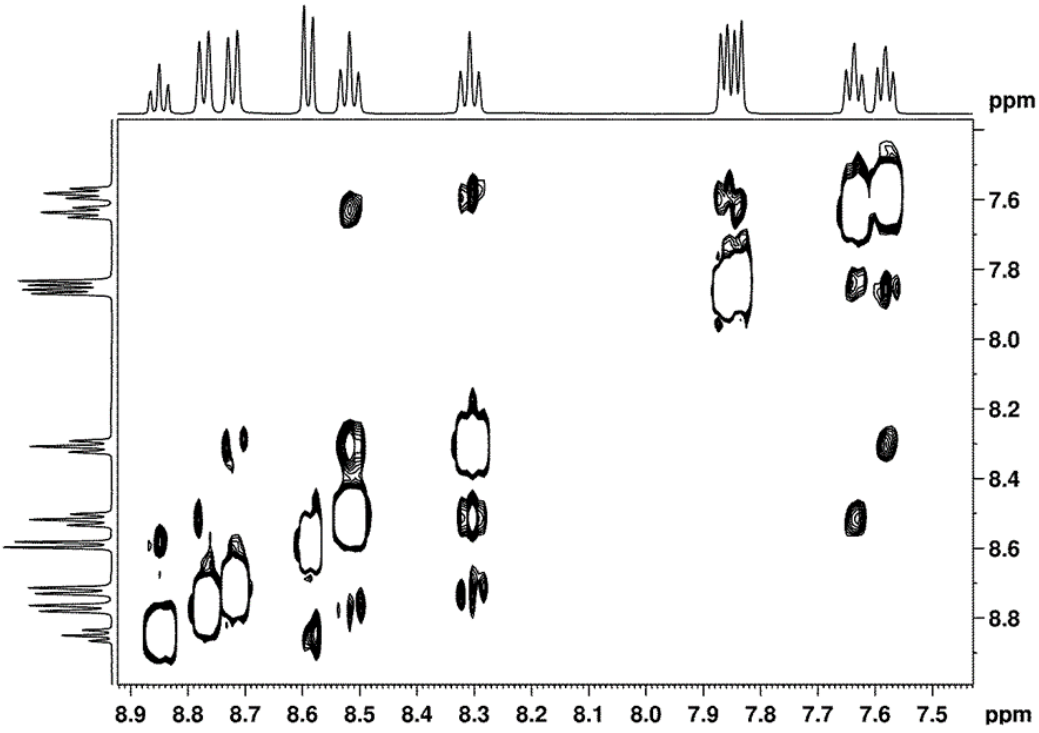
ppm
7.6
7.8
8.0
8.2
8.4
8.6
8.8
8.9 8.8 8.7 8.6 8.5 8.4 8.3 8.2 8.1 8.0 7.9 7.8 7.7 7.6 7.5 ppm

c)

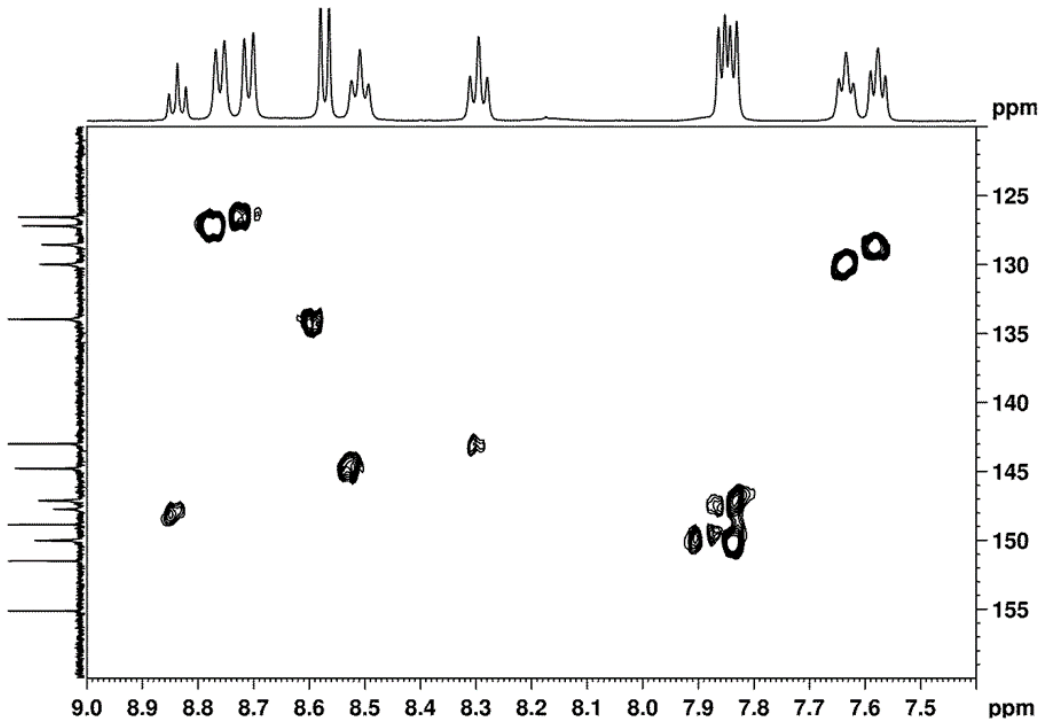
ppm
125
130
135
140
145
150
155
9.0 8.9 8.8 8.7 8.6 8.5 8.4 8.3 8.2 8.1 8.0 7.9 7.8 7.7 7.6 7.5
ppm

d)

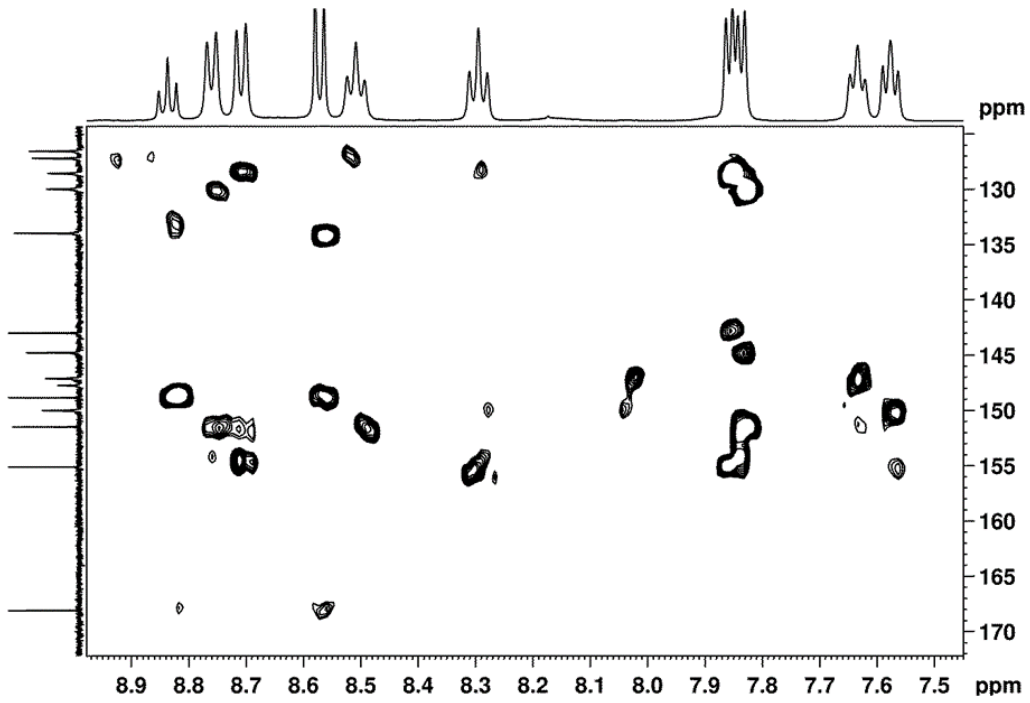
ppm
130
135
140
145
150
155
160
165
170
8.9 8.8 8.7 8.6 8.5 8.4 8.3 8.2 8.1 8.0 7.9 7.8 7.7 7.6 7.5
ppm

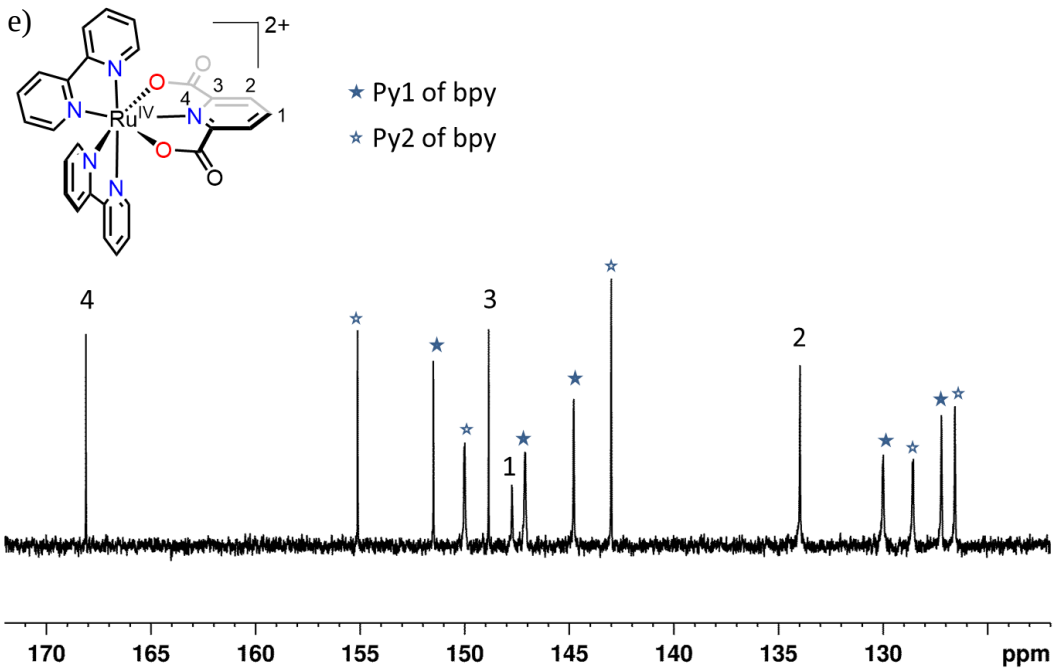

Figure S6. NMR data collected with a 500 MHz spectrometer at 298 K in $[d_2]$-D_2O of complex $[Ru^{IV}(pdc\text{-}\kappa^3\text{-}N^1O^2)(bpy)_2]^{2+}$, $\mathbf{2}^{IV}$, prepared by adding 2 equivalents of Ce(IV) in pD 1 to a solution of $[Ru^{II}(pdc\text{-}\kappa^2\text{-}N^1O^1)(bpy)_2]$, $\mathbf{2}^{II}$ in $[d_2]$-D_2O: a) COSY; b) NOESY; c) HSQC; d) HMBC and e) ^{13}C NMR (125 MHz, 298 K, $[d_2]$-D_2O).

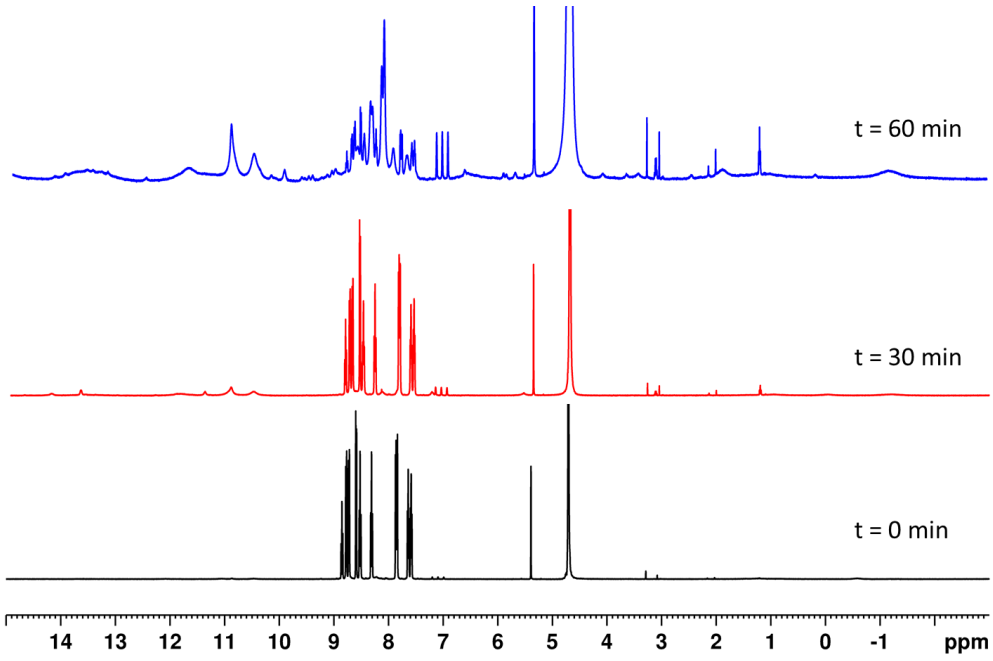

Figure S7. ^1H NMR spectra (500 MHz, 298 K, $[d_2]$-D_2O) of $[Ru^{IV}(pdc\text{-}\kappa^3\text{-}N^1O^2)(bpy)_2]^{2+}$,$\mathbf{2}^{IV}$ prepared by adding 2 equivalents of Ce^{IV} in pD 1 to a solution of $[Ru^{II}(pdc\text{-}\kappa^2\text{-}N^1O^1)(bpy)_2]$, $\mathbf{2}^{III}$ in $[d_2]$-D_2O. As prepared (black), after 30 min (red) and after 60 min (blue).

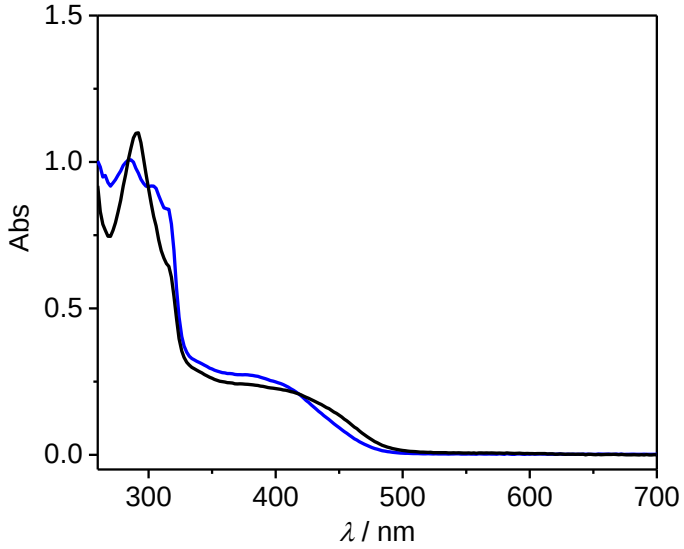

Figure S8. UV–vis spectra of [Ru^{III}(pdc-κ^3-N^1O^2)(bpy)Cl], **1**^{III} (blue) and [Ru^{II}(pdc-κ^2-N^1O^1)(bpy)(DMSO)Cl]$^-$ (black) in dimethyl sulfoxide. [Ru^{II}(pdc-κ^2-N^1O^1)(bpy)(DMSO)Cl]$^-$ was prepared from [Ru^{III}(pdc-κ^3-N^1O^2)(bpy)Cl], **1**^{III} by in situ reduction with excess of triethylamine.

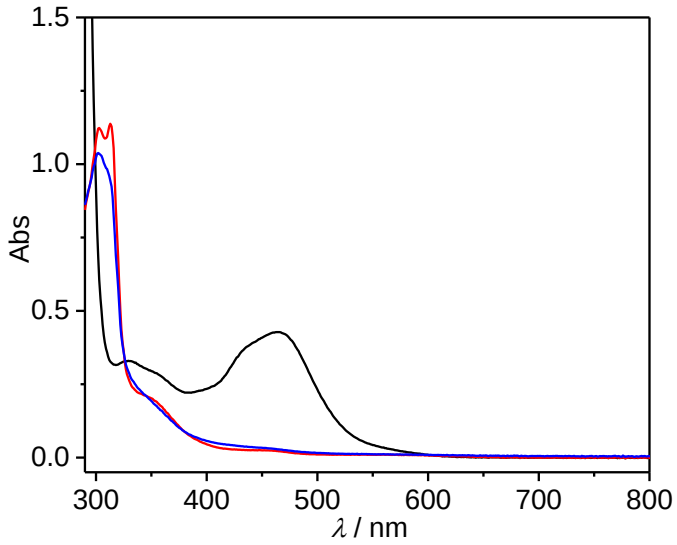

Figure S9. UV–vis spectra of [Ru^{II}(pdc-κ^2-N^1O^1)(bpy)$_2$], **2**^{II} (black), [Ru^{III}(pdc-κ^2-N^1O^1)(bpy)$_2$]$^+$, **2**^{III} (red), and [Ru^{IV}(pdc-κ^3-N^1O^2)(bpy)$_2$]$^{2+}$, **2**^{IV} (blue), in a 0.1 M triflic acid aqueous solution. [Ru^{III}(Hpdc-κ^2-N^1O^1)(bpy)$_2$]$^{2+}$, **2**^{III} and [Ru^{IV}(pdc-κ^3-N^1O^2)(bpy)$_2$]$^{2+}$, **2**^{IV} were prepared *in situ* by adding 1 or 2 equivalents of Ce^{IV} to a 0.2 mM solution of [Ru^{II}(pdc-κ^2-N^1O^1)(bpy)$_2$], **2**^{II} respectively.

a)

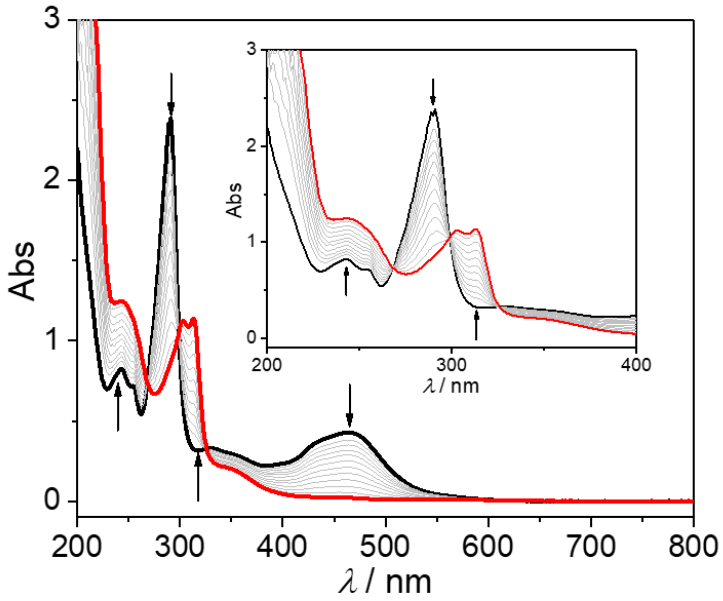

b)

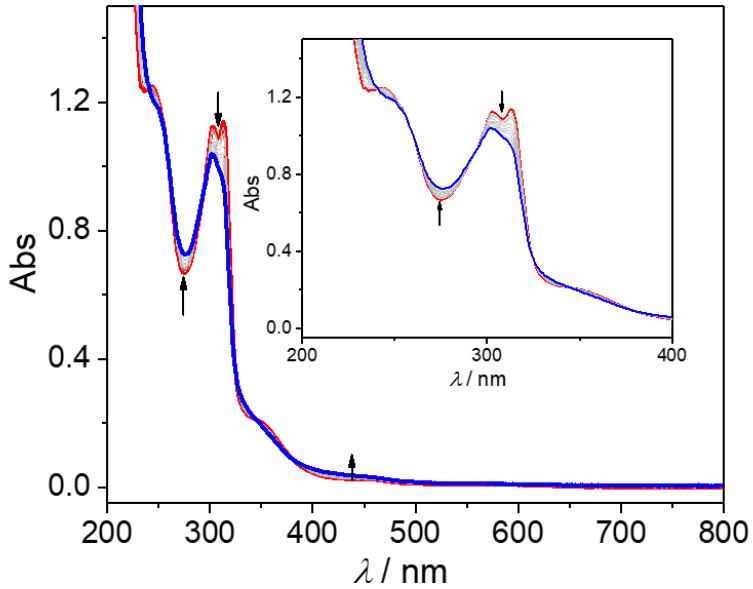

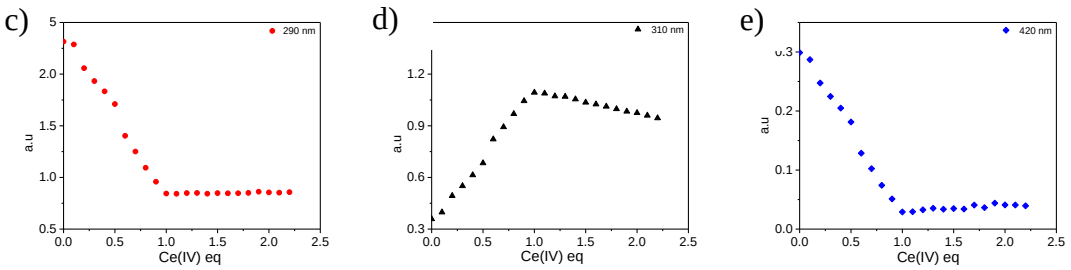

Figure S10: Spectrophotometric redox titration of [Ru^{II}(pdc-κ^2-N^{1}O^1)(bpy)$_2$], **2**^{II} at pH = 1.0 by adding cerium(IV) ammonium nitrate (10 μL, 6 mM). a): UV-vis spectra of [Ru^{II}(pdc-κ^2-N^{1}O^1)(bpy)$_2$], **2**^{II} (solid black line) and successive additions of 0.1 eq of Ce^{IV} (grey solid lines). b): UV-vis spectra of one-electron oxidized derivative [Ru^{III}(Hpdc-κ^2-N^{1}O^1)(bpy)$_2$]$^{2+}$, **2**^{IV} (red solid line), and successive additions of 0.1 eq. of Ce^{IV} (grey solid lines). Plot of absorbance versus equivalents of Ce^{IV} added at selected wavelengths: c) 290 nm, d) 310 nm and e) 420 nm.

a)

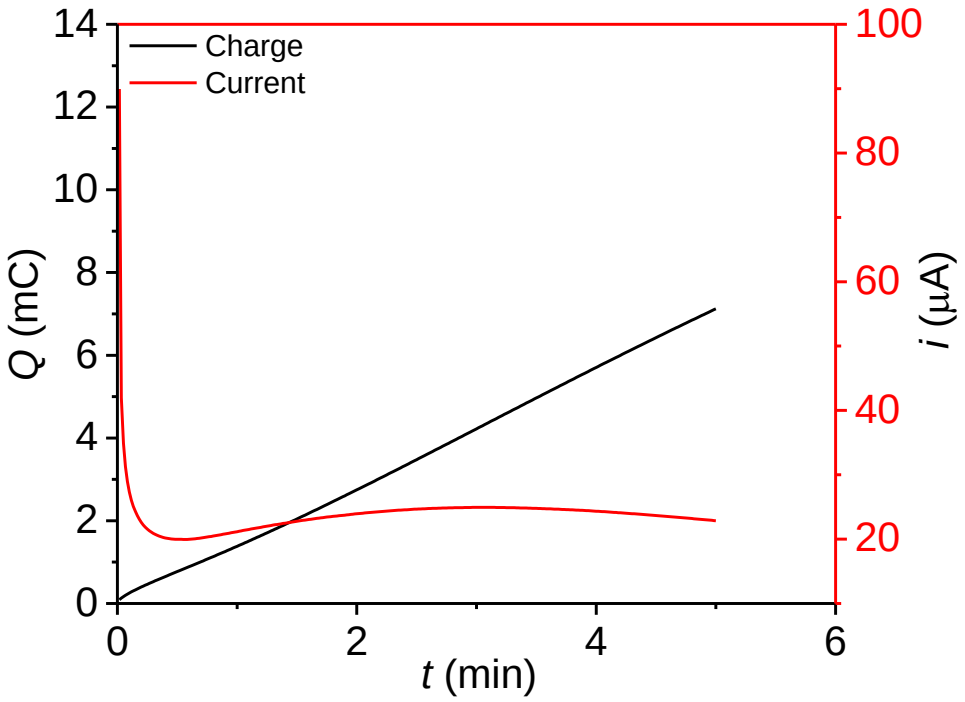
Charge
Current
Q (mC)
i (μA)
t (min)
0
2
4
6
8
10
12
14
20
40
60
80
100

b)

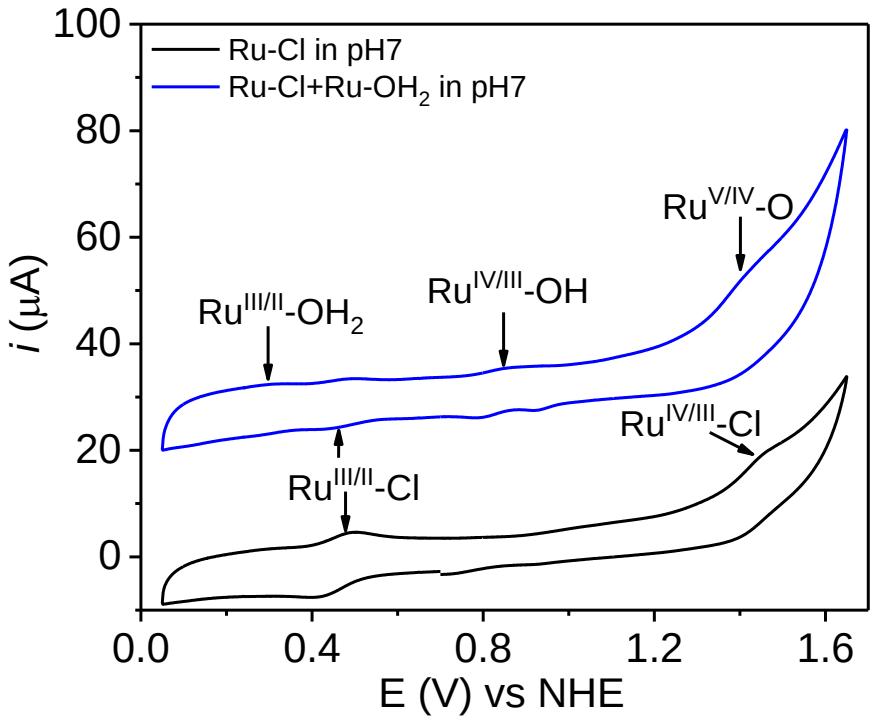
Ru-Cl in pH7
Ru-Cl+Ru-OH2 in pH7
i (μA)
E (V) vs NHE
RuV/IV-O
RuIV/III-OH
RuIII/II-OH2
RuIV/III-Cl
RuIII/II-Cl
0.0
0.4
0.8
1.2
1.6
0
20
40
60
80
100

c)

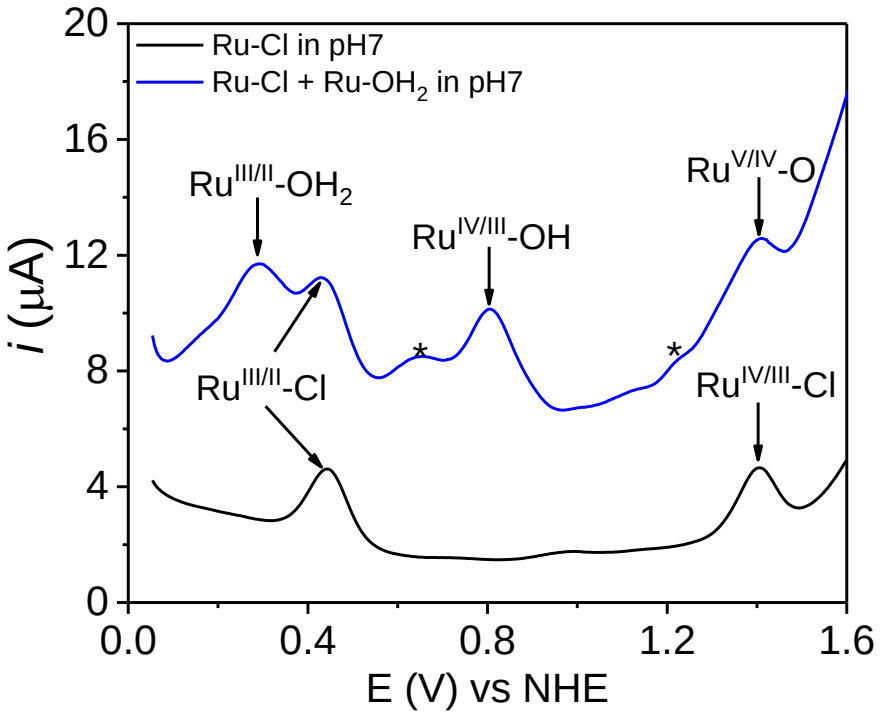

Figure S11. a) Bulk electrolysis of 2 mL of a pH 7 phosphate buffer solution of 1 mM of [Ru^{III}(pdc-κ^3-N^1O^2)(bpy)Cl], $\mathbf{1}^{III}$ at E_{app} = 1.6 V for 5 min (7.2 mC; 0.037 mols of e^-/mol of $\mathbf{1}^{III}$).

b) CV of [Ru^{III}(pdc-κ^3-N^1O^2)(bpy)Cl], $\mathbf{1}^{III}$, in pH 7 phosphate buffer: fresh complex solution (black) and after 5 min bulk at 1.6 V, mixture of Ru-Cl and Ru-OH_2 (blue).

c) DPV in pH 7 phosphate buffer: fresh complex solution (black) and after 5 min bulk electrolysis at 1.6 V, mixture of Ru-Cl and Ru-OH_2 (blue). For both CV and Bulk electrolysis experiment, WE: Glassy carbon disk, CE: Pt disk, RE: Hg/Hg_2SO_4 * Unidentified species.

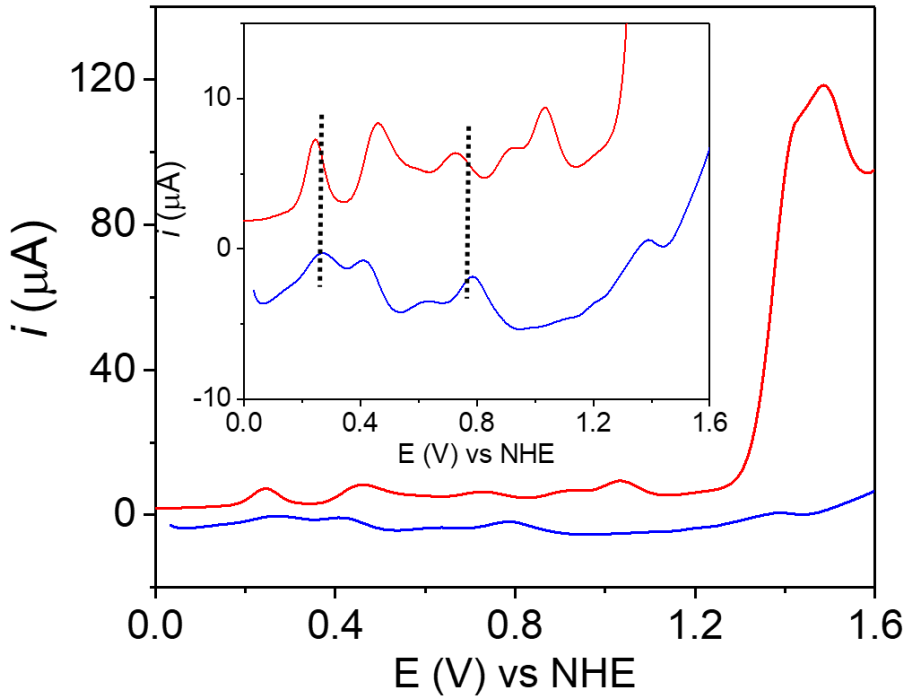

Figure S12. Differential pulse voltammetry of [Ru^{II}(pdc-κ^2-N^1O^1)$(bpy)_2$] in pH 7 after bulk electrolysis experiment at E_{app} = 1.45 V for 2 h (red) and differential pulse voltammetry of [Ru^{III}(pdc-κ^3-N^1O^2)bpy(Cl)] in pH 7 after bulk electrolysis experiment at E_{app} = 1.6 V for 5 min (blue).

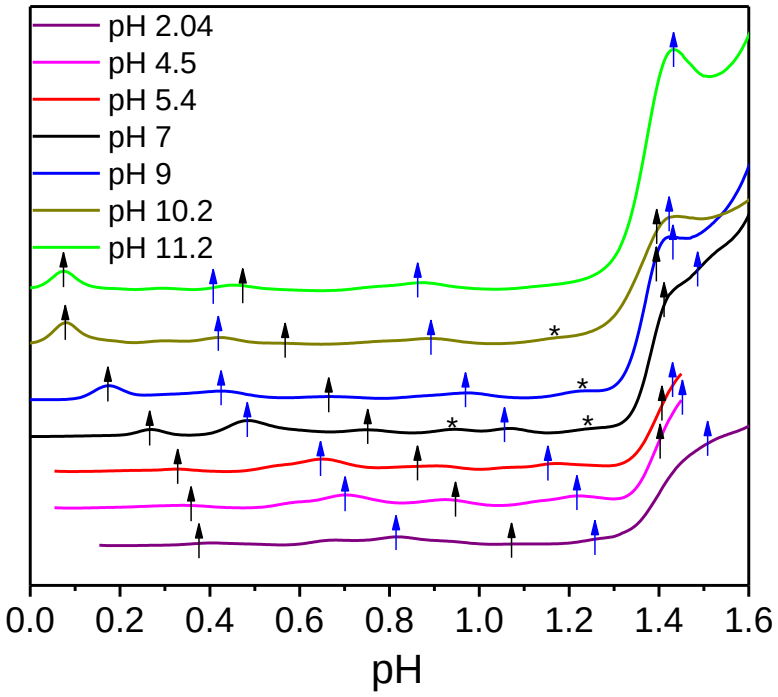

Figure S13. DPVs after bulk electrolysis experiments of a solution of [Ru^{II}(pdc-κ^2-N^1O^1)$(bpy)_2$], **2^{II}** in different pH phosphate buffers solution; pH 2.04 (purple) pH 4.5 (magenta), pH 5.4 (red), pH 7.0 (black), pH 9.0 (blue), pH 10.2 (dark yellow) and pH 11.2 (green). Redox potential values for pourbaix diagram of species A were shown with black arrows and species B with blue arrows. * starting material and unidentified species.

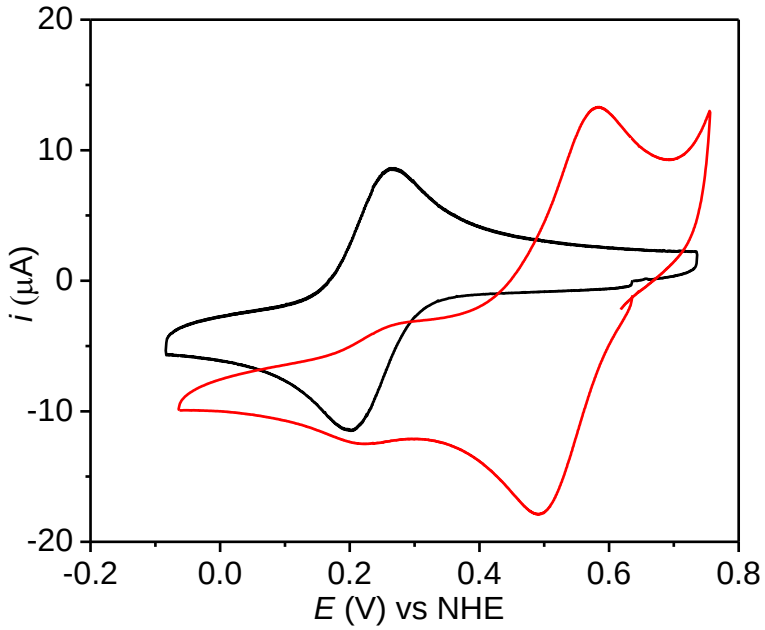

Figure S14. CV in acetone-0.1 M [(*n*-Bu)$_4$N][PF$_6$] of [Ru^{III}(pdc-κ^3-N^{1}O^2)(bpy)Cl] (black) and [Ru^{III}(pdc-κ^3-N^{1}O^2)(bpy)(OH$_2$)]$^+$ (red).

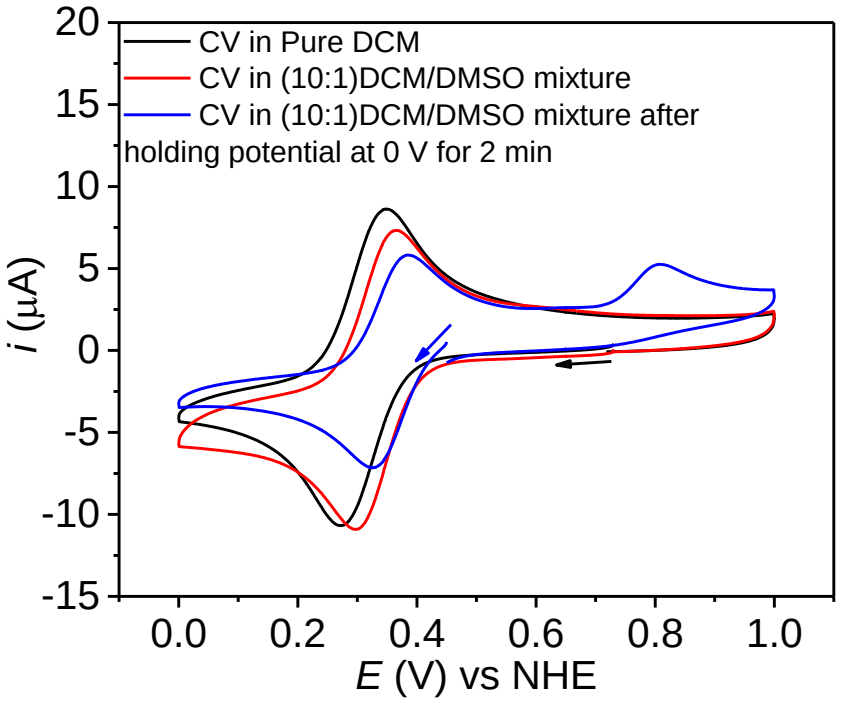

FigureS15: Cyclic voltammetry experiments of a 1 mM solution of [Ru^{III}(pdc-κ^3-N^{1}O^2)(bpy)Cl], **1^{III}** in dichloromethane-0.1 M [(*n*-Bu)$_4$N][PF$_6$]; pure DCM (black), DCM/DMSO(10:1) mixture (red), c) DCM/DMSO(10:1) mixture after bulk electrolysis at E_{app} = 0 V for 2 min (blue). WE: glassy carbon disk, CE: Pt disk, RE: Hg/Hg$_2$SO$_4$.

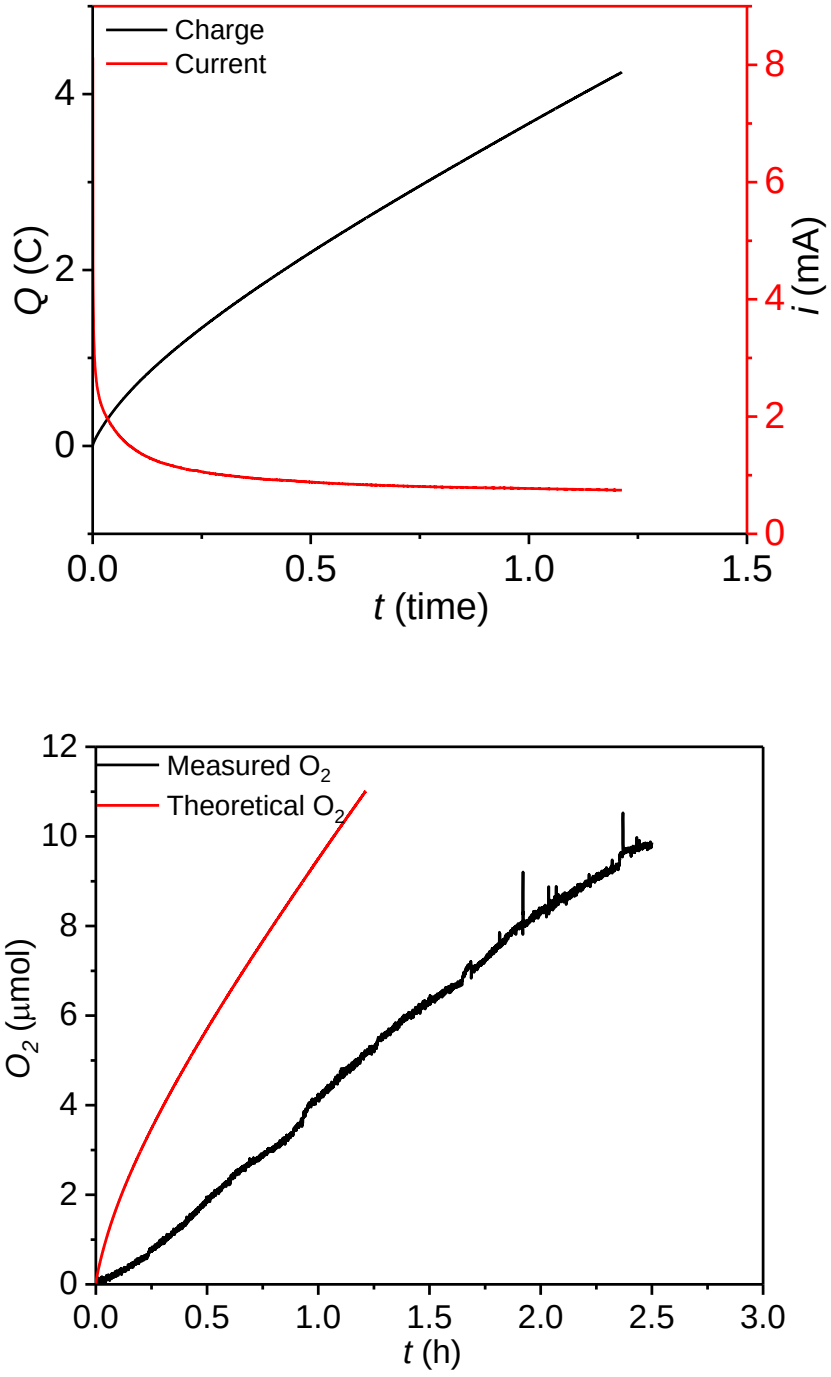

Figure S16: Bulk electrolysis of a 3 mL solution of [Ru^{II}(pdc-κ^2-N^{1}O^1)(bpy)$_2$], **2**^{II} (1 mM) at pH = 7.0 phbf at E_{app} = 1.45 V *vs.* NHE (4.25 C; 15 mols of e^-/mol of **2**^{II}). A glassy carbon rod was used as working electrode, a Pt grid as counter electrode and Ag/AgCl (sat KCl) as a reference electrode. Top, *I* and *Q vs. t* plot. Bottom, oxygen evolution *vs.* time monitored with a Clark electrode (black line) and the theoretical amount of oxygen obtained assuming 100 % Faradaic efficiency from the measured current density (red solid line). The E_{app} was stopped at 1.2 h, but oxygen evolution continued till approx. 2.3 h due to large number of bubbles trapped in the working electrode. The Faradaic efficiency turned out to be 90%.

Chapter 5

Linear coordination polymers with general formula {[Ru(tda)(4,4-bpy)]$_n$(4,4-bpy)} using 4,4'-bypridine as bridging ligand are synthesized and characterized. These materials show a unique anchoring strategy on multiwall carbon nanotubes via several CH-π interactions. The molecular hybrid materials are very active and rugged electroanodes for water oxidation reaching extremely high current densities up to 240 mA/cm^2 at 1.45 V in pH 7 and are comparable to commercial electrolyzers with much less catalyst loading.

Chapter 5

5. New Functional Coordination Oligomers Strongly Attached to MWCNT via Multiple CH-π Interactions as Powerful Molecular Electroanodes for Water Oxidation Catalysis

Md Asmaul Hoque[1,2], Marcos Gil-Sepulcre[1], Adiran de Aguirre[1], Hans Elemans[3], Dooshaye Moonshiram[5], Roc Matheu[1], Carolina Gimbert-Suriñach[1], Feliu Maseras[1,4] and Antoni Llobet*[1,4]

[1]*Institute of Chemical Research of Catalonia (ICIQ), Avinguda Països Catalans 16, 43007 Tarragona, Spain*

[2]*Departament de Química Física i Inorganica, Universitat Rovira i Virgili, Campus Sescelades, C/Marcel·lí Domingo, s/n, 43007 Tarragona, Spain*

[3]*Institute for Molecules and Materials Radboud University, Heyendaalseweg 135 Nijmegen, 6525AJ, Netherlands*

[4]*Departament de Química, Universitat Autonoma de Barcelona, 08193 Cerdanyola del Valles, Barcelona, Spain*

[5]*Instituto Madrileño de Estudios Avanzados en Nanociencia (IMDEA-Nanociencia), Calle Faraday, 9, 28049 Madrid, Spain*

V

Contributions

Md Asmaul Hoque synthesized and characterized all the complexes and performed the electrochemical, spectroscopic analysis together with the catalytic tests and prepared the manuscript.

Chapter 5

Abstract

Linear coordination polymers with different chain length based on the repetitive unit [Ru(tda)(4,4'-bpy)] have been developed where tda^{2-} is the pentadentate equatorial ligand [2,2':6',2''-terpyridine]-6,6''-dicarboxylato and 4,4'-bpy is the linear bridging ligand 4,4'-bipyridine. These coordination polymers of general formula $\{[Ru(tda)(4,4'\text{-}bpy)]_n(4,4'\text{-}bpy\}$ (n = 1-15; **n**) have been characterized by NMR spectroscopy, electrochemical and electron microscopy techniques, and further complemented with DFT calculations. These new coordination polymers have a strong affinity for graphitic surfaces in general and are readily adsorbed into multiwall carbon nanotubes (MWCNT) in particular, generating very stable hybrid molecular materials labeled as **n@CNT** that are subsequently deposited onto glassy carbon electrodes, **n@CNT@GC**. The strong affinity displayed by **n** to graphitic surfaces is associated with the formation of multiple concerted aromatic C-H (tda)-π interactions (4 per each repetitive unit) with the graphitic surface that provide for an increased stabilization as the number of units increase due largely to the entropic factor. They also provide for an additional stabilization factor due to the reversible formation and cleavage of CH-π interactions that for a monomer $[Ru(tda)(4,4'\text{-}bpy)_2]$, **1** would represent a complete lose of material from the surface. In basic solutions under an applied potential of 1.25 V *vs*. NHE, an aquo ligand can access the first coordination sphere of the Ru center generating **n-H_2O@CNT@GC**. The Ru-aquo derivatives behave as electroanodes that catalyze the water oxidation to dioxygen reaction at pH 7, reaching unprecedented current densities in the range of 0.3 A/cm^2 at 1.45 V *vs.* NHE. Further bulk electrolysis experiments sustain current densities of 30 mA/cm^2 for 12 h, which implies more than 199121 turnovers (TONs) without loss of activity and with Faradic efficiencies close to 100%.

Chapter 5

Graphical Abstract

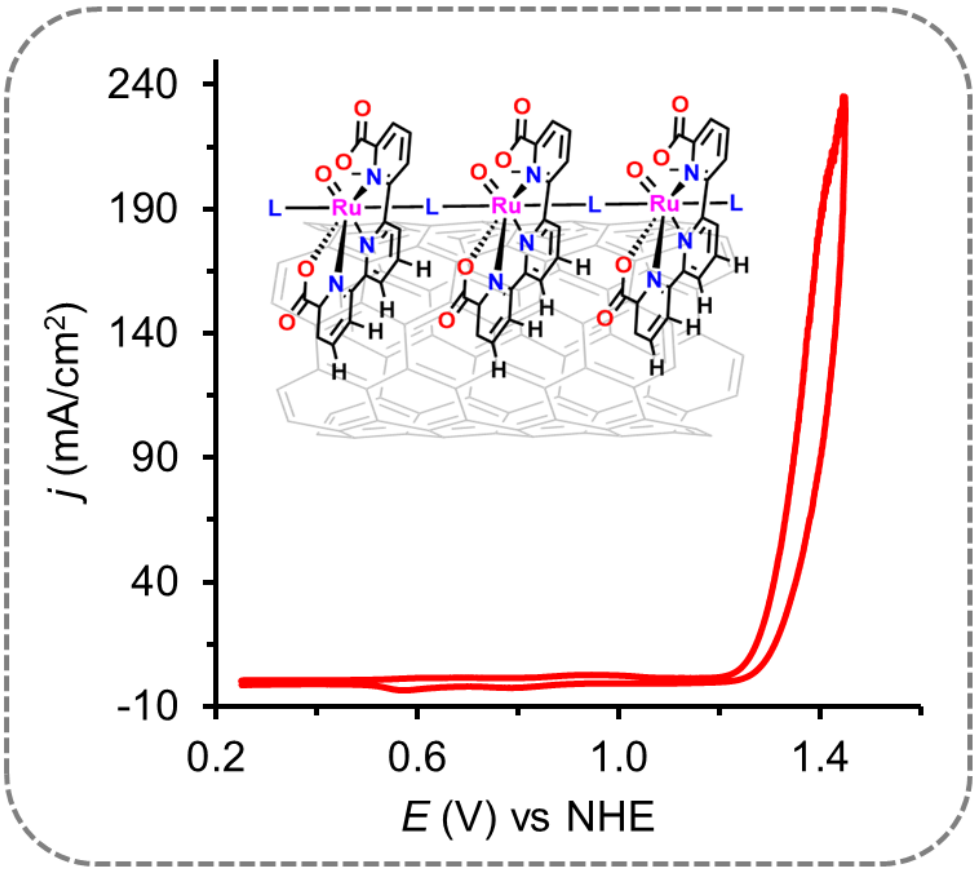

Keywords: Ruthenium, Linear coordination polymer, CH-π interaction, Electroanode, Water oxidation

Chapter 5

5. 1. Introduction

Molecular water oxidation catalysts (WOCs) have experienced a large development over the last decades[1-4] even beating nature in terms of turnover frequency (TOF).[5,6] Thanks to the capacity to tailor not only the first coordination sphere of the metal center but also the second coordination via supramolecular effects or intramolecular H-bonding and acid-base properties. From device objective perspective, the generation of molecular solid electroanodes and electrocathodes based on molecular complexes anchored into solid surfaces has received much less attention. However, a few examples exist that show all sorts of behaviors when compared to their homogeneous counterparts.[7-16]

Among the key parameters to predict and understand the performance of a molecular catalyst anchored on a conductive surface are the mechanism of O-O[17] bond formation and the functionality that links the catalyst to the surface.[18] One of the most successful examples in terms of turnover numbers (TONs) and robustness is based on the mononuclear complexes [Ru(O)(tda)(pyp)$_2$], (**1-O-pyp)** or [Ru(O)(tda)(pypA)$_2$], (**1-O-pypA)** that are capable of achieving more than a million TONs without apparent deactivation reactions associated (tda = [2,2':6',2''-terpyridine]-6,6''-dicarboxylato and pyp is 4-(pyren-1-yl)pyridine and pypA is 4-(pyren-1-yl)-N-(pyridin-4-ylmethyl)butanamide).[19] With molecular anodes however modest current densities have been achieved in the range of 10 mA/cm^2 at pH 7 with an overpotential of about 400 mV at the foot of the catalytic wave.[19] The limiting factor to improve absolute current densities is the small amount of catalyst that can be deposited at the surface of the electrode.

On the other hand, water oxidation electroanodes based on oxides as WOCs can achieve current densities in the range of 0.2-1 A/cm^2,[20-25] that is the typical range of current densities operating in commercial electrolyzers.[26,27] This large current density is achieved by depositing a large amount of the catalyst oxide on top of electrode surface although only around 1-0.1% of the oxide deposited ends up being active, depending on the deposition methodology.[28,29] Furthermore, only a limited number of oxides are capable of performing decently at pH 7 and the TOF are in general lower than those obtained with molecular catalysts.[30,31] Thus giving the benefits of the molecular catalysts with regard to oxides in terms of not only synthetic versatility but also in terms of TOF we seek to discover molecular catalysts that could be vastly attached to electrode surfaces in a robust manner and that could potentially deliver large current densities.

Chapter 5

Here on we report a new functional coordination polymer that strongly and massively adsorbs into graphitic surfaces such as multiwall carbon nanotubes (MWCNT), via aromatic catalyst-surface CH-π interactions. This type of anchoring has never been described previously for molecular catalyst. The resulting molecular material behaves as a rugged and powerful electroanode for the water oxidation reaction achieving unprecedented current densities in the range of 0.3 A/cm^2.

V

5. 2. Results and Discussion

5. 2. 1. Synthesis of Coordination Polymers Based on the Ru-tda Core

Reaction of 1 eq. of [Ru(tda)(DMSO)(H_2O)], with 1.5 eq. of the bridging ligand 4,4'-bypridine (4,4'-bpy) in MeOH:Water (1:1) generates a range of neutral oligomers of general formula {[Ru(tda)(4,4-bpy)]$_n$(4,4-bpy} ranging from n = 1-4, as indicated in Scheme 1. From now on we will use the **n** value as the label for the corresponding oligomer/polymer. The oligomer with n=4, **4**, is not soluble in the reaction conditions and precipitates out of the solution. The oligomers **1-3** are soluble and are separated via column chromatography, which allows to obtain pure samples of **1** and **2**. We could not obtain pure samples of complex **3** possibly due to the low amount of this complex generated under the present reaction conditions. The 1:1.5 reaction of [Ru(tda)(DMSO)(H_2O)] and 4,4'-bpy in TFE at reflux for 3 days generates the oligomer **5** whereas the 1:1 reaction of [Ru(tda)(DMSO)(H_2O)] and 4,4'-bpy in TFE generates a 1D linear polymer **15**, with 15 units.

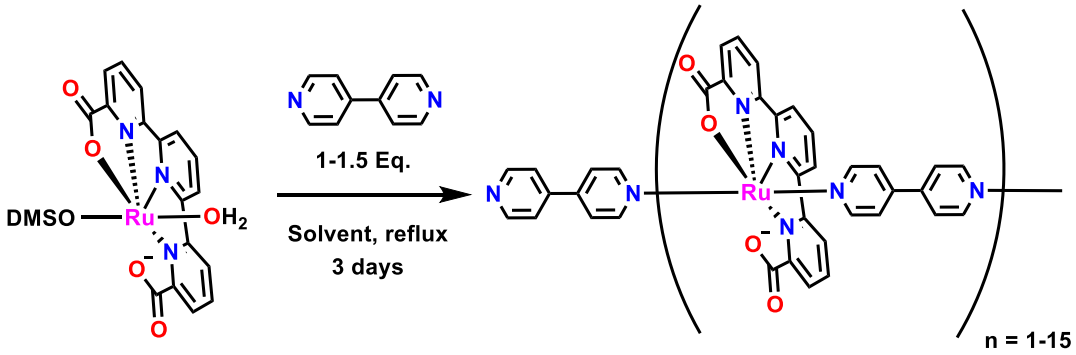

Scheme 1. Synthetic strategy for the preparation of {[Ru(tda)(4,4'-bpy)]$_n$(4,4'-bpy)} oligomers.

The characterization of these oligomers and the 1D polymer were carried out by elemental analysis, (Experimental section) mass spectrometry (Figure S10-S11) UV-vis spectroscopy (Figure S12), powder XRD (Figure S13) and NMR (Figure S2-S7). ^{1}H-NMR spectroscopy is especially useful because it not only allows to assign all resonances that appear in the spectra but in addition, the relative integration of key protons, allows to obtain the number of repeating units [Ru(tda)(4,4-bpy)]$_n$, as can be observed in Figure 1. Furthermore, DOSY experiments reflect the increasing volume of the polymer as the number of units grow (see SI Figure S8-S9). However, it does not display a linear relationship because the available equations for these experiments assume a spherical shape of the molecule while the Ru polymers described here possess a cylindrical shape.

Chapter 5

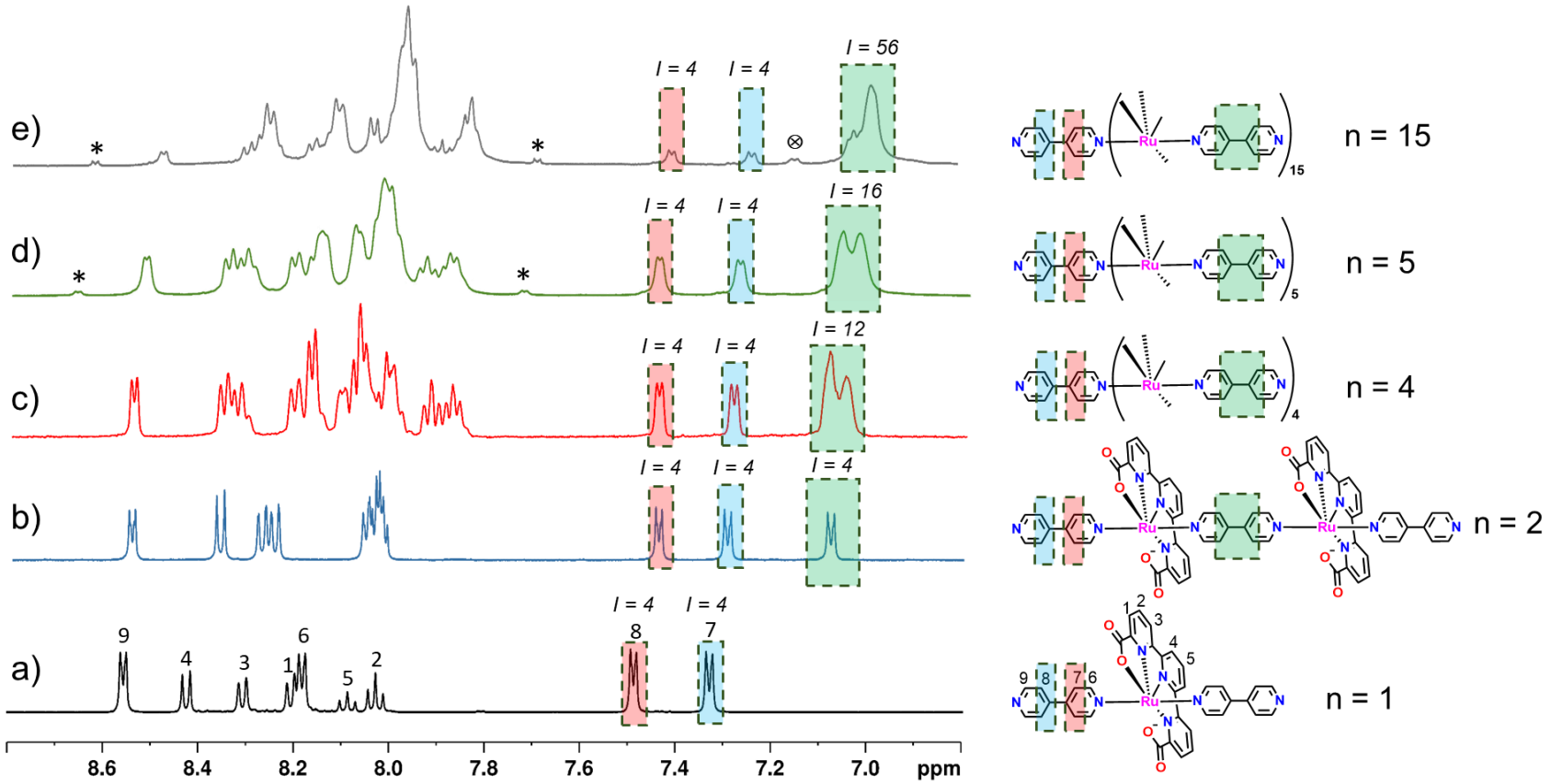

Figure 1. Left, ^{1}H NMR spectra (500 MHz, 298 K, [d_2]-DCM/[d_3]-TFE (4:1)) for {[Ru(tda)(4,4'-bpy)]$_n$(4,4'-bpy)} oligomers. Right, drawing of the oligomers. The color shades relate to the assignment of key protons and their resonances. * indicates free 4,4'-bpy resonances and ⊗ indicates polymer that terminates with the DMSO ligand.

5. 2. 2. Anchoring on Graphitic Surfaces via Aromatic CH-π Interaction

One of the most striking properties of this new family of coordination complexes is their capacity to strongly attach to graphitic surfaces in sharp contrast with their monomeric counterpart, **1** that does not adsorb.

The addition of a concentrated solution of coordination polymers, **5** (See SI and Figure S1) or **15** dissolved in TFE to a solution of THF containing dispersed MWCNT, results in the immediate discoloration of the final mixture, indicating the adsorption of **5** or **15**, onto the MWCNT. These materials are labeled **5@CNT** and **15@CNT** respectively. Kinetics of polymer desorption (See Figure S14) from the electrode clearly indicate a stronger affinity for polymer containing a larger number of units. This together with the absence of affinity of the monomer, **1-py**, or $[Ru(tda)(py)_2]$,[32] (py represents the monodentate pyridine ligand) suggests a synergic effect of the strength of the interaction of the polymers and MWCNT as the number of repeating units increases that can be associate with an entropic effect that will be discussed later on.

The interaction of MWCNT and the polymers were further studied by scanning tunneling microscopy (STM) in collaboration with Prof. Hans Elemans. Figure 2 shows the image obtained in which the white spots are associated with the Ru-tda fragment of the polymer. Each of these fragments is separated by 10.9 Å which is exactly the distance between two Ru centers linked by the 4,4'-bpy bridging ligands. The latter is not observed in the microscopy image because the electron density associated with it, is relatively small. It is also interesting to notice that the oligomers align parallel to one another and the distance between each polymer is about 12 Å, see Figure 2 (right). All these data points out that the site of interaction of the polymers with the surface is the tda ligand that will be situated perpendicular to the graphitic surface. Thus the bonding interaction will occur with the H atoms of the aromatic central pyridyl ring of tda that will interact with the π-system of the MWCNT in a CH-π type of interaction.[33,34]

To further understand these hybrid materials, Density Functional Theory/Molecular Mechanics (DFT/MM) calculations at the ONIOM (B97D:MM3:UFF) level were carried out in collaboration with Prof. F. Maseras to analyze the interaction of the oligomer with the graphitic surface (see Computational Details/Supporting Information for partition and further details). A 10-unit $[Ru(tda)(4,4\text{-bpy})]_{10}$ oligomer was placed on a monolayer graphite shield composed of multiple carbon atoms, and the structure was optimized in vacuum. The overall

arrangement, shown in Figure 3 is in good agreement with the microscopy image, the Ru centers being in a mostly linear arrangement, and is separated by 11.4 Å (experiment 11.1 Å).

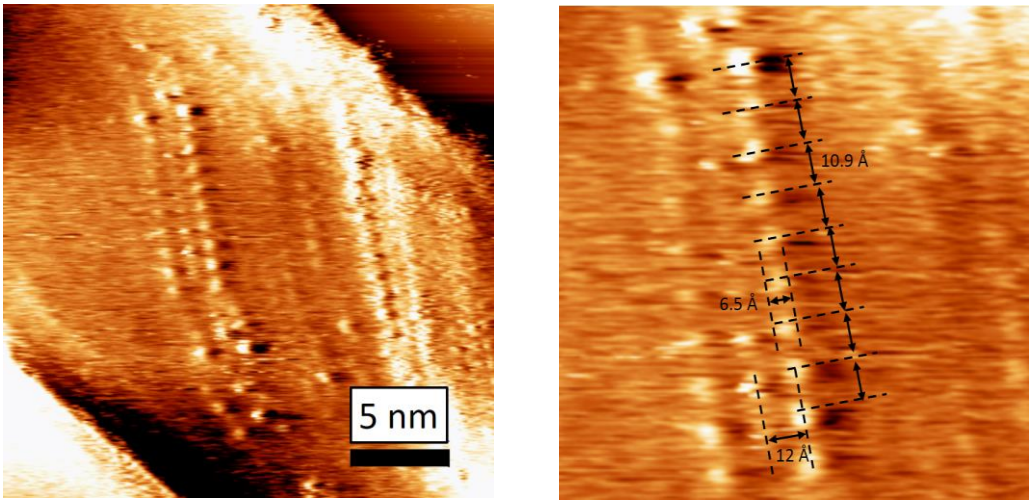

Figure 2. Scanning tunneling microscopic image (STM) of **15** on pyrolytic graphite (HOPG) surface, left) image full range, right) zoom.

The DFT/MM model in Figure 3 and Figure S27 demonstrates that the binding between oligomer and surface consists of aromatic CH-π interactions. Four CH groups in each Ru core interact with the surface, the shortest H...C distances being between 2.74 and 3.03 Å, and are within the expected range for C-H-π interaction.[33,34] The computed energetics are especially informative. The Gibbs energy of binding between oligomer and surface is 160 kcal/mol, which can be decomposed into a binding enthalpy of 180 kcal/mol and an entropic penalty of 20 kcal/mol. Binding enthalpy is in principle additive, thus we can assign a value of *ca* 18 kcal/mol per Ru unit. The entropic penalty is mostly associated with bringing two fragments (surface plus oligomer) together, and has only a minor dependence on the size of the oligomer. It follows that the interaction free energy of a monomeric complex with the surface would be approximately +2 kcal/mol (-18 plus 20 kcal/mol), thus non-binding. It is the large number of small binding interactions that makes feasible the strong attachment of the polymer onto the surface. We can estimate a relatively modest value of 4.5 kcal/mol per C-H π interaction, but there are 40 of them in our model. We admit that our calculations were carried out in vacuum, and the specific numbers would be modified if we carried much more demanding calculations in solvent, but we are convinced that the general observations would hold.

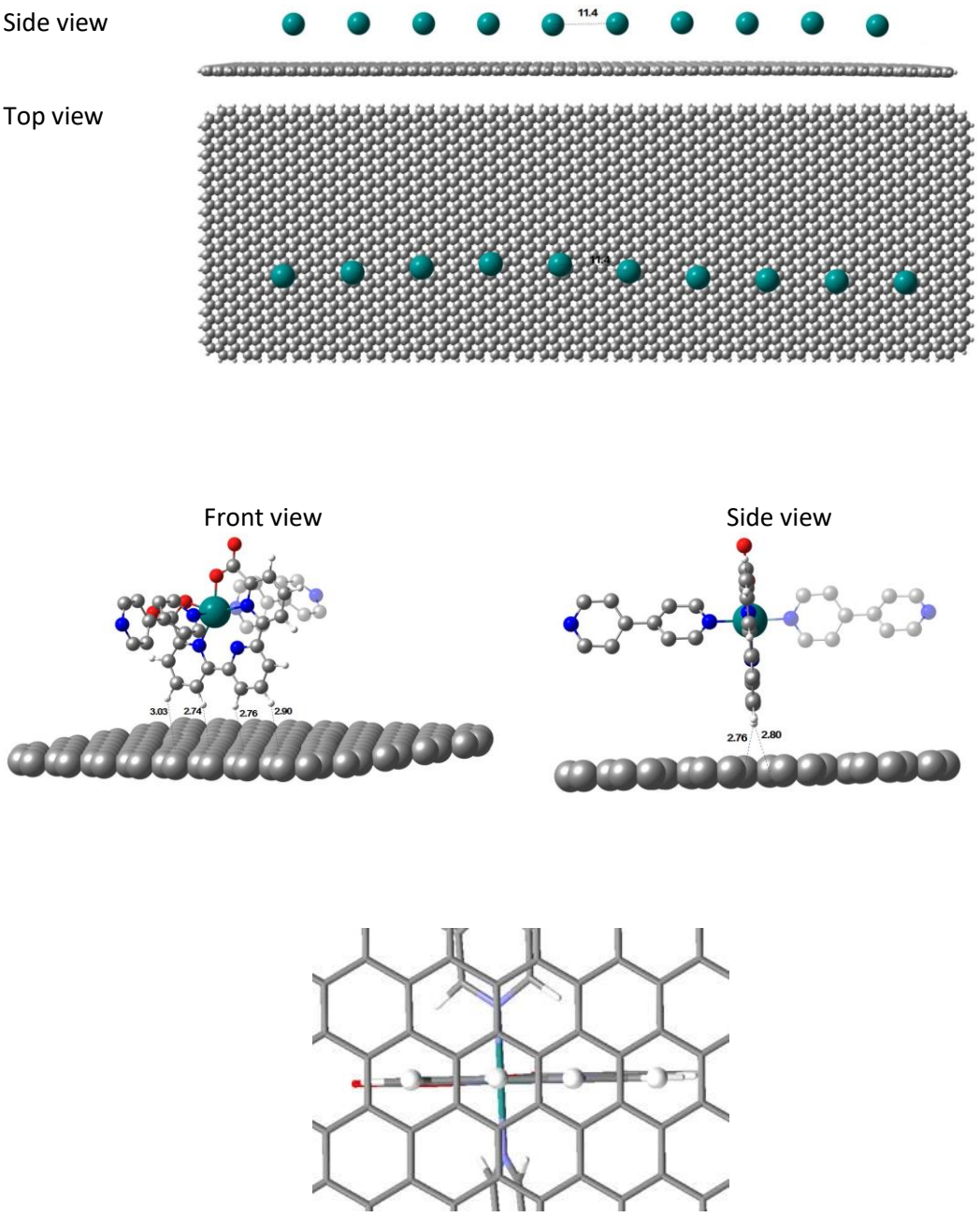

Figure 3. General view of the interaction of polymer **10** with a graphitic surface from different sides in DFT/MM model.

The access to a second pair of CH tda groups with the surface gives rise to a rocking type of polymeric movement that is synchronized with its immediate neighbor polymeric molecules via a carboxylato interactions as can be inferred from closeness of the polymeric units (12 Å) displayed in the microscopy image shown in Figure 2.

It is worth mentioning here that the high affinity of **15** for graphitic surfaces also allows to obtained large surface coverage as compared to other anchoring strategies. For instance, the surface coverage of **15@CNT** in terms of Ru centers per surfaces area, is about 2-5 times larger than in the cases of mononuclear Ru-tda complexes using pyrene as an anchoring functionality, such as [Ru(O)(tda)(pyp)$_2$], (**1-O-pyp)** or [Ru(O)(tda)(pypA)$_2$], (**1-O-pypA)**, because of a better surface coverage efficiency achieved by the polymeric complexes (Figure S23 and Table S2).[19] Further, when comparing to other mononuclear complexes using a phosphonate type of functionality attached to oxide surfaces, the new Ru polymers generate surface coverages that are about 10-100 times higher[35] depending on the oxides surface and thus manifest the convenience and effectiveness of the CH-π strategy described here (Table S2).

5. 2. 3. Electrochemical Properties and Catalysis

The [Ru(O)(tda)(py)$_2$], **1-O** complex is at present the best water oxidation catalyst in terms of TOF[32] in homogeneous phase and is actually about two orders of magnitude better than OEC-PSII (OEC-PSII stands for oxygen evolving complex in photosystem II). In addition, it follows at water nucleophilic attack (WNA) O-O bond formation mechanism and for these two reasons, it constitutes one of the best options for anchoring into surfaces to generate highly efficient electro- and photo-anodes. Indeed, the anchoring of **1-O-pypA** in MWCNT generates highly efficient electroanodes, **1-O-pypA@CNT**, for the water oxidation reaction as has been recently described.[19] Here the anchoring has been achieved via pyrene functionalization and even though it results in a very stable WO electroanode, the current densities obtained are in the 5-10 mA/cm^2 range and thus still far from the ones operating in commercial electrolyzers which are in the range of 0.2-1.0 A/cm^2.

The present polymers **n@CNT** thanks to its high affinity for graphitic surfaces are expected to generate unprecedented powerful electroanodes due to both, the enhancement of surface coverages and the enormously improved stability provided by the nature of the new anchoring interactions.

The electrochemical properties of the **n@CNT** were evaluated based on cyclic voltammetry (CV) and bulk electrolysis techniques. Figure 4 shows the CV of the **15@CNT** deposited at the surface of glassy carbon electrode via drop casting that is labelled as **15@CNT@GC**. See the supporting information for the protocols used here and for related electrochemical properties displayed by **5@CNT@GC** (Figure S15-S18). As can be seen in the Figure 4 two one electron redox process are observed at $E_{1/2}$ = 0.65 V (ΔE = 45 mV) and $E_{1/2}$ = 1.10 V (ΔE = 70 mV) due to the $Ru^{III/II}$ and $Ru^{IV/III}$ couples, respectively. The redox potentials obtained here are very similar to those obtained for the monomer **1** in homogenous solution at the same pH, and thus suggests that each individual Ru center of the polymer acts in a similar manner as in the discrete mononuclear complex. This is a consequence of the anchoring nature of the polymer at MWCNT, where each metal center has the same access to the surface and thus facilitates a synchronized transfer process to the electrode.

The **n@CNT** hybrid materials are used as precursors to generate the corresponding Ru-OH_2 complexes, that are labeled as **n-H_2O@CNT**, and that are actually the species that behaves as water oxidation catalysts.

To generate **15-H_2O@CNT@GC**, the precursor complex **15@CNT@CG** is exposed to 1.25 V applied potential for 1000 s in a pH = 12 solution. Afterwards, the hybrid electrode is rinsed with water and placed again in pH 7 solution (additional details of this protocol are described in the SI). Figure 4 shows the CV of **15-H_2O@CNT@GC**, where two new waves due the $Ru^{III/II}$ and $Ru^{IV/III}$ electron transfers at 0.60 and 0.90 V are observed. The initial waves due the precursor complex have totally disappeared and thus indicates a complete conversion from the precursor complex to the corresponding Ru-OH_2 species. This is in sharp contrast to the **1-O-pypA@CNT** homologue where the ratio of precursor *vs.* activated complex is at approximately 2:1.[19] The ratio of activated *vs*. precursor reflects the equilibrium that operates between the capacity of the dangling carboxylate to coordinate back to the metal center and ejection of the coordinated aquo group from the first coordination sphere of the metal center. This equilibrium is thus affected by the packing organization of the anchored polymers and the proximity of the Ru-aquo active site to the surface of the electrode.

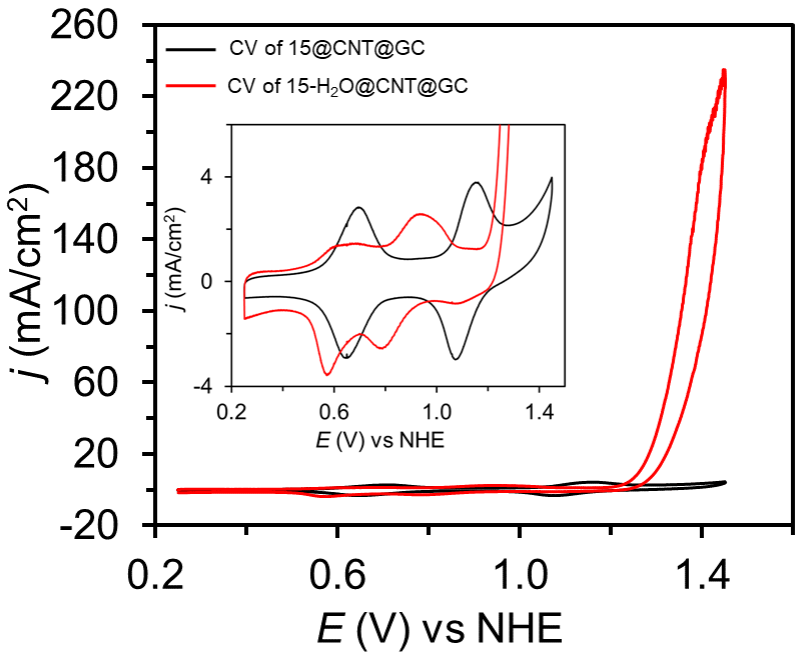

Figure 4. CV of 1**5@CNT@GC** (black line) and **15-H_2O@CNT@GC** (red line) with a surface coverage of 17.7 nmol·cm^{-2} in 1.0 M phosphate buffer (pH 7) at scan rate of 100 mV/s. Inset, enlargement of the non-catalytic redox waves.

The supramolecular interaction among neighboring polymer units through hydrogen bonding with water molecules can also influence the relative strength of interactions between the intramolecular carboxylate coordination and the Ru-aquo formation, and thus can also be responsible for the activity of **15-H_2O@CNT@GC** over the whole pH range 0-14 (Figure S24).

In sharp contrast its monomeric counterpart in homogeneous phase that is only active above pH 5.5.[32]

At high anodic potentials, a huge anodic current is observed that is due to the electrocatalytic oxidation of water to dioxygen whose onset is at 1.20 V and that reaches unprecedented current densities in the range of 240 mA/cm^2 at 1.45 V (Figure 4) for molecularly based electroanodes. The current density obtained here is about 20 times larger than the highest current densities reported for **1-O-pyp@CNT** and about two orders of magnitude larger than any other molecular catalyst anchored on an electrode surfaces (see Table S2).

Bulk electrolysis experiments at 1.45 V were carried out for **15-H_2O@CNT@GC,** with this electrode that sustained current densities of 32 mA/cm^2 for 12 hours with practically no decay (Figure S21) giving Faradaic efficiencies in the range of 99% (Figure S25) and thus highlighting the superb performance of these new hybrid anodes (Figure S19-S22). Similar experiments were carried with **5@CNT** drop casted into glassy carbon disk (GC_d), **5-H_2O@CNT@GC_p** showing comparable electrochemical behavior and stability as evidenced by CVs (Figure S15-S18).

5. 2. 4. Structural Characterization

Finally, X-ray absorption near edge structure (XANES) and Extended X-ray absorption fine structure (EXAFS) of the polymers and materials were performed in collaboration with Dr. D. Moonshiram at ALBA synchrotron and Advanced Photon Source (APS) to further spectroscopically characterize them both as a powder for **15** and attached to the surface of glassy carbon plate, **15@CNT@GC_p**. The trip to the synchrotron resulted in a mixture of 96% Ru^{III} and 4% Ru^{II} as was the case of **1-pypA@CNT** base on half-edge energies obtained from XANES.[19] The stability of the catalyst was also evaluated after a bulk electrolysis catalytic experiments generating **15-O@CNT@GC_p** at 1.45 V, that based on half-edge energies obtained from XANES turned out to be 59% Ru^{IV}=O and 41% Ru^{III}-OH.

Chapter 5

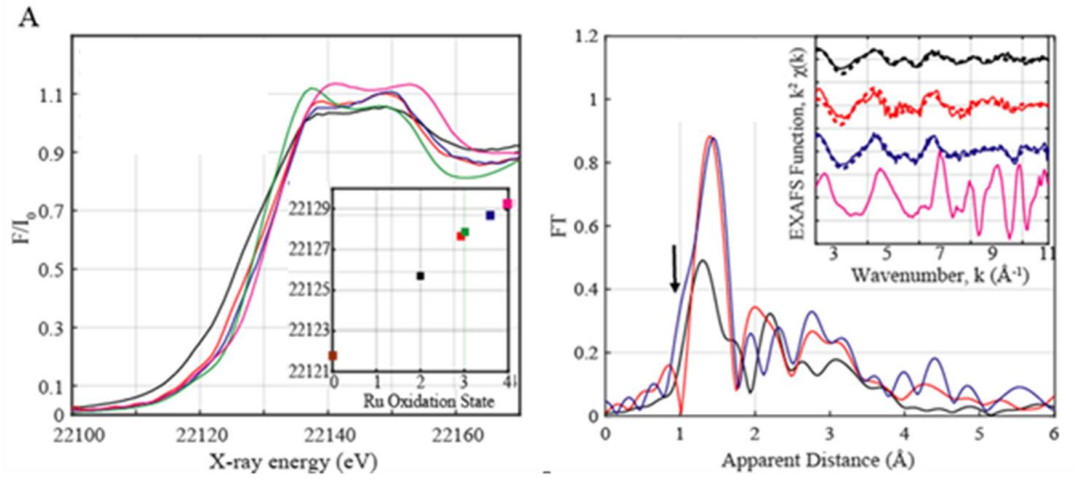

Figure 5. Left, normalized Ru K-edge XANES for **15** (black), **15@CNT@GC$_p$** (red), $[Ru^{III}(tda)(py)_2]^+$ (green), **15-O@CNT@GC$_p$** obtained after catalysis (blue; SEE SI for details), and RuO_2 (magenta). Inset, plot of half peak k-edge energy vs. oxidation state including Ru^0. Right, Fourier transforms of k^2-weighted Ru EXAFS. Inset, Back Fourier transformed experimental (solid lines) and fitted (dashed lines) Re[χ (k)] for Ru complexes together with RuO_2. Experimental spectra were calculated for *k* values of 2-11 $Å^{-1}$. Same color code as in left.

The parameters obtained by EXAFS (Figure 5 and Figure S26, Table S3-S5). The simulated EXAFS spectra for the complexes deposited in the GC_p before and after catalysis gave very good fits similar to that of the reference $[Ru(tda)(pypA)_2]^+$, (**1-pypA)** complex reported earlier.[19] It is worth mentioning the increase in amplitude of the first coordination sphere shown in Figure 4B associated with an increase in the Ru-N/O coordination number of the complexes after deposition and catalysis where oxidation state III and IV are reached and coordination number increase from the regular 6 at oxidation state II up to 6.5 and 7 for oxidation state III and IV respectively.[36]

Lastly, XAS spectroscopy unambiguously showed the absence of any traces of RuO_2 after catalysis as can be seen in the SI further supporting the molecular nature of the whole catalytic process.

5. 3. Conclusion

In conclusion, we have introduced for the first time functional coordination polymers with all catalytically active repetitive units. The judicious choice of solvent and relative ratios of complex and bridging ligand together with column chromatography allows obtaining pure samples of the polymer with the desired number of repetitive units, up to 15. They have shown a new and unique anchoring strategy using simultaneous and concurrent aromatic-CH-π interactions, extremely robust easy and convenient allowing higher surface coverage as compared to pyrene or phosphonates type of linkages. These new materials give extremely active electroanodes with giant current densities in the range of commercial electrolyzers but with two orders of magnitude less catalysts mass needed. Another interesting features of the material is that, the packing organization of the anchored polymers produces a carboxylate-craboxylate interaction with neighboring polymers that changes the relative K values of the reaction [Ru(OCarbox)-OH_2] -> [Ru-Ocarbox] + H_2O. As a consequence of this, now the Ru-tda type of polymer can be activated 100% to generate Ru-OH_2, as opposed to the initial monomer. Further, the polymer is now active at pH lower than 5.5, where the initial complex was not active. It thus constitutes an example of how the anchoring on the surface can strongly improve the homogeneous phase catalyst.

On the other hand, metal oxides as catalysts have also experienced a large improvement this time based on improvement of particle size and morphology.[37-41] Here we use a rational bottom up molecular approach for improvement. Transferring these concepts into first raw transition metals will be highly valuable for a practical point of view.

5. 4. Reference

(1) Blakemore, J. D.; Crabtree, R. H.; Brudvig, G. W. *Chem. Rev.* **2015**, *115*, 12974.
(2) Berardi, S.; Drouet, S.; Francas, L.; Gimbert-Suriñach, C.; Guttentag, M.; Richmond, C.; Stoll, T.; Llobet, A. *Chem. Soc. Rev.* **2014**, *43*, 7501.
(3) Garrido-Barros, P.; Gimbert-Suriñach, C.; Matheu, R.; Sala, X.; Llobet, A. *Chem. Soc. Rev.* **2017**, *46*, 6088.
(4) Matheu, R.; Garrido-Barros, P.; Gil-Sepulcre, M.; Ertem, M. Z.; Sala, X.; Gimbert-Suriñach, C.; Llobet, A. *Nat. Rev. Chem.* **2019**, *3*, 331.
(5) Duan, L.; Bozoglian, F.; Mandal, S.; Stewart, B.; Privalov, T.; Llobet, A.; Sun, L. *Nat. Chem.* **2012**, *4*, 418.
(6) Suga, M.; Akita, F.; Hirata, K.; Ueno, G.; Murakami, H.; Nakajima, Y.; Shimizu, T.; Yamashita, K.; Yamamoto, M.; Ago, H. *Nature* **2015**, *517*, 99.
(7) Francàs, L.; Richmond, C.; Garrido-Barros, P.; Planas, N.; Roeser, S.; Benet-Buchholz, J.; Escriche, L.; Sala, X.; Llobet, A. *Chem. Eur. J.* **2016**, *22*, 5261.
(8) Hyde, J. T.; Hanson, K.; Vannucci, A. K.; Lapides, A. M.; Alibabaei, L.; Norris, M. R.; Meyer, T. J.; Harrison, D. P. *ACS Appl. Mater. Interfaces.* **2015**, *7*, 9554.
(9) Wadsworth, B. L.; Beiler, A. M.; Khusnutdinova, D.; Jacob, S. I.; Moore, G. F. *ACS Catal.* **2016**, *6*, 8048.
(10) Chen, Z.; Concepcion, J. J.; Jurss, J. W.; Meyer, T. J. *J. Am. Chem. Soc.* **2009**, *131*, 15580.
(11) Ashford, D. L.; Gish, M. K.; Vannucci, A. K.; Brennaman, M. K.; Templeton, J. L.; Papanikolas, J. M.; Meyer, T. J. *Chem. Rev.* **2015**, *115*, 13006.
(12) Wu, L.; Eberhart, M.; Nayak, A.; Brennaman, M. K.; Shan, B.; Meyer, T. J. *J. Am. Chem. Soc.* **2018**, *140*, 15062.
(13) Kaminsky, C. J.; Wright, J.; Surendranath, Y. *ACS Catal.* **2019**, *9*, 3667.
(14) Jackson, M. N.; Oh, S.; Kaminsky, C. J.; Chu, S. B.; Zhang, G.; Miller, J. T.; Surendranath, Y. *J. Am. Chem. Soc.* **2018**, *140*, 1004.
(15) Oh, S.; Gallagher, J. R.; Miller, J. T.; Surendranath, Y. *J. Am. Chem. Soc.* **2016**, *138*, 1820.
(16) Blakemore, J. D.; Gupta, A.; Warren, J. J.; Brunschwig, B. S.; Gray, H. B. *J. Am. Chem. Soc.* **2013**, *135*, 18288.
(17) Sala, X.; Maji, S.; Bofill, R.; Garcia-Anton, J.; Escriche, L. s.; Llobet, A. *Acc. Chem. Res.* **2013**, *47*, 504.
(18) Garrido-Barros, P.; Matheu, R.; Gimbert-Suriñach, C.; Llobet, A. *Curr. Opin. Electrochem.* **2019**, DOI: 10.1016/j.coelec.2019.04.027.
(19) Creus, J.; Matheu, R.; Peñafiel, I.; Moonshiram, D.; Blondeau, P.; Benet-Buchholz, J.; García-Antón, J.; Sala, X.; Godard, C.; Llobet, A. *Angew. Chem. Int. Ed.* **2016**, *55*, 15382.
(20) McCrory, C. C.; Jung, S.; Peters, J. C.; Jaramillo, T. F. *J. Am. Chem. Soc.* **2013**, *135*, 16977.
(21) McCrory, C. C.; Jung, S.; Ferrer, I. M.; Chatman, S. M.; Peters, J. C.; Jaramillo, T. F. *J. Am. Chem. Soc.* **2015**, *137*, 4347.
(22) Smith, R. D.; Prévot, M. S.; Fagan, R. D.; Zhang, Z.; Sedach, P. A.; Siu, M. K. J.; Trudel, S.; Berlinguette, C. P. *Science* **2013**, *340*, 60.
(23) Merrill, M. D.; Dougherty, R. C. *J. Phys. Chem. C* **2008**, *112*, 3655.
(24) Smith, R. D.; Prévot, M. S.; Fagan, R. D.; Trudel, S.; Berlinguette, C. P. *J. Am. Chem. Soc.* **2013**, *135*, 11580.
(25) Salvatore, D.; Pena, B.; Dettelbach, K.; Berlinguette, C. *J. Mater. Chem. A* **2017**, *5*, 1575.
(26) Carmo, M.; Fritz, D. L.; Mergel, J.; Stolten, D. *Int. J. Hydrog. Energy* **2013**, *38*, 4901.
(27) Zeng, K.; Zhang, D. *Progress in Energy and Combustion Science* **2010**, *36*, 307.
(28) Xu, J.; Murphy, S.; Xiong, D.; Cai, R.; Wei, X.-K.; Heggen, M.; Barborini, E.; Vinati, S.; Dunin-Borkowski, R. E.; Palmer, R. E. *ACS Appl. Energy Mater.* **2018**, *1*, 3013.

(29) Li, W.; Gao, X.; Wang, X.; Xiong, D.; Huang, P.-P.; Song, W.-G.; Bao, X.; Liu, L. *J. Power Sources* **2016**, *330*, 156.
(30) Kanan, M. W.; Nocera, D. G. *Science* **2008**, *321*, 1072.
(31) Surendranath, Y.; Kanan, M. W.; Nocera, D. G. *J. Am. Chem. Soc.* **2010**, *132*, 16501.
(32) Matheu, R.; Ertem, M. Z.; Benet-Buchholz, J.; Coronado, E.; Batista, V. S.; Sala, X.; Llobet, A. *J. Am. Chem. Soc.* **2015**, *137*, 10786.
(33) Neel, A. J.; Hilton, M. J.; Sigman, M. S.; Toste, F. D. *Nature* **2017**, *543*, 637.
(34) Nishio, M. *Phys. Chem. Chem. Phys.* **2011**, *13*, 13873.
(35) Concepcion, J. J.; Jurss, J. W.; Hoertz, P. G.; Meyer, T. J. *Angew. Chem. Int. Ed.* **2009**, *48*, 9473.
(36) Matheu, R.; Ertem, M. Z.; Gimbert-Suriñach, C.; Sala, X.; Llobet, A. *Chem. Rev.* **2019**, *119*, 3453.
(37) Graetzel, M. *Acc. Chem. Res.* **1981**, *14*, 376.
(38) Toshima, N.; Yonezawa, T. *New J. Chem.* **1998**, *22*, 1179.
(39) Cao, S.; Tao, F. F.; Tang, Y.; Li, Y.; Yu, J. *Chem. Soc. Rev.* **2016**, *45*, 4747.
(40) Kotani, H.; Hanazaki, R.; Ohkubo, K.; Yamada, Y.; Fukuzumi, S. *Chem. Eur. J.* **2011**, *17*, 2777.
(41) Roy, C.; Sebok, B.; Scott, S.; Fiordaliso, E.; Sørensen, J.; Bodin, A.; Trimarco, D.; Damsgaard, C.; Vesborg, P.; Hansen, O. *Nat. Catal.* **2018**, *1*, 820.

5. 5. Supporting Information

Table of Contents

1. Experimental Section

Materials

Instrumentation and Methods

Electrochemical Methods

O_2 evolution Experiments

X-ray Absorption Spectroscopy (XAS) Methods

Synthesis of {[Ru(tda)(4,4-bpy)]n(4,4-bpy}, (n= 1-15)

2. Spectroscopic Characterization

NMR Spectroscopy

Mass Spectroscopy

UV-Vis Spectroscopy

3. Electrochemical Characterization

4. O_2 Evolution Experiments

5. XANES & EXAFS

6. Scanning Tunneling Microscopy

7. Density Functional Theory

8. References

Chapter 5

Experimental Section

Materials

All the chemicals used in this work were provided by Sigma Aldrich and they have been used without further purification unless explicitly indicated. $RuCl_3 \cdot \times H_2O$ was purchased from Alfa-Aesar, 6,6'-Dicarboxylic acid-[2,2':6',2"-terpyridyl] (H_2tda), the precursor complexes {$RuCl_2(DMSO)_4$} and Ru(tda)(DMSO)(OH_2) were prepared according to a reported procedure.[1]

MultiWall Carbon Nanotubes (MWCNTs) were purchased from HeJi, Inc. (Zengcheng city, China) in bulk with >95% purity, >50 nm OD and ~10 µm length.

Solvents were dried with a SPS® system and degassed by bubbling nitrogen before starting the reactions. High purity de-ionized water used for the electrochemistry experiments was obtained by passing distilled water through a nanopure Mili-Q water purification system. For other spectroscopic and electrochemical studies, HPLC-grade solvents were used. GC plate electrodes (GC_p) were purchased from HTW, Germany, and are made of glassy carbon SIGRADUR® with the dimensions 20x10x0.18 mm.

Instrumentation and Methods

Bruker Avance 400 MHz and/or 500 MHz were used to carry out NMR spectroscopy. All the measurements were carried out at room temperature in the corresponding deuterated solvent using residual protons as internal reference.

ESI-Mass spectra were recorded using micromass Q-TOF mass spectrometer.

The pH of the solutions was determined by a pH meter (CRISON, Basic 20^+) calibrated before measurements through standard solutions at pH 4.01, 7.00 and 9.21.

Powder X-ray diffraction (PXRD) was performed on D8 Advanced Powder Diffractometer (Bruker) equipped with a vertical 2theta-theta goniometer in transmission configuration, with a Kα1 germanium monochromator for Cu radiation (λ = 1.5406 Å), at a scan step of 0.02° s^{-1} from 10° to 80°.

Elemental Analysis of the samples was carried out in a Thermo Finnigan elemental analyzer Flash 1112 model.

UV-vis spectrometry was performed ot using a Cary 50 (Varian) UV-vis spectrophotometer.

Electrochemical Methods

All the electrochemical experiments were performed in an IJ-Cambria CHI-660 potentiostat. Either a glassy carbon disk (GC_d, ϕ = 0.3 cm, S = 0.07 cm^2) or a glassy carbon plate (GC_p, 20 mm x 10 mm x 0.18 mm) were used as working electrode (WE). In the case of GC_p the surface

dipped in the electrochemical solution was 1 cm^2. A Pt disk (ϕ = 0.2 cm, S = 0.03 cm^2) was used as counter electrode (CE) and a Hg/Hg_2SO_4 (K_2SO_4 sat.) electrode was used as a reference electrode (RE), except for the oxygen monitored bulk electrolysis that a Ag/AgCl (KCl sat.) was used as RE and a Pt mesh as a CE. Electrochemical experiments in organic solvent were carried out in trifluoroethanol (TFE) containing 0.1 M of $[(n\text{-}Bu)_4N][PF_6]$ ($TBAPF_6$) as supporting electrolyte.

Preparation of different pH phosphate buffers:

- *pH 2, Ionic strength 0.1 M:* H_3PO_4 (0.104 mol, 10.19 g) and NaH_2PO_4 (0.0955 mol, 11.45 g) in 1 L of Mili-Q water.
- *pH 7, Ionic strength 1 M:* NaH_2PO_4 (0.153 mol, 18.31 g) and Na_2HPO_4 (0.282 mol, 40.07 g) in 1 L of Mili-Q water.
- *pH 7, Ionic strength 0.1 M:* NaH_2PO_4 (0.019 mol, 2.32 g) and Na_2HPO_4 (0.027 mol, 3.78 g) in 1 L of Mili-Q.
- *pH 12, Ionic strength 0.1 M:* Na_2HPO_4 (0.0073 mol, 1.04 g) and Na_3PO_4 (0.013 mol, 2.07 g) in 1 L of Mili-Q.

Note: During pH dependent experiments the solutions were basified or acidified by addition of the corresponding amount of 1 M NaOH or 0.1 M CF_3SO_3H aqueous solutions, respectively.

Cyclic Voltammetry (CV): In a typical CV experiment, a 20 mL vial was used as an electrochemical cell. A home-made teflon cap with holes for the three electrodes was used as a lid to ensure a reproducible distance between the electrodes. The scan rate was 100 $mV \cdot s^{-1}$ unless otherwise stated. iR compensation was applied at 90% when the current density was above 10 $mA \cdot cm^{-2}$.

Differential Pulse Voltammetry (DPV): In a typical DPV experiment, a 20 mL vial was used as an electrochemical cell. A home-made teflon cap with holes for the three electrodes was used as a lid to ensure a reproducible distance between the electrodes. The DPV parameters were ΔE= 4 mV, Amplitude = 50 mV, Pulse width = 0.05 s, Sampling width = 0.0167 s, Pulse period = 0.5 s. iR compensation was applied at 90%.

Bulk electrolysis: For activation of catalyst, controlled potential electrolysis (CPE) was carried out in pH 12 phosphate buffer solution for 1000 s at 1.25 V vs NHE in 20 mL one compartment three electrode electrochemical cell with constant stirring. CPE experiment for checking the stability was also carried out in 20 mL electrochemical cell containing stirring bar using glassy carbon disk as WE, Pt disk as CE and Hg/Hg_2SO_4 (K_2SO_4 saturated) as RE.

Surface Coverage (Γ) Calculation

The surface coverage of the complexes on the electrode was calculated following the formula:

$$\Gamma\ (mol \cdot cm^{-1}) = \frac{Q_{av}}{n \cdot S \cdot F} \qquad \text{(S1)}$$

$$Q_{av} = \frac{Q_{ap,Ru^{III/II}} + Q_{cp,Ru^{III/II}} + Q_{ap,Ru^{IV/III}} + Q_{cp,Ru^{IV/III}}}{4} \qquad \text{(S2)}$$

Where Q_{av} is average of the charge under anodic (Q_{ap}) and cathodic (Q_{cp}) peaks for $Ru^{III/II}$ and $Ru^{IV/III}$ electron transfer processes, obtained by integration in the CV. n is the number of electrons involved in each oxidation process, which is 1 for both complexes. S is the geometric surface area of the electrode (GC_d, S= 0.07 cm^2 and GC_p, S = 1 cm^2) and F is Faradaic constant. The average coverage of the catalyst was estimated from 5 independent experiments and an error between the sample was considered as standard deviation. Moreover, the surface coverage of each electrode used for different analyses was calculated and indicated in the caption.

O_2 Evolution Experiments

For Oxygen monitored bulk electrolysis experiments, a 10 mL two-compartment cell with a separation membrane between the two compartments was used. Both compartments were filled with 5 mL of 1 M phosphate buffer solution (pH = 7) and were equipped with a stirring bar. A functionalized GC_p was used as WE, a Pt grid as CE and a Ag/AgCl (KCl sat.) as a RE. Oxygen evolution was analyzed with a gas phase Clark type oxygen electrode (Unisense Ox-N needle microsensor) and calibrated by the addition of small quantities of oxygen (99%) at the end of the experiment. The CE was placed in one compartment and the other was provided with WE, RE and Clark electrode.

X-ray Absorption Spectroscopy (XAS) Methods

X-ray absorption spectra were collected at the CLAESS beamline at ALBA synchrotron light source and the Advanced Photon Source (APS) at Argonne National Laboratory on bending magnet beamline 20 at electron energy 23 KeV and average current of 100 mA. The radiation was monochromatized using a pair of Si (111) crystals at ALBA and by a Si (110) crystal monochromator at APS. The intensity of the X-rays were monitored by three ion chambers (I_0, I_1 and I_2) filled with 70% nitrogen and 30% argon and placed before the sample (I_0) and after the sample (I_1 and I_2). Ru metal was placed between ion chambers I_1 and I_2 and its absorption was recorded with each scan for energy calibration. At APS, the samples were kept at 20 K in a He atmosphere at ambient pressure. Hybrid materials on glassy carbon surfaces

were thereby recorded as fluorescence excitation spectra using a 13-element energy-resolving detector. Solid reference sample {[Ru^{II}(tda)(4,4'-bpy)]$_{15}$(4,4'-bpy} and RuO_2 were diluted with Boron Nitride pressed between 3 µm polypropylene film and mylar tape and measured in the continuous helium flow cryostat in transmission mode. On the other hand, fluorescence absorption measurements at ALBA were carried out with an Amptek silicon drift solid state detector (XR-100 SDD)[2] placed at 90 degrees to the incoming beam. The silicon drift detector was placed on a motorized stage allowing the sample-detector distance to be easily changed between 30-110 mm[2]. Around 25 XAS spectra of each sample were collected. Care was to measure at several sample positions on each sample and no more than 5 scans were taken at each sample position. In order to reduce the risk of sample damage by X-ray radiation, 80% flux was used in the defocused mode (beam size 5500 µm (horizontal) x 600 µm (vertical)) and no damage was observed after scan to any samples. All samples were also protected from the X-ray beam during spectrometer movements by a shutter synchronized with the scan program. Ru XAS energy was calibrated by the first maxima in the second derivative of the ruthenium metal X-ray Absorption Near Edge Structure (XANES) spectrum.

V

Extended X-ray Absorption Fine Structure (EXAFS) Analysis

Athena software[3] was used for data processing. The energy scale for each scan was normalized using Ruthenium metal standard. Data in energy space were pre-edge corrected, normalized, deglitched (if necessary), and background corrected. The processed data were next converted to the photoelectron wave vector (k) space and weighted by k^3. The electron wave number is defined as $k = [2m(E - E_0)/\hbar^2]^{1/2}$, E_0 is the energy origin or the threshold energy. K-space data were truncated near the zero crossings k =2 to 11 $Å^{-1}$ for the hybrid complexes on FTO and glassy carbon surfaces, in Ru EXAFS before Fourier transformation. The k-space data were transferred into the Artemis Software for curve fitting. In order to fit the data, the Fourier peaks were isolated separately, grouped together, or the entire (unfiltered) spectrum was used. The individual Fourier peaks were isolated by applying a Hanning window to the first and last 15% of the chosen range, leaving the middle 70% untouched. Curve fitting was performed using *ab initio*-calculated phases and amplitudes from the FEFF8[4] program from the University of Washington. *Ab initio*-calculated phases and amplitudes were used in the EXAFS equation

$$\chi(k) = S_0^2 \sum_j \frac{N_j}{kR_j^2} f_{eff_j}(\pi, k, R_j) e^{-2\sigma_j^2 k^2} e^{\frac{-2R_j}{\lambda_j(k)}} \sin(2kR_j + \phi_{ij}(k)) \qquad \text{(S3)}$$

where N_j is the number of atoms in the j^{th} shell; R_j the mean distance between the absorbing atom and the atoms in the j^{th} shell; $f_{eff_j}(\pi,k,R_j)$ is the *ab initio* amplitude function for shell *j*, and the Debye-Waller term $e^{-2\sigma_j^2 k^2}$ accounts for damping due to static and thermal disorder in absorber-backscatterer distances. The mean free path term $e^{\frac{-2R_j}{\lambda_j(k)}}$ reflects losses due to inelastic scattering, where $\lambda_j(k)$, is the electron mean free path. The oscillations in the EXAFS spectrum are reflected in the sinusoidal term $\sin(2kR_j + \phi_{ij}(k))$, where $\phi_{ij}(k)$ is the *ab initio* phase function for shell *j*. This sinusoidal term shows the direct relation between the frequency of the EXAFS oscillations in k-space and the absorber-backscatterer distance. S_0^2 is an amplitude reduction factor.

The EXAFS equation[5] (Eq. S3) was used to fit the experimental Fourier isolated data (q-space) as well as unfiltered data (k-space) and Fourier transformed data (R-space) using *N*, S_0^2, E_0, *R*, and σ^2 as variable parameters (Table S4, S5). *N* refers to the number of coordination atoms surrounding Ru for each shell. The quality of fit was evaluated by R-factor and the reduced Chi^2 value. The deviation in E_0 ought to be less than or equal to 10 eV. R-factor less than 2% denotes that the fit is good enough[5] whereas R-factor between 2 and 5% denotes that the fit is correct within a consistently broad model. The reduced Chi^2 value is used to compare fits as more absorber-backscatter shells are included to fit the data. A smaller reduced Chi^2 value implies a better fit. Similar results were obtained from fits done in k, q, and R-spaces.

Synthesis of {[Ru(tda)(4,4-bpy)]$_n$(4,4-bpy}, (n= 1-15)

Synthesis of {[Ru(tda)(4,4-bpy)]$_n$(4,4-bpy}, (n= 1-4), 1,2 and **4**: In 100 mL two neck round bottom flask, [Ru(tda)(DMSO)(OH$_2$)] (100 mg, 0.2 mmol) and 4,4'-bipyridine (47 mg, 0.3 mmol) were dissolved in 20 mL of degassed MeOH/H$_2$O (3:2) and refluxed for 3 days under N$_2$ atmosphere. Afterwards, the reaction mixture was cooled down to room temperature affording a black-red precipitate, which was filtered through, washed with MeOH, H$_2$O, acetone and Et$_2$O and dried under vacuum yielding complex **{[Ru^{II}(tda)(4,4´-bpy)]$_4$(4,4´-bpy)}** (**4**) as a brown-red solid. The red deep filtrate collected during the first filtration was evaporated to dryness. The resulting brown-red solid was dissolved in DCM/MeOH (10:1) and purified by column chromatography (Silica). The first brown red color fraction obtained using DCM/MeOH (1:1) as eluent corresponds to monomeric complex **{[Ru^{II}(tda)(4,4´-bpy)](4,4´-bpy)}** (**1**). The second deep red fraction was collected by changing the polarity of the eluent to DCM/MeOH (1:4) yielding the dimeric complex **{[Ru^{II}(tda)(4,4´-bpy)]$_2$(4,4´-bpy)}** (**2**).

V

Synthesis of {[Ru^{II}(tda)(4,4´-bpy)]$_5$(4,4´-bpy)}, 5: In 100 mL two neck round bottom flask, [Ru(tda)(DMSO)(OH$_2$)] (100 mg, 0.2 mmol) and 4,4'-bipyridine (47 mg, 0.3 mmol) were dissolved in 20 mL of degassed TFE and refluxed for 3 days under N$_2$ atmosphere. Afterwards, the reaction mixture was evaporated to dryness and to this resulting solid, methanol was added and a nice black red precipitate was observed along with deep red color solution. The precipitate was filtered through frit and washed with MeOH, H$_2$O, acetone and Et$_2$O and dried under vacuum yielding the pentamer complex **{[Ru^{II}(tda)(4,4´-bpy)]$_5$(4,4´-bpy)}** (**5**).

Synthesis of {[Ru^{II}(tda)(4,4´-bpy)]$_{15}$(4,4´-bpy)}, 15 : In 100 mL two neck round bottom flask, [Ru(tda)(DMSO)(OH$_2$)] (100 mg, 0.2 mmol) and 4,4'-bipyridine (31.0 mg, 0.2 mmol) were dissolved in 20 mL of degassed TFE and refluxed for 3 days under N$_2$ atmosphere. Afterwards, the reaction mixture was evaporated to dryness and to this resulting solid, methanol was added and a nice black red precipitate was observed along with deep red color solution. The precipitate was filtered through frit and washed with MeOH, H$_2$O, acetone and Et$_2$O and dried under vacuum yielding the oligomeric complex **{[Ru^{II}(tda)(4,4´-bpy)]$_{15}$(4,4´-bpy)}** (**15**).

{[Ru^{II}(tda)(4,4´-bpy)](4,4´-bpy)}, 1:

Yield: 30 mg, 0.04 mmol (20 %). ^{1}H-NMR (500 MHz, [d$_4$]-MeOD) δ: 8.71 (d, J = 8.05 Hz, 2H), 8.60 (dd, J=4.87 and 1.59 Hz, 4H), 8.56 (d, J=7.92 Hz, 2H), 8.32 (dd, J=5.52 and 1.45 Hz, 4H), 8.16 (t, J = 8.25 Hz, 1H), 8.10 (d, J=7.64 Hz, 2H), 8.06 (t, J=7.72 Hz, 2H), 7.64 (dd, J=4.92 and 1.59 Hz, 4H), 7.52 (dd, J=5.55 and 1.44Hz, 4H). ^{13}C-NMR (125 MHz, [d$_4$]-MeOD) δ: 170.8, 161.9,

158.1, 157.0, 153.2, 149.7, 145.5, 144.5, 136.8, 132.7, 126.5, 124.0, 123.9, 122.2 and 121.5. (+)-HRMS-ESI (MeOH). Calcd for $[M+H]^+$, ($C_{37}H_{26}N_7O_4Ru$) : 734.1012, found 734.1117. Elemental analysis (% found): C, 49.61%; H, 4.01%; N, 9.82%. Calcd for $C_{37}H_{25}N_7O_4Ru \cdot 1.8\ C_2H_2OF_3 \cdot 4\ H_2O$: C, 49.51%; H, 3.93%; N, 9.96%.

{[Ru^{II}(tda)(4,4´-bpy)]$_2$(4,4´-bpy)}, 2:

Yield: 15 mg, 0.01 mmol (6 %). ^{1}H-NMR (500 MHz, [d_4]-MeOD) δ: 8.71 (d, J = 7.97 Hz, 4H), 8.65 (dd, J=4.71 and 1.65 Hz, 4H), 8.56 (d, J=7.67 Hz, 4H), 8.34 (dd, J=5.53 and 1.35 Hz, 4H), 8.29 (dd, J = 5.68 and 1.47 Hz, 4H), 8.17 (t, J=8.09 Hz, 2H), 8.13 (m, 4H), 8.08 (t, J=7.82 Hz, 4H), 7.67 (dd, J=4.84 and 1.64 Hz, 4H), 7.54 (dd, J=5.50 and 1.52 Hz, 4H), 7.31 (dd, J=5.54 and 1.49 Hz, 4H). ^{13}C-NMR (125 MHz, [d_4]-MeOD) δ: 170.9, 162.0, 160.0, 157.9, 157.4, 153.2, 153.0, 149.7, 145.5, 144.4, 143.9, 136.8, 132.8, 126.6, 123.9, 123.8, 122.2 and 121.5. (+)-HRMS-ESI (MeOH). [M/2+Na^+], ($C_{32}H_{21}N_6O_4Ru$+Na^+): 678.0668, found 678.0588. Elemental analysis (% found): C, 43.98%; H, 3.59%; N, 8.52%. Calcd for $C_{64}H_{42}N_{12}O_8Ru_2 \cdot 7\ C_2H_2OF_3 \cdot 6\ H_2O$: C, 44.24%; H, 3.57%; N, 7.98%.

{[Ru^{II}(tda)(4,4´-bpy)]$_4$(4,4´-bpy)}, 4:

Yield: 45 mg, 0.02 mmol (37 %). ^{1}H-NMR (500 MHz, [d_2]-DCM/[d_3]-TFE(4:1)) δ: 8.54 (d, J = 5.68 Hz, 4H), 8.34 (m, 8H), 8.20 (d, J=8.87 Hz, 4H), 8.17 (d, J=6.61, 8H), 8.11-7.98 (m, 24H), 7.92 (t, J=7.10 Hz, 4H), 7.87 (t, J=7.24 Hz 4H), 7.44 (d, J=5.06 Hz, 4H), 7.29 (d, J=6.18, 4H), 7.08 (m, 8H), 7.05 (m, 4H.

{[Ru^{II}(tda)(4,4´-bpy)]$_5$(4,4´-bpy)}, 5:

Yield: 60 mg, 0.02 mmol (49 %). ^{1}H-NMR (500 MHz, [d_2]-DCM/[d_3]-TFE (4:1)) δ: 8.52 (d, J = 4.53 Hz, 4H), 8.37-8.28 (m, 10H), 8.21 (d, J=7.98 Hz, 5H), 8.18-8.12 (3, 9H), 8.08 (d, J=4.98 Hz, 8H), 8.05-7.96 (m, 23H), , 7.93 (t, J=7.71 Hz 5H), 7.88 (t, J=7.51 Hz 5H), 7.45 (d, J=4.64 Hz, 4H), 7.27 (d, J=5.31, 4H), 7.06 (m, 8H), 7.03 (m, 8H).

{[Ru^{II}(tda)(4,4´-bpy)]1$_5$(4,4´-bpy)}, 15:

Yield: 100 mg, 0.011 mmol (85 %). ^{1}H-NMR (500 MHz, [d_2]-DCM/[d_3]-TFE (4:1)) δ: 8.48 (d, J = 5.4 Hz, 4H), 8.32-8.222 (m, 28H), 8.18-8.07 (m, 36H), 8.04 (d, J=7.06 Hz, 16H), 8.02-7.92 (m, 79H), 7.89 (t, J=7.75 Hz, 8H), 7.87-7.79 (m, 28H), 7.41 (d, J=5.76 Hz 4H), 7.23 (d, J=6.22 Hz, 4H), 7.06-6.91 (m, 56H. Elemental analysis (% found): C, 46.51%; H, 3.18%; N, 9.71%. Calcd for $C_{415}H_{263}N_{77}O_{60}Ru_{15} \cdot 26\ C_2H_2OF_3 \cdot 27\ H_2O$: C, 46.79%; H, 3.34%; N, 8.92%.

Preparation and Activation of 5@CNT@GC and 15@CNT@GC Electrodes

Preparation of 5@CNT and 15@CNT

Figure S1 shows a schematic drawing of the procedure employed for preparation of **5@CNT** and **15@CNT**. Solution A was prepared by disolving 1 mg of the corresponding oligomer (**5** or **15**) in 1 mL of TFE. Suspension B was prepared parallely by sonication of 5 mg of MWCNTs (HeJi, Inc., China) in 5 mL of THF during 60 minutes. Afterwards, 0.1 mL of Solution A was added to 1 mL of Suspension B. Upon addition, the red color disappeared immediately from the solution indicating that oligomeric species are quickly anchored on MWCNT yielding suspension C, which contains **5@CNT** or **15@CNT**.

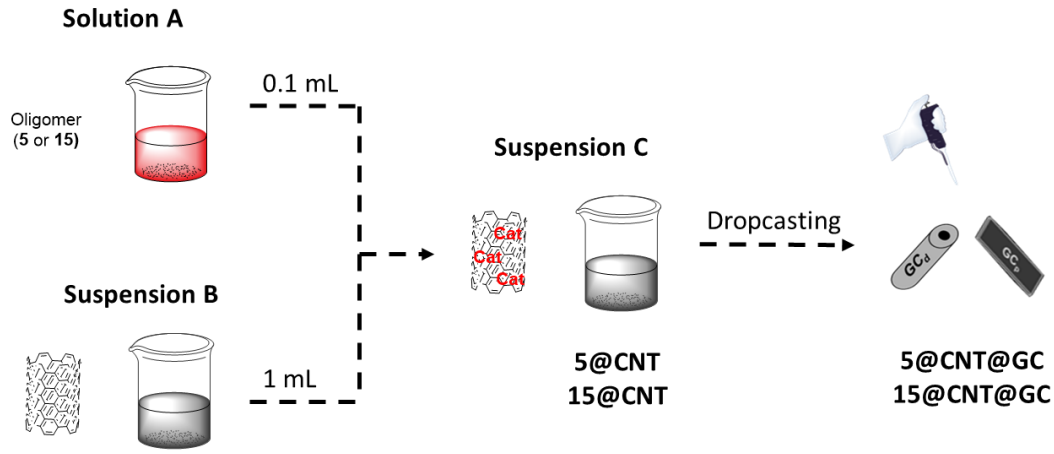

Figure S1. Schematic diagram for preparation of **5@CNT@GC** and **15@CNT@GC.**

Preparation of 5@CNT@GC_d and 15@CNT@GC_d

Solution C was dropcasted (4 x 20 μL) onto GC_d electrodes. Each drop was placed after the last drop is totally dried. Electrode was then ready for electrochemical measurements.

Preparation of 5-H_2O@CNT@GC_d and 15-H_2O@CNT@GC_d

The electrodes prepared above (**5@CNT@GC** and **15@CNT@GC**) were immersed in 0.1 M phosphate buffer solution (pH 12) and CPE was performed at 1.25 V vs NHE for 1000 s under constant stirring to generate **5-H_2O@CNT@GC** or **15-H_2O@CNT@GC**. Afterwards, the activated electrodes were rinsed with distillated water and dried at room temperature.

Note: Preparation of electrodes on glassy carbon plates (**GC_p**) were carried out using a similar methodology but some differences were introduced. Suspension C was dropcasted (4 x 30 μL) onto GC_p electrodes. Each drop was placed after the last drop is totally dried. The coating was applied only to one side of the plates and a tape was used to limit this coating to 1 cm^2.

For XAS analysis, **15@CNT@GC_p** as deposited and **15-H_2O@CNT@GC_p** after 12 h bulk electrolysis at 1.45 V were wrapped in thin 3 μm mylar film separately and analyzed. The samples were then kept under ambient conditions until the XAS measurement (approx. a week). See the XAS methods section for further details about the XAS analysis.

Surface coverage (*Γ*) Calculation

The modified electrodes (both **GC_d** and **GC_p**) were immersed in 1 M phosphate buffer solution (pH 7) and cyclic voltammetry was performed (E_i = 0.25 V, E_c = 1.45 V, E_f = 0.25 V, total scans = 6, where E_i is initial potential, E_c is the change potential and E_f is the final potential), (CE = Pt disk, RE = Hg/Hg_2SO_4) to estimate the coverage of the electrodes. The surface coverage (Γ) of the complexes on the electrodes was estimated by applying the formula Γ (mol·cm^{-2}) = Q / (n*S*F).

Table S1. Summary of calculated surface coverage (Γ, nmol·cm^{-2}) for the prepared electrodes.

	5@CNT@GC_d	**5-H_2O@CNT@GC_d**	**15@CNT@GC_d**	**15-H_2O@CNT@GC_d**
Γ, (nmol·cm^{-2})	14±1	10.1±1	21±2	16±1.5

Chapter 5

Spectroscopic Characterization

NMR Spectroscopy

a)

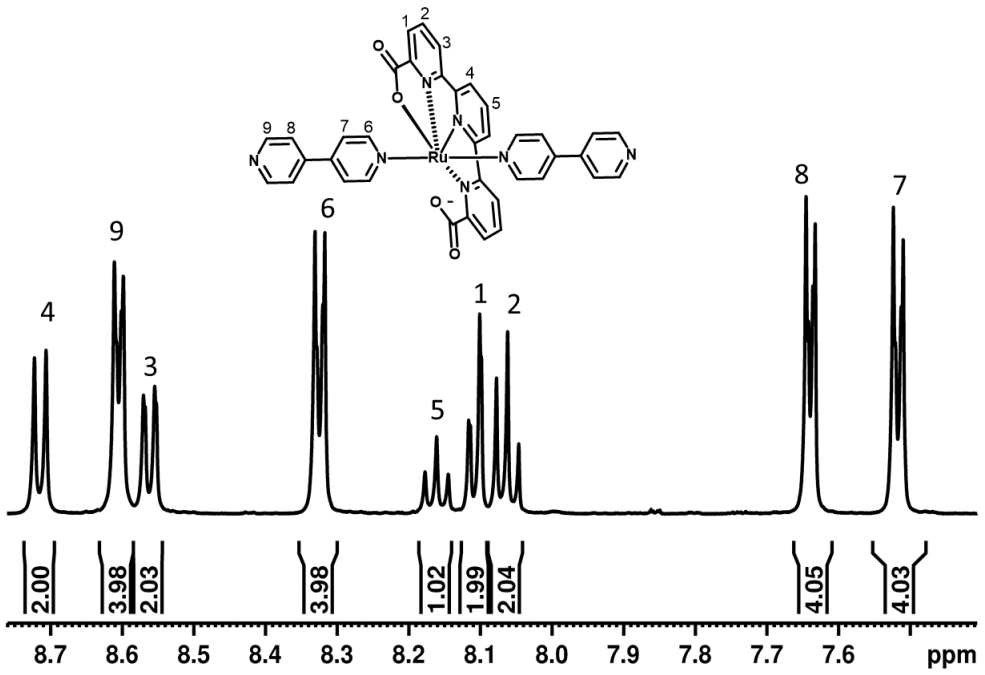

b)

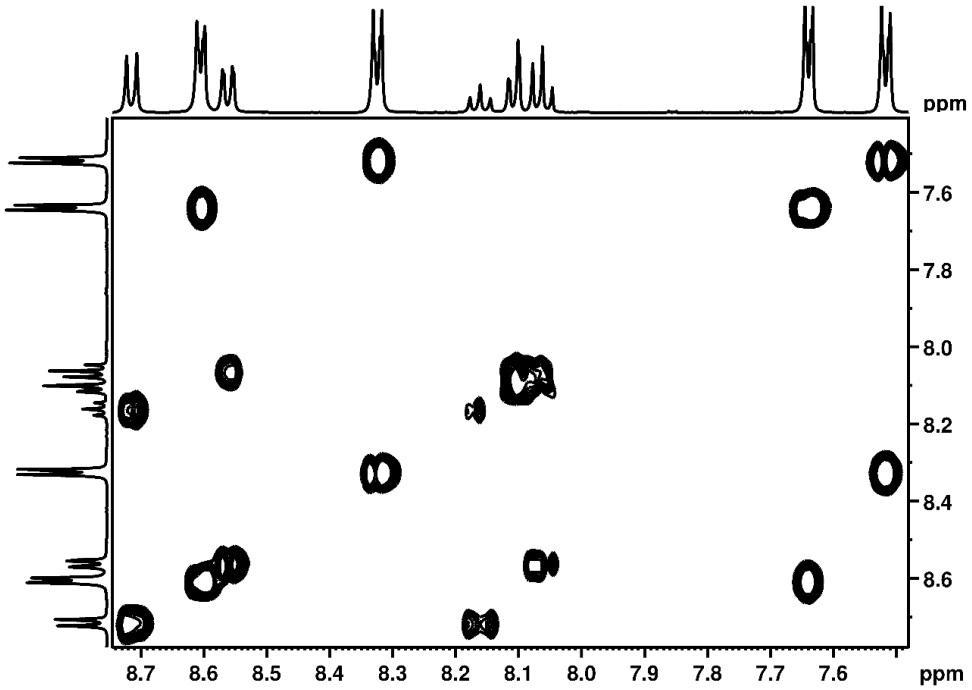

c)

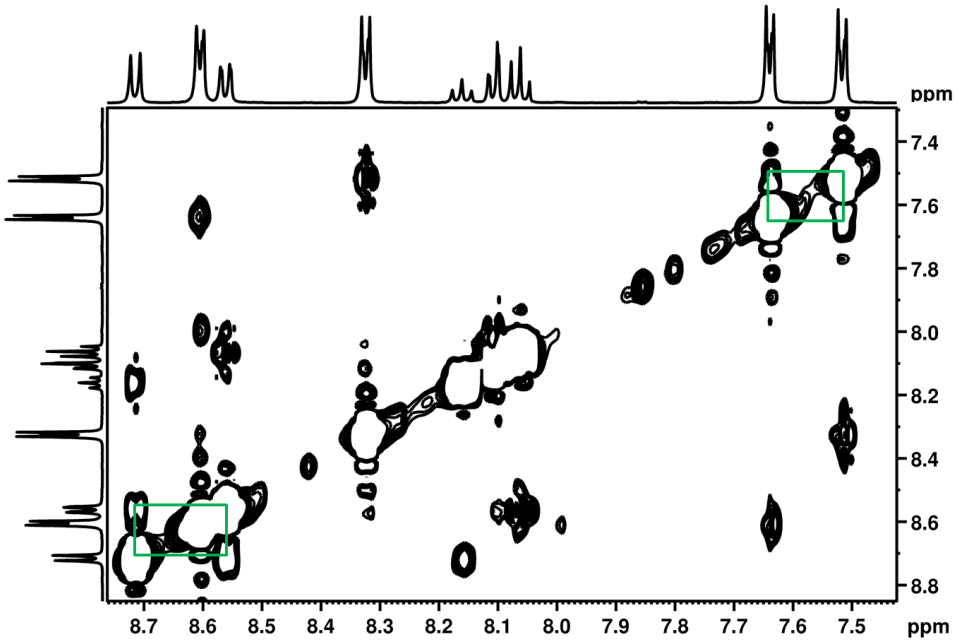
ppm
7.4
7.6
7.8
8.0
8.2
8.4
8.6
8.8
8.7 8.6 8.5 8.4 8.3 8.2 8.1 8.0 7.9 7.8 7.7 7.6 7.5 ppm

d)

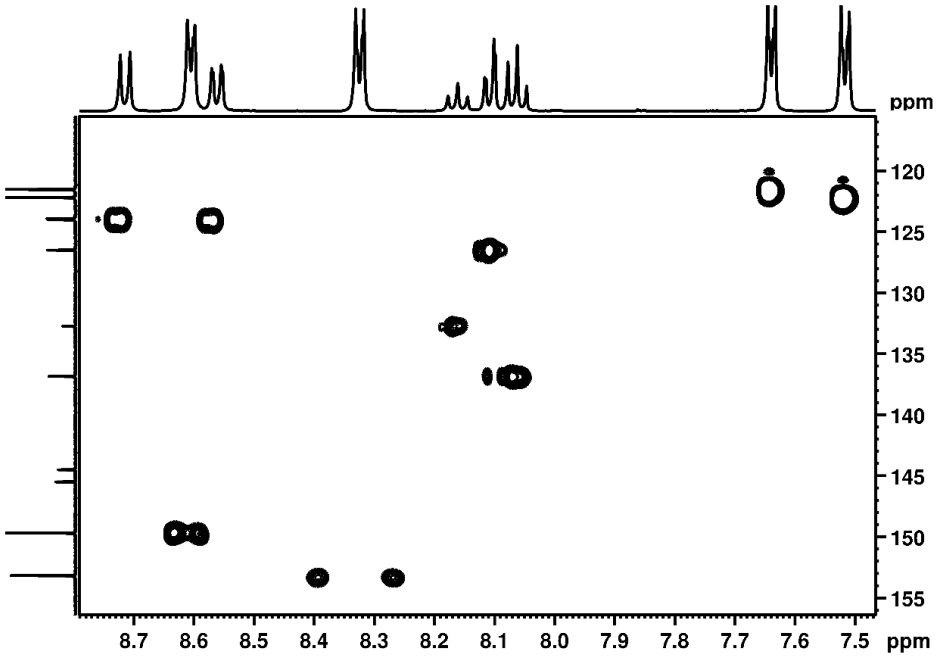
ppm
120
125
130
135
140
145
150
155
8.7 8.6 8.5 8.4 8.3 8.2 8.1 8.0 7.9 7.8 7.7 7.6 7.5 ppm

e)

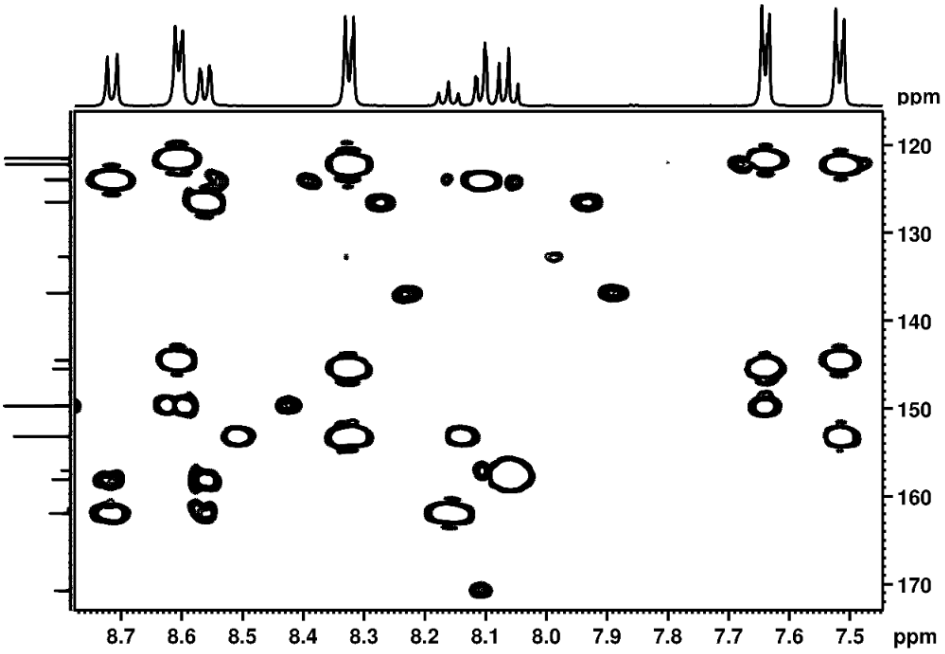

f)

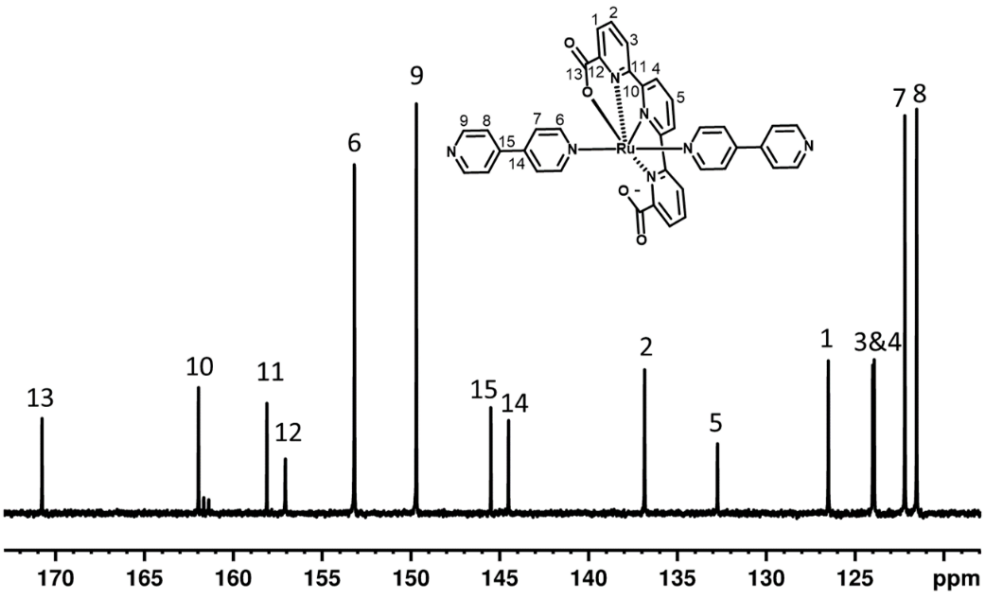

Figure S2. NMR spectra (500 MHz, 298 K, [d_4]-MeOD) for **1** a) ^{1}H-NMR, b) COSY, c) NOESY, d) HSQC, e) HMBC and f) ^{13}C NMR (125 MHz).

a)

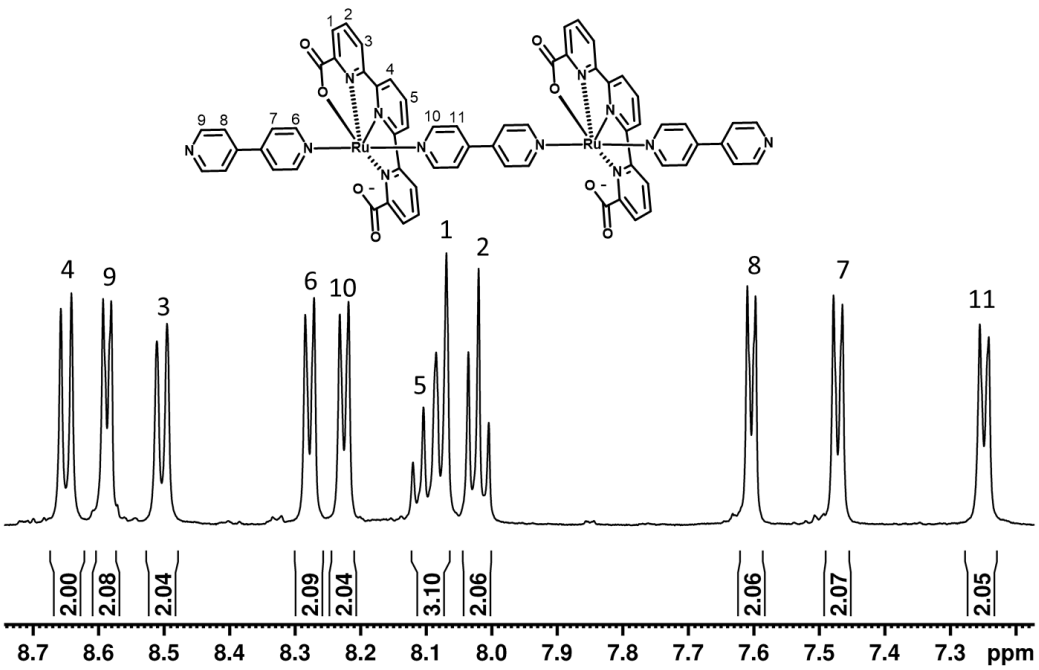
4
9
3
6
10
1
2
5
8
7
11
2.00
2.08
2.04
2.09
2.04
3.10
2.06
2.06
2.07
2.05
8.7
8.6
8.5
8.4
8.3
8.2
8.1
8.0
7.9
7.8
7.7
7.6
7.5
7.4
7.3
ppm

b)

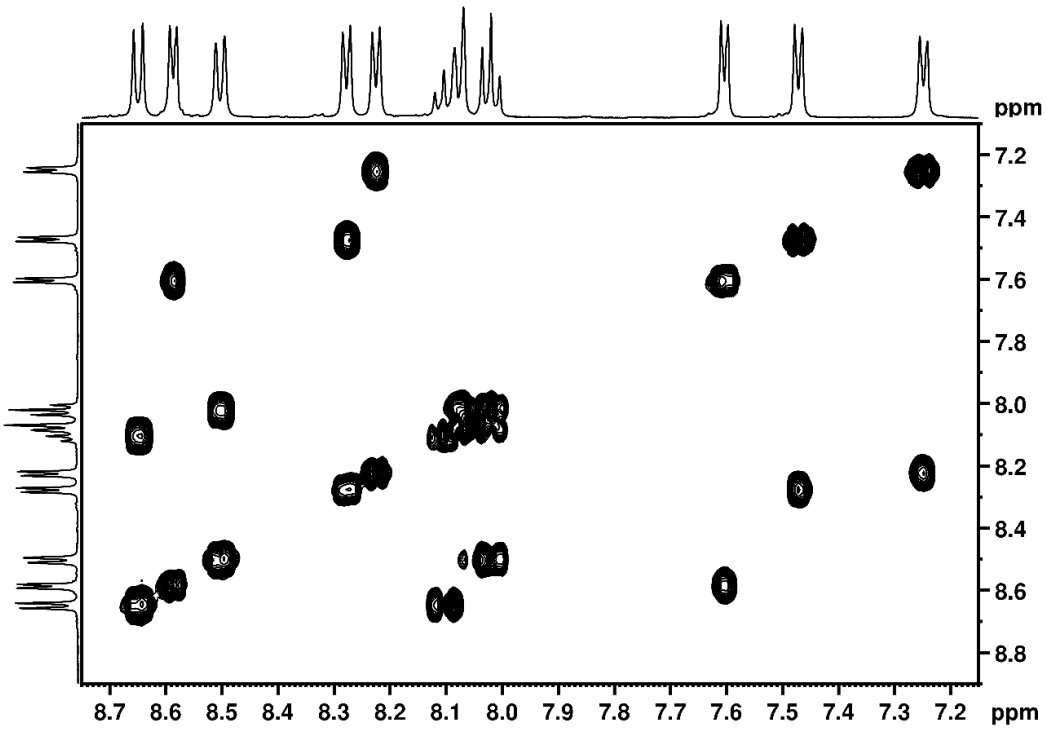
ppm
7.2
7.4
7.6
7.8
8.0
8.2
8.4
8.6
8.8
8.7
8.6
8.5
8.4
8.3
8.2
8.1
8.0
7.9
7.8
7.7
7.6
7.5
7.4
7.3
7.2
ppm

V

c)

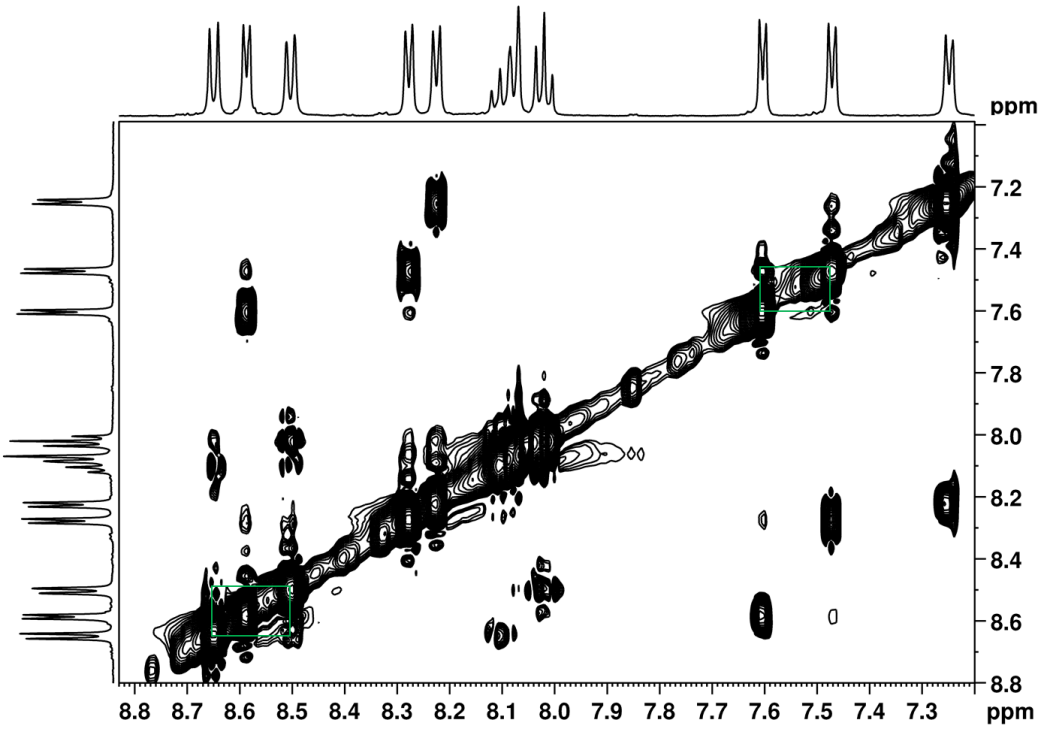
ppm
7.2
7.4
7.6
7.8
8.0
8.2
8.4
8.6
8.8
8.8 8.7 8.6 8.5 8.4 8.3 8.2 8.1 8.0 7.9 7.8 7.7 7.6 7.5 7.4 7.3
ppm

d)

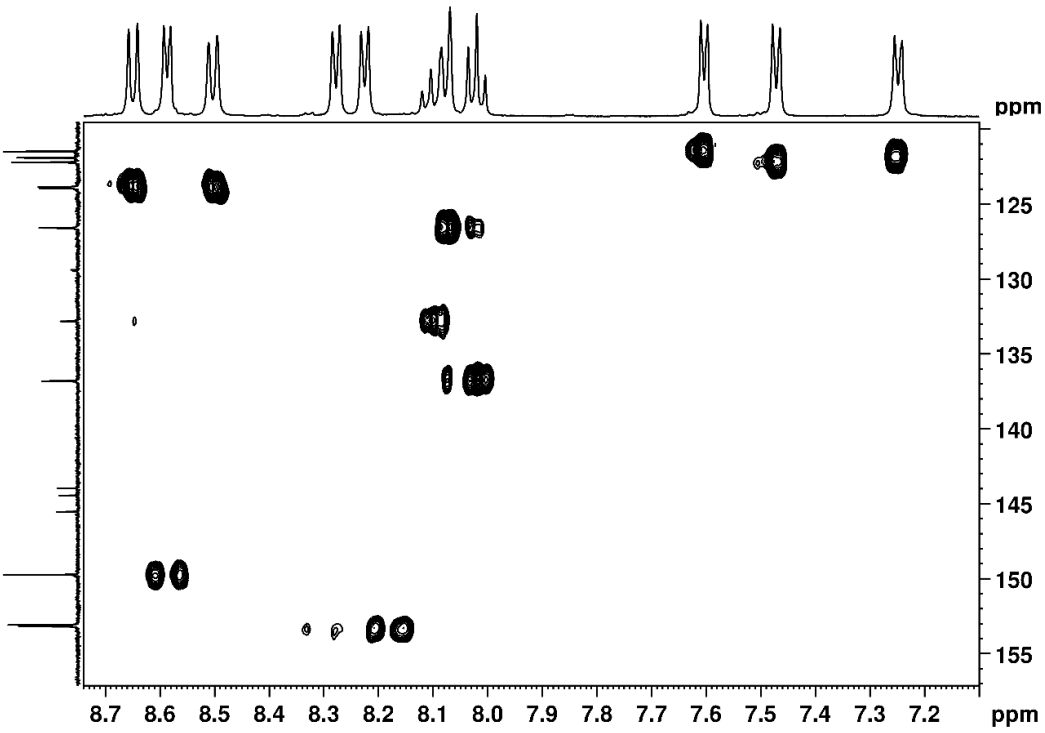
ppm
125
130
135
140
145
150
155
8.7 8.6 8.5 8.4 8.3 8.2 8.1 8.0 7.9 7.8 7.7 7.6 7.5 7.4 7.3 7.2
ppm

e)

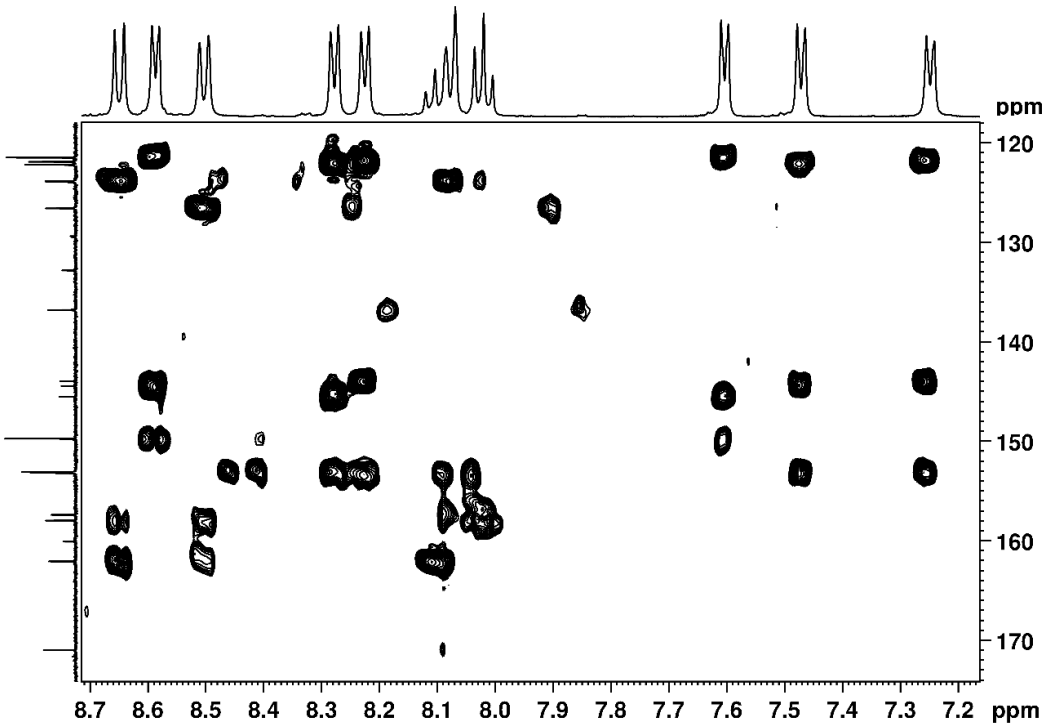

f)

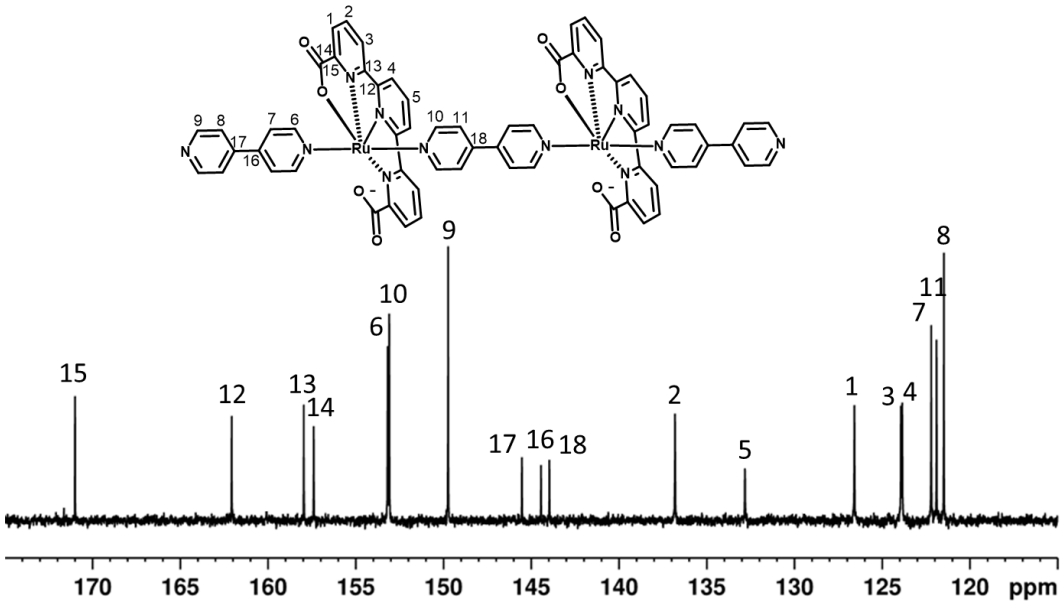

Figure S3. NMR spectra (500 MHz, 298 K, [d_4]-MeOD) for **2** a) ^{1}H-NMR, b) COSY, c) NOESY, d) HSQC, e) HMBC and f) ^{13}C NMR (125 MHz).

Chapter 5

a)

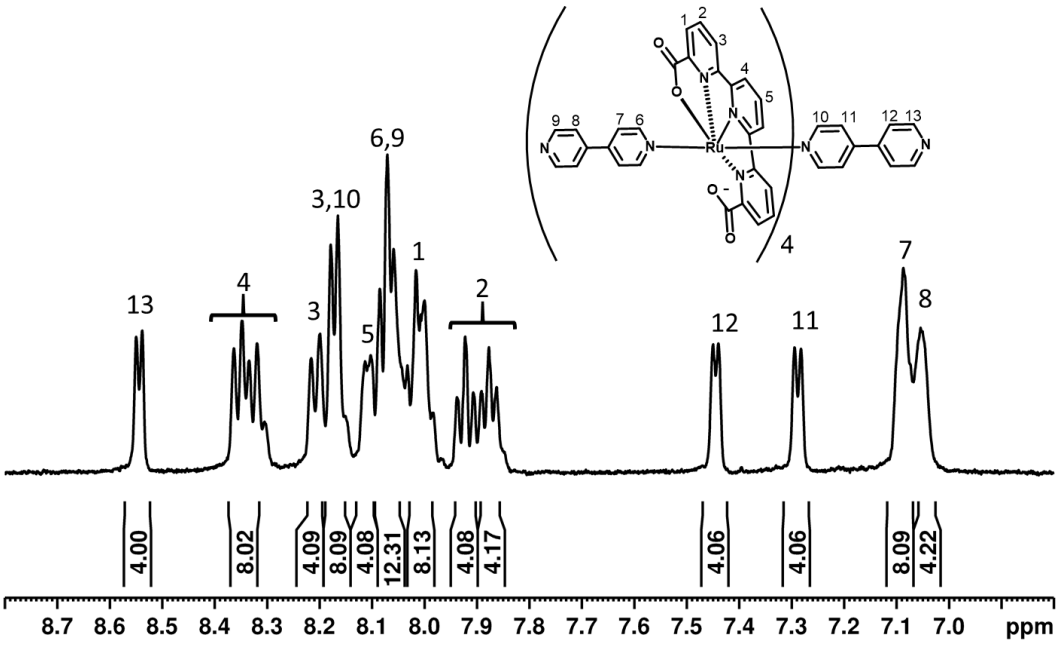
13
4
3
3,10
5
6,9
1
2
12
11
7
8
4.00
8.02
4.09
8.09
4.08
12.31
8.13
4.08
4.17
4.06
4.06
8.09
4.22
8.7 8.6 8.5 8.4 8.3 8.2 8.1 8.0 7.9 7.8 7.7 7.6 7.5 7.4 7.3 7.2 7.1 7.0
ppm

b)

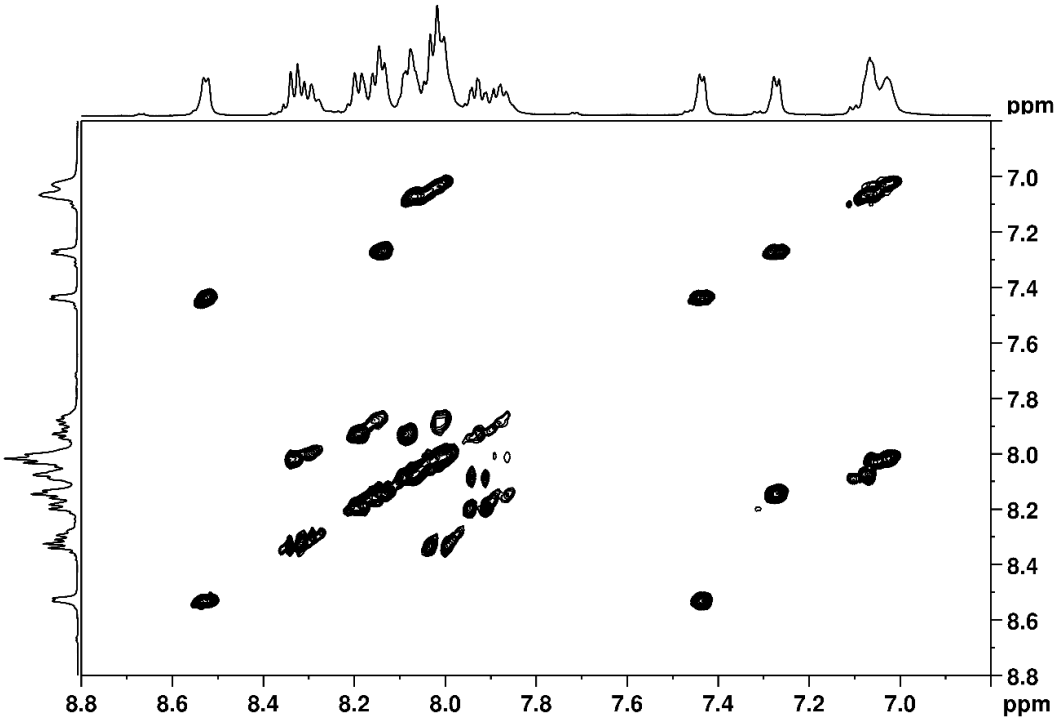
ppm
7.0
7.2
7.4
7.6
7.8
8.0
8.2
8.4
8.6
8.8
8.8 8.6 8.4 8.2 8.0 7.8 7.6 7.4 7.2 7.0
ppm

c)

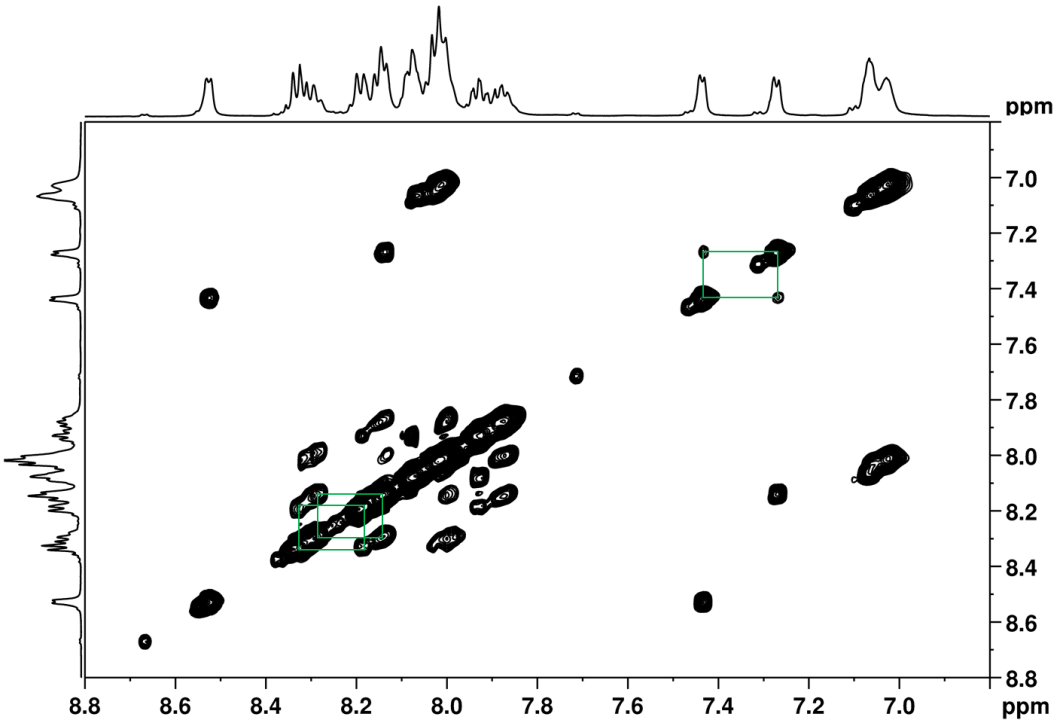

Figure S4. NMR spectra (500 MHz, 298 K, [d_2]-DCM/[d_3]-TFE (4:1)) for **4.** a) ^{1}H-NMR, b) COSY and c) NOESY.

Chapter 5

a)

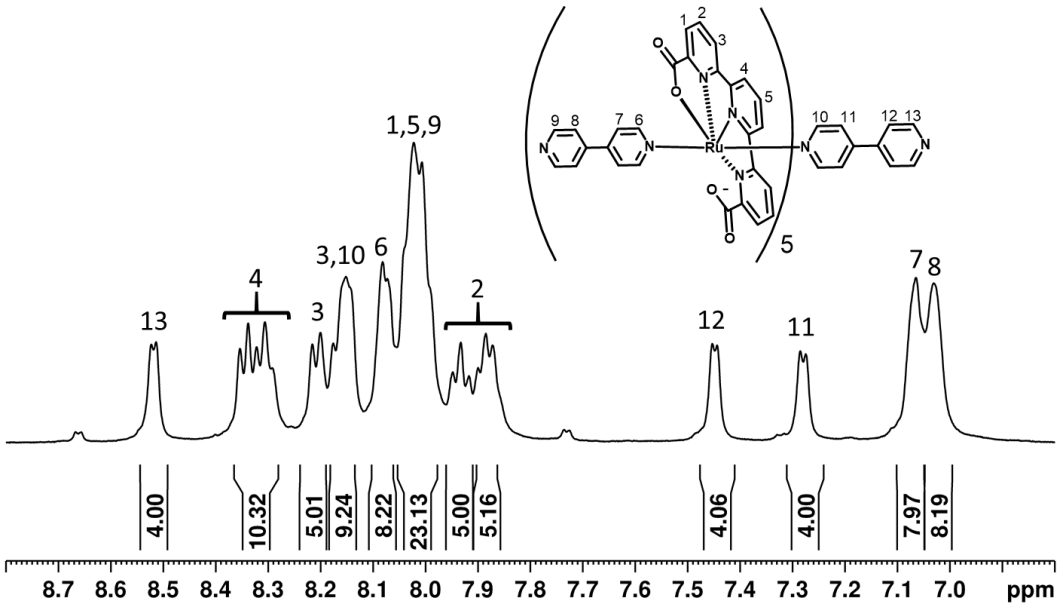
1,5,9
3,10
6
4
2
13
3
12
11
7
8
4.00
10.32
5.01
9.24
8.22
23.13
5.00
5.16
4.06
4.00
7.97
8.19
8.7 8.6 8.5 8.4 8.3 8.2 8.1 8.0 7.9 7.8 7.7 7.6 7.5 7.4 7.3 7.2 7.1 7.0
ppm

b)

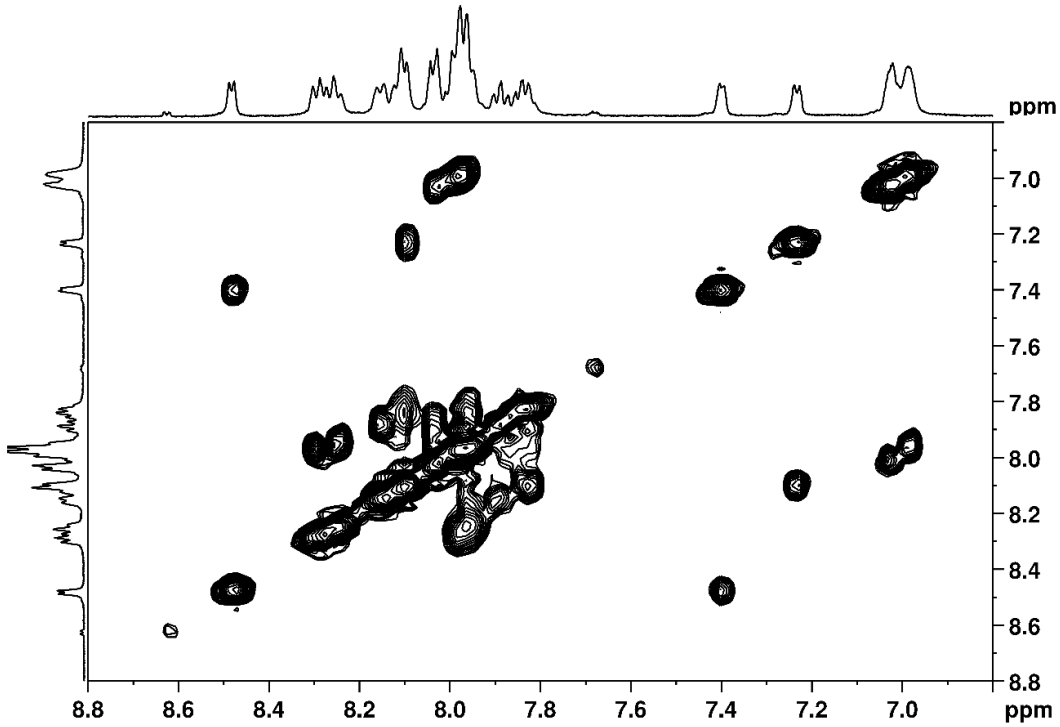
ppm
7.0
7.2
7.4
7.6
7.8
8.0
8.2
8.4
8.6
8.8
8.8 8.6 8.4 8.2 8.0 7.8 7.6 7.4 7.2 7.0
ppm

c)

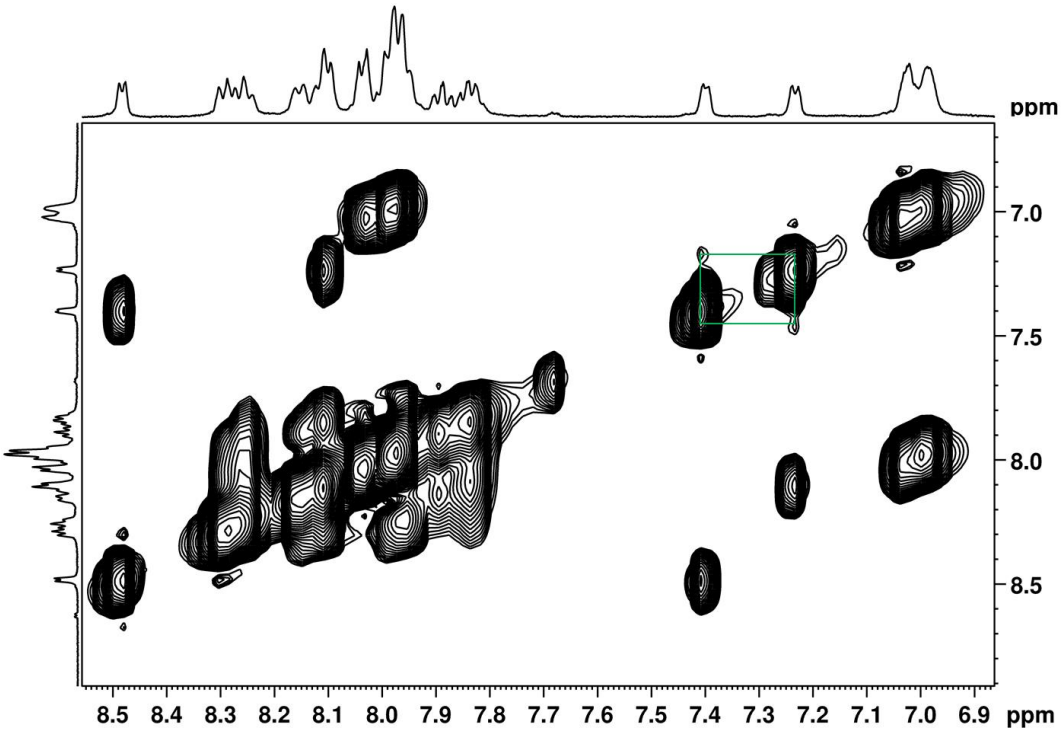

Figure S5. NMR spectra (500 MHz, 298 K, [d_2]-DCM/[d_3]-TFE (4:1)) for **5**. a) ^{1}H-NMR, b) COSY and c) NOESY.

a)

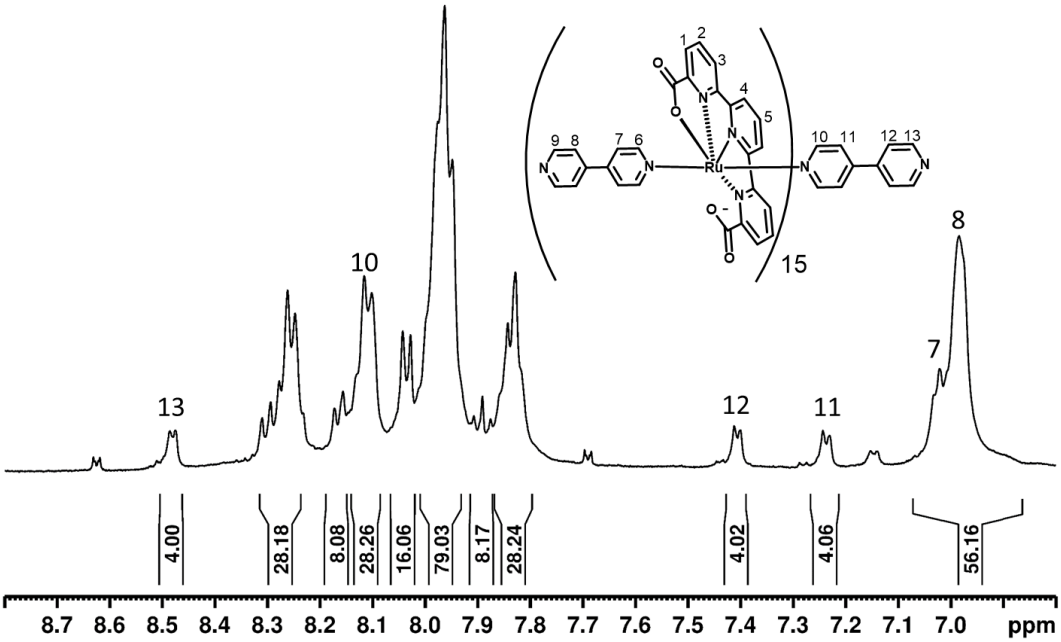
13
10
8
7
12
11
15
4.00
28.18
8.08
28.26
16.06
79.03
8.17
28.24
4.02
4.06
56.16
8.7 8.6 8.5 8.4 8.3 8.2 8.1 8.0 7.9 7.8 7.7 7.6 7.5 7.4 7.3 7.2 7.1 7.0 ppm

b)

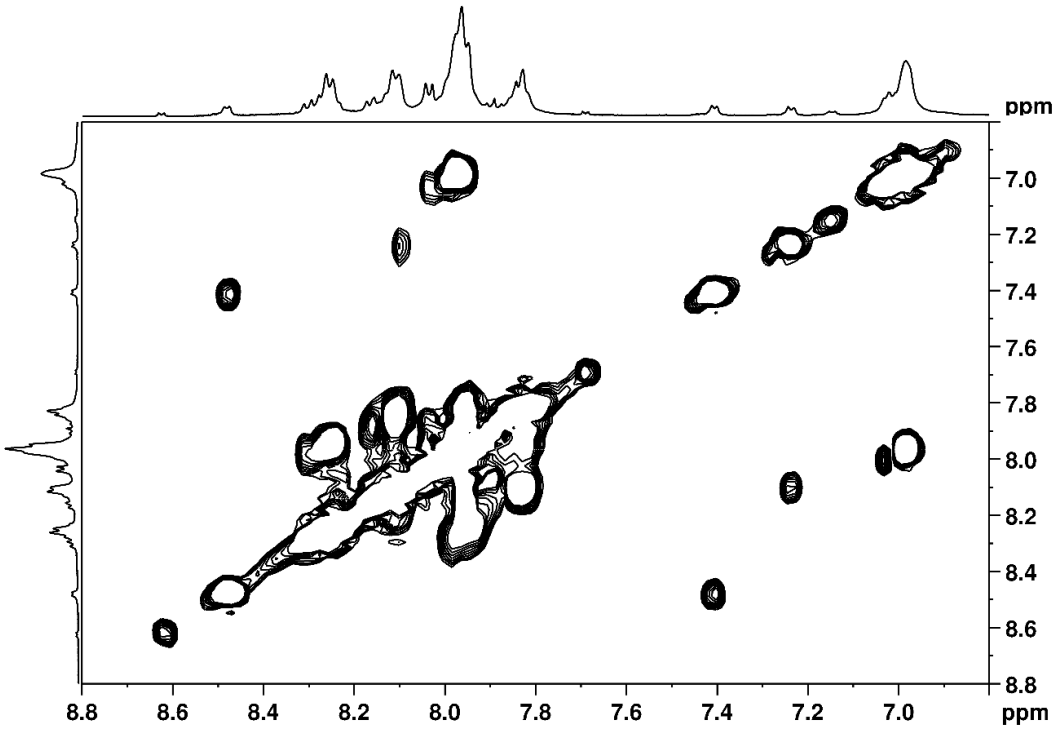
ppm
7.0
7.2
7.4
7.6
7.8
8.0
8.2
8.4
8.6
8.8
8.8 8.6 8.4 8.2 8.0 7.8 7.6 7.4 7.2 7.0 ppm

c)

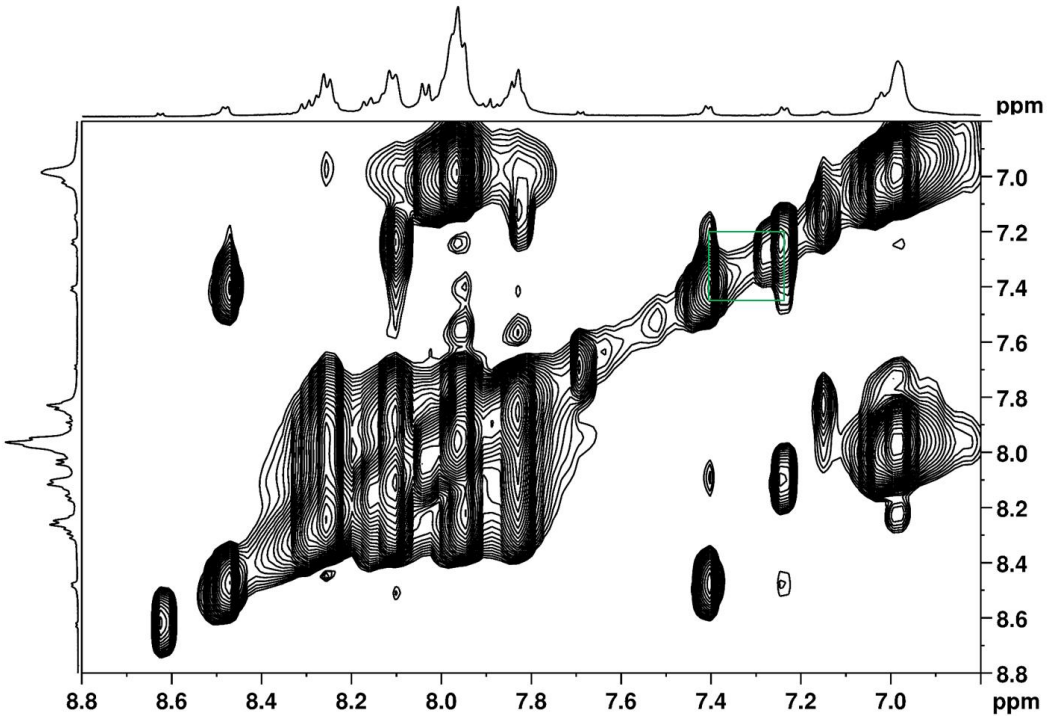

Figure S6. NMR spectra (500 MHz, 298 K, [d_2]-DCM/[d_3]-TFE (4:1)) for **15.** a) ^{1}H-NMR, b) COSY and c) NOESY.

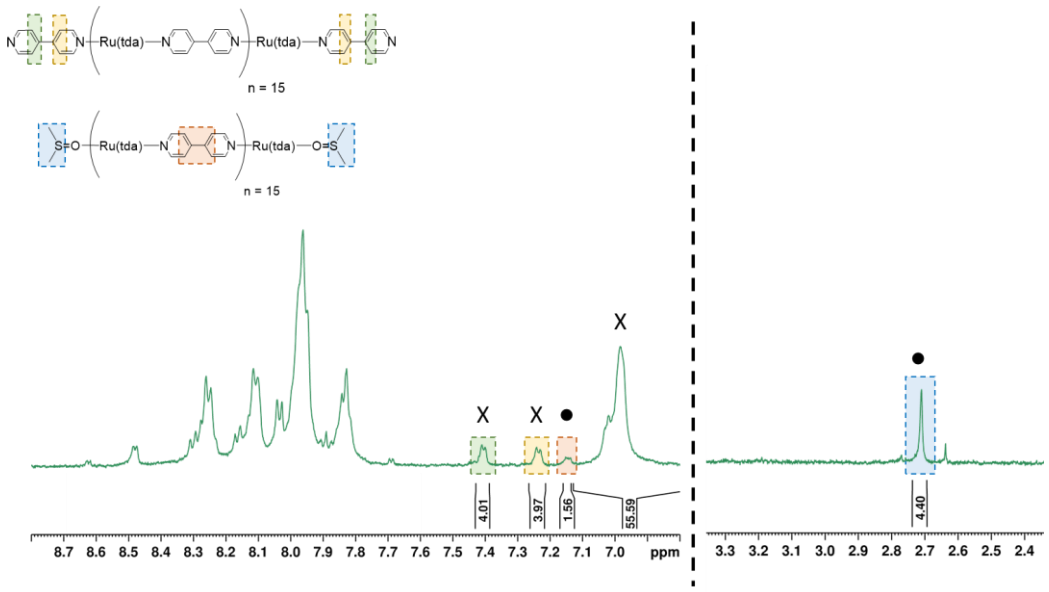

Figure S7. ^{1}H NMR spectra (500 MHz, 298 K, [d_2]-DCM/[d_3]-TFE (4:1)) for **15**. The spectra shows a mixture of **15** with 4,4'-bpy (X) and DMSO ending (•), 97% and 3% respectively.

a)

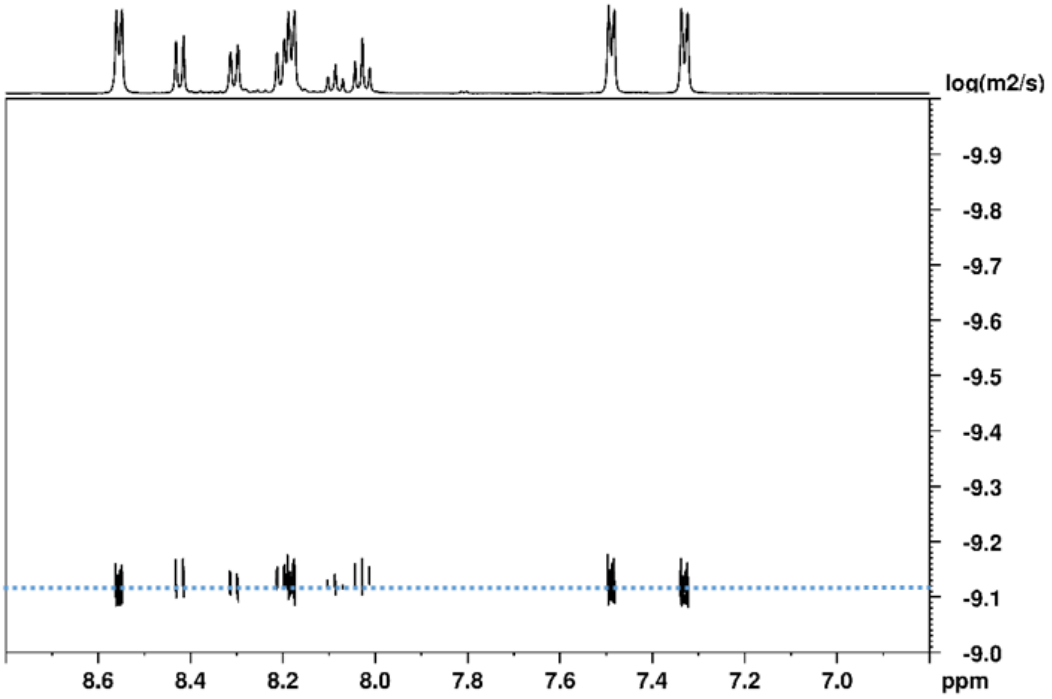
log(m2/s)
-9.9
-9.8
-9.7
-9.6
-9.5
-9.4
-9.3
-9.2
-9.1
-9.0
8.6
8.4
8.2
8.0
7.8
7.6
7.4
7.2
7.0
ppm

b)

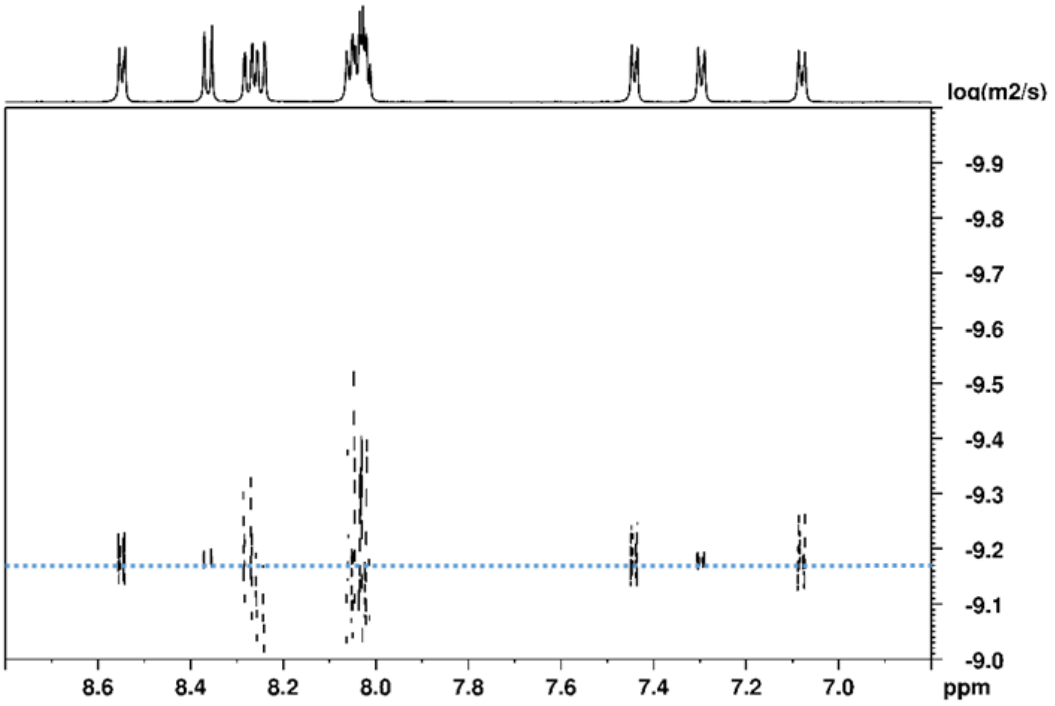
log(m2/s)
-9.9
-9.8
-9.7
-9.6
-9.5
-9.4
-9.3
-9.2
-9.1
-9.0
8.6
8.4
8.2
8.0
7.8
7.6
7.4
7.2
7.0
ppm

c)

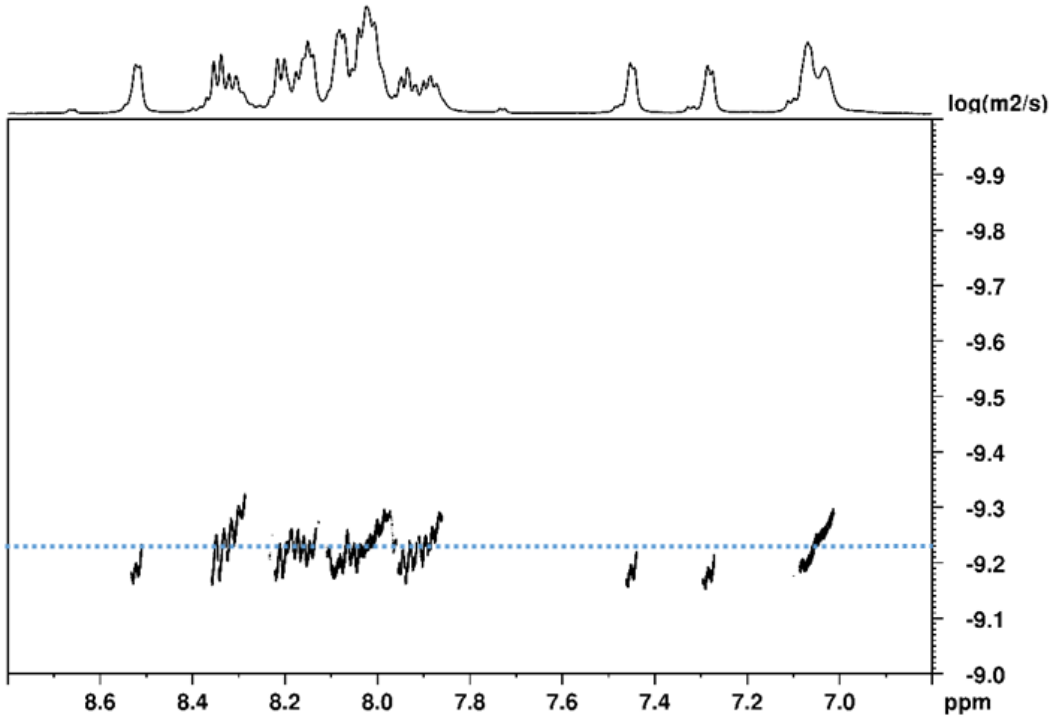
log(m2/s)
-9.9
-9.8
-9.7
-9.6
-9.5
-9.4
-9.3
-9.2
-9.1
-9.0
8.6
8.4
8.2
8.0
7.8
7.6
7.4
7.2
7.0
ppm

d)

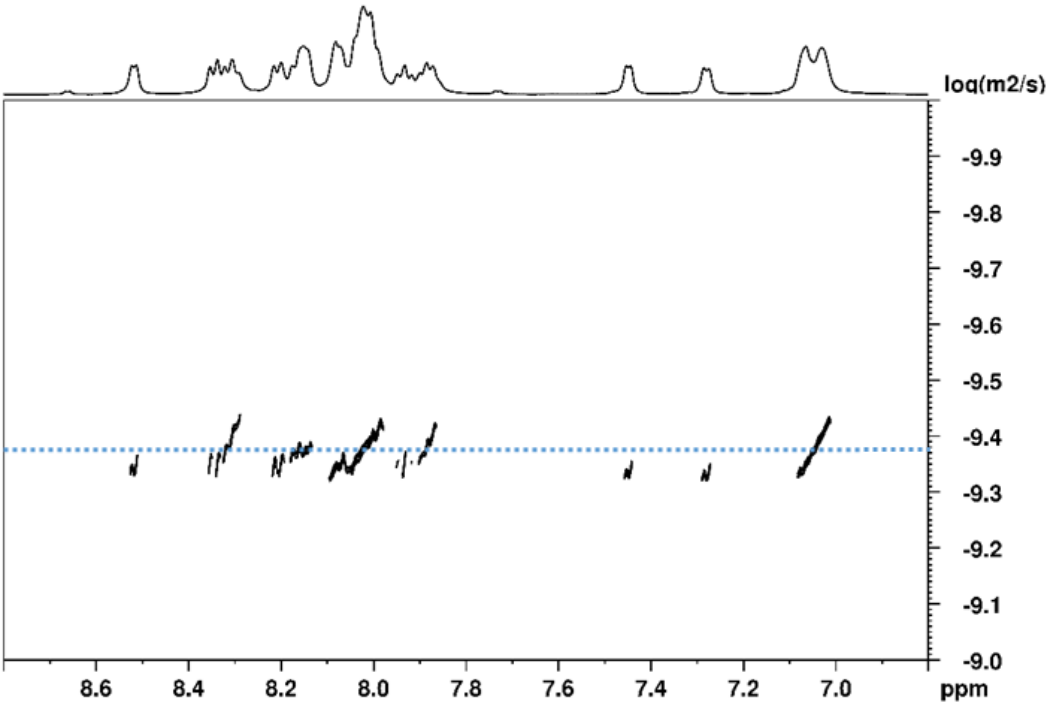
log(m2/s)
-9.9
-9.8
-9.7
-9.6
-9.5
-9.4
-9.3
-9.2
-9.1
-9.0
8.6
8.4
8.2
8.0
7.8
7.6
7.4
7.2
7.0
ppm

e)

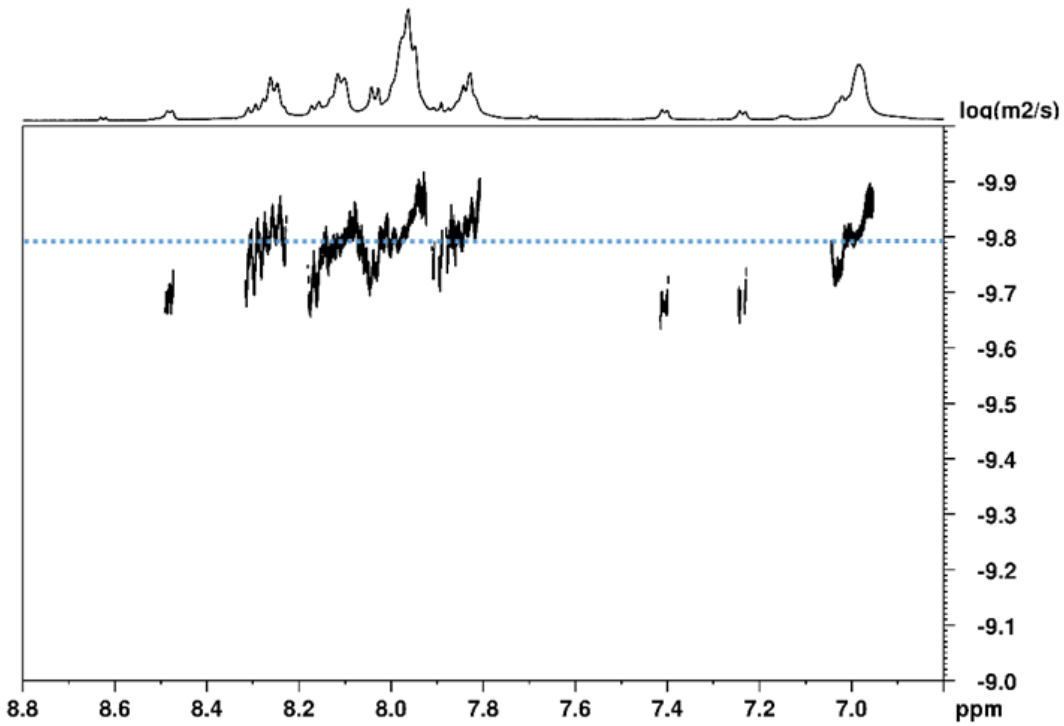

Figure S8. DOSY NMR spectra (500 MHz, 298 K, [d_2]-DCM/[d_3]-TFE (4:1)) for complexes a) **1**, b) **2**, c) **4**, d) **5** and e) **15**.

f)

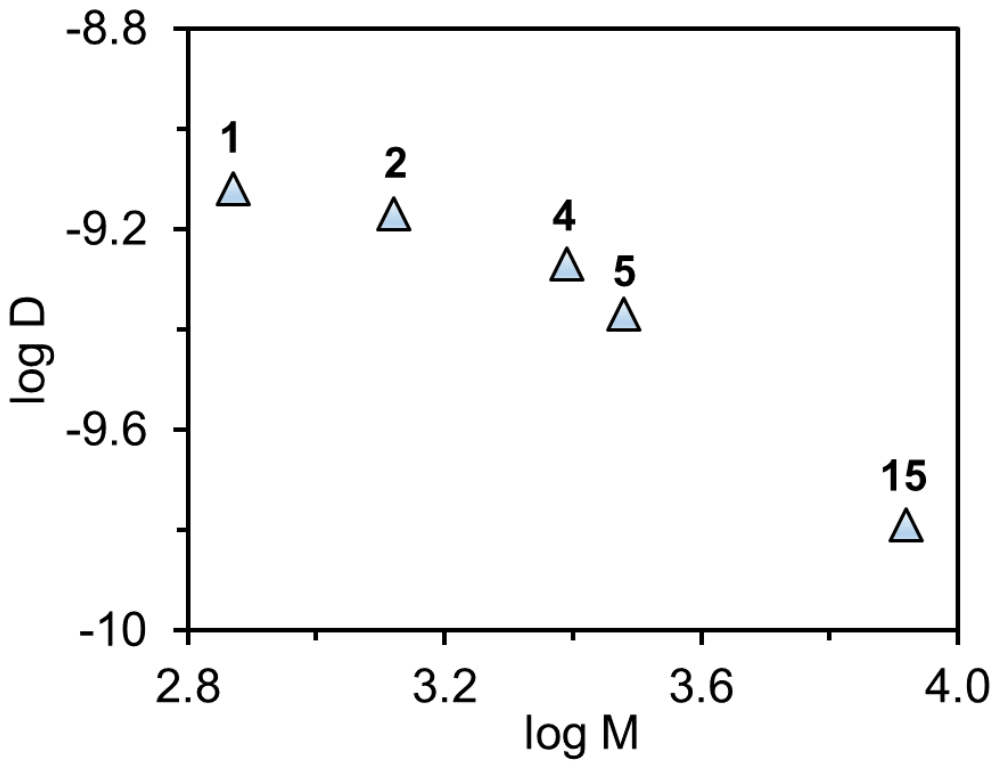

Figure S9. Correlation between logarithm of the diffusion coefficient calculated by DOSY NMR experiments (500 MHz, 298 K, [d_2]-DCM/[d_3]-TFE (4:1)) for **1**, **2**, **4**, **5** and **15** and logarithm of the molecular weight (log M).

Chapter 5

Mass Spectrometry

a)

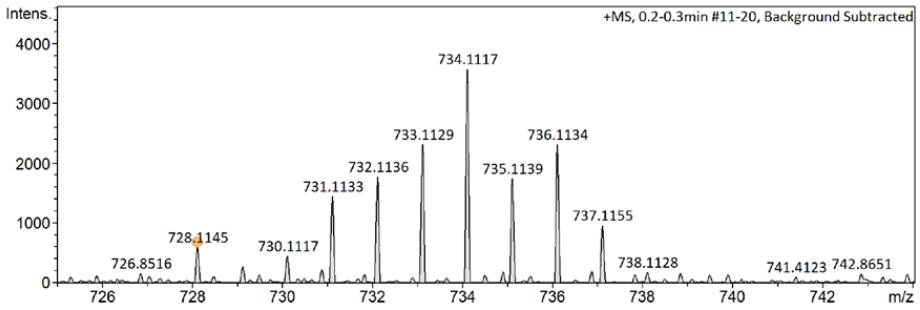

b)

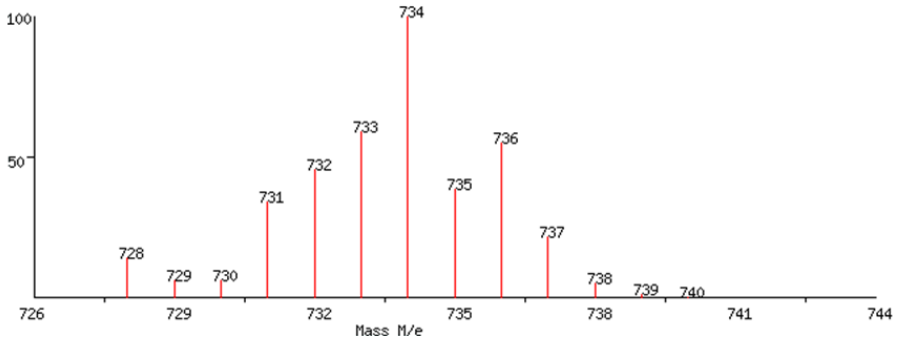

Figure S10. a) HRMS-ESI for **1**. Calcd for [M+H$^+$], ($C_{37}H_{25}N_7O_4Ru$ + H$^+$) : 734.1012, found 734.1117. b) Simulated isotopic pattern for ($C_{37}H_{25}N_7O_4Ru$ + H$^+$)

a)

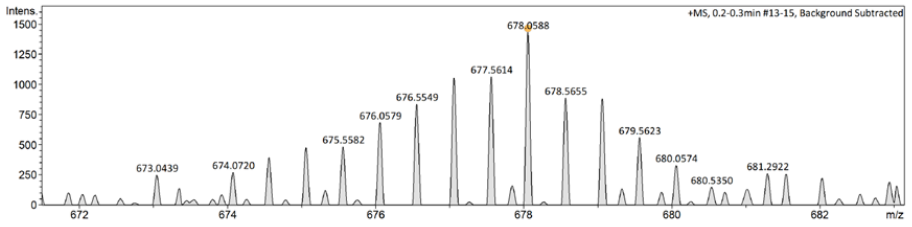

b)

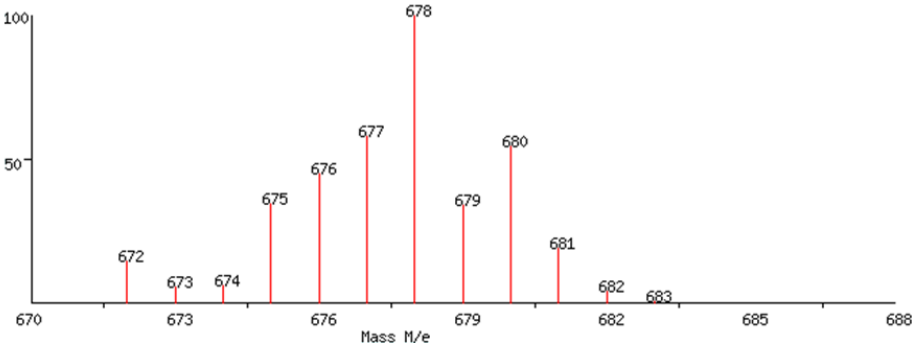

Figure S11. a) HRMS-ESI for **2**. Calcd for [M/2+Na$^+$], ($C_{32}H_{21}N_6O_4Ru$+Na$^+$): 678.0668, found 678.0588. b) Simulated isotopic pattern for ($C_{32}H_{21}N_6O_4Ru$+Na$^+$).

UV-Vis Spectroscopy

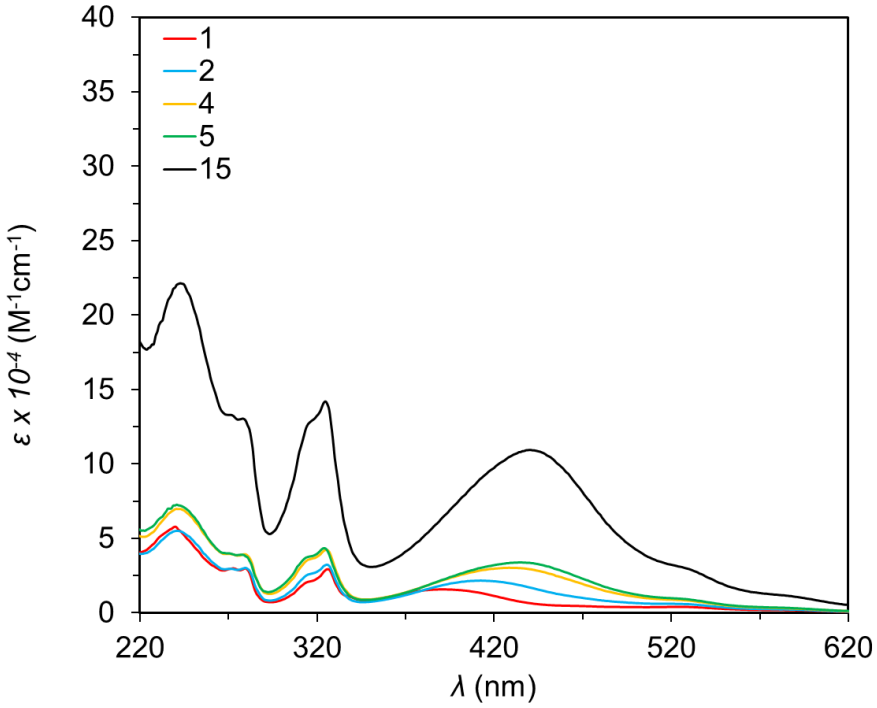

Figure S12. UV-Vis absorption spectrum of **1** (red line), **2** (blue line), **4** (yellow line), **5** (green line) and **15** (black line). Conditions: 5-20 µM of complexes in TFE.

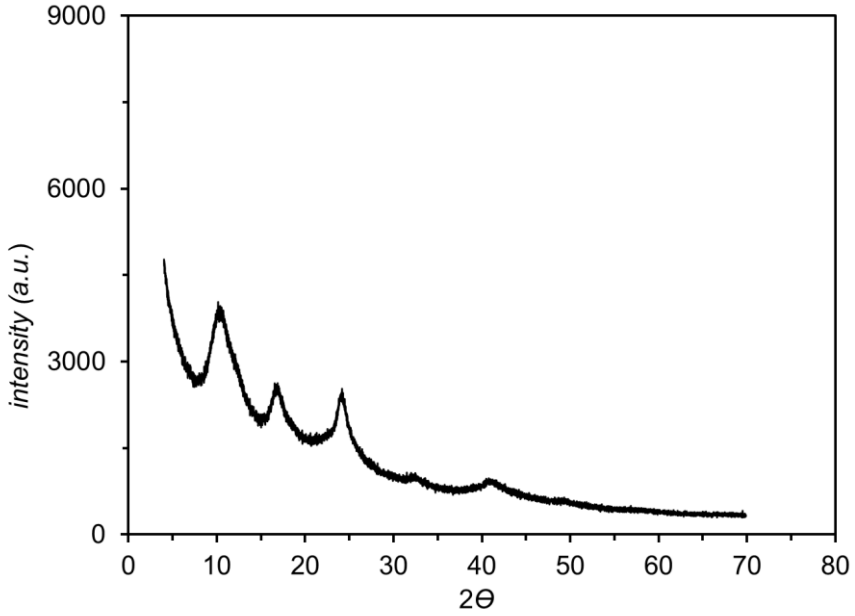

Figure S13. Powder x-ray diffraction pattern of **15.**

Electrochemical Characterization

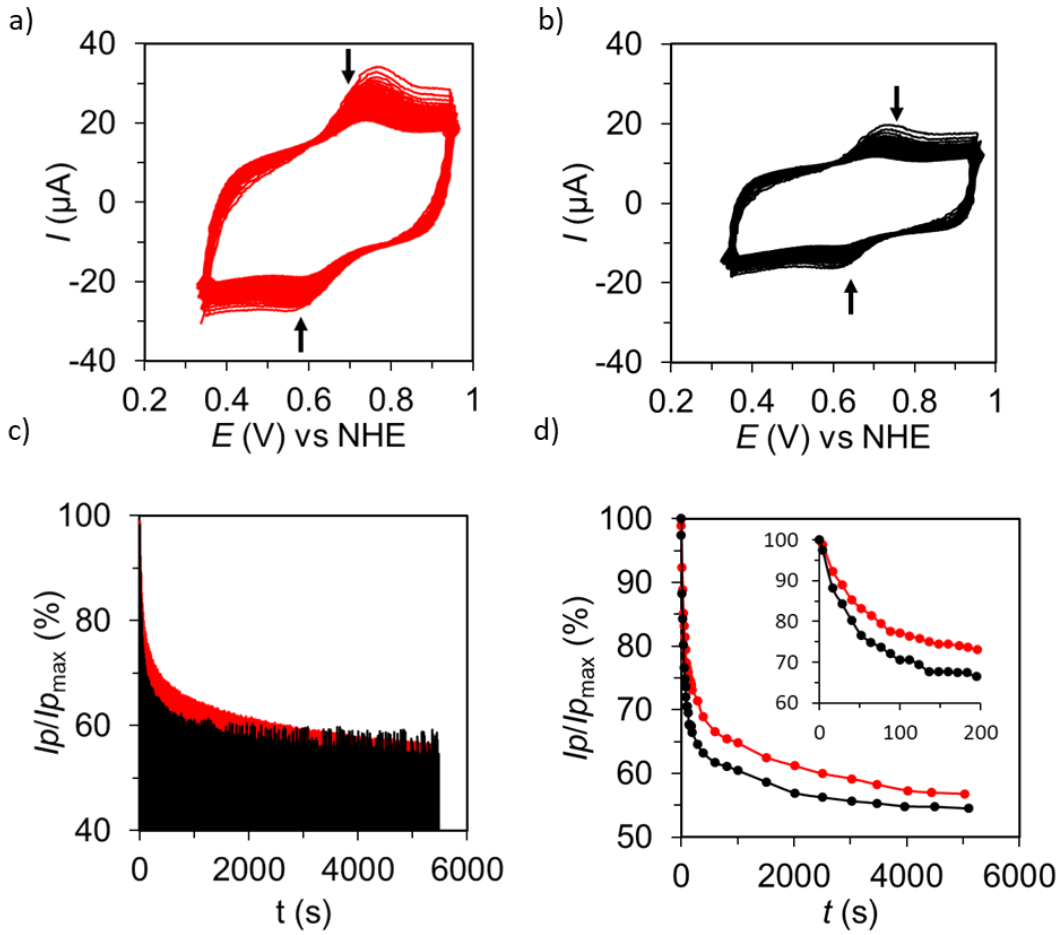

Figure S14. a) CV evolution of the **5@CNT@GC** (a) and **15@CNT@GC** (b) in 0.1 M solution of $TBAPF_6$ in TFE during 1.5 h at 25 ˚C. CV cycles show the detachment of the oligomers from the MWCNTs and ulterior solubilization in TFE. c) Plot of I/I_p (%) *vs.* t for **5@CNT@GC** (black line) and **15@CNT@GC** (red line); ***Note:*** Current of the anodic peak (I) has been normalized by dividing the intensity of the anodic peak in the initial cycle (I_p). d) Plot of I/I_p (%) *vs.* t at the potential of the anodic peak (0.77 for **5@CNT@GC** and 0.73 for **15@CNT@GC**) showing a clear difference in the detachment kinetics between **5** and **15**, which is much more stabilized due to the multiple CH-π interactions with the graphitic surface.

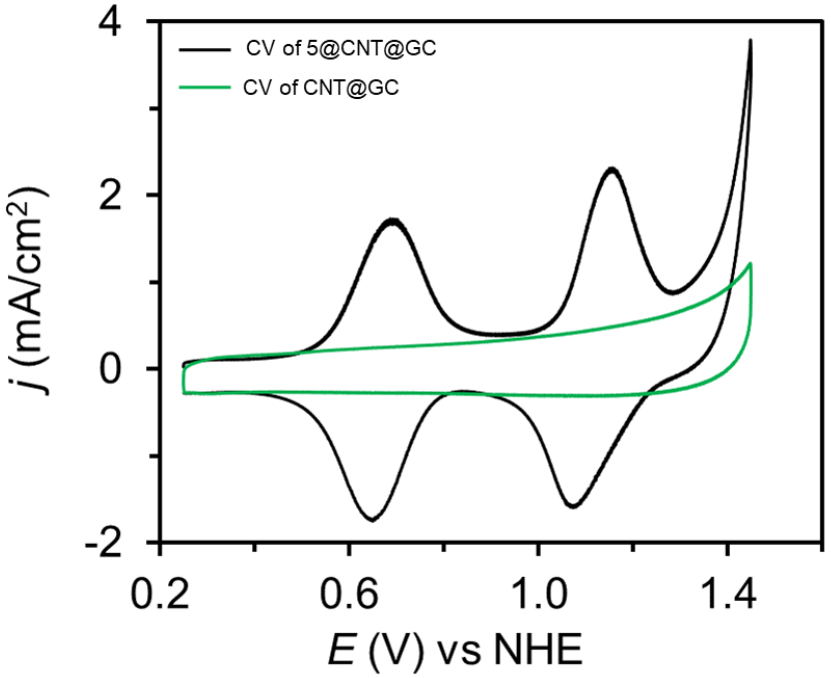

Figure S15. CV of **5@CNT@GC** (black line) and the blank (green line) in 1 M phosphate buffer (pH 7) at a scan rate of 100 mV/s. Conditions: Γ_5= 14.2 nmol·cm^{-2}.

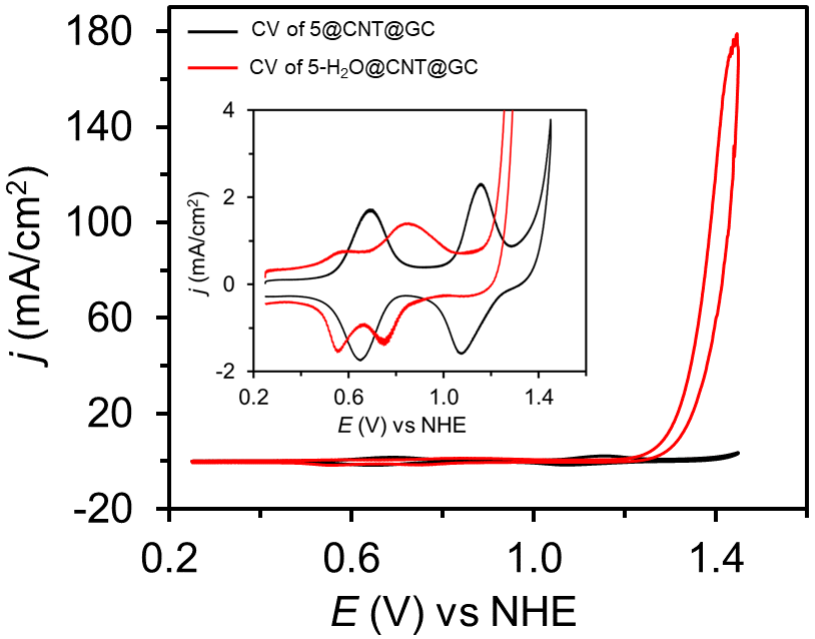

Figure S16. CV of **5@CNT@GC** (black line) and **5-H_2O@CNT@GC** (red line) in 1M phosphate buffer (pH 7) at scan rate of 100 mV/s. Inset*:* enlargement of the non-catalytic redox waves. Conditions: $\Gamma_{5\text{-}H2O}$ = 9.7 nmol·cm^{-2}.

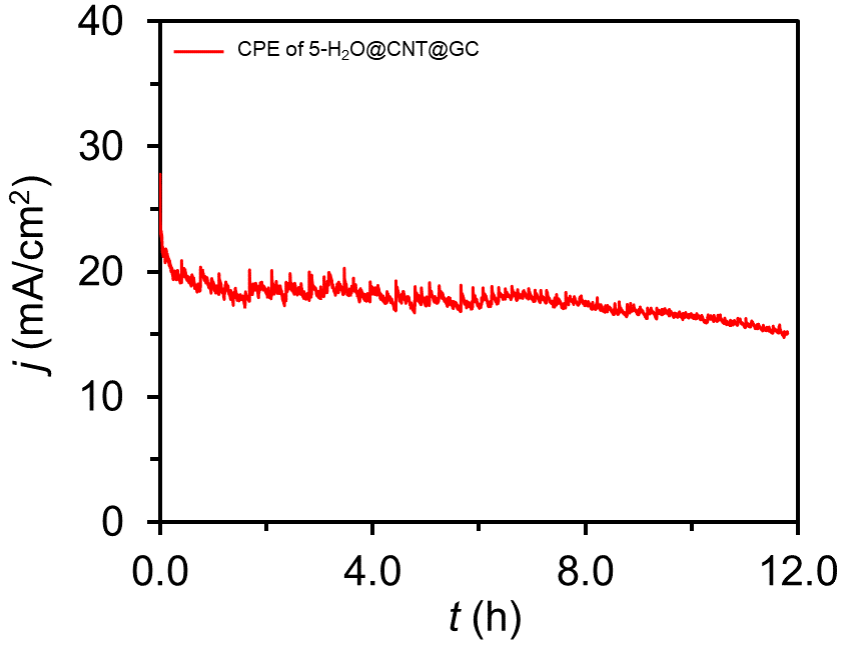

Figure S17. Controlled potential electrolysis (CPE) of **5-H_2O@CNT@GC** at 1.45 V vs NHE in 1 M phosphate buffer (pH 7) during 12 h. Conditions: $\Gamma_{5\text{-}H2O}$ = 9.5 nmol·cm^{-2}. Charge passed in 12 h is 52.6 C and TONs is 0.2×10^6.

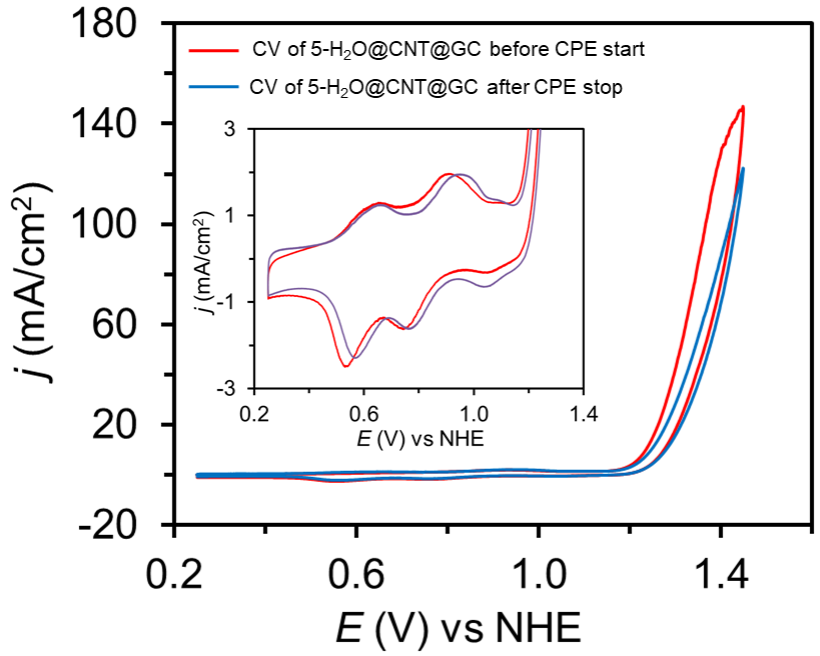

Figure S18. CV of **5-H_2O@CNT@GC** before (red line) and after (blue line) CPE experiment at 1.45 V vs NHE for 12 h in a freshly prepared 1M phosphate buffer solution (pH 7) at a scan rate of 100 mV/s. Inset: enlargement of the non-catalytic redox waves. Conditions: $\Gamma_{5\text{-}H2O}$ = 9.5 nmol·cm^{-2}.

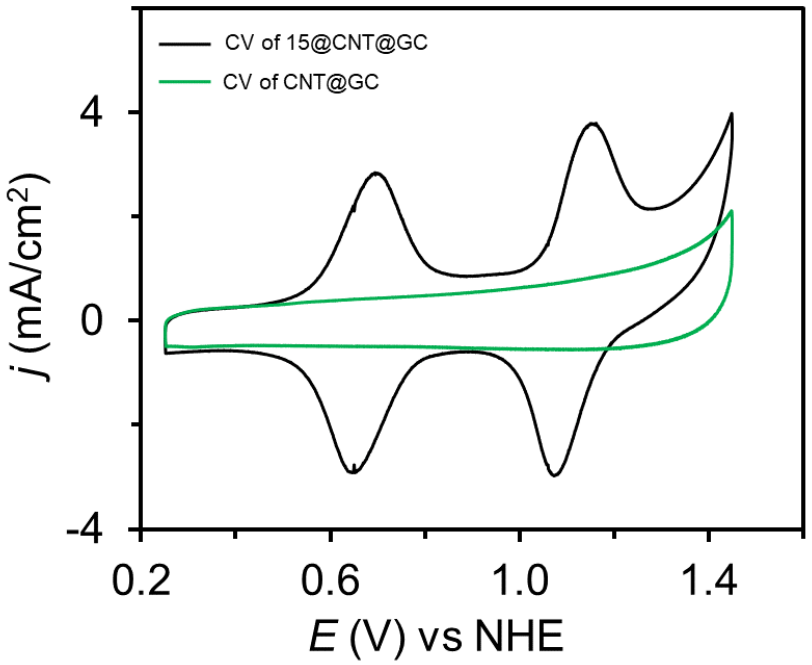

Figure S19. CV of **15@CNT@GC** (black line) and the blank (green line) in 1M phosphate buffer (pH 7) at a scan rate of 100 mV/s. Conditions: Γ_{15} = 21.2 nmol·cm^{-2}.

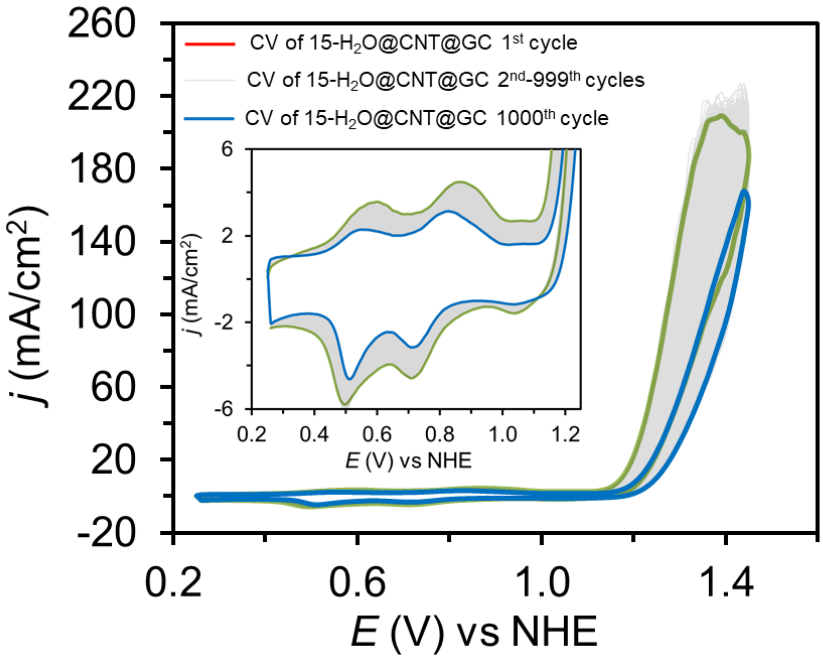

Figure S20. CV evolution of **15-H_2O@CNT@GC** during 1000 repetitive CV cycles in 1 M phosphate buffer (pH 7), red line corresponds to the first cycle, grey line is 2nd– 999th cycles and blue line is the 1000th cycle at a scan rate of 100 mV/s. Inset: enlargement of the non-catalytic redox waves. Conditions: $\Gamma_{15\text{-}H2O}$ = 17.3 nmol·cm^{-2}.

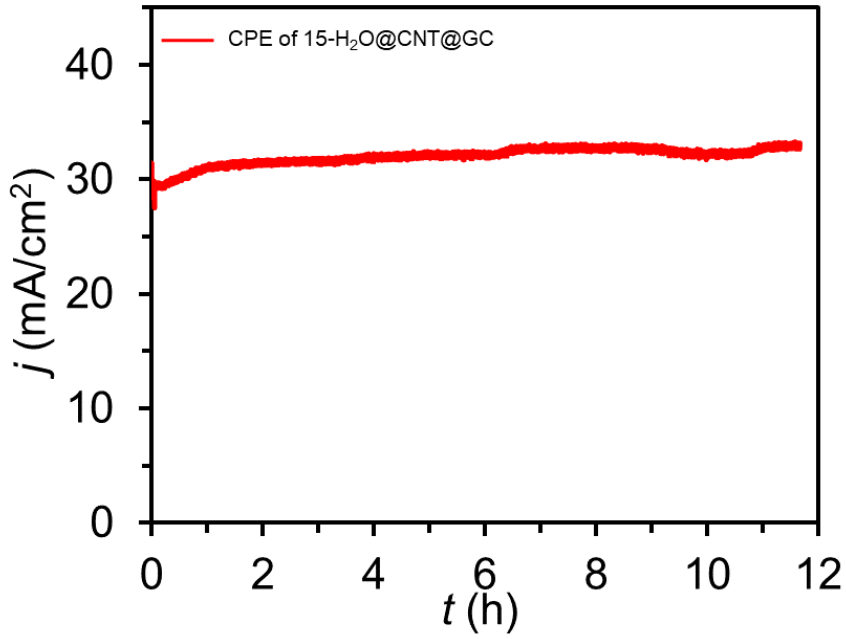

Figure S21. Controlled potential electrolysis (CPE) of **15-H₂O@CNT@GC** at 1.45 V vs NHE in 1 M phosphate buffer (pH 7) during 12 h. Conditions: $\Gamma_{15\text{-}H2O}$ = 17.5 nmol·cm^{-2}. Charge passed in 12 h is 94.1 C and TONs is 0.2×10^{6}.

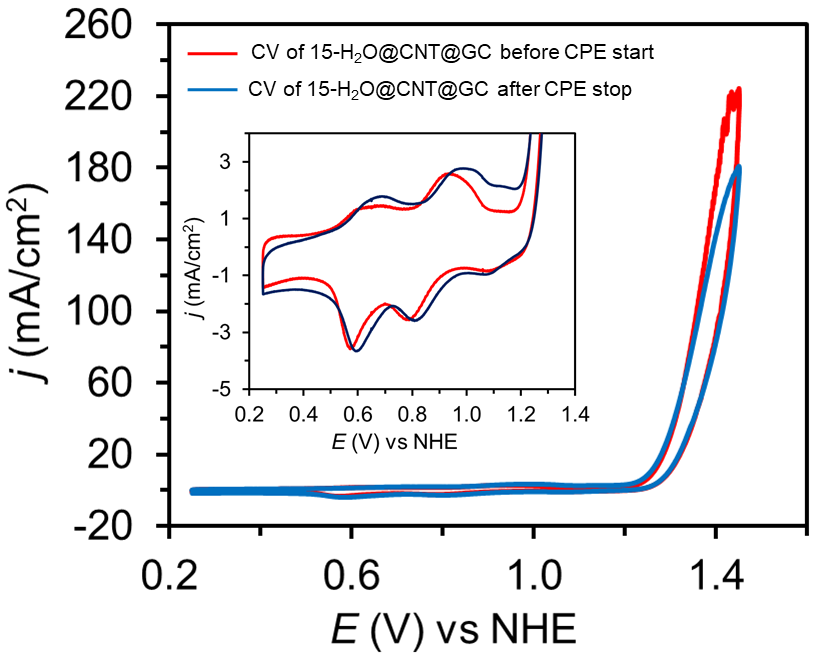

Figure S22. CV of **15-H₂O@CNT@GC** before (red line) and after (blue line) CPE experiment at 1.45 V vs NHE for 12 h in a freshly prepared 1 M phosphate buffer solution (pH 7) at a scan rate of 100 mV/s. Inset: enlargement of the non-catalytic redox waves. Conditions: $\Gamma_{15\text{-}H2O}$ = 17.5 nmol·cm^{-2}.

a)

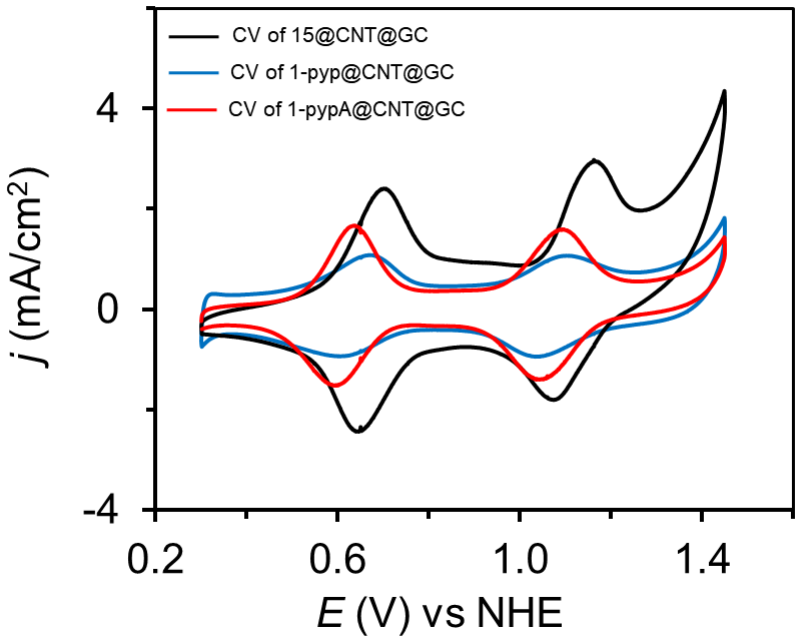

b)

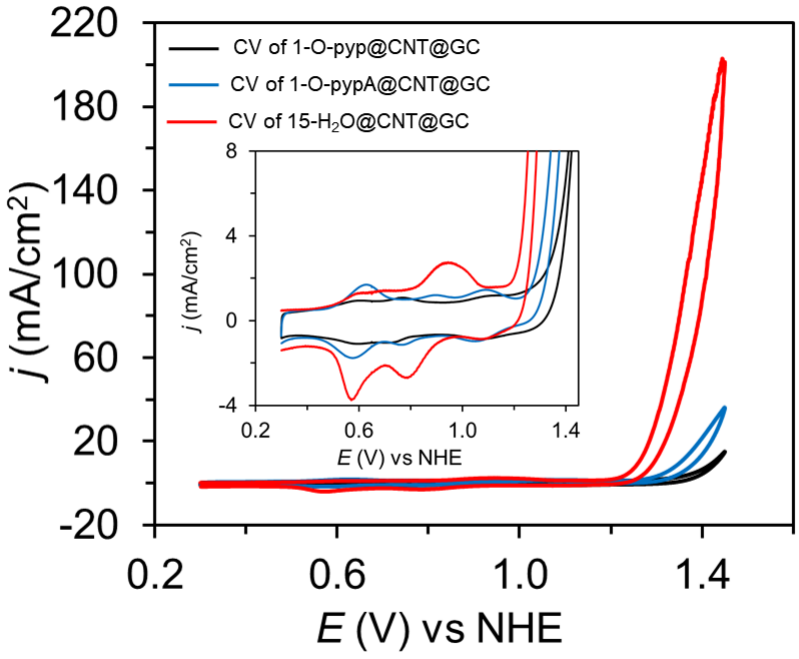

Figure S23. a) CV of **15@CNT@GC** (black line), **1-pyp@CNT@GC** (blue line) and **1-pypA@CNT@GC** (red line) in 1 M phosphate buffer (pH 7) at a scan rate of 100 mV/s; b) CV of **15-H_2O@CNT@GC** (red line**), 1-O-pyp@CNT@GC** (black line) and **1-O-pypA@CNT@GC** (blue line) in 1 M phosphate buffer (pH 7) at a scan rate of 100 mV/s. Inset: enlargement of the non-catalytic redox waves.

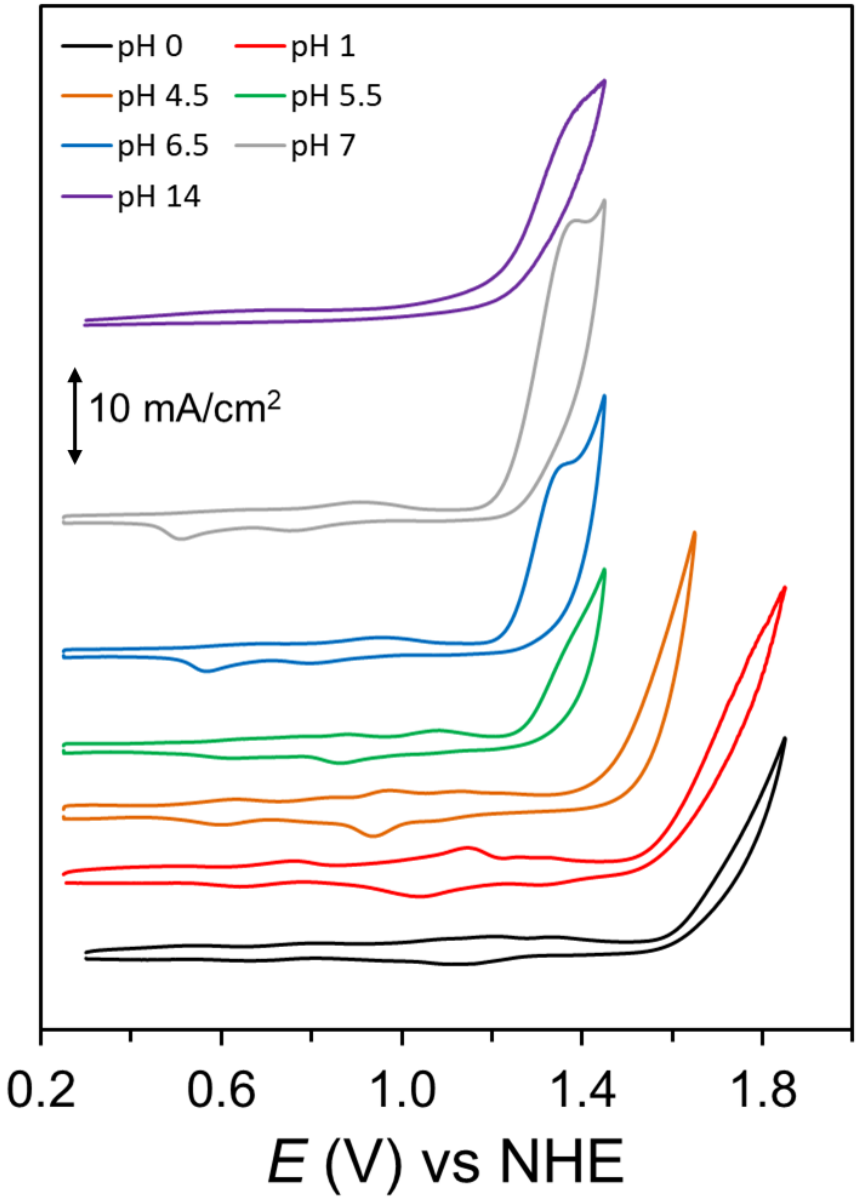

Figure S24. CV of **15-H_2O@CNT@GC** at different pH values in 0.1 M phosphate buffer solutions (pH 4.5-7), 1 M NaOH solution (pH 14), 1 M and 0.1 M CF_3SO_3H solution (pH 0 and 1, respectively) at a scan rate of 100 mV/s. Conditions: $\Gamma_{15\text{-}H2O}$ = 15±1.5 nmol·cm^{-2}.

Chapter 5

Table S2. Catalytic performance of related molecular anodes described previously in the literature.

Entry	Catalyst	*Γ* (nmol cm^{-2})	*pH*	*J* (mA cm^{-2})[d]	*E* vs NHE (V)	*Anchoring*	*Support*
1[tw]	5@CNT	14	7	-	-	CH-π	GC
2[tw]	15@CNT	21	7	-	-	CH-π	GC
3[tw]	1-pyp@CNT	5	7	-	-	π-π	GC
4[tw]	1-pypA@CNT	9	7	-	-	π-π	GC
5[tw]	5-H_2O@CNT	9.5	7	190	1.45	CH-π	GC
6[tw]	15-H_2O @CNT	17.5	7	240	1.45	CH-π	GC
7[tw]	1-O-pyp@CNT	0.4	7	20	1.45	π-π	GC
8[tw]	1-O-pypA@CNT	0.9	7	39	1.45	π-π	GC
9[6]	1-pyp@CNT	0.2	7	-	-	π-π	GC
10[6]	1-pypA@CNT	6.3	7	-	-	π-π	GC
11[6]	1-O-pyp@CNT	0.03	7	2.2	1.45	π-π	GC
12[6]	1-O-pypA@CNT	0.55	7	10.5	1.45	π-π	GC
13[7]	[(bpy-$CH_2PO_3H_2$)Ru(Mebimpy)(OH_2)]$^{2+}$	0.12[c]	5	0.015	1.85	[R-PO_3H^-]-M	ITO/FTO
14[8]	[(bpy-$CH_2PO_3H_2$)$_2$Ru(bpm)Ru(tpy)(OH_2)]$^{4+}$	85[c]	1	0.083	1.8	[R-PO_3H^-]-M	TiO_2/FTO
15[8]		0.7[c]	1	0.007	1.8	[R-PO_3H^-]-M	ITO
16[8]	[(bpy-$CH_2PO_3H_2$)$_2$Ru(bpm)Ru(Mebimpy)(OH_2)]$^{4+}$	0.57[c]	1	0.002	1.5	[R-PO_3H^-]-M	ITO
17[9]	[(bpy-PO_3H_2)$_2$Ru(4-Mebpy-4'-bimpy)Ru(tpy)(OH_2)]$^{4+}$	5.5	1	~0.27	1.55	[R-PO_3H^-]-M	nanoITO/GC
18[10]	[Ru(bda)(I-py)(py-Thiophene)]	0.96	7.2	5	1.3	P-thiophene	GC
19[10]	[Ru(bda)(F-Isoq)(py-Thiophene)]	0.96	7.2	4	1.3	P-thiophene	GC

Abbreviations: (a) tw refers to the catalysts reported in this work (b) CNT is MultiWall Carbon Nanotubes; pyp is 4-(pyren-1-yl)pyridine; pypA is 4-(pyren-1-yl)-N-(pyridin-4-ylmethyl)butanamide; bpy-$CH_2PO_3H_2$ is ([2,2'-bipyridine]-4,4'-diylbis(methylene))bis(phosphonic acid); bpm is 2,2'-bipyrimidine; Mebimpy is 2,6-bis(1-methylbenzimidazol-2-yl)pyridine; tpy is 2,2':6',2''-terpyridine; 4-Mebpy-4'-bimpy is 4-(methylbipyridin-4'-yl)-N-(benzimid)-N'-pyridine); bda is 2,2'-bipyridine–6,6'–dicarboxylate; I-py is 4-iodopyridine; F-Isoq is 6-fluroisoquinoline. (c) Calculated from UV-vis measurements using the expression $\Gamma = A(\lambda)/[10^3\varepsilon(\lambda)]$, where $A(\lambda)$ and $\varepsilon(\lambda)$ are the absorbance and molar absorptivity at wavelength λ.(d) Calculated from CV or CPE experiments at the indicated potential (*E*).

O_2 Evolution experiments

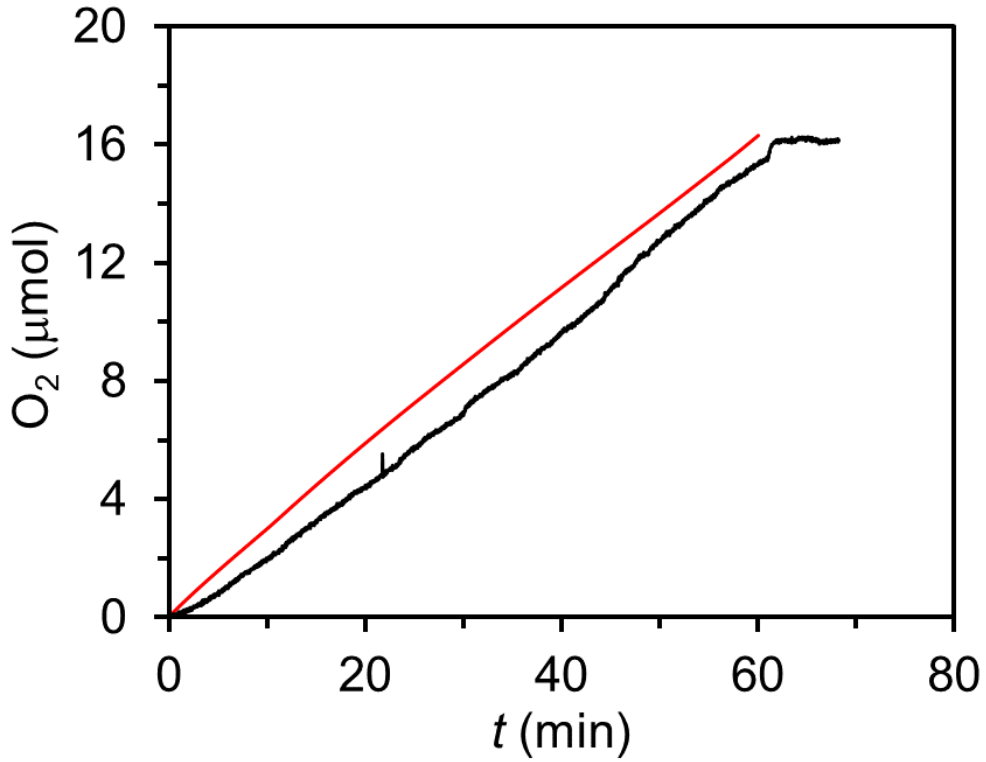

Figure S25. Oxygen evolution *vs*. time (min) for **15-H_2O@CNT@GC** ($\Gamma_{15\text{-}H2O}$ = 14.5 nmol·cm^{-2}) using a Clark probe electrode during a CPE at 1.45 V vs NHE in 1 M phosphate buffer (pH 7). Black line corresponds to the O_2 measured in the gas phase by a Clark electrode during CPE experiment, Red line corresponds to the theoretical amount of oxygen generated based on the charge passed during the CPE assuming 100% Faradaic efficiency. A Faradaic efficiency value of 99.1% was calculated at 70 min. ***Note:*** The applied potential was stopped at 60 min, but the O_2 evolution continued until 70 min due to the O_2 bubbles trapped at the working electrode.

Chapter 5

XANES & EXAFS

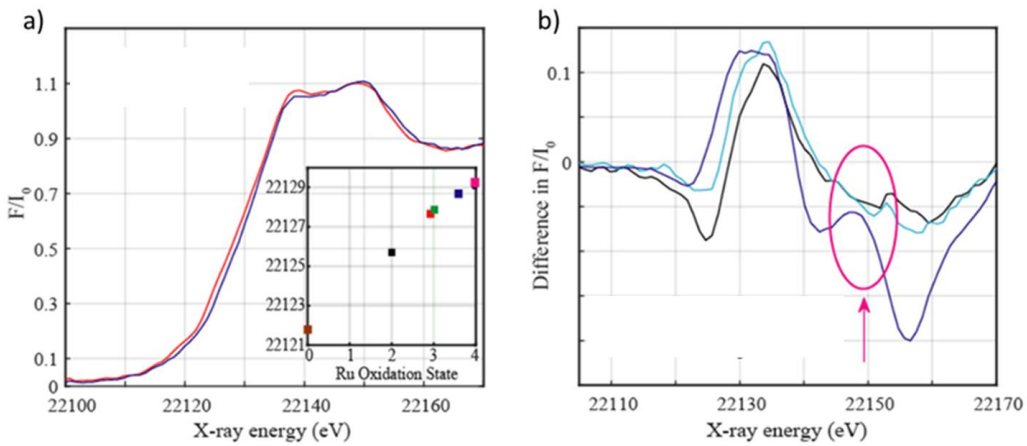

Figure S26. a) Normalized XANES spectra of **15@CNT@GC** on GC surface after deposition (red line) and **15-H_2O@CNT@GC** after catalysis (blue line). b) Difference normalized XANES spectra for: **15@CNT@GC** (Ru^{III}) on GC surface after deposition (black line), **15-H_2O@CNT@GC** (Ru^{IV}) on GC surface after catalysis (light blue line), and RuO_2 (Ru^{IV}) (blue line).

Table S3: Comparison of XANES energies for all Ru complexes on GC plates.

Sample	Energy at Normalized Fluorescence 0.5 (eV)	**Percentage Presence of Ru(II),Ru(III) and Ru(IV)**	**REF**
Ru^0	22121.74	--	
15	22125.71	**100 % Ru(II)**	**tw**
15@CNT@GCp	22127.70	**6 % Ru(II) + 94 % Ru(III)**	**tw**
1-pyp@CNT@GCp	22127.83	**100 % Ru(III)**	Ref6
15-O@CNT@GCp	22128.68	**41 % Ru(III) + 59 % Ru(IV)**	**tw**
RuO_2	22129.18	**100 % Ru(IV)**	**tw**

Table S4. Summary of EXAFS Fits parameters

Sample	Shell,N	R, Å
15	Ru-N/O,5 Ru-N, 1	2.02 2.49
15-O@CNT@GCp	Ru-N/O,6 Ru-O, 0.6 Ru-O, 0.4	1.99 1.64 2.56

Table S5. EXAFS Fits parameters

Sample	Fit	Peak	Shell,N	R, Å	E_0	ss.^{2} (10^{-3})	R-factor	Reduced Chi-square
15-@CNT@GC	1	1	Ru-N/O, 6	2.04	-7.5	22.1	0.0131	43
	2	I	Ru-N/O,5 Ru-N,1	2.05 2.30	-5.1	18.4	0.0131	43
	3	**All**	**Ru-N/O,5** **Ru-N, 1** **Ru-C,8** **Ru-C,5** **Ru-C,8** **Ru-C,5**	**2.02** **2.49** **2.96** **3.36** **3.63** **4.01**	**-9.6**	**20.3** **20.3** **18.4** **12.7** **59.3** **3.5**	**0.0299**	**43**
GC as deposited	14	I	Ru-N/O, 7	2.032.49	-12.9	13.1	0.1694	480
	15	I	Ru-N/O,6 Ru-O,1	2.04 2.34	-9.5	10.0 10.0	0.1130	424
	16	**All**	**Ru-N/O,6** **Ru-O, 1** **Ru-C,8** **Ru-C,5** **Ru-C,8** **Ru-C,5**	**2.03** **2.35** **2.87** **3.43** **3.83** **3.97**	**-12.9**	**10.1** **10.1** **37.1** **8.1** **22.5** **2.2**	**0.1016**	**136**
GC after catalysis	17	**I**	Ru-N/O, 7	2.03	-8.5	14.7	0.0353	198
	18	**I**	Ru-N/O,6 Ru-O, 1	2.05 2.36	-5.2	11.6 11.6	0.0160	76
	19	**All**	Ru-N/O, 6 Ru-O, 1 Ru-C, 8 Ru-C, 5 Ru-C, 8 Ru-C, 5	2.04 2.51 3.03 3.35 3.55 3.99	-7.1	12.9 12.9 13.8 2.2 7.5 1.6	0.0340	105
	20	**All**	**Ru-N/O,6** **Ru-O, 0.4** **Ru-O,0.6** **Ru-C,8** **Ru-C,5** **Ru-C,8** **Ru-C,5**	**1.99** **2.56** **1.65** **3.05** **3.34** **3.54** **3.97**	**-8.7**	**14.7** **14.7** **1.4** **12.5** **0.5** **6.1** **1.9**	**0.0165**	**66**

Scanning Tunneling Microscopy

STM image was taken after immobilizing the complex **15** on the solid surface electrode. In this case a solution of **15** in TFE/ethylene glycol/1-phenyloctane was dropcasted onto an atomically flat surface of highly oriented pyrolytic graphite (HOPG).

Density Functional Theory

Top view

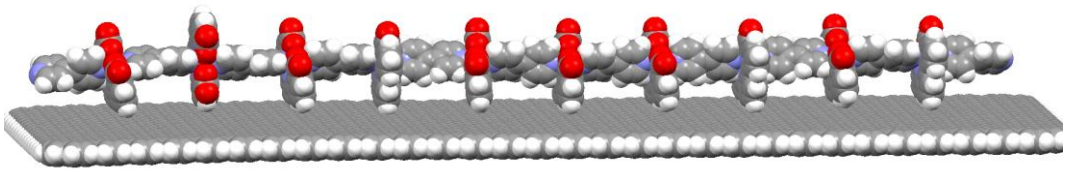

Side view

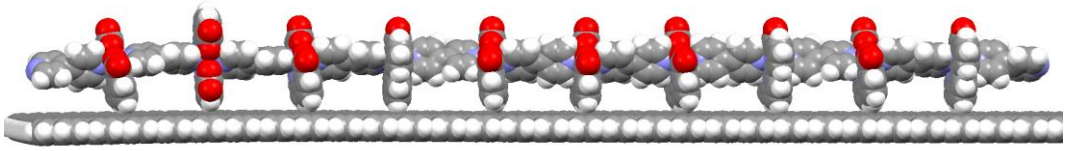

Figure S27. General view of the interaction of polymer **10** with a graphitic surface from different sides in DFT/MM model.

References

(1) Matheu, R.; Benet-Buchholz, J.; Sala, X.; Llobet, A. *Inorg. Chem.* **2017**, *57*, 1757.
(2) Simonelli, L.; Marini, C.; Olszewski, W.; Ávila Pérez, M.; Ramanan, N.; Guilera, G.; Cuartero, V.; Klementiev, K. *Cogent Physics* **2016**, *3*, 1231987.
(3) Ravel, B.; Newville, M. *J. Synchrotron Radiat.* **2005**, *12*, 537.
(4) Rehr, J. J.; Albers, R. C. *Rev. Mod. Phys.* **2000**, *72*, 621.
(5) Koningsberger, D.; Prins, R. **1988**.
(6) Creus, J.; Matheu, R.; Peñafiel, I.; Moonshiram, D.; Blondeau, P.; Benet-Buchholz, J.; García-Antón, J.; Sala, X.; Godard, C.; Llobet, A. *Angew. Chem. Int. Ed.* **2016**, *55*, 15382.
(7) Chen, Z.; Concepcion, J. J.; Jurss, J. W.; Meyer, T. J. *J. Am. Chem. Soc.* **2009**, *131*, 15580.
(8) Concepcion, J. J.; Jurss, J. W.; Hoertz, P. G.; Meyer, T. J. *Angew. Chem. Int. Ed.* **2009**, *48*, 9473.
(9) Norris, M. R.; Concepcion, J. J.; Fang, Z.; Templeton, J. L.; Meyer, T. J. *Angew. Chem. Int. Ed.* **2013**, *52*, 13580.
(10) Wang, L.; Fan, K.; Chen, H.; Daniel, Q.; Philippe, B.; Rensmo, H.; Sun, L. *Catal. Today* **2017**, *290*, 73.

Chapter 5

Chapter 6

A functional coordination polymer with 2 dimensional framework with a ruthenium catalyst as a core unit and 2,4,6-tris(4-pyridyl)-1,3,5-triazine as a linker is reported. This material shows solid state interactions between different layers and changes its properties from solution to solid state. It strongly and massively anchores on the surface of multiwall carbon nanotubes. This new hybrid material is a precursor of extremely active and robust water oxidation catalyst that shows impressive catalytic current densities in the range of 0.1-0.2 A/cm^2 with over 1 million Turnover number in 6 h.

Chapter 6

6. A Powerful Hybrid Molecular Electroanode for Efficient Water Oxidation Based on 2D Ru Coordination Polymer

Md Asmaul Hoque,[1,2] Marcos Gil-Sepulcre,[1] Carolina Gimbert-Suriñach,[1] Antoni Llobet[1,3]

[1] Institute of Chemical Research of Catalonia (ICIQ), Barcelona Institute of Science and Technology (BIST), Av. Països Catalans 16, 43007 Tarragona, Spain

[2]Departament de Química Física i Inorganica, Universitat Rovira i Virgili, Campus Sescelades, C/Marcel·lí Domingo, s/n, 43007 Tarragona, Spain

[3]Universitat Autònoma de Barcelona, Departament de Química, Cerdanyola del Vallès, 08193 Barcelona, Spain

VI

Contributions

Md Asmaul Hoque synthesized and characterized all the materials and performed the electrochemical, spectroscopic analysis together with the catalytic tests and prepared the manuscript.

Chapter 6

Abstract

We report a functional coordination polymer based on ruthenium within a 2 dimensional framework with general formula $[\{Ru(tda)\}(tpt)_3]_n$ where tda is the pentadentate equatorial ligand [2,2':6',2''-terpyridine]-6,6''-dicarboxylato and tpt is the bridging ligand 2,4,6-tris(4-pyridyl)-1,3,5-triazine. This polymer shows the existence of solid state interactions among 2D sheets within the packing structure upon changing from solution to the solid state. They are strongly and massively anchored on multiwall carbon nanotube (MWCNT) surfaces through supramolecular interactions. This new hybrid material is a precursor of extremely active and robust water oxidation anode that shows impressive catalytic current densities in the range of 0.1-0.2 A/cm^2 with over 1 million turnover number in 6 h.

Graphical Abstract

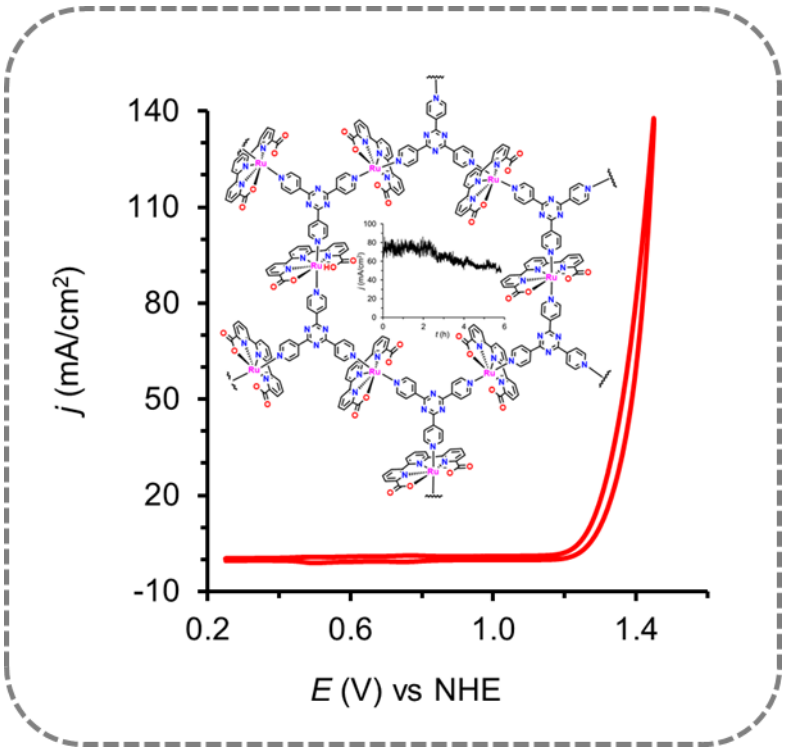

Keywords: 2D polymer, Solid state properties, Adsorption, Electroanode, Water oxidation

Chapter 6

6. 1. Introduction

The energy infrastructure for the future relies on our capacity to develop renewable technologies that can be converted into fuels.[1,2] Water splitting with sunlight is one of the most promising technology that can achieve this goal in the form of H_2 fuel.[3-6] Oxidation of water to molecular oxygen is the half reaction for the water splitting reaction that occurs at 1.23 V vs NHE at pH 0 and is both thermodynamically and kinetically unfavourable. In nature, this reaction is carried out by a Mn_4CaO_5 cluster of the photosystem II during the photosynthesis process.[7-10] Inspired by nature, there has been a tremendous progress in the field of water oxidation catalysis in the past few years including both molecular catalysts[11] and metal oxide catalysts.[12] Among the most efficient molecular water oxidation catalysts described so far are ruthenium based complexes due to the detailed understanding of their mode of action and the mechanistic details with the help of spectroscopic, electrochemical and analytical techniques together with the valuable complementary information provided by computational studies.[13]

The most extensively studied homogeneous water oxidation catalysts are based on mononuclear ruthenium complexes containing flexible, adaptative, multidentate and equatorial (FAME) ligands that are the fastest water oxidation catalyst reported in the literature[14-17] with TOF_{max} in the range of 10^2 to 10^4 s^{-1} which exceed by 1-2 orders of magnitude that of the oxygen evolving cluster in the natural photosystem II. Despite of the synthetic challenge to prepare polynuclear complexes, they have important benefits from the perspective of water oxidation catalyst (WOC). For example, multiple electronically coupled redox active metal centres can cooperate during the four-electron transfer needed for the water oxidation reaction. In addition, non-redox active ligand environment can exert the electronic perturbation over the redox active centres in the polynuclear system.[18-22]

On the other, hand study of heterogeneous catalyst based on transition metal based oxides or hydroxides in WOCs dated back to more than a half century ago.[22] This heterogeneous electrocatalysts exhibit greater stability and could readily be integrated into functional energy conversion devices such as fuel cells, electrolyzers and photoelectrochemical cells for water splitting.[23] The catalytic activity of these heterogeneous inorganic catalysts is still limited to harsh conditions that require either very high acidic or basic condition and lose their activity over time. Moreover, the catalytic activity with heterogeneous catalysts are difficult to tune as they are much less amenable to systematic modification of the active site. Hence, to mimic

natural photosynthesis and designing efficient water splitting device in neutral water still remains challenging.

Thus, constructing a molecularly well-defined and tunable heterogeneous catalyst that combines the advantages of both molecular homogeneous and metal oxide heterogeneous WOC is highly desirable. To achieve this goal, there are numerous ways of anchoring the molecular catalyst on the electrode ranging from those that utilize weak physisorption or electrostatic interactions[24-26] to those that form strong covalent linkages.[27,28] On the other hand, incorporation of molecular catalysts inside the metal organic frameworks (MOFs)[29-31] has also recently gained a significant attention. In this context, coordination polymers are very promising candidates for efficient heterogeneous catalyst for proton reduction[32,33] but they have been much less explored for the application on the water oxidation field.[34,35]

Recently, our group has reported the synthesis of the complex $[Ru(tda)(py)_2]$ (where tda is [2,2':6',2''-terpyridine]-6,6''-dicarboxylato and py is pyridine),[15] a precursor for the most powerful water oxidation catalyst described to date in the literature showing impressive TOF_{max} = 8.000 s^{-1} in neutral pH. Replacing the simple py axial ligand with pyrene substituted py, later our group reported the best hybrid molecular electroanode based on Ru-functionalized multiwall carbon nanotube (MWCNT) with over a million turnover number.[24] However, the absolute current density of this material range within 1-10 mA/cm^2 and for technological purposes, it is indispensable to reach much higher current densities, in the range of A/cm^2.

Here, we report for the first time that the ruthenium based 2-dimensional coordination polymer with Ru(tda) as a core and with 2,4,6-tris(4-pyridyl)-1,3,5-triazine (tpt) ligand as a linker, that can be easily and massively adsorbed on MWCNT. The resulting hybrid material is a powerful molecular electroanode for water oxidation to dioxygen with an impressive current densities above 0.1 A/ cm^2 and remarkable stability at neutral pH.

6. 2. Results and Discussion

6. 2. 1. Synthesis and Characterization

The 2-dimentional coordination polymer containing Ru-tda unit, **2D** polymer (Scheme 1) was synthesized by heating $[Ru(tda)(OH_2)_2]PF_6$[36] with 2,4,6-tris(4-pyridyl)-1,3,5-triazine with 1:1.5 molar ratio in trifluoroethanol at 78˚C in the presence of triethylamine for 3 days. The **2D** polymer was isolated through precipitation by adding methanol solvent into the reaction mixture at room temperature followed by washing with water, methanol, diethyl ether and air dried with almost quantitative yield. A similar product can be obtained using $[Ru(tda)(DMSO)(OH_2)]$[36] as a starting material. The surprising fact about this 2D polymer is that before isolation, it was completely soluble in trifluoroethanol but the isolated solid was partially soluble in the same solvent, clearly indicating the existence of solid state interactions among 2D sheets within the packing structure. These solid state interactions are further manifested by the change in color, from red in solution to violet in the solid state.

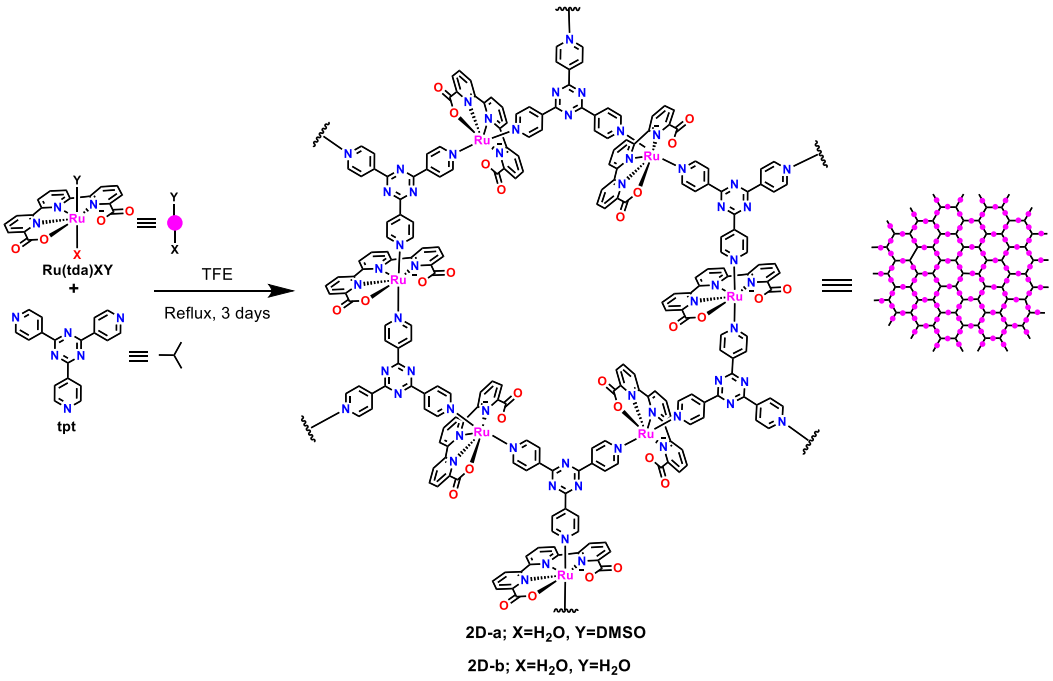

Scheme 1. Schematic representation of the synthesis of **2D** Polymer.

Powder X-ray diffraction measurements show that this **2D** polymer is semi crystalline in nature that might be due to the highly distorted structure of the whole molecule (Figure S1). UV-vis spectra of the polymer shows $\pi-\pi^*$ transitions due to the aromatic ligands below 350 nm and metal to ligand charge transfer (MLCT) d–π^* bands between 350 and 550 nm and are similar to those of the mononuclear complex $Ru(tda)(4,4'\text{-bpy})_2]$ (Chapter 5), where 4,4'-bpy is 4,4'-bypridine) with an additional strong transition at 240 nm. The latter additional

transition is due to the presence of the aromatic triazine bridging ligand present in the 2D polymer (Figure S2).

6. 2. 2. Anchoring on Graphitic Surface

The polymer **2D** shows very strong affinity for graphitic surfaces strongly absorbing on them. This behavior is similar to the parent 1D polymer described in Chapter 5 and in sharp contrast to the mononuclear [Ru(tda)(4,4'-bpy)$_2$] complex that does not adsorb. MWCNT were chosen as a solid conductive support due to their high surface area, high thermal and chemical stability, excellent electrical conductivity and insolubility in most solvents. The addition of a saturated solution of **2D** in trifluoroethanol to a suspension of MWCNT dispersed in tetrahydrofuran, results in the immediate decoloration of the final mixture, indicating the complete adsorption of the 2D polymer onto the MWCNT (Scheme S1 in the supporting information). This new hybrid material is represented as **2D@MWCNT**.

6. 2. 3. Electrochemistry

6. 2. 3. 1. Redox Properties in Homogeneous Solution

The electrochemical behavior of **2D** was analyzed by cyclic voltammetry (CV) and differential pulse voltammetry (DPV) experiments in trifluoroethanol (TFE) containing 0.1 M of [(*n*-Bu)$_4$N][PF$_6$] (TBAH). All the redox potentials reported in this work have been measured by using Hg/Hg$_2$SO$_4$ (Satuarated solution of K$_2$SO$_4$) reference electrode and have been converted to normal hydrogen electrode (NHE) by adding 0.65 V to the measure potential.

As shown in Figure 1, **2D** shows two one electron redox features at $E_{1/2}$ = 0.69 V (ΔE = 60 mV) and $E_{1/2}$ = 1.18V (ΔE = 80 mV) that correspond to the III/II and IV/III redox couples of the ruthenium in the **2D** polymer respectively in trifluoroethanol and are similar to the analogous mononuclear complexes.[15]

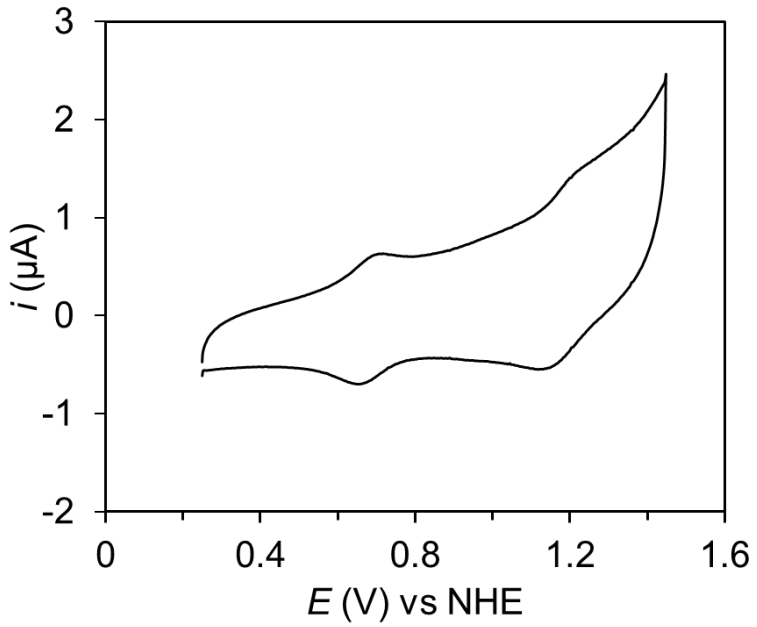

Figure 1. CV of the **2D** polymer in 0.1 M solution of TBAH in trifluoroethanol solvent.

6. 2. 3. 2. Redox Properties on Solid Surface and Catalysis

The **2D** polymer is insoluble in water and it is not possible to carry out homogeneous electrochemistry in this solvent. However, this polymer can be strongly adsorbed on MWCNT and generate the hybrid material denoted as **2D@MWCNT**. This hybrid material was then dropcasted on graphitic electrode such as glassy carbon disk (GC$_d$) or glassy carbon plates (GC$_p$) denoted as **2D@MWCNT@GC$_d$** and **2D@MWCNT@GC$_p$** respectively and used to

analyze it electrochemical properties in aqueous conditions. This hybrid material shows two chemically reversible and electrochemically quasi-reversible waves at $E_{1/2}$ = 0.71 V (ΔE = 50 mV) and 1.17 V (ΔE = 40 mV) attributed to the $Ru^{III/II}$ and $Ru^{IV/III}$ couples respectively (Figure 2 black line). This CV clearly indicates that the redox potential obtained here are very similar to the mononuclear $[Ru(tda)(pyp)_2]$[24] complex containing a pyrene group in the axial pyridine ligand in solution at the same pH and suggesting each Ru center of the polymer acts in a similar manner as the discrete molecule. It also indicate that all the Ru centers of the polymer have the same access to the electrode during electron transfer process. The total amount of the catalyst precursor anchored on the surface of the electrode turned out to be Γ_{2D}= 5.1±1 nmol/cm^2 based on electrochemical response (loading was calculated by taking the average of both anodic and cathodic charge under both Ru $^{III/II}$ and Ru $^{IV/III}$ waves, see supporting information for details). The high affinity of the **2D** polymer for graphitic surfaces allows us to obtain large surface coverages, as compared to other anchoring strategies. For instance, the surface coverage in **2D@MWCNT** is about 50 times higher than the typical phosphonates in oxides surfaces (Table S1 in the supporting information).[37]

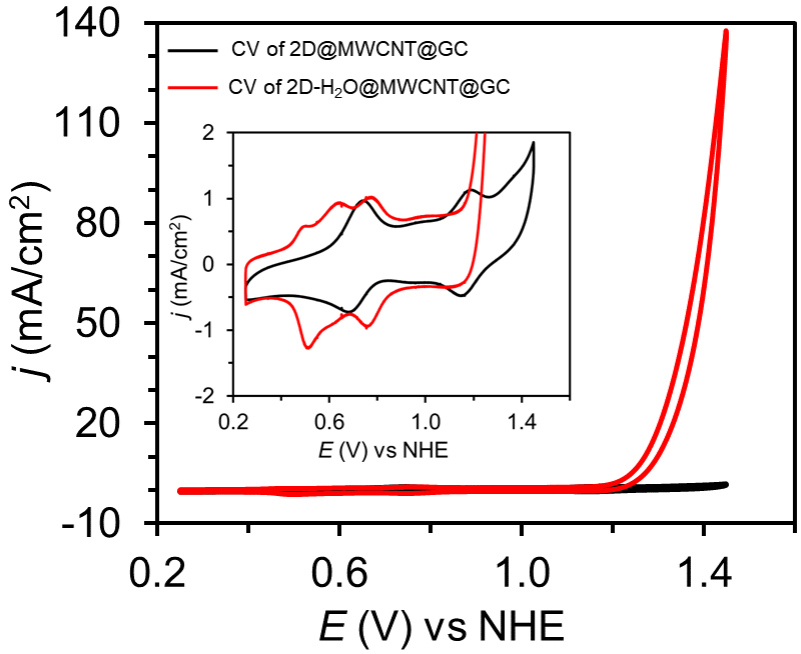

Figure 2. a) CV of **2D@MWCNT@GC** (black line) and **2D-H_2O@MWCNT@GC** (red line) in 1 M phosphate buffer (pH 7) at scan rate of 100 mV/s. *Inset:* Zoom in the region of the non-catalytic redox waves. Surface coverage: Γ_{2D} = 4.8 nmol·cm^{-2}, $\Gamma_{2D\text{-}H2O}$ = 4.2 nmol·cm^{-2}.

To generate the active catalyst at the surface of the electrode, a bulk electrolysis at 1.25 V for 1000 s was applied under stirring at pH 12. During this process, the initial Ru^{II} species oxidizes to oxidation state Ru^{IV} and the coordination of aquo occurs at the Ru metal center, generating

an active hybrid material denoted as **2D-H_2O@MWCNT@GC**. Once generated, this electrode was removed from pH 12, rinsed with water and then introduced to a fresh solution at pH 7. This active hybrid material **2D-H_2O@MWCNT@GC** shows two redox waves at $E_{1/2}$ = 0.51 V (ΔE = 120 mV) and 0.71 V (ΔE = 20 mV) attributed to the $Ru^{III/II}$ and $Ru^{IV/III}$ couples respectively (Figure 2 red line). As can be seen from this Figure 2, two additional redox waves appear with anodic peak at $E_{p,a}$ = 0.44 V and cathodic peak at $E_{p,c}$ = 0.55 V that are pH dependent suggesting they are involved in proton coupled electron transfer (PCET) processes that point out to the presence of Ru-OH species (Figure S4). These additional redox waves might belong to different redox couples with overlapping electroactivity, due to slightly different coordinating environment around the metal center. Finally, a large electrocatalytic current corresponding to the oxidation of water to molecular oxygen associated with the $Ru^{V/IV}$ couple occurs with onset potential at 1.2 V, manifesting very high activity of this catalytic hybrid material (Figure 2 red line). Moreover, current densities above 140 mA/cm^2 at 1.45 V *vs*. NHE were achieved in neutral pH 7 phosphate buffer solution with molecularly well define hybrid material, that is around 15 times higher than the best reported molecular electroanode[24] and almost two orders of magnitude higher than any other molecular catalyst anchored on the solid surface. These results prove the benefits of having a well-defined polynuclear material with a high density of catalytic centers.[25,37]

VI

The **2D-H_2O@MWCNT@GC** electrode shows exceptional stability and durability for oxygen evolution reaction. The long-term stability of this electrode was evaluated at pH 7 based on repetitive CV cycles and bulk electrolysis. After 1000 repetitive CV cycles from 0.25 V to 1.45 V at pH 7 solution with 100 mV/s scan rate shows deterioration of the catalytic current from 70 mA/cm^2 to 20 mA/cm^2 (Figure S3a). The long-term durability of this hybrid material was analysed by applying constant potential at 1.45 V at pH 7. The initial current density reaches 75 mA/cm^2 and remain constant for 2 h. After this time, the current density starts to decrease and decays to 50 mA/cm^2 after 6 h (Figure 3). The decay of the current density might be due to the de-attachment of the active catalyst from the MWCNT or the partial de-attachment of the **2D-H_2O@MWCNT** material from the GC electrode or convert to some other species with no catalytic activity. The cyclic voltammetry after 6 h control potential electrolysis shows that the catalyst is still present on the electrode surface with slightly less catalytic current (Figure S3b). Moreover, a small increase of the capacitive current can be attributed to the partial oxidation of electrode surface during this long experiment at this high potential. After 6 h of control potential electrolysis experiment in pH 7 at 1.45 V gives a remarkable turnover number (TONs) of 1.3 million (Figure S8).

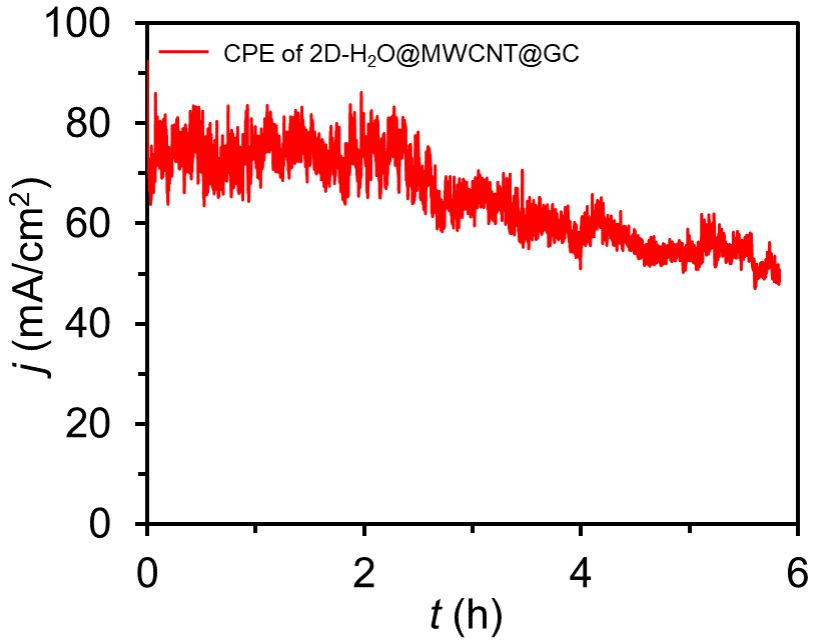

Figure 3. Controlled potential electrolysis (CPE) of **2D-H_2O@MWCNT@GC** at 1.45 V vs NHE in 1 M phosphate buffer (pH 7) during 6 h. Surface coverage: $\Gamma_{2D\text{-}H2O}$ = 4.1 nmol·cm^{-2} (TONs was calculated up to 6 h and turns out to 1.3 million).

The mass loading of the **2D** polymer is four times lower as compare to **1D** polymer described in Chapter 5 but the relative current density with respect to the mass loading, for the **2D** polymer is 2.5 times better than that of the **1D** polymer (Table S1). The extraordinary activity of this **2D-H_2O@MWCNT@GC** might be due to the presence of some unique supramolecular interaction present between the 2D layers of the coordination polymers when they are anchored on MWCNT surface.

Interestingly, the **2D** polymer also adsorbed strongly on the glassy carbon electrode in the absence of MWCNT to give the hybrid **2D@GC**. As can be seen in Figure S5, the cyclic voltammetry of the surface functionalized glassy carbon electrode via physisorption was carried out in pH 7 phosphate buffer. It shows two one electron redox features at $E_{1/2}$ = 0.64 V and $E_{1/2}$ = 1.13 V, which correspond to the III/II and IV/III redox couples of the Ru-polymer respectively, clearly confirming the adsorption of the Ru-polymer on the surface of the GC electrode (Figure S5a black line). The activation of **2D@GC** was performed following the same procedure used for **2D@MWCNT@GC** giving the hybrid electrode **2D-H_2O@GC**, which showed significant electrocatalytic current corresponding to oxidation of water to molecular oxygen (Figure S5a red line). The catalyst on the electrode shows robustness without any deactivation of the catalysis upon 100 repetitive CV cycles (Figure S6).

All these results manifest the importance of supramolecular/polynuclear nature of the **2D** materials prepared in this work for the production of highly active and robust electroanodes for water splitting devices, that can perform similar or sometimes better than commercial electrolyzer.[38] Finally, an analysis of the gas phase of a bulk electrolysis experiment of this molecular hybrid anode at an applied potential of 1.45 V for 1.5 h confirms the evolution of O_2 gas with a faradaic efficiency of 99.5% (Figure S7), showing the robustness of this system.

6. 3. Conclusion

In conclusion, we have reported for the first time a functional 2D coordination polymer for water oxidation catalysis based on the Ru(tda) core. This material strongly adsorbs on MWCNT and can be used to build extremely active and highly robust molecular electroanodes for the oxidation of water to molecular oxygen with 1.3 million Turn over number in 6 h and is about six times higher than **1D** polymer with 0.2 million TON over 12 h under the same condition (Chapter 5). Current density achieved by this material is comparable to that of metal oxide catalysts in commercial electrolyzers but with two orders of magnitude lower mass loading.[38] The results show that the judicious design of functional coordination polymer can open a new horizon for the generation of molecularly well-defined heterogeneous catalyst for energy application devices.

6. 4. References

(1) McKone, J. R.; Lewis, N. S.; Gray, H. B. *Chem. Mater.* **2013**, *26*, 407.
(2) Montoya, J. H.; Seitz, L. C.; Chakthranont, P.; Vojvodic, A.; Jaramillo, T. F.; Nørskov, J. K. *Nat. Mater.* **2017**, *16*, 70.
(3) Lewis, N. S. *Science* **2016**, *351*, 1920.
(4) Karkas, M. D.; Verho, O.; Johnston, E. V.; Åkermark, B. r. *Chem. Rev.* **2014**, *114*, 11863.
(5) Kunz, V.; Schmidt, D.; Röhr, M. I.; Mitrić, R.; Würthner, F. *Adv. Energy Mater.* **2017**, *7*, 1602939.
(6) Berardi, S.; Drouet, S.; Francas, L.; Gimbert-Suriñach, C.; Guttentag, M.; Richmond, C.; Stoll, T.; Llobet, A. *Chem. Soc. Rev.* **2014**, *43*, 7501.
(7) Croce, R.; Van Amerongen, H. *Nat. Chem. Biol.* **2014**, *10*, 492.
(8) McEvoy, J. P.; Brudvig, G. W. *Chem. Rev.* **2006**, *106*, 4455.
(9) Ferreira, K. N.; Iverson, T. M.; Maghlaoui, K.; Barber, J.; Iwata, S. *Science* **2004**, *303*, 1831.
(10) Suga, M.; Akita, F.; Hirata, K.; Ueno, G.; Murakami, H.; Nakajima, Y.; Shimizu, T.; Yamashita, K.; Yamamoto, M.; Ago, H. *Nature* **2015**, *517*, 99.
(11) Matheu, R.; Garrido-Barros, P.; Gil-Sepulcre, M.; Ertem, M. Z.; Sala, X.; Gimbert-Suriñach, C.; Llobet, A. *Nat. Rev. Chem.* **2019**, *3*, 331.
(12) Song, F.; Bai, L.; Moysiadou, A.; Lee, S.; Hu, C.; Liardet, L.; Hu, X. *J. Am. Chem. Soc.* **2018**, *140*, 7748.
(13) Matheu, R.; Ertem, M. Z.; Gimbert-Suriñach, C.; Sala, X.; Llobet, A. *Chem. Rev.* **2019**, *119*, 3453.

(14) Duan, L.; Bozoglian, F.; Mandal, S.; Stewart, B.; Privalov, T.; Llobet, A.; Sun, L. *Nat. Chem.* **2012**, *4*, 418.
(15) Matheu, R.; Ertem, M. Z.; Benet-Buchholz, J.; Coronado, E.; Batista, V. S.; Sala, X.; Llobet, A. *J. Am. Chem. Soc.* **2015**, *137*, 10786.
(16) Hoque, M. A.; Benet-Buchholz, J.; Llobet, A.; Gimbert-Suriñach, C. *ChemSusChem.* **2019**, *12*, 1949.
(17) Shatskiy, A.; Bardin, A. A.; Oschmann, M.; Matheu, R.; Benet-Buchholz, J.; Eriksson, L.; Kärkäs, M. D.; Johnston, E. V.; Gimbert-Suriñach, C.; Llobet, A.; Åkermark, B. *ChemSusChem.* **2019**, *12*, 2251.
(18) Richmond, C. J.; Llobet, A. *Catal. Sci. Technol.* **2016**, *6*, 6697.
(19) Mognon, L.; Mandal, S.; Castillo, C. E.; Fortage, J.; Molton, F.; Aromí, G.; Benet-Buchhlolz, J.; Collomb, M.-N.; Llobet, A. *Chem. Sci.* **2016**, *7*, 3304.
(20) Schulze, M.; Kunz, V.; Frischmann, P. D.; Würthner, F. *Nat. Chem.* **2016**, *8*, 576.
(21) Zhang, L.; Gao, Y.; Liu, Z.; Ding, X.; Yu, Z.; Sun, L. *Dalton. Trans.* **2016**, *45*, 3814.
(22) Coehn, A.; Gläser, M. *Z. anorg. allg.* **1902**, *33*, 9.
(23) McCrory, C. C.; Jung, S.; Ferrer, I. M.; Chatman, S. M.; Peters, J. C.; Jaramillo, T. F. *J. Am. Chem. Soc.* **2015**, *137*, 4347.
(24) Creus, J.; Matheu, R.; Peñafiel, I.; Moonshiram, D.; Blondeau, P.; Benet-Buchholz, J.; García-Antón, J.; Sala, X.; Godard, C.; Llobet, A. *Angew. Chem. Int. Ed.* **2016**, *55*, 15382.
(25) Li, F.; Zhang, B.; Li, X.; Jiang, Y.; Chen, L.; Li, Y.; Sun, L. *Angew. Chem. Int. Ed.* **2011**, *50*, 12276.
(26) Toma, F. M.; Sartorel, A.; Iurlo, M.; Carraro, M.; Parisse, P.; Maccato, C.; Rapino, S.; Gonzalez, B. R.; Amenitsch, H.; Da Ros, T. *Nat. Chem.* **2010**, *2*, 826.
(27) Ashford, D. L.; Lapides, A. M.; Vannucci, A. K.; Hanson, K.; Torelli, D. A.; Harrison, D. P.; Templeton, J. L.; Meyer, T. J. *J. Am. Chem. Soc.* **2014**, *136*, 6578.
(28) Matheu, R.; Francàs, L.; Chernev, P.; Ertem, M. Z.; Batista, V.; Haumann, M.; Sala, X.; Llobet, A. *ACS Catal.* **2015**, *5*, 3422.
(29) Wang, C.; Wang, J.-L.; Lin, W. *J. Am. Chem. Soc.* **2012**, *134*, 19895.
(30) Hansen, R. E.; Das, S. *Energy Environ. Sci.* **2014**, *7*, 317.
(31) Johnson, B. A.; Bhunia, A.; Ott, S. *Dalton. Trans.* **2017**, *46*, 1382.
(32) Zhang, G.; Lan, Z. A.; Wang, X. *Angew. Chem. Int. Ed.* **2016**, *55*, 15712.
(33) Li, L.; Cai, Z.; Wu, Q.; Lo, W.-Y.; Zhang, N.; Chen, L. X.; Yu, L. *J. Am. Chem. Soc.* **2016**, *138*, 7681.
(34) Zheng, T.; Li, L. *New J. Chem.* **2018**, *42*, 2526.
(35) Najafpour, M. M. *Mol. Cryst. Liq. Cryst.* **2010**, *517*, 167.
(36) Matheu, R.; Benet-Buchholz, J.; Sala, X.; Llobet, A. *Inorg. Chem.* **2017**, *57*, 1757.
(37) Chen, Z.; Concepcion, J. J.; Jurss, J. W.; Meyer, T. J. *J. Am. Chem. Soc.* **2009**, *131*, 15580.
(38) Carmo, M.; Fritz, D. L.; Mergel, J.; Stolten, D. *Int. J. Hydrog. Energy* **2013**, *38*, 4901.

6. 5. Supporting Information

Table of Contents

Experimental Section and Spectroscopic Characterization

Experimental section

Figure S1. Powder X-ray diffraction of **2D** polymer

Figure S2. UV-Vis absorption spectrum of **2D** polymer

Electrochemistry

Figure S3. Electrochemical data of **2D-H_2O@MWCNT@GC**

Figure S4. CV of **2D-H_2O@MWCNT@GC** in different pHs

Figure S5-S6. Electrochemical data of **2D-H_2O @GC**

Figure S7. Oxygen evolution profile of **2D-H_2O@MWCNT@GC**

Figure S8. plot of TON *vs.* time of **2D-H_2O@MWCNT@GC**

Table S1. Electrochemical data for anchored molecule

References

Chapter 6

Experimental Section

Materials

All the chemicals used in this work were provided by Sigma Aldrich and they have been used without further purification unless explicitly indicated. $RuCl_3 \cdot \times H_2O$ was purchased from Alfa-Aesar, 6,6'-Dicarboxylic acid-[2,2':6',2"-terpyridyl] (H_2tda), the precursor complexes $\{RuCl_2(DMSO)_4\}$ and $Ru(tda)(DMSO)(OH_2)$ were prepared according to a reported procedure.[1]

MultiWall Carbon Nanotubes (MWCNTs) were purchased from HeJi, Inc. (Zengcheng city, China) in bulk with >95% purity, >50 nm OD and ~10 μm length.

Solvents were dried with a SPS® system and degassed by bubbling nitrogen before starting the reactions. High purity de-ionized water used for the electrochemistry experiments was obtained by passing distilled water through a nanopure Mili-Q water purification system. For other spectroscopic and electrochemical studies, HPLC-grade solvents were used. GC plate electrodes (GC_p) were purchased from HTW, Germany, and are made of glassy carbon SIGRADUR® with the dimensions 20x10x0.18 mm.

Instrumentation and Methods

The pH of the solutions was determined by a pH meter (CRISON, Basic 20^+) calibrated before measurements through standard solutions at pH 4.01, 7.00 and 9.21.

Powder X-ray diffraction (PXRD) was performed on D8 Advanced Powder Diffractometer (Bruker) equipped with a vertical 2theta-theta goniometer in transmission configuration, with a Kα1 germanium monochromator for Cu radiation (λ = 1.5406 Å), at a scan step of 0.02° s^{-1} from 10° to 80°.

UV-vis spectrometry was performed using a Cary 50 (Varian) UV-vis spectrophotometer.

Electrochemical Methods

All the electrochemical experiments were performed in an IJ-Cambria CHI-660 potentiostat. Either a glassy carbon disk (GC_d, ϕ = 0.3 cm, S = 0.07 cm^2) or a glassy carbon plate (GC_p, 20 mm x 10 mm x 0.18 mm) were used as working electrode (WE). In the case of GC_p the surface dipped in the electrochemical solution was 1 cm^2. A Pt disk (ϕ = 0.3 cm, S = 0.07 cm^2) was used as counter electrode (CE) and a Hg/Hg_2SO_4 (K_2SO_4 sat.) electrode was used as a reference electrode (RE), except for the oxygen monitored bulk electrolysis that a Ag/AgCl (KCl sat.) was used as RE and a Pt mesh as a CE. Electrochemical experiments in organic solvent were carried

out in trifluoroethanol (TFE) containing 0.1 M of [(*n*-Bu)$_4$N][PF$_6$] (TBAH) as supporting electrolyte.

Preparation of different pH phosphate buffers:

- *pH 2, Ionic strength 0.1 M:* H_3PO_4 (0.104 mol, 10.19 g) and NaH_2PO_4 (0.0955 mol, 11.45 g) in 1 L of Mili-Q water.
- *pH 7, Ionic strength 1 M:* NaH_2PO_4 (0.153 mol, 18.31 g) and Na_2HPO_4 (0.282 mol, 40.07 g) in 1 L of Mili-Q water.
- *pH 7, Ionic strength 0.1 M:* NaH_2PO_4 (0.019 mol, 2.32 g) and Na_2HPO_4 (0.027 mol, 3.78 g) in 1 L of Mili-Q.
- *pH 12, Ionic strength 0.1 M:* Na_2HPO_4 (0.0073 mol, 1.04 g) and Na_3PO_4 (0.013 mol, 2.07 g) in 1 L of Mili-Q.

Note: During pH dependent experiments the solutions were basified or acidify by addition of the corresponding amount of 1 M NaOH or 0.1 M CF_3SO_3H aqueous solutions, respectively.

Cyclic Voltammetry (CV): In a typical CV experiment, a 20 mL vial was used as an electrochemical cell. A home-made Teflon cap with holes for the three electrodes was used as a lid to ensure a reproducible distance between the electrodes. The scan rate was 100 $mV \cdot s^{-1}$ unless otherwise stated. IR compensation was applied at 90% when the current density was above 10 mA/cm^2.

Differential Pulse Voltammetry (DPV): In a typical DPV experiment, a 20 mL vial was used as an electrochemical cell. A home-made Teflon cap with holes for the three electrodes was used as a lid to ensure a reproducible distance between the electrodes. The DPV parameters were ΔE = 4 mV, Amplitude = 50 mV, Pulse width = 0.05 s, Sampling width = 0.0167 s, Pulse period = 0.5 s. iR compensation was applied at 90%.

Bulk electrolysis: For activation of catalyst, controlled potential electrolysis (CPE) was carried out in pH 12 phosphate buffer solution for 1000 s at 1.25 V vs NHE in 20 mL one compartment three electrode electrochemical cell with constant stirring. CPE experiment for checking the stability was also carried out in 20 mL electrochemical cell containing stirring bar using glassy carbon disk as WE, Pt disk as CE and Hg/Hg_2SO_4 (K_2SO_4 saturated) as RE.

Surface Coverage (Γ) Calculation

The surface coverage of the complexes on the electrode was calculated following the formula:

$$\Gamma\ (mol \cdot cm^{-1}) = \frac{Q_{av}}{n \cdot S \cdot F} \qquad \text{(S1)}$$

$$Q_{av} = \frac{Q_{pa,Ru^{III/II}} + Q_{pc,Ru^{III/II}} + Q_{pa,Ru^{IV/III}} + Q_{pc,Ru^{IV/III}}}{4} \qquad \text{(S2)}$$

Where Q_{av} is average of the charge under anodic (Q_{ap}) and cathodic (Q_{cp}) peaks for $Ru^{III/II}$ and $Ru^{IV/III}$ electron transfer processes, obtained by integration in the CV. n is the number of electrons involved in each oxidation process, which is 1 for both complexes. S is the geometric surface area of the electrode (GC_d, S= 0.07 cm^2 and GC_p, S = 1 cm^2) and F is Faradaic constant. The average coverage of the catalyst was estimated from 5 independent experiments and an error between the sample was considered as standard deviation. Moreover, the surface coverage of each electrode used for different analyses was calculated and indicated in the caption.

O_2 Evolution Experiments

For Oxygen monitored bulk electrolysis experiments, a 10 mL two-compartment cell with a separation membrane between the two compartments was used. Both compartments were filled with 5 mL of 1 M phosphate buffer solution (pH = 7) and were equipped with a stirring bar. A functionalized GC_p was used as WE, a Pt grid as CE and a Ag/AgCl (KCl sat.) as a RE. Oxygen evolution was analyzed with a gas phase Clark type oxygen electrode (Unisense Ox-N needle microsensor) and calibrated by the addition of small quantities of oxygen (99%) at the end of the experiment. The CE was placed in one compartment and the other was provided with WE, RE and Clark electrode.

Synthesis of $[\{Ru(tda)\}_2(tpt)_3]_n$ (n= x)

Synthesis of $[\{Ru(tda)\}_2(tpt)_3]_n$·DMSO (2D): In 100 mL two neck round bottom flask, [Ru(tda)(DMSO)(OH_2)] (50 mg, 0.1 mmol) 2,4,6-tris(4-pyridyl)-1,3,5-triazine (tpt) (47 mg, 0.15 mmol) were dissolved in 20 mL of degassed TFE and refluxed for 3 days under N_2 atmosphere. Afterwards, the reaction mixture was evaporated to dryness and to this resulting solid, methanol was added and a violet precipitate was observed along with red color solution. The precipitate was filtered through frit and washed with MeOH, H_2O, acetone and Et_2O and dried under vacuum and gives the **2D** polymer **$[\{Ru(tda)\}_2(tpt)_3]_n$·DMSO** (**2D**) with 70 mg as an isolated solid.

Synthesis of $[\{Ru(tda)\}_2(tpt)_3]n\cdot H_2O$ (2D): In 100 mL two neck round bottom flask, [Ru(tda)(OH_2)$_2$]PF_6 (50 mg, 0.09 mmol) and 2,4,6-tris(4-pyridyl)-1,3,5-triazine (tpt) (42 mg, 0.13 mmol) were dissolved in 20 mL of degassed TFE and refluxed for 3 days under N_2

atmosphere. Afterwards, the reaction mixture was evaporated to dryness and to this resulting solid, methanol was added and a violet precipitate was observed along with deep red color solution. The precipitate was filtered through frit and washed with MeOH, H_2O, acetone and Et_2O and dried under vacuum yielding the 2-D polymer complex **[{Ru(tda)}$_2$(tpt)$_3$]n·H2O** (**2D**) with 60 mg as an isolated yield.

Preparation and Activation of 2D@MWCNT@GC Electrodes

Preparation of 2D@MWCNT

Scheme S1 shows a schematic drawing of the procedure employed for preparation of **2D@MWCNT**. Solution A was prepared by disolving 1 mg of the corresponding 2D polymer in 1 mL of TFE. Suspension B was prepared parallely by sonication of 5 mg of MWCNTs (HeJi, Inc., China) in 5 mL of THF during 60 minutes. Afterwards, 0.1 mL of Solution A was added to 1 mL of Suspension B. Upon addition, the red color disappeared inmediately from the solution indicating that polymeric complexes are quickly anchored on MWCNT yielding suspension C, which contains **2D@MWCNT**.

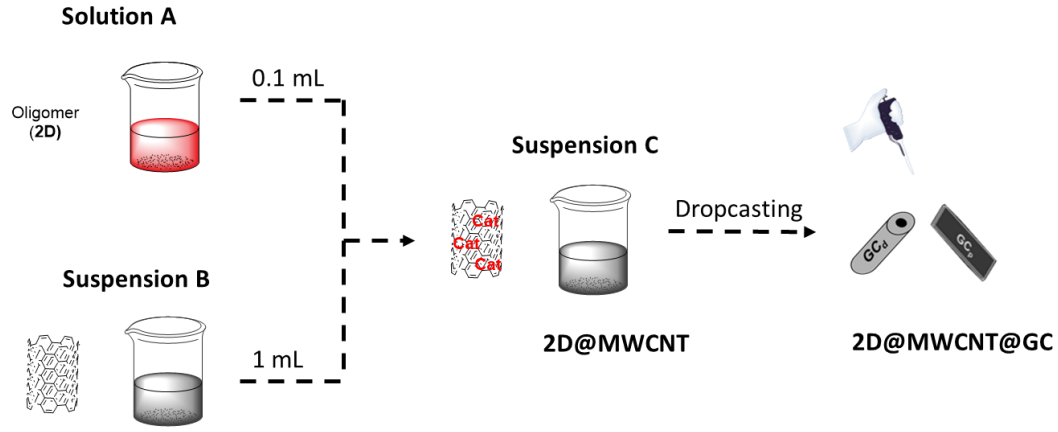

Scheme S1. Schematic diagram for the preparation of **2D@MWCNT@GC.**

Preparation of 2D@MWCNT@GC$_d$

Solution C was dropcasted (4 x 20 µL) onto GC$_d$ electrodes. Each drop was placed after the last drop is totally dried. Electrode was then ready for electrochemical measurements.

Preparation of 2D-H$_2$O@MWCNT@GC$_d$

The electrodes prepared above (**2D@MWCNT@GC**) was immersed in 0.1 M phosphate buffer solution (pH 12) and CPE was performed at 1.25 V vs NHE for 1000 seconds under constant

stirring to generate **2D-H_2O@MWCNT@GC**. Afterwards, the activated electrodes were rinsed with distillated water and dried at room temperature.

Note: Preparation of electrodes on glassy carbon plates (**GC_p**) was carried out using a similar methodology but some differences were introduced. Solution C was dropcasted (4 x 30 μL) onto GC_p electrodes. Each drop was placed after the last drop is totally dried. The coating was applied only to one side of the plates and a tape was used to limit this coating to 1 cm^2.

Surface Coverage (Γ*)* Calculation

The modified electrodes were immersed in 1 M phosphate buffer solution (pH 7) and cyclic voltammetry was performed (E_i = 0.25 V, E_c = 1.45 V, E_f = 0.25 V, total scans = 6, where E_i is initial potential, E_c is the change potential and E_f is the final potential), (CE = Pt disk, RE = Hg/Hg_2SO_4) to estimate the coverage of the electrodes. The surface coverage (Γ) of the complexes on the electrodes was estimated by applying the formula Γ (mol·cm^{-2}) = Q / (n*S*F).

Physisorption Method

1 mg of **2D** polymer was dissolved in 1 mL of trifuloroethanol solvent. To this solution glassy carbon electrode (GC_d) was dipped for 1 min and the electrode was taken out from the solution. The electrode was then washed with water and dried. The electrode was then ready for the electrochemical experiments.

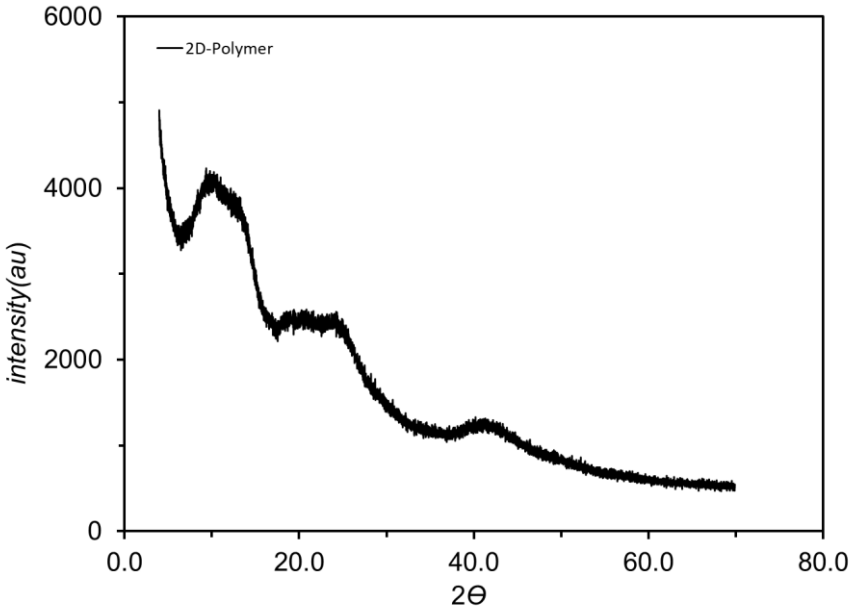

Figure S1. Powder X-ray diffraction of representative **2D** polymer.

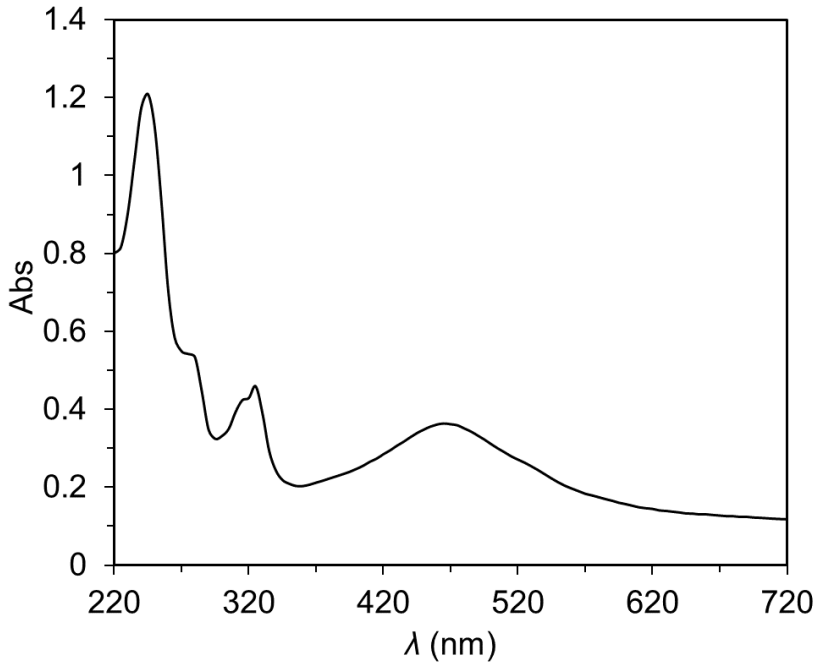

Figure S2. UV-Vis absorption spectrum of representative **2D** polymer.

a)

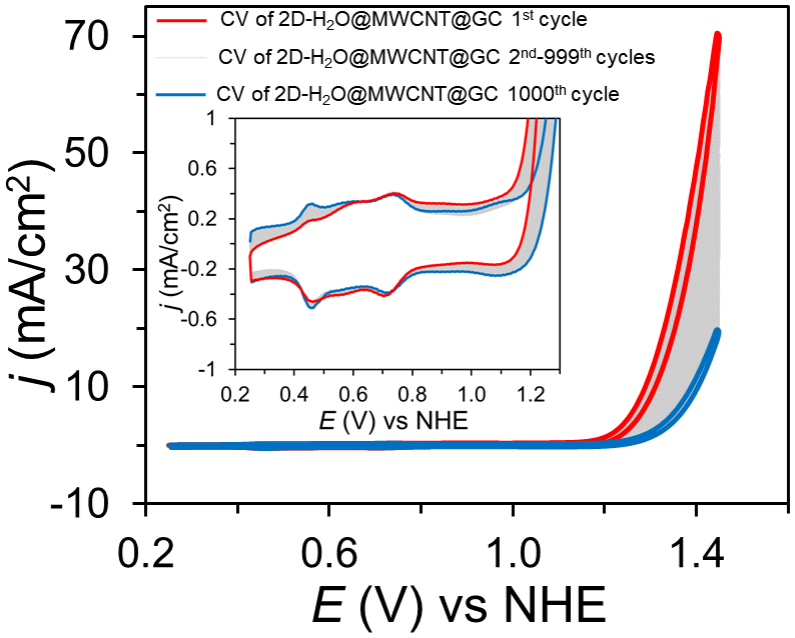

b)

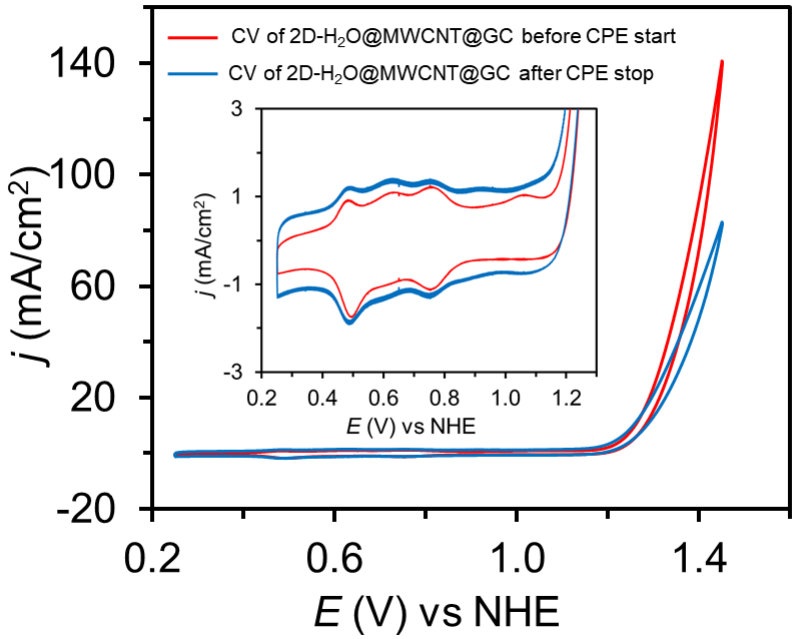

Figure S3. a) CV evolution of **2D-H_2O@MWCNT@GC** during 1000 repetitive CV cycles in 1 M phosphate buffer (pH 7), red line corresponds to the 1st cycle, grey line is 2nd– 999th cycles and blue line is the 1000th cycle at a scan rate of 100 mV/s. Inset: non catalytic redox waves. Surface coverage: $\Gamma_{2D\text{-}H2O}$ = 2.9 nmol·cm^{-2}.
b) CV of **2D-H_2O@MWCNT@GC** before (red line) and after (blue line) CPE experiment at 1.45 V vs NHE for 6 h in a freshly prepared 1 M phosphate buffer solution (pH 7) at a scan rate of 100 mV/s. Inset:, non catalytic redox waves. Surface coverage: $\Gamma_{2D\text{-}H2O}$ = 4.1 nmol·cm^{-2}.

a)

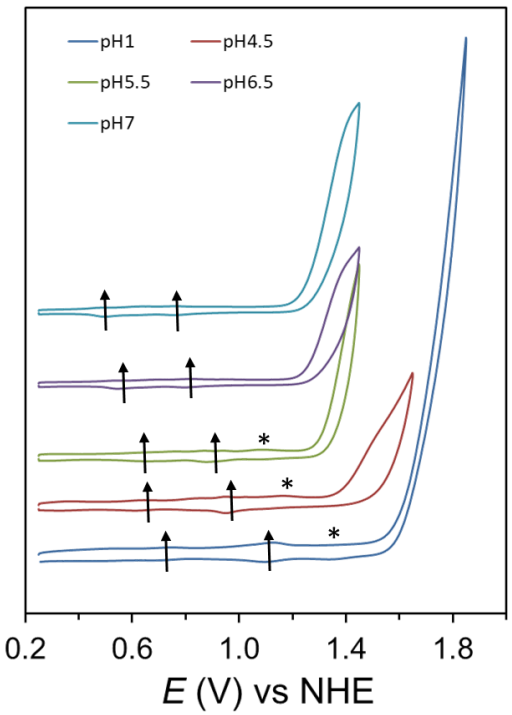

b)

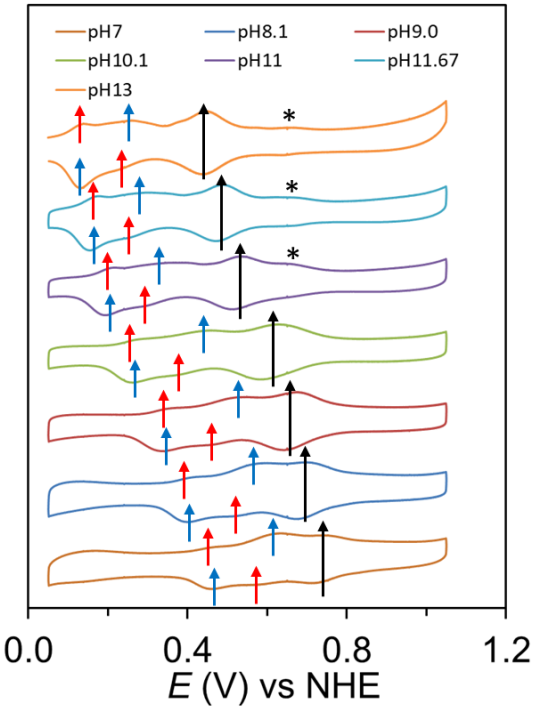

Figure S4. CV of **2D-H_2O@MWCNT@GC** at different pHs. a) acidic pH ranges, b) basic pH ranges. Arrow indicates the shift of redox waves upon changing the pHs, asterisk indicates unidentified species. (Note: in higher pHs, upon catalysis, local pHs of the solution changes near the electrode and cothodic waves are not appearing in the expected zone after catalysis).

a)

b)

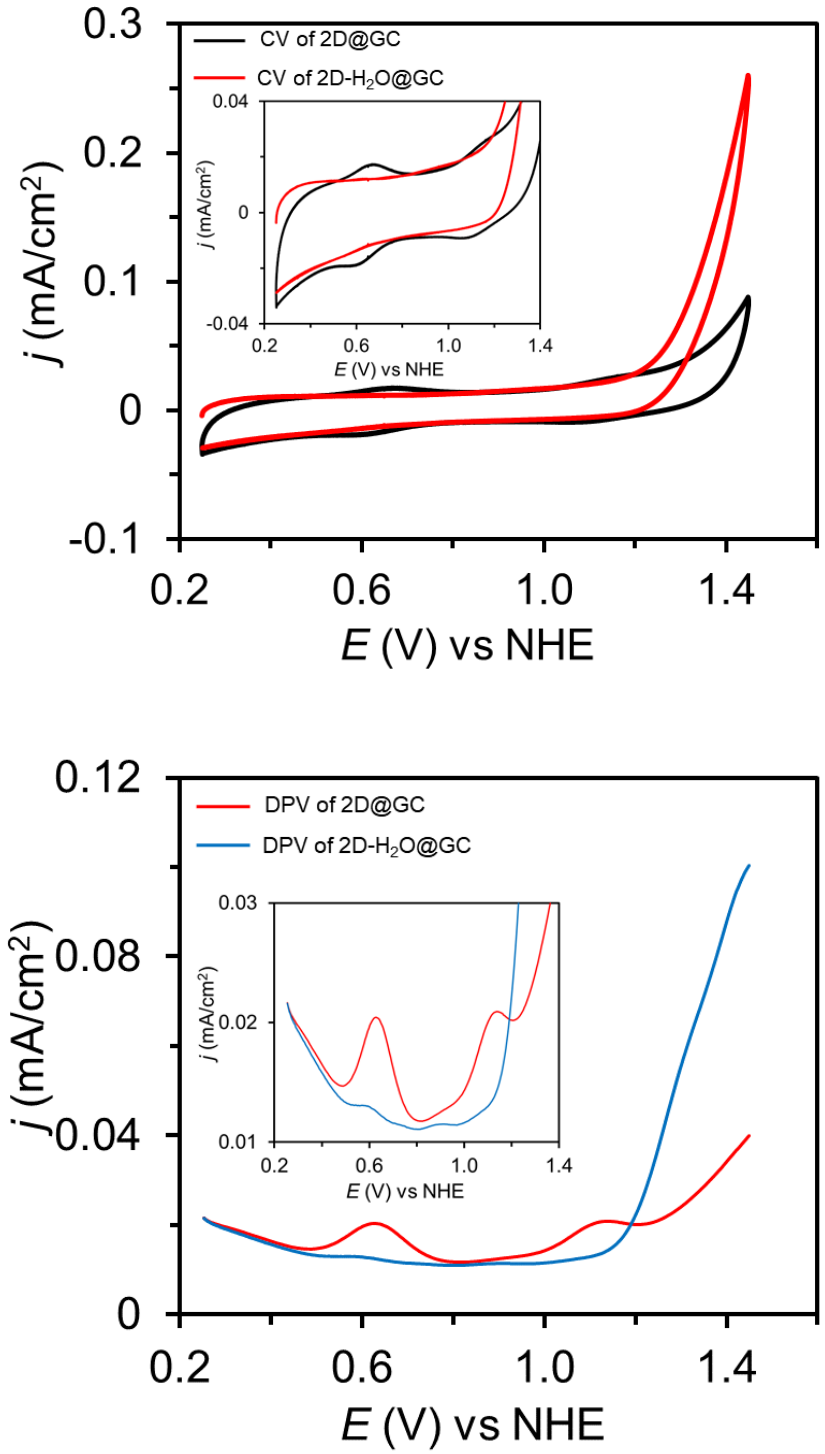

Figure S5. a) CV of **2D@GC** (black line) and **2D-H₂O@GC** (red line) in 1 M phosphate buffer (pH 7) at scan rate of 100 mV/s. Inset*:* enlargement of non catalytic redox waves. b) DPV of **2D@GC** (red) and **2D-H₂O@GC** (blue line) in 1 M phosphate buffer (pH 7) at scan rate of 100 mV/s. Inset: enlargement of non catalytic redox waves.

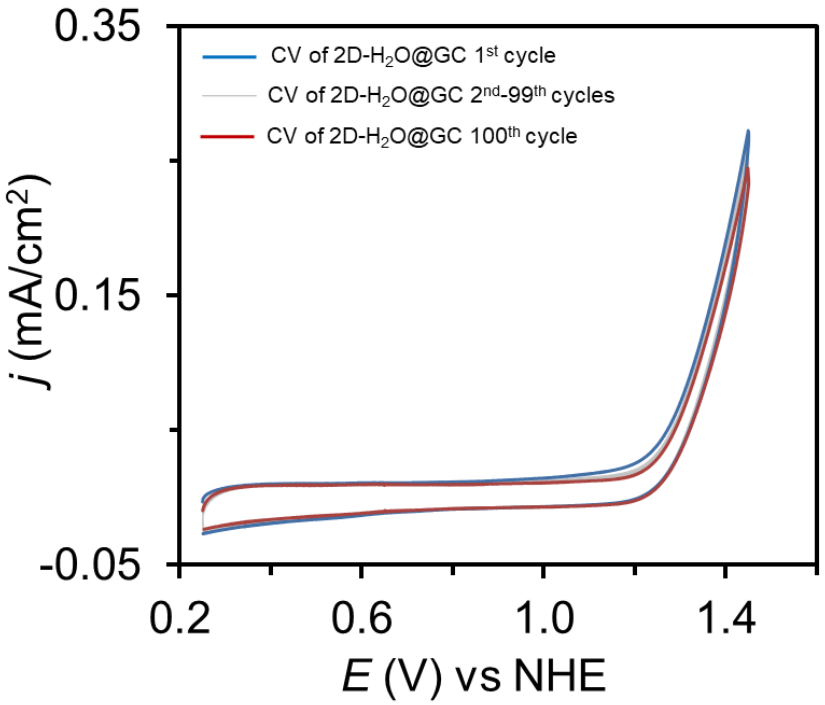

Figure S6. CV evolution of **2D-H_2O@GC** during 100 repetitive CV cycles in 1 M phosphate buffer (pH 7), red line corresponds to the first cycle, grey line is 2^{nd}– 99^{th} cycles and blue line is the 100^{th} cycle at a scan rate of 100 mV/s.

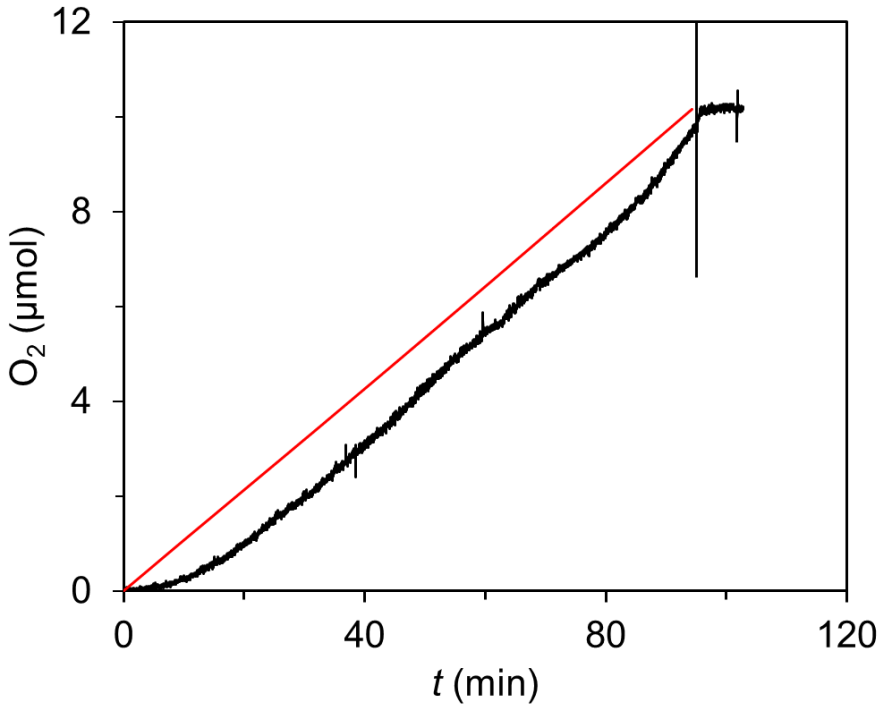

Figure S7. Oxygen evolution vs time (min) for **2D-H_2O@MWCNT@GC** $\Gamma_{2D\text{-}H2O}$ = 3.1 nmol·cm^{-2} using a Clark probe electrode during a CPE at 1.45 V vs NHE in 1 M phosphate buffer (pH 7). Black line corresponds to the O_2 measured in the gas phase by a Clark electrode during CPE experiment, Red line corresponds to the calculated amount of oxygen generated based on the charge passed during the CPE assuming 100% Faradaic efficiency. A Faradaic efficiency value of 99.5% was calculated at 100 min. ***Note:*** The applied potential was stopped at 95 min, but the O_2 evolution continued until 110 min due to the O_2 bubbles trapped at the working electrode. (Spike in the black line is due to the slight movement of the bulk electrolysis set up at the end of bulk electrolysis experiment to take out the oxygen bubble from the working electrode. Slight decrease in the slope of Clark response after 80 min of the experiment might be due to the change of the headspace of the bulk electrolysis set up due to the generation of the different amount gas in both compartment cell).

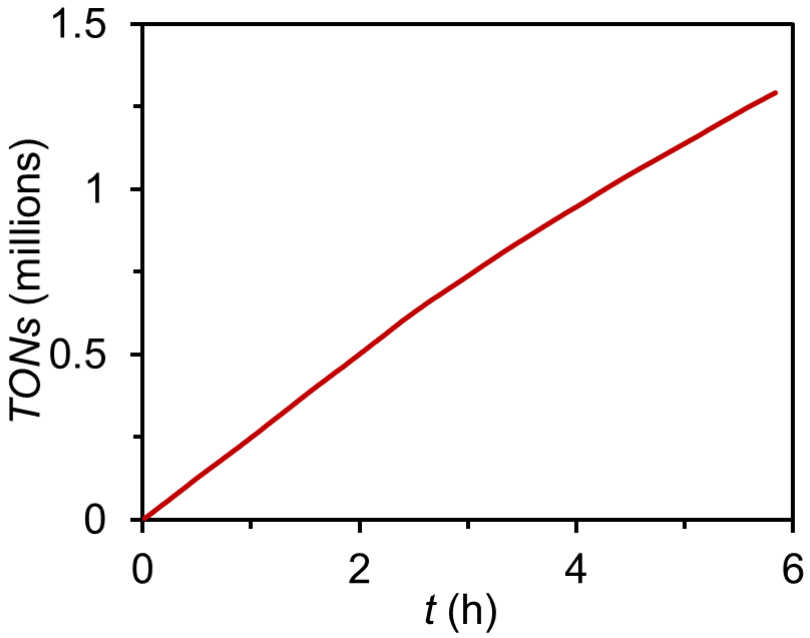

Figure S8. Plot of TONs *vs.* time obtained from the bulk electrolysis experiment for **2D-H_2O@MWCNT@GC** with $\Gamma_{2D\text{-}H2O}$ = 4.1 nmol·cm^{-2} at pH = 7 at an *E*app = 1.45 V. Charge after 6 h is 143 C and the total amount of catalyst is 0.287 nmol.

Chapter 6

Table S1. Catalytic performance of related molecular anodes described previously in the literature.

Entry	Catalyst	*Γ* (nmol cm^{-2})	*pH*	*J* (mA cm^{-2})[a]	*E* vs NHE (V)[a]	*Anchoring*	*Support*
1[1D]	5@CNT	14	7	-	-	CH-π	GC
2	15@CNT	21	7	-	-	CH-π	GC
3[tw]	2D@MWCNT	4.8	7			-	GC
3[1D]	1-pyp@CNT	5	7	-	-	π-π	GC
4[1D]	1-pypA@CNT	9	7	-	-	π-π	GC
5[1D]	5-H_2O@CNT	9.5	7	190	1.45	CH-π	GC
6[1D]	15-H_2O @CNT	17.5	7	240	1.45	CH-π	GC
7[tw]	2D-H_2O @CNT	4.2	7	140	1.45	-	GC
8[1D]	1-O-pyp@CNT	0.4	7	20	1.45	π-π	GC
9[1D]	1-O-pypA@CNT	0.9	7	39	1.45	π-π	GC
10[2]	1-pyp@CNT	0.2	7	-	-	π-π	GC
11[2]	1-pypA@CNT	6.3	7	-	-	π-π	GC
12[2]	1-O-pyp@CNT	0.03	7	2.2	1.45	π-π	GC
13[2]	1-O-pypA@CNT	0.55	7	10.5	1.45	π-π	GC
14[3]	[(bpy-$CH_2PO_3H_2$)Ru(Mebimpy)(OH_2)]$^{2+}$	0.1	5	0.015	1.85	[R-PO_3H^-]-M	ITO/FTO
15[4]	[Ru(bda)(F-Isoq)(py-Thiophene)]	0.96	7.2	4	1.3	P-thiophene	GC

Abbreviations: 1D refers to 1D polymer in Chapter 6, tw refers to the catalysts reported in this work, **CNT** and **MWCNT** is Multi Wall Carbon Nanotubes; pyp is 4-(pyren-1-yl)pyridine; pypA is 4-(pyren-1-yl)-N-(pyridin-4-ylmethyl)butanamide; bpy-$CH_2PO_3H_2$ is ([2,2'-bipyridine]-4,4'-diylbis(methylene))bis(phosphonic acid); Mebimpy is 2,6-bis(1-methylbenzimidazol-2-yl)pyridine; bda is 2,2'-bipyridine–6,6'–dicarboxylate; F-Isoq is 6-fluroisoquinoline. [a]Calculated from CV or CPE experiments at the indicated potential (*E*).

References

(1) Matheu, R.; Benet-Buchholz, J.; Sala, X.; Llobet, A. *Inorg. Chem.* **2017**, *57*, 1757.
(2) Creus, J.; Matheu, R.; Peñafiel, I.; Moonshiram, D.; Blondeau, P.; Benet-Buchholz, J.; García-Antón, J.; Sala, X.; Godard, C.; Llobet, A. *Angew. Chem. Int. Ed.* **2016**, *55*, 15382.
(3) Chen, Z.; Concepcion, J. J.; Jurss, J. W.; Meyer, T. J. *J. Am. Chem. Soc.* **2009**, *131*, 15580.
(4) Wang, L.; Fan, K.; Chen, H.; Daniel, Q.; Philippe, B.; Rensmo, H.; Sun, L. *Catal. Today* **2017**, *290*, 73.

Chapter 7

Mononuclear complexes based on the [Ru(tda)(Py')(py")] as a catalyst precursor are described (where tda = 2,2':6',2"-terpyridine-6,6"-dicarboxylate, py' and py" = functionalized pyridine). Here the pyridine py' or py" contain a functional group that allows attaching the complex to conductive substrates via covalent bonding. For instance, carboxylate and vinyl groups are used to attach the complex onto metal oxides, diazonium salts for C-C bonding attachment to graphitic materials or pyrazine linkages to anodized graphitic materials. Finally, non-covalent interactions are explored as a means to heterogenize mononuclear and coordination polymers on graphitic materials or metal oxides.

Chapter 7

7. Anchoring Strategies for Molecular Water Oxidation Catalysts on Solid Surfaces

Md Asmaul Hoque,[1,2] Marcos Gil-Sepulcre,[1] Carolina Gimbert-Suriñach,[1] Antoni Llobet[1,3]

[1]Institute of Chemical Research of Catalonia (ICIQ), Barcelona Institute of Science and Technology (BIST), Av. Països Catalans 16, 43007 Tarragona, Spain

[2]Departament de Química Física i Inorganica, Universitat Rovira i Virgili, Campus Sescelades, C/Marcel`·lí Domingo, s/n, 43007 Tarragona, Spain.

[3]Universitat Autònoma de Barcelona, Departament de Química, Cerdanyola del Vallès, 08193 Barcelona, Spain

VII

Contributions

Md Asmaul Hoque synthesized and characterized all the complexes and prepared the electrode and performed the electrochemical, spectroscopic analysis together with the catalytic tests and prepared the manuscript.

Chapter 7

Abstract

Mononuclear complexes based on the [Ru(tda)(Py')(py")] pre-catalytic center are described (where tda = 2,2':6',2"-terpyridine-6,6"-dicarboxylate, py' and py" = functionalized pyridine). Here the pyridine py' and py" contain a functional group that allows attaching the complex to conductive substrates via covalent bonding. For instance, carboxylate and vinyl groups are used to attach the complex onto metal oxides, diazonium salts for C-C bonding attachment to graphitic materials or pyrazine linkages to anodized graphitic materials. Finally, non-covalent interactions are explored as a means to heterogenize mononuclear and coordination polymers on graphitic materials or metal oxides. Covalent linkage of carboxylate groups on metal oxide surfaces is unstable under working conditions pH 7 while polyvinyl pyridine films show a very robust linkage on the same surface. Covalent linkage of the molecular catalyst on graphite surface through C-C bonds are also very stable while pyrazine groups are sensitive to high potential. Interestingly, physisorbed polymers on graphite surface are promising candidates for water oxidation as opposed to analogous mononuclear derivatives. The high activity observed in the former case is not translated to conductive metal oxides due to deactivation of the catalyst in contact with this type of surface.

VII

Graphical abstract

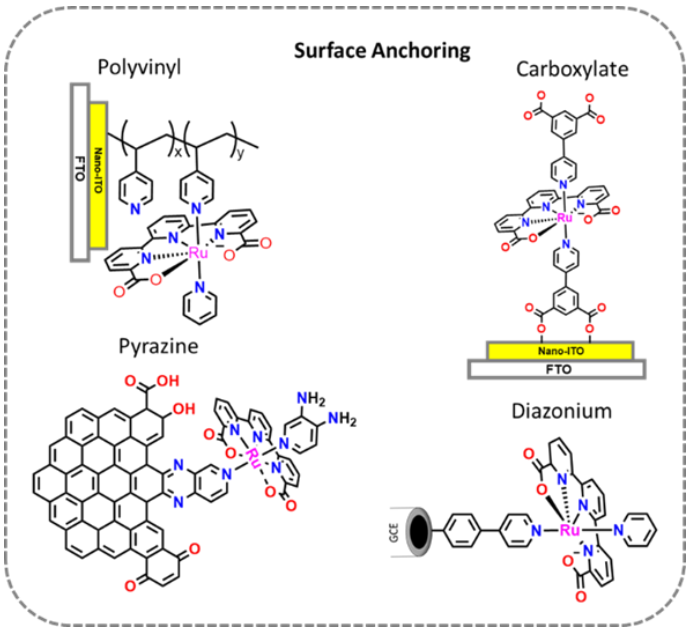

Keywords: Anchoring, Carboxylate, Vinyl pyridine, Pyrazine, Diazonium, Water oxidation

Chapter 7

7. 1. Introduction

Molecular electrocatalysis consists of using well defined transition metal complexes to carry out catalytic transformations by electrochemical means. Although the ease of synthetic tuning of homogeneous molecular electrocatalyst represents a powerful strategy to optimize the kinetics and/or thermodynamics of the substrate activation,[1-3] when a catalyst is used in homogeneous phase it often experiences lower reaction rates as compared to heterogeneous catalysts because catalytic turnover only occurs when the catalyst is in diffusive contact with the electrodes. These limitations can be overcome if the molecular catalyst is anchored onto the electrode. Often, heterogeneous electrocatalysts based on metallic surfaces of metal oxides exhibit greater stability than molecular analogues. However, the catalytic activity of such materials is difficult to control since systematic modification of the active site is generally limited to morphology and pore size as opposed to molecular complexes where the first and even second coordination spheres can be easily and judiciously tuned. For all these reasons, it is of interest to develop methodologies that can allow to anchor molecular catalysts that have been previously optimized in homogeneous phase onto conductive surfaces.

A variety of methods have been developed to immobilized molecules on conductive solid surfaces such as thiol based self-assembled monolayers (SAMs),[4] click chemistry,[5] alkyne linkage,[6] diazonium grafting[7,8] and non-covalent linkage that rely on π–π[9] interactions for many applications. In the particular field of water oxidation catalysis, the reports on molecular catalysts anchored on solid surfaces is limited but it has recently become an attractive strategy to generate hybrid material to build up photoelectrochemical cells for water splitting. In chapter 5 and 6 of the present thesis the deposition of coordination polymers containing water oxidation catalysts (WOC) centers on graphitic surfaces through CH-π-interaction have been explored. This chapter focuses on exploring a wide range of anchoring strategies to immobilize WOC on solid surfaces via covalent linkage (Figure 1). The first strategy consists of using a pyridine dicarboxylate[10,11] group that is expected to bind to metal oxide surfaces such as nano-ITO particles (where ITO is indium doped tin oxide) forming covalent bonds as indicated in the top left of Figure 1. The second approach is based on the polymerization of vinyl pyridine induced by UV-light[12] that forms stable films on both metal oxide and graphitic electrodes (Figure 1, bottom left). Next, a simple and powerful method of linking the WOC on graphitic carbon electrode through conjugated aromatic pyrazine linkage[13] will be explored. This approach requires a pre-treatment of the glassy carbon that ensures that there are enough oxidized sites to be able to react with the diaminobenzene group (Figure 1, top right). The last method is based on diazonium electrografting,[14] which generates stable covalent (C-

C) bonds on any graphitic surface with the molecular catalyst. In the last part of the chapter, a quick note on the supramolecular interaction between monomeric water oxidation catalysts and graphitic materials will be explored and the results compared with those obtained for coordination polymers described in Chapter 5 and 6.

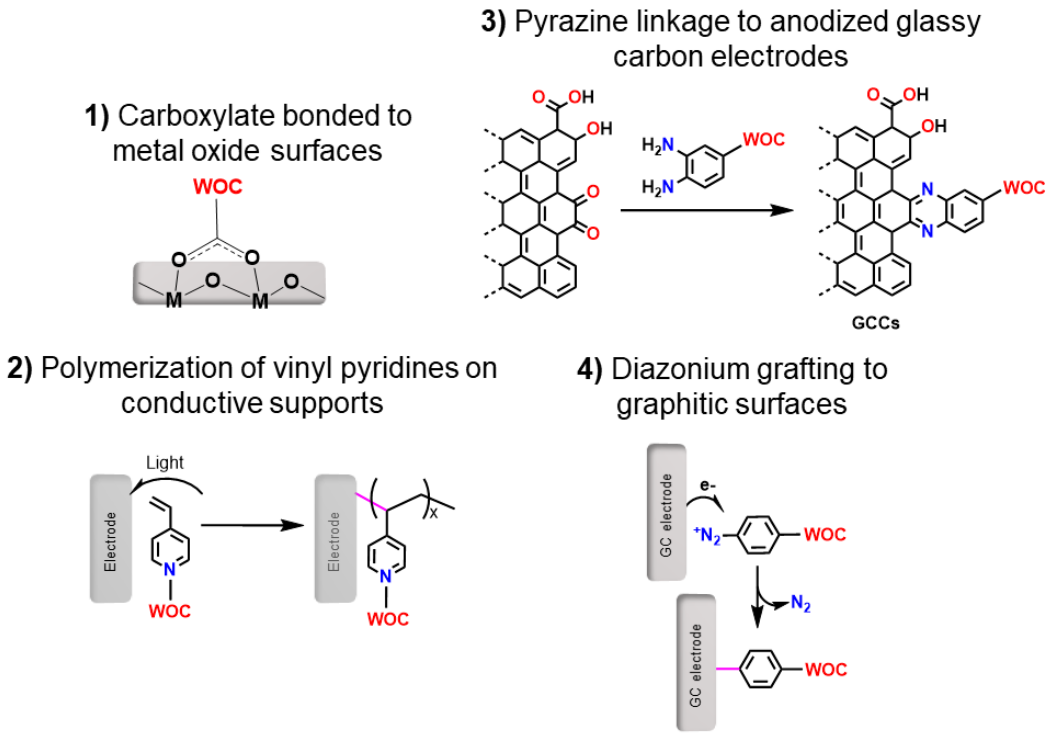

Figure 1. Strategies to anchor water oxidation catalysts (WOC) on conductive substrates used in this work.

The water oxidation catalyst selected to perform this study is the [Ru(tda)(py)$_2$] catalyst (where tda is [2,2':6',2''-terpyridine]-6,6''-dicarboxylato and py is pyridine), which is the fastest molecular WOC described to date (Figure 2).[15] In order to incorporate this catalyst on electrode surfaces, the axial pyridines have been modified with appropriate functional groups. The family of pyridines used in this work as well as the molecular structure of the catalytic center are given in Figure 2.

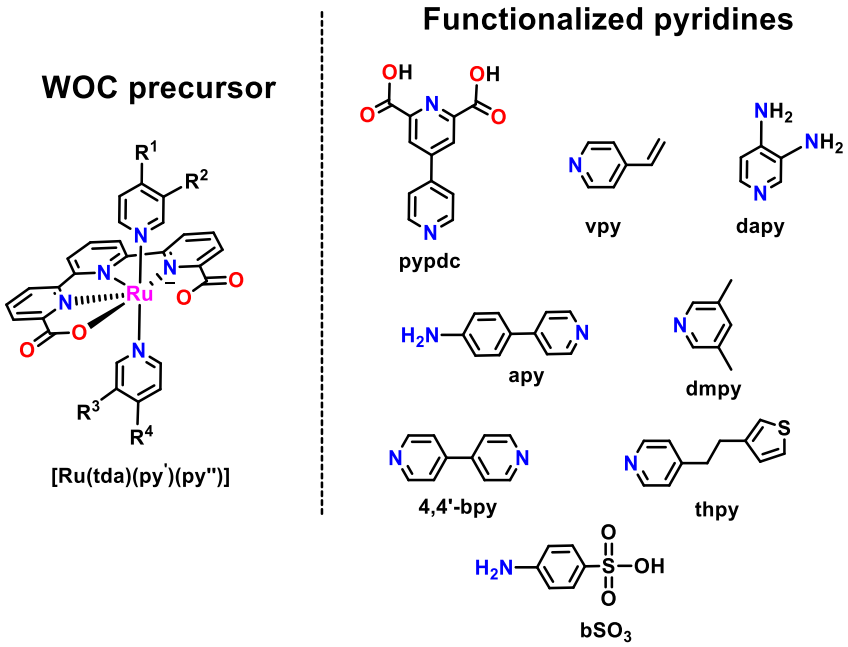

Figure 2. Water oxidation catalyst precursor (left) and functionalized pyridines and aniline (right) used in this work and their corresponding labeling .

VII

7. 2. Experimental Section

Materials

$RuCl_3 \cdot \times H_2O$ was purchased from Alfa-Aesar. The precursor complex $[RuCl_2(DMSO)_4]$,[16] $[Ru(tda)(DMSO)(OH_2)]$[17] and $[Ru(tda)(py)(OH_2]$[17] were prepared according to a reported procedures. [4,4'-bipyridine]-2,6-dicarboxylic acid, vinyl pyridine, 3,5-pyridine diamine, 4-(pyridin-4-yl)aniline and other chemicals were obtained from commercial source and used as received. Indium doped tin oxide (ITO) electrodes were purchase from SPI supplies/ALPHA BIOTECH (R = 8-12 ohms/sq) and fluorine doped tin oxide (FTO) from Xop Glass (FTO TEC-15, thickness: 2.2 mm, R=12-15ohms/sq). nano-ITO was purchased by Aldrich and the paste for doctor blading were prepared following reported procedures.[18,19] Solvents were dried with a SPS® system and degassed by bubbling nitrogen before starting the reactions. High purity de-ionized water used for the electrochemistry experiments was obtained by passing distilled water through a nanopure Mili-Q water purification system. For other spectroscopic and electrochemical studies, HPLC-grade solvents were used.

Instrumentation and Methods

A 400 MHz Bruker Avance II spectrometer and a Bruker Avance 500 MHz were used to carry out NMR spectroscopy. ESI-Mass spectra were recorded using micromass Q-TOF mass spectrometer. Elemental analyses were carried out on Perkin-Elmer 240C elemental analyzer. The pH of the solutions was determined by a pHmeter (CRISON, Basic 20^+) calibrated before

measurements through a standard solutions at pH 4.01, 7.00 and 9.21. Oxygen evolution was analyzed with a gas phase Clark type oxygen electrode (Unisense Ox-N needle microsensor) and calibrated by the addition of small quantities of oxygen (99%) at the end of the experiment. Spin coater 3000 with WS-650 spin processor from Laurell technology was used. All electrochemical experiments were performed in an IJ-Cambria CHI-660 potentiostat using a three-electrode one compartment cell for cyclic voltammetry (CV) and differential pulse voltammetry (DPV) or two compartment cell for bulk electrolysis. $E_{1/2}$ values reported in this work were estimated from CV experiments as the average of the oxidative and reductive peak potentials ($E_{p,a}$ + $E_{p,c}$)/2 or from DPV. The Reference Electrode (RE) was Hg/Hg_2SO_4 (K_2SO_4 saturated) and potentials were converted to NHE by adding 0.65 V. Either a glassy carbon disk (GC_d, ϕ = 0.3 cm, S = 0.07 cm^2), a glassy carbon rotatory disk (ϕ = 0.5 cm, S = 0.196 cm^2) or ITO/FTO plates (*ca.* 10 mm x 12 µm) with or without functionalization were used as working electrodes (WE). A Pt disk (ϕ = 0.2 cm, S = 0.03 cm^2) was used as counter electrode (CE). Glassy carbon electrodes were polished with 0.05 µm alumina (Al_2O_3) and rinsed with water. Before catalyst deposition, ITO-coated glass slides were cleaned using consecutive ultrasonic treatment with isopropanol and acetone for 20 min each. The slides were then dried under nitrogen flow and used immediately after being cleaned. Before catalyst deposition, FTO electrodes we cleaned by an alkaline solution ($V_{HELLANEX}$: $V_{Milli\text{-}Q\ water}$ =100:1, Hellmanex is an alkaline solution purchased from Hellma GmbH & CO. KG), Milli-Q water and ethanol. Each cleaning step are under 10 min sonication and then rinsed by the corresponding solvents. After all these steps, the FTO/ITO coated glass is dried in the oven at 100˚C overnight, and then annealed at 300 ˚C for 30 min in the furnace to remove the organic contaminations on the surface and ensure a good conductivity. CVs and DPVs were iR compensated by the potentiostat in all the measurements. CVs were recorded at 100 $mV{\cdot}s^{-1}$ scan rate. DPV parameters were Δ*E* = 4 mV, Amplitude = 50 mV, Pulse width = 0.05 s, Sampling width = 0.0167 s, Pulse period = 0.5 s. The complexes were dissolved in acetonitrile or trifluoroethanol containing [(*n*-Bu)$_4$N][PF_6] (0.1 M) as supporting electrolyte. In aqueous solution the electrochemical experiments were carried out in *I* = 0.1 M phosphate buffer solutions with desired pH. For routine bulk electrolysis experiments, a functionalized electrode was used as a WE, another Pt grid as a CE and a Hg/Hg_2SO_4 (K_2SO_4 saturated) as a RE. iR compensation by the potentiostat was not applied in this technique.

NanoITO@ITO preparation using spin coating: Freshly cleaned ITO-coated glass slides were partially covered with scotch tape in order to leave flat surface for electrical connection. The uncovered area was filled with ITO nanoparticles via spin coating to have a homogeneous

layer on it following the reported procedures.[18,19] The coated slides (nanoITO@ITO) were then placed on a hot plate (100 °C) for 5 min to dry off excess solvent and followed by annealing under the atmospheric pressure in a tube furnace at 350 °C.

GC Rotating Disk Electrode Preparation

Glassy carbon rotating disk electrodes, 5 mm diameter, were polished by hand against an alumina slurry using a circular motion for 30 seconds following by sonication in Milli-Q water for 1 min. This process was repeated in sequence using 1.0 µm, 0.3 µm, and 0.05 µm alumina slurries. To further clean the glassy carbon electrode surface and expose a high population of quinone moieties the electrodes were briefly anodized via potentiostatic electrolysis at 3.5 V vs NHE for 10 seconds in 0.1 M H_2SO_4. Electrodes were subsequently washed with copious amount of water and ethanol prior to electrochemical evaluation or further functionalization.

Electrode Activation Protocol

The molecular system $[Ru(tda)(py)_2]$ that is used in this work, is not a real water oxidation catalyst but a catalyst precursor. An aquo ligand needs to coordinate to the Ruthenium at high oxidation states. This process is regarded as activation of the electrode. In order to do this activation, the functionalized electrode was submitted to a Controlled Potential Electrolysis. Unless otherwise mentioned, the protocol consisted in applying a potential of 1.25 V vs NHE at the hybrid electrode in a pH 12 phosphate buffer solution for *ca.* 500 s.

GC Functionalization with Aromatic Diazonium Salts

Procedure: The clean glassy carbon electrodes were put in three electrode set up CV cell containing 4-(pyridin-4-yl)aniline or 1:1 mixture of 4-(pyridin-4-yl)aniline, 4-amino-benzenesulfonic acid or the complexes containing aromatic amine with *tert*-butyl nitrite under argon at 4 ˚C in acetonitrile or trifluoroethanol solvent containing 0.1 M $[(n\text{-}Bu)_4N][PF_6]$ for 10 min. Then 10 CV cycles were carried out starting from 0.9 to -0.35V vs NHE with the same solution. The electrodes were removed from the set up and rinsed with acetonitrile, water and dried with airflow. Ligand or complex modified electrodes were then ready for further experiment.

Preparation of GC with MWCNT and Functionalization with Aromatic Diazonium Salts

MWCNT@GC was prepared by dropcasting 20 µL dispersed solution of MWCNT on the top of glassy carbon electrode and allowed to dry. This electrode was then dipped into 1 mM

solution of complex **4** in trifluoroethanol containing *tert*-butyl nitrite under argon at 4 ˚C for 10 min and similar procedure as describe above was applied.

Physisorption Method

A clean glassy carbon electrode was dipped into a solution that contain 1 mg of complex in 1 mL of trifluoroethanol solvent for 1 min. The complex functionalized electrode was then rinsed with trifluoroethanol and water. It was then dried by airflow and was ready for electrochemical experiment. In this process, complexes are adsorbed by physisorption method.

Synthesis of [Ru^{II}(tda)(pypdc)$_2$], 1: [Ru(tda)(DMSO)(OH_2)] (100 mg, 0.19 mmol) and [4,4'-bipyridine]-2,6-dicarboxylic acid (pypdc, 100mg, 0.4 mmol) were stirred in 30 mL of a mixture methanol/water (3:2) under reflux overnight under argon atmosphere. The volume of the solvent was reduced to 5 mL and 1 mL of 1 M H_2SO_4 was added. The blackish red color precipitate was obtained by filtration and cleaned with cold water and dried under vacuum. The amount of isolated material was low and the compound was not analytically pure and therefore, full characterization of **1** is not given. Nevertheless, the compound is electrochemically pure allowing to perform preliminary anchoring tests. Approximate yield: 18 mg (0.02 mmol, 10 %). The nominal mass of **1**, $[1\text{-}2H + 2Na]^+$ ($C_{41}H_{21}N_7Na_2O_{12}Ru$). 951.0 (expt); 950.7 (calculated).

Synthesis of [Ru^{II}(tda)(dapy)$_2$], 2: [Ru(tda)(DMSO)(OH_2)] (100 mg, 0.19 mmol) and 3,4-diaminopyridine (dapy, 75 mg, 0.69 mmol) were refluxed in 20 mL of a mixture methanol/water (1:1) overnight under argon atmosphere. Solvent was then removed and 5 mL of methanol were added. To this resulting solution, 10 mL of ether were added to get a precipitate. The solid was filtered and washed with a little amount of methanol and diethyl ether and dried under vacuum. Yield: 90 mg (0.14 mmol, 70 %). ^{1}H-NMR (500 MHz, [d_6]-DMSO) δ: 8.61 (H^4, d, J=8.0 Hz, 2H), 8.47 (H^3, dd, J=5.9 Hz and J=2.2 Hz, 2H), 7.88 ($H^{1,2,5}$, m, 5H), 7.31 (H^6, d, J=6.1 Hz, 2H), 6.54 (H^{10}, s, 2H), 6.06 (H^7, d, J=6.15 Hz, 2H), 5.63 (H^8, s, 4H),4.31 (H^9, s, 4H). ^{13}C-NMR (125 MHz, [d_6]-DMSO) δ: 123.7, 124.0, 124.4, 127.0, 132.7, 136.9, 143.3, 152.7, 155.8, 158.3, 162.1, 167.7 and 170.3. ESI (-) HRMS m/z: calc. for ($C_{29}H_{18}N_5O_8Ru$): 660.0237, found m/z: 660.0259 (3.3 ppm error). *Anal. Calc.* for $C_{29}H_{17}N_5O_{12}Ru$ (compound + 4 H_2O): C, 47.16 %; H, 3.68 %; N, 9.48 %. Found: C, 47.00 %; H, 3.34 %; N, 9.15 %.

Synthesis of [Ru^{II}(tda)(apy)(OH_2)], 3: [Ru(tda)(DMSO)(OH_2)] (100 mg, 0.19 mmol) and 4-(pyridin-4-yl)aniline (apy, 70 mg, 0.41 mmol) were stirred in 40 mL of water overnight at 45˚C

under N_2 atmosphere. The mixture was then evaporated to dryness and the resulting solid dissolved in methanol and purified by column chromatography with neutral alumina using a mixture of CH_2Cl_2/MeOH/Et_3N (1:1:0.001, v/v) as eluent. An orange red fraction was collected giving the product [Ru^{II}(tda)(apy)(DMSO)] (40 mg, 0.06 mmol, Yield: 33 %). This product was then heated at 90˚C with 0.2 mL neat triflic acid for 4 h and 2 mL of a saturated aqueous solution of KPF_6 were added and kept in the fridge overnight. The precipitate was then filtered and washed with cold water and dried under vacuum. The amount of isolated material was low and the compound was not analytically pure and therefore, full characterization of **3** is not given. Nevertheless, the impurities have no electrochemical activity and thus allow to perform preliminary anchoring tests. Approximate yield: 15 mg (0.02 mmol, 10 %).

Synthesis of [Ru^{II}(tda)(dmpy)(apy)], 4: [Ru(tda)(DMSO)(OH_2)] (100 mg, 0.19 mmol) and 3,5-lutidine (dmpy, 2 mL, 0.69 mmol) were stirred in 20 mL water for 4h at room temperature. This generated a brown solution that was extracted with DCM (3 x 100 mL). A brown solid was obtained by removal of the water and was then dissolved in MeOH and 4-(4-pyridinyl) benzenamine (apy, 40 mg, 0.23 mmol) were added and the mixture heated to reflux for 2 days. The mixture was then evaporated to dryness and the resulting solid dissolved in CH_2Cl_2 and purified by column chromatography with neutral alumina using a mixture of CH_2Cl_2/MeOH (100:25, v/v) as eluent. A brown red fraction was collected giving a solid identified as compound **4**, which was not enough to fully characterize the compound. Nevertheless, it was possible to assign ^{1}H NMR resonance and perform preliminary anchoring tests. Yield; 12 mg (0.02 mmol, 10 %).^{1}H-NMR (500 MHz, [d_6]-DMSO) δ: 8.72 (d, J=8.2 Hz, 2H), 8.54 (dd, J=7.9 Hz and 1.1 Hz, 2H), 8.05 (t, J=8.2 Hz, 1H), 8.0 (d, J=7.3 Hz, 2H), 7.95 (t, J=8.2 Hz, 2H), 7.87 (dd, J=7.9 Hz and J=1.0 Hz, 2H), 7.75 (s, 2H), 7.37 (d, J=8.57 Hz, 2H), 7.24 (d, J=6.9 Hz, 2H), 7.21 (s, 1H), 6.52 (d, J=8.75 Hz, 2H) 5.63 (s, 2H), 1.96 (s, 6H). ^{13}C-NMR (125 MHz, [d_6]-DMSO) δ: 18.1, 114.3, 119.8, 121.7, 123.4, 124.0, 126.2, 128.1, 131.8, 133.7, 136.2, 138.3, 147.5, 149.9, 151.4, 152.5, 157.7, 160.2, 161.9 and 169.3.

7. 3. Results and Discussion

7. 3. 1. Pyridine Dicarboxylate Linkage to Metal Oxides

Synthesis and Characterization of Complex 1

Complex **1** was synthesized by using the precursor [Ru(tda)(DMSO)(OH_2)] and two equivalents of [4,4'-bipyridine]-2,6-dicarboxylic acid (pypdc) in a mixture of methanol/water (3:2) (Scheme 1). The complex has been characterized by mass spectrometry and ^{1}H NMR spectroscopy with the expected resonances and integration (Figure S1 in the SI). The amount of isolated compound **1** was low but it was possible to perform preliminary electrochemical and anchoring experiments described in the next sections.

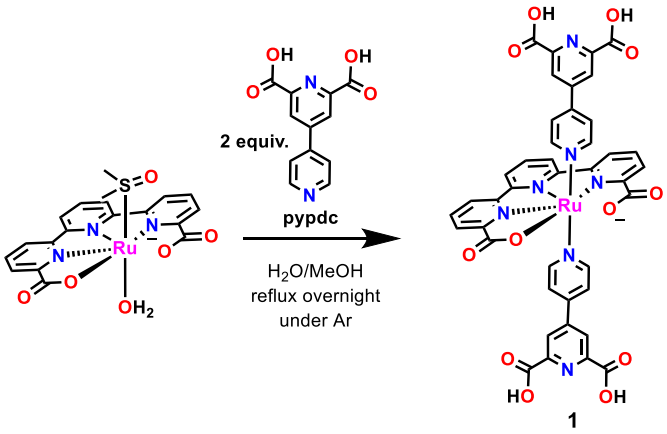

Scheme 1. Synthesis of complex **1**.

Electrochemistry and surface modification

The electrochemical properties of complex **1** in homogeneous phase were analyzed in pH 7 phosphate buffer (I = 0.1 M). All the redox potential here are reported versus the normal hydrogen electrode (NHE) unless otherwise explicitly mentioned.

Cyclic voltammogram of **1** in Figure 3 shows two one-electron redox waves at $E_{1/2}$ = 0.56 V (ΔE = 60 mV) and $E_{1/2}$ = 1.07 V (ΔE = 60 mV) corresponding to the $Ru^{III/II}$ and $Ru^{IV/III}$ redox couples of the complex respectively and are similar to the reported complex [Ru(tda)($py)_2$],[20] indicating that the electronic effect of the functionalized axial ligand is weak.

The complex was anchored on nano-ITO supported on conductive FTO plates by dipping the electrode inside a 1 mM solution of complex **1** in methanol for 2 h. The electrode was then rinsed with methanol and water and dried by airflow. A cyclic voltammetry of this new hybrid electrode **1**@nanoITO@FTO was carried out in fresh pH 7 phosphate buffer (Figure 3b and 3c). It shows a one-electron redox wave at $E_{1/2}$ = 0.6 V (ΔE = 440 mV) assigned to the $Ru^{III/II}$

redox couple. A second one-electron redox wave also appears at $E_{1/2}$ = 1.02 V (ΔE = 260 mV) corresponding to the $Ru^{IV/III}$ redox couple. Both electron transfer processes are very slow as indicated by the broad shape of the waves and the large peak-to-peak separation as compared to the homogeneous characterization (compare Figure 3a and 3c, black solid line). This is attributed to the lower conductivity of the nanoITO/FTO electrode compared to the glassy carbon electrode used to perform the electrochemistry in homogeneous conditions.

a)

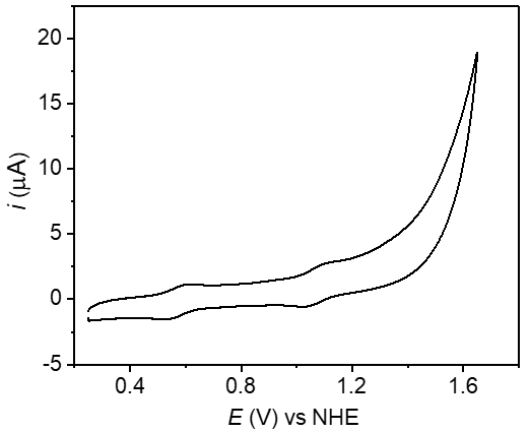

b) c)

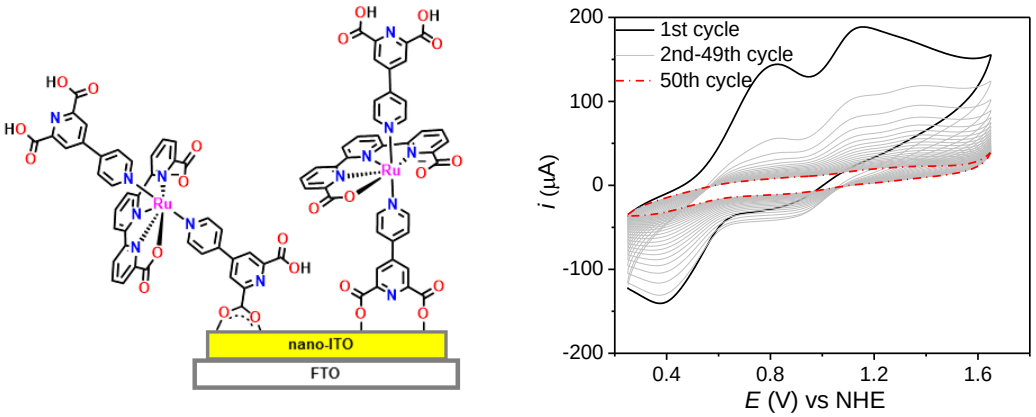

Figure 3. a) CV of complex **1** in homogeneous phase at pH 7 and using glassy carbon disk as working electrode; b) A schematic representation of the hybrid electrode **1**@nanoITO@FTO; c) Repetitive CV cycles using the hybrid electrode **1**@nanoITO@FTO as working electrode: first CV cycle (black solid line), 2nd to 49th CV cycles (grey solid line), 50th cycle (red dotted line) at pH 7.

To check the stability of the complex anchored on the surface repetitive cyclic voltammetry experiments were carried out (Figure 3c, grey lines). After 50 cycles, the electrochemical response of the ruthenium complex is completely gone (red dotted line in Figure 3c). In addition, it is visually possible to see that the complex has leached to the solution as shown in the pictures of Figure 4. A CV of the colored solution after the 50 cycles using a clean glassy

carbon electrode shows exactly the same CV as in Figure 3a, indicating no decomposition of complex **1** upon anchoring on the surface.

Similar results were obtained when a flat FTO plate and a nano-TiO_2 coated FTO plate were used, indicating that the behavior is the same for different type of oxides. In the former case, the loading was extremely low and the stability as poor as for the described for **1**@nanoITO@FTO. For the latter, the loading was significant but the electrochemical response of the hybrid electrode **1**@nanoTiO_2@FTO were difficult to characterize in the dark and under light, due to the semiconducting properties of the TiO_2 materials.

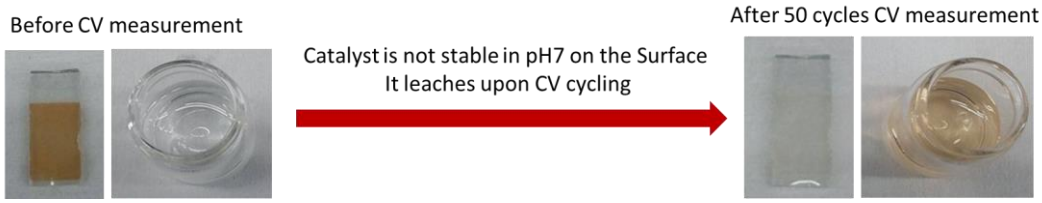

Figure 4. Pictorial view of the electrode and the electrolytic solution before and after 50 CV cycles. A full decoloration of the electrode is observed indicative of the weak linkage of the pyridine dicarboxylate group in pH 7 phosphate buffer solutions.

7. 3. 2. Polyvinyl Pyridine Films as Anchoring Platform

Electrode Preparation and Surface Functionalization

It is known that 4-vinylpyridine (vpy) polymerizes to polyvinyl pyridine (PVP) under UV light.[12] If this reaction is carried out on top of a flat surface, it results in a homogeneous film with controlled thickness depending on several reaction parameters such as amount of vpy or time of exposure to UV light. This conductive film contains a high density of dangling pyridine groups that are excellent anchoring platforms to attach the ruthenium precursor [Ru(tda)(py)(OH_2)] to generate a conductive material containing the catalytic site precursor [Ru(tda)(py)(py')] as indicated in the top of Scheme 2.

Following this strategy, nanoITO coated slides (nanoITO@ITO) were placed inside an oxygen free glove box and a few drops of inhibitor-free vpy were added on top of the slides to cover the whole surface. In order to keep the liquid vpy, a wall of epoxy resin compatible with the reaction conditions was deposited on the edges of the electrode (see Scheme 2, bottom). The slides containing the vpy were exposed to 254 nm UV light for 2 h giving a polyvinyl modified nanoITO electrodes (PVP@nanoITO@ITO). Then, they were rinsed thoroughly with methanol, dried under nitrogen and stored under vacuum.

The complex functionalization was achieved by dipping the PVP@nanoITO@ITO electrode in a solution of [Ru(tda)(py)(OH_2)] (1 mM) and triethylamine (1 mM) in methanol under argon. The solution was heated up at 50 °C overnight. The resulting modified electrode Ru(tda)(py)PVP@nanoITO@ITO was then rinsed with methanol and water and dried with airflow. As seen in the bottom of Scheme 2, the colour of the electrode changes significantly from transparent to redish/brownish after the functionalization, indicating the successful incorporation of the Ruthenium on the surface.

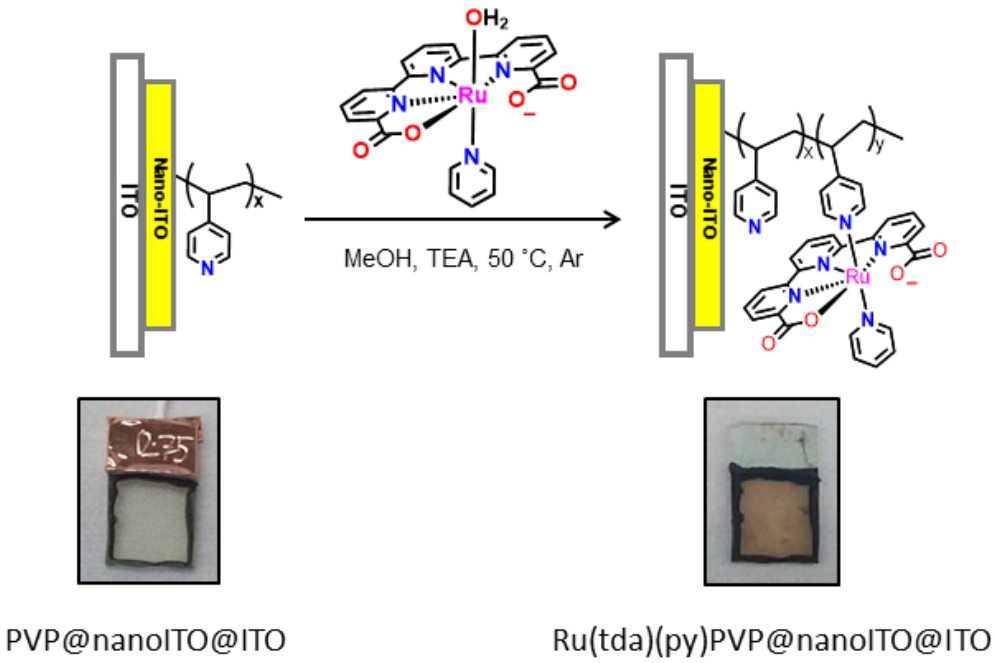

Scheme 2. Top) Schematic representation of the preparation of the hybrid electrode Ru(tda)(py)PVP@nanoITO@ITO. **Bottom)** Picture of the real electrodes before (left) and after (right) functionalization with the ruthenium catalyst. A clear change of color of the surface due to anchored Ruthenium is observed.

Electrochemistry

Cyclic voltammetry experiments using Ru(tda)(py)PVP@nanoITO@ITO as working electrode were recorded in pH 7 phosphate buffer. As shown in Figure 5, two one-electron redox process appear at $E_{1/2}$ = 0.54 V (ΔE = 80 mV) and $E_{1/2}$ = 1.03 V (ΔE = 100 mV) corresponding to the $Ru^{III/II}$ and $Ru^{IV/III}$ redox couples, respectively. These values are comparable to those obtained for homogeneous analog $[Ru(tda)(py)_2]$,[20] indicative of the negligible electronic effect exerted by the polymeric structure connected to the axial pyridine, as expected. The absence of any pH dependent wave due to proton couple electron transfer process (PCET) of Ru-OH_2 groups indicates that there is no adsorbed $[Ru(tda)(Py)(OH_2)]$ precursor on the surface.

The stability of the hybrid electrode was carried out by repetitive CV cycles. As shown in Figure 5, the intensity of the redox waves of the complex on the surface remain constant after 100 cycles. This results indicate the extremely robustness of the linkage between the metal oxide surface and the Ru-modified PVP film over a wide potential window.

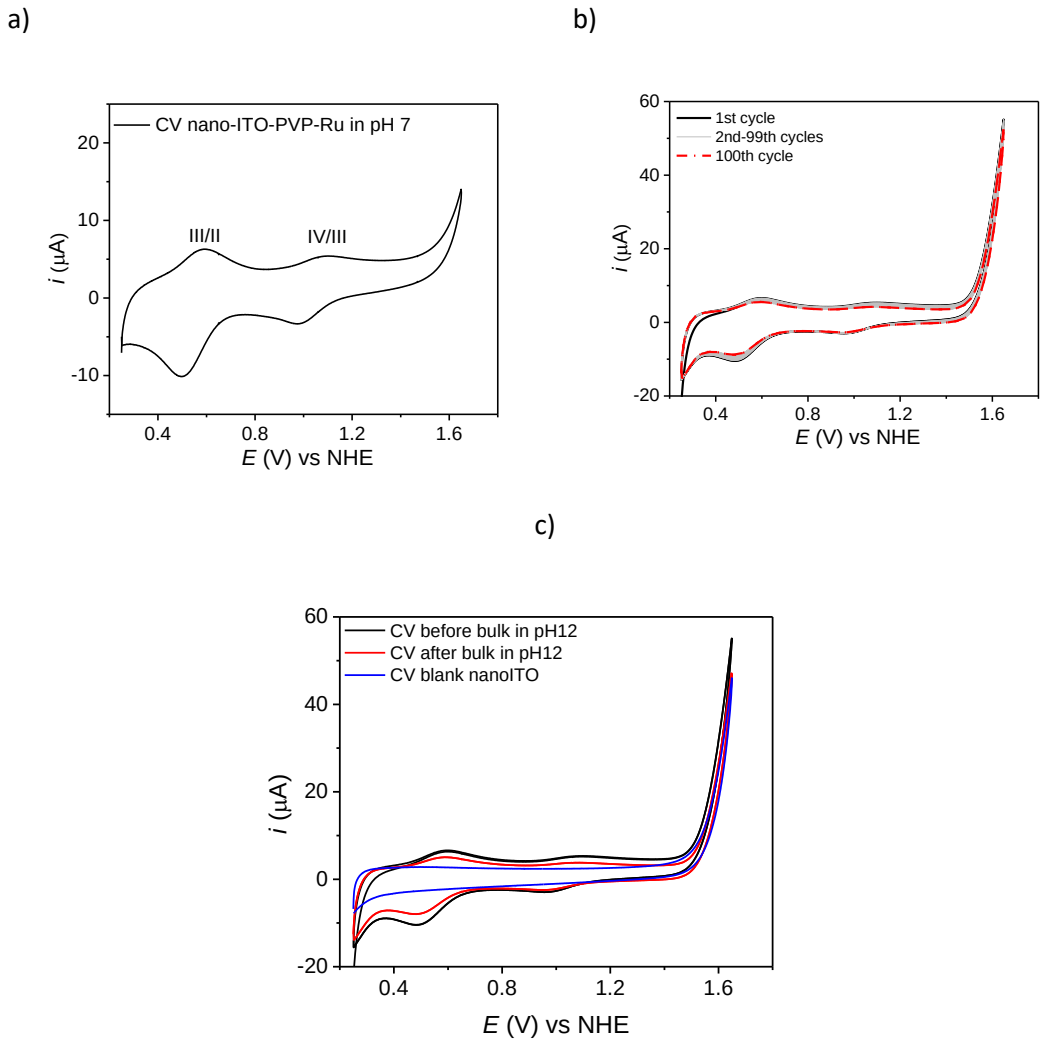

Figure 5. a) CV of freshly prepared Ru(tda)(py)PVP@nanoITO@ITO as working electrode in pH 7. b) Repetitive CV cycles of Ru(tda)(py)PVP@nanoITO@ITO as working electrode: 1st CV cycle (black solid line), 2nd to 99th CV cycles (grey solid line), 100th cycle (red dotted line). c) CV of the Ru(tda)(py)PVP@nanoITO@ITO before activation (black solid line), after activation as described in the main text (red solid line) and blank electrode (PVP@nanoITO@ITO) (blue solid line). All CVs in Figure 5a-c are performed in pH 7 buffered solution.

The Ruthenium centers in the Ru(tda)(py)PVP@nanoITO@ITO electrode in Scheme 2 are catalyst precursors. In order to generate the active Ru-aquo catalyst on the electrode (Ru(OH)(tda)(py)PVP@nanoITO@ITO) a control potential electrolysis was carried out at E_{app} = 1.25 V in basic pH 12 for a few minutes as described in detailed in the experimental section. We usually call this process the activation of the catalyst. After prolonged activation of the electrode, no changes appeared indicating that the formation of the corresponding Ru-OH_2 complex on the surface did not occurred, as opposed to previous results in homogeneous and heterogeneous phase on graphitic surfaces.[20,21] These results could be a consequence of two effects: i) the lack of effective concentration of hydroxide ion around the first coordination sphere of the metal center on the electrode due to the hydrophobicity of the PVP film

embedding the ruthenium centers and/or ii) deactivation of the catalyst due to coordination of the dangling carboxylate group on the metal oxide surface. Strategies to increase hydrophilicity of the PVP film by introducing polar groups in the polymeric backbone such as sulfonic or carboxylic acids are currently under way.

7. 3. 3. Aromatic Pyrazine on Anodized Glassy Carbon

The strategies discussed in the last two sections 7.3.1 and 7.3.2 are characterized by a relatively poor electronic coupling between the appended molecule and the conductive electrode surface, due to the organic moiety acting as a link between the two entities. Recently Yogesh *el al.* reported[22] a new and simple surface functionalization strategy for conjugating molecular units with anodized graphitic surfaces by aromatic pyrazine linkage (Figure 1, top right) for CO_2 reduction showing very impressive results. They have also shown that this anchoring method gives a very strong electronic coupling between the appended molecule and the surface electrode and thus the molecular catalytic site behaves like metallic heterogeneous surface sites.[13]

For this approach the axial pyridine of the Ru-tda type of complex was functionalized with two ortho-amino groups (diapy in Figure 2). This diamino group can condense with the orthoquinone moiety of the exploited native surface of graphitic electrode and form a conjugated aromatic pyrazine linkage (Figure 1, top right). While the synthesis and full characterization of the new ruthenium complex was performed at ICIQ, (Figure S2-S4) the anchoring and catalytic studies were performed during a three months stay with Prof. Yogesh group at the Massachusetts Institute of Technology (MIT).

Synthesis and Characterization of 2

The synthetic strategy used to prepare complex **2** is outline in Scheme 3. It consists of reacting the ruthenium precursor [Ru(tda)(DMSO)(OH_2)] with slight excess of 3,4-pyridinediamine (dapy). The solid product is isolated with 70% yield and the compound characterized by spectroscopic, electrochemical and analytical techniques. Full assignment of the ^{1}H NMR resonances is given in Figure S2-S4 in the supporting information and shows the characteristic singlet proton signals for the two distinct amine groups at δ = 5.63 ppm and 4.31 ppm as expected.

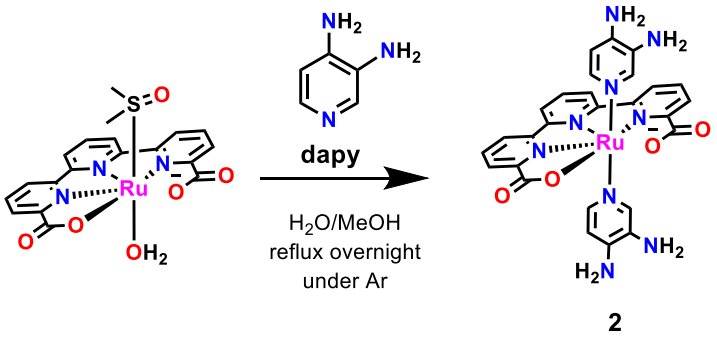

Scheme 3. Synthesis of complex [Ru^{II}(tda)(dapy)$_2$], **2**.

Surface Anchorage and Characterization

In order to perform the condensation reaction between complex **2** and glassy carbon electrodes, a pretreatment of the latter is needed to ensure there are enough orthoquinone groups to react with the diamino moiety. This pretreatment is done under an inert atmosphere and consists in polarizing a polished glassy carbon (GC) electrode +3.5 V vs NHE in a 0.1 M H_2SO_4 solution for 10 s.[23] The pretreated electrodes (GCC hereafter) were then immersed in a 1 mM solution of of **2** in trifluoroethanol (TFE) and heated up to 60 °C for 12 h (Scheme 4). The electrodes were then removed from the reaction medium, rinsed with TFE and placed in 5 mL of 0.1 M H_2SO_4 for 1 h. Finally, it was rinsed with copious amount of water and ethanol and dried under vacuum to give the functionalized electrode (**2**@GCC, Scheme 4).

Surface analysis of **2**@GCC was carried out by X-ray Photoelectron Spectroscopy (XPS). The survey XPS spectrum shows a new peak at 462.5 eV corresponding to Ru 3d (Figure S8) as well as increased intensity in the N 1s peak relative to the native N concentration of unmodified GC electrode. The peak integration reveals an increase in atomic surface concentration of 0.51 and 4.32 % for Ru and N respectively and consistent with the expected Ru/N ratio (1:9) based on the structure of **2**@GCC. High resolution XPS spectra give additional information about the surface of this new electrode. The N 1s spectrum of this freshly prepared GCC-Ru shows the introduction of three new peaks corresponding to three different nitrogen environment on the surface in 2:5:2 ratio at 401.67, 400.17and 398.77 eV (Figure S8) corresponding to aromatic amine, pyridine and pyrazine nitrogen, respectively.

Chapter 7

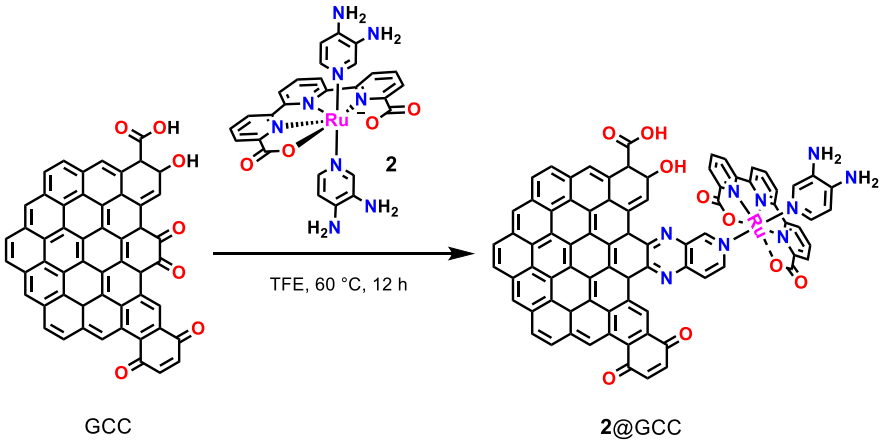

Scheme 4. Preparation of hybrid electrode **2**@GCC.

Electrochemistry

A cyclic voltammogram of **2**@GCC in aqueous electrolyte solution at pH 13 (0.1 M KOH) shows two one-electron redox processes at $E_{1/2}$ = -0.78V (ΔE = 48 mV) and $E_{1/2}$ = -0.42 V (ΔE = 52 mV) (Figure 6), that are characteristic of the pyrazine system and are associated with the sequential proton coupled electron transfer processes (PCET) indicated in the top of Figure 6. The potential values are fully consistent with reported values and with control experiments done with an analogous organic molecule,[23] which doesn't contain any metallic center (Figure S9 and S10). All these results confirm that the coupling reaction in Scheme 4 was successful.

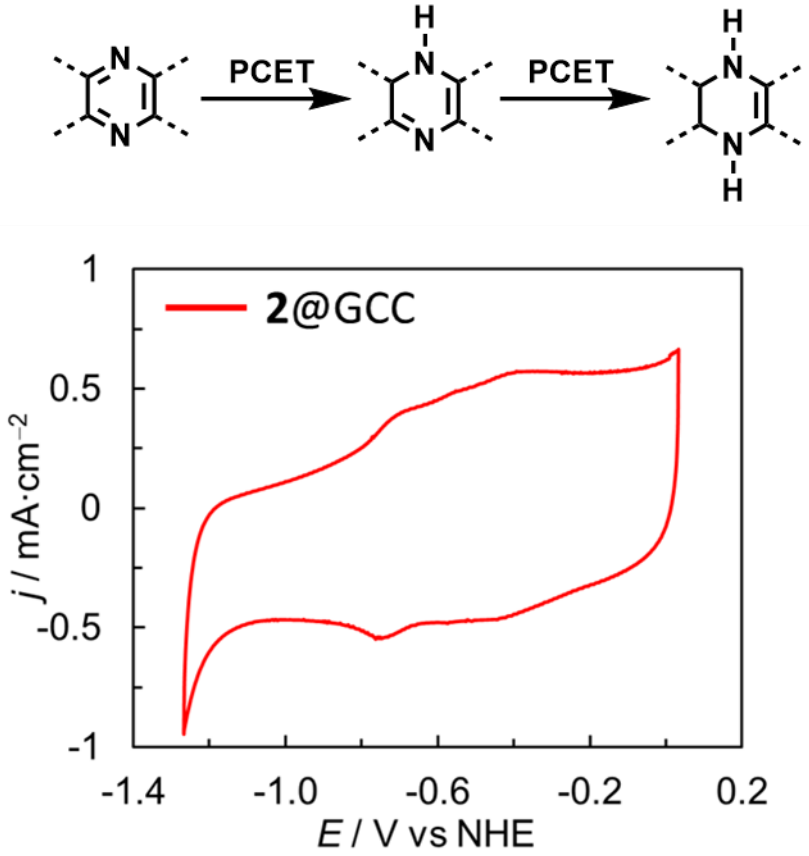

Figure 6. Top) PCET processes involved for pyrazine groups. **Bottom**) CV of **2**@GCC in 0.1 M KOH solution in the lower potential range to see features of the pyrazine group.

Cyclic voltammetry experiments of **2**@GCC at pH 7 don't show the typical features related to the $Ru^{III/II}$ and $Ru^{IV/III}$ redox couples at $E_{1/2} \approx 0.55$ V and $E_{1/2} \approx 1.00$ V, respectively (Figure 7, red trace) as expected for a strong electronic coupling between the molecular complex and the conductive graphitic surface.[13] On the other hand, a large current is observed starting at $E_{1/2} \approx 0.95$ V, that could be related to an electrocatalytic process of **2**@GCC. If this is true for the water oxidation reaction with a thermodynamic potential of 0.82 V at pH 7, it would represent an overpotential of only 130 mV. However, consecutive CV cycles show that the high current decreases significantly after every cycle (Figure 7, grey traces). In addition, the capacitive current also decreases, indicating that the electroactive surface of the electrode is lost, *i.e.*, the Ru-pyrazine linkage is breaking and coming out from GC electrode upon scanning at high potentials. In order to test the stability of the pyrazine linkage, a model electrode containing an organic molecule attached to the GCC via a pyrazine group was submitted to a controlled potential electrolysis at different applied potentials (Figure S10). We found that while the pyrazine linkage is relatively stable at E_{app} = 1.1 V, it is almost completely gone after a 10 minutes electrolysis at E_{app} = 1.4 V. Due to the instability of the system, it was not possible to further study the electrochemical water oxidation properties of **2**@GCC.

Chapter 7

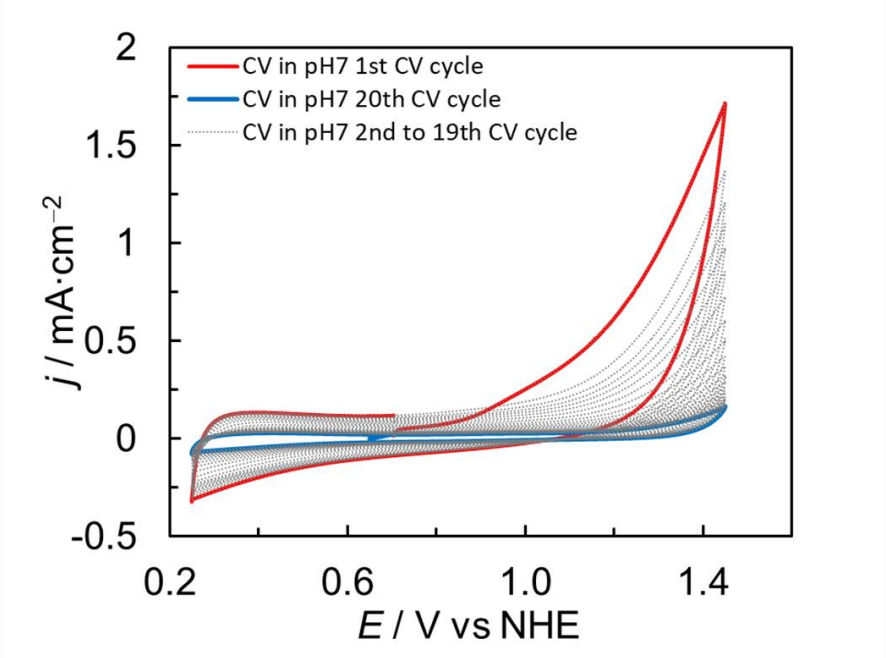

Figure 7. Repetitive CV cycles of **2**@GCC in pH 7 phosphate buffer 0.1 M to explore the water oxidation catalytic activity: 1st CV cycle (red solid line), 2nd to 19th CV cycles (grey dashed line), 20th cycle (blue solid line).

7. 3. 4. Aromatic Diazonium Salt as an Anchoring Group

A well-known and promising way of anchoring molecular catalysts onto conductive supports is the electrochemical grafting by either oxidation or reduction of versatile organic functional groups. One example is the dediazonation reaction, *i.e,* the loss of dinitrogen with the formation of an aryl radical upon reduction. This process generates a covalent linkage between the surface and the appended molecule through C-C bond.[24] In this strategy, 4-(pyridin-4-yl) aniline ligand (apy in Figure 2) was used to generate the corresponding aromatic diazonium salt and further be anchored on the carbon surface.

Three different approaches have been explored for anchoring the [Ru(tda)(py')(py'')] catalyst (py' and py'' are pyridine with different functional group) precursor following the electrografting of aromatic diazonium salts: i) electrografting of the ligand followed by complexation, ii) electrografting of a ruthenium precursor containing a ligand with a diazonium salt followed by aqua ligand exchange, and iii) electrografting of the final [Ru(tda)(py')(py'')] catalytic precursor containing at least one ligand (py' or py'') with a diazonium salt.

7. 3. 4. 1. Approach 1: Ligand Attachment Followed by Complexation

In general, surface functionalization of the electrode was carried with electroreduction of *in situ* generated aromatic diazonium salt. In an electrochemical set up cell, 4-(pyridin-4-yl)aniline (apy) ligand was first treated with *tert*-butyl nitrite in acetonitrile solvent at 4 ˚C for 10 min under N_2 atmosphere in order to convert the amino group to the corresponding diazonium salt. Once generated, a cyclic voltammetry experiment was carried out starting from 0.9 V to -0.35 V up to 10 CV cycles (see Scheme 4 top and experimental section for the detailed procedure). As shown in Figure 8a, the 1st CV cycle shows a broad irreversible redox wave corresponding to the reduction of the diazonium salt with the formation of aryl radical, that irreversibly anchors on the carbon surface through C-C covalent bond. Later from the 2nd CV to the 10th cycle the wave disappears completely due to the formation of an organic layer of aromatic pyridine on the surface that covers the electroactive area during the 1st cycle.[25] The ligand modified electrodes were then put into a solution containing the precursor Ru(tda)(py)(OH_2) complex in methanol or the 1D polymer, {[Ru(tda)(4,4´bpy)]$_{15}$(4,4´bpy)}, (see Chapter 5, 4,4´bpy is 4, 4´-bipyridine and Scheme 4, bottom) in trifluoroethanol at 50 ˚C overnight. The functionalized electrodes were rinsed with the respective solvents to remove all the adsorbed complexes for 10 min and with copious amount of water and dried with

airflow. With this process, two kind of hybrid electrodes were produced that will be referred as Ru(tda)(py)(apy)@GC and Ru1Dpolymer(apy)@GC, respectively.

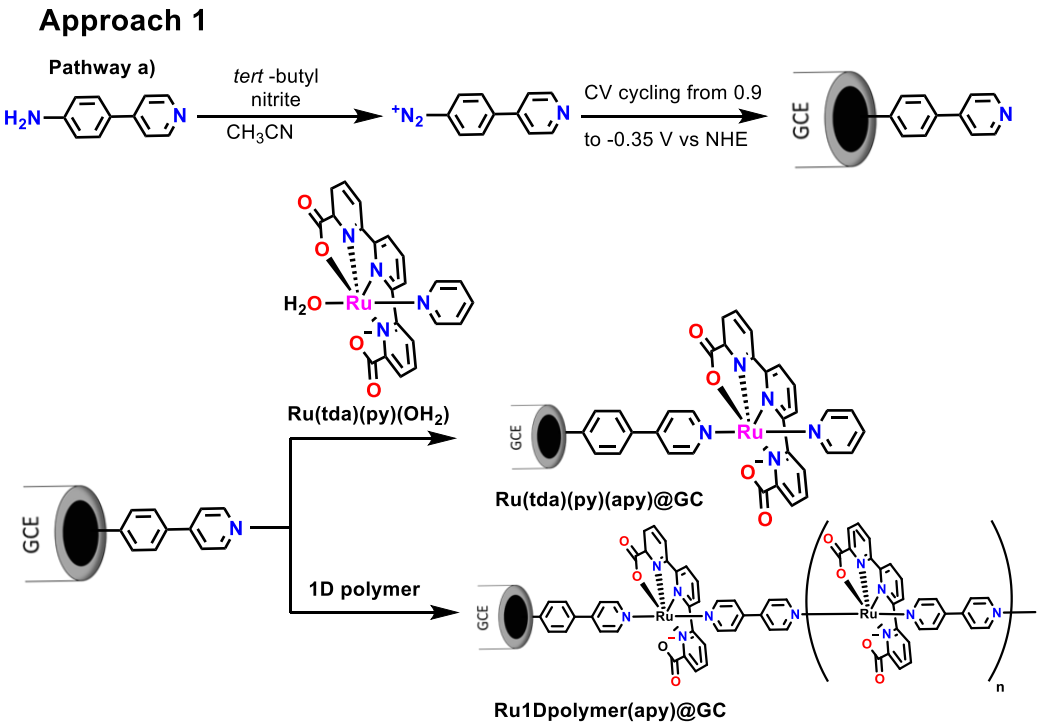

Scheme 4. General scheme of anchoring ligand on graphite surface followed by complexation.

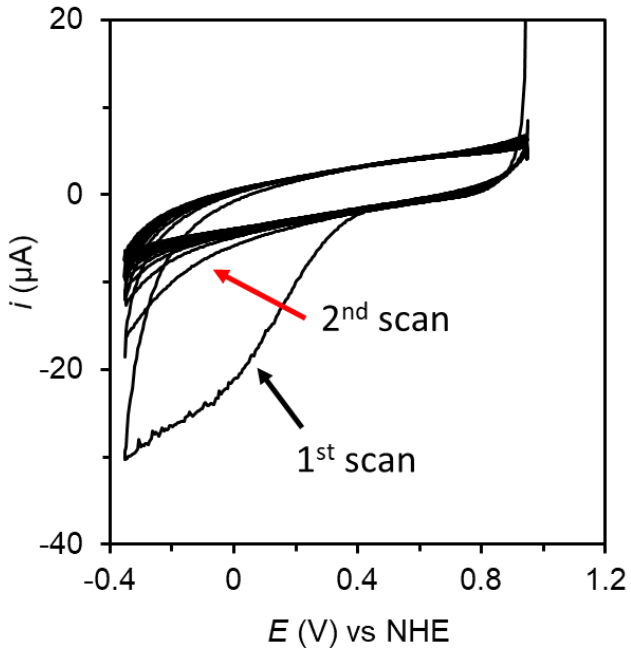

Figure 8. Electrografting process: CV of 4-(pyridin-4-yl) benzenediazonium salt in 0.1 M [(*n*-Bu)$_4$N][PF$_6$] acetonitrile.

Electrochemistry

Cyclic voltammetry and differential pulse voltammetry experiments of the electrode Ru(tda)(py)(apy)@GC were carried out in pH 7 phosphate buffer solution. As shown in Figure 9, two weak one-electron redox waves at $E_{1/2}$ = 0.59 V (ΔE = 53 mV) and $E_{1/2}$ = 1.06 V (ΔE = 60 mV) are observed. As already discussed in previous sections, these values are within the expected range for the the $Ru^{III/II}$ and $Ru^{IV/III}$ redox couples, respectively, of a typical [Ru(tda)(py')(py'')] complex. Therefore, we concluded that the complexation reaction using the precursor Ru(tda)(py)(OH_2) was successful.

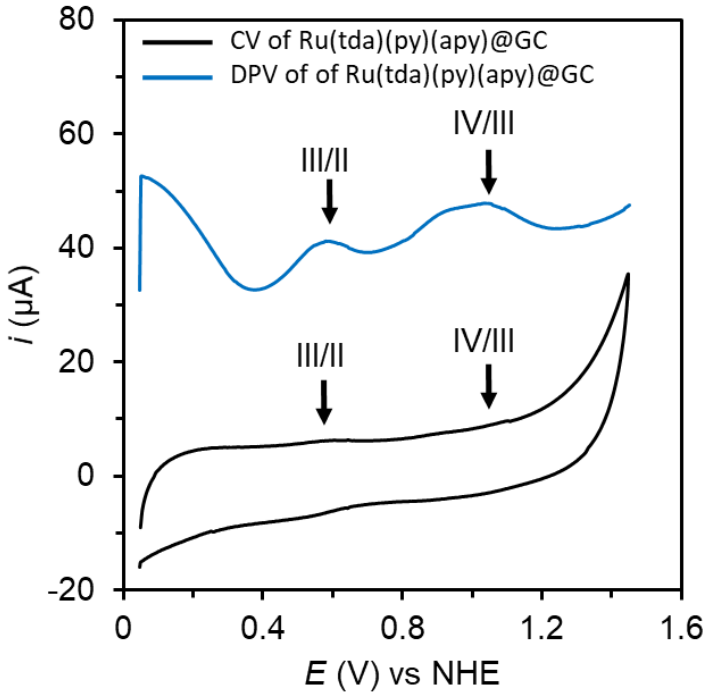

Figure 9. CV (black) and DPV (blue) of Ru(tda)(py)(apy)@GC in 0.1 M pH 7 phosphate buffer.

In section 7.3.2, we already explained that the [Ru(tda)(py')(py'')] type of complexes are catalyst precursors and need activation to get the real catalyst for water oxidation catalysis. Thus, a control potential electrolysis at E_{app}= 1.25 V of the Ru(tda)(py)(apy)@GC electrode in basic pH was carried out for a few minutes. As shown in Figure 10, the intensities of the waves decrease slightly but most importantly, no new waves appeared after prolonged activation of the electrode, indicating no formation of the active Ru(OH)(tda)(py)(apy)@GC electrode. This behavior is similar to that of the electrode Ru(tda)(py)PVP@nanoITO@ITO in section 7.3.2 and suggests that the hydrophobic organic layer on top of the electrode hinders the coordination of the hydroxide to the metal.

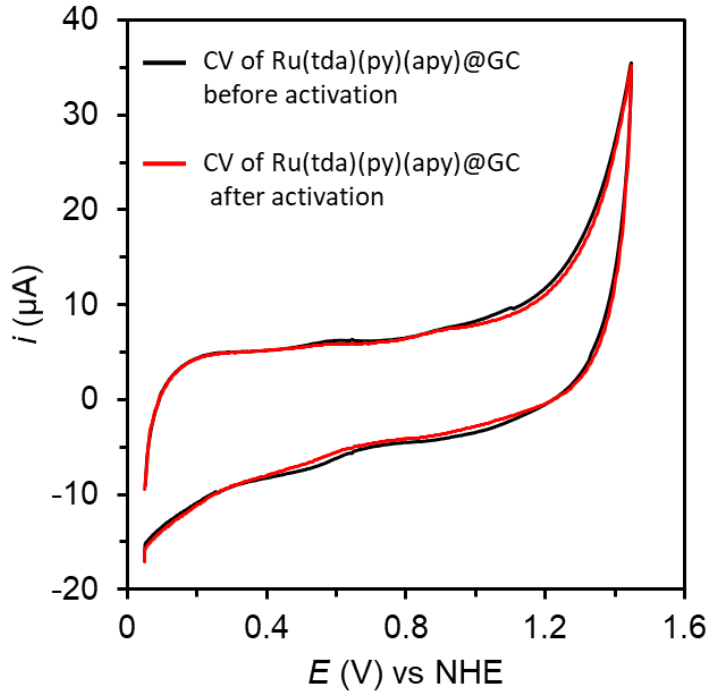

Figure 10. CV of Ru(tda)(py)(apy)@GC in 0.1 M pH 7 phosphate buffer: before (black) and after (red) activation.

The Ru1Dpolymer(apy)@GC electrode shows similar electrochemical behavior as Ru(tda)(py)(apy)@GC indicating successful attachment of the polymer on the electrode (Scheme 4, bottom). Interestingly, the electrochemical response of this electrode is much better, indicating higher catalyst loading on the surface with values of $\Gamma_{Ru1Dpolymer(apy)@GC}$ = 0.05 nmol/cm^2 and $\Gamma_{Ru(tda)(py)(apy)@GC}$ = 0.001 nmol/cm^2 (compare CVs in Figure 10 and 11). However, there were no changes in the redox chemistry after prolonged activation in pH 12, once again indicating no formation of the active Ru(OH)1Dpolymer(apy)@GC electrode. On the other hand, it is worth to mention that there was no loss of catalyst after the activation process, indicative for the high robustness of the electrode (Figure 11).

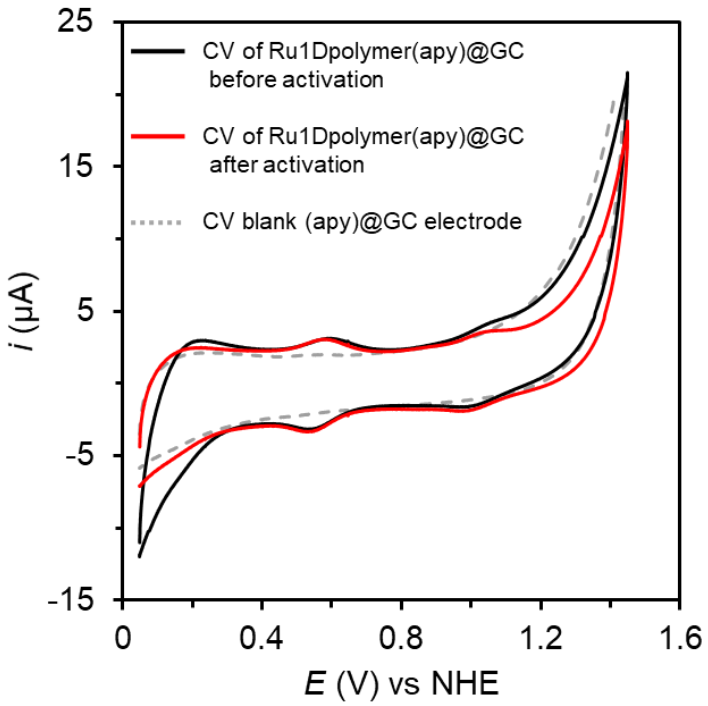

Figure 11 CV of Ru1Dpolymer(apy)@GC in 0.1 M pH 7 phosphate buffer: before (black), after (red) activation and blank (apy)@GC (grey dotted line).

One of the possible reason why Ru(tda)(py)(apy)@GC and Ru1Dpolymer(apy)@GC electrodes do not activate is the hydrophobic nature of the electrode surface that is covered by organic pyridines and the ruthenium centers. In order to tackle this problematic, a co-electrografting method using a mixture of apy and 4-amino-benzenesulfonic acid (bSO_3) was developed. The latter pyridine contains a hydrophilic sulfonate group that should increase the overall hydrophilicity of the final electrode surface (Scheme 5, top). As shown in Figure S11, the electrografting of a 1:1 molar ratio of the two ligands on a glassy carbon electrode shows the electrochemical behavior, suggesting successful anchoring of the ligands.

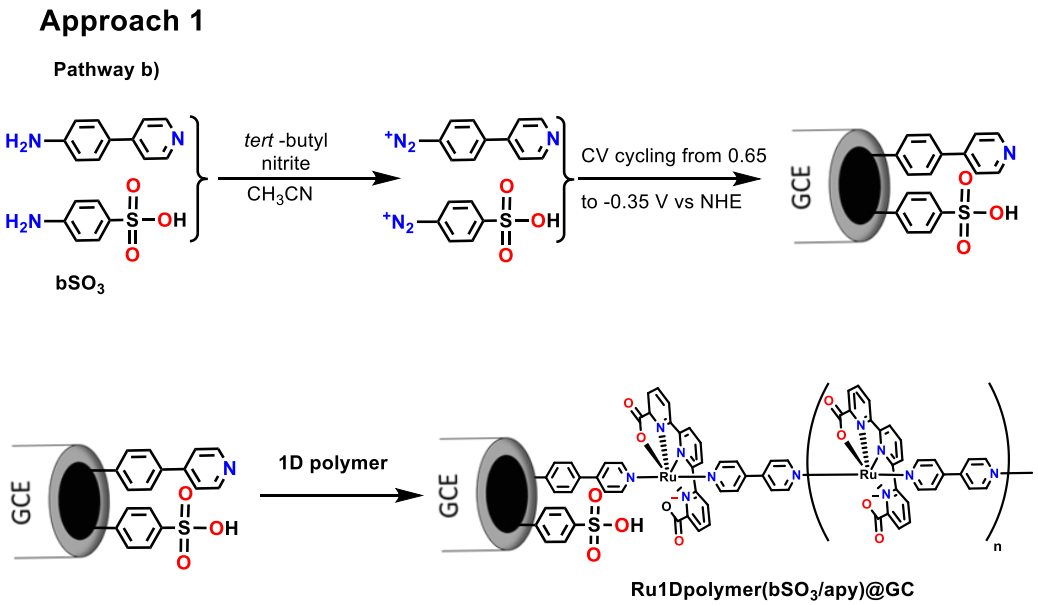

Scheme 5. General scheme of anchoring ligand on graphite surface followed by complexation.

The following complexation reaction of the hybrid electrode (bSO_3/apy)@GC with the 1D polymer indicated in the bottom of Scheme 5 was successful as indicated in the CV of Figure 12 (black line). However, the activation of the precursor was not possible as indicated by the red trace of Figure 12, only an increase of the capacitive current was achieved in this case. These results are preliminary and more experiments are necessary to make definitive conclusions about this strategy. A thorough study of electrografting using different ratios of the two anilines apy and bSO_3 as well as their concentration are currently underway.

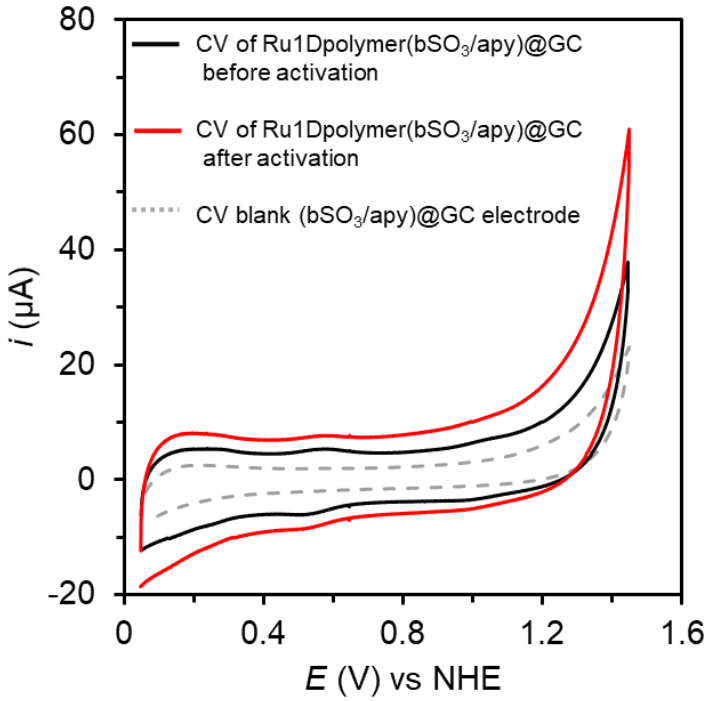

Figure 12. CV of Ru1Dpolymer(bSO_3/apy)@GC in 0.1 M pH 7 phosphate buffer: before (black), after (red) activation and blank (bSO_3/apy)@GC (grey dotted line).

7. 3. 4. 2. Approach 2: Ru-aqua Complex Attachment Followed by Aqua Ligand Exchange

Synthesis and Characterization

In a second approach, a Ruthenium complex containing an aromatic amine group was prepared. For this purpose, the complex [Ru^{II}(tda)(apy)(OH_2)], **3** was prepared following the literature precedent.[17] It consists of reacting the precursor [Ru(tda)(DMSO)(OH_2)] with 4-(pyridin-4-yl)aniline (apy) at 1:1 molar ratio in water and heating at 50˚C for 4 h. The resulting complex [Ru(tda)(apy)(DMSO)] was obtained which upon treatment with neat triflic acid produced the desired complex [Ru^{II}(tda)(apy)(OH_2)], **3**. The complex was characterized by ^{1}H NMR spectroscopy with the expected resonances and integration (Figure S5).

Surface Functionalization and Electrochemistry

The surface functionalization of the glassy carbon electrode was achieved by a similar electrografting procedure as described before. In this case, complex **3** is used to generate the diazonium derivative *in situ* in trifluoroethanol solvent (Scheme 6, top and Figure S12).

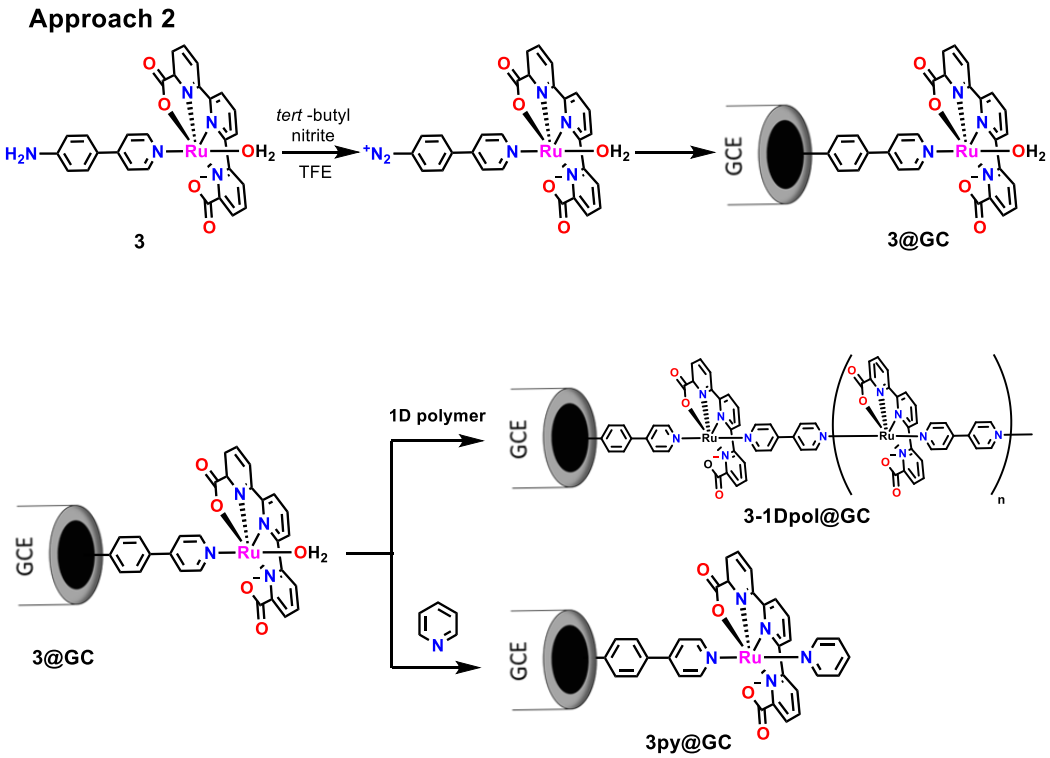

Scheme 6. General scheme for anchoring Ruthenium complexes on graphite surface followed by aqua ligand exchange.

An electrochemical analysis of the modified electrode **3**@GC confirmed the successful attachment of the complex on the graphite surface. The DPV in Figure 13a shows two one electron redox couples that are similar to those of the reported homogeneous complex [Ru(tda)(py)(OH_2)].[17] Further, both redox waves are pH dependent confirming the presence of a Ru-aqua group on the electrode.

In the next step, the **3**@GC electrode was dipped into a solution of pyridine and heated up to 40 ˚C overnight. Then, the electrode was rinsed with methanol, water and dried with airflow. As shown in the DPV experiments of Figure 13b, the initial redox waves of **3**@GC at $E_{1/2}$ = 0.49 V and 0.92 V disappeared with the appearance of two new redox couples at $E_{1/2}$ = 0.54 V and 1.0 V which are in the expected potential zone for the [Ru(tda)(py')(py'')] type of complex, confirming the generation of **3py**@GC by replacing the aqua group of **3**@GC with pyridine.

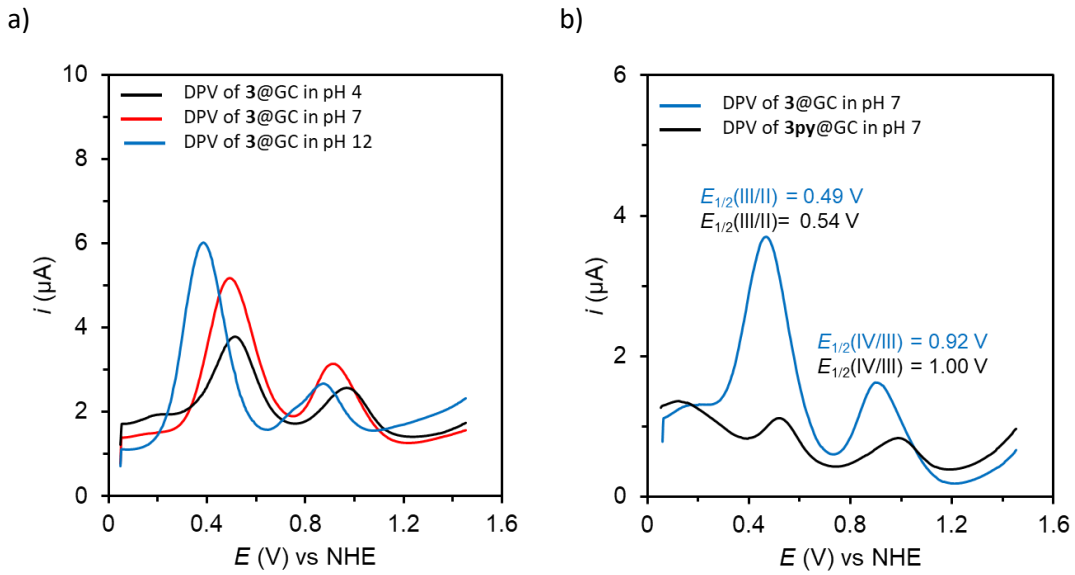

Figure 13. a) DPV of **3**@GC in different pHs; b) DPV of **3**@GC and **3py**@GC in pH 7.

The coordination of the 1D polymer on the **3**@GC was also achieved by treating this electrode with a 1D polymer solution in trifluoroethanol at 50˚C. In this case, a much longer time is required to achieve full conversion as illustrated in Figure 14. After 16 h the DPV shows the presence of both complexes on the electrode, i.e., **3**@GC and **3**-1Dpol@GC indicating the partial aqua ligand coordination. After 32 h the presence of the 1D polymer increases with decreasing of the **3**@GC as can be seen in (compare red and blue lines in Figure 14).

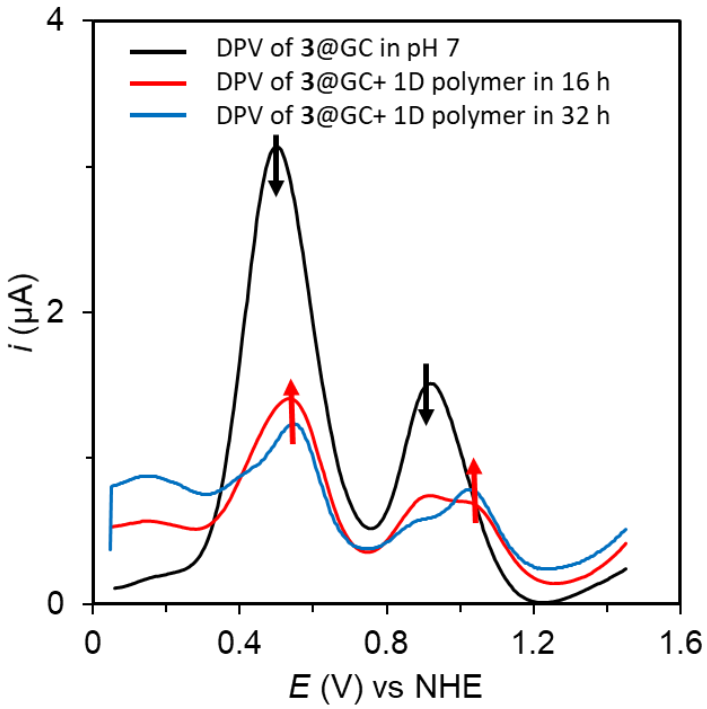

Figure 14. DPV of **3**@GC with 1D polymer in different reaction time. Black arrows indicate the disappearance of **3**@GC and red arrows indicate the appearance **3**-1Dpol@GC. Black trace: **3**@GC at time = 0 h, red trace: **3**@GC + 1D polymer at time = 16 h and blue trace: **3**@GC + 1D polymer at time = 32 h. All experiments are measured in pH 7.

Both electrodes **3py**@GC and **3**-1Dpol@GC were place in basic solution and submitted to a bulk electrolysis in order to generate the active species on the electrode as explained before. As shown in Figure 15, it was not possible to generate the active species on the electrode, a behavior that was also observed in the previous approach. This result is not surprising if one consider that the final functionalized electrodes obtained using approach 1 and 2 should be analogous, despite the different sequence of reactions.

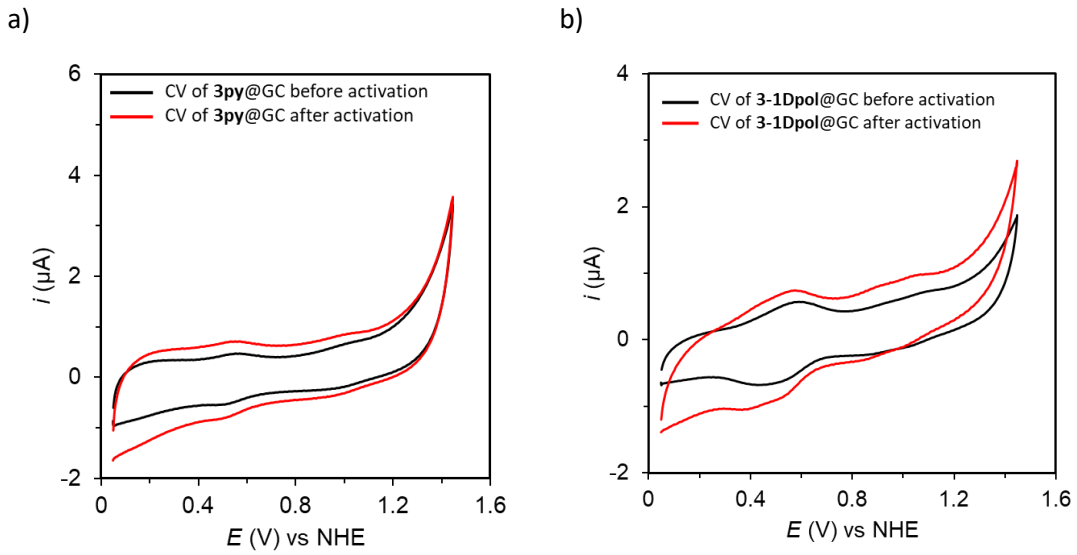

Figure 15 a) CV of **3py**@GC in 0.1 M pH 7 phosphate buffer: before (black) and after (red) activation. b) CV of **3**-1Dpol@GC in 0.1 M pH 7 phosphate buffer: before (black) and after (red) activation.

7. 3. 4. 3. Approach 3: Ru-Catalyst Precursor [Ru(tda)(py')(py'')] Attachment

Synthesis and Characterization

VII

In order to attach a [Ru(tda)(py')(py'')] pre-catalytic center directly on a graphitic surface, the non-symmetric complex [Ru^{II}(tda)(dmpy)(apy)], **4**, was prepared following the synthetic route outlined in Scheme 7. It starts with the reaction of [Ru(tda)(DMSO)(OH$_2$)] with 3,5-lutidine (dmpy in Figure 2) in water for 4 h at room temperature. This procedure generated a brown solution that was extracted with DCM (3 x 100 mL). Upon removal of the aqueous solvent, a brown solid identified as the intermediate Ru^{II}(tda)(dmpy)(DMSO)] was obtained. This product was then dissolved in MeOH and 1 equivalent of 4-(pyridin-4-yl)aniline (apy) was added and refluxed for 2 days. Compound [Ru^{II}(tda)(dmpy)(apy)], **4** was isolated upon column chromatography of the resulting mixture using neutral alumina in a 10 % yield. It was fully characterized by ^{1}H and ^{13}C NMR spectroscopy (Figures S6-S7).

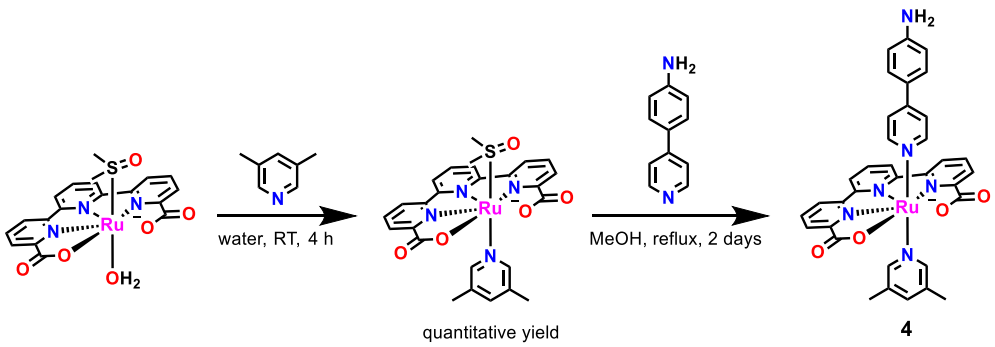

Scheme 7. Synthetic scheme for the complex [Ru^{II}(tda)(dmpy)(apy)], **4**.

Chapter 7

Surface Functionalization and Electrochemistry

Surface functionalization of the electrode via diazonium salt was achieved following the same procedure described above using a trifluoroethanol solution of complex **4** to give the hybrid electrode **4**@GC (pathway a) in Scheme 8 and Figure S13). The CV of **4**@GC shows the successful attachment of the complex on the graphite surface by the presence of two one-electron redox waves at $E_{1/2}$ = 0.56 V (ΔE = 65 mV) and $E_{1/2}$ = 1.02 V (ΔE = 60 mV), which are similar to those of the homogeneous catalyst and former hybrid electrodes with similar Ru centers (Figure 14 black trace).

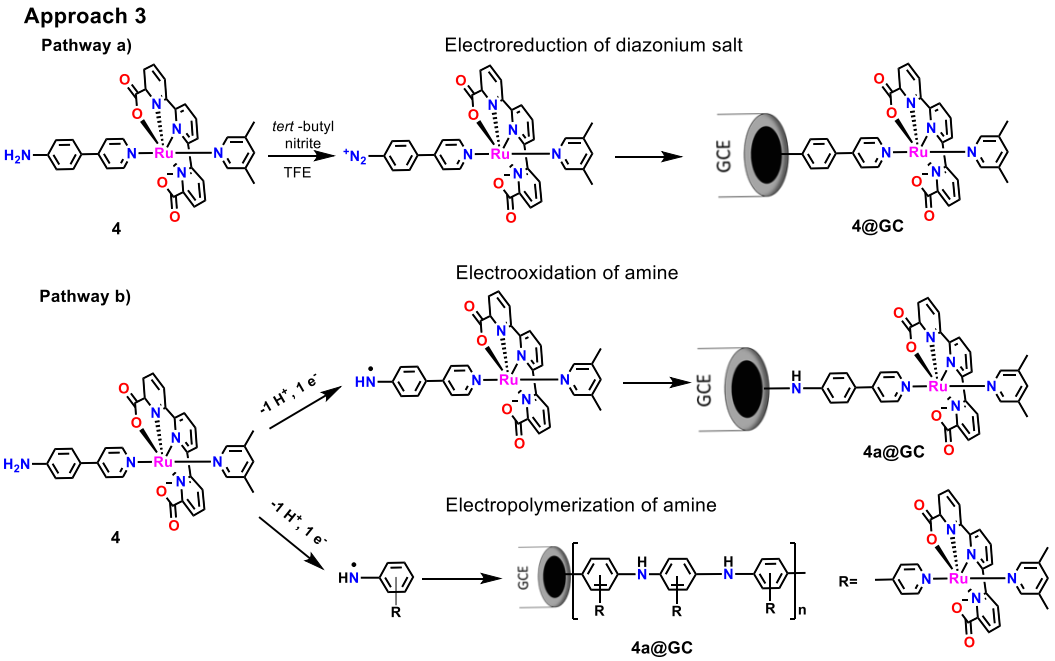

Scheme 8. General scheme for anchoring complex **4** on graphite surface. Pathway a) electroreduction of diazonium salt and b) electrooxidation and electropolymerization of aniline group.

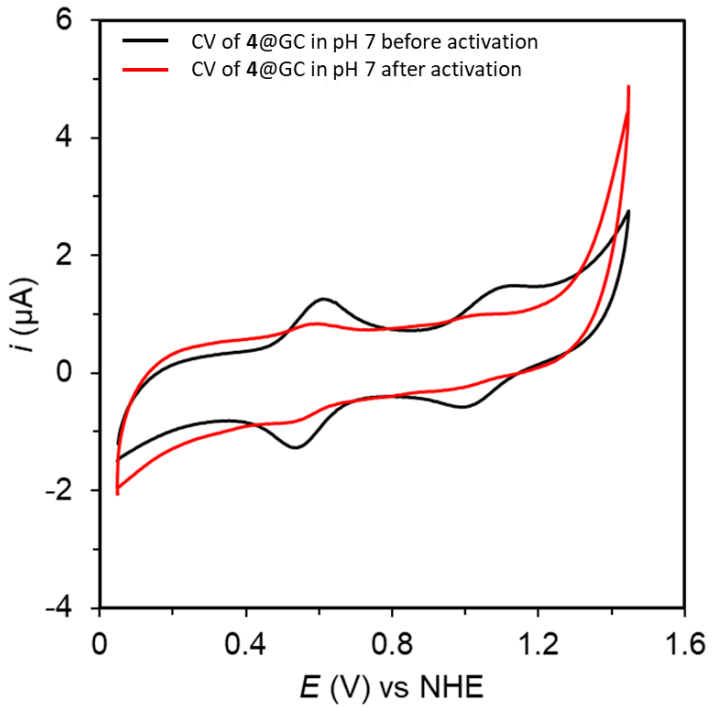

Figure 14. CV of **4**@GC in 0.1 M pH 7 phosphate buffer: before (black) and after (red) activation.

The **4**@GC electrode was then placed in basic solution and submitted to a bulk electrolysis in order to generate the active species as described before. Interestingly, **4**@GC shows some changes in the CV profile after this treatment as opposed to what we had observed using approaches 1 and 2 above (compare black and red traces in Figure 14). In particular, an increase of the current in the 1.2 to 1.3 V range suggests the presence of electrocatalytic activity of the electrode, presumably with the formation of oxygen from water. Additionally, a weak redox wave at 0.8 V appears, which matches with that of the corresponding Ru-aqua type of complexes, and therefore we assign it to the $Ru^{IV/III}$ redox couple of the active electrode denoted as **4(OH)**@GC. The new redox wave and the catalytic current are in good agreement with the formation of the active catalyst and closely resemble the analogous molecular anodes reported in the literature.[9]

In order to improve the mass loading of the catalyst on the surface, multiwall carbon nanotubes (MWCNT) were used as a conductive support on the glassy carbon disk. The resulting electrode **4**@MWCNT@GC shows two one-electron waves at $E_{1/2}$ = 0.58 V (ΔE = 60 mV) and $E_{1/2}$ = 1.07 V (ΔE = 60 mV) in pH 7 corresponding to the $Ru^{III/II}$ and $Ru^{IV/III}$ redox couples (Figure 15 black line inset).[9] The electrode was then exposed to the activation procedure to generate the **4(OH)**@MWCNT@GC electrode, which shows a huge electrocatalytic current

with an onset potential at 1.2 V as expected for this kind of catalytic centers (Figure 15 red line).

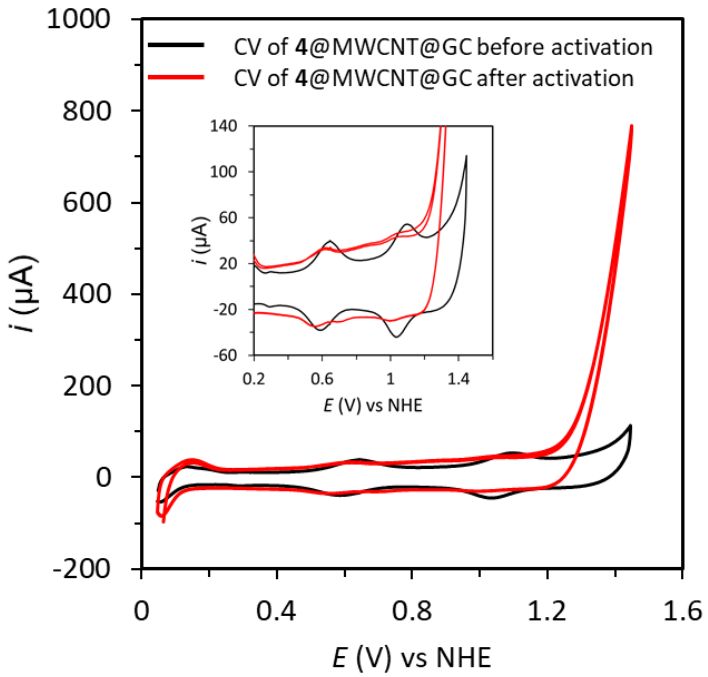

Figure 15 CV of **4**@MWCNT@GC in 0.1 M pH 7 phosphate buffer: before (black) and after (red) activation.

All these results are in sharp contrast to those obtained using approaches 1 and 2 described earlier and suggest a completely different nature of the electrode surface in **4**@GC as compared to the others. This could be related to distinct mechanisms operating in the anchoring process involving the aniline derivatives. Indeed, aniline groups are known to be sensitive to oxidation upon applying a potential, a phenomenon that can lead to either aniline polymerization[26,27] or electrografting.[28] An example of both cases are shown in pathway b in Scheme 8 that generates a polyaniline attached to the surfaces and formation of C-N bond on the graphite surface. This kind of procedures are strongly dependent on the type of aniline involved as well as the solvent used in the electrografting process that could have a big influence on the oxidation potential in which the process happens. Although the electrografting method to prepare the hybrid electrodes described until now are similar (Figure 8 and Figures S11-S13), the process is carried out in different solvents depending on the solubility of the precursors. For the first two electrodes Ru(tda)(py)(apy)@GC and Ru1D(polymer)(apy)@GC in approach 1, pure acetonitrile is used while pure trifluoroethanol is needed for the preparation of **3py**@GC or **3**-1Dpol@GC in approach 2 and **4**@GC and **4**@MWCNT@GC in approach 3.

In order to investigate the putative role of pathway b in Scheme 8, a new electrode was functionalized using the same conditions as **4**@MWCNT@GC in the absence of the *tert*-butyl nitrite to prevent the electrografting via diazonium salt. This new hybrid electrode was denoted as **4a**@MWCNT@GC. Surprisingly this electrode also shows successful attachment of the complex on the surface, as evidenced by the presence of the two typical redox waves that characterize this Ru center (Figure 16, black trace). After activation, a huge electrocatalytic current associated with the oxidation of water to molecular oxygen together with the appearance of two new redox couples at 0.5 and 0.8 V confirmed the successful preparation of the active electrode **4(OH)a**@MWCNT@GC (Figure 16, red trace). This experiment is a clear evidence of a plausible involvement of the amine oxidation grafting shown in pathway b in Scheme 8 and the big influence it has in the nature of the final electrode surface, particularly increasing its hydrophilicity and facilitating the access of hydroxides in order to generate the active Ru-OH centers. Further experiments are currently underway to fully confirm this hypothesis.

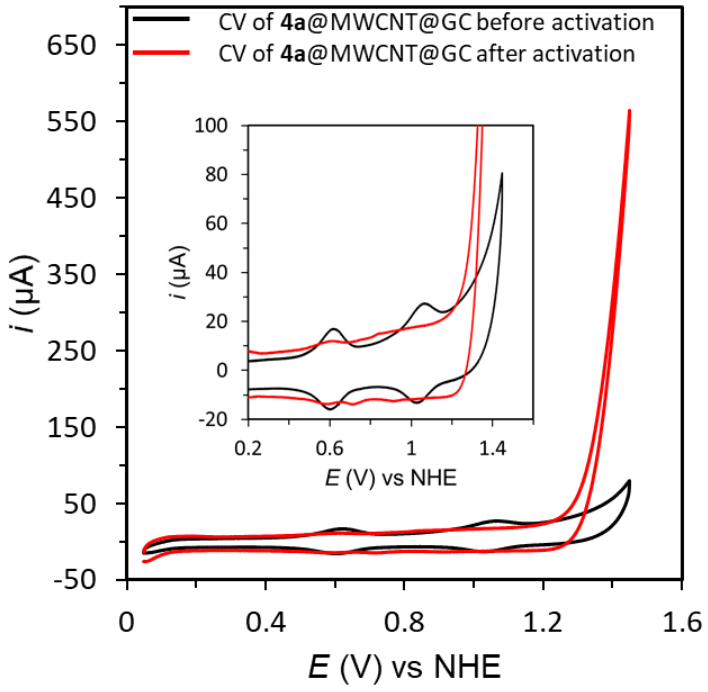

Figure 16 CV of **4a**@MWCNT@GC in 0.1 M pH 7 phosphate buffer: before (black) and after (red) activation.

7. 3. 5. Supramolecular Interaction of [Ru(tda)(py')(py")] Complexes on the Surface

7. 3. 5. 1. Interaction with Graphitic materials

So far in this chapter, only covalently bound [Ru(tda)(py')(py")] type of complexes have been considered. Although promising results showing strong and stable attachment of the surface were obtained, in most of the cases the activation of the catalyst precursor was not possible. In contrast, the **1D** polymer discussed in Chapter 5, which binds to graphitic surfaces through CH-π interactions and has shown to activate easily giving impressive current densities related to the water oxidation to dioxygen reaction.

In order to get further insights into the role of the π-π and CH-π interactions, two mononuclear compounds **5** and **6** in Scheme 9 were prepared and deposited into glassy carbon electrode disks as conductive supports and the results compared with those obtained for the supramolecularly anchored **1D** polymer. Details of the physisorption procedure is given in the experimental sections, briefly it consists of dipping the electrode in a solution of the complex or polymer in trifluoroethanol, followed by washing with clean solvent.

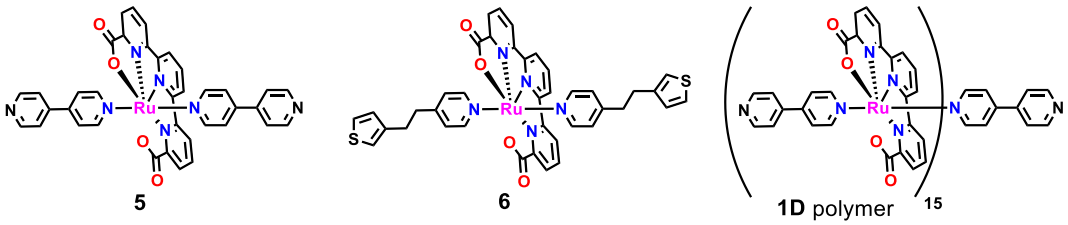

Scheme 9. Mononuclear complexes **5** and **6** and **1D** polymer to study supramolecular interactions.

Electrochemistry

Cyclic voltammetry experiments of the electrodes resulting from the physisorption method in pH 7 phosphate buffer are shown in Figure 17 and evidence the absence of any redox feature associated with the Ru centers of complexes **5** and **6**.

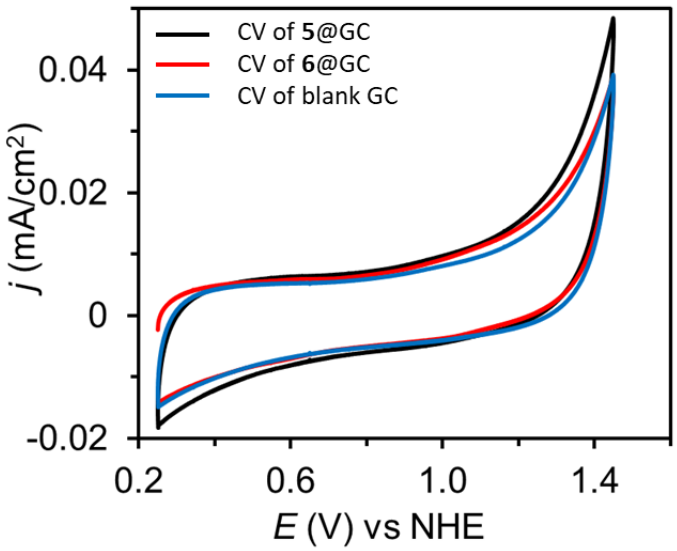

Figure 17. CV of the GC electrodes that were submitted to physisorption of mononuclear complexes **5** (black) and **6** (red) and a blank (blue) in pH 7.

In contrast, an analogous electrode prepared from a supramoleculary anchored solution of the **1D** polymer produced the hybrid electrode **1Dpol**@GC with the expected two-one electron redox features at $E_{1/2}$ = 0.61 V and $E_{1/2}$ = 1.08 V, corresponding to the $Ru^{III/II}$ and $Ru^{IV/III}$ redox couples as expected for the adsorbed complex on the surface (Chapter 5 and Figure 18).

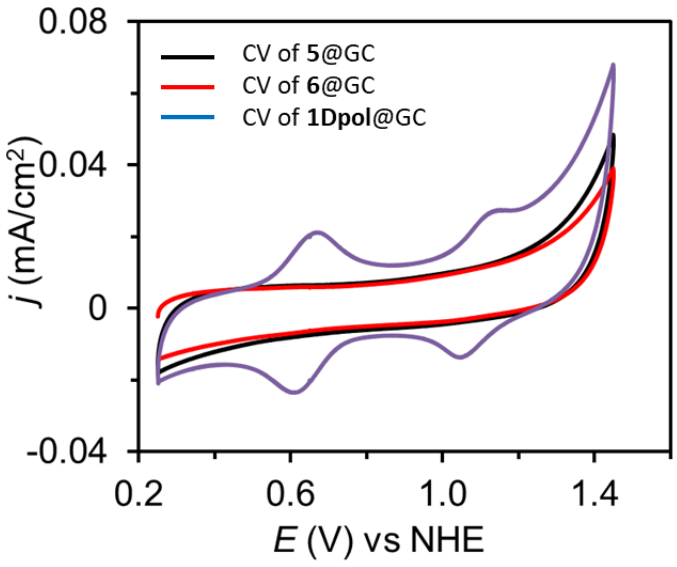

Figure 18. CV of the GC electrodes that were submitted to physisorption of mononuclear complexes **5** (black), **6** (red)and supramoelcuarly anchored **1D** polymer (blue)in pH 7 using similar methodology.

The activation of **1Dpol**@GC was successful showing electrocatalytic current corresponding to the oxidation of water to molecular oxygen with onset potential at 1.2 V in pH 7 (Figure

19). These results are fully consistent with the work presented in Chapter 5 and highlight the importance of having a multinuclear structure to guarantee an efficient attachment of molecular complexes on the surface of graphitic materials through π-π or CH-π interactions.

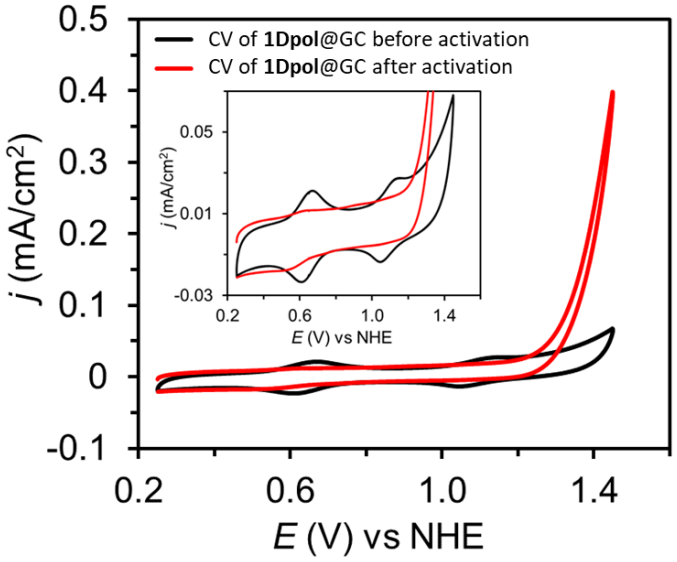

Figure 19. CV of **1Dpol**@GC in pH 7 phosphate buffer before (black) and after (red) activation. The inset shows a zoom in the range of the precatalytic waves and the catalyst precursor.

7. 3. 5. 2. Interaction with Metal oxide Surfaces

In this last section, we explore the adsorption of the **1D** polymer catalyst precursor on metal oxide surfaces, in particular to nanoITO@ITO for its high surface area. For the functionalization, the electrode was dipped into a solution of the 1D polymer in trifluoroethanol for 5 min and washed with clean solvent to generate the hybrid electrode **1Dpol**@nanoITO@ITO.

The CV of **1Dpol**@nanoITO@ITO shows two redox waves at $E_{1/2}$ = 0.68 V (ΔE = 150 mV) and $E_{1/2}$ = 1.08 V (ΔE = 70 mV) corresponding to the $Ru^{III/II}$ and $Ru^{IV/III}$ redox couples, respectively, indicating the successful attachment of the polymer on the metal oxide (Figure 20, black trace). Interestingly, the intensity of the two waves is significantly different, a fact that we attribute to the lower conductivity of the nanoITO/ITO electrode as compared to the glassy carbon electrode.

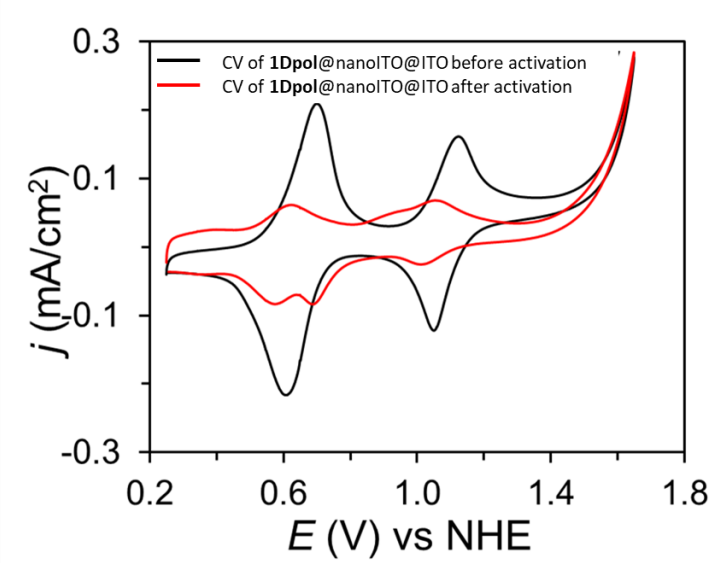

Figure 20. CV of **1Dpol**@nanoITO@ITO: before (black), after (red), 1 hour of activation, measured in pH 7 phosphate buffer.

The electrode **1Dpol**@nanoITO@ITO was submitted to the activation procedure to generate the Ru-OH derivative **1Dpol(OH)**@nanoITO@ITO. As shown in Figure 20 (red line) the CV of the electrode in pH 7 after 1 h activation shows a decrease of the electrochemical response and the appearance of a pH dependent broad redox couple at $E^1_{p,c}$ = 0.69 V and $E^1_{p,a}$ = 0.92 V (Figure 21). The fact that the new redox wave potential changes with the pH is a clear indication of the presence of a Ru-OH/Ru-OH_2 group on the electrode, consistent with the formulation of the **1Dpol(OH)**@nanoITO@ITO electrode. However, **1Dpol(OH)**@nanoITO@ITO electrode did not show any catalytic current related to water oxidation as opposed to graphite electrode, only in pH 9 a catalytic current is observed but is the same to that obtained with an analogous blank nanoITO@ITO electrode (see Figures 20 and 21).

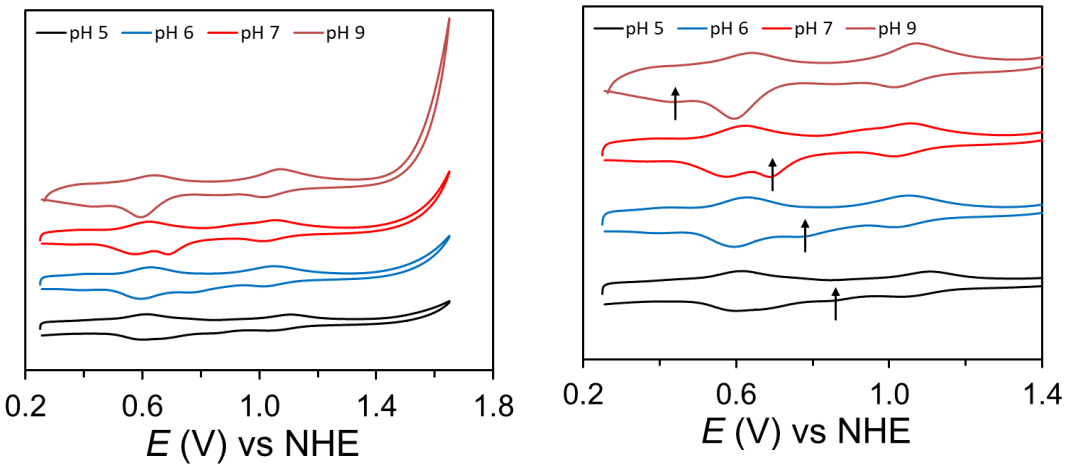

Figure 21. CV of **1Dpol(OH)**@nanoITO@ITO in different pHs. Left, full potential windows. Right, enlargement of the non catalytic redox waves (arrows indicates the RuOH/Ru-OH_2 waves).

The lack of catalytic activity of **1Dpol(OH)**@nanoITO@ITO is attributed to the deactivation of the catalyst via binding of the carboxylate group of the equatorial tda ligand to the metal oxide. Indeed, the impressive catalytic activity of Ru(tda)(py´)$_2$ type of complexes is due to the presence of a dangling carboxylate group that favors intramolecular H-bonding during the catalysis process reducing the activation barrier for the O-O bond formation. Thus, we conclude that although it was possible to coordinate the hydroxido ligand to the ruthenium generating the hybrid electrode **1Dpol(OH)**@nanoITO@ITO, it was not possible to observe catalysis due to the blocking of carboxylate group that prefers to bind to the conductive surface.

7. 4. Conclusion

In summary, the attachment of molecular catalysts on different conductive surfaces via different anchoring groups have been studied extensively. For this study four new Ruthenium complexes (**1**, **2**, **3** and **4**) containing functionalized axial pyridine ligands such as [4,4'-bipyridine]-2,6-dicarboxylic acid, vinyl pyridine, 3,5-pyridine diamine and 4-(pyridin-4-yl)aniline have been synthesized and characterized with spectroscopic and electrochemical techniques.

The surface attachment of catalyst **1** containing a pyridine dicarboxylate group on metal oxide surface through covalent bonding was achieved successfully. However, upon applying potential in the range of 0.2 to 1.6V vs NHE in pH 7 phosphate buffer, this covalent bond seems to be unstable and the complex fully de-attached from the electrode surface and did not allow us to further study this system.

The next anchoring strategy was based on the polymerization of vinyl pyridine on metal oxide surfaces under UV light giving polyvinyl films decorated with pendant pyridine groups, which are readily available for complexation. Subsequent reaction with a Ruthenium precursor generated a Ru-functionalized electrode, with a very robust linkage that is stable in aqueous solution for prolonged electrolysis times. Unfortunately, the activation of this electrode was unsuccessful, most likely due to the hydrophobic organic layer created by the polyvinylpyridine films, which did not allow hydroxide coordination to the metal center.

The 3rd strategy was based on the aromatic pyrazine linkage, resulting from the reaction of a diaminobenzene derivative and the orthoquinone groups of an anodized glassy carbon electrodes. Although the hybrid electrode containing the Ru molecular moiety was successfully prepared, the pyrazine group resulted to be very sensitive to positive applied potentials required for the water oxidation reaction and was broken before water oxidation catalysis could be tested.

The most promising anchoring strategy developed in this chapter was the electrografting of complexes having aromatic diazonium salt on graphite surface. This C-C covalent linkage is very robust over a wide potential range from acidic to basic aqueous solution. It was not possible to activate the complex anchored on glassy carbon electrode, mainly due to the formation of hydrophobic organic layer during the electrografting procedure that is highly hydrophobic; hence, hindering the access of hydroxide ion to the first coordination sphere of the metal. This phenomenon was similar to that observed for the polyvinylpyridine film approach. An interesting preliminary result was obtained with electrografting via oxidation of

the aniline group or electropolymerization of aniline group, particularly in the presence of MWCNT, showing a high current for the water oxidation catalysis.

In the last part of this chapter, we have also shown that the mononuclear complexes are not physisorbed on the surface through π-π or CH-π interactions but they can anchor through covalent bonds on the same surface. On the other hand, the **1D** polymer is supramoleculary anchored on the surface and undergoes water oxidation catalysis on graphitic surfaces as expected considering the results in Chapter 5. In sharp contrast, when **1D** polymer is adsorbed on metal oxide surfaces the polymer did not work presumably due to the binding of the dangling carboxylate group to the metal oxide surface, deactivating the Ru catalytic site.

7. 5. References

(1) Savéant, J.-M. *Chem. Rev.* **2008**, *108*, 2348.
(2) Smieja, J. M.; Kubiak, C. P. *Inorg. Chem.* **2010**, *49*, 9283.
(3) Agarwal, J.; Shaw, T. W.; Stanton III, C. J.; Majetich, G. F.; Bocarsly, A. B.; Schaefer III, H. F. *Angew. Chem. Int. Ed.* **2014**, *53*, 5152.
(4) Love, J. C.; Estroff, L. A.; Kriebel, J. K.; Nuzzo, R. G.; Whitesides, G. M. *Chem. Rev.* **2005**, *105*, 1103.
(5) McCrory, C. C. L.; Devadoss, A.; Ottenwaelder, X.; Lowe, R. D.; Stack, T. D. P.; Chidsey, C. E. D. *J. Am. Chem. Soc.* **2011**, *133*, 3696.
(6) Sheridan, M. V.; Lam, K.; Geiger, W. E. *J. Am. Chem. Soc.* **2013**, *135*, 2939.
(7) Mahouche-Chergui, S.; Gam-Derouich, S.; Mangeney, C.; Chehimi, M. M. *Chem. Soc. Rev.* **2011**, *40*, 4143.
(8) Matheu, R.; Francàs, L.; Chernev, P.; Ertem, M. Z.; Batista, V.; Haumann, M.; Sala, X.; Llobet, A. *ACS Catal.* **2015**, *5*, 3422.
(9) Creus, J.; Matheu, R.; Peñafiel, I.; Moonshiram, D.; Blondeau, P.; Benet-Buchholz, J.; García-Antón, J.; Sala, X.; Godard, C.; Llobet, A. *Angew. Chem. Int. Ed.* **2016**, *55*, 15382.
(10) Zhang, L.; Cole, J. M. *ACS Appl. Mater. Interfaces.* **2015**, *7*, 3427.
(11) Baktash, A.; Khoshnevisan, B.; Sasani, A.; Mirabbaszadeh, K. *Org. Electron.* **2016**, *33*, 207.
(12) Wadsworth, B. L.; Beiler, A. M.; Khusnutdinova, D.; Jacob, S. I.; Moore, G. F. *ACS Catal.* **2016**, *6*, 8048.
(13) Jackson, M. N.; Oh, S.; Kaminsky, C. J.; Chu, S. B.; Zhang, G.; Miller, J. T.; Surendranath, Y. *J. Am. Chem. Soc.* **2018**, *140*, 1004.
(14) Shul, G.; Weissmann, M.; Bélanger, D. *Electrochim. Acta* **2015**, *162*, 146.
(15) Matheu, R.; Ertem, M. Z.; Benet-Buchholz, J.; Coronado, E.; Batista, V. S.; Sala, X.; Llobet, A. *J. Am. Chem. Soc.* **2015**, *137*, 10786.
(16) Evans, I.; Spencer, A.; Wilkinson, G. *J. Chem. Soc., Dalton Trans.* **1973**, 204.
(17) Matheu, R.; Ertem, M. Z.; Gimbert-Suriñach, C.; Benet-Buchholz, J.; Sala, X.; Llobet, A. *ACS Catal.* **2017**, *7*, 6525.
(18) Kato, M.; Cardona, T.; Rutherford, A. W.; Reisner, E. *J. Am. Chem. Soc.* **2012**, *134*, 8332.
(19) Hoertz, P. G.; Chen, Z.; Kent, C. A.; Meyer, T. J. *Inorg. Chem.* **2010**, *49*, 8179.
(20) Matheu, R.; Ertem, M. Z.; Benet-Buchholz, J.; Coronado, E.; Batista, V. S.; Sala, X.; Llobet, A. *J. Am. Chem. Soc.* **2015**, *137*, 10786.
(21) Creus, J.; Matheu, R.; Peñafiel, I.; Moonshiram, D.; Blondeau, P.; Benet-Buchholz, J.; García-Antón, J.; Sala, X.; Godard, C.; Llobet, A. *Angew. Chem. Int. Ed.* **2016**, *55*, 15382.
(22) Oh, S.; Gallagher, J. R.; Miller, J. T.; Surendranath, Y. *J. Am. Chem. Soc.* **2016**, *138*, 1820.
(23) Fukushima, T.; Drisdell, W.; Yano, J.; Surendranath, Y. *J. Am. Chem. Soc.* **2015**, *137*, 10926.
(24) McCreery, R. L. *Chem. Rev.* **2008**, *108*, 2646.
(25) Bouden, S.; Pinson, J.; Vautrin-Ul, C. *Electrochemistry Communications* **2017**, *81*, 120.
(26) Santos, L. M.; Ghilane, J.; Fave, C.; Lacaze, P.-C.; Randriamahazaka, H.; Abrantes, L. M.; Lacroix, J.-C. *J. Phys. Chem. C* **2008**, *112*, 16103.
(27) Zhang, L.; Shi, Z.; Lang, Q.; Pan, J. *Electrochim. Acta* **2010**, *55*, 641.
(28) Belanger, D.; Pinson, J. *Chem. Soc. Rev.* **2011**, *40*, 3995.

7. 6. Supporting Information

Table of Content

NMR Spectroscopy and Mass Spectrometry

Figure S1. NMR spectraum **1**

Figure S2-S4. NMR spectra of **2**

Figure S5. NMR spectra of **3**

Figure S6-S7. NMR spectra of **4**

Figure S8. XPS data of **2**@GC

Electrochemistry

Figure S9. CV of **py**GCC in pH 7 and pH 13.

Figure S10. CV of **OPBAN@**GCC in pH 7 after CPE at 1.1 and 1.4 V

Figure S11. Electrografting of apy and bSO_3 in acetonitrile

Figure S12. Electrografting of **3** in TFE

Figure S13. Electrografting of **4** in TFE

Figure S14. CV and DPV of the complex **4** in pH 7

Chapter 7

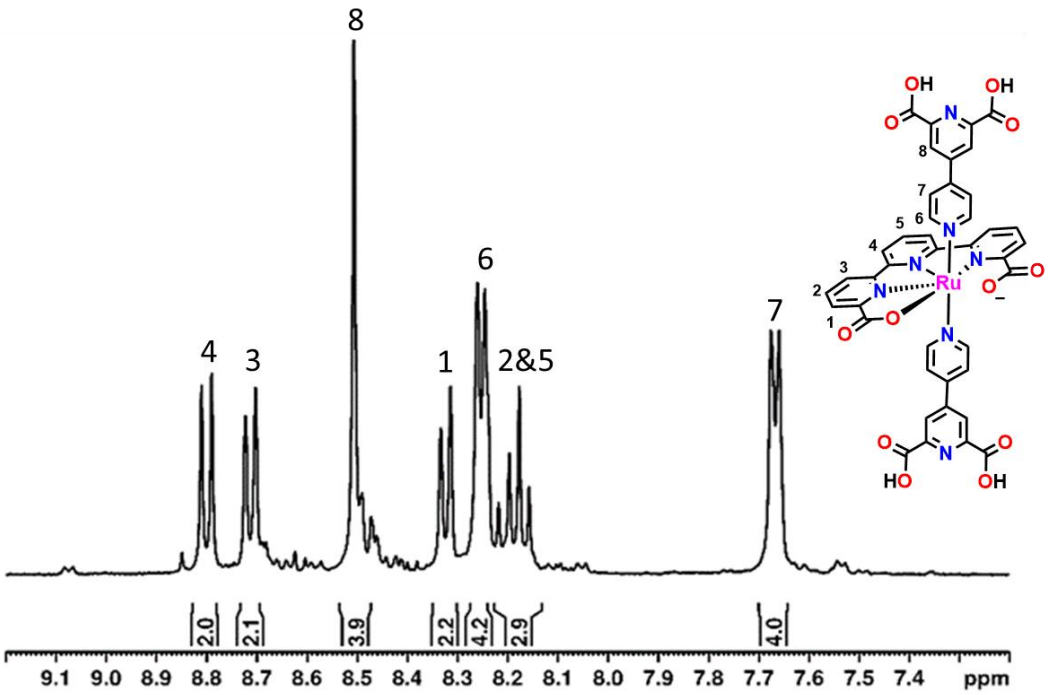

Figure S1. ^{1}H NMR (500 MHz, 298 K, [d$_4$]-MeOD) spectrum of [Ru^{II}(tda)(pypdc)$_2$], **1.** Full assignment has not been completed yet, but integrals match the expected values.

VII

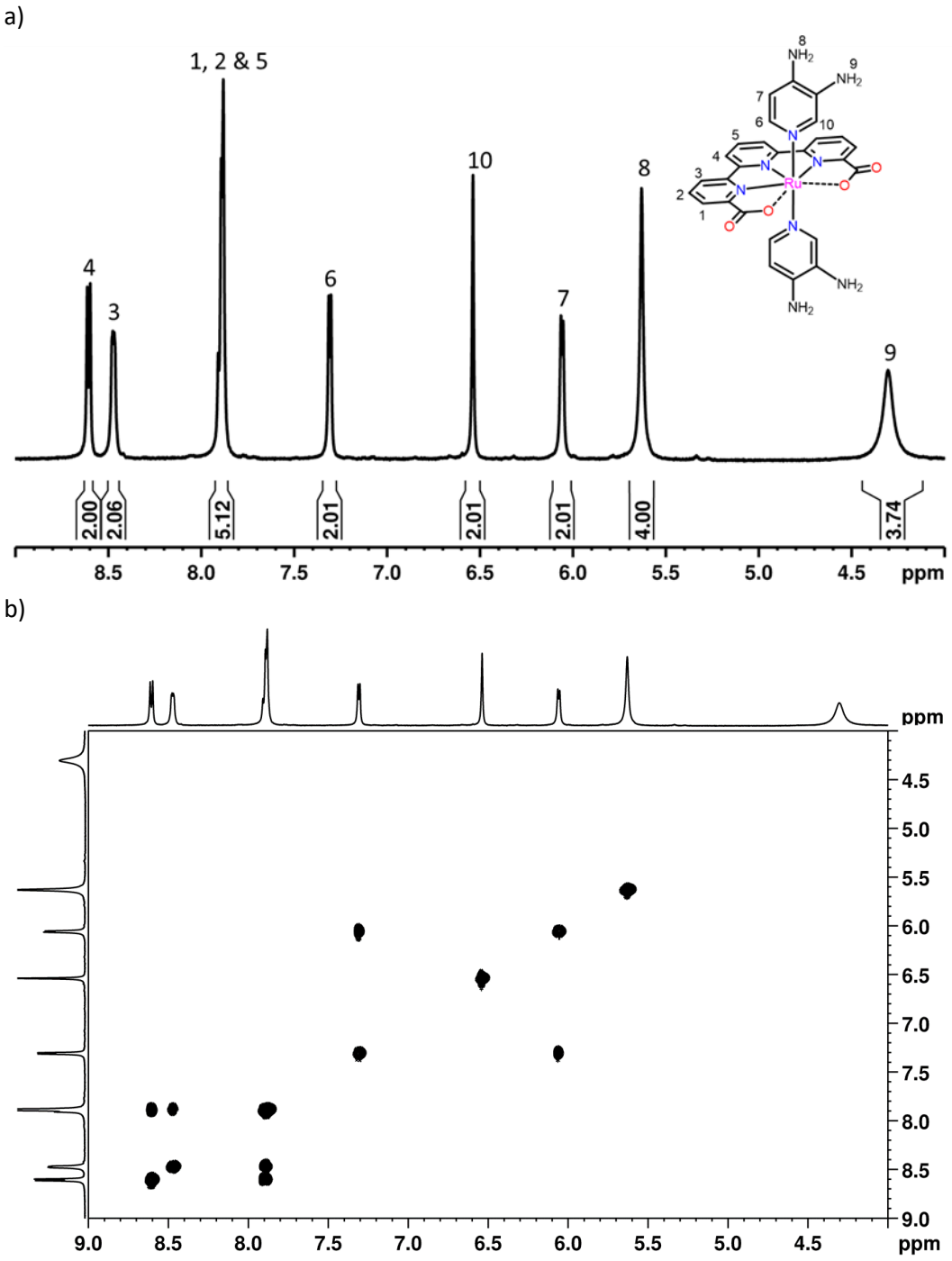

Figure S2. NMR spectra (500 MHz, 298 K, [d_6]-DMSO) for complex [Ru^{II}(tda)(dapy)$_2$], **2**. a) ^{1}H NMR. b) COSY.

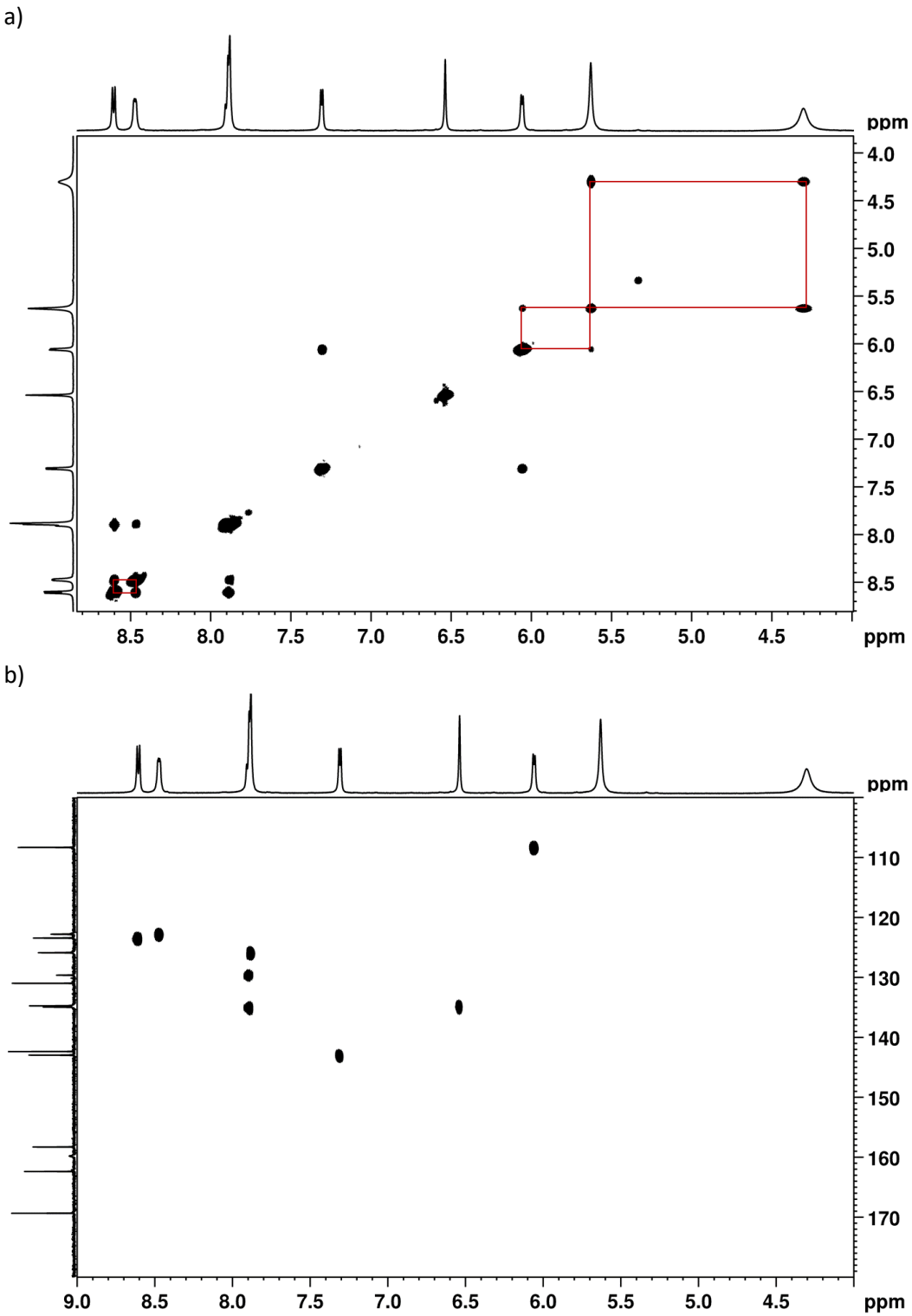

Figure S3. NMR spectra (500 MHz, 298 K, [d_6]-DMSO) for complex [Ru^{II}(tda)(dapy)$_2$], **2**; a) NOESY and b) HSQC.

Chapter 7

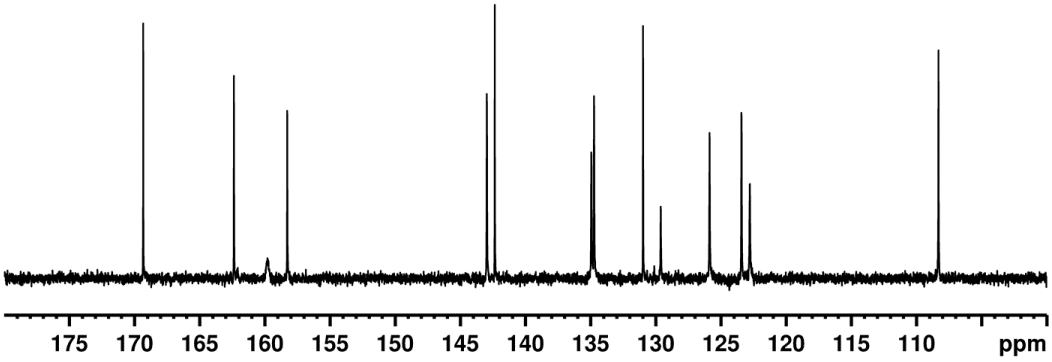

Figure S4. ^{13}C NMR spectra (125 MHz, 298 K, [d_6]-DMSO) for complex [Ru^{II}(tda)(dapy)$_2$], **2**.

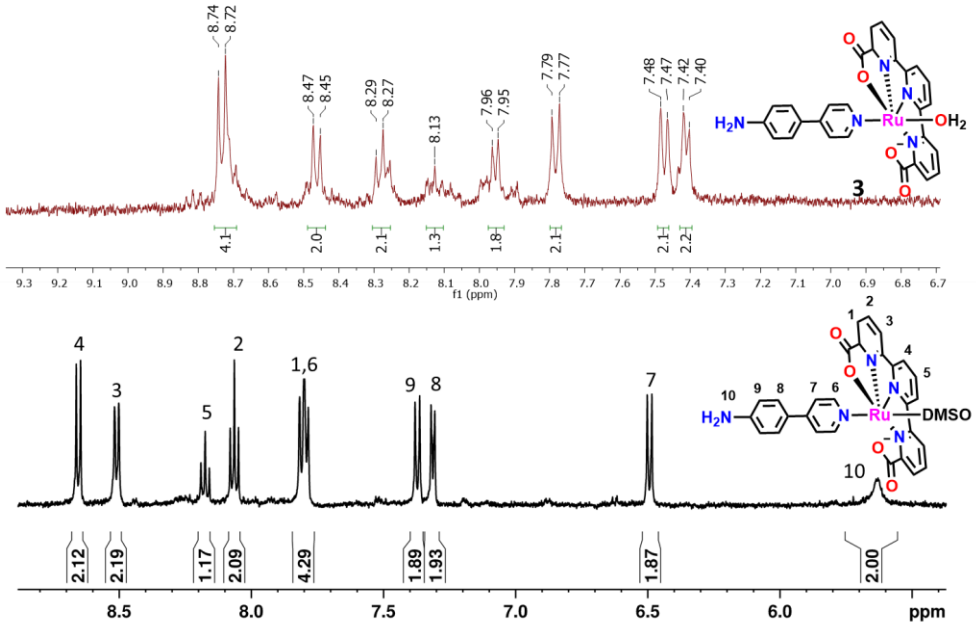

Figure S5. ^{1}H NMR of the intermediate complex (500 MHz, 298 K, [d_6]-DMSO) and [Ru^{II}(tda)(apy)(OH_2)], **3** (500 MHz, 298 K, [d_4]-MeOD).

VII

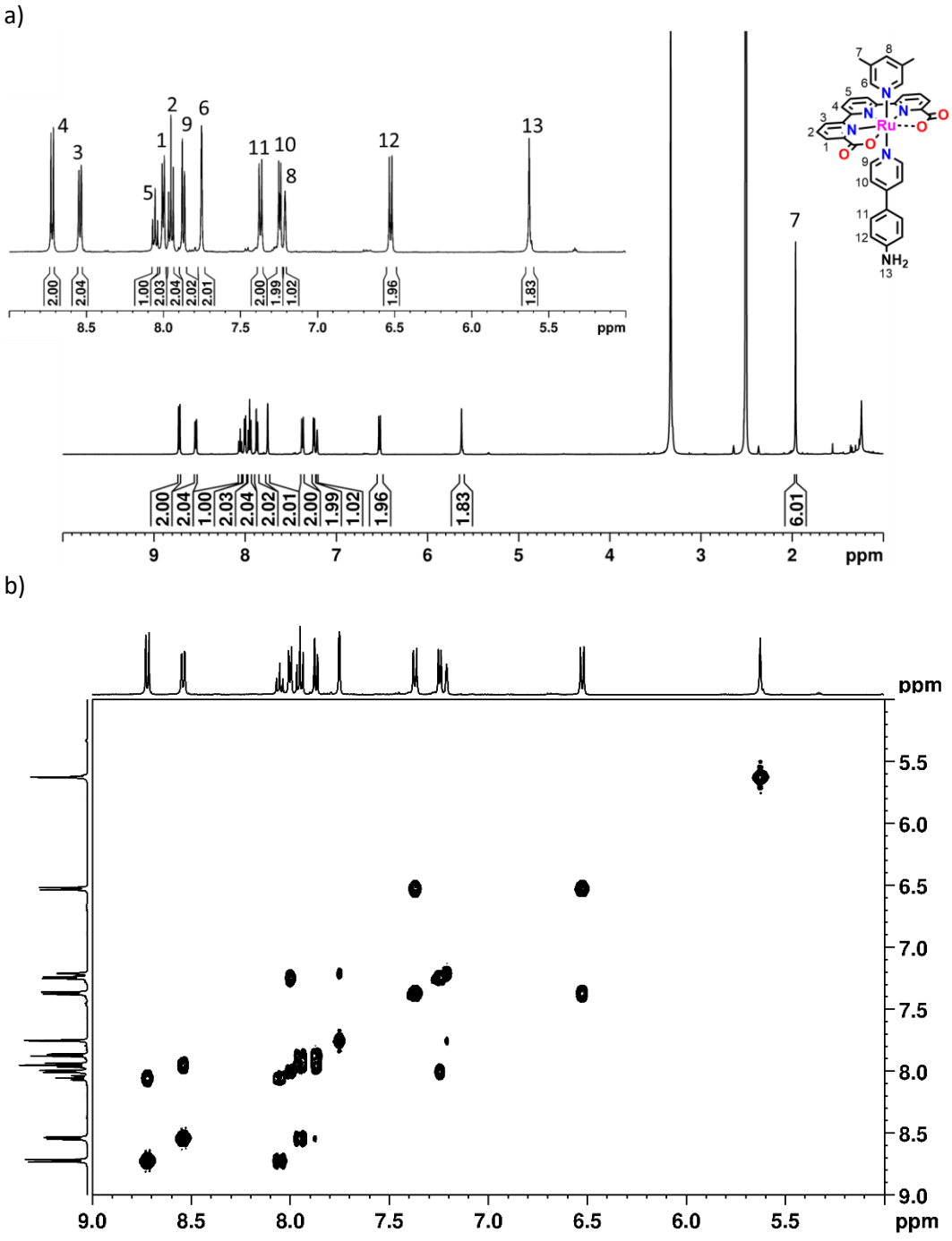

Figure S6. NMR spectra (500 MHz, 298 K, [d_6]-DMSO) for complex [Ru^{II}(tda)(dmpy)(apy)], **4**. a) ^{1}H NMR and b) COSY.

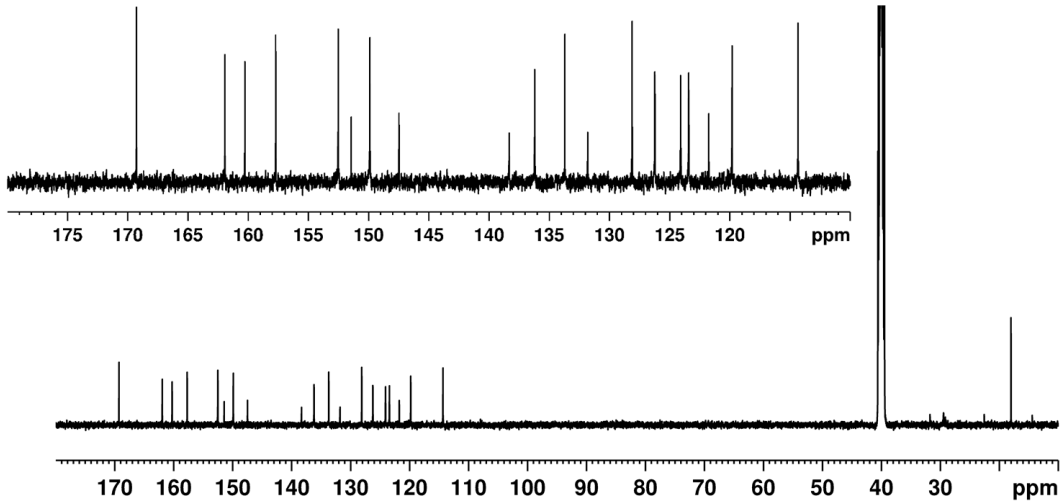

Figure S7. ^{13}C NMR spectra (125 MHz, 298 K, [d_6]-DMSO) for complex [Ru^{II}(tda)(dmpy)(apy)], **4**.

a)

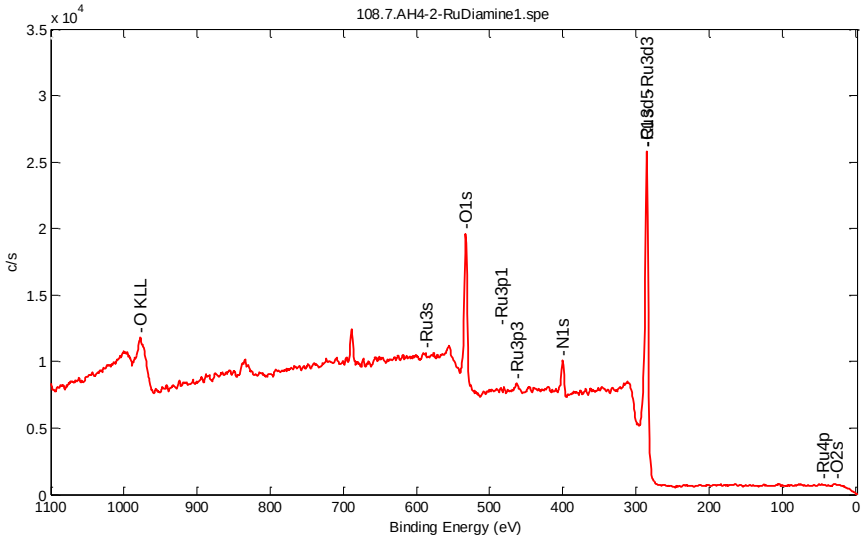

b) c)

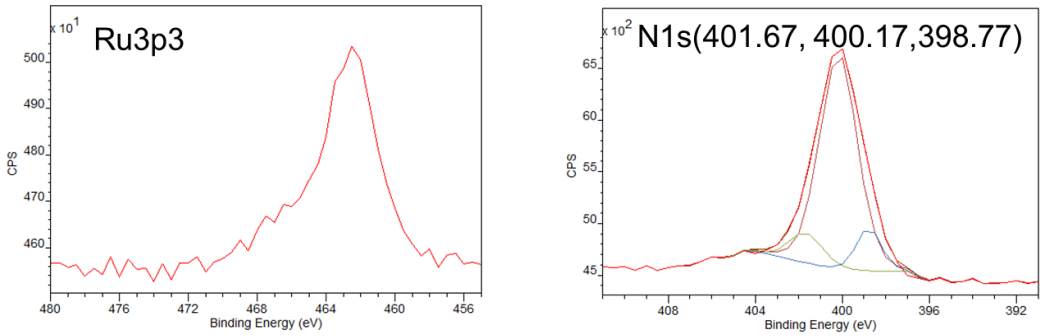

Figure S8. XPS characterization of **2**@GCC: a) full energy range, b) high resolution XPS of Ru and c) high resolution XPS of N.

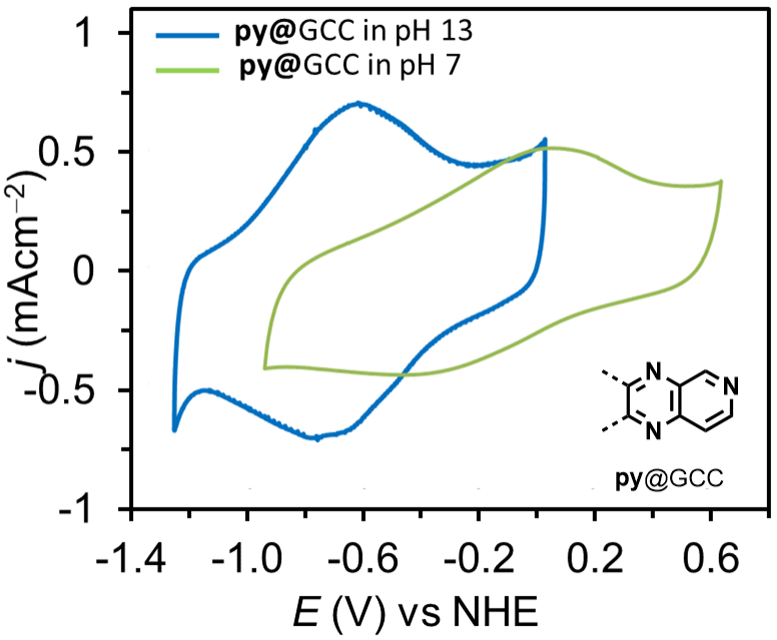

Figure S9. CV of **py**@GCC in pH 7 (green) and pH 13 (blue).

a)

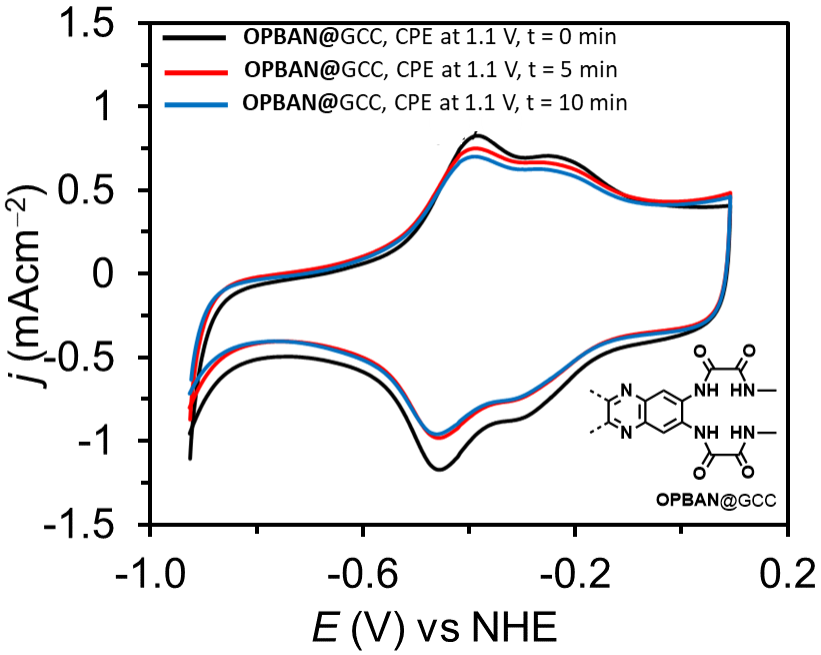

b)

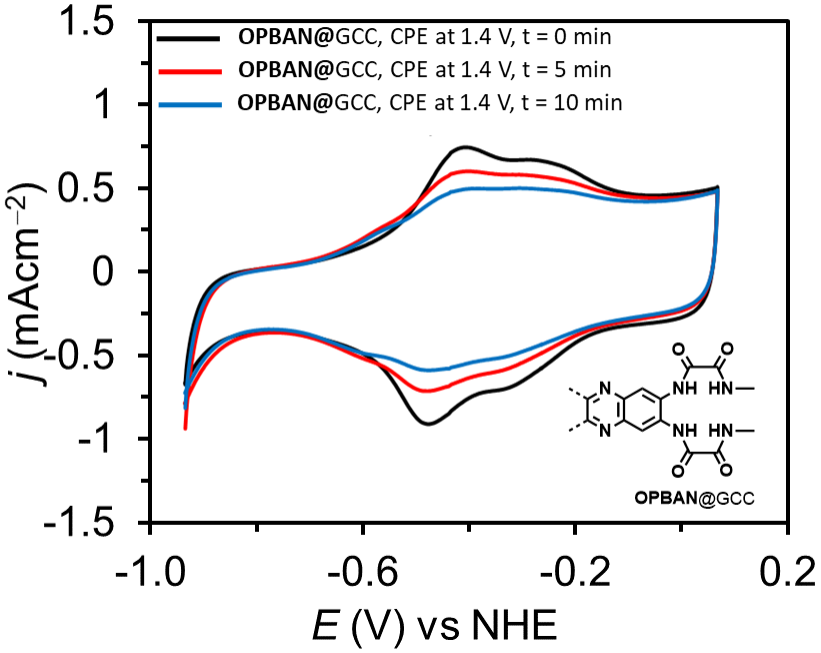

Figure S10. CV of **OPBAN**@GCC in pH 7 after control potential electrolysis (CPE) in different time interval, a) E_{app} = 1.1 V and b) E_{app} = 1.4 V *vs.* NHE; Color code: CPE time= 0 min (black), time = 5 min (red line), time = 10 min (blue). OPBAN stands for tetradentate N_1,N_1'-(1,2 phenylene)bis(N_2methyloxalamide) ligand.

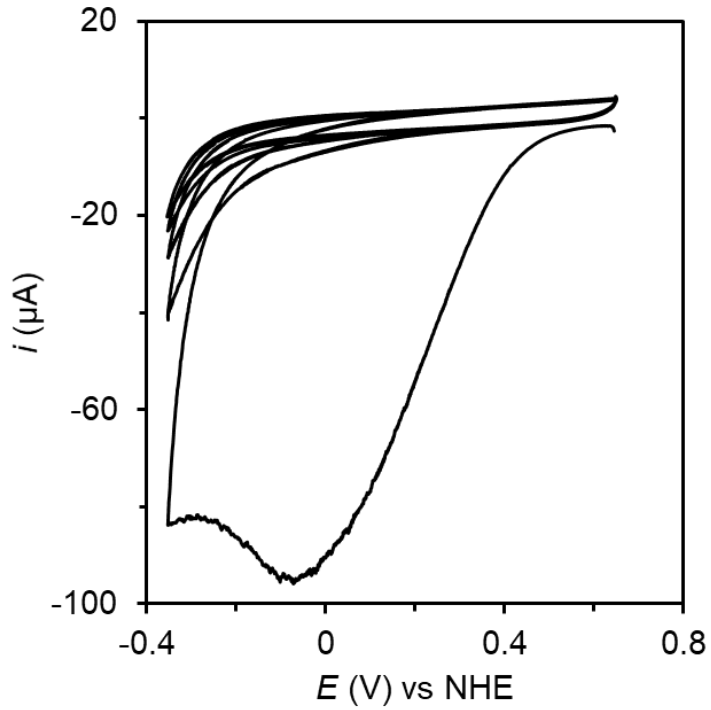

Figure S11. a) CV of 1:1 mixture of 4-(pyridin-4-yl) benzenediazonium salt and 4-diazo-benzenesulfonate salt in 0.1 M [(*n*-Bu)$_4$N][PF$_6$] acetonitrile.

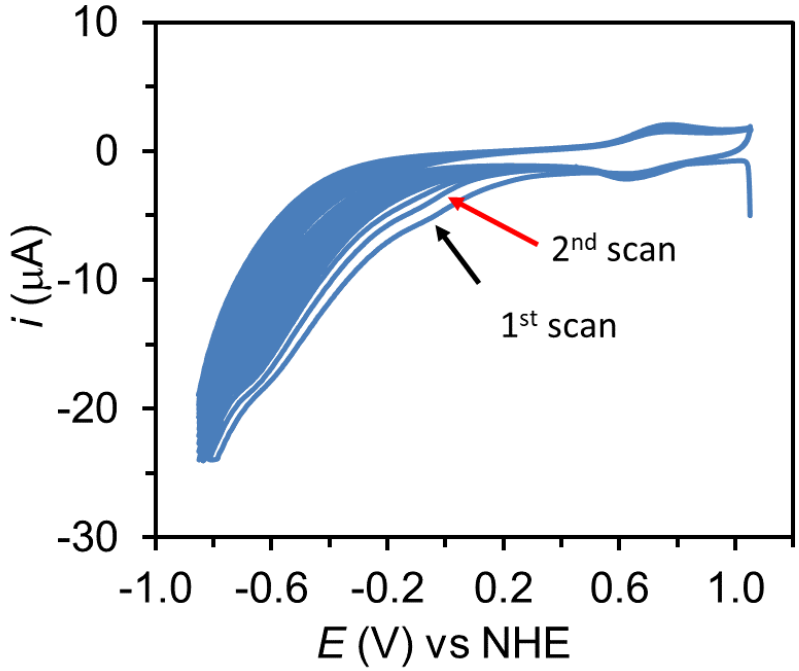

Figure S12. a) CV of **3** in 0.1 M [(*n*-Bu)$_4$N][PF$_6$] trifluoroethanol solvent containing *tert*-butyl nitrite under N_2 scanning form 0.9 V to -0.35 V up to 10 cycles. The irreversible waves at 0.4 V in the reduction waves of the diazonium salt.

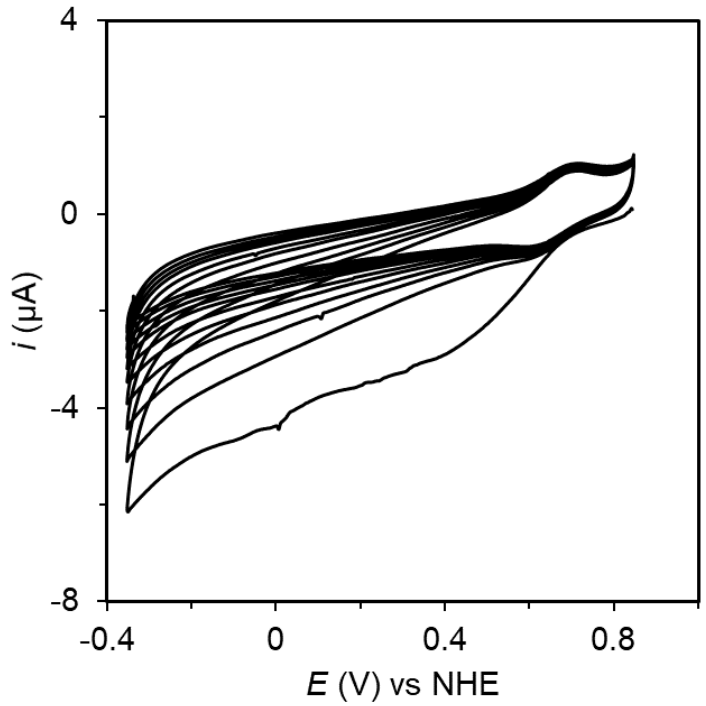

Figure S13. a) CV of [Ru^{II}(tda)(dmpy)(apy)], **4** in 0.1 M [(*n*-Bu)$_4$N][PF_6] trifluoroethanol solvent containing *tert*-butyl nitrite under N_2 scanning form 0.9 V to -0.35 V up to 10 cycles. The irreversible waves at 0.4 V in the reduction waves of the diazonium salt.

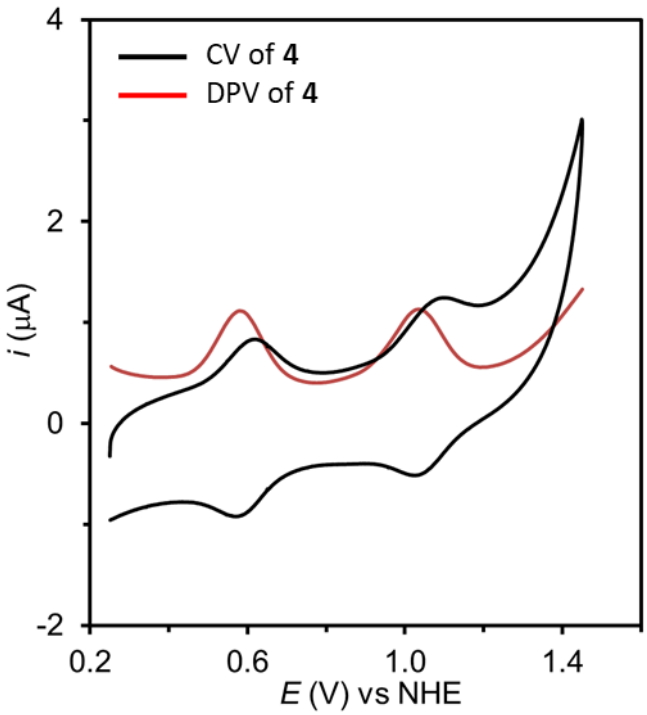

Figure S14. CV of complex **4** in pH 7 in homogeneous solution.

Chapter 8

An end-on superoxido intermediate involved in the water oxidation reaction catalysed by a dinuclear Co- complex is characterized by resonance Raman, Electron paramagnetic resonance and X-ray absorption spectroscopy and complemented by Density Functional Theory. Isotopic labeling experiments under turnover conditions prove that this is a key intermediate of the water oxidation reaction.

Chapter 8

8. Structural and Spectroscopic Characterization of Reaction Intermediates Involved in a Dinuclear Co-Hbpp Water Oxidation Catalyst

Carolina Gimbert-Suriñach,[1] Dooshaye Moonshiram,[2] Laia Francàs,[1] Nora Planas,[3] Varinia Bernales,[3] Fernando Bozoglian,[1] Alexander Guda,[4] Lorenzo Mognon,[1] Isidoro López,[1] Md Asmaul Hoque,[1,6] Laura Gagliardi,[3] Christopher J. Cramer*,[3] and Antoni Llobet*,[1,5]

[1] *Institute of Chemical Research of Catalonia (ICIQ), Barcelona Institute of Science and Technology (BIST), Av. Països Catalans 16, 43007 Tarragona, Spain*

[2] *Chemical Sciences and Engineering Division, Argonne National Laboratory, 9700 S. Cass Avenue, Lemont IL 60439, U.S.A*

[3] *Department of Chemistry, Supercomputing Institute and Chemical Theory Center, University of Minnesota, 207 Pleasant St. SE, Minneapolis, MN, U.S.A*

[4] *International Research Center "Smart Materials", Southern Federal University, 344090 Rostov-on-Don, Russia*

[5] *Departament de Química, Universitat Autònoma de Barcelona, 08193 Cerdanyola del Vallès, Barcelona, Spain*

[6] *Departament de Química Física i Inorganica, Universitat Rovira i Virgili, Campus Sescelades, C/Marcel·lí Domingo, s/n, 43007 Tarragona, Spain*

VIII

Published Article: Gimbert-Suriñach, C.; Moonshiram, D.; Francàs, L.; Planas, N.; Bernales, V.; Bozoglian, F.; Guda, A.; Mognon, L.; López, I.; **Hoque, M. A**.; Gagliardi, L.; Cramer, C. J.; Llobet, A. *J. Am. Chem. Soc.* **2016**, *138*, 15291.

Contributions

Md Asmaul Hoque design the experimental set up for the electrochemical oxygen evolution measurement and perform the experiment for the oxygen evolution with the isotopic labeling during the catalysis.

Chapter 8

Abstract

An end-on superoxido complex with formula {[$Co^{III}(OH_2)$(trpy)][Co^{III}(OO·)(trpy)](μ-bpp)}c^{4+}, **3**$^{4+}$, (bpp^- is bis-2-pyridyl-3,5-pyrazolate; trpy is 2,2';6':2"-terpyridine) has been characterized by resonance Raman, electron paramagnetic resonance and X-ray absorption spectroscopies. These results together with on-line mass spectrometry experiments using ^{17}O and ^{18}O isotopically labeled compounds prove that this compound is a key intermediate of the water oxidation reaction catalyzed by the peroxido bridging complex {[Co^{III}(trpy)]$_2$(μ-bpp)(μ-OO)}$^{3+}$, **1**$^{3+}$. Density Functional Theory calculations agree and complement the experimental data, and offer a complete description of the transition states and the intermediates involved in the catalytic cycles.

Graphical Abstract

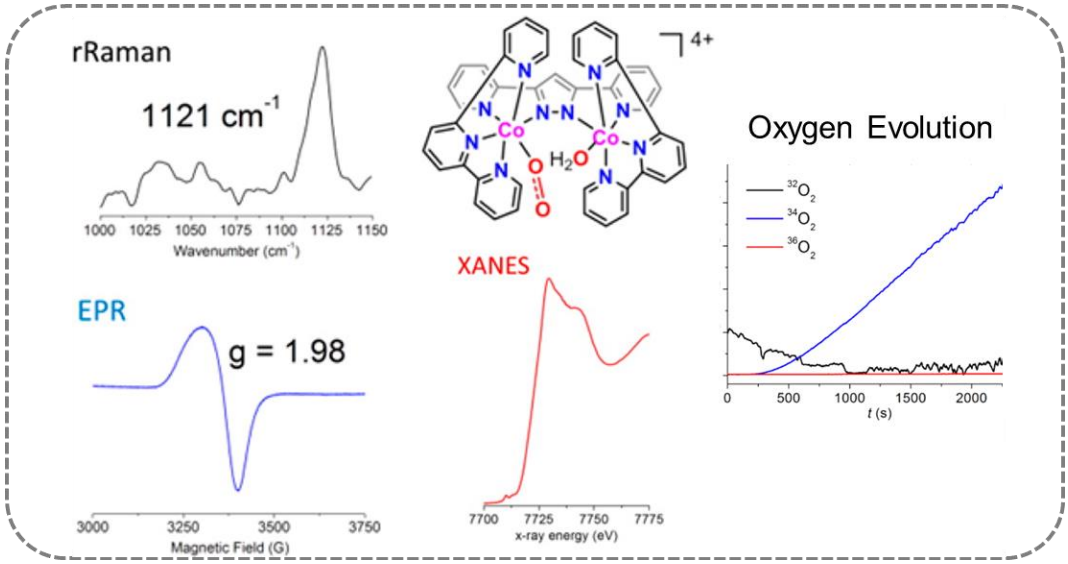

Keywords: Cobalt superoxo, Intermediate, rRaman, EPR, Oxygen evolution

VIII

Chapter 8

8. 1. Introduction

Oxygen activation by first-row transition metal complexes in low oxidation states has been a very active field of research for the last two decades.[1-4] A plethora of transition metal peroxido and superoxido complexes in different coordination modes have been prepared and characterized with spectroscopic techniques and even via single-crystal X-ray diffraction in selected instances.[5,6] The reverse reaction, the oxidation of water to molecular oxygen assisted by first row-transition metal complexes is a field that has emerged recently and the proper characterization of the potential peroxido and/or superoxido reaction intermediates is practically nonexistent.[7,8] The characterization of such intermediates is hampered by the lability of the metal-ligand bonds that can undergo substitution by water solvent molecules and by the relatively low temperature range at which the reaction can be operated. In sharp contrast, the inverse reaction *i.e*. the oxygen activation can be carried out in organic solvents and at very low temperatures. Additionally, for the water oxidation reaction, in a number of cases, a competing and/or preferential ligand oxidation occurs[9-11] which prevents extraction of reliable and meaningful information. In previous work, we have reported the synthesis and X-ray structure of the dinuclear μ-peroxido complex $\{[Co^{III}(trpy)]_2(\mu\text{-bpp})(\mu\text{-OO})\}^{3+}$, denoted as $\mathbf{1}^{3+}$ or $[Co^{III}\text{-OO-}Co^{III}]^{3+}$ hereafter, (trpy is 2,2';6';2"-terpyridine; bpp^- is the bis-2-pyridyl-3,5-pyrazolate) that behaves as powerful catalyst for the $4e^-$ reduction of dioxygen to water.[12] The key structures are depicted in Scheme 1. Further, we have electrochemically characterized the properties of $\mathbf{1}^{3+}$ and have shown by voltammetric and potentiometric techniques its capacity to act as a catalyst for the $4e^-$ oxidation of water to dioxygen.[13]

VIII

In this work, we present the preparation of a dinuclear Co superoxido end-on complex, denoted as $\mathbf{3}^{4+}$ or $[H_2O\text{-}Co^{III}Co^{III}\text{-}OO^{\cdot}]^{4+}$, and its thorough characterization based on vibrational, X-ray absorption near edge structure (XANES), Extended X-ray absorption fine structure (EXAFS), Electron Paramagnetic Resonance (EPR) spectroscopies, and by density functional theory, DFT, calculations. In addition, we show for the first time that sequential oxidation of the peroxido derivative, $\mathbf{1}^{3+}$, leads to the just mentioned superoxido $\mathbf{3}^{4+}$, and that further oxidation of the latter generates dioxygen. These two reactions have been carried out using ^{16}O, ^{17}O and ^{18}O labeled complexes to monitor them and to properly characterize potential intermediates. In addition, a coherent mechanistic description of the catalytic cycle is presented based on DFT calculations that agree with the available experimental data.

Chapter 8

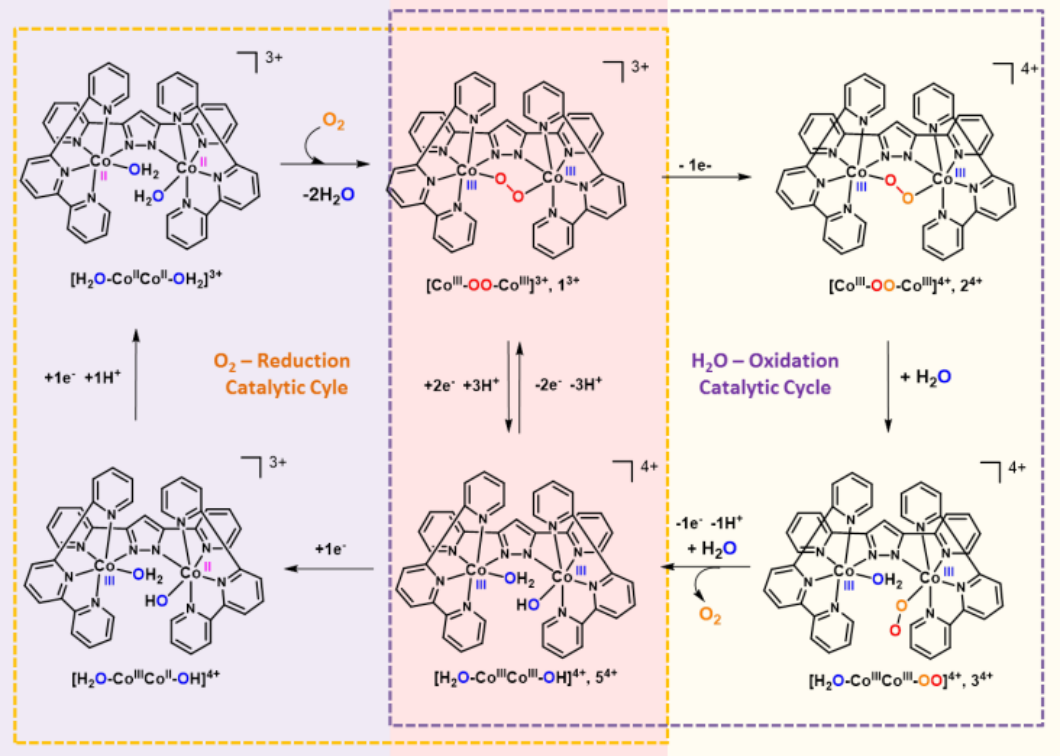

Scheme 1. Simplified Oxygen Reduction (left) and Water Oxidation (right) catalytic cycles based on the Co-Hbpp complex. In the center (red shadow) the intermediates shared by the two catalytic cycles, $[Co^{III}\text{-}OO\text{-}Co^{III}]^{3+}$ (**1^{3+}**) and $[H_2O\text{-}Co^{III}Co^{III}\text{-}OH]^{4+}$ (**5^{4+}**).

VIII

8. 2. Results and Discussion

The dinuclear Co μ-peroxido complex $\mathbf{1}^{3+}$ is prepared in good yields following literature procedures by reacting $\{[Co^{II}(OH_2)(trpy)]_2(\mu\text{-bpp})\}^{3+}$ or its chlorido bridge derivative with molecular dioxygen (Scheme 1).[12] Using dioxygen labeled with different isotopes (^{16}O, ^{17}O or ^{18}O), we have prepared the peroxido complexes $\mathbf{1(32)}^{3+}$ $[Co^{III}\text{-}^{16}O^{16}O\text{-}Co^{III}]^{3+}$, $\mathbf{1(34)}^{3+}$ $[Co^{III}\text{-}^{17}O^{17}O\text{-}Co^{III}]^{3+}$, and $\mathbf{1(36)}^{3+}$ $[Co^{III}\text{-}^{18}O^{18}O\text{-}Co^{III}]^{3+}$, respectively. Figure 1 (left) shows the resonance Raman (rR) spectra obtained for the $\mathbf{1}^{3+}$ set of complexes with the different labeling. A prominent vibration appears at 839 cm^{-1} for $\mathbf{1(32)}^{3+}$ associated with the O-O bond stretching mode. This vibrational transition shifts to 814 cm^{-1} for $\mathbf{1(34)}^{3+}$ and to 795 cm^{-1} for $\mathbf{1(36)}^{3+}$ as expected for a quantum mechanical harmonic oscillator having such changes in reduced mass. For the case of the $\mathbf{1(36)}^{3+}$, rR spectroscopy shows the presence of two bands at 839 and 795 cm^{-1} of similar intensity that are due to a 1:1 ratio of $\mathbf{1(32)}^{3+}$ and $\mathbf{1(36)}^{3+}$ since the dioxygen used in the synthesis contained a 1:1 mixture of $^{36}O_2$:$^{32}O_2$ (See Experimental Section in SI). Similarly, the ^{17}O labeling experiment that used a 9:1 mixture $^{34}O_2$:$^{32}O_2$ of dioxygen shows a small shoulder at 839 cm^{-1} in the corresponding rR spectrum.

Chemically, the addition of 1 equivalent of Ce^{IV} to the peroxido complexes $\mathbf{1}^{3+}$ at pH=1.0 generates the corresponding superoxido complexes $\mathbf{2}^{4+}$ or $[Co^{III}\text{-}O^{\cdot}O\text{-}Co^{III}]^{4+}$ that undergo hydrolysis to yield end-on superoxido complexes $\mathbf{3}^{4+}$ or $[H_2O\text{-}Co^{III}Co^{III}\text{-}OO^{\cdot}]^{4+}$ as suggested by DFT calculations and in agreement with XAS spectroscopy. DFT calculations using the SMD(water)/M11-L/ 6-311G(2f,d) predict that the end-on form $\mathbf{3}^{4+}$ is 19.8 kcal/mol more stable than the bridging one $\mathbf{2}^{4+}$ (Scheme 2). Figure 2 shows the optimized DFT structure for the end-on superoxido complex together with the singly occupied molecular orbital (SOMO). The spin density in this orbital is mainly localized on the superoxido group, which forms a hydrogen bond with the neighboring Co-OH_2 group supporting the peroxide bridge as the main oxidation site. Previous electrochemical experiments showed that the oxidation of the peroxido complex $\mathbf{1}^{3+}$ to the superoxido $\mathbf{3}^{4+}$ is chemically and electrochemically reversible and occurs at E^o = 1.49 V *vs*. NHE.[13] DFT calculations using again SMD(water)/M11-L/ 6-311G(2f,d) predict a value of 1.37 V *vs*. NHE for this oxidation in good agreement with the experimental value and thus suggests that this level of theory will be useful and sufficiently accurate for modeling other properties of the system.

Chapter 8

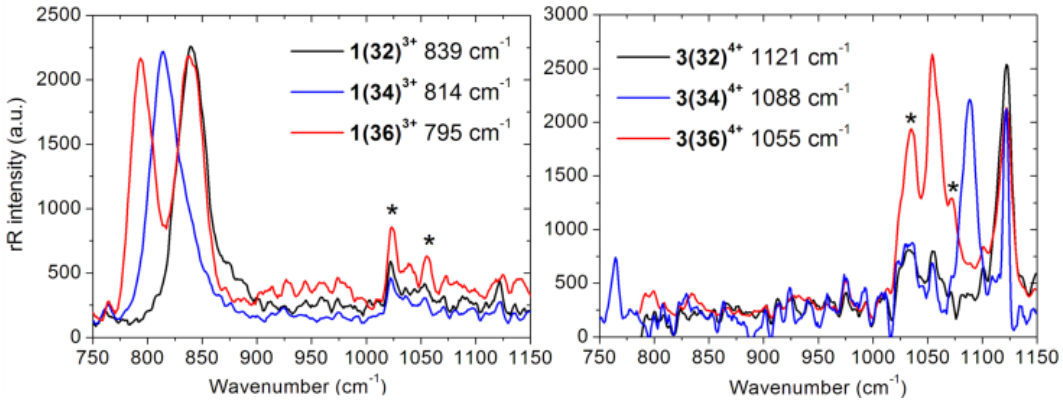

Figure 1. Normalized rR spectra for peroxido complexes **1(32)**$^{3+}$ (black line), **1(34)**$^{3+}$ (blue line) and **1(36)**$^{3+}$ (red line) (Left) and superoxido complexes **3(32)**$^{4+}$ (black line), **3(34)**$^{4+}$ (blue line) and **3(36)**$^{4+}$ (red line) (Right). λ_{exc} = 514 nm. Asterisks: solvent resonances.

Vibrational rR spectroscopy was also carried out for the superoxido complexes with the different O_2 isotopologues, and the results are shown in Figure 1 (right). The O-O bond vibration for the **3(32)**$^{4+}$ oxidized complex appears at 1121 cm^{-1}, which is consistent with a superoxido group,[14-17] although experimentally the end-on and side-on isomers are virtually undistinguishable.[17-19] Furthermore, the labeled complexes shift to 1088 cm^{-1} and 1055 cm^{-1} for **3(34)**$^{4+}$ and **3(36)**$^{4+}$, respectively, as expected. Here again, the mixture of isomers is clearly observed in the spectra since we use the peroxido complexes mentioned earlier as starting materials. It is worth noting here that the potential use of mixed labeled oxygen atoms would generate one band for the symmetric side-on complex (Co-O^{16}O^{18}-Co) and two for the end-on (CoCo-O^{16}O^{18} and CoCo-O^{18}O^{16}). However the energy difference for the two bands generated by the latter complex would be too small to be clearly differentiated in the spectrum (theory predicts a shift of 1-3 cm^{-1} for related complexes).[19 18]

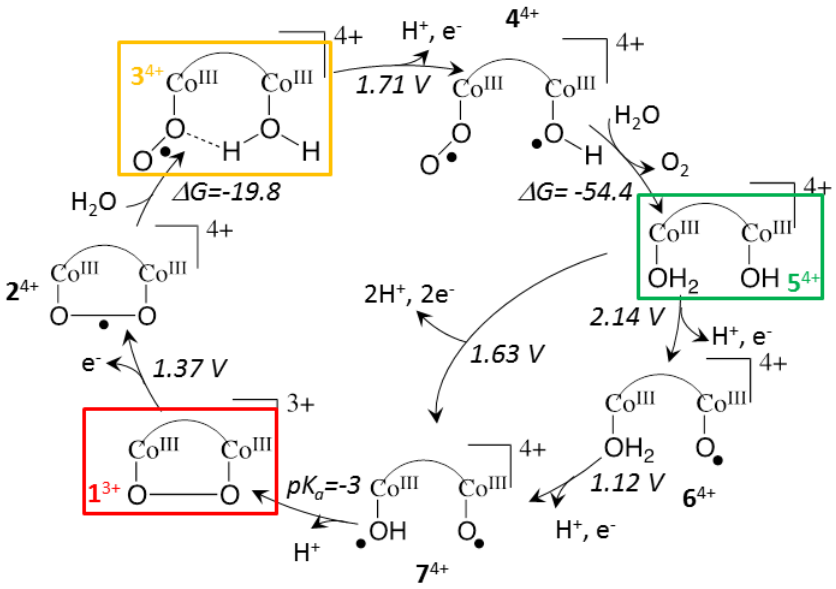

Scheme 2. Calculated water oxidation catalytic cycle associated with the Co-Hbpp complex. The arc connecting the two Co centers represents the bpp$^-$ bridging ligand. The trpy ligands are not represented for clarity purposes. Red box: starting material [Co^{III}-OO-Co^{III}]$^{3+}$, **1**$^{3+}$. Yellow box: hydrated one electron oxidation of the former [H$_2$O-Co^{III}Co^{III}-OO$^{\cdot-}$]$^{3+}$, **3**$^{4+}$. Green box: [H$_2$O-Co^{III}Co^{III}-OH]$^{4+}$, **5**$^{4+}$, species formed after oxygen ejection. Potentials are indicated in V *vs*. the NHE reference electrode at pH = 2.0 whereas ΔG are reported in kcal/mol.

VIII

The superoxido complexes were also characterized by EPR spectroscopy. For complex **3(32)**$^{4+}$ and **3(36)**$^{4+}$ a broad band centered at g = 1.98 is observed in the EPR spectrum, which is due to the unpaired electron of the superoxido group. The broadness of the peaks is a consequence of the coupling of the superoxido unpaired electron with the nuclear spins of ^{59}Co (I = 7/2) that are not well resolved (See Figure S1 in the SI). In sharp contrast, the EPR for **3(34)**$^{4+}$ shows a similar spectrum as for **3(32)**$^{4+}$ but with a fine structure due to the coupling to the nuclear spin of ^{17}O (I = 5/2) as can be observed in Figure 2 together with its mathematical simulation.

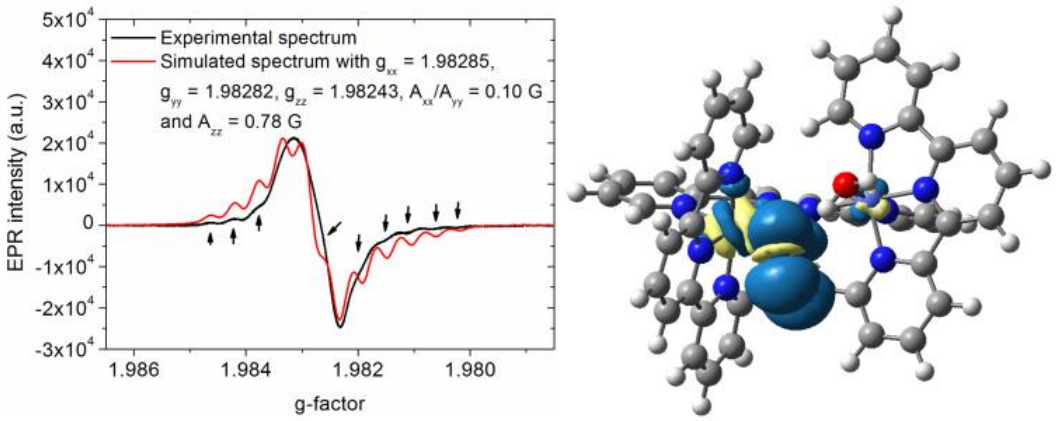

Figure 2. Left, experimental (black line) and simulated (red line) EPR spectrum of **3(34)**$^{4+}$. Right, SOMO for the optimized end-on superoxido complex **3(32)**$^{4+}$.

XANES analysis of the superoxido complex **3**$^{4+}$ reveals a small positive shift of the rising edge (0.4 eV) compared to the peroxido **1**$^{3+}$ (top left of Figure 3). The shift in energy indicates a change in the electron density and local geometry around the Co metal center and is well reproduced by theoretical XANES simulations shown in Figure 3 (right) thus supporting a peroxido centered oxidation in agreement with rR and EPR results. More interesting is the predominant characteristic multiplet feature in the pre-edge region that distinguishes the superoxido compound from its parent peroxido derivative (Figure 3, bottom). The presence of pre-edge features corresponds to the 1s to 3d quadrupole transitions and dipole excitations of the core electrons into the valence 3d levels hybridized with p orbitals. Upon oxidation with 1 eq. Ce^{IV}, local distortions around the Co center and increased hybridization of the valence 3d states with N/O ligand p-orbitals[20-23] results in the clear formation of a second pronounced pre-edge feature. As shown by the Gaussian fits in Figure 3 (bottom), the pre-edge region has contribution of two main absorptions centered at *ca.*7709.9 eV and 7712.2 eV for the peroxido derivative. Upon oxidation, the peak at 7712.2 eV slightly shifts to higher energy (7712.7 eV), and becomes more pronounced giving rise to an apparent doublet feature that is not as obvious for the starting peroxido compound (compare black and red traces). Theoretical DFT-MO XANES calculations of the superoxido derivatives **2**$^{4+}$ and **3**$^{4+}$ in Scheme 2 reproduce well this shift especially for the non-symmetric end-on compound **3**$^{4+}$, where the doublet feature is more noticeable (Figure 3 and Figure S3). In addition, EXAFS analysis show a slightly better fit for **3**$^{4+}$ (see supporting information). Previous electrochemical experiments revealed that the superoxido complex **3**$^{4+}$ can be further oxidized by one electron at 1.80 V *vs*. NHE.[13] M11-L/DFT calculations suggest the formation of a diradical hydroxyl-superoxido species $[HO^{\cdot}\text{-}Co^{III}Co^{III}\text{-}OO^{\cdot}]^{4+}$, **4**$^{4+}$, obtained from a PCET process occurring at a potential of 1.71 V *vs*. NHE (Scheme 2).

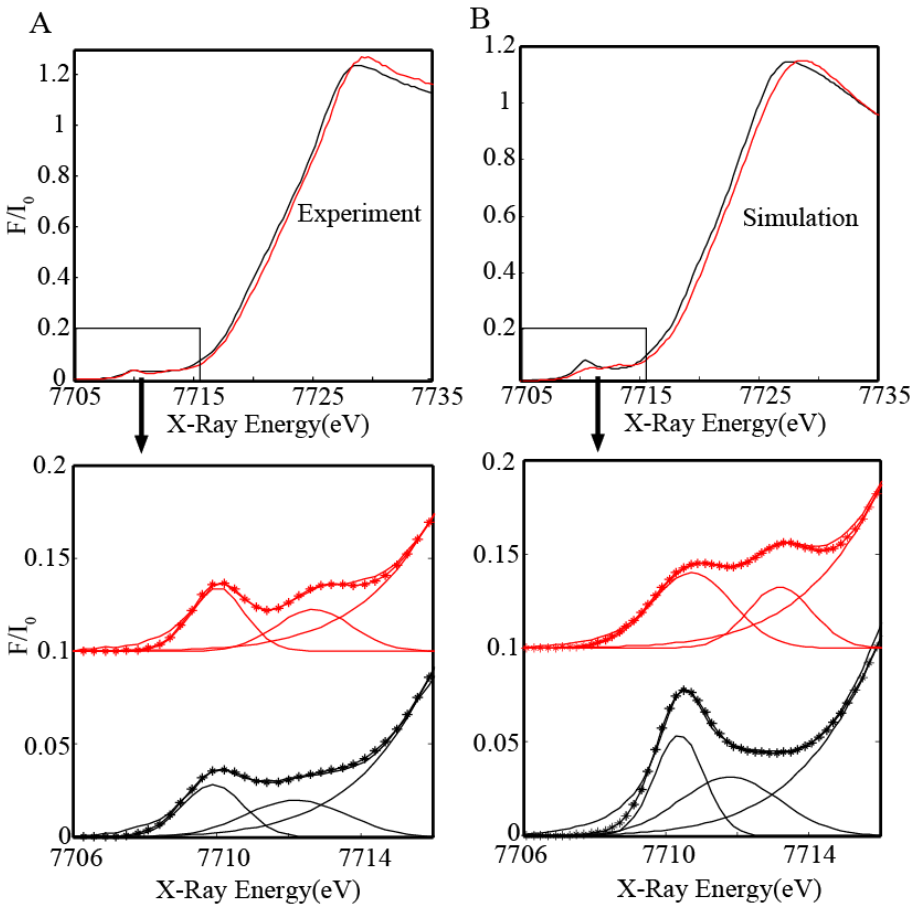

Figure 3. O_2 evolution profile monitored via on-line MS for a mixture containing **1(34)**$^{3+}$ and 4 equivalents of $(NH_4)_2Ce(NO_3)_6$ in 0.1 M triflic acid (pH=1.0).

This new redox couple (**3**$^{4+}$/**4**$^{4+}$) is responsible for a large electrocatalytic wave in the 1.8-2.0 V *vs*. NHE potential range associated with catalytic water oxidation to dioxygen.[13] In agreement with these electrochemical results, further addition of Ce^{IV} to the superoxido complexes **3**$^{4+}$ should generate dioxygen. Indeed, Figure 4 shows the on-line mass spectrometry (MS) results of adding 4 equivalents of Ce^{IV} to a solution of **1(34)**$^{3+}$ that generates a mixture of approximately 10:1 of $^{34}O_2$:$^{32}O_2$ in very good agreement with the expected 9:1 ratio of the starting materials. In a similar manner **3(32)**$^{4+}$ and **3(36)**$^{4+}$ also give the expected ratios of labeled dioxygen (Figure S8).

Further DFT calculations were undertaken to complete the catalytic cycle (Scheme 2). Oxygen ejection from $\mathbf{4}^{4+}$ concomitant with solvent coordination generates a dicobalt aquo-hydroxo complex at oxidation state III, $[HO\text{-}Co^{III}Co^{III}\text{-}OH_2]^{4+}$, $\mathbf{5}^{4+}$. Species $\mathbf{5}^{4+}$ is predicted to be further oxidized by a two-electron/two-proton single step at a potential of 1.63 V *vs*. NHE (which is slightly lower than that required for the oxidation of $\mathbf{3}^{4+}$ to $\mathbf{4}^{4+}$) to generate the highly reactive oxyl-hydroxyl species, $[HO^{\cdot}\text{-}Co^{III}Co^{III}\text{-}O^{\cdot}]$, $\mathbf{7}^{4+}$. The aqueous pK_a of $\mathbf{7}^{4+}$ is predicted to be -3, so proton loss is expected to be spontaneous to generate the initial peroxo species $\mathbf{1}^{3+}$. Indeed, it cannot be ruled out that the oxidation of $\mathbf{5}^{4+}$ may occur as an overall two-electron/three-proton step, as we have not attempted to model the specific kinetics of these PCET transformations. The resulting bis-[cobalt(III)-oxyl] compound, $\mathbf{7}^{4+}$, is not predicted to be stationary at the M11/L level, but spontaneously forms an O–O bond leading to the bridged peroxido complex $\mathbf{1}^{3+}$, closing the catalytic cycle. Theory indicates that $\mathbf{7}^{4+}$ will have extremely short lifetimes, thereby disfavoring O–O bond formation through nucleophilic attack of water on the oxyl fragment. It is interesting to note here the fundamental role played by the bpp^- ligand in maintaining the two metal centers in close proximity. In the O-O bond formation step, the ligand pre-organizes the two Co-O moieties in $\mathbf{7}^{4+}$ so that the O-O bond formation is entropically favored.

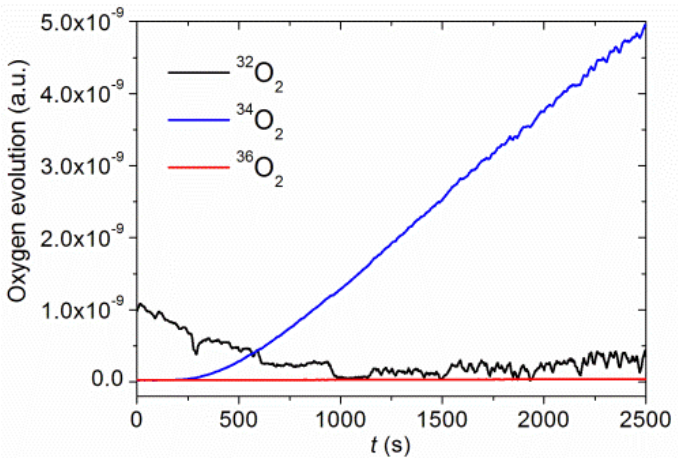

Figure 4. O_2 evolution profile monitored via on-line MS for a mixture containing $\mathbf{1(34)}^{3+}$ and 4 equivalents of $(NH_4)_2Ce(NO_3)_6$ in 0.1 M triflic acid (pH=1.0).

Further, the last step before oxygen ejection involves the formation of a diradical hydroxyl-superoxido species $\mathbf{4}^{4+}$, where the Co-O$^{\cdot}$H and the Co-OO$^{\cdot}$H moieties are situated in close proximity. Electron transfer to the cobalt hydroxyl moiety from the superoxido ligand is then ultimately responsible for the oxygen ejection. The need to generate a Co-hydroxyl simultaneously with a Co-superoxido cannot occur at a single-site as would be required in a mononuclear complex. Notice also that the water oxidation reaction cycle involves oxygen

only (not metal-centered) redox processes involving the superoxido and the aquo ligands in different protonation states (i.e., oxyl or hydroxyl radicals). The Co^{III} centers act as scaffolds strategically supporting the reactive oxygen radical species but do not undergo metal center redox processes.

Scheme 1 shows the interplay between the oxygen reduction and water oxidation catalytic cycles for the Co-Hbpp complex. The two catalytic cycles share two common reactive intermediates, $[Co^{III}\text{-}OO\text{-}Co^{III}]^{3+}$, **1**$^{3+}$, and $[H_2O\text{-}Co^{III}Co^{III}\text{-}OH]^{4+}$, **5**$^{4+}$, (shown in the center of Scheme 1, whose X-ray structures have been described previously).[5,6] Oxidation of $[Co^{III}\text{-}OO\text{-}Co^{III}]^{3+}$ leads to the water oxidation cycle (yellow box in Scheme 1) whereas reduction of $[H_2O\text{-}Co^{III}Co^{III}\text{-}OH]^{4+}$ leads to the oxygen reduction cycle (purple box in Scheme 1). The use of similar type of species for O-O bond formation and O-O bond cleavage but at different oxidation states parallels the chemistry that occurs at the chloride dismutase (Chl-D)[24,25] and Cyt-P450[26,27] respectively in nature. For Cyt-P450 cycle the Fe(II) porphyrin active center reacts with oxygen to generate an Fe(III)-superoxido species that eventually leads to O-O bond scission forming an Fe^{IV}=O high oxidation state species responsible for organic substrate oxidations. On the other hand, the catalytic cycle proposed for Chl-D, the lowest oxidation state proposed for the Fe porphyrin is “III” at which point molecular oxygen is released.

VIII

8. 3. Conclusion

In conclusion, we report detailed characterization of reaction intermediates involved in the catalytic cycle of a first-row transition-metal-based water-oxidation catalyst. This work is also important because it can be taken as a low molecular weight model of Co oxides,[8,28-30] although it is important to keep in mind that the electronic coupling through the bpp^- ligand can be significantly different from that of oxo-bridged Co oxides. The latter together with Ni oxides are amongst the most active earth abundant water oxidation heterogeneous catalysts.[31,28,32] For those oxides, thorough structural characterizations and mechanistic studies of active species are inherently difficult, given their heterogeneous nature. In addition, we also show that the same transition metal complex can be used for both the water oxidation and oxygen reduction catalytic reactions.

8. 4. References

(1) Hematian, S.; Garcia-Bosch, I.; Karlin, K. D. *Acc. Chem. Res.* **2015**, *48*, 2462.
(2) Nam, W. *Acc. Chem. Res.* **2015**, *48*, 2415.
(3) Cramer, C. J.; Tolman, W. B. *Acc. Chem. Res.* **2007**, *40*, 601.
(4) Citek, C.; Herres-Pawlis, S.; Stack, T. D. P. *Acc. Chem. Res.* **2015**, *48*, 2424.
(5) Cho, J.; Jeon, S.; Wilson, S. A.; Liu, L. V.; Kang, E. A.; Braymer, J. J.; Lim, M. H.; Hedman, B.; Hodgson, K. O.; Valentine, J. S. *Nature* **2011**, *478*, 502.
(6) Bukowski, M. R.; Koehntop, K. D.; Stubna, A.; Bominaar, E. L.; Halfen, J. A.; Münck, E.; Nam, W.; Que, L. *Science* **2005**, *310*, 1000.
(7) Concepcion, J. J.; Tsai, M.-K.; Muckerman, J. T.; Meyer, T. J. *J. Am. Chem. Soc.* **2010**, *132*, 1545.
(8) Zhang, M.; De Respinis, M.; Frei, H. *Nat. Chem.* **2014**, *6*, 362.
(9) Wang, J.-W.; Sahoo, P.; Lu, T.-B. *ACS Catal.* **2016**, *6*, 5062.
(10) Hoffert, W. A.; Mock, M. T.; Appel, A. M.; Yang, J. Y. *Eur. J. Inorg. Chem.* **2013**, *2013*, 3846.
(11) Radaram, B.; Ivie, J. A.; Singh, W. M.; Grudzien, R. M.; Reibenspies, J. H.; Webster, C. E.; Zhao, X. *Inorg. Chem.* **2011**, *50*, 10564.
(12) Fukuzumi, S.; Mandal, S.; Mase, K.; Ohkubo, K.; Park, H.; Benet-Buchholz, J.; Nam, W.; Llobet, A. *J. Am. Chem. Soc.* **2012**, *134*, 9906.
(13) Rigsby, M. L.; Mandal, S.; Nam, W.; Spencer, L. C.; Llobet, A.; Stahl, S. S. *Chem. Sci.* **2012**, *3*, 3058.
(14) Barraclough, C. G.; Lawrance, G. A.; Lay, P. A. *Inorg. Chem.* **1978**, *17*, 3317.
(15) Schmidt, S.; Heinemann, F. W.; Grohmann, A. *Eur. J. Inorg. Chem.* **2000**, *2000*, 1657.
(16) Rajani, C.; Kincaid, J. R.; Petering, D. H. *J. Am. Chem. Soc.* **2004**, *126*, 3829.
(17) *Nakamoto, K. Infrared and raman Spectra of Inorganic and Coordi-nation Compounds, 6th Edn., John wiley & Sons Inc., Hoboken, New Jersey, 2009*.
(18) Kinsinger, C. R.; Gherman, B. F.; Gagliardi, L.; Cramer, C. J. *J. Biol. Inorg. Chem.* **2005**, *10*, 778.
(19) Shan, X.; Que, L. *Proc. Natl. Acad. Sci.* **2005**, *102*, 5340.
(20) Loeb, K. E.; Westre, T. E.; Kappock, T. J.; Mitić, N.; Glasfeld, E.; Caradonna, J. P.; Hedman, B.; Hodgson, K. O.; Solomon, E. I. *J. Am. Chem. Soc.* **1997**, *119*, 1901.
(21) Westre, T. E.; Kennepohl, P.; DeWitt, J. G.; Hedman, B.; Hodgson, K. O.; Solomon, E. I. *J. Am. Chem. Soc.* **1997**, *119*, 6297.
(22) De Groot, F. *Chem. Rev.* **2001**, *101*, 1779.
(23) Chandrasekaran, P.; Stieber, S. C. E.; Collins, T. J.; Que Jr, L.; Neese, F.; DeBeer, S. *Dalton. Trans.* **2011**, *40*, 11070.
(24) Mlynek, G.; Sjöblom, B.; Kostan, J.; Füreder, S.; Maixner, F.; Gysel, K.; Furtmüller, P. G.; Obinger, C.; Wagner, M.; Daims, H. *J. Bacteriol.* **2011**, *193*, 2408.
(25) Sun, S.; Li, Z.-S.; Chen, S.-L. *Dalton trans. (Cambridge, England: 2003)* **2014**, *43*, 973.
(26) Ener, M. E.; Lee, Y.-T.; Winkler, J. R.; Gray, H. B.; Cheruzel, L. *Proc. Natl. Acad. Sci.* **2010**, *107*, 18783.
(27) Guengerich, F. P. *J. Biochem. Mol. Toxicol.* **2007**, *21*, 163.
(28) McCrory, C. C.; Jung, S.; Ferrer, I. M.; Chatman, S. M.; Peters, J. C.; Jaramillo, T. F. *J. Am. Chem. Soc.* **2015**, *137*, 4347.
(29) Nguyen, A. I.; Ziegler, M. S.; Oña-Burgos, P.; Sturzbecher-Hohne, M.; Kim, W.; Bellone, D. E.; Tilley, T. D. *J. Am. Chem. Soc.* **2015**, *137*, 12865.
(30) Coehn, A.; Gläser, M. *Z. anorg. allg.* **1902**, *33*, 9.
(31) Hu, S.; Shaner, M. R.; Beardslee, J. A.; Lichterman, M.; Brunschwig, B. S.; Lewis, N. S. *Science* **2014**, *344*, 1005.
(32) Kenney, M. J.; Gong, M.; Li, Y.; Wu, J. Z.; Feng, J.; Lanza, M.; Dai, H. *Science* **2013**, *342*, 836.

8. 5. Supporting Information

Table of Contents

Experimental, Materials and Methods

Figure S1 EPR spectra of **3(32)**$^{4+}$ and **3(36)**$^{4+}$

Figure S2 Additional EPR spectra simulations for **3(34)**$^{4+}$

Figure S3 DFT-MO XANES simulations of bridging superoxido complexes

Figure S4 EXAFS spectra of **1(32)**$^{3+}$and **3(32)**$^{4+}$

Figure S5 Simulated EXAFS fitting from XRD and DFT coordinates of **1(32)**$^{3+}$

Figure S6 EXAFS fitting for **1(32)**$^{3+}$and **3(32)**$^{4+}$. Superoxido bridging versus end-on

Figure S7 Back Fourier experimental and fitted lines *q Re[χ(k)]* for **1(32)**$^{3+}$ and **3(32)**$^{4+}$. Superoxido bridging versus end-on

Figure S8A On-line mass spectrometry for oxygen gas detection with **1(32)**$^{3+}$and **1(36)**$^{3+}$

Figure S8B Electrocatatlytic on line gas evolution experiment for **1(36)**$^{3+}$ at pH 2.0

Table S1 Comparison of structural parameters from EXAFS, DFT and XRD data of **1(32)**$^{3+}$ and **3(32)**$^{4+}$

Table S2 EXAFS fits for **1(32)**$^{3+}$ and **3(32)**$^{4+}$. Superoxido bridging versus end-on

Figure S9 Summary Reaction scheme at pH 2. At pH 8 PCETE(M06-L/M11-L)=1.10/1.35, PCETB3(M06-L/M11-L)=1.61/1.98, PCETC2(M06-L/M11-L)=0.65/0.76.

Figure S10 Summary of Computed Reaction scheme at pH 8.

Figure S11 Computational Reactivity and Pourbaix diagram: Energies, pKa's and Redox Potentials. All relevant speciation studied at pH 2.

Figure S12 Computational Reactivity and Pourbaix diagram: Energies, pKa's and Redox Potentials. All relevant speciation studied at pH 8.

Figure S13 Labeling scheme of the species and ET, PT and PCET steps involved in the Pourbaix diagram.

Figure S14 Labeling scheme of the species and ET, PT, PCET and substitution steps involved in the oxygen evolution process.

Table S3 Reduction potentials and ΔG values for the different Electron Transfer (ET) steps at the different levels of theory tested.

Table S4 pKa's and ΔG of proton dissociation values for the different steps at the different levels of theory tested.

Table S5 Reduction potentials and ΔG values for the different Proton Coupled Electron Transfer (PCET) steps at pH 2 at the different levels of theory tested

Table S6 Reduction potentials andΔG values for the different Proton Coupled Electron Transfer (PCET) steps at pH 8 at the different levels of theory tested

Table S7 ΔG values for the different water insertion reactions at the different levels of theory tested.

Table S8 ΔG= activation energy values for the transition states considered at the different levels of theory tested.

Table S9 Compilation of the, electronic energy, the as computed Gibbs free energy, the Gibbs free energy after removing the contribution of the frequencies that are under 50 cm^{-1} and the Composite Gibbs Free energy considering water as a solvent. All calculated with M06-L on M06-L optimized geometries. <S2> represents the spin operator expectation value.

Table S10 Compilation of the Composite Gibbs Free energies calculated with M06-L considering water as a solvent, at the gas phase concentration and then 1 Molar concentration. The latter corresponds to the standard state for the computation of standard potentials and activation energies.

Table S11 Compilation of the, electronic energy, the Gibbs free energy corrected by removing the contributions of the frequencies under 50, the electronic energy at the M11-L level of theory considering the solvation with water on the M06-L optimized geometry, the resulting composite Gibbs free energy. All calculated with on M06-L optimized geometries. <S2> represents the spin operator expectation value.

Table S12 Compilation of the Composite Gibbs Free energies calculated with M11-L, considering water as a solvent, at the gas phase concentration and then 1 Molar concentration. The latter corresponds to the standard state for the computation of standard potentials and activation energies.

Experimental, Materials and Methods

Materials

Complexes **1(32)**$^{3+}$, **1(34)**$^{3+}$ and **1(36)**$^{3+}$ were synthesized following a modified reported procedure.[1] Purity of all compounds was verified by ^{1}H-NMR, cyclic voltammetry and/or UV-Vis spectroscopy. All reagents used for the synthesis of ligands and complexes were obtained from Aldrich Chemical Co. and were used without further purification. Labeled oxygen gas samples ($^{18}O_2$(97%) and $^{17}O_2$ (90%)) and $(NH_4)_2Ce(NO_3)_6$ (99.99+% metal basis) were purchased from Aldrich Chemical Co and Trifluoromethanesulfonic acid (HOTf) from CYMIT. Although the purity of the $^{18}O_2$ gas sample was as high as 97%, the rRaman characterization of the obtained compound confirmed that there was a contamination of the oxygen atmosphere during the reaction generating a 1:1 mixture of **1(32)**$^{3+}$ and **1(36)**$^{3+}$. High-purity deionized water was obtained by passing distilled water through a nanopure Milli-Q water purification system.

Resonance Raman Spectroscopy

rR spectra were measured with a Renishaw in Via Reflex RAMAN confocal microscope instrument (Gloucestershire, UK), equipped with an Ar ion laser, operating at 514 nm. The spectrometer was equipped with a Peltier-cooled CCD detector (-70°C) coupled to a Leica DM-2500 microscope. Calibration was carried out with respect to Si standard. A temperature controlled stage from Linkam Scientific Instruments was used to keep the sample at -150˚C during the measurement. Spectra integration time was 20 seconds and spectra shown correspond to five accumulations. Laser power used was 50% of the nominal power (25 mW). The samples were prepared by mixing a 3 mM solution of **1**$^{3+}$ in Milli-Q water (300 µL) and a 30 mM solution of $(NH_4)_2Ce(NO_3)_6$in 1 M HOTf (pH 0, 30 µL) at room temperature and freezing the mixture after 30 seconds.

Electron Paramagnetic Resonance

EPR spectra were measured in aEMX Micro EPR spectrometer with an X-band bridge of 9.1-9.9 GHz at 4K. The samples were prepared by adding one equivalent of $(NH_4)_2Ce(NO_3)_6$ to a 0.5mM solution of **1**$^{3+}$ in 0.1 M HOTf (pH 1)at room temperature and freezing the mixture within minutes. Tensor components values of g_{xx} = 1.982850, g_{yy} = 1.982820, and g_{zz} =1.98243 were used to simulate the EPR spectra of **3(32)**$^{4+}$ and **3(36)**$^{4+}$with good agreement with experimental data (Figure S1). Simulations with line width of 1,1 and 0.30 G at g_{xx}, g_{yy} and g_{zz}were used (Figure S1). For the simulation of the **3(34)**$^{4+}$spectrum, a hyperfine splitting of

A_{zz} = 0.78 G due to the two ^{17}O (I = 5/2) atoms were well resolved, and could be fitted. However the values of A_{yy} and A_{zz} are uncertain. Simulations were carried out with A_{zz} = 0.78 G and A_{yy} varying from 0.10-0.30 Gauss, and with A_{zz} = 0.78 G and A_{xx} varying between 0.10-0.30 G. We estimated upper limit for A_{yy} and A_{zz} as 0.10 G (Figure S2).

Oxygen Detection Experiments

A 1 mM solution of $\mathbf{1}^{3+}$ in 0.1 M HOTf (pH 1, 1.5 mL) was connected to a Mass Spectrometer OmniStar™ for on-line gas analysis. Four equivalents of $(NH_4)_2Ce(NO_3)_6$ in 0.5 mL of 0.1 M HOTf (pH 1) were added quickly and the evolution of $^{32}O_2$, $^{34}O_2$ and $^{36}O_2$ gases were monitored simultaneously.

XAS

X-ray absorption spectra were collected at the Advanced Photon Source (APS) at Argonne National Laboratory on bending magnet beamline 20 at electron energy 7.7 keV and average current 100 mA. The radiation was monochromatized by a Si(110) crystal monochromator. The intensity of the X-ray was monitored by three ion chambers (I_0, I_1 and I_2) filled with 70% nitrogen and 30% helium and placed before the sample (I_0) and after the sample (I_1 and I_2). A Co metal foil was placed between the I_1 and I_2 and its absorption recorded with each scan for energy calibration. Plastic (Lexan) EXAFS sample holders (inner dimensions of 12 mm x 3 mm x 3 mm) filled with frozen solutions were inserted into a pre-cooled (20 K) cryostat. The samples were kept at 20 K in a He atmosphere at ambient pressure. Data was recorded as fluorescence excitation spectra using a 13-element energy-resolving detector. In order to reduce the risk of sample damage by X-ray radiation, 80% flux was used in the defocused mode (beam size 1 x 10 mm) and no damage was observed to any samples scan after scan. The samples were also protected from the X-ray beam during spectrometer movements by a shutter synchronized with the scan program. No more than 5 scans were taken at each sample position in any condition. The Co XAS energy was calibrated by the first maximum of the second derivative of the cobalt metal XANES spectrum.

EXAFS Data Analysis

Athena software[2] was used for data processing. The energy scale for each scan is normalized using the cobalt metal standard. Data in energy space are pre-edge corrected, normalized, deglitched (if necessary), and background corrected. The processed data are next converted to the photoelectron wave vector (k) space and weighted by k^3. The electron wave number is defined as $k = [2m(E - E_0)/\hbar^2]^{1/2}$, E_0 is the energy origin or the threshold energy. K-space data

were truncated near the zero crossings (k = 1.403 to 12.103 $Å^{-1}$) in Co EXAFS before Fourier transformation. The k-space data are transferred into the Artemis Software for curve fitting. In order to fit the data, the Fourier peaks are isolated separately, grouped together, or the entire (unfiltered) spectrum was used. The individual Fourier peaks were isolated by applying a Hanning window to the first and last 15% of the chosen range, leaving the middle 70% untouched. Curve fitting is performed using *ab initio*-calculated phases and amplitudes from the FEFF8[3] program and *ab initio*-calculated phases and amplitudes are used in the EXAFS equation[4]

$$\chi(k) = S_0^2 \sum_j \frac{N_j}{kR_j^2} f_{eff_j}(\pi, k, R_j) e^{-2\sigma_j^2 k^2} e^{\frac{-2R_j}{\lambda_j(k)}} \sin(2kR_j + \phi_{ij}(k)) \quad (1)$$

where $N_j$is the number of atoms in thej^{th}shell; R_j the mean distance between the absorbing atom and the atoms in the j^{th}shell; $f_{eff_j}(\pi,k, R_j)$ is the *ab initio* amplitude function for shell *j*, and the Debye-Waller term $e^{-2\sigma_j^2 k^2}$ accounts for damping due to static and thermal disorder in absorber-backscatterer distances. The mean free path term $e^{\frac{-2R_j}{\lambda_j(k)}}$ reflects losses due to inelastic scattering, where $\lambda_j(k)$, is the electron mean free path. The oscillations in the EXAFS spectrum are reflected in the sinusoidal term $\sin(2kR_j + \phi_{ij}(k))$, where $\phi_{ij}(k)$ is the *ab initio* phase function for shell *j*. This sinusoidal term shows the direct relation between the frequency of the EXAFS oscillations in k-space and the absorber-back scatterer distance. S_0^2 is an amplitude reduction factor.

The EXAFS equation (Eq. 1) is used to fit the experimental Fourier isolated data (in q-space) as well as unfiltered data (in k-space) and Fourier transformed data (in R-space) using *N*, S_0^2, E_0, *R,* and σ^2 as variable parameters**.** *N* refers to the number of coordination atoms surrounding Co for each shell. The quality of fit is evaluated by R-factorand the reduced Chi^2 value. The deviation in E_0 was required to be less than or equal to 10 eV. An R-factor less than 2% denotes that the fit is good enough whereas an R-factor between 2 and 5% denotes that the fit is correct within a consistently broad model.[4] The reduced Chi^2 value is used to compare fits as more absorber-backscatter shells are included to fit the data. A smaller reduced Chi^2 value indicates a better fit. Similar results were obtained from fits done in k, q, and R-spaces.

DFT Methods for Geometry Optimization and Free Energy Calculations

All molecular geometries were fully optimized at the M06-L[5-7] level of density functional theory using the Stuttgart [8s7p6d2f|6s5p3d2f] ECP28MWB contracted pseudopotential basis set[8] on Co and the 6-31G(d) basis set[9] on all other atoms. Non-analytical integral

evaluations made use of a pruned grid having 99 radial shells and 590 angular points per shell and an automatically generated density-fitting basis set was used within the resolution- of-the- identity approximation to speed the evaluation of the Coulomb integrals. The nature of all stationary points was verified by analytical computation of vibrational frequencies, which were also used for the computation of zero-point vibrational energies, molecular partition functions (with all frequencies below 50 cm^{-1} replaced by 50 cm^{-1} when computing free energies), and for determining the reactants and products associated with each transition-state structure (by following the normal modes associated with imaginary frequencies). Partition functions were used in the computation of 298 K thermal contributions to free energy employing the usual ideal-gas, rigid-rotator, harmonic oscillator approximation.[10] Free energy contributions were added to single-point M06-L and M11-L[11] electronic energies computed with the SDD basis set on cobalt and the 6-311+G(2df,p) basis set on all other atoms to arrive at final, composite, aqueous free energies. As M11-L predictions were found to be in near quantitative agreement with experiment for key oxidation potentials, we report energetics exclusively at that level (M06-L oxidation potentials were generally predicted to be 200-300 mV lower than those at the M11-L level).

Solvation effects associated with water as solvent were accounted for using the SMD continuum solvation model.[12] A 1 M standard state was used for all species in aqueous solution except for water itself, for which a 55.6 M standard state was employed. Thus, for all molecules but water, the free energy in aqueous solution is computed as the 1 atm gas-phase free energy, plus an adjustment for the 1 atm to 1 M standard state concentration change of RTln(24.5), or 1.9 kcal mol-1, plus the 1 M to 1 M transfer (solvation) free energy computed from the SMD model. In the case of water, the 1 atm gas-phase free energy is adjusted by the sum of a 1 atm to 55.6 M standard-state concentration change, or 4.3 kcal mol^{-1},[13-16] and the experimental 1 M to 1 M solvation free energy, -6.3 kcal mol-1. The 1 M to 1 M solvation free energy of the proton was taken from experiment as -265.9 kcal mol-1. Standard reduction potentials were calculated for various possible redox couples to assess the energetic accessibility of different intermediates at various oxidation states. For a redox reaction of the form:

$$O_{(aq)} + n\ e^-_{(g)} \rightarrow R_{(aq)} \qquad (2)$$

where O and R denote the oxidized and reduced states of theredox couple, respectively, and *n* is the number of electron*s* involved in redox reaction, the reduction potential E^o for the O/R couple relative to the standard hydrogen electrode (SHE) was computed as:

$$E°_{O/R} = -(\Delta G°_{O/R} - \Delta G°_{SHE})/nF \quad (3)$$

Where $\Delta G°_{O/R}$ is the free energy change associated with Eq. 4 (using Boltzmann statistics for the electron),[17,18] and $\Delta G°_{NHE}$ is the SHE free energy change associated with

$$H^+_{(aq)} + e^-_{(g)} \rightarrow (1/2)\ H_{2(g)} \quad (4)$$

which is -4.28 eV with Boltzmann statistics for the electron, and *F* is the Faraday constant. The 298 K difference between the normal hydrogen electrode (NHE; which is what is employed in actual measurements) and SHE (which is a formal construct) is –0.006 V.[19]

DFT-MO XANES Methods

The optimized geometries calculated as described above were used to calculate unoccupied molecular orbitals which were subsequently used for XANES calculations.The X-ray absorption cross section obeys the Fermi golden rule, and the matrix element for the electron transition can be written as

$$\sigma(E) \sim \left|\left\langle \psi_f \left| \boldsymbol{\varepsilon}\cdot\mathbf{r}\cdot e^{i\mathbf{k}\cdot\mathbf{r}} \right| \psi_{1s} \right\rangle\right|^2 \cdot \delta(E - E_f - E_{1s}) \quad (5)$$

where ψ_{1s} is a core−electron wave function, ψ_f is a wave function for the unoccupied state, **ε** is a photon polarization, **k** is a photon wavevector. Both dipole and quadrupole terms were taken into account:

$$\sigma(E) \sim \left|\left\langle \psi_f \left| \boldsymbol{\varepsilon}\cdot\mathbf{r}\cdot(1+i\mathbf{k}\cdot\mathbf{r}) \right| \psi_{1s} \right\rangle\right|^2 \cdot \delta(E - E_f - E_{1s}) \quad (6)$$

The averaging was performed for all directions of photon polarization and wave vector with a restriction of perpendicularity of these two vectors. Calculation of the wave function for unoccupied states is based on a basis set method within the molecular orbital DFT approach already described above (DFT-MO in the text). Molecular orbitals of the 1s core level and unoccupied levels are used to calculate dipole and quadrupole matrix elements and Lorentzian convolution is subsequently applied for comparison with experiment.[20] In order to represent a final state after the photon absorption process, a core hole is introduced on a 1s cobalt level in a self-consistent way subsequently for two inequivalent Co sites. For the DFT-MO calculations shown in text, we first obtain eigenvalues and corresponding wave functions for both spin polarizations for a given Co complex in the presence of a core hole. The matrix elements are then evaluated for transitions between 1s core level and unoccupied MOs using dipole and quadrupole transition operators. In order to compare with experimental results, a convolution of calculated matrix elements was performed with a Lorentzian profile using energy dependent linewidth. In the pre-edge region, the width of the Lorentzian profile

corresponds to a core hole lifetime broadening for Co. This value is then increased in higher energy interval with a smooth arctangent function. The parameters of the matrix elements calculations (grid step, size number of unoccupied MOs) and energy convolution are fixed once for all complexes. The DFT-MO calculated spectra were subsequently aligned according to the energy value of the Co 1s orbital, thus reproducing the chemical shift for different Co oxidation states. A constant shift with the identical value was applied for all spectra in order to align the energy scale between experimental data and theoretical calculations.

It is important to note that metal to ligand charge transfer shakedown transitions can cause a shift in the energy position[21] and intensity[22] of the shoulder on the rising edge of the XANES spectrum. However, the proper theoretical description of such state requires the use of multi-reference computational methods which are at present capable of dealing only with the first several transitions.[23]

In our simulations, we intended to reproduce both pre-edge transitions and main edge features which require calculation of energies and wave functions of more than 500 electronic states that were possible only within DFT level of theory. Thus, we expect the discrepancies between energy position of the shakedown transition observed in the experiment and calculated spectra to be in the order of 1eV. However, the effect of the intensity of the peak associated with shakedown transitions is much suppressed for complexes with metal-oxygen bonds.[16]

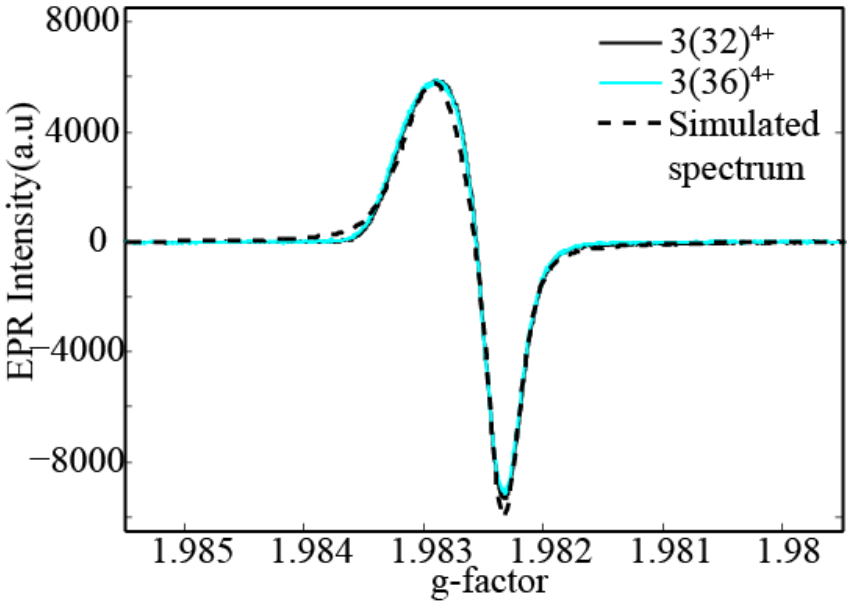

Figure S1. Experimental EPR spectrum of **3(32)**$^{4+}$ (black) and **3(36)**$^{4+}$ (cyan) measured at -4 ˚C together with simulated EPR spectrum (dashed line) calculated withg_{xx} = 1.982850, g_{yy} = 1.982820 and g_{zz} = 1.98243.

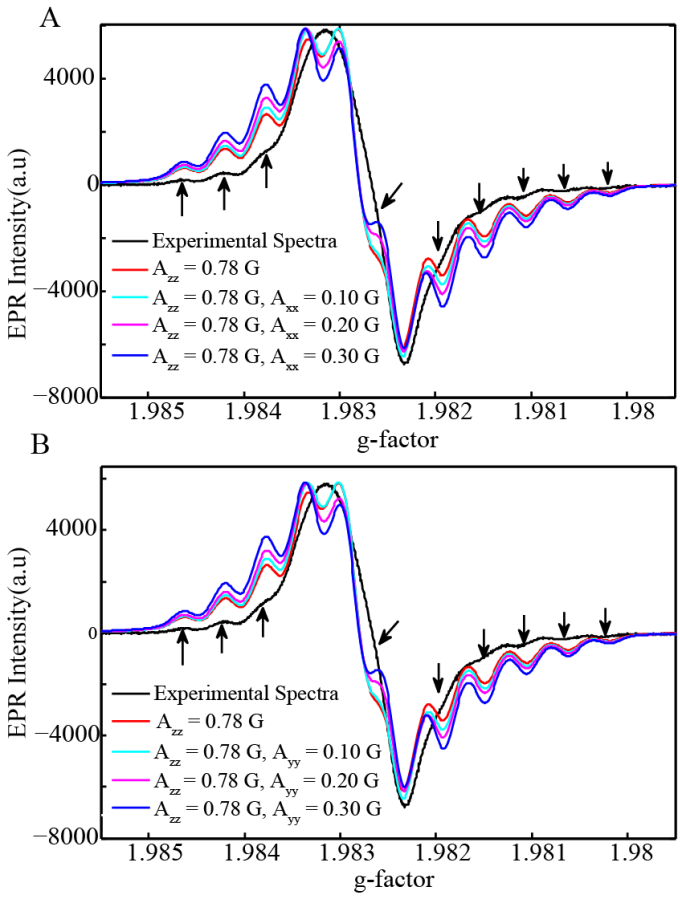

Figure S2. Experimental EPR spectrum of **3(34)**$^{4+}$ (black) measured at -4 ºC together with simulated EPR spectra with different hyperfine splitting parameters: A_{zz} = 0.78 G with addition of A_{yy} = 0.10-0.30 G (A) and with addition of A_{zz} = 0.10-0.30 G (B).

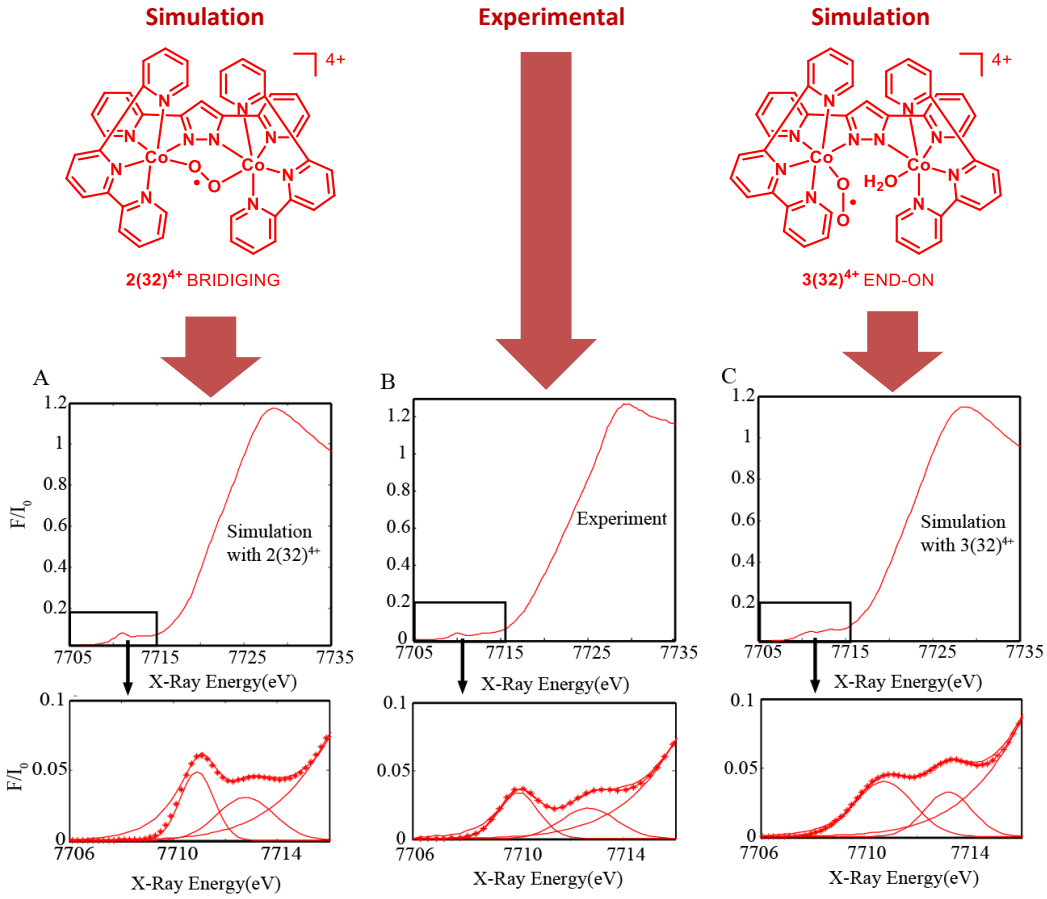

Figure S3. DFT-MO XANES spectra simulations for the one-electron oxidized symmetric superoxido-bridged product (left), the asymmetric superoxido-end-on product (right) compared to the experimental spectrum (middle).In the bottom figures, a zoom in of the pre-edge region and Gaussian fits of the 2 pre-edge peaks are shown. Note that the doublet pre-edge feature in the calculated spectrum of the superoxido-bridged derivative is less pronounced than that observed for the simulated superoxido end-on derivative.

The near edge fit and pre-edge peak fits were carried out with an error function and 2 gaussian functions respectively. The formulas for the error (erf) and Gaussian(gauss) functions are as follows:

Error function: $A\left[erf\left(\frac{e-E_0}{w}\right)+1\right]$ (Eq.1)

Gaussian function: $\left(\frac{A}{w\sqrt{2\pi}}\right)\exp\left[\frac{-(e-E_0)^2}{(2w^2)}\right]$ (Eq.2)

Where A corresponds to the amplitude; w, the width; E_0, the centroid of the pre-edge and near edge peaks and *e*, the x-ray energy.

The parameters E_0, *A* and *w* used for each sets of functions for the experimental and theoretical fits together with their uncertainties are tabulated below.

1(32)$^{3+}$peroxo experimental			
Function	**Centroid**	**Amplitude**	**Width**
Erf	7722.45	0.688	6.024
Gauss	7709.90	0.060	0.850
Gauss	7712.20	0.070	1.4
1(32)$^{3+}$ peroxo simulation			
Function	**Centroid**	**Amplitude**	**Width**
Erf	7722.1	0.688	6.024
Gauss	7710.38	0.089	0.665
Gauss	7711.80	0.110	1.4
3(32)$^{4+}$superoxo experimental			
Function	**Centroid**	**Amplitude**	**Width**
Erf	7722.9	0.688	6.024
Gauss	7710.04	0.064	0.750
Gauss	7712.70	0.059	1.05
3(32)$^{4+}$superoxo -bridging simulation			
Function	**Centroid**	**Amplitude**	**Width**
Erf	7722.8	0.688	6.024
Gauss	7710.91	0.080	0.650
Gauss	7712.79	0.085	1.1
3(32)$^{4+}$superoxo-end on simulation			
Function	**Centroid**	**Amplitude**	**Width**
Erf	7722.55	0.688	6.024
Gauss	7710.74	0.112	1.118
Gauss	7713.20	0.073	0.9

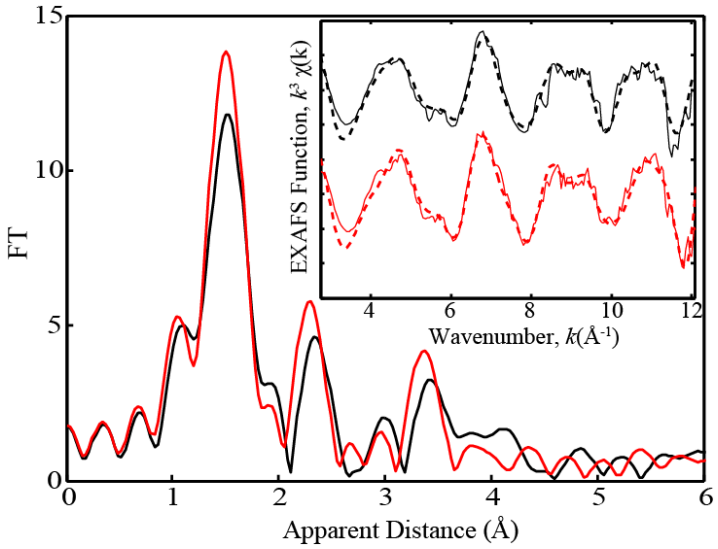

Figure S4. Fourier transforms of k^3-weighted Co EXAFS of the **1(32)**$^{3+}$ (black) and **3(32)**$^{4+}$(red).

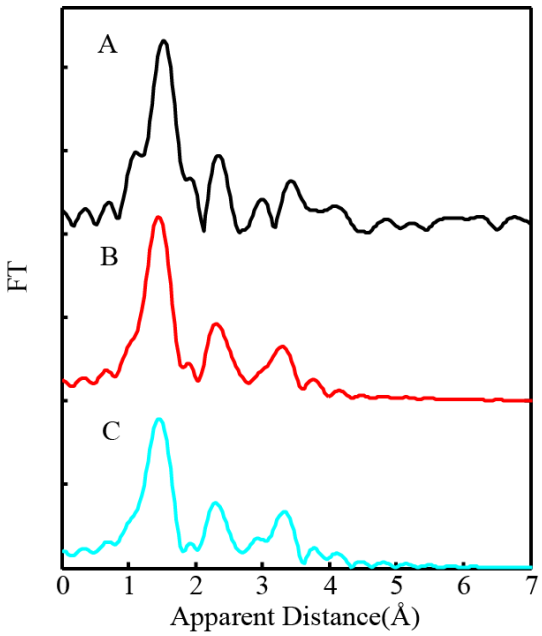

Figure S5. A) Fourier transforms of k^3-weighted Co EXAFS of **1(32)**$^{3+}$. B) EXAFS spectrum simulated with FEFF software, coordinates of all atoms were obtained from published XRD structure of **1(32)**$^{3+}$.[1] C) EXAFS spectrum simulated with FEFF software, coordinates of all atoms from DFT calculations were used as input.

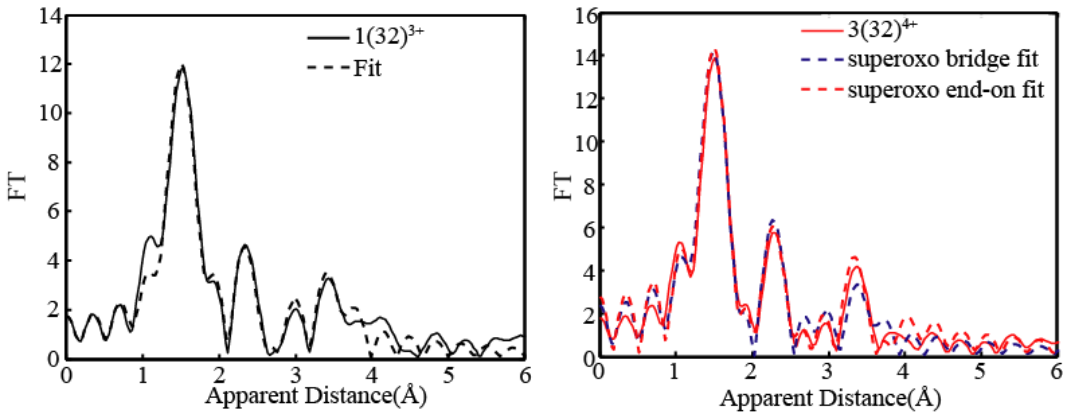

Figure S6. Left) **1(32)**$^{3+}$ EXAFS Fourier transforms and its corresponding fit (fit 5 in Table S2, below). Right) **3(32)**$^{4+}$ EXAFS Fourier transforms and its corresponding fit: fit 12 (in Table S2 below) for blue dotted line corresponding to a **superoxo bridged** and fit 14 (in Table S2 below) red dotted line corresponding to a **superoxo end-on**.

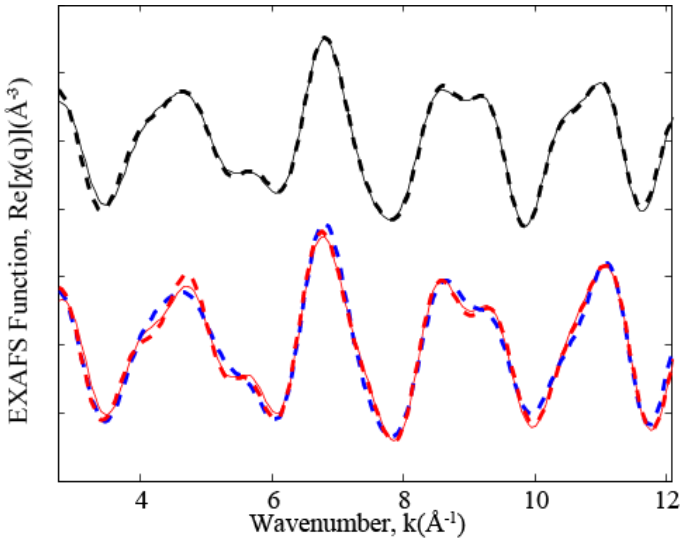

Figure S7. Back fourier experimental and fitted lines *q Re[χ(k)]* for **1(32)**$^{3+}$ (black, fit 5, Table 2 below) and **3(32)**$^{4+}$ (red). The blue dotted line corresponding to a superoxo bridged (fit 12 in Table S2 below) and red dotted line, corresponding to a superoxo end-on (fit 14 in Table S2 below).

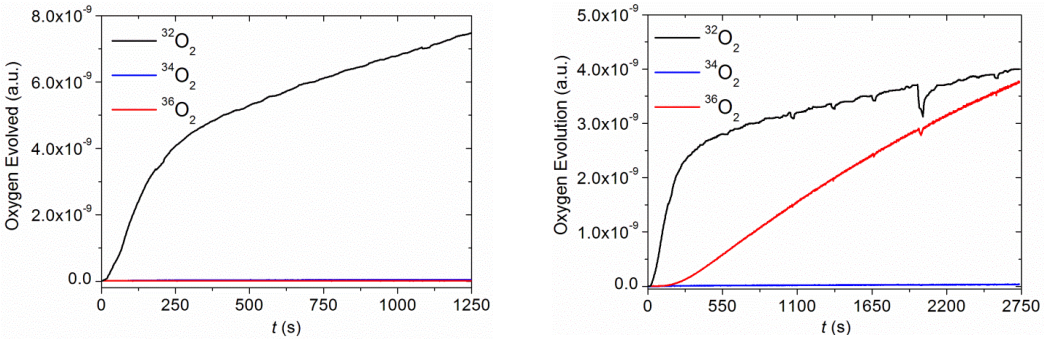

Figure S8A. O_2 evolution profile monitored via on-line MS for a mixture containing pure **1(32)**$^{3+}$ (Left) or a mixture of **1(32)**$^{3+}$:**1(36)**$^{3+}$ 50:50 (Right) in the presence of 4 equivalents of $(NH_4)_2Ce(NO_3)_6$in 0.1 M HOTf (pH 1).

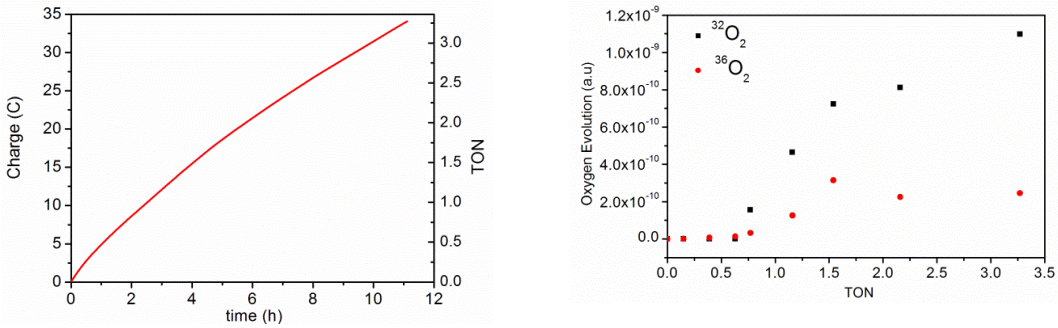

Figure S8B. Left, charge *vs.* time profile of a bulk electrolysis experiment performed in a two compartment cell containing an FTO working electrode (4.5 cm^2), Ag/AgCl reference electrode and a 8.5 mL of a 2.4 mM solution of **1(36)**$^{3+}$ in a pH = 2.0 phosphate buffer solution at an E_{app} = 1.80 V (*vs.* Ag/Ag^+). The second compartment contained a platinum wire counter electrode in 8.5 mL of a pH = 2.0 phosphate buffer solution. The TONs are calculated assuming a Faradaic efficiency of 77% (see Ref 6 main ms). Right, oxygen evolution *vs.* TON profile for the same experiment.

The electrocatalytic experiment for **1(36)**$^{3+}$ shows the initial formation of $^{32}O_2$ and $^{36}O_2$, and as the catalysis proceeds the gas phase gets enriched with $^{32}O_2$ as expected.

Chapter 8

Table S1. Comparison of structural parameters from EXAFS, DFT and XRD data of **1(32)**$^{3+}$ and **3(32)**$^{4+}$.

	EXAFS Analysis Distances (Å)	**DFT Distances (Å)**	**XRD Distances**
1(32)$^{3+}$ peroxido	Co-N/O,5: 1.93 Co-N,1: 2.17 Co-O,1: 2.75 Co-C,5: 2.89 Co-C,3: 3.31 Co-Co,1: 3.82 O-O distance = 1.005 R-factor = 0.0001 Reduced Chi^2 value: 40 (Fit 5 in Table 2)	Co(1)-O(1): 1.9092 Co(2)-O(2): 1.9096 Co(1)-O(2): 2.7501 Co(2)-O(1): 2.7501 Co(1)-N(1): 2.1001 Co(1)-N(2): 1.9067 Co(1)-N(3): 1.9694 Co(1)-N(4): 1.8848 Co(1)-N(5): 1.9980 Co(2)-N(1): 1.9068 Co(2)-N(2): 2.1003 Co(2)-N(3): 1.9698 Co(2)-N(4): 1.8848 Co(2)-N(5): 1.9990 Co(1)-Co(2): 3.8174 O(1)-O(2): 1.3516	Co(1)-O(1): 1.882(3) Co(2)-O(2): 1.884(2) Co(1)-O(2): 2.763(2) Co(2)-O(1): 2.757(2) Co(1)-N(1): 2.006(3) Co(1)-N(2): 1.875(2) Co(1)-N(3): 1.952(2) Co(1)-N(4): 1.863(2) Co(1)-N(5): 1.9939(2) Co(2)-N(1): 1.875(3) Co(2)-N(2): 1.929(3) Co(2)-N(3): 1.862(3) Co(2)-N(4): 1.958(3) Co(2)-N(5): 2.009(2) Co(1)-Co(2): 3.7967 O(1)-O(2): 1.397
2(32)$^{4+}$ superoxido bridge	Co-N,6: 1.91 Co-O,1: 2.70 Co-C,5: 2.89 Co-C,3: 3.32 Co-Co,1: 3.78 O-O distance = 0.963 R-factor = 0.0008 Reduced Chi^2 value: 98 (Fit 12 in Table 2)	Co(1)-O(1): 1.9446 Co(1)-O(2): 1.9446 Co(1)-O(2): 2.7128 Co(2)-O(1): 2.7130 Co(1)-N(1): 2.0114 Co(1)-N(2): 1.9293 Co(1)-N(3): 1.9968 Co(1)-N(4):1.9748 Co(1)-N(5):1.8876 Co(2)-N(1): 1.9293 Co(2)-N(2): 2.0114 Co(2)-N(3): 1.9749 Co(2)-N(4): 1.8876 Co(2)-N(5): 1.9976 Co(1)-Co(2): 3.9587 O(1)-O(2): 1.3097	No crystal structure of complex
3(32)$^{4+}$ superoxido end-on	Co-N,6: 1.92 Co-O,0.5: 2.70 Co-C,5: 2.89 Co,C,3: 3.29 Co-Co,1 :3.78 Co-O,1: 3.95 R-factor = 0.0001 Reduced Chi^2 value = 41 (Fit 14 in Table 2)	Co(2)-O(1):2.7833 Co(2)-O(2):1.9187 Co(1)-O(3):1.9873 Co(1)-N(1): 1.9566 Co(1)-N(2): 1.9906 Co(1)-N(3):1.9951 Co(1)-N(4):1.8833 Co(1)-N(5):1.9745 Co(2)-N(1):2.0084 Co(2)-N(2):2.0215 Co(2)-N(3):1.9933 Co(2)-N(4):1.8756 Co(2)-N(5):1.9818 Co(1)-Co(2):4.4416 O(1)-O(2):1.2883	No crystal structure of this complex

Chapter 8

Table S2. EXAFS fits for **1(32)**$^{3+}$ and **3(32)**$^{4+}$ (Superoxo bridging (Fit 12) versus end-on (Fit 14) structure).

Sample	Fit	Peak	Shell, N	R, Å	E_0	$\sigma^2(10^{-3})$	R-factor	ReducedChi-square
1(32)$^{3+}$ peroxido	1	I	Co-N,6	1.91	2.3	4.3	0.0021	936
	2	I	Co-N/O,5 Co-N,1	1.92 2.21	5.7	3.2	0.0001	399
	3	I,II	Co-N/O,5 Co-N,1 Co-C,5 Co-C,3	1.92 2.17 2.83 3.33	6.6	2.8 4.1 4.1 5.2	0.0003	110
	4	all	Co-N/O,5 Co-N,1 Co-O,1 Co-C,5 Co-C,3	1.93 2.17 2.74 2.90 3.32	7.6	2.9 4.8 2.3 6.4 7.2	0.0002	1294
	5	all	Co-N/O,5 Co-N,1 Co-O,1 Co-C,5 Co-C,3 Co-Co,1	1.93 2.17 2.75 2.89 3.31 3.82	7.3	3.0 6.3 2.0 9.8 0.5 4.6	0.0001	40
superoxido	6	I	Co-N,6	1.90	2.4	3.6	0.0015	482
	7	I	Co-N/O,5 Co-N,1	1.91 2.11	5.5	1.8 2.1	0.0005	2634
	8	I,II	Co-N,6 Co-C,5 Co-C,3	1.90 2.78 3.36	2.4	3.7 2.8 18.4	0.0029	510
	9	I,II	Co-N,6 Co-O,1 Co-C,5 Co-C,3	1.91 2.70 2.90 3.28	5.8	4.0 6.9 1.5 14.7	0.0003	131
	10	I,II	Co-N,6 Co-O,0.5 Co-C,5 Co-C,3	1.91 2.69 2.87 3.32	5.5	4.0 9.6 1.6 25.1	0.0002	92
	11	all	Co-N,6 Co-C,5 Co-C,3 Co-Co,1	1.90 2.79 3.32 3.77	2.7	3.7 2.8 6.2 0.3	0.0025	272
	12	all	Co-N,6 Co-O,1 Co-C,5 Co-C,3 Co-Co,1	1.91 2.70 2.89 3.32 3.78	5.7	3.9 6.7 1.2 25.4 2.2	0.0006	98
	13	all	Co-N,6 Co-O,0.5 Co-C,5 Co-C,3 Co-Co,1	1.91 2.69 2.87 3.32 3.78	5.6	4.0 9.4 1.1 26.1 2.4	0.0005	80
	14	all	Co-N,6 Co-O,0.5 Co-C,5 Co-C,3 Co-Co,1 Co-O,1	1.92 2.70 2.89 3.29 3.78 3.95	6.0	4.2 9.6 4.4 9.2 3.7 10.6	0.0001	41

- *Peak I refers to the region between 1.2-2.05 Å, peak I,II to 1.2-3.0 Å and all to 1.2-3.8 Å

DFT M06-L and M11-L Studied Reactions with the Corresponding Energies

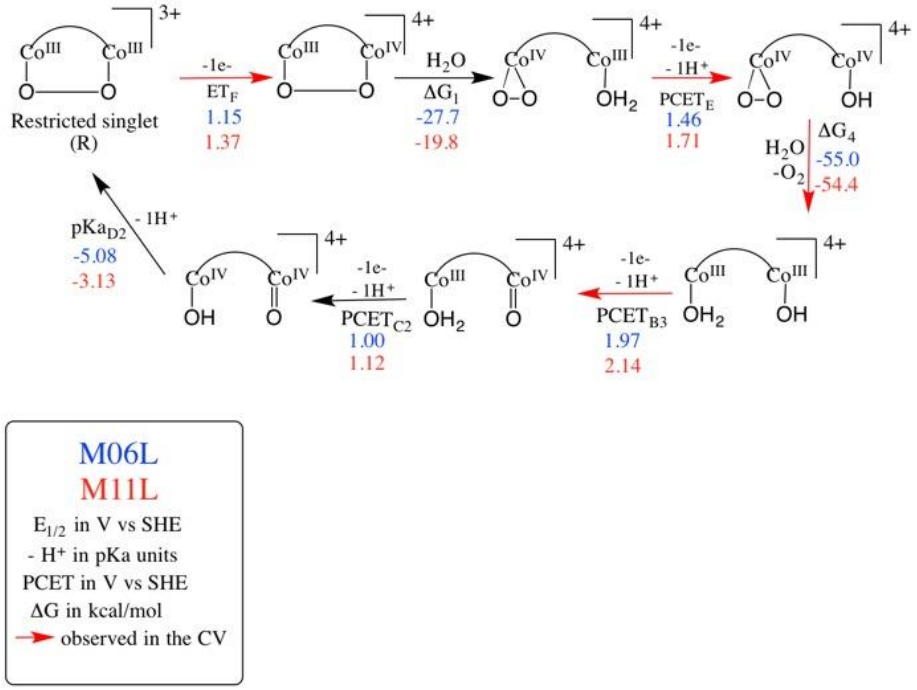

Figure S9. Summary Reaction scheme at pH=2. At pH=8 $PCET_E$(M06-L/M11-L)=1.10/1.35, $PCET_{B3}$(M06-L/M11-L)=1.61/1.98, $PCET_{C2}$(M06-L/M11-L)=0.65/0.76.

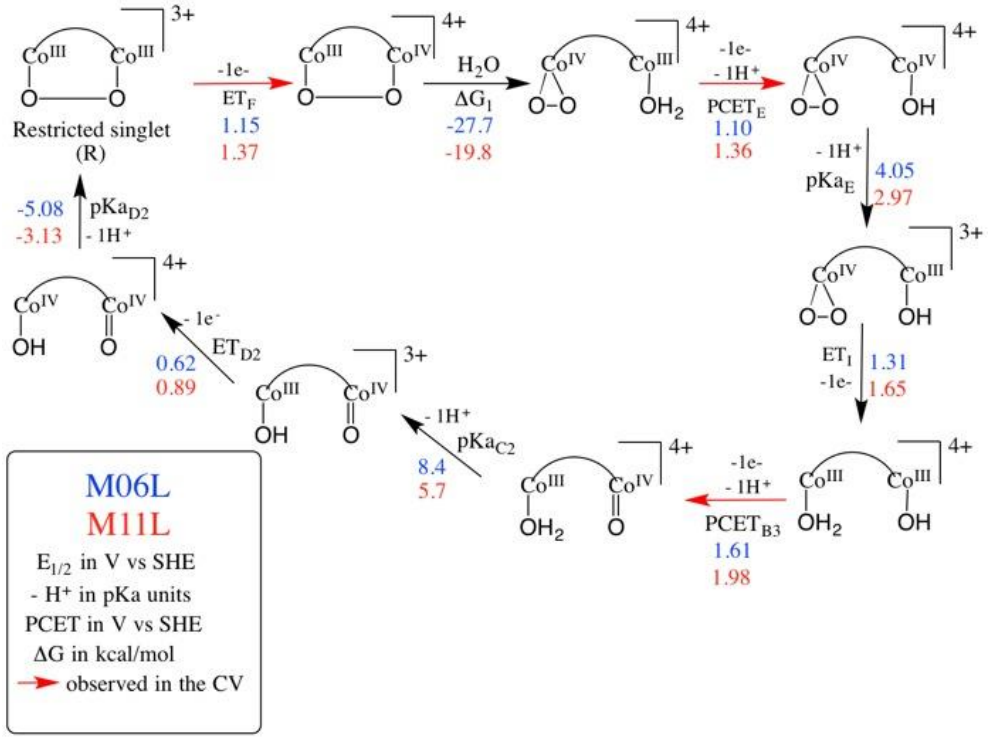

Figure S10. Summary Reaction scheme at pH 8.

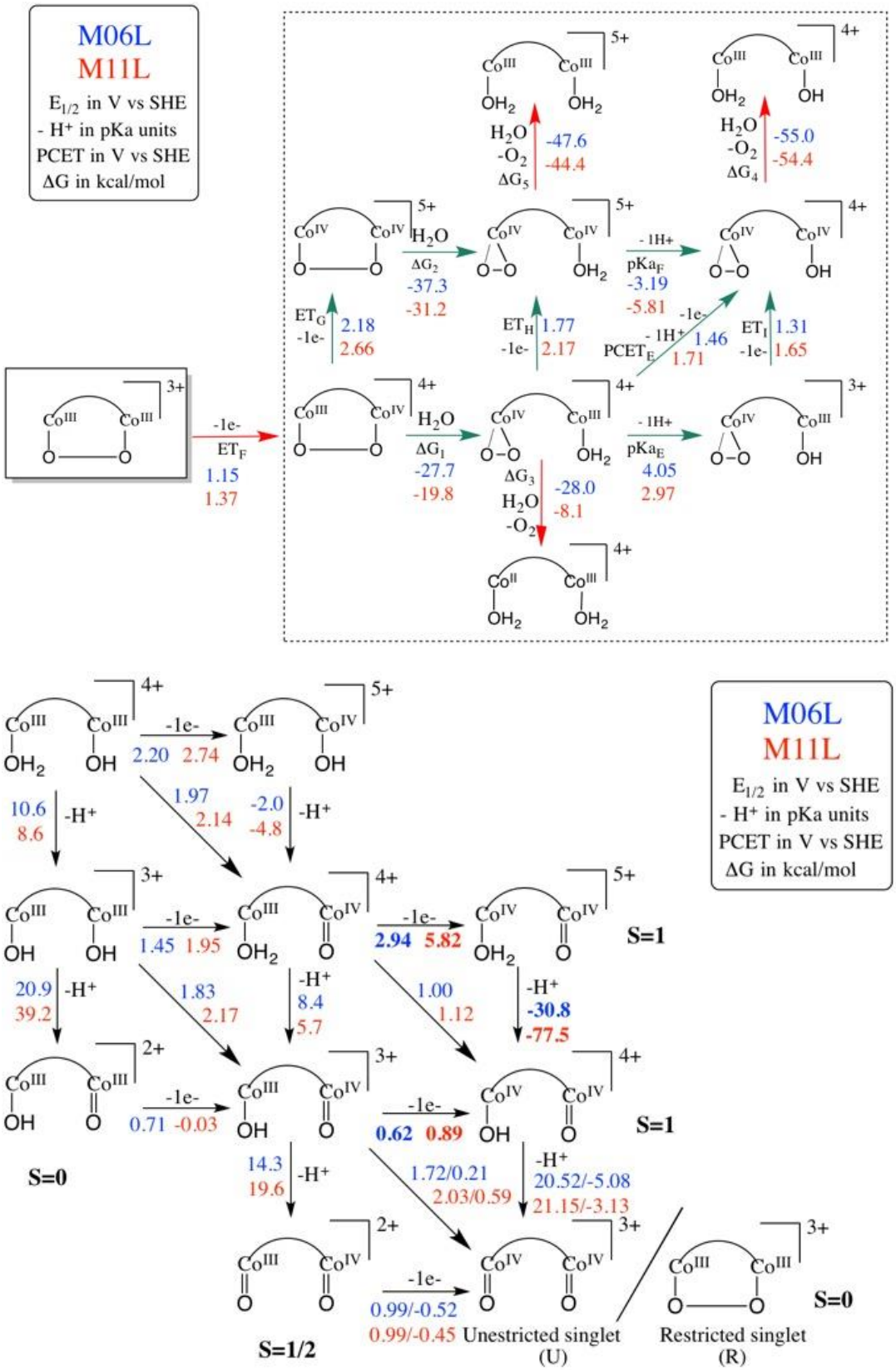

Figure S11. All relevant speciation studied at pH 2.

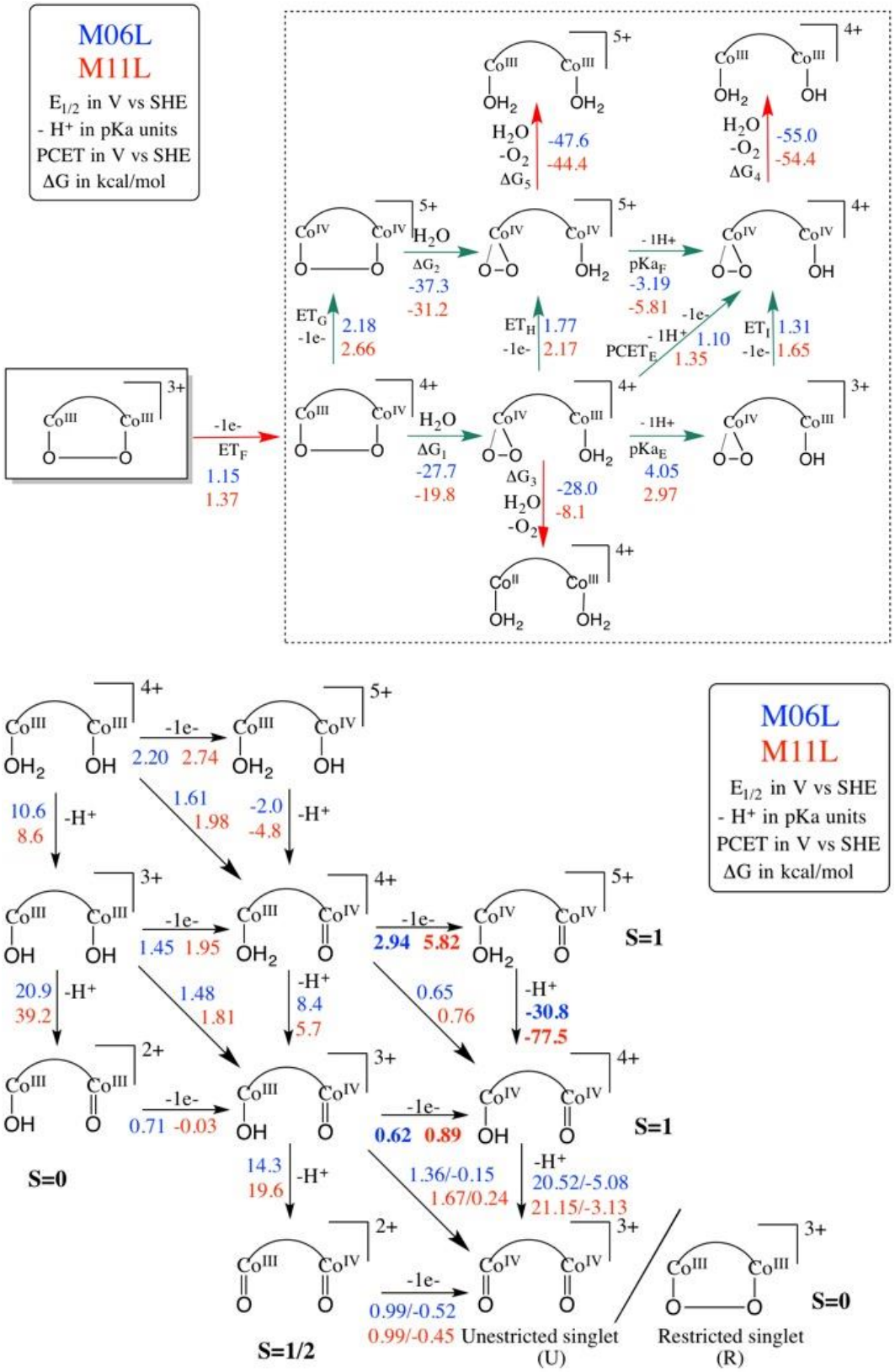

Figure S12. All relevant speciation studied at pH 8.

Compiled Energy Information with Corresponding Labeling Graphs

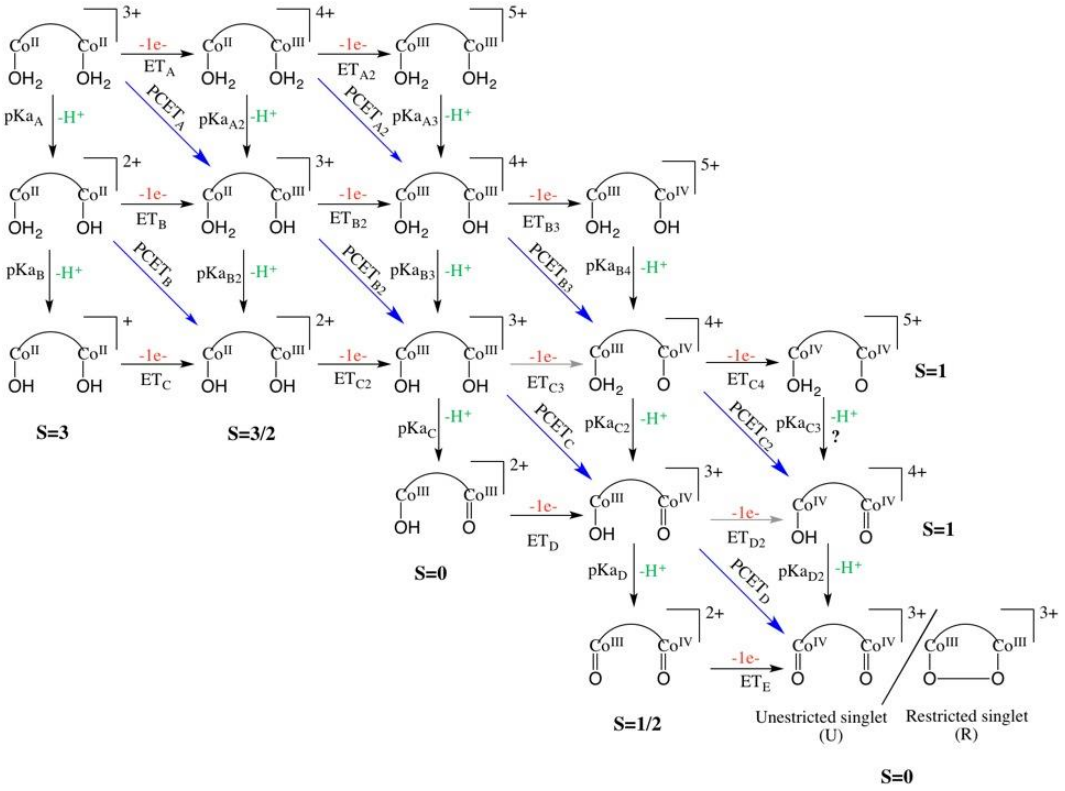

Figure S13. Labeling scheme of the species and ET, PT and PCET steps involved in the Pourbaix diagram.

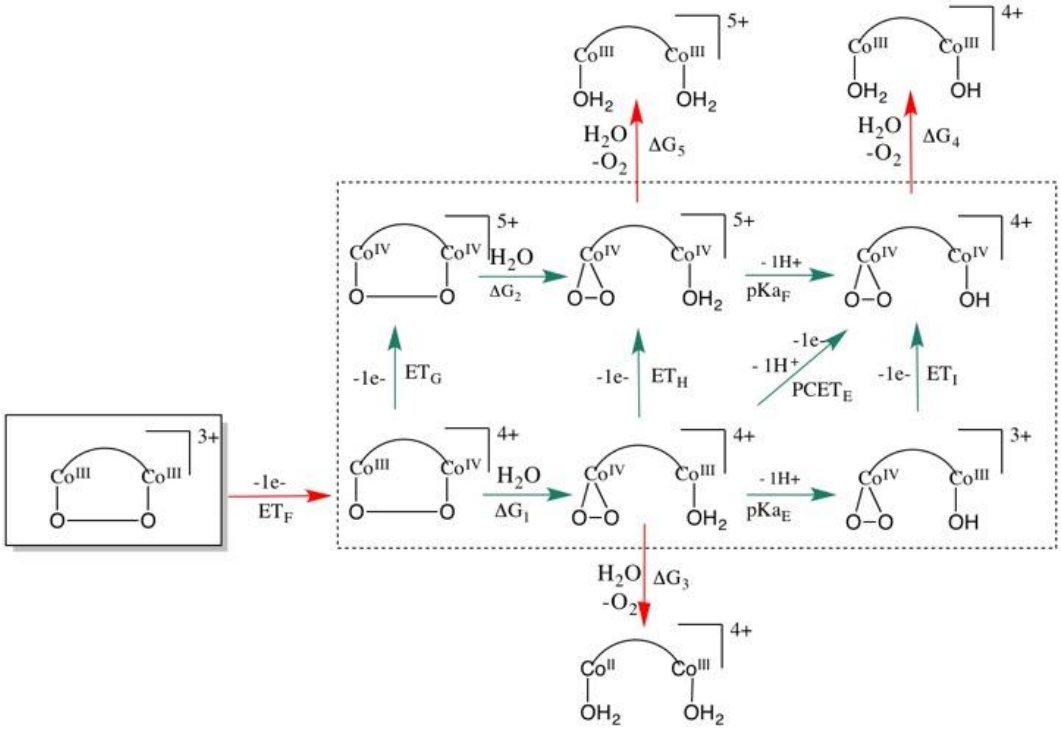

Figure S14. Labeling scheme of the species and ET, PT, PCET and substitution steps involved in the oxygen evolution process.

Table S3. Reduction potentials and ΔG values for the different Electron Transfer (ET) steps at the different levels of theory tested.

	M06-L		M06-L-Gcorr[a]		M11-L-Ecorr[b]	
ET	ΔGred (kcal/mol)	Ered vs SHE (V)	ΔGred (kcal/mol)	Ered vs SHE (V)	ΔGred (kcal/mol)	Ered vs SHE (V)
ET_A	-108.85	**0.44**	-109.21	**0.46**	-97.96	**-0.03**
ET_{A2}	-120.74	**0.96**	-119.79	**0.91**	-112.35	**0.59**
ET_B	-97.60	**-0.05**	-96.53	**-0.09**	-83.80	**-0.65**
ET_{B2}	-107.75	**0.39**	-107.06	**0.36**	-94.18	**-0.20**
ET_{B3}	-149.80	**2.22**	-149.50	**2.20**	-161.88	**2.74**
ET_C	-87.38	**-0.49**	-90.05	**-0.38**	-78.87	**-0.86**
ET_{C2}	-96.12	**-0.11**	-95.25	**-0.15**	-83.76	**-0.65**
ET_{C3}	-132.17	**1.45**	-132.24	**1.45**	-143.58	**1.95**
ET_{C4}	-150.75	**2.26**	-166.51	**2.94**	-232.80	**5.82**
ET_D	-116.03	**0.75**	-115.17	**0.71**	-98.03	**-0.03**
ET_{D2}	-115.00	**0.71**	-113.08	**0.62**	-119.32	**0.89**
ET_E (u)	-124.79	**1.13**	-121.51	**0.99**	-121.46	**0.99**
ET_E (r)	-87.84	**-0.47**	-86.62	**-0.52**	-88.37	**-0.45**
ET_F	-125.66	**1.17**	-125.15	**1.15**	-130.27	**1.37**
ET_G	-149.09	**2.19**	-149.01	**2.18**	-160.07	**2.66**
ET_H	-139.39	**1.76**	-139.41	**1.77**	-148.69	**2.17**
ET_I	-129.00	**1.31**	-128.87	**1.31**	-136.72	**1.65**

[a]M06-L/6-31G(d) free energy contributions (corrected for frequencies below 50 cm^{-1}) added to single-point M06-L/6-311+G(2df,p).

[b] M06-L/6-31G(d) free energy contributions (corrected for frequencies below 50 cm^{-1}) added to single-point M11-L/6-311+G(2df,p).

Table S4.pKa's and ΔG of proton dissociation values for the different steps at the different levels of theory tested.

	M06-L		**M06-L-Gcorr[a]**		**M11-L-Ecorr[b]**	
pKa	ΔGdissoc (kcal/mol)	pKa	ΔGdissoc (kcal/mol)	pKa	ΔGdissoc (kcal/mol)	pKa
pKa_A	12.27	**9.00**	13.60	**9.98**	14.46	**10.61**
pKa_{A2}	1.01	**0.74**	0.92	**0.68**	0.30	**0.22**
pKa_{A3}	-11.98	**-8.79**	-11.80	**-8.66**	-17.87	**-13.11**
pKa_B	36.38	**26.69**	32.79	**24.06**	27.09	**19.88**
pKa_{B2}	26.17	**19.20**	26.31	**19.31**	22.16	**16.26**
pKa_{B3}	14.55	**10.67**	14.50	**10.64**	11.74	**8.61**
pKa_{B4}	-3.08	**-2.26**	-2.76	**-2.02**	-6.56	**-4.81**
pKa_C	27.49	**20.17**	28.47	**20.89**	53.40	**39.18**
pKa_{C2}	11.35	**8.33**	11.40	**8.37**	7.86	**5.76**
pKa_{C3}	-24.39	**-17.90**	-42.03	**-30.83**	-105.63	**-77.50**
pKa_D	18.16	**13.33**	19.54	**14.34**	26.69	**19.58**
pKa_{D2}(u)	27.96	**20.51**	27.97	**20.52**	28.83	**21.15**
pKa_{D2}(r)	-8.99	**-6.60**	-6.92	**-5.08**	-4.27	**-3.13**
pKa_E	5.94	**4.36**	6.18	**4.53**	4.05	**2.97**
pKa_F	-4.45	**-3.26**	-4.35	**-3.19**	-7.92	**-5.81**

[a]M06-L/6-31G(d) free energy contributions (corrected for frequencies below 50 cm^{-1}) added to single-point M06-L/6-311+G(2df,p).

[b] M06-L/6-31G(d) free energy contributions (corrected for frequencies below 50 cm^{-1}) added to single-point M11-L/6-311+G(2df,p).

Chapter 8

Table S5. Reduction potentials and ΔG values for the different Proton Coupled Electron Transfer (PCET) steps at pH=2 at the different levels of theory tested

	M06-L		**M06-L-Gcorr[a]**		**M11-L-Ecorr[b]**	
PCET (pH=2)	ΔG_{PCET}red (kcal/mol)	Ered vs SHE (V)	ΔG_{PCET}red (kcal/mol)	Ered vs SHE (V)	ΔG_{PCET}red (kcal/mol)	Ered vs SHE(V)
$PCET_A$	-107.14	**0.37**	-107.41	**0.38**	-95.54	**-0.14**
$PCET_{A2}$	-106.04	**0.32**	-105.26	**0.28**	-91.76	**-0.30**
$PCET_B$	-121.05	**0.97**	-120.12	**0.93**	-103.24	**0.20**
$PCET_{B2}$	-119.57	**0.91**	-118.84	**0.87**	-103.20	**0.19**
$PCET_{B3}$	-144.00	**1.96**	-144.02	**1.97**	-152.59	**2.14**
$PCET_{B4}$	-144.95	**2.01**	-161.03	**2.70**	-223.52	**5.41**
$PCET_C$	-140.80	**1.83**	-140.93	**1.83**	-148.71	**2.17**
$PCET_{C2}$	-123.64	**1.08**	-121.76	**1.00**	-124.46	**1.12**
$PCET_D$(u)	-140.24	**1.80**	-138.33	**1.72**	-145.43	**2.03**
$PCET_D$(r)	-103.29	**0.20**	-103.44	**0.21**	-112.34	**0.59**
$PCET_E$	-132.22	**1.45**	-132.33	**1.46**	-138.05	**1.71**

[a]M06-L/6-31G(d) free energy contributions (corrected for frequencies below 50 cm^{-1}) added to single-point M06-L/6-311+G(2df,p).

[b] M06-L/6-31G(d) free energy contributions (corrected for frequencies below 50 cm^{-1}) added to single-point M11-L/6-311+G(2df,p).

Chapter 8

Table S6. Reduction potentials and ΔG values for the different Proton Coupled Electron Transfer (PCET) steps at pH=8 at the different levels of theory tested

	M06-L		**M06-L-Gcorr[a]**		**M11-L-Ecorr[b]**	
PCET (pH=8)	ΔG_{PCET}red (kcal/mol)	Ered vs SHE (V)	ΔG_{PCET}red (kcal/mol)	Ered vs SHE (V)	ΔG_{PCET}red (kcal/mol)	Ered vs SHE (V)
$PCET_A$	-98.98	**0.01**	-99.25	**0.02**	-87.38	**-0.49**
$PCET_{A2}$	-97.88	**-0.04**	-97.10	**-0.07**	-83.60	**-0.65**
$PCET_B$	-112.89	**0.62**	-111.96	**0.57**	-95.08	**-0.16**
$PCET_{B2}$	-111.41	**0.55**	-110.68	**0.52**	-95.04	**-0.16**
$PCET_{B3}$	-135.84	**1.61**	-135.86	**1.61**	-144.43	**1.98**
$PCET_{B4}$	-136.79	**1.65**	-152.87	**2.35**	-215.36	**5.06**
$PCET_C$	-132.64	**1.47**	-132.77	**1.48**	-140.55	**1.81**
$PCET_{C2}$	-115.48	**0.73**	-113.60	**0.65**	-116.30	**0.76**
$PCET_D$(u)	-132.08	**1.45**	-130.17	**1.36**	-137.27	**1.67**
$PCET_D$(r)	-95.13	**-0.15**	-95.28	**-0.15**	-104.18	**0.24**
$PCET_E$	-124.06	**1.10**	-124.17	**1.10**	-129.89	**1.35**

[a] M06-L/6-31G(d) free energy contributions (corrected for frequencies below 50 cm^{-1}) added to single-point M06-L/6-311+G(2df,p).[b] M06-L/6-31G(d) free energy contributions (corrected for frequencies below 50 cm^{-1}) added to single-point M11-L/6-311+G(2df,p).

VIII

Table S7. ΔG values for the different water insertion reactions at the different levels of theory tested.

	M06-L	**M06-L-Gcorr[a]**	**M11-L-Ecorr[b]**
Substitution Reactions	ΔGsubs (kcal/mol)	ΔGsubs (kcal/mol)	ΔGsubs (kcal/mol)
ΔG_1	-27.87	-27.73	-19.85
ΔG_2	-37.57	-37.34	-31.24
ΔG_3	-28.88	-27.95	-8.11
ΔG_4	-55.06	-55.02	-54.40
ΔG_5	-47.52	-47.57	-44.43

[a] M06-L/6-31G(d) free energy contributions (corrected for frequencies below 50 cm^{-1}) added to single-point M06-L/6-311+G(2df,p). [b] M06-L/6-31G(d) free energy contributions (corrected for frequencies below 50 cm^{-1}) added to single-point M11-L/6-311+G(2df,p).

Table S8. ΔG= activation energy values for the transition states considered at the different levels of theory tested.

	M06-L-Gcorr[a]	**M11-L-Ecorr[b]**
Substitution Reactions	ΔGsubs (kcal/mol)	ΔGsubs (kcal/mol)
ΔG_{TSA}[c]	-13.0	-8.4
ΔG_{TSB}[d]	-1.1	41.1
ΔG_{TSC}[e]	-16.1	46.6

[a] M06-L/6-31G(d) free energy contributions (corrected for frequencies below 50 cm^{-1} for all species but TS) added to single-point M06-L/6-311+G(2df,p).

[b] M06-L/6-31G(d) free energy contributions (corrected for frequencies below 50 cm^{-1} for all species but TS) added to single-point M11-L/6-311+G(2df,p).

[c] TSA: $^{III}Co\text{-}OO\text{-}Co^{IV} + H_2O \rightarrow OO\text{-}Co^{III}\text{-}Co^{IV}\text{-}OH_2$

[d] TSB: $OO\text{-}Co^{IV}\text{-}Co^{IV}\text{-}OH + H_2O \rightarrow H_2O\text{-}Co^{III}\text{-}Co^{III}\text{-}OH + O_2$

[e] TSC: $O\text{-}Co^{IV}\text{-}Co^{III}\text{-}O \rightarrow Co^{IV}\text{-}OO\text{-}Co^{III}$

Chapter 8

M06-L- ENERGIES

Table S9. Compilation of the, electronic energy, the as computed Gibbs free energy, the Gibbs free energy after removing the contribution of the frequencies that are under 50 cm-1 and the Composite Gibbs Free energy considering water as a solvent. All calculated with M06-L on M06-L optimized geometries. <*S*2> represents the spin operator expectation value.

Compound	Formal. Ox. St.	spin	$<S^2>$	E-gas-M06-L (Hartree)	G-gas-M06-L (Hartree)	G-gas corr-M06-L (Hartree)	$<S^2>$	E-sol-M06-L (Hartree)	G-sol-M06-L (Hartree)
H2O-CoCo-H2O	**II,II**	**septet**	12.02	-2,648.6602	-2,648.0345	-2,648.0309	12.0	-2,649.7041	-2,649.0778
H2O-CoCo-H2O	**II,III**	**Q**	3.76	-2,648.1882	-2,647.5557	-2,647.5515	3.76	-2,649.5375	-2,648.9044
H2O-CoCo-H2O	**III,III**	**s**	0.	-2,647.6108	-2,646.9688	-2,646.9661	0.	-2,649.3546	-2,648.7122
OH-CoCo-H2O	**II,II**	**sept**	12.03	-2,648.4108	-2,647.7993	-2,647.7936	12.0	-2,649.2396	-2,648.6288
OH-CoCo-H2O	**III-II**	**q**	3.76	-2,648.0590	-2,647.4357	-2,647.5515	3.76	-2,649.0959	-2,648.4722
OH-CoCo-H2O	**III,III**	**s**	0.	-2,647.5867	-2,646.9585	-2,646.9555	0.	-2,648.9292	-2,648.3000
OH-CoCo-H2O	**III,IV**	**d**	0.75	-2,646.9652	-2,646.3373	-2,646.3348	0.76	-2,648.6902	-2,648.0622
OH-CoCo-OH	**II,II**	**sept**	12.08	-2,648.0155	-2,647.4149	-2,647.4114	12.0	-2,648.7435	-2,648.1399
OH-CoCo-OH	**III,II**	**q**	3.77	-2,647.7641	-2,647.1554	-2,647.1512	3.77	-2,648.6088	-2,648.0000
OH-CoCo-OH	**III,III**	**s**	0.	-2,647.4236	-2,646.8041	-2,646.8012	0.	-2,648.4665	-2,647.8477

O-CoCo-OH2	**III,III**	**q**	6.02	-2,647.4059	-2,646.7941	-2,646.7905	6.02	-2,648.4392	-2,647.827
OH-CoCo-OH	**IV,III**	**d**	0.76	-2,646.9196	-2,646.3033	-2,646.3004	0.76	-2,648.2501	-2,647.633
O-CoCo-OH2	**IV,III**	**d**	0.76	-2,646.9177	-2,646.2998	-2,646.2968	0.76	-2,648.2543	-2,647.636
OH-CoCo-OH	**IV,IV**	**t**	2.01	-2,646.2927	-2,645.6801	-2,645.6801		-2,648.0087	-2,647.396
O-CoCo-OH	**III,III (II-OH /IV=O)**	**q**	6.03	-2,647.1355	-2,646.5370	-2,646.5326	6.03	-2,647.9710	-2,647.372
O-CoCo-OH	**IV,III**	**d**	0.76	-2,646.7577	-2,646.1513	-2,646.1482	0.76	-2,647.7940	-2,647.187
O-CoCo-OH	**IV,IV**	**s**	0.	-2,646.2809	-2,645.6698	-2,645.6698	0.	-2,647.6154	-2,647.004
O-CoCo-O	**III,IV**	**d**	1.20	-2,646.4955	-2,645.9080	-2,645.9027	0.82	-2,647.3154	-2,646.727
O-CoCo-O	**IV,IV**	**U**	0.87	-2,646.0899	-2,645.4935	-2,645.4935	0.85	-2,647.1254	-2,646.529
CoCo-peroxo	**III,III**	**s**	0.	-2,646.1566	-2,645.5585	-2,645.5553	0.	-2,647.1860	-2,646.587
CoCo-peroxo	**IV,III**	**d**	0.80	-2,645.6626	-2,645.0636	-2,645.0611	0.80	-2,646.9867	-2,646.387
CoCo-peroxo	**IV,IV**	**t**	2.06	-2,645.0327	-2,644.4378	-2,644.4355	2.06	-2,646.7450	-2,646.150

CoCo-OO-OH2	**IV,IV**	t	2.04	-2,721.4752	-2,720.8587	-2,720.8560	2.02	-2,723.2258	-2,722.609
CoCo-OO-OH	**IV,IV**	**t**	2.02	-2,721.4409	-2,720.8339	-2,645.6545	2.02	-2,722.7927	-2,722.185
CoCo-OO-OH2	**III,IV**	**d**	0.81	-2,722.0899	-2,721.4688	-2,721.4661	0.79	-2,723.4525	-2,722.831
CoCo-OO-OH	**III,IV**	**d**	0.93	-2,721.9395	-2,721.3318	-2,646.1482	0.85	-2,722.9989	-2,722.391
TSC: Co2-O2-association	**III,IV**	**d**	0.79	-2645.58513	-2644.98814	-2644.987408	0.79	-2646.910308	-2646.31257
	III,IV	**q**	3.75	-2645.58119	-2644.98808	-2644.986626	3.75	-2646.902728	-2646.30815
	III,IV	**Sext**	8.75	-2645.56982	-2644.98207	-2644.979357	8.75	-2646.886541	-2646.29607
TSA: Co2-O2-1stsubstitution	**IV,III**	**d**	0.76	-2722.063983	-2721.446433	-2721.446433	0,76	-2723.42272	-2722.805169
TSB:Co2-O2-liberation	**IV,IV**	**s**	0.00	-2721.38924	-2720.78020	-2720.778992	0.00	-2722.75527	-2722.14502
	IV,IV	**t**	2.00	-2721.42829	-2720.82111	-2720.820103	2.00	-2722.791738	-2722.18354

Chapter 8

Table S10. Compilation of the Composite Gibbs Free energies calculated with M06-L considering water as a solvent, at the gas phase concentration and then 1 Molar concentration. The latter corresponds to the standard state for the computation of standard potentials and activation energies.

Compound	Formal. Ox. St.	spin	G-sol-M06-L(Kcal/mol)	G-sol-M06-L*-1M (kcal/mol)
H2O-CoCo-H2O	**II,II**	**sept**	-1,662,321.7880	-1662319.90
H2O-CoCo-H2O	**II,III**	**q**	-1,662,212.9370	-1662211.05
H2O-CoCo-H2O	**III,III**	**s**	-1,662,092.1929	-1662090.30
OH-CoCo-H2O	**II,II**	**sept**	-1,662,039.2417	-1662037.35
OH-CoCo-H2O	**III-II**	**q**	-1,661,941.6461	-1661939.76
OH-CoCo-H2O	**III,III**	**s**	-1,661,833.8974	-1661832.01
OH-CoCo-H2O	**III,IV**	**d**	-1,661,684.1005	-1661682.21
OH-CoCo-OH	**II,II**	**sept**	-1,661,732.5779	-1661730.69
OH-CoCo-OH	**III,II**	**q**	-1,661,645.1940	-1661643.30
OH-CoCo-OH	**III,III**	**s**	-1,661,549.0716	-1661547.18
O-CoCo-OH2	**III,III**	**q**	-1,661,536.7315	-1661534.84
OH-CoCo-OH	**IV,III**	**d**	-1,661,415.3123	-1661413.42
O-CoCo-OH2	**IV,III**	**d**	-1,661,416.9025	-1661415.01
OH-CoCo-OH	**IV,IV**	**t**	-1,661,266.1511	-1661264.26
O-CoCo- OH	**III,III (II-OH/IV=O)**	**q**	-1,661,251.3029	-1661249.41
O-CoCo- OH	**IV,III**	**d**	-1,661,135.2682	-1661133.38
O-CoCo- OH	**IV,IV**	**s**	-1,661,020.2664	-1661018.38

O-CoCo-O	**III,IV**	**d**	-1,660,846.8251	-1660844.94
O-CoCo-O	**IV,IV**	**U**	-1,660,722.0307	-1660720.14
CoCo-peroxo	**III,III**	**s**	-1,660,758.9803	-1660757.09
CoCo-peroxo	**IV,III**	**d**	-1,660,633.3167	-1660631.43
CoCo-peroxo	**IV,IV**	**t**	-1,660,484.2253	-1660482.34
CoCo-OO-OH2	**IV,IV**	t	-1,708,463.1006	-1708461.21
CoCo-OO-OH	**IV,IV**	**t**	-1,708,197.2670	-1708195.38
CoCo-OO-OH2	**III,IV**	**d**	-1,708,602.4896	-1708600.60
CoCo-OO-OH	**III,IV**	**d**	-1,708,326.2677	-1708324.38
TSC: Co2-O2-association	**III,IV**	**d**	-1660584.96	-1,660,583.07
	III,IV	**q**	-1660582.184	-1,660,580.30
	III,IV	**Sext**	-1660574.605	-1,660,572.72
TSA: Co2-O2-1stsubstitution	**III,IV**	**d**	-1,708,586.0261	-1708584.14
TSC:Co2-O2-liberation	**IV,IV**	**s**	-1708170.5	-1,708,168.61
	IV,IV	**t**	-1708194.675	-1,708,192.79

Chapter 8

Table S11. Compilation of the, electronic energy, the Gibbs free energy corrected by removing the contributions of the frequencies under 50, the electronic energy at the M11-L level of theory considering the solvation with water on the M06-L optimized geometry, the resulting composite Gibbs free energy. All calculated with on M06-L optimized geometries. $<S^2>$ represents the spin operator expectation value.

Compound	Formal. Ox. St.	spin	$<S^2>$	E-gas-M06-L (Hartree)	G-gas corr-M06-L (Hartree)	$<S^2>$	E-sol-M11-L (Hartree)	G-sol-M11-L (Hartree)
H2O-CoCo-H2O	II,II	sept	12.02	-2,648.6602	-2,648.0309	12.03	-2649.78	-2,649.1547
H2O-CoCo-H2O	II,III	q	3.76	-2,648.1882	-2,647.5515	3.76	-2649.64	-2,648.9986
H2O-CoCo-H2O	III,III	s	0.	-2,647.6108	-2,646.9661	0.	-2649.46	-2,648.8195
OH-CoCo-H2O	II,II	sept	12.03	-2,648.4108	-2,647.7936	12.03	-2649.32	-2,648.7009
OH-CoCo-H2O	III-II	q	3.76	-2,648.0590	-2,647.5515	3.76	-2649.19	-2,648.5674
OH-CoCo-H2O	III,III	s	0.	-2,647.5867	-2,646.9555	0.	-2649.05	-2,648.4173
OH-CoCo-H2O	III,IV	d	0.75	-2,646.9652	-2,646.3348	0.75	-2,648.78	-2,648.1593
OH-CoCo-OH	II,II	sept	12.08	-2,648.0155	-2,647.4114	12.04	-2,648.831	-2,648.2270
OH-CoCo-OH	III,II	q	3.77	-2,647.7641	-2,647.1512	3.77	-2648.71	-2,648.1013
OH-CoCo-OH	III,III	s	0.	-2,647.4236	-2,646.8012	0.	-2648.590	-2,647.9679
O-CoCo-OH2	III,III	q	6.02	-2,647.4059	-2,646.7905	6.01	-2,648.517	-2,647.9019

OH-CoCo-OH	**IV,III**	**d**	0.76	-2,646.9196	-2,646.3004	0.75	-2,648.350	-2,647.7310
O-CoCo-OH2	**IV,III**	**d**	0.76	-2,646.9177	-2,646.2968	0.75	-2,648.359	-2,647.7391
OH-CoCo-OH	**IV,IV**	**t**	2.01	-2,646.2927	-2,645.6801	2.01	-2,648.008	-2,647.3930
O-CoCo-OH	**III,III (II-OH/IV=O)**	**q**	6.03	-2,647.1355	-2,646.5326	6.02	-2,648.054	-2,647.4520
O-CoCo-OH	**IV,III**	**d**	0.76	-2,646.7577	-2,646.1482	0.76	-2,647.905	-2,647.2958
O-CoCo-OH	**IV,IV**	**s**	0.	-2,646.2809	-2,645.6698	0.	-2647.72	-2,647.1057
O-CoCo-O	**III,IV**	**d**	1.20	-2,646.4955	-2,645.9027	0.81	-2647.42	-2,646.8226
O-CoCo-O	**IV,IV**	**U**	0.87	-2,646.0899	-2,645.4935	0.85	-2,647.225	-2,646.6290
CoCo-peroxo	**III,III**	**s**	0.	-2,646.1566	-2,645.5553	0.	-2647.28	-2,646.6818
CoCo-peroxo	**IV,III**	**d**	0.80	-2,645.6626	-2,645.0611	0.79	-2,647.075	-2,646.4742
CoCo-peroxo	**IV,IV**	**t**	2.06	-2,645.0327	-2,644.4355	2.06	-2,646.816	-2,646.2191
CoCo-OO-OH2	**IV,IV**	t	2.04	-2,721.4752	-2,720.8560	2.03	-2,723.287	-2,722.6682
CoCo-OO-OH	**IV,IV**	**t**	2.02	-2,721.4409	-2,645.6545	2.02	-2,722.860	-2,722.2501
CoCo-OO-OH2	**III,IV**	**d**	0.81	-2,722.0899	-2,721.4661	0.79	-2,723.528	-2,722.9051
CoCo-OO-OH	**III,IV**	**d**	0.93	-2,721.9395	-2,646.1482	0.85	-2,723.078	-2,722.4680
TS1: Co2-O2-association	**III,IV**	**d**	0.79	-2645.58513	-2644.98740	0.79	-2646.9103	-2646.31257

	III,IV	**q**	3.75	-2645.58119	-2644.98662	3.75	-2646.9027	-2646.30815
	III,IV	**Sext**	8.75	-2645.56982	-2644.97935	8.75	-2646.8865	-2646.29607
TSA: Co2-O2-1st substitution	**IV,III**	**d**	0.76	-2722.063983	-2721.446433	0,76	-2723.504412	-2722.886862
TS4:Co2-O2-liberation	**IV,IV**	**s**	0.00	-2721.38924	-2720.77899	0.00	-2722.7552	-2722.14502
	IV,IV	**t**	2.00	-2721.42829	-2720.82010	2.00	-2722.7917	-2722.18354

Table S12. Compilation of the Composite Gibbs Free energies calculated with M11-L, considering water as a solvent, at the gas phase concentration and then 1 Molar concentration. The latter corresponds to the standard state for the computation of standard potentials and activation energies.

Compound	Formal. Ox. St.	spin	Gsol-M11-L(Kcal/mol)	Gsol-M11-L*-1M (kcal/mol)
H2O-CoCo-H2O	**II,II**	**sept**	-1,662,369.6504	-1662367.76
H2O-CoCo-H2O	**II,III**	**q**	-1,662,271.6872	-1662269.80
H2O-CoCo-H2O	**III,III**	**s**	-1,662,159.3341	-1662157.44
OH-CoCo-H2O	**II,II**	**sept**	-1,662,084.9134	-1662083.02
OH-CoCo-H2O	**III-II**	**q**	-1,662,001.1088	-1661999.22
OH-CoCo-H2O	**III,III**	**s**	-1,661,906.9290	-1661905.04
OH-CoCo-H2O	**III,IV**	**d**	-1,661,745.0530	-1661743.16
OH-CoCo-OH	**II,II**	**sept**	-1,661,787.5409	-1661785.65
OH-CoCo-OH	**III,II**	**q**	-1,661,708.6707	-1661706.78
OH-CoCo-OH	**III,III**	**s**	-1,661,624.9124	-1661623.02
O-CoCo- OH2	**III,III**	**q**	-1,661,583.5079	-1661581.62
OH-CoCo-OH	**IV,III**	**d**	-1,661,476.2458	-1661474.36
O-CoCo-OH2	**IV,III**	**d**	-1,661,481.3348	-1661479.44
OH-CoCo-OH	**IV,IV**	**t**	-1,661,264.1898	-1661246.64
O-CoCo- OH	**III,III (II-OH/IV=O)**	**q**	-1,661,301.2281	-1661299.34
O-CoCo- OH	**IV,III**	**d**	-1,661,203.1996	-1661201.31
O-CoCo- OH	**IV,IV**	**s**	-1,661,083.8774	-1661081.99
O-CoCo-O	**III,IV**	**d**	-1,660,906.2304	-1660904.34
O-CoCo-O	**IV,IV**	**U**	-1,660,784.7697	-1660782.88
CoCo-peroxo	**III,III**	**s**	-1,660,817.8643	-1660815.97

CoCo-peroxo	**IV,III**	**d**	-1,660,687.5955	-1660685.71
CoCo-peroxo	**IV,IV**	**t**	-1,660,527.5217	-1660525.63
CoCo-OO-OH2	**IV,IV**	t	-1,708,500.0633	-1708498.17
CoCo-OO-OH	**IV,IV**	**t**	-1,708,237.7022	-1708235.81
CoCo-OO-OH2	**III,IV**	**d**	-1,708,648.7484	-1708646.86
CoCo-OO-OH	**III,IV**	**d**	-1,708,374.4199	-1708372.53
TS1: Co2-O2-association	**III,IV**	**d**	-1660579.668	-1,660,577.78
	III,IV	**q**	-1660576.891	-1,660,575.00
	III,IV	**Sext**	-1660569.312	-1,660,567.42
TSA: Co2-O2-1stsubstitution	**III,IV**	**d**	-1,708,637.2890	-1708635.40
TS4:Co2-O2-liberation	**IV,IV**	**s**	-1708165.056	-1,708,163.17
	IV,IV	**t**	-1708189.231	-1,708,187.34

References

(1) Fukuzumi, S.; Mandal, S.; Mase, K.; Ohkubo, K.; Park, H.; Benet-Buchholz, J.; Nam, W.; Llobet, A. *J. Am. Chem. Soc.* **2012**, *134*, 9906.
(2) Ravel, B.; Newville, M. *J. Synchrotron Radiat.* **2005**, *12*, 537.
(3) Rehr, J. J.; Albers, R. C. *Rev. Mod. Phys.* **2000**, *72*, 621.
(4) Koningsberger, D.; Prins, R. **1988**.
(5) Zhao, Y.; Truhlar, D. G. *J. Chem. Phys.* **2006**, *125*, 194101.
(6) Zhao, Y.; Truhlar, D. G. *Acc. Chem. Res.* **2008**, *41*, 157.
(7) Zhao, Y.; Truhlar, D. G. *J. Chem. Theory Comput.* **2008**, *4*, 1849.
(8) Andrae, D.; Haeussermann, U.; Dolg, M.; Stoll, H.; Preuss, H. *Theor. Chim. Acta* **1990**, *77*, 123.
(9) Hehre, W.; Radom, L.; Schleyer, P.; Wiley: New York: 1986.
(10) Cramer, C. J.; John Wiley & Sons Chichester: 2004.
(11) Peverati, R.; Truhlar, D. G. *J. Phys. Chem. Lett.* **2011**, *3*, 117.
(12) Marenich, A. V.; Cramer, C. J.; Truhlar, D. G. *J. Phys. Chem. B* **2009**, *113*, 6378.
(13) Tissandier, M. D.; Cowen, K. A.; Feng, W. Y.; Gundlach, E.; Cohen, M. H.; Earhart, A. D.; Coe, J. V.; Tuttle, T. R. *J. Phys. Chem. A* **1998**, *102*, 7787.
(14) Camaioni, D. M.; Schwerdtfeger, C. A. *J. Phys. Chem. A* **2005**, *109*, 10795.
(15) Kelly, C. P.; Cramer, C. J.; Truhlar, D. G. *J. Phys. Chem. B* **2006**, *110*, 16066.
(16) Bryantsev, V. S.; Diallo, M. S.; Goddard Iii, W. A. *J. Phys. Chem. B* **2008**, *112*, 9709.
(17) Cramer, C. J.; Truhlar, D. G. *Acc. Chem. Res.* **2008**, *41*, 760.
(18) Winget, P.; Cramer, C. J.; Truhlar, D. G. *Theor. Chem. Acc.* **2004**, *112*, 217.
(19) Marenich, A. V.; Ho, J.; Coote, M. L.; Cramer, C. J.; Truhlar, D. G. *Phys. Chem. Chem. Phys.* **2014**, *16*, 15068.
(20) Alperovich, I.; Smolentsev, G.; Moonshiram, D.; Jurss, J. W.; Concepcion, J. J.; Meyer, T. J.; Soldatov, A.; Pushkar, Y. *J. Am. Chem. Soc.* **2011**, *133*, 15786.
(21) Bair, R. A.; Goddard III, W. A. *Phys. Rev. B* **1980**, *22*, 2767.
(22) Kau, L. S.; Spira-Solomon, D. J.; Penner-Hahn, J. E.; Hodgson, K. O.; Solomon, E. I. *J. Am. Chem. Soc.* **1987**, *109*, 6433.
(23) Tomson, N. C.; Williams, K. D.; Dai, X.; Sproules, S.; DeBeer, S.; Warren, T. H.; Wieghardt, K. *Chem. Sci.* **2015**, *6*, 2474.

Chapter 9

General Conclusions

Herein, I highlight the general conclusions in the direction of the objectives mentioned in chapter 2, while the specific conclusions have been discussed in each chapters from 3 to 8.

Chapter 9

A new family of the ruthenium complexes containing pyridine carboxylate ligands for the water oxidation reaction have been prepared and characterized.

A series of mononuclear ruthenium complexes with one or two anionic carboxylate moieties connected to an aromatic pyridine ligands have been prepared and characterized thoroughly. The σ-donating anionic carboxylate ligand reduces the redox potential of the complexes and lower the overpotential for the water oxidation catalysis process. It has been shown that each carboxylate moiety can reduce the overpotential in the range of 200-300 mV. In addition, the different orientation of the ligand arrangement around the metal center gives different isomeric complexes with different geometric constrains on the metal center. These differences have a strong influence on the redox as well as catalytic properties of the complexes.

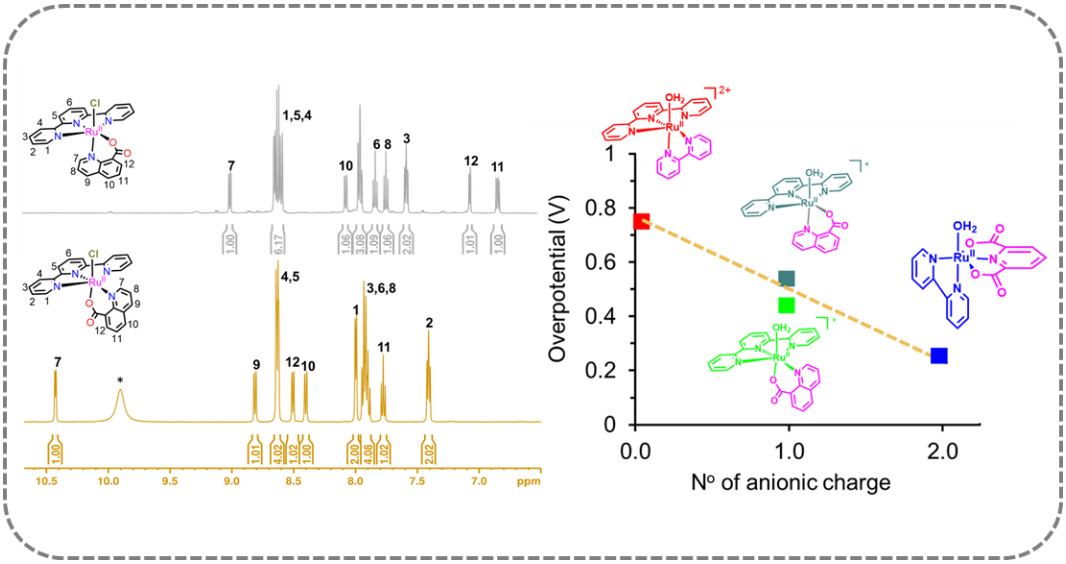

IX

Chapter 9

Seven coordinated ruthenium complex containing the pyridine dicarboxylate ligand (pdc) for the fast water oxidation catalysis.

A new ruthenium complex with tridentate meridional 2,6-pyridine-dicarboxylate (pdc) ligand has been prepared and fully characterized. This complex at high oxidation state Ru^{IV} generates a seven coordination complex (CN7) with pentagonal bipyramidal geometry. It has been shown that this complex serves as a precursor for highly active water oxidation catalyst with TOF values in the range of 2.4-3.4 × 10^3 s^{-1}. The extremely fast kinetics of the catalyst is attributed to the involvement of intramolecular H-bonding of a dangling carboxylate group with the active site of the catalyst.

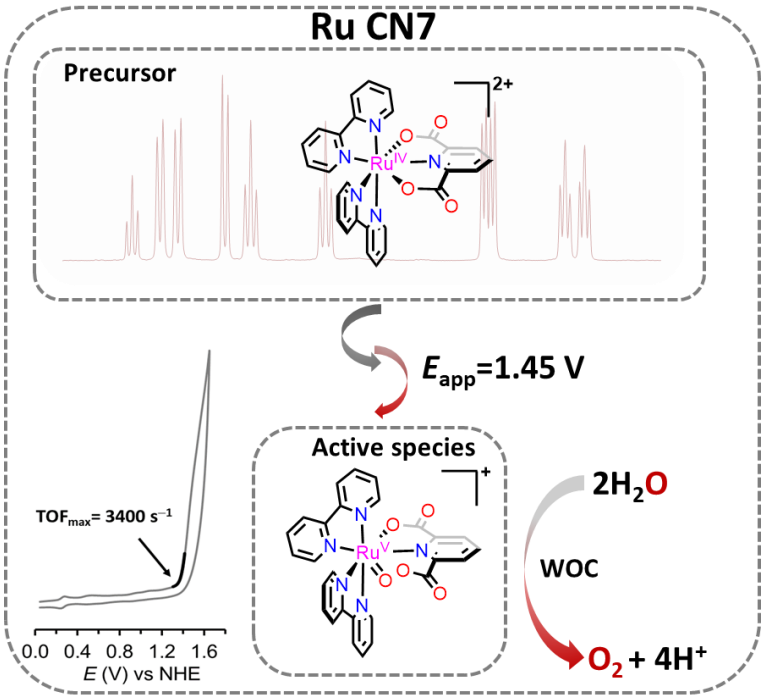

Chapter 9

Functional coordination polymers for the generation of powerful molecular electroanodes for water oxidation.

New functional coordination polymers using the [Ru(tda)(py')$_2$] (where tda = 2,2':6',2"-terpyridine-6,6"-dicarboxylate and py' = functionalized pyridine) as a core unit and 4,4´-bipyridine (4,4´-bpy) or 2,4,6-tri(pyridin-4-yl)-1,3,5-triazine (tpt) organic linkers have been prepared. Different organic linkers allowed us to synthesize polymers with different dimensions (1D or 2D). The ratio of the core unit and the organic linker together with the solvent nature play a crucial role for the chain length of the polymers. These polymers exhibit very strong adsorption on multiWall carbon nanotubes (MWCNT) with a unique CH-π interaction that allows for the high mass loading of the polymer and stability on the surface of electrodes. These hybrid materials are extremely powerful catalyst precursors for the water oxidation catalysis giving current densities in the range of 0.1-0.3 A/cm^2 and are comparable to those of commercial electrolizers. The current density provided by these materials are stable over long periods without any deactivation, thus proving the robustness of the hybrid materials and making them suitable for water splitting devices.

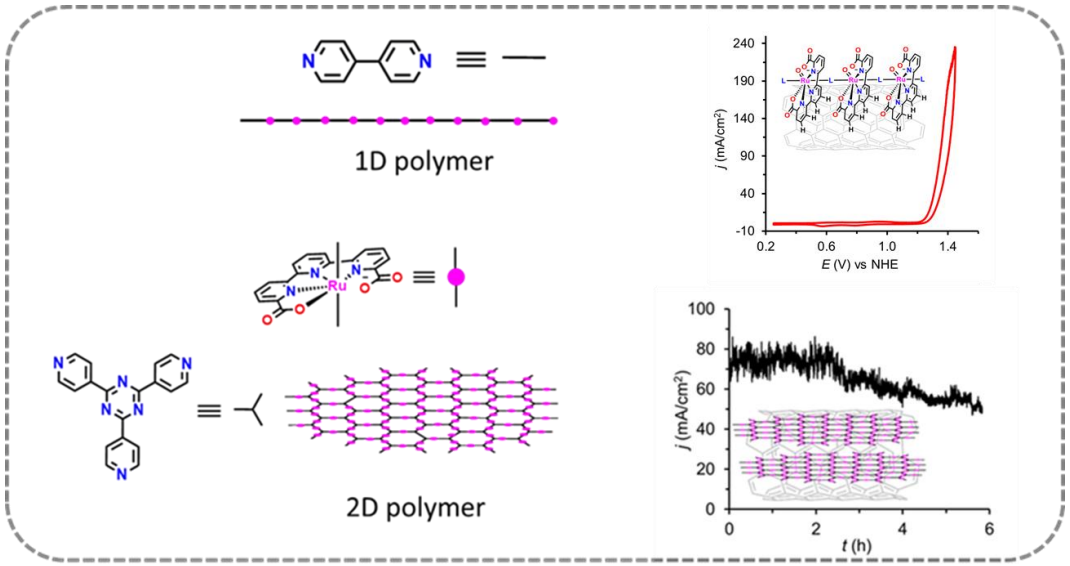

Chapter 9

Anchoring Strategies for Molecular Water Oxidation Catalysts on Solid Surfaces.

Mononuclear complexes based on the [Ru(tda)(py')(py")] catalyst have been prepared (where tda = 2,2':6',2"-terpyridine-6,6"-dicarboxylate and py'and py" = functionalized pyridine). Here the pyridine py' or py" contain a functional group that allows to attach the complex to conductive substrates via covalent bonding. For instance, carboxylate and vinyl groups have been used to attach the complex onto metal oxides, diazonium salts for C-C bonding attachment to graphitic materials or pyrazine linkages to anodized graphitic materials. Preliminary tests of the resulting electroanodes have been performed with very distinct results depending on the anchoring group and the nature of conductive support. In the case of the carboxylate linkage, the stability is very poor, showing full deattachment from the surface after few minutes in aqueous conditions. On the other hand, the covalent linkages on graphitic materials are very strong but the hydrophobicity nature of the resulting hybrid anode hinders the activation of the catalyst precursor. However, the adsorbed molecule on metal oxide surface shows the formation of active species with absence of catalytic activity, which is attributed to the deactivation of the catalyst by coordinating the dangling carboxylate group to the metal oxide surface.

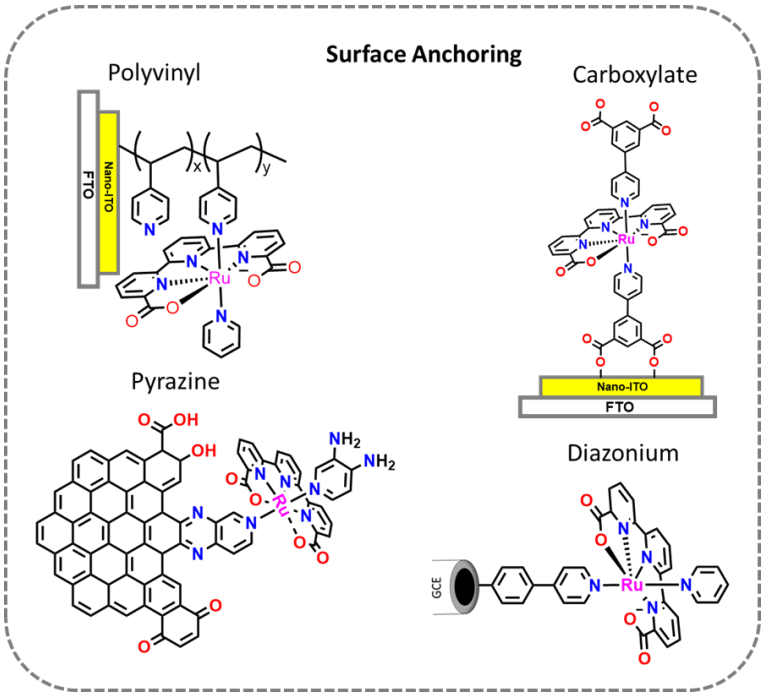

IX

Chapter 9

Mechanistic understanding and characterization of reaction intermediate species involved in the water oxidation catalytic cycle with a dinuclear cobalt complex.

Herein, the catalytic cycle of the water oxidation catalysis carried out by $\{[Co^{III}(trpy)]_2(\mu\text{-}bpp)(\mu\text{-}OO)\}^{3+}$ (where trpy = 2,2';6':2''-terpyridine and bpp^- = bis(2-pyridyl)-3,5-pyrazolate) has been studied in detail. The first one electron oxidation of the initial Co^{III}-O-O-Co^{III} complex occurs at the peroxo ligand and generates a side on superoxo intermediate species that rearranges to produce an end-on superoxo species in the catalytic cycle. These intermediates have been characterized by resonance Raman, electron paramagnetic resonance (EPR) and X-ray absorption (XAS) spectroscopies and complemented with Density Functional Theory (DFT). In addition, O_2 labelling experiments have proved that the produced O_2 in first turnover number is originated from the catalyst and beyond that O_2 is resulted from the oxidation of the water substrate.

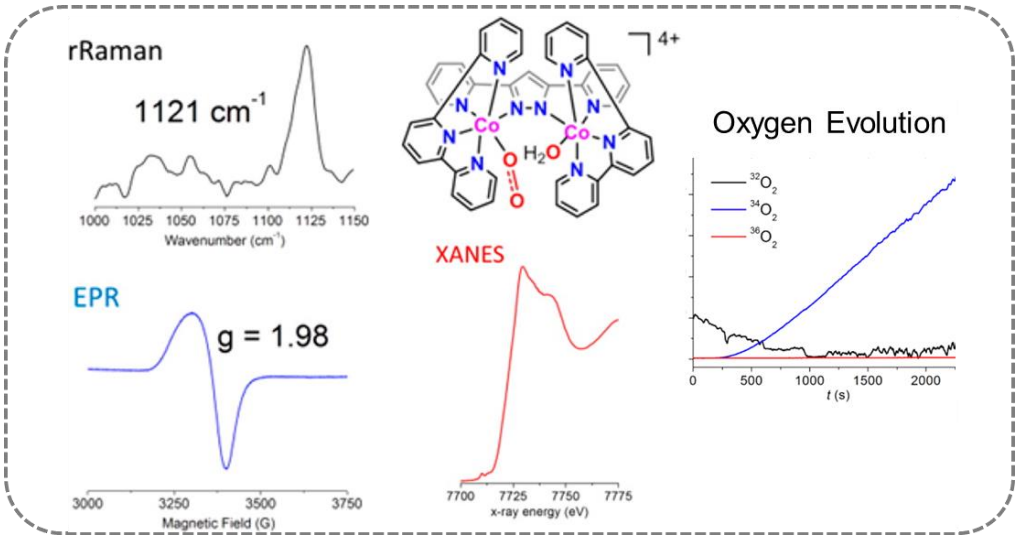

IX


ICIQ
Institut
Català
d'Investigació
Química


UNIVERSITAT
ROVIRA i VIRGILI